Stephan Baer Klaus Ensslin

Transport Spectroscopy of Confined Fractional Quantum Hall Systems



Springer Series in Solid-State Sciences

Volume 183

Series editors

Bernhard Keimer, Stuttgart, Germany Roberto Merlin, Ann Arbor, MI, USA Hans-Joachim Queisser, Stuttgart, Germany Klaus von Klitzing, Stuttgart, Germany The Springer Series in Solid-State Sciences consists of fundamental scientific books prepared by leading researchers in the field. They strive to communicate, in a systematic and comprehensive way, the basic principles as well as new developments in theoretical and experimental solid-state physics.

More information about this series at http://www.springer.com/series/682

Transport Spectroscopy of Confined Fractional Quantum Hall Systems



Stephan Baer Solid State Physics Laboratory ETH Zürich Zürich Switzerland Klaus Ensslin Solid State Physics Laboratory ETH Zürich Zürich Switzerland

ISSN 0171-1873 ISSN 2197-4179 (electronic) Springer Series in Solid-State Sciences ISBN 978-3-319-21050-6 ISBN 978-3-319-21051-3 (eBook) DOI 10.1007/978-3-319-21051-3

Library of Congress Control Number: 2015944176

Springer Cham Heidelberg New York Dordrecht London

© Springer International Publishing Switzerland 2015

This work is subject to copyright. All rights are reserved by the Publisher, whether the whole or part of the material is concerned, specifically the rights of translation, reprinting, reuse of illustrations, recitation, broadcasting, reproduction on microfilms or in any other physical way, and transmission or information storage and retrieval, electronic adaptation, computer software, or by similar or dissimilar methodology now known or hereafter developed.

The use of general descriptive names, registered names, trademarks, service marks, etc. in this publication does not imply, even in the absence of a specific statement, that such names are exempt from the relevant protective laws and regulations and therefore free for general use.

The publisher, the authors and the editors are safe to assume that the advice and information in this book are believed to be true and accurate at the date of publication. Neither the publisher nor the authors or the editors give a warranty, express or implied, with respect to the material contained herein or for any errors or omissions that may have been made.

Printed on acid-free paper

Springer International Publishing AG Switzerland is part of Springer Science+Business Media (www.springer.com)

Preface

At very low temperatures and at certain filling factors ν , the ground state of a high mobility electron gas exposed to a strong magnetic field becomes incompressible, forming an integer quantum Hall (IQH) or fractional quantum Hall (FQH) state. The $\nu=5/2$ state is one of the most exceptional of these states, as it is believed to exhibit non-Abelian quasiparticle excitations. This property makes it not only interesting from a fundamental physics point of view, but also for possible applications in topological quantum computing.

In this book, we investigate the properties of the IQH and FQH states, using transport measurements in the bulk, in quantum point contacts (QPCs) and through quantum dots (QDs) or interferometers implemented in high mobility GaAs samples. One important goal of the work presented in this book has been to study the properties of the $\nu=5/2$ state by investigating its tunneling and confinement properties and to make progress towards the realization of an experiment that allows to probe the statistics of the quasiparticle excitations at $\nu=5/2$.

This book gives an insight into the work on the $\nu=5/2$ state that has been conducted at ETH Zürich in a collaboration of the groups of Werner Wegscheider and Klaus Ensslin, since 2010. The book is based on a dissertation written by Stephan Baer in the group of Klaus Ensslin [1].

This book provides an overview of recent developments in experiments probing the fractional quantum Hall (FQH) states of the second Landau level, especially the $\nu=5/2$ state. It summarizes the state-of-the-art understanding of these FQH states. It furthermore describes how the properties of the FQH states can be probed experimentally, by investigating tunneling and confinement properties. The progress towards the realization of an experiment, allowing to probe the potentially non-Abelian statistics of the quasiparticle excitations at $\nu=5/2$ is discussed. The book is intended as a reference for graduate students and postdocs starting in the field. The experimental part of this book gives practical advice for solving the experimental challenges which are faced by researchers studying highly fragile FQH states.

We thank the following colleagues for their contribution to this work or for discussions: Clemens Rössler, Thomas Ihn, Szymon Hennel, Werner Wegscheider,

vi Preface

Christian Reichl, Anastasia Varlet, Tobias Krähenmann, Ernst de Wiljes, Per-Lennart Ardelt, Thomas Hasler, Hiske Overweg, Sebastian Butz, Dominic Blosser, Bernd Rosenow, Rudolf Morf, Lars Tiemann and many others.

Zürich July 2015 Stephan Baer Klaus Ensslin

Reference

 S. Baer, Transport spectroscopy of confined fractional quantum Hall systems, Ph.D. thesis, ETH Zürich, Zürich, 2014. http://dx.doi.org/10.3929/ethz-a-010252603

Contents

Pai	.4 T]	Fundame	entals of Quantum Hall Physics	
1 ai			vant Experiments	
2	Two	-Dimens	ional Electron Gases	
	2.1	Introdu	action	
	2.2	Basic 1	Properties of Two-Dimensional Electron Gases	1
	2.3		field Magnetoresistance of Two-Dimensional	
			on Gases	1
	2.4		h Schemes for High Electron Mobilities]
	2.5	-	of Disorder on the Gap of the $\nu = 5/2$ State]
	Refe	erences		2
3	The		m Hall Effect	2
	3.1	Introdu	action	2
	3.2		Spectrum in a Magnetic Field	2
	3.3		ikov-De Haas Effect	2
	3.4		Quantum Hall Effect	2
		3.4.1	Landauer-Büttiker Formalism	2
		3.4.2	. 3	
			Landau Level	2
	3.5	Fractio	onal Quantum Hall Effect	2
		3.5.1	Laughlin's Wavefunction	3
		3.5.2	Composite Fermion Theory	3
	3.6		onal Quantum Hall Effect in the Second	
		Landau	ı Level	3
		3.6.1	Candidate States for $\nu = 5/2$	3
		3.6.2	Candidate States for $v = 7/3$ and $v = 8/3 \dots$	3

viii Contents

		3.6.3 Candidate States for $\nu = 12/5 \dots \dots \dots$	41			
	3.7	Conclusion	43			
	Refe	rences	43			
4	Physics at the Edge					
	4.1	Introduction	47			
	4.2	Spatial Edge State Picture	47			
		4.2.1 Self-consistency at the Edge	48			
		4.2.2 FQH Edge States	50			
	4.3	Energetic Edge State Picture	5:			
		4.3.1 Hydrodynamic Theory	5:			
		4.3.2 Hierarchical States and Bulk-Edge Correspondence	5			
		4.3.3 Tunneling in a QPC	5			
	Refe	rences	6			
5	Non-	-Abelian Statistics and Its Signatures in Interference				
		eriments	6			
	5.1	From Fermions to Anyons	6.			
	5.2	Non-Abelian Anyons in the Moore-Read Pfaffian State	6			
	5.3	Interferometry with Non-Abelian Anyons	6			
	5.4	Aharonov-Bohm Versus Coulomb-Dominated Physics	6			
	Refe	rences	7			
6	Ove	rview of Experiments Probing the Properties				
•		we $\nu = 5/2$ State	7.			
	6.1	Introduction	73			
	6.2	Numerical Studies	74			
	6.3	Detecting the Quasiparticle Charge	7:			
		6.3.1 Shot Noise Measurements	7			
		6.3.2 Local Compressibility Measurements	7			
	6.4	Bulk Experiments: Probing the Spin Polarization	7			
		6.4.1 Transport: Density Dependence of the Gap	7			
		6.4.2 Transport: In-Plane Magnetic Fields	7			
		6.4.3 Optics	8			
		6.4.4 Nuclear Magnetic Resonance Techniques	8			
		6.4.5 Conclusion	82			
	6.5	Probing the Edge Properties	82			
		6.5.1 Quasiparticle Tunneling	82			
		6.5.2 Neutral Mode Experiments	84			
	6.6	Interference Experiments at $\nu = 5/2$	80			
	6.7	Summary	90			
		rancas	o.			

Contents ix

Part 1	T S	etun s	and	Sample	Optimiza	ition
ı aıı ı	u o	Եւսբ Շ	mu ı	Sample	Opunnza	uou

7	Measurement Setup Optimization for Low Electron						
		peratures	97				
	7.1	Introduction	97				
	7.2	Dilution Refrigerator Setup	98				
		7.2.1 Vibration Minimization and Insulation	101				
		7.2.2 Electronic Noise	106				
	7.3	Cryostat Cabling and Cold Filtering	108				
		7.3.1 General Remarks	108				
		7.3.2 Thermocoax Cables	111				
		7.3.3 π -Filters	111				
		7.3.4 Quartz Heat Sinks	112				
		7.3.5 RC Low-Pass Filters	113				
		7.3.6 Silver Cold-Finger	113				
		7.3.7 Filter Attenuation	115				
	7.4	Estimation of the Electronic Temperature	117				
	7.5	Outlook	120				
	7.6	Conclusion	121				
	Refe	rences	121				
8	Opti	imization of Samples and Sample Fabrication	123				
	8.1	Introduction	123				
	8.2	Non-invasive Processing	123				
	8.3	Mesa and Contact Geometry	125				
	8.4	Ohmic Contacts and Contact Resistance	127				
	8.5	Conclusion	129				
	Refe	rences	129				
n.	4 777	O A B'AGAAF					
Pal	rt III	Quantum Point Contact Experiments					
9	Oua	ntum Point Contacts	133				
	9.1	Introduction	133				
	9.2	Conductance of Ideal and Non-ideal QPCs	135				
		9.2.1 Transmission of an Ideal Quantum Wire	135				
		9.2.2 Non-ideal QPC	137				
		9.2.3 Saddle-Point Potential	138				
		9.2.4 Magneto-Electric Depopulation.	139				
	9.3	QPC Simulations	139				
	9.4	Transport Properties of Clean QPCs	142				
	⊅. 4	9.4.1 Lateral Shifting of the QPC Channel	142				
		9.4.2 Finite Bias Transmission	142				
		9.4.2 Fillite Dids Hallshillssion	143				

x Contents

		9.4.4	Spin-Resolved Transport	151
		9.4.5	Bias Dependence in the Quantum Hall Regime	153
	9.5	Conclu	sion	155
	Refer	ences		156
10	Integ		Fractional Quantum Hall States in QPCs	159
	10.1	Introdu	ction	159
	10.2	Experir	mental Details	161
	10.3	Results	and Discussion	162
		10.3.1	Quantum Hall Phase Diagram of a QPC	162
		10.3.2	Influence of QPC Geometry on Incompressible	
			Separating Region and Density Distribution	165
		10.3.3	Characterization of QPC Resonances	
			and Microscopic Model	167
		10.3.4	Spatial Dependence of QPC Resonances	174
		10.3.5	Fragile Fractional Quantum Hall States in QPCs	177
		10.3.6	Energy Gap of the $v_{QPC} = 1/3$ State	180
	10.4	Conclu	sion	183
	Refer	ences		184
11	Quas	iparticle	Tunneling in the Second Landau Level	187
	11.1	Introdu	ction	187
	11.2	Experir	mental Details	189
	11.3	Measur	rement Results	189
		11.3.1	Tunneling Conductance at $v = 5/2$	191
		11.3.2	Tunneling Conductance at $\nu = 8/3$	195
		11.3.3	Effect of Varying the Coupling via	100
		1101	the Magnetic Field	198
		11.3.4	Effect of Varying the Coupling via	200
		1105	the QPC Transmission	200
		11.3.5	Breakdown of the Weak Tunneling Regime	201
	11.4		etation and Discussion	202
		11.4.1	$v = 8/3 \dots \dots$	202
		11.4.2	$v = 5/2 \dots \dots$	203
		11.4.3	$\nu = 7/3$	204
		11.4.4	Experimental Limitations and Origin of Systematic Errors	205
	11.5	Conclu		206
				207
	· ·ppc		I of Tunneling Peaks	207
			Proposed Parameter Pairs— $\nu = 5/2$	207
			Proposed Parameter Pairs— $\nu = 3/2$	208
			onal Fits— V_{OPC} Dependence	209
	Refer	ences	•	215

Contents xi

Par	t IV	Quantum Dot and Interferometer Experiments	
12	Ouar	ntum Dots and Charge Detection Techniques	221
	12.1	Introduction	221
	12.2	Basics of Quantum Dots	222
		12.2.1 Energy Scales	222
		12.2.2 Coulomb Blockade	223
		12.2.3 Principle of Charge Detection	225
	12.3	Improving the Charge Detection Sensitivity	226
	12.4	Conclusion	230
	Refer	rences	231
13	Quar	ntum Dots in the Quantum Hall Regime	233
	13.1	Introduction	233
	13.2	Experimental Details	234
	13.3	Results and Discussion	235
		13.3.1 Zero Magnetic Field Transport	235
		13.3.2 Non-cyclic Depopulation of Edge Channels	235
		13.3.3 Transport in the Fabry-Pérot Regime	243
	13.4	Conclusion	245
	Refer	rences	245
14	Preli	minary Results of Interference Experiments	
		e Second Landau Level	247
	14.1	Introduction	247
	14.2	Design Considerations	248
	14.3	Transport Measurements	250
		14.3.1 Sample Stability Issues	251
		14.3.2 Optimizing the Transmission by Sample	
		Illumination	253
	14.4	Conclusion and Outlook	261
		rences.	261
Par	t V	Bulk Transport Experiments	
15		equilibrium Transport in Density Modulated Phases	
	of th	e Second Landau Level	265
	15.1	Introduction	265
	15.2	Experimental Details	266
	15.3	Results and Discussion	267
		15.3.1 Phase Diagram of Reentrant Integer Quantum	
		Hall Phases	260

xii Contents

	15.3.2	Transition from RIQH Phase to Isotropic		
		Compressible Phase	271	
	15.3.3	Discussion of the Bias Dependence	274	
	15.3.4	Reentrant Integer Quantum Hall Phases in a QPC	276	
	15.3.5	Orientation Dependence	278	
15.4	Conclu	sion	279	
Apper	ndix		280	
	Depend	lence on Magnetic Field Direction	280	
	Hystere	esis of Current Sweeps	280	
	Negativ	ve Differential Resistance from DC Measurement	280	
	Bias Do	ependence of the Longitudinal Resistance	281	
Refere	ences		283	
Part VI	Conclus	ion		
16 Concl	usion		289	
Appendices				
Index			305	

Symbols and Abbreviations

Physical Constants

 $\begin{array}{lll} a_{\rm B} & {\rm Bohr\ radius} \\ -e < 0 & {\rm Electron\ charge} \\ \varepsilon & {\rm Dielectric\ permittivity} \\ \varepsilon_o & {\rm Vacuum\ dielectric\ constant} \\ h = 2\pi\hbar & {\rm Planck's\ constant} \\ k_{\rm B} & {\rm Boltzmann\ constant} \\ \mu_{\rm B} & {\rm Bohr\ magneton} \\ R_{\rm K} = h/e^2 & {\rm Von\ Klitzing\ constant} \end{array}$

Symbols

System size (length, width) L,W В Magnetic field \vec{A} Vector potential $E_{\mathbf{C}}$ Constant interaction energy Gate lever arm $\alpha_{
m G}$ Spin degenerate single particle level spacing Δ_N $E_{\rm F}$ Fermi energy QCharge Ι Current VVoltage GConductance Resistance ρ Fermi velocity $v_{\rm F}$ Fermi wavenumber $k_{\rm F}$ $\lambda_{\rm F}$ Fermi wavelength Magnetic length l_B Elastic mean free path l_e

 au_{tr} Transport scattering time

 τ_q Quantum life time

 m^* Effective electron mass in GaAs

 μ Electron mobility n_s Electron sheet density

u Filling factor u_{QPC} QPC filling factor u_{bulk} Bulk filling factor ω_c Cyclotron frequency u_c Cyclotron radius

 ω_y, ω_x Confinement strength of a harmonic potential

 r_s Interaction parameter g^* Effective g-factor T Temperature

Abbreviations

2DEG Two-dimensional electron gas

AC Alternating current

AFM Atomic force microscope

CB Coulomb blockade
CF Composite Fermion
DC Direct current
DOS Density of states

ES Excited state

FIRST Frontiers in research, space and time (Cleanroom at ETH Zürich)

FQH(E) Fractional quantum Hall (effect) FWHM Full width at half maximum

GS Ground state

IQH(E) Integer quantum Hall (effect)

LL Landau level

MBE Molecular beam epitaxy

QD Quantum dot

QPC Quantum point contact

RIQH(E) Reentrant integer quantum Hall (effect)

SdH Shubnikov de Haas

Chapter 1 Introduction

This work contains many things which are new and interesting. Unfortunately, everything that is new is not interesting, and everything which is interesting, is not new.

Lev Landau, not in reference to this book

Motivation

Some of the most intriguing physical phenomena, like superconductivity, superfluidity or Bose-Einstein condensation, are many-body effects. Here the interaction of the particles that constitute the physical system can change the system's behavior dramatically. Many of these effects have been discovered unintentionally in experiments which were conducted for example at very low temperatures and in very pure or very regular systems. Under such conditions, interaction effects that otherwise do not play a role and which often were not anticipated, become relevant.

Two-dimensional electron gases (2DEGs) are the ideal system for the experimentalist studying many-body effects in solid state physics. These systems are exceptionally pure and can be cooled to temperatures below 10 mK with state-of-the-art experimental setups. The fractional quantum Hall (FQH) effect is a many-body effect that has been discovered under these conditions. Electrons in a two-dimensional system exposed to a strong magnetic field interact with each other via the Coulomb interaction. It turns out that under certain conditions electrons form a collective ground state, described by a many-body wavefunction proposed by Laughlin [1]. The interacting electrons in this state can be understood as new quasiparticles, socalled composite Fermions [2]. In this description, they are only weakly interacting and have different physical properties than the original electrons. For example, the charge of the quasiparticles no longer corresponds to the original electron charge, but is only a fraction of it. Another far-reaching consequence of the correlations in a two-dimensional system is that composite particles do not behave as Fermions or Bosons. While a particle exchange of Fermions or Bosons changes the phase of the wavefunction by 0 or π , it can be any value for the quasiparticles of the fractional quantum Hall effect, making them "anyons".

2 1 Introduction

With the chase for new physics, samples have been further improved, revealing new interesting phenomena. One of the most remarkable subsequent discoveries was the $\nu = 5/2$ state [3], which could no longer be understood in the framework developed for the ordinary FOH effect. A possible explanation for this groundstate suggests a BCS-like p-wave pairing of composite Fermions [4]. However, alternative less exciting explanations exist (see Sect. 3.6). The p-wave paired Moore-Read Pfaffian groundstate would possess another property, which has tremendously increased the interest in the $\nu = 5/2$ state: it is believed to exhibit non-Abelian anyonic excitations. In a very simplified picture, this can be understood in the following way [5]: given an ensemble of N quasiparticles, an exchange of two quasiparticles transforms the total wavefunction to a different final state. The system is said to be non-Abelian, if performing exactly the same exchange operations in a different sequence leads to a different final state. By exchanging quasiparticles in a particular sequence, this might allow to apply a desired unitary transformation to the wavefunction, which could for example be used for quantum computation. Here, the exact trajectories on which the quasiparticles are exchanged are irrelevant and the system is protected from decoherence. Such a system is said to be "topologically protected".

Though numerical and first experimental results favor the non-Abelian candidates for ν =5/2, the definite proof is still missing. Also the nature of most of the other FQH states in the second Landau level (LL), like the ν =7/3 and ν =8/3 FQH states is not fully clarified yet. Given the large theoretical effort that is invested to explore the potential properties of these states, answering the open questions is one of the most important experimental tasks in the quantum Hall research community.

However, even without non-Abelian statistics, the FQH states in the second LL contain interesting many-body physics and are worth studying. The physics in the second Landau level is not only influenced by FQH states, but also by electron crystal phases which compete with the FQH states. The properties of those states are still largely unexplored and require further experimental study.

Impact of this work and outlook

An important goal of the experiments presented in this book was to investigate the properties of the FQH states in the second LL, especially the $\nu = 5/2$ state. Our work intends to advance towards the realization of an interference experiment that clarifies the nature of the $\nu = 5/2$ state and its potential suitability for quantum computing.

This book is the result of the first Ph.D. project conducted on the ν =5/2 state in the Ensslin group at ETH Zürich by Stephan Baer. Hence we describe the experimental tasks, necessary for starting this project. For example, it was necessary to improve a dry dilution refrigerator setup for low electronic temperatures and a new low temperature cabling, filtering setup and silver cold finger had to be designed and built. Furthermore the sample processing had to be carefully checked and optimized, in order to avoid a degradation of the quality of the 2DEGs. Due to a close collaboration with the Wegscheider group, we could identify and characterize wafers that exhibit a pronounced ν =5/2 state and which were suitable for the experiments conducted by us. By accomplishing these tasks we were finally able to observe the most fragile FQH states and could reach an electronic temperature of approximately

1 Introduction 3

12–13 mK at a cryostat temperature of approximately 9–10 mK. Compared to the best electronic temperatures of around 50 mK that have been reached in the Ensslin group before, this is a large improvement. This preliminary work paves the way for future FQH experiments at very low temperatures in the Ensslin group. Starting from the prototype cabling and filtering employed by us, cold filtering techniques have been further improved. In the Ensslin group's new cryostat with a base temperature of less than 3.5 mK, these developments might allow the study of even more fragile FQH states, like for example the $\nu = 12/5$ state.

Quantum point contacts (QPCs) allow a local manipulation of FQH states and are a basic building block for interferometers that try to investigate the ν =5/2 state. We have investigated the transport properties of QPCs fabricated on high-mobility electron gases. Finite-bias measurements have allowed us to investigate the confinement potential and its influence on the QPC transmission in magnetic fields. Here correlation effects show up in the transport. They arise from an interplay of the FQH states with localized states, which are described by single- or many-electron physics. In the FQH regime, disorder has a large influence on the transmission and we observe effects related to the localization of fractionally charged quasiparticles in the constriction. We have investigated the transmission properties of QPCs, which is necessary in order to be able to correctly interpret tunneling and interferometer experiments using QPCs, especially at ν =5/2.

Gating high-mobility 2DEGs is experimentally challenging and requires optimizing the gating procedure to the doping scheme of the heterostructure. By doing this, we succeeded to define QPCs, with a perfect transmission of the ν =5/2 state. We have demonstrated that this state can survive fully gapped in a top-gate defined interferometer, with an energy gap exceeding 200 mK. This is a crucial prerequisite for interference experiments at this filling factor. To our knowledge, this has not been clearly demonstrated before.

Using the gating techniques, we were able to define a QPC in a weak backscattering regime, where quasiparticle tunneling in the FQH states at $\nu = 5/2$, 7/3 and 8/3 could be observed. Previous experiments were only conducted with a single sample and were not fully conclusive regarding the question whether the tunneling properties at $\nu = 5/2$ favor an Abelian (3,3,1)-state or the non-Abelian Anti-Pfaffian or SU(2)₂states. Hence, repeating those experiments with a different sample, fabricated with a different growth technique was desirable. Furthermore, a correct interpretation of the experiment in terms of the weak tunneling theory might depend sensitively on the experimental situation, like the backscattering strength and the local filling factor. We have addressed these open questions in detail and found that the Abelian (3,3,1)- and (1,1,3)-states describe our data best. Though this result is for example inconsistent with numerical findings, the quality of agreement of our data and theoretical predictions for the (3,3,1)- and (1,1,3)-states is astonishing. The nature of the $\nu = 8/3$ and 7/3 states is not fully clear and non-Abelian candidate states have also been proposed here. We present the first systematic investigation of these states in a tunneling experiment. We find that the $\nu = 8/3$ state is best described by a particle-hole conjugate Laughlin state. This finding is not only relevant for $\nu = 8/3$, but is also an important crosscheck for the tunneling experiments that have investigated the $\nu = 5/2$ state. Our 4 1 Introduction

quasiparticle tunneling experiments will be supplemented by further experiments at $\nu = 1/3$ and $\nu = 2/3$, which are currently being performed in the Ensslin group. These studies might reveal whether additional interaction effects which have not been taken into account in the theory modify the quasiparticle tunneling signatures.

In addition to the OPC measurements, we have performed transport measurements of large quantum dots and interferometers in magnetic fields. We have optimized charge detection techniques, which allow a time-resolved single-electron charge detection on micron-sized quantum dots, which are suitable for interference experiments in the quantum Hall regime. In order to perform charge detection on such large QDs, the sensitivity had to be greatly enhanced. We have shown how this can be accomplished using localized states. These optimized charge detection techniques might be employed in the future to study the behavior of Coulomb dominated Fabry-Pérot interferometers in the FQH regime. Here, (time-resolved) charge detection techniques might allow to study quasiparticle charges and the inner structure of edge states, which are only accessible by direct transport in very special cases. Subsequently, we have investigated such a special case: here, the transport properties of a single QD were modified due to the presence of different compressible and incompressible regions in the dot. The transport behavior of the system could be described in analogy to the physics of a double quantum dot. Our results show that the inner structure of a QD can strongly influence the charging spectrum, which is relevant for Coulomb blockade experiments trying to investigate the statistics of the $\nu = 5/2$ edge excitations. Finally, transport in top-gate defined interferometers has been investigated. Here we have used different high-mobility 2DEGs that employ different doping techniques. We have investigated the experimental problems that arise, for example due to the lack of stability of the structures. We have demonstrated how a fully gapped $\nu = 5/2$ state can be confined in a top-gate defined interferometer without destroying the quantization, by careful choice of the 2DEG in combination with gating and illumination techniques. This is one of the experimentally most challenging prerequisites for the implementation of an interference experiment at $\nu = 5/2$ and has to our knowledge not yet been clearly demonstrated in literature. Unfortunately, no interference could be found at $\nu = 5/2$. This was mainly attributed to an inappropriate QPC geometry. Implementing an optimized interferometer geometry with the techniques described by us, might in the future allow interference experiments at $\nu = 5/2$.

The physics of the second LL is not only influenced by FQH states, but also by density modulated phases corresponding to the reentrant integer quantum Hall (RIQH) effect. A better understanding of the density-modulated phases might also improve our understanding of the physics of the second Landau level as a whole. Hence we have investigated the RIQH phases in non-equilibrium transport. Due to their extreme fragility and high requirements to the sample quality, only few research groups were able to investigate those states. Because of this, many properties of these phases are still unknown and are still under experimental study. Our results suggest that either these phases are not electron-hole symmetric as expected from theory or that they possibly are of a more complicated nature than anticipated. As these phases

1 Introduction 5

reside in the same LL as the ν = 5/2 state, such a particle-hole asymmetry might be of relevance for the physics at ν = 5/2 and the groundstate that is formed at this filling factor

Organization of this book

This book is structured in five parts:

Part I gives an introduction to two-dimensional electron gases, the quantum Hall effect and edge states. We discuss the possibility of non-Abelian statistics and how this could be probed with interference experiments. Finally, we give a short overview of experiments at $\nu = 5/2$ by other authors and discuss their relevance for our results and whether they are compatible with our findings.

Part II describes how the measurement setup and samples were optimized, which in the end allowed us to perform experiments with the most fragile FQH states.

Part III discusses the QPC experiments: we start with investigating transport at zero magnetic field and the QPC confinement potential. Then we turn to the question of the magnetic field transmission of QPCs and how to observe a $\nu = 5/2$ state in a QPC. Finally, we discuss the quasiparticle tunneling experiments in the second LL.

Part IV shows the results of quantum dot and interferometer experiments. After a discussion of how charge detection techniques can be pushed towards the technical limit, we investigate a quantum dot, where the transport properties are strongly modified due to the presence of compressible and incompressible regions inside the dot. Then we discuss progress towards an interference experiment at $\nu = 5/2$.

Part V summarizes the non-equilibrium transport measurements in the reentrant integer quantum Hall phases of the second Landau level.

References

- 1. R.B. Laughlin, Phys. Rev. Lett. 50, 1395 (1983). doi:10.1103/PhysRevLett.50.1395
- 2. J.K. Jain, *Composite Fermions* (Cambridge University Press, Cambridge, 2007)
- 3. R. Willett, J.P. Eisenstein, H.L. Störmer, D.C. Tsui, A.C. Gossard, J.H. English, Phys. Rev. Lett. 59, 1776 (1987). doi:10.1103/PhysRevLett.59.1776
- 4. G. Moore, N. Read, Nucl. Phys. B 360, 362 (1991). doi:10.1016/0550-3213(91)90407-O
- 5. S.D. Sarma, M. Freedman, C. Nayak, Phys. Today 59, 32 (2006). doi:10.1063/1.2337825

Part I Fundamentals of Quantum Hall Physics and Relevant Experiments

Chapter 2 Two-Dimensional Electron Gases

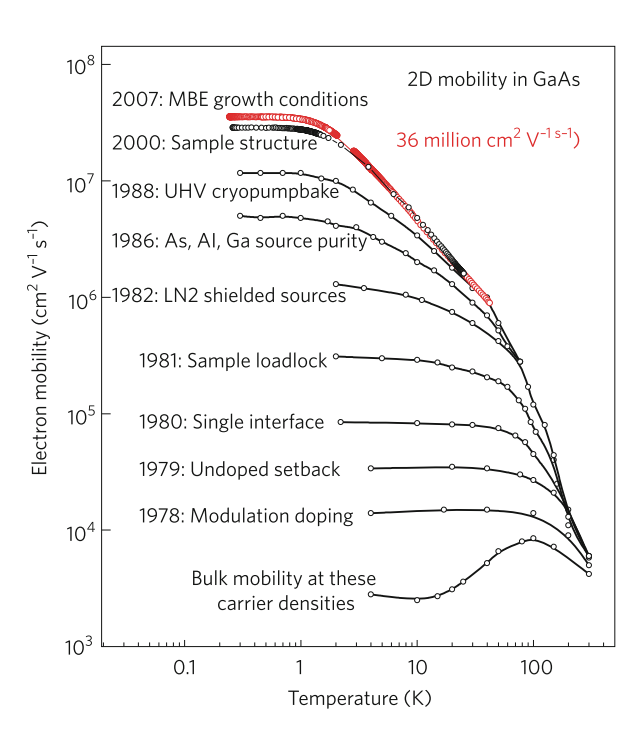
Abstract We review the basic low magnetic field properties of two-dimensional electron gases (2DEGs). The influence of growth techniques on the observation of the most fragile fractional quantum Hall states is discussed.

2.1 Introduction

Two-dimensional electron gases (2DEGs) in Gallium Arsenide (GaAs) represent the cleanest solid state system that is accessible to experimentalists. Continuous technological progress in molecular beam epitaxy (MBE) growth (Fig. 2.1), has allowed fabricating 2DEGs of higher and higher mobilities. In these systems new single- and many-body quantum phenomena, like the integer quantum Hall (IQH) effect and the fractional quantum Hall (FQH) effect, have been discovered. The Nobel prizes of 1985 (Klaus von Klitzing) and 1998 (Robert B. Laughlin, Horst L. Störmer and Daniel C. Tsui) attest the great importance of these discoveries and the large interest they have raised, not only in the solid state physics community.

More recent discoveries, like the exotic fractional quantum Hall (FQH) states at $\nu=5/2$ and $\nu=12/5$ show that still many interesting many-body phenomena remain to be studied in these systems. In the following, we will shortly review the basic properties and characteristics of 2DEGs. We will quickly discuss the sophisticated growth techniques that make the observation of exotic FQH states possible and hence provide the foundation for the experiments described in this book. Furthermore, these techniques have a large influence on the gating properties of top-gated structures, which is of great relevance for the experiments discussed later in this book.

Fig. 2.1 Electron mobilities versus temperature for state-of-the-art GaAs 2DEGs grown in different years. The main lever for the mobility improvement is indicated for each *curve*. The best currently available 2DEGs reach mobilities of more than 30 million cm²/Vs (Taken from [1]. Reprinted by permission from Macmillan Publishers Ltd)



2.2 Basic Properties of Two-Dimensional Electron Gases

The growth of two-dimensional AlGaAs/GaAs heterostructures relies on the combination of layers of GaAs with layers of the ternary compound $Al_xGa_{1-x}As$. GaAs and AlAs have a small lattice mismatch of only 0.14% [2], but different band gaps $E_{\rm g}$ ($E_{\rm g}$ = 1.424 eV for GaAs and $E_{\rm g}$ = 2.168 eV for AlAs [3]). Thus GaAs and $Al_xGa_{1-x}As$ layers can be combined without creating significant strain, but creating large discontinuities in the conduction band edge energy $E_{\rm CB}$. Figure 2.2 illustrates how this technique is used to specifically engineer the conduction band edge, in order to create a two-dimensional electron gas. Figure 2.2a shows a layer sequence of a single-side doped heterostucture. A conduction band energy, obtained from numerically solving Poisson and Schrödinger equations self-consistently, is shown on the right hand side (Fig. 2.2b) as a function of the reversed growth direction z. The surface of the heterostructure is capped by a thin layer of GaAs to prevent oxidation. The conduction band bottom at the surface is raised due to surface reconstruction or due to a Schottky barrier with a metallic top-gate and is far above the Fermi energy $E_{\rm F} = 0$. Below the GaAs cap, a thick layer of Al_{0.24}Ga_{0.76}As is grown, which leads to a discontinuity of the conduction band energy at the interface between these two materials. At z = 250 nm, the conduction band energy is pinned close to the Fermi energy due to strong local doping with silicon (Si). At z > 320 nm, another wide region of GaAs has been grown. Due to the pinning of the conduction band edge at

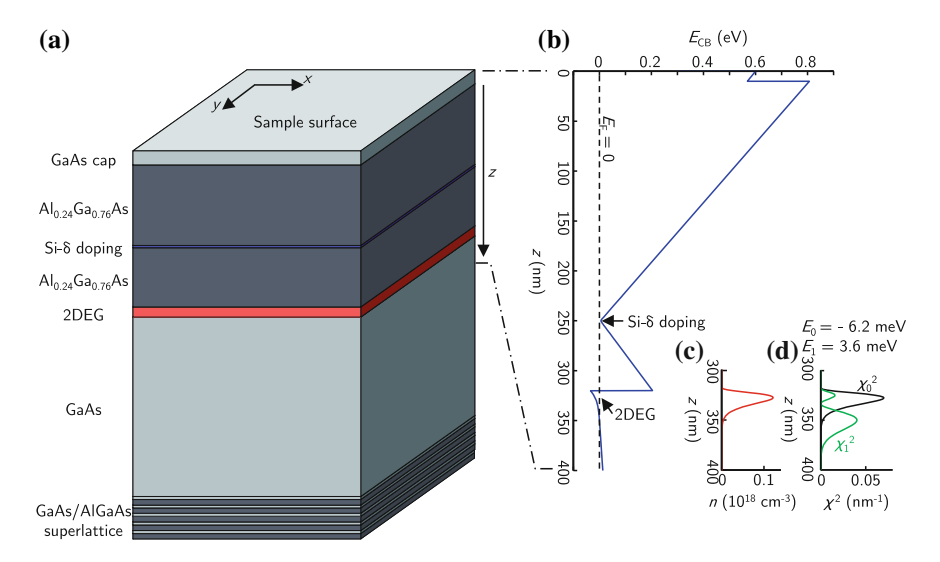


Fig. 2.2 a Layer structure of a single-side doped high-mobility heterostructure. The conduction band edge, obtained from a numerical self-consistent solution of Poisson and Schrödinger equations is shown in (b). The electron densities and *square* of the electronic wavefunctions of the two lowest subbands are shown in $\bf c$ and $\bf d$ as a function of z. Here, only the lowest subband has a negative eigenenergy and is occupied

the doping plane and due to the discontinuity of the conduction band at $z=320\,\mathrm{nm}$, the conduction band edge is pulled below the Fermi energy at the interface between $\mathrm{Al}_x\mathrm{Ga}_{1-x}\mathrm{As}$ and $\mathrm{Ga}\mathrm{As}$. Here, free states in the conduction band are filled by electrons up to the Fermi energy, leading to a finite electron density close to the interface. The calculated electron density of the sample is shown in Fig. 2.2c. The conduction band electrons are confined in an approximately triangular confinement potential. The calculated square of the electron wavefunction in z direction, $\chi^2(z)$, is shown in Fig. 2.2d for the two lowest subbands (χ^2_0 and χ^2_1). In this situation, only the lowest subband, with an eigenenergy of $E_0=-6.2\,\mathrm{meV}$ is occupied, while the second subband with $E_1=3.6\,\mathrm{meV}$ remains empty. In this situation, the electron wavefunction $\psi(x,y,z)$ can be written as a plane wave for the in-plane directions x and y [4]:

$$\psi(x, y, z) = \chi(z)e^{i(k_x x + k_y y)}$$
(2.1)

with a parabolic dispersion relation [4]:

$$E_{n,\mathbf{k}} = E_n + \frac{\hbar^2}{2m^*} (k_x^2 + k_y^2)$$
 (2.2)

We have used $\mathbf{k} = (k_x, k_y)^T$. E_n is the eigenenergy of the *n*th subband and m^* is the effective mass of the 2DEG electrons. In this situation, the small *z*-extent of the

volume occupied with electrons becomes negligible and we are dealing with a quasi two-dimensional system.

The following list comprises the most important quantities for the description of a 2DEG (partially taken from [4]). We give typical values of the quantities for a high mobility 2DEG with $n_s \approx 2.5 \times 10^{11} \text{ cm}^{-2}$ and $\mu \approx 20 \times 10^6 \text{ cm}^2/\text{Vs}$.

Electron density The electron density mainly depends on the doping concentration and the thickness of the AlGaAs spacer between 2DEG and doping plane. Typical electron densities are of the order of 1.0×10^{11} cm⁻²– 1.7×10^{11} cm⁻² for single-side doped heterostructures and 2.0×10^{11} cm⁻²– 3.5×10^{11} cm⁻² for double-side doped quantum wells (QWs).

Electron mobility The electron mobility μ relates to the effective mass m^* and the momentum relaxation time τ via [4]:

$$\mu = \frac{e\tau}{m^*} \tag{2.3}$$

In the best samples available, typical magnitudes of the mobility are 5×10^6 cm²/Vs- 10×10^6 cm²/Vs for single-side doped heterostructures and $\mu \geq 15\times10^6$ cm²/Vs for double-side doped QWs.

Elastic mean free path The elastic mean free path l_e is given as:

$$l_e = \tau v_{\rm F} \tag{2.4}$$

where v_F is the Fermi velocity. In the best samples, the elastic mean free path can be as large as 175 μ m.

Effective mass The in-plane effective mass m_{\parallel}^* is given by [4]:

$$\frac{1}{m_{\parallel}^*} = \frac{p_{\rm A}}{m_{\rm A}^*} + \frac{p_{\rm B}}{m_{\rm B}^*} \tag{2.5}$$

Here, p_A and p_B are the probabilities for finding the electron in material A or B [4]. For typical 2DEGs, the envelope of the electronic wavefunction is small outside the GaAs region in which the 2DEG is defined. Hence, the in-plane effective mass corresponds with a good accuracy to the bulk GaAs effective mass: $m_{\parallel}^* \approx m_{\text{GaAs}}^* \approx 0.063 \, m_e$ [3].

Density of states The parabolic dispersion relation leads to a constant density of states:

$$\mathcal{D}_{2d}(E) = \frac{g_s m^*}{2\pi\hbar^2} \tag{2.6}$$

where g_s denotes the spin degeneracy.

Fermi energy The Fermi energy of the two-dimensional system is given as:

$$E_{\rm F} = \frac{2\pi n_s \hbar^2}{g_s m^*} \tag{2.7}$$

In typical high-mobility 2DEGs, $E_F \approx 30$ meV is found.

Fermi wavevector The Fermi wavevector is defined as:

$$k_{\rm F} = \sqrt{\frac{4\pi n_s}{g_s}} \tag{2.8}$$

It has a typical size of $k_{\rm F} \approx 1.3 \times 10^8 \ {\rm m}^{-1}$.

Fermi wavelength From this, the Fermi wavelength is obtained:

$$\lambda_{\rm F} = \sqrt{\frac{g_{\rm s}\pi}{n_{\rm s}}} \tag{2.9}$$

where typically $\lambda_{\rm F} \approx 50\,{\rm nm}$ in our samples.

Fermi velocity The Fermi velocity is the group velocity of an electron at the Fermi energy and is given by:

$$v_{\rm F} = \frac{\hbar k_{\rm F}}{m^*} \tag{2.10}$$

For our samples we find $v_{\rm F} \approx 2.4 \times 10^5$ m/s.

Classical cyclotron radius The cyclotron radius is the radius of a classical circular orbit described by an electron in a magnetic field *B* due to the Lorentz force:

$$R_c = \frac{\hbar k_{\rm F}}{eB} \tag{2.11}$$

At a given magnetic field B, we find: $R_c \times B \approx 85$ nmT.

Magnetic length The magnetic length at a given magnetic field *B* is given as:

$$l_B = \sqrt{\hbar/eB} \tag{2.12}$$

Typical magnetic lengths in quantum Hall experiments are of the order of 10 nm: $l_B \times \sqrt{B} = 25.6 \text{ nm}\sqrt{T}$.

Cyclotron energy Using the cyclotron frequency $\omega_c = \frac{eB}{m^*}$, the cyclotron energy E_{cyc} is given as:

$$E_{cyc} = \hbar\omega_c = \frac{\hbar eB}{m^*} \tag{2.13}$$

Expressed in terms of thermal energy k_BT , the cyclotron energy corresponds to: $\frac{E_{cyc}}{B} = 20 \text{ K}$.

Coulomb energy The Coulomb energy is given as [5]:

$$E_{Coulomb} = \frac{e^2}{4\pi\varepsilon\varepsilon_0 l_{\rm B}} \tag{2.14}$$

Here, ε_0 denotes the vacuum permittivity and ε the relative dielectric constant (in our case GaAs: $\varepsilon=12.9$). Expressed in terms of thermal energy, this corresponds to: $\frac{E_{Coulomb}}{\sqrt{B}} \stackrel{.}{=} 50.8$ K.

Zeeman energy The size of the Zeeman splitting is given as [6]:

$$E_Z = 2g\mu_{\rm B}\mathbf{B} \cdot \mathbf{S} = \frac{g}{2} \frac{m^*}{m_e} \hbar \omega_c \tag{2.15}$$

where m_e is the mass of a free electron. In bulk GaAs, the size of the Zeeman splitting corresponds to: $\frac{E_Z}{B} = 0.3$ K. In reality, the effective g-factor and also the Zeeman splitting can be strongly enhanced.

2.3 Low Field Magnetoresistance of Two-Dimensional Electron Gases

A classical Hall measurement [7] at low magnetic fields can be performed in a setup depicted in Fig. 2.3. Here, a four-terminal measurement scheme is used, where the current is passed in the x-direction along the long axis of the Hall-bar. A homogeneous external magnetic field B is applied perpendicular to the 2DEG. The voltages V_{xx}

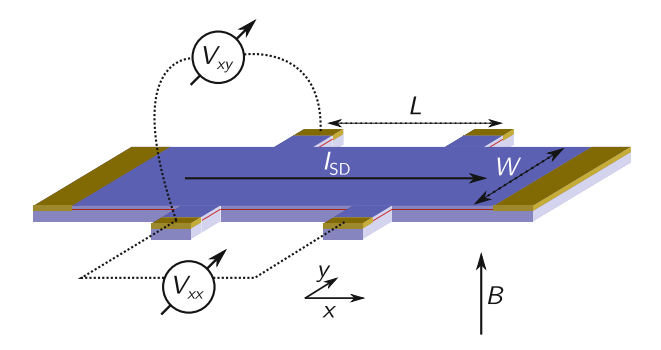


Fig. 2.3 Hall-bar measurement configuration. While a current $I_{\rm SD}$ is passed along the long axis of the Hall-bar, voltages V_{xx} and V_{xy} are measured. The voltage contacts define an area of a geometry factor (W/L). An external magnetic field B is applied perpendicular the 2DEG plane

and V_{xy} are measured on separate voltage contacts that define a geometry factor (W/L).

In two dimensions, the electric field $\mathbf{E} = (E_x, E_y)^T$ and the current density $\mathbf{j} = (j_x, j_y)^T$ are related via:

$$\begin{pmatrix} E_x \\ E_y \end{pmatrix} = \begin{pmatrix} \rho_{xx} & \rho_{xy} \\ \rho_{yx} & \rho_{yy} \end{pmatrix} \begin{pmatrix} j_x \\ j_y \end{pmatrix}$$
(2.16)

In the configuration of Fig. 2.3, we have $j_x = I_{SD}/W$ and $j_y = 0$. Hence we can relate the components of the resistivity tensor to our measurement quantities via $\rho_{xx} = (W/L) \frac{V_{xx}}{I_{SD}}$ and $\rho_{xy} = \frac{V_{xy}}{I_{SD}}$.

Classical diffusive transport At low magnetic fields when quantization effects are absent, the transport properties of the system can be well described by the Drude model [8]. With an external electric field **E** and a magnetic field **B**, the equation of motion of an electron between two scattering events can be written as [4]:

$$m^* \frac{d\mathbf{v}}{dt} = -|e|(\mathbf{E} + \mathbf{v} \times \mathbf{B})$$
 (2.17)

Scattering processes can be taken into account by assuming a statistical distribution of scattering angles and scattering times. Taking this statistical averaging into account, the components of the drift velocity $\mathbf{v}_D = (\overline{v}_x, \overline{v}_y)^T$ can be found [4]. At B = 0, the following relation between the external electric field \mathbf{E} and the drift velocity \overline{v}_x is found:

$$\overline{v}_x = -\underbrace{\frac{e\tau}{m^*}}_{\mu} E_x = -\mu E_x \tag{2.18}$$

Here μ is the electron mobility. Using the definition of the current density, $\mathbf{j} = -n_s|e|\mathbf{v}_D$ and (2.16) we find [4]:

$$\rho_{xx} = \frac{m^*}{n_s e^2 \tau} \tag{2.19}$$

$$\rho_{xy} = \frac{B}{|e|n_s} \tag{2.20}$$

These measurement quantities are connected to the electron density and mobility via:

$$n_s = \frac{1}{|e|d\rho_{xy}/dB|_{B=0}}$$
 (2.21)

$$\mu = \frac{d\rho_{xy}/dB|_{B=0}}{\rho_{xx}(B=0)}$$
 (2.22)

2.4 Growth Schemes for High Electron Mobilities

High mobility quantum wells used for the experiments presented in this book were grown in the group of Werner Wegscheider at ETH Zürich, by Christian Reichl and Werner Wegscheider. The MBE system in use is optimized for highly pure MBE growth and incorporates only a very small amount of residual background impurities in the wafers. The technical challenges that arise for the growth of a high-mobility 2DEG, for example providing pure metal sources and optimized growth temperature, rate, etc. are far beyond the scope of this book. A discussion with respect to an optimization of 2DEGs for the observation of the $\nu=5/2$ state can for example be found in [9].

However, the doping schemes employed for the 2DEGs are of great experimental relevance. Thus we will give a short overview of the different techniques used. The details of the doping strongly influence the gating properties of a heterostructure and hence influence the behavior of top-gate defined devices. The samples that have been used for the experiments presented in this book employ either conventional DXdoping or quantum-well doping and are optimized for the formation of a pronounced $\nu = 5/2$ state without the requirement of prior illumination with a light emitting diode (LED) [9]. For DX-doping, a δ -doping plane of Si dopants is located in a wide $Al_xGa_{1-x}As$ region. Apart from the shallow donors with hydrogenic energy levels, deep donor levels, the DX-centers exist. Here, the binding of an electron involves a lattice deformation and leads to a strongly bound electron state [10, 11]. The energy difference between conduction band edge and DX energy level, Δ_{DX} , scales linearly for 0.22 < x < 0.4 (from $\Delta_{DX} = 0$ at x = 0.22 to $\Delta_{DX} = -0.16$ eV at x = 0.4) [12]. Hence DX centers become shallow energy levels for a small Al mole fraction. Illuminating a DX-doped sample at low temperatures ionizes the electrons bound in DX-centers and enhances the electron density. We will discuss in the next section why illumination is often necessary in such samples, in order to observe a quantized $\nu = 5/2$ state.

An example of a DX-doped structure is shown in Fig. 2.4a. The corresponding schematics of the conduction band edge is shown in Fig. 2.4b. Here a 27 nm wide QW is defined approximately 200 nm below the surface and a DX-doping scheme in $Al_{0.24}Ga_{0.76}As$ is used, at a setback distance of approximately 100 nm. Within the $Al_{0.24}Ga_{0.76}As$ spacers, two 1.5 nm wide GaAs QWs are defined, which are expected to provide additional screening of the QW from long-range remote impurity scattering. However, without illumination of the sample, these narrow QWs are not expected to be occupied by charge carriers. 1

Quantum well doping [13–15] is an efficient technique for screening the 2DEG from long-range remote impurity scattering. Here, the doping region consists of a narrow GaAs quantum well, defined between thin barriers of AlAs [9]. The δ -Si doping plane lies in the center of the narrow GaAs QW, hence no DX centers are formed [10]. When the layer thicknesses are chosen appropriately, the X-band minima of the AlAs layers reside below the conduction band edge of the narrow GaAs

¹C. Reichl, private communication.

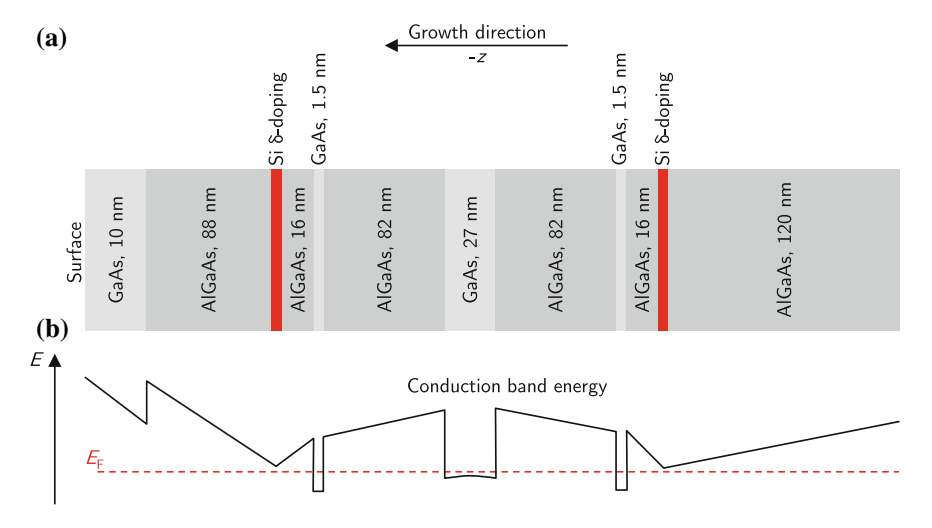


Fig. 2.4 a Layer sequence of a 27 nm wide QW grown 200 nm below the sample surface and using a DX-doping scheme. **b** Schematic conduction band energy as a function of position. The *dashed red line* indicates the Fermi energy

quantum wells (Γ -band) and excess electrons occupy the AlAs X-band [15]. The high effective mass X-band electrons provide additional screening of the 2DEG from long range potential fluctuations [9], but do not contribute to the 2DEG conductance if the growth parameters are suitably chosen.

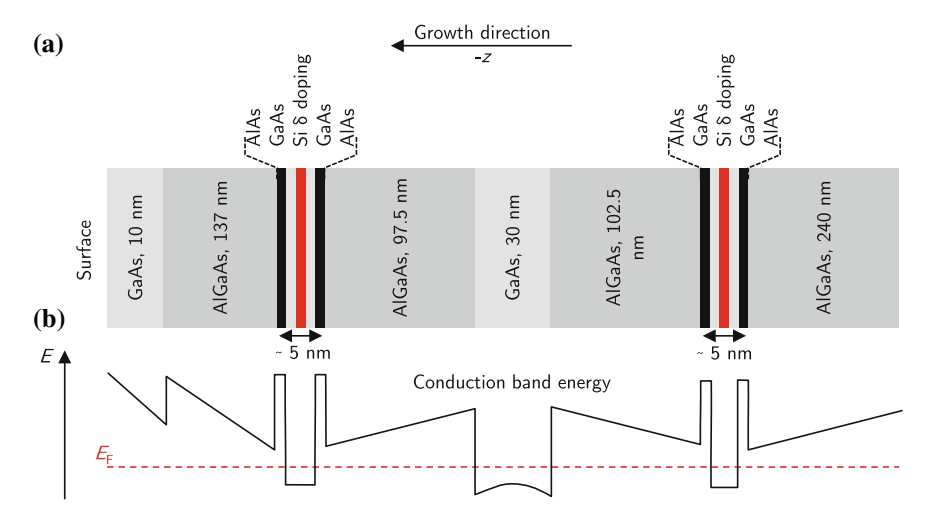


Fig. 2.5 a Layer sequence of a 30 nm wide QW grown 250 nm below the sample surface and using a QW-doping scheme. **b** Schematic conduction band energy as a function of position. The *dashed red line* indicates the Fermi energy

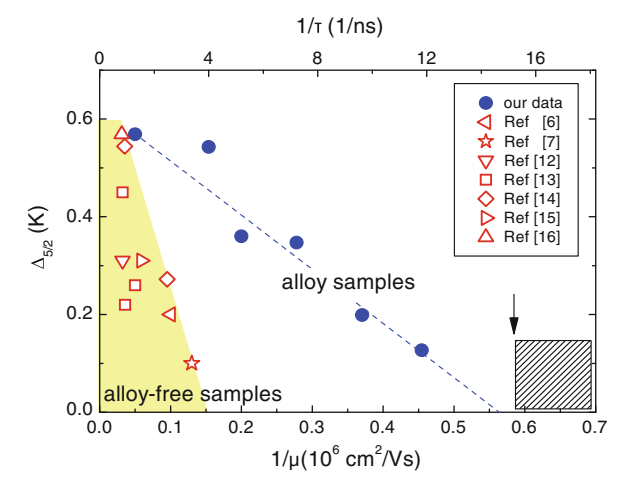
Figure 2.5 shows an example of a sample employing such a doping scheme. Here, a 30 nm wide QW is formed approximately 250 nm below the surface. The AlAs/GaAs doping regions lie approximately 100 nm below and above the 2DEG. Such a QW doping scheme allows to reach extremely high mobilities, as high as 36 million cm²/Vs [1, 15]. However, this doping scheme poses serious experimental challenges for the gating. Experiments investigating gate induced density variations on such samples [16] found pronounced hysteresis effects, which arise from the long time constants for a density relaxation of the X-band screening layers. At millikelvin temperatures, this density relaxation can take several days and makes working with top-gates structures challenging. We will discuss in Chap. 10, how this problem can be dealt with by depleting the screening layers at higher temperatures where the relaxation time constants are much shorter.

2.5 Impact of Disorder on the Gap of the $\nu = 5/2$ State

With respect to experiments at $\nu=5/2$, the main goal for a sample optimization is maximizing the energy gap $\Delta_{5/2}$ at this filling factor and not the electron mobility. Contrary to what is naively expected, there is not always a clear correlation between electron mobility and $\Delta_{5/2}$. Recent experiments showed that the contribution of different scattering mechanisms is crucial for the size of $\Delta_{5/2}$, which seems to be mainly limited by long-range scattering mechanisms [17–19].

An especially impressive demonstration of the different influence of scattering mechanisms is shown in Fig. 2.6 (from [19]). In this work, the 2DEG mobility was reduced intentionally by adding a finite Al mole fraction to the GaAs QW region. This leads to alloy scattering, which is believed to be a short-range scattering mechanism [19]. Figure 2.6 shows the energy gap $\Delta_{5/2}$ as a function of the inverse mobility for

Fig. 2.6 Energy gap $\Delta_{5/2}$ versus inverse mobility $1/\mu$. Samples with intentionally reduced mobility due to alloy scattering (*blue dots*) exhibit a gapped $\nu = 5/2$ state down to much lower mobilities than conventional high mobility samples (*red symbols*). (Reprinted figure with permission from [19]. Copyright 2014 by the American Physical Society)



the alloy samples (blue dots), compared to gap values from literature (red symbols) for samples where no intentional alloy scattering has been induced. Surprisingly, a finite energy gap $\Delta_{5/2}$ is found for the alloy samples for mobilities as low as 2.2×10^6 cm²/Vs, while for conventional samples the energy gap typically vanishes for $\mu < 10 \times 10^6$ cm²/Vs. Hence the short range alloy scattering has only a small influence on $\Delta_{5/2}$. Other recent experiments [15, 17, 18] indicate that the energy gap $\Delta_{5/2}$ in very pure heterostructures is mainly limited by remote impurity (RI) scattering.

As discussed in the previous section, the influence of RI scattering can be minimized by using a QW doping scheme. However, due to the difficult gating properties, observing a $\nu=5/2$ state in more "simple" structures would be desirable. In the experiments of Gamez et al., this has been achieved using conventionally DX-doped QWs with mobilities $\mu<10\times10^6~{\rm cm^2/Vs}$ [18]. Figure 2.7a–c shows the magneto-transport signatures of a QW before illumination with a LED (Fig. 2.7a), after intermediate illumination (Fig. 2.7b) and after strong illumination (Fig. 2.7c). During the illumination process, the mobility rose from $\mu=4\times10^6~{\rm cm^2/Vs}$ to $\mu=4.8\times10^6~{\rm cm^2/Vs}$ [18], which alone cannot account for the improved visibility of FQH features in Fig. 2.7c. A similar behavior is observed in Fig. 2.7d for samples with different Al mole fractions (from x=0.34-0.25). At x=0.25, the $\nu=5/2$ state is clearly much more pronounced than for higher Al mole fractions.

The behavior observed is attributed to the properties of the DX centers in the doping plane. Illumination at low temperatures is believed to lead to an ionization of

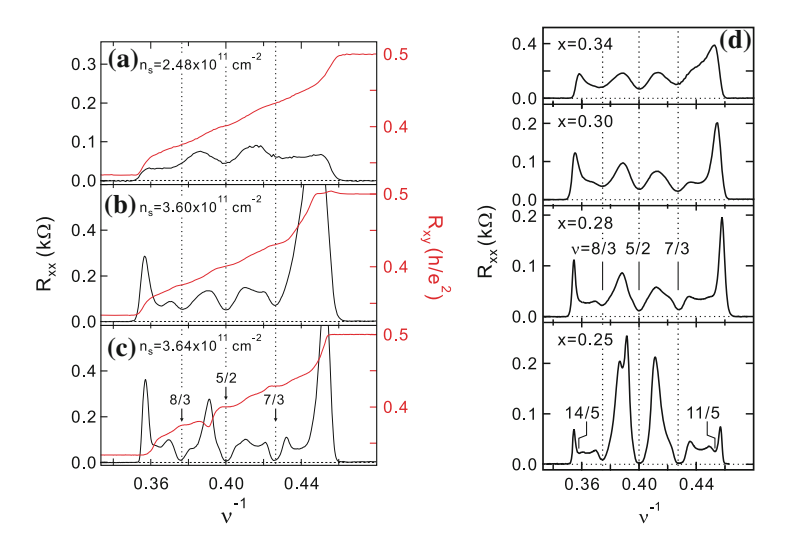


Fig. 2.7 Magnetotransport signatures of a QW for filling factors between 2 and 3 without illumination (**a**), after intermediate illumination (**b**) and after strong illumination (**c**). **d** Shows the longitudinal resistance R_{xx} versus the filling factor for different Al mole fractions x. At x = 0.25, features related to FQH states are most strongly pronounced. (Reprinted figure with permission from [18]. Copyright 2013 by the American Physical Society)

the DX centers and transforming them in shallow donors [10]. Similarly, the energy splitting of the DX centers from conduction band edge, $\Delta_{\rm DX}$, shrinks for a reduced Al mole fraction towards zero at x=0.22. Hence donors are expected to occupy more shallow energy levels at x=0.25 than at higher values of x. In this situation, the wavefunction of the bound electrons is less localized, which might lead to an improved screening of remote impurity potentials and hence explain the enhanced energy gap $\Delta_{5/2}$. The DX-doped samples used by us employ a reduced Al mole fraction x=0.24 compared to the typically employed values x=0.30-0.33. Thus these samples are optimized for a large energy gap at $\nu=5/2$.

References

- 1. D.G. Schlom, L.N. Pfeiffer, Nat. Mater. 9, 881 (2010). doi:10.1038/nmat2888
- 2. S. Adachi, Properties of Aluminium Gallium Arsenide (IET, London, 1993)
- 3. J.S. Blakemore (ed.), in *Gallium Arsenide* (Springer Science and Business Media, New York, 1961)
- T. Ihn, Semiconductor Nanostructures: Quantum States and Electronic Transport (OUP, Oxford, 2010)
- 5. Z. F. Ezawa, Quantum Hall Effects: Field Theoretical Approach and Related Topics (World Scientific, Singapore, 2008)
- 6. J. K. Jain, Composite Fermions (Cambridge University Press, Cambridge, 2007)
- 7. E.H. Hall, Am. J. Math. 2, 287 (1879). doi:10.2307/2369245
- 8. P. Drude, Ann. Phys. 306, 566 (1900). doi:10.1002/andp.19003060312
- C. Reichl, J. Chen, S. Baer, C. Rössler, T. Ihn, K. Ensslin, W. Dietsche, W. Wegscheider, New J. Phys. 16, 023014 (2014). doi:10.1088/1367-2630/16/2/023014
- 10. P.M. Mooney, J. Appl. Phys. 67, R1 (1990). doi:10.1063/1.345628
- 11. P. Yu, M. Cardona, Fundamentals of Semiconductors: Physics and Materials Properties (Springer Science and Business Media, New York, 2010)
- M. Henini, Molecular Beam Epitaxy: From Research to Mass Production (Newnes, Oxford, 2012)
- T. Baba, T. Mizutani, M. Ogawa, Jpn. J. Appl. Phys. 22, L627 (1983). doi:10.1143/JJAP.22. L627
- K.-J. Friedland, R. Hey, H. Kostial, R. Klann, K. Ploog, Phys. Rev. Lett. 77, 4616 (1996). doi:10.1103/PhysRevLett.77.4616
- V. Umansky, M. Heiblum, Y. Levinson, J. Smet, J. Nübler, M. Dolev, J. Cryst. Growth 311, 1658 (2009). doi:10.1016/j.jcrysgro.2008.09.151
- C. Rössler, T. Feil, P. Mensch, T. Ihn, K. Ensslin, D. Schuh, W. Wegscheider, New J. Phys. 12, 043007 (2010). doi:10.1088/1367-2630/12/4/043007
- W. Pan, N. Masuhara, N.S. Sullivan, K.W. Baldwin, K.W. West, L.N. Pfeiffer, D.C. Tsui, Phys. Rev. Lett. 106, 206806 (2011). doi:10.1103/PhysRevLett.106.206806
- 18. G. Gamez, K. Muraki, Phys. Rev. B 88, 075308 (2013). doi:10.1103/PhysRevB.88.075308
- N. Deng, G. Gardner, S. Mondal, E. Kleinbaum, M. Manfra, G. Csáthy, Phys. Rev. Lett. 112, 116804 (2014). doi:10.1103/PhysRevLett.112.116804

Chapter 3 The Quantum Hall Effect

Abstract We review the basics of the integer quantum Hall effect and the fractional quantum Hall effect. We furthermore discuss the fractional quantum Hall states in the second Landau level and their properties.

3.1 Introduction

More than 100 years after the discovery of the Hall effect [1], a quantum mechanical version of this effect, the quantum Hall effect was discovered by Klaus von Klitzing [2]. When von Klitzing realized that the quantized resistivities in a Hall measurement are only related to the natural constants h, the Planck constant and e, the electron charge, the importance of this discovery became obvious.

Only shortly afterwards, the FQH effect has been discovered by Tsui et al. [3]. These works have sparked a large number of theoretical and experimental studies, trying to understand the physics behind these effects. Though a huge progress has been made in the field, new interesting phenomena still appear as experimental methods and sample quality improve. Many of these phenomena are complicated many-particle effects and are not yet understood, making the quantum Hall effect still a "hot" research topic. In the following, we will give a short overview of the understanding of the integer and fractional quantum Hall effect.

3.2 Energy Spectrum in a Magnetic Field

When a strong perpendicular magnetic field is applied to a 2DEG, the constant DOS is strongly modified due to energy quantization of the in-plane motion of the electrons. In the presence of a magnetic field B, the Hamiltonian of an electron with effective mass m^* in a parabolic band can be written as:

$$H = \frac{1}{2m^*} (\mathbf{p} + |e|\mathbf{A})^2 + V(z)$$
 (3.1)

[©] Springer International Publishing Switzerland 2015 S. Baer and K. Ensslin, *Transport Spectroscopy of Confined Fractional Quantum Hall Systems*, Springer Series in Solid-State Sciences 183, DOI 10.1007/978-3-319-21051-3_3

Here the canonical momentum is given as $\mathbf{p} = -i\hbar\nabla$, V(z) is the confinement potential in z-direction and we have $\mathbf{B} = (0, 0, B)^T = \nabla \times \mathbf{A}$. In the Landau gauge we choose: $\mathbf{A} = (-By, 0, 0)^T$.

The eigenvalue problem in the x-y plane can be solved making an Ansatz of the following form [4]: $\psi(x,y)=e^{ik_xx}\eta(y)$. Introducing the new variables $y'=\frac{y}{l_B}-l_Bk_x$ and $p'_y=\frac{l_Bp_y}{\hbar}$ the Hamiltonian can be rewritten as [5]:

$$H = H_{x,y} + H_z \tag{3.2}$$

$$H_z = -\frac{\hbar^2}{2m^*} \frac{\partial^2}{\partial z^2} + V(z)$$
 (3.3)

$$H_{x,y} = \hbar\omega_c \left[\frac{1}{2} y'^2 + \frac{1}{2} \left(p_y' \right)^2 \right]$$
 (3.4)

where $\omega_c = |e|B/m^*$ is the cyclotron frequency. H_z is independent of the magnetic field and describes the confinement in the z-direction. The Hamiltonian for the inplane motion, $H_{x,y}$, is independent of the confinement potential V(z). This is the Hamiltonian of a one-dimensional harmonic oscillator with a center coordinate $y_0 = l_B^2 k_x = \frac{\hbar k_x}{|e|B}$. The energy eigenvalues are given as [4]:

$$E_n = \left(n + \frac{1}{2}\right)\hbar\omega_c\tag{3.5}$$

These energy levels are called Landau levels (LLs). The eigenmodes of the Hamiltonian have the structure of a plane wave in the x-direction and a localized harmonic oscillator wavefunction in y-direction [5]:

$$\psi_{n,k_x}(x,y) = \left[\pi 2^{2n} (n!)^2\right]^{-1/4} e^{ik_x x} \exp\left[-\frac{1}{2} \left(\frac{y}{l_B} - l_B k_x\right)^2\right] H_n \left(\frac{y}{l_B} - l_B k_x\right)$$
(3.6)

Here H_n are the Hermite polynomials. The harmonic oscillator wavefunction is localized at $y_0 = \frac{\hbar k_x}{|e|B}$ in y-direction with a semiclassical spread in the y-direction $R_c = \sqrt{2n+1}l_{\rm B}$, the cyclotron radius [6].

We see that in the presence of a quantizing magnetic field, the constant DOS of the 2DEG evolves into a discrete DOS with an energy spacing $\hbar\omega_c$. If the Zeeman splitting is included, the energy eigenstates are modified [4]:

$$E_n^{\pm} = \hbar\omega_c \left(n + \frac{1}{2} \right) \pm \frac{1}{2} g^* \mu_{\rm B} B \tag{3.7}$$

where $\mu_{\rm B}=\frac{\hbar|e|}{2m_e}$ is Bohr's magneton. Here, g^* is the effective g-factor, which can be substantially enhanced compared to the bare GaAs g-factor (see Sect. 9.4.4).

The degeneracy of the LLs can be found from the following consideration: the center coordinate of the eigenmodes (3.6) y_0 is required to lie within the width W of

the sample: $0 \le y_0 \le W$. We find that the number of allowed k_x states per unit area increases with B and is given as:

$$n_{\rm L} = \frac{|e|B}{h} = \frac{B}{\phi_0} \tag{3.8}$$

where $\phi_0 = h/|e|$ is the flux quantum. Hence exactly $2n_L$ electrons per unit area are allowed to lie within one LL (for a spin degeneracy of two). The filling factor is defined as $\nu = n_s/n_L = hn_s/|e|B$ and represents the number of electrons per free state in a LL. A filling factor $\nu = 2$ corresponds to the lowest LL completely filled, whereas for $\nu = 1$ only the energetically lower spin-split branch of the lowest LL is filled.

The relation between the LL energy eigenvalues and the magnetic field is linear and can be illustrated in a Landau fan (Fig. 3.1a). Here the LL energies are plotted

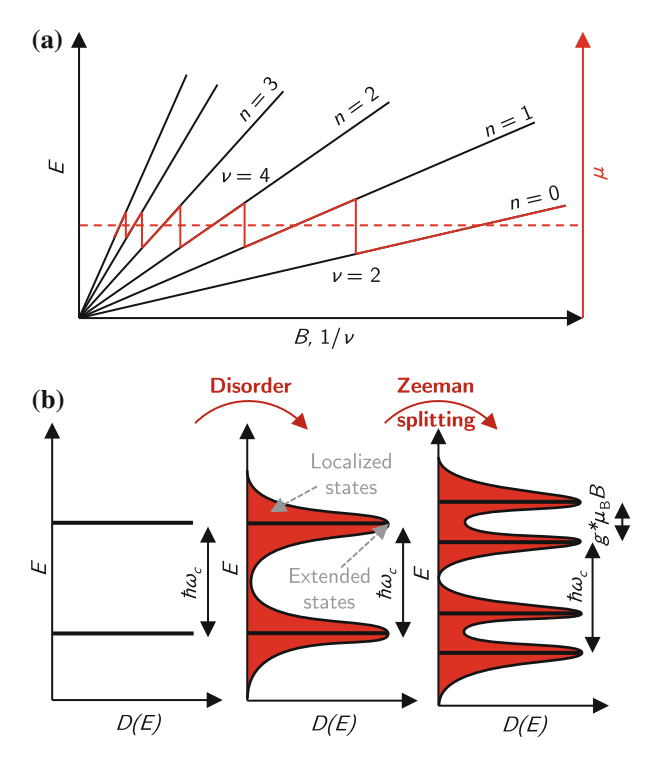


Fig. 3.1 a LL energies for n = 0, 1, 2,... versus the magnetic field. At a fixed electron density, increasing the magnetic field increases the degeneracy of the LLs and thus subsequently depletes higher LLs. This results in 1/*B*-periodic jumps of the electrochemical potential (*red*). **b** Electronic density of states in a strong magnetic field. The δ-shaped DOS peaks are broadened by scattering and disorder, leading to localized states in the tails of the DOS peaks. When the Zeeman splitting is included, the spin degeneracy of the LLs is lifted and the DOS peaks split in energy by $g^* μ_B B$

for $n=0,1,\ldots$ as a function of B or $1/\nu$. Increasing the magnetic field increases the degeneracy of the LLs (3.8). Hence, at a fixed electron density n_s , electrons are transferred from higher LLs to lower LLs as the magnetic field strength is increased. Decreasing the filling factor across $\nu=2,4,6,\ldots$, the topmost LL is emptied, causing 1/B-periodic jumps of the Fermi energy. When also the spin-splitting is taken into account, jumps in the Fermi energy occur at $\nu=1,2,3,\ldots$

In this simplified picture, the DOS of the electrons is perfectly quantized (left column, Fig. 3.1b). When disorder and scattering processes are present like in any realistic sample, the δ -peaked DOS is broadened . The states which lie in the tails of the broadened DOS are localized (red areas in Fig. 3.1b, middle column) and do not contribute to the transport. In contrast states at the DOS maximum are extended and span throughout the sample (black lines in Fig. 3.1b, middle column) [4]. When the magnetic field is changed now, the Fermi energy no longer jumps between extended states, but localized states are depopulated at certain *B*-field intervals. As the conductivity σ_{xx} of localized states is expected to vanish at low T, this implies a vanishing longitudinal resistivity at low temperatures whenever only localized states are (de)populated.

3.3 Shubnikov-De Haas Effect

A clear deviation of the ordinary Drude-model behavior can be seen when the LL splitting becomes larger than the broadening due to disorder and scattering. This is true when $\omega_c \tau_{\text{tot}} \approx 1$, where τ_{tot} is the total scattering time. Here, the quantized DOS affects the longitudinal resistivity that can be measured in a Hall measurement. The result of such a measurement is shown in Fig. 3.2a. At low magnetic fields (B < 40 mT), ρ_{xx} depends only weakly on the magnetic field. In this regime, the Drude model is expected to be a good description. At B > 40 mT, 1/B-periodic oscillations in the longitudinal resistivity due to the modulation of the DOS set in, the Shubnikov-de Haas (SdH) oscillations. At low magnetic fields and assuming a Lorenzian DOS broadening and dominant long-range scattering potentials, an expression for ρ_{xx} can be found [4]:

$$\rho_{xx}(B,T) = \frac{m^*}{n_s e^2 \tau} \left[1 - 2e^{-\pi/\omega_c \tau_q} \frac{2\pi^2 k_{\rm B} T / \hbar \omega_c}{\sinh(2\pi^2 k_{\rm B} T / \hbar \omega_c)} \cos\left(2\pi \frac{h n_s}{2eB}\right) \right]$$
(3.9)

The Dingle factor $2e^{-\pi/\omega_c\tau_q}$ accounts for the finite lifetime broadening of the LLs [4]. The quantum lifetime τ_q can be obtained from temperature-dependent measurements of the SdH oscillations and comparison with (3.9).

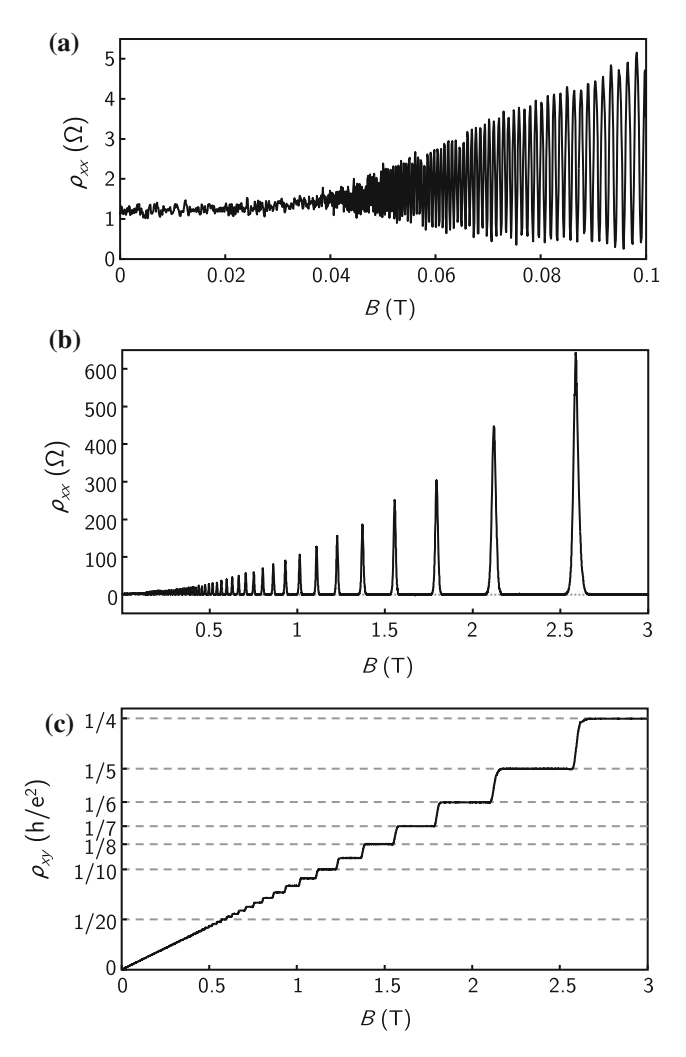


Fig. 3.2 a Shubnikov-de Haas oscillations of the longitudinal resistivity ρ_{xx} at small magnetic fields. At higher magnetic fields, ρ_{xx} develops distinct peaks and wide regions of $\rho_{xx} \approx 0$ in between the peaks (**b**). Whenever zeroes in ρ_{xx} are observed, the Hall resistivity ρ_{xy} develops a plateau with a quantized resistance value described by $\rho_{xy} = \frac{h}{ie^2}$ with an integer ν (**c**)

3.4 Integer Quantum Hall Effect

At low temperatures and in a strong magnetic field, where the energy quantization of the DOS becomes dominant, the quantities measured in a Hall measurement also become quantized. A measurement where this becomes obvious is shown in Fig. 3.2b, c. As the magnetic field strength is increased, a transition from the Drude

regime (B < 40 mT) to a regime where SdH oscillations are observed occurs. At even stronger magnetic fields, ρ_{xx} no longer oscillates, but exhibits wide zeroes with sharp peaks in between. Whenever ρ_{xx} exhibits a zero, a plateau in the Hall resistance ρ_{xy} is observed. The plateau values correspond to resistances given by

$$\rho_{xy}^{plateau} = \frac{h}{ie^2} \tag{3.10}$$

where *i* is an integer number. This effect is called (integer) quantum Hall effect (and has been discovered by Klaus von Klitzing [2]). The quantization of ρ_{xy} was found to be independent of the details of the sample and even of the material system in which the measurement was implemented. The constant $R_{\rm K} = \frac{h}{e^2} = 25812.807449$ Ω is called the von Klitzing constant.

In the center of a quantum Hall plateau, ρ_{xx} is exponentially suppressed in temperature. Here ρ_{xx} follows an Arrhenius law [7]:

$$\rho_{xx} \propto \exp\left(-\frac{E_{\text{gap},xx}}{2k_{\text{B}}T}\right) \tag{3.11}$$

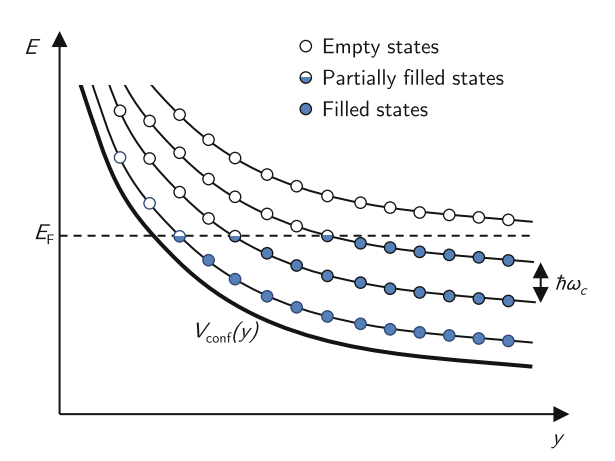
The energy gap $E_{\text{gap},xx}$ is the energy difference between the Fermi energy and the energetically lowest unoccupied extended state. Similarly, the deviation of the Hall resistance from the quantized plateau value is described by an activated behavior [7]:

$$\Delta \rho_{xy}(T, B) = \left| \rho_{xy}(T, B) - \frac{h}{\nu e^2} \right| \propto \exp\left(-\frac{E_{\text{gap}, xy}}{2k_{\text{B}}T}\right)$$
(3.12)

3.4.1 Landauer-Büttiker Formalism

Shortly after the discovery of the QHE, the importance of the sample edges has been recognized [8]. The most simple picture in which transport in a multi-terminal system in the QH regime can be described is the Landauer-Büttiker picture. Though this model neglects complications arising from self-consistency of charge distribution and potential at the edge, it is still very useful and accurately describes the physics in many situations. The situation of a sample edge is shown schematically in Fig. 3.3. At the boundary of the 2DEG to vacuum, LL energies are adiabatically lifted due to a confinement potential $V_{\rm conf}(y)$ (thick black line). In the situation shown, the extended states of the lowest three LLs are occupied in the bulk. Close to the edge, the LLs intersect with the Fermi energy. Here, partially filled extended states contribute to the conductance. In the simplest picture, the intersection of the non-interacting LLs with the Fermi energy is referred to as "edge channel" and seen as one-dimensional channel where the current flows. This current is dissipationless due to the chirality of the edge states and the suppressed backscattering across the wide bulk of the sample. Electrons in the edge states propagate with a group velocity of [4]:

Fig. 3.3 Non-interacting LL energies at the edge. Due to a confinement potential $V_{\rm conf}(y)$ (thick black line), single-particle energies are lifted towards the edge. In the situation shown, the extended states of three LLs are fully populated in the bulk. Towards the edge, they intersect the Fermi energy, defining one-dimensional channels of partially filled states



$$v_x = \frac{1}{\hbar} \frac{\partial V_{\text{conf}}}{\partial k_x} = \frac{\partial V_{\text{conf}}(y)}{\partial y} \bigg|_{y = \frac{\hbar k_x}{\partial B}} \frac{1}{|e|B}$$
(3.13)

and contribute $2e^2/h$ to the conductance. If the spin degeneracy is lifted by the Zeeman splitting, each LL splits into two edge channels which each contribute e^2/h to the conductance. In the generalized multi-terminal Landauer-Büttiker formalism [9–11], we can relate the currents I_1, I_2, \ldots, I_n entering into the contacts $1, 2, \ldots, n$ with the potential V_1, V_2, \ldots, V_n of the contacts via [4]:

$$\begin{pmatrix} I_{1} \\ I_{2} \\ \vdots \\ I_{n} \end{pmatrix} = \frac{e^{2}}{h} \begin{pmatrix} N_{1} - \mathcal{R}_{1} & -\mathcal{T}_{12} & \dots & -\mathcal{T}_{1n} \\ -\mathcal{T}_{21} & N_{2} - \mathcal{R}_{2} & \dots & -\mathcal{T}_{2n} \\ \vdots & \vdots & & \vdots \\ -\mathcal{T}_{n1} & -\mathcal{T}_{n2} & \dots & N_{n} - \mathcal{R}_{n} \end{pmatrix} \begin{pmatrix} V_{1} \\ V_{2} \\ \vdots \\ V_{n} \end{pmatrix}$$
(3.14)

Here N_k modes are inserted in the contact k and we have used the reflection probabilities \mathcal{R}_k and the transmission probabilities $\mathcal{T}_{k,l}$ from contact l to contact k. Making use of this framework, we will now try to understand the observations of the IQH effect.

For this, we first look at a situation where the Fermi energy lies in the tails of the DOS peaks in the bulk. This situation is depicted in Fig. 3.4a. In such a situation where disorder is present, the LL energies are shown as a function of the spatial coordinate y in the middle row of Fig. 3.4a. Intersections of Fermi energy and LL energies occur close to the edge, but also in the bulk where the disorder potential exhibits a minimum. A schematic configuration of edge states in such a situation is shown in the rightmost row of Fig. 3.4a. Here, the edge state corresponding to the lowest LL is flowing dissipationless along the edge and is decoupled from the counterpropagating edge state at the other side of the Hall-bar. The second LL is

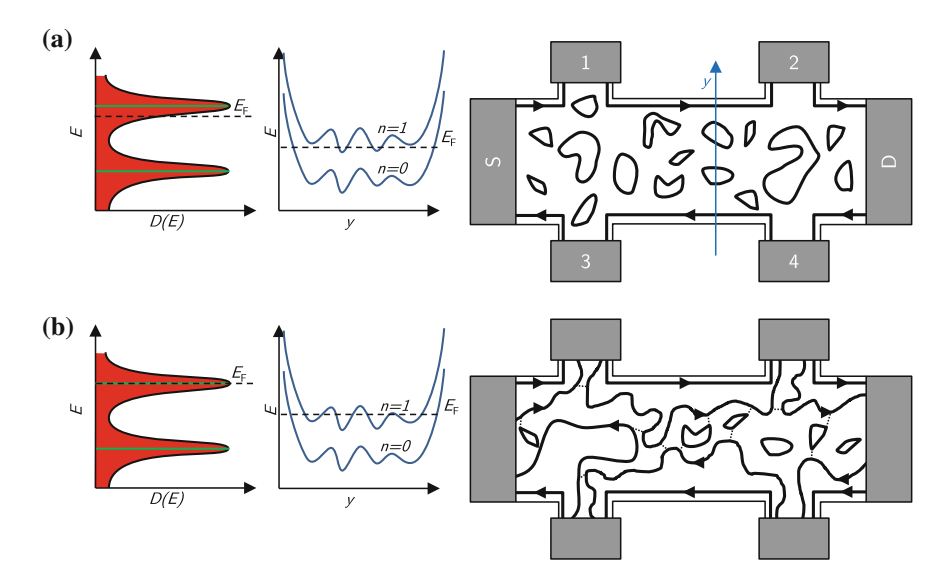


Fig. 3.4 Landauer-Büttiker edge channel picture for different filling factors. The spin-splitting is neglected in this picture. For $\nu \approx 2$, the Fermi energy is located in the tails of the DOS (a). In this case, extended states are either localized in the bulk or propagate along the edge. In a situation where the filling factor has been increased and no quantized Hall resistance is observed (b), the Fermi energy lies near the DOS peaks corresponding to extended states. In this situation extended states percolate through the bulk, connecting both edges and causing finite backscattering

occupied in certain areas of the bulk, leading to localized states and an additional edge state encircling them.

We now consider a situation where current is only inserted or extracted via the source or drain contacts of the Hall-bar (S or D in Fig. 3.4a, right column). Due to the dissipationless flow of current along the edges, the potential of source, contact 1 and contact 2 are identical: $V_S = V_1 = V_2$. The same is true for drain and contacts 3 and 4: $V_D = V_3 = V_4$. Hence, ρ_{xx} measured between contacts 1 and 2 or 3 and 4 vanishes in this situation. The conductance from source to drain is contributed by ν edge states, with a total conductance of $\nu \frac{e^2}{h}$. Without backscattering, we find from (3.14) (see Appendix B) a quantized Hall resistance $\rho_{xy} = \frac{h}{e^2} \frac{1}{\nu}$. Thus, we can identify the integer number i (3.10) as the filling factor: $i = \nu$.

When the Fermi energy lies at the center of the DOS maxima (Fig. 3.4b), the second edge state is no longer confined to localized states but percolates throughout the whole sample (rightmost row in Fig. 3.4). This leads to backscattering between counterpropagating edge states and hence finite ρ_{xx} and a deviation of ρ_{xy} from the plateau value.

3.4.2 Many-Body Wavefunction of the Lowest Landau Level

In the lowest LL and in the symmetric gauge, the electron single-particle wavefunctions can be written as [5]:

$$\eta_l(z) = \left(2\pi 2^l l!\right)^{-1/2} z^l e^{-\frac{1}{4}|z|^2}$$
(3.15)

where z = x - iy is the complex coordinate and l is the angular momentum. A many-body wavefunction Ψ_{LLL} can be written as the product of the single-particle wavefunctions and the Slater determinant, which guarantees antisymmetry under particle exchange [5]:

$$\Psi_{\text{LLL}} = \begin{vmatrix} 1 & 1 & 1 & \dots \\ z_1 & z_2 & z_3 & \dots \\ z_1^2 & z_2^2 & z_3^2 & \dots \\ \vdots & \vdots & \ddots & \vdots \\ \vdots & \vdots & \ddots & \dots \end{vmatrix} \exp \left[-\frac{1}{4} \sum_{i} |z_i|^2 \right] = \prod_{j < k} (z_j - z_k) \exp \left[-\frac{1}{4} \sum_{i} |z_i|^2 \right]$$
(3.16)

Here, and for the rest of this chapter, we have set $l_B = 1$. The determinant is known as Vandermonde determinant and equals $\prod_{j < k} (z_j - z_k)$. This factor takes account for

Pauli's exclusion principle by demanding that the wavefunction vanishes for two identical electron coordinates.

3.5 Fractional Quantum Hall Effect

The IQH effect is a single-particle effect and can be understood without taking electron-electron interaction into account. In 2DEGs of even higher purity and at even lower temperature than necessary for the observation of the IQH effect, electron-electron interaction effects eventually become important. An effect where this becomes obvious is the FQH effect.

One of the most impressive measurements of this effect available in literature is shown in Fig. 3.5 (taken from [12]). There, the longitudinal resistance of a high mobility electron gas has been measured as a function of the magnetic field B at very low temperature ($T \approx 35$ mK). At integer filling factors $\nu = 1, 2, ...$ the longitudinal resistance drops to zero, as seen before. However, for filling factors $\nu < 1$, a large number of new states with $\rho_{xx} \approx 0$ appear. Also in the upper spin-branch of the lowest LL, $1 < \nu < 2$, several states with $\rho_{xx} \approx 0$ are visible. The zeroes of ρ_{xx} appear at filling factors $\nu = p/q$, where p and q are integers and q is odd. At the same time, plateaus in the Hall resistance are observed at the corresponding values $R_{xy} = \frac{h}{\nu \rho^2}$. The effect giving rise to these observations is called the fractional

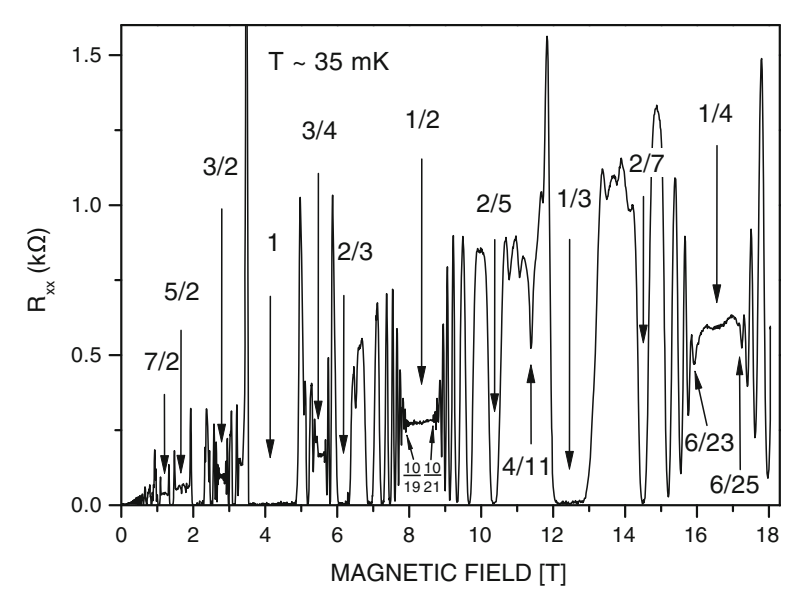


Fig. 3.5 Longitudinal resistance versus the magnetic field of a high-mobility electron gas at low temperature. Many IQH and FQH states are observed. (Reprinted figure with permission from [12]. Copyright 2002 by the American Physical Society.)

quantum Hall effect. We point out some of the experimental observations that have been made from transport measurements:

- The most prominent FQH states that are observed are $\nu = 1/3, 2/5, 3/7, \ldots$ and $\nu = 2/3, 3/5, 4/7, \ldots$
- Many FQH states are observed in the lowest LL (ν < 2). In contrast, only a few FQH states are observed in the second LL (2 < ν < 4) and usually no FQH states are observed in even higher LLs (4 < ν).
- The spectrum of the FQH states (Fig. 3.5) resembles a fractal pattern with a certain self-similarity. For example, FQH states seem to occur symmetrically around $\nu = 1/2$ and 1/4 and also around $\nu = 3/2$. Furthermore, around $\nu = 1/2$ for example, the behavior of R_{xx} resembles its behavior around B = 0.

3.5.1 Laughlin's Wavefunction

Much of the theory of the FQH effect developed from the wavefunction proposed by Laughlin [13]:

$$\Psi_{\text{Laughlin}}^{1/m} = \prod_{j < k} (z_j - z_k)^m \exp\left[-\frac{1}{4} \sum_i |z_i|^2\right]$$
 (3.17)

where $z_j = x_j + iy_j$ is the complex coordinate. Theoretical and experimental findings strongly suggest that this is the correct wavefunction for the FQH states at $\nu = 1/m$ (also referred to as Laughlin sequence). Let us mention why this wavefunction is a good choice for the groundstate at $\nu = 1/m$. The basic requirements for a many-body wavefunction believed to be relevant at $\nu = 1/m$ are [6]:

- As the FQH effect is not a single-particle effect, pairwise correlations (i.e. the Coulomb repulsion) have to be taken into account. This can be done via a term ∏ f (z_j − z_k).
- The many-particle wavefunction is required to be an eigenstate of the total angular momentum, hence $\prod_{j < k} f(z_j z_k)$ must be a polynomial of z_1, z_2, \ldots, z_N of degree L [6], where L is the total angular momentum.
- The last requirement for a Fermionic wavefunction is the antisymmetry under electron exchange. The only function f that fulfills all three criteria is given by $f(z) = z^m$ [5] where m is an odd integer.

Overall, this wavefunction is able to explain the FQH states at $\nu=1/m$ and the states at $\nu=1-1/m$ by particle-hole inversion. As a consequence of the electron-electron interaction, the quasiparticle excitations of a 1/m FQH state carry a quasiparticle charge $e^*/e=1/m$.

So how can the other FQH states be explained? Early approaches have tried to construct other filling factors iteratively from the Laughlin sequence in a hierarchical approach, like for example the Haldane-Halperin hierarchy [14, 15]. The most successful approach that is able to explain most of the FQH states is however the composite Fermion theory, which is discussed in the next section.

3.5.2 Composite Fermion Theory

The composite Fermion theory introduced by Jain (for an overview see [5]) allows to draw an analogy between the FQH effect and the IQH effect and tries to unify both phenomena. In this theory, we no longer consider the behavior of electrons, but of quasiparticles called composite Fermions (CFs). When the Coulomb interaction which is crucial for the FQH effect is taken into account, the system can be described in terms of weakly interacting CFs. These quasiparticles have the same function for the FQH effect as electrons have for the IQH effect [5].

Chern-Simons approach In order to motivate the CF theory, we consider interacting electrons at a filling factor ν which are exposed to an external magnetic field B and an interaction V. Following [16] we now would like to transform this system to a description of only weakly interacting quasiparticles. This can be done by a Chern-Simons gauge transformation where the electron wavefunction Ψ is written as [5]:

$$\Psi = \prod_{j < k} \left(\frac{z_j - z_k}{|z_j - z_k|} \right)^{2p} \Psi_{\text{CS}}$$
(3.18)

With this, the system can be described in terms of Ψ_{CS} [16]:

$$H'\Psi_{\rm CS} = E\Psi_{\rm CS} \tag{3.19}$$

$$H' = \frac{1}{2m^*} \sum_{i} (\mathbf{p}_i + e\mathbf{A}(\mathbf{r}_i) - e\mathbf{a}(\mathbf{r}_i))^2 + V$$
 (3.20)

where $\mathbf{a}(\mathbf{r}_i) = 2p\phi_0 \frac{1}{2\pi} \sum_{j \neq i} \nabla_i \theta_{ij}$ and $\theta_{jk} = i \ln \left(\frac{z_j - z_k}{|z_j - z_k|}\right)$ [5]. Naively, the vector potential $\mathbf{a}(\mathbf{r}_i)$ can be understood to attach 2p flux quanta to every electron at $\mathbf{r}_j \neq \mathbf{r}_i$, which are then experienced by the electron at coordinate \mathbf{r}_i . In order to be able to construct an effective theory, we now use a mean-field approximation: the electron at \mathbf{r}_i sees an uniform effective magnetic field B^* instead of the flux quanta attached to the other electrons. In this approximation, we can write [16]:

$$\mathbf{A} - \mathbf{a} = \mathbf{A}^* + \delta \mathbf{A} \tag{3.21}$$

from which we find the effective magnetic field experienced by the CFs:

$$B^* = B - 2pn_s\phi_0 \tag{3.22}$$

In this approximation, the Hamiltonian can be now written as [16]:

$$H' = \underbrace{\frac{1}{2m^*} \sum_{i} (\mathbf{p}_i + e\mathbf{A}^*(\mathbf{r}_i))^2 + V + V'(\delta \mathbf{A})}_{H'_{\delta}}$$
(3.23)

FQH effect as IQH effect of composite Fermions From this approximation we see the following: the new quasiparticles, the CFs, can be described in analogy to electrons in an effective magnetic field $B^* = B - 2pn_s\phi_0$, described by the Hamiltonian H'_0 . In this effective field, CFs occupy the analog of LLs, commonly referred to as Λ -levels. The CF filling factor ν^* is related to the electron filling factor ν via [5]:

$$\nu = \frac{\nu^*}{2p\nu^* \pm 1} \tag{3.24}$$

Here, the \pm in the denominator corresponds to a positive or negative sign of B^* . We furthermore notice that the effective magnetic field B^* disappears at filling factors $\nu=1/2p$. In these situations a "sea" of CFs (with 2p flux quanta) is observed, in analogy to an electron Fermi liquid. Looking back to Fig. 3.5, we now can understand the fractal structure as a result of series of CF states around $B^*=0$ at $\nu=1/2,1/4,\ldots$ Furthermore, the similarity of transport at $\nu=1/2,1/4,\ldots$ to the transport at B=0

		2pv 1								
-5	-4	-3	-2	-1	ν^*	1	2	3	4	5
5/9	4/7	3/5	2/3	1	$ \nu = {}^{2p}CF_{\nu^*} $	1/3	2/5	3/7	4/9	5/11
$^2CF_{-5}$	² CF ₋₄	² CF ₋₃	² CF ₋₂	² CF ₋₁		² CF ₁	² CF ₂	² CF ₃	² CF ₄	² CF ₅
5/19	4/15	3/11	2/7	1/3	$ \nu = {}^{2p}CF_{\nu^*} $	1/5	2/9	3/13	4/17	5/21
$^4\mathrm{CF}_{-5}$	⁴ CF ₋₄	⁴ CF ₋₃	⁴ CF ₋₂			⁴ CF ₁	⁴ CF ₂	⁴ CF ₃	⁴ CF ₄	⁴ CF ₅
		3/17	2/11	1/5	$ \nu = {}^{2p} CF_{\nu^*} $	1/7	2/13	3/19		
		⁶ CF ₋₃	⁶ CF ₋₂	⁶ CF ₋₁		⁶ CF ₁	⁶ CF ₂	⁶ CF ₃		

Table 3.1 Composite Fermion states ${}^{2p}CF_{\nu^*}$ for different ν^* and 2p and the corresponding electron filling factors $\nu = \frac{\nu^*}{2n\nu^*+1}$

Adapted from [5]

is a result of the analogy of the physics of electron transport at B = 0 to the transport of CFs at $B^* = 0$.

Table 3.1 shows different CF states ${}^{2p}\text{CF}_{\nu^*}$, where 2p flux quanta are attached, and CFs form Λ -levels with an integer filling factor ν^* . The corresponding electron filling factors ν of those states are calculated from (3.24) and are given in Table 3.1.

Comparing the FQH states listed in Table 3.1 with experimental observations (for example Fig. 3.5), we realize the power of the CF theory: it is able to predict (nearly) all FQH states observed. Furthermore, FQH states that are very prominent in the experiment arise from the "lowest orders" of the theory, i.e. for small p and ν^* .

From this approach, the CF wavefunction $\psi_{\frac{\nu^*}{2p\nu^*\pm 1}}$ can be constructed from an IQH wavefunction at filling factor ν^* via [17]:

$$\psi_{\frac{\nu^*}{2p\nu^*\pm 1}} = \phi_{\pm\nu^*} \prod_{j< k} (z_j - z_k)^{2p}$$
(3.25)

Here, $\phi_{\pm\nu^*}$ is the many-body wavefunction of an IQH state at $\pm\nu^*$. Let us have a look at the result that is obtained from this for the Laughlin sequence. Here we have $\nu^* = 1$ and $p = 1, 2, \ldots$ Inserting the many-body wavefunction of the lowest LL (3.16) into (3.25), we find again Laughlin's wavefunction (3.17).

Beyond the CF approach While most of the FQH states can be explained in the picture of non-interacting CFs, there are a few exceptions where this cannot be done. One example is the FQH states in the second LL, where the residual interaction between CFs can no longer be neglected. We will discuss these states in the next section. Another example is the FQH states at the filling factors $\nu=4/11$ (see Fig. 3.5) and $\nu=5/13$ which are not described by the sequence of (3.24) [18, 19]. Also here, the residual CF interaction is believed to be relevant. These both FQH states can be seen as a FQH effect of composite Fermions, with CF filling factors $\nu^*=4/3$ or $\nu^*=5/3$ [5].

3.6 Fractional Quantum Hall Effect in the Second Landau Level

As we have seen, a large number of FQH states is found in the lowest LL. Most of these states can be well understood in terms of the composite Fermion theory. In contrast, only a small number of FQH states is observed in the second LL, even in samples with mobilities exceeding 20×10^6 cm²/Vs and at extremely low temperatures T < 15 mK. Two exemplary measurements of longitudinal and Hall resistivities in high mobility samples at an estimated electron temperature $T_{\rm el} \approx 12$ –13 mK are shown in Fig. 3.6a–d.

Reentrant integer quantum Hall effect The first big difference of this measurement to the behavior in the lowest LL can be seen from the Hall resistance. At certain *B*-field positions, the Hall resistance is strongly non-monotonic and reaches the quantized resistance plateau of the neighboring IQH state. In these configurations, longitudinal resistivity vanishes at the lowest temperatures, but does not exhibit an activated behavior [20]. This effect is known as reentrant integer quantum Hall (RIQH) effect. The RIQH effect is a result of the competition between the long range repulsive and short range attractive contributions to the Coulomb interaction [21]. In higher LLs, this can lead to a situation where the bulk breaks into regions

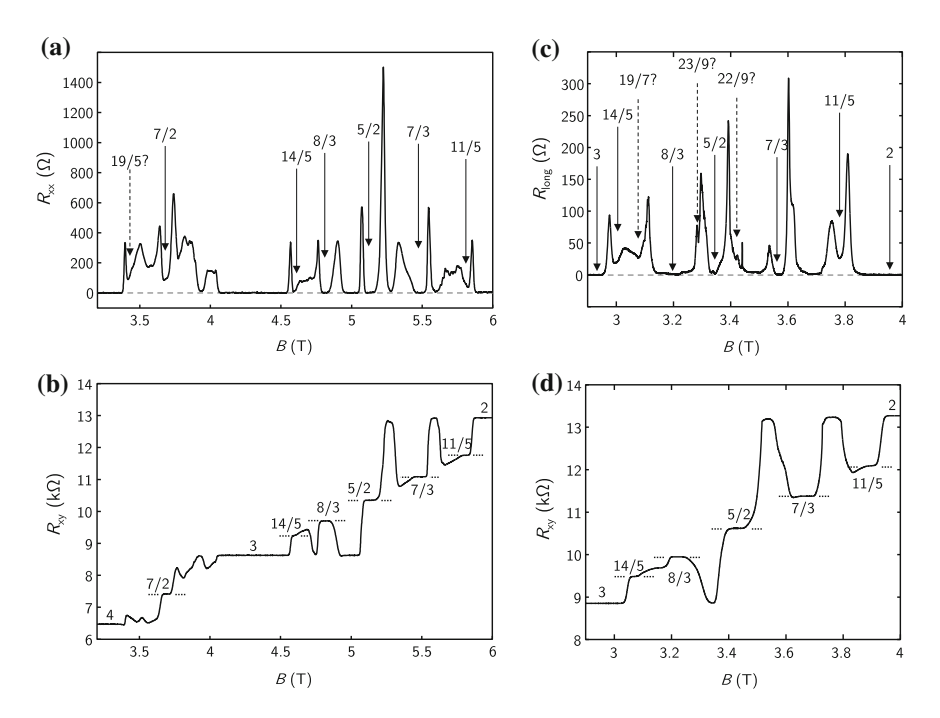


Fig. 3.6 Longitudinal and Hall resistance of two different high-mobility electron gases at $T_{\rm el} \approx 12$ –13 mK. The filling factors corresponding to minima in R_{xx} or plateaus in R_{xy} are indicated

with different filling factors [22–24]. In the simplest charge density wave picture, these density modulated phases appear as stripes or bubbles with a local filling factor higher or lower by one than the background filling factor [21]. The bubble phase in the bulk is insulating and localized by disorder. Hence the transport properties are determined by the integer filling factor of the background. In the second LL, the density modulated phases are believed to be one- or two electron or hole bubble phases [25, 26]. In the second LL, these bubble phases lead to a lower ground-state energy than FQH states at the corresponding filling factors. Hence FQH and density-modulated phases compete, explaining why less FQH states are observed here. In even higher LLs, the density-modulated phases are even more favorable compared to FQH states, explaining why FQH states are absent. We remark that in more realistic models of the density-modulated phases, quantum fluctuations have to be taken into account. In the Electron Liquid Crystal picture, this leads to a modified phase diagram of the density modulated phases [27]. For more details, we refer the reader to a review article by Fogler [21].

FQH states FQH states at $\nu=14/5, 8/3, 7/3$ and 11/5 are clearly observed in the measurements of Fig. 3.6a–d. Furthermore, a pronounced FQH state is observed at $\nu=5/2$. This even-denominator state obviously cannot be explained by a theory of non-interacting CFs, which predicts a compressible CF sea at $\nu=5/2$. In the following sections, we will discuss certain candidate wavefunctions that have been proposed for the FQH states in the second LL and their properties.

3.6.1 Candidate States for $\nu = 5/2$

The $\nu=5/2$ state has been discovered by Willett and coworkers [28] and has caused a lot of excitement among theorists and experimentalists since then. One reason lies in the fact that a state with quasiparticle excitations that possess non-Abelian statistics might be realized at $\nu=5/2$ [29, 30]. This property would make that state potentially interesting for topological quantum computing applications [31]. We will explore the implications of this possibility in more detail in Chap. 5.

The $\nu=5/2$ state is extremely fragile and is only observed in the best high mobility electron gases and at very low temperatures. We have already discussed in Chap. 2 how growth techniques can be optimized in order to maximize the energy gap of this state.

In the following, we will discuss the candidate wavefunctions that have been proposed for the $\nu=5/2$ state and some of their properties. In Chap. 6 we will review the most important experiments at $\nu=5/2$ and discuss which candidate wavefunctions are compatible with the experimental findings. An overview of the candidate wavefunctions at $\nu=5/2$ can be found in Table 3.2. Here, we quote the quasiparticle charge e^*/e and the Coulomb interaction parameter g that will be relevant for the quasiparticle tunneling experiments discussed later in this book (g is twice the scaling dimension of the quasiparticle creation and annihilation operators [32]). In a tunneling experiment, g describes the scaling of the quasiparticle tunneling

FF	State	e^*/e	g	n-A?	Edge modes	Spin-pol.	
$\nu = 5/2$	K = 8	1/4	1/8	No	$1\rho_{\rm D} + 2\rho_{\rm D}$	^↑ or ↑↓	
		1/2	1/2	No			
	MR Pf	1/4	1/4	Yes	$1\rho_{\rm D} + 1\psi_{\rm D} + 2\rho_{\rm D}$	$\uparrow \uparrow$	
		1/2	1/2	No			
	(3,3,1)	1/4	3/8	No	$2\rho_{\mathrm{D}} + 2\rho_{\mathrm{D}}$	↑ ↑ or ↑ ↓	
		1/2	1/2	No			
	(1,1,3)	1/4	≈3/8 ^a	No	$1\rho_{\rm D} + 1\tilde{\rho}_{\rm U} + 2\rho_{\rm D} \ (?)$	↑ ↑ or ↑ ↓	
		1/2	1/2 (?)	No			
	Pf	1/4	1/2	Yes	$1\rho_{\rm D} + 3\psi_{\rm U} + 2\rho_{\rm D}$	$\uparrow \uparrow$	
		1/2	1/2	No			
	SU(2) ₂	1/4	1/2	Yes	$1\rho_{\rm D} + 1\tilde{\rho}_{\rm D} + 1\psi_{\rm D} + 2\rho_{\rm D}$ (?)	$\uparrow \uparrow$	
		1/2	1/2	No			
	(3, 3, 1)	1/4	5/8	No	$1\rho_{\rm D} + 4\psi_{\rm U} + 2\rho_{\rm D}$	$\uparrow \uparrow$	
		1/2	1/2	No			
	<u>SU(2)</u> ₂	1/4	3/4	Yes	$1\rho_{\rm D} + 5\psi_{\rm U} + 2\rho_{\rm D}$	↑ ↑ (?)	
		1/2	1/2 (?)	No			
	Majorana-gapped edge-rec. Pf	1/4	1/2	Yes	$2\rho_{\rm D} + 1\psi_{\rm U} + 2\rho_{\rm D} \ (?)$	$\uparrow \uparrow$	
		1/2	1/2	No			
	Majorana-gapped	1/4	0.55-0.75	Yes	?	$\uparrow \uparrow$	
	Pf	1/2	0.5-0.7	No			

Table 3.2 Overview of the theoretically proposed parameter pairs g and e^*/e for $\nu = 5/2$, the proposed edge modes and the spin-polarization for different states. ('n-A' non-Abelian; taken from [32–36])

Question marks denote entries that could not (or not with full certainty) be identified from the literature

conductance g_{tun} as a function of the temperature via $g_{\text{tun}} \propto T^{2g-2}$. The relevant edge excitations, i.e. the edge excitations which are expected to be dominant in tunneling at low temperatures, are the edge excitations which possess the smallest g.

All candidate wavefunctions shown in Table 3.2 possess e/4 edge excitations, with g between 1/8 and 3/4. Furthermore, all candidate wavefunctions possess Abelian e/2 edge excitations, which have a scaling parameter g=0.5 (apart from the Majorana-gapped Anti-Pfaffian where g=0.5-0.7 and the Anti-SU(2)₂-state where we are not aware of the size of g for the e/2 excitations). Hence tunneling of e/2 quasiparticles might be present at low temperatures for all candidate wavefunctions with $g\geq 0.5$ for the e/4 quasiparticle excitations.

In the column "Edge modes", we specify the edge modes expected for each of the wavefunctions. Here, ρ_D denotes a downstream charge mode, which propagates

^aIn a gate-defined geometry [34]

in the direction expected in a simplified Landauer-Büttiker edge-state picture. ψ_D or ψ_U denote downstream or counterpropagating upstream Majorana Fermion modes and $\tilde{\rho}_D$ or $\tilde{\rho}_U$ denote electrically neutral Bosonic modes, propagating downstream or upstream. For example the Anti-Pfaffian state is expected to exhibit one downstream charge mode and three upstream Majorana Fermion modes (plus two downstream charge modes from the additional IQH edge channels). Finally, the rightmost column of Table 3.2 indicates if the corresponding state is spin-polarized ($\uparrow \uparrow$) or spin-unpolarized ($\uparrow \downarrow$). Some states may be both, spin-polarized or spin-unpolarized.

3.6.1.1 K = 8 State, Anti-K = 8 State

The K=8 state is a strong pairing state, where electrons first pair in Bosons of charge 2e and then condense in a Laughlin state [32, 37]. Here single-electron excitations are gapped and tunneling of single electrons in the $\nu=5/2$ edge is not possible at low energies [36]. The wavefunction is given as:

$$\Psi\left(\{z_i\}\right) = \prod_{i < j} \left(z_i - z_j\right)^8 e^{-\frac{1}{4}\sum_i |z_i|^2}$$
(3.26)

The particle-hole conjugate of this state, the anti-K=8 state does not exhibit a universal behavior in tunneling experiments [36]. Also, no quantized conductance at $5/2 \times e^2/h$ is expected at low temperatures and voltages where QP tunneling properties become relevant [36]. Hence the anti-K=8 state is most likely not of any practical relevance for the physics at $\nu=5/2$.

3.6.1.2 Moore-Read Pfaffian State, Anti-Pfaffian and Relatives

The probably most widely recognized state for $\nu = 5/2$ is the Pfaffian state, proposed by Moore and Read [29]. The reason for this is that it is the exact ground state for a three-body repulsive interaction [29] and that numerical studies strongly favor this state, or closely related states (see Sect. 6.2). The Moore-Read Pfaffian (MR Pf) state is a *p*-wave paired state of composite Fermions and is fully spin-polarized. The wavefunction can be written as [29]:

$$\Psi_{\text{Pf}}(\{z_i\}) = \text{Pf}\left(\frac{1}{z_i - z_j}\right) \prod_{i < j} (z_i - z_j)^2 e^{-\frac{1}{4}\sum_i |z_i|^2}$$
(3.27)

where the Pfaffian Pf (M_{ij}) of an antisymmetric $N \times N$ (N even) matrix M is defined by [29]:

$$Pf(M_{ij}) = \frac{1}{2^{N/2}(N/2)!} \sum_{\sigma \in S_N} sign(\sigma) \prod_{k=1}^{N/2} M_{\sigma(2k-1),\sigma(2k)}$$
(3.28)

which is the antisymmetrized sum over all pairs $\frac{1}{(z_i-z_j)}$ [30]. The anti-Pfaffian state [38, 39] is obtained from the MR Pf state by particle-hole conjugation. The anti-Pfaffian state is also spin-polarized and possesses edge excitations with non-Abelian statistics.

Edge reconstruction in a smooth confinement potential can change the edge properties of FQH states [40]. These states share the bulk properties with their parent state, but may possess different edge modes and show different signatures in a tunneling experiment. This leads for example to the edge-reconstructed Pfaffian state, which shares the bulk properties of the Pfaffian state but shows different edge modes [32].

It has been shown that an interaction involving charge transfer between edge modes can lead to an opening of a gap for a pair of left- and right-moving Majorana Fermion modes [32]. This leads to the Majorana-gapped edge-reconstructed Pfaffian state and the Majorana-gapped anti-Pfaffian state, which have different edge properties than Pfaffian and anti-Pfaffian states (see Table 3.2).

3.6.1.3 (3,3,1)-State, Anti-(3,3,1)-State

The (3,3,1)-state [41] is an Abelian candidate state for $\nu=5/2$. It exists as a spin-polarized and as a spin-unpolarized state, which share the same edge properties but are of a different physical origin [36]. The spin-unpolarized (3,3,1)-state at $\nu=5/2$ is an analog to the bilayer (3,3,1)-state originally proposed by Halperin [41]. Here, spin-up and spin-down electrons take the role of the electrons in the two different layers [36]. Halperin's (n,n,m)-wavefunction can be written as:

$$\Psi_{n,n,m} = \prod_{k < l} (z_k - z_l)^n \prod_{\alpha < \beta} (w_\alpha - w_\beta)^n \prod_{k,\alpha} (z_k - w_\alpha)^m \exp\left[-\frac{1}{4} \sum_{l,\alpha} \left(|z_l|^2 + |w_\alpha|^2 \right) \right]$$
(3.29)

where $z_k = x_k + iy_k$ and $w_\alpha = x_\alpha + iy_\alpha$ are the positions of the two flavors of electrons [34]. Hence in the case of the spin-unpolarized (3,3,1)-state, z_k and w_α denote coordinates of spin-up and spin-down electrons.

The spin-polarized (3,3,1)-state in contrast arises when charge 2e/3 quasiparticles, on top of a $\nu = 1/3$ Laughlin liquid, condense [36].

The particle-hole conjugate state, the anti-(3,3,1)-state is also a potential candidate for $\nu = 5/2$. However, here only the spin-polarized version has the correct filling factor $\nu = 5/2$ [36].

3.6.1.4 (1,1,3)-State

Very recently it was argued that the Abelian (1,1,3)-state is a possible candidate wavefunction for $\nu = 5/2$ and is in best agreement with the existing experimental results [34]. This state possesses a similar topological order as the (3,3,1)-state and is expected to show similar signatures in a tunneling experiment [34]. However,

in contrast to the (3,3,1)-state, it possesses a (Bosonic) counterpropagating neutral mode and is hence in agreement with experiments that found evidence for this (see Chap. 6). A wavefunction for the (1,1,3)-state can be constructed from (3.29), in analogy to the (1,1,2)-state which is believed to describe the spin-singlet state at $\nu=2/3$ [42]. With this, the following wavefunction is found for the (n,n,m)-state [34]:

$$\Psi_{n,n,m} = \hat{P} \exp \left[-\frac{1}{4} \sum_{l,\alpha} \left(|z_l|^2 + |w_{\alpha}|^2 \right) \right] \prod_{k < l} (\partial_{z_k} - \partial_{z_l})^{m-n} \prod_{\alpha < \beta} (\partial_{w_{\alpha}} - \partial_{w_{\beta}})^{m-n}$$

$$\times \prod_{k < l} (z_k - z_l)^m \prod_{\alpha < \beta} (w_{\alpha} - w_{\beta})^m \prod_{k,\alpha} (z_k - w_{\alpha})^m$$

where \hat{P} antisymmetrizes the wavefunction with respect to the flavor degree of freedom [34].

3.6.1.5 SU(2)₂ State, Anti-SU(2)₂ State

The $SU(2)_2$ state has been proposed by Blok and Wen [43, 44]. Here, electrons are split in three partons, a charge e/2 Fermion and two e/4 Fermions with respective filling factors one and two. For decoupled partons, the resulting wavefunction would simply be a product of three IQH wavefunctions [36]. However, an independent motion of the partons gives rise to unphysical degrees of freedom, which is resolved by demanding identical coordinates for the partons [43]. With this, the following wavefunction is found [32]:

$$\Psi(\{z_i\}) = [\chi_2(\{z_i\})]^2 \prod_{i < j} (z_i - z_j) e^{-\frac{1}{4} \sum_i |z_i|^2}$$
(3.30)

Here $\chi_2(\{z_i\})$ is the Fermion wavefunction of two filled LLs [32]. The anti-SU(2)₂ state has been treated in literature and is a possible candidate for $\nu=5/2$ (see Table 3.2). Here, the disorder-dominated particle-hole conjugate of the SU(2)₂ state was considered, as the non-equilibrated state does not exhibit universal physical properties [36].

3.6.2 Candidate States for $\nu = 7/3$ and $\nu = 8/3$

In the following, we will discuss different candidate wavefunctions for $\nu=7/3$ and 8/3. Possible states are (particle-hole conjugate) Laughlin states $(L_{1/3}, \overline{L}_{1/3})$, different (particle-hole conjugate) Bonderson-Slingerland states $(\overline{BS}_{2/3}, BS_{1/3}^{\psi}, BS_{2/3}, \overline{BS}_{1/3}^{\psi})$ or the four-clustered Read-Rezayi state $(RR_{k=4})$ and its particle-hole

FF	State	e^*/e	g	n-A?
$\nu = 7/3$	L _{1/3}	1/3	1/3	No
	BS _{2/3}	1/3	23/24	Yes
		1/3	1/3	No
	$BS^\psi_{1/3}$	1/3	17/24	Yes
	,	1/3	1/3	No
	$\overline{RR}_{k=4}$	1/6	1/3	Yes
$\nu = 8/3$	$\overline{L}_{1/3}$	1/3	2/3	No
		2/3	2/3	No
	BS _{2/3}	1/3	7/24	Yes
		1/3	2/3	No
		2/3	2/3	No
	$\overline{\mathrm{BS}}_{1/3}^{\psi}$	1/3	13/24	Yes
	,	1/3	2/3	No
		2/3	2/3	No
	$RR_{k=4}$	1/6	1/6	Yes

Table 3.3 Overview of the theoretically proposed parameter pairs g and e^*/e for different states at $\nu = 7/3$ and 8/3 ('n-A' non-Abelian; taken from [35])

conjugate $(\overline{RR}_{k=4})$. An overview of the edge modes of the candidate states is given in Table 3.3. We would like to stress that at $\nu=7/3$, only the tunneling of the lowest quasiparticle excitations is relevant, while for $\nu=8/3$, all candidate wavefunctions possess an $e^*/e=2/3$ edge mode with g=2/3, which thus might also lead to the observation of $e^*/e=2/3$ quasiparticle tunneling for a particle-hole conjugate Laughlin state.

3.6.2.1 (Particle-hole Conjugate) Laughlin State

The simplest explanation for the FQH states at $\nu=7/3$ and 8/3 would be a (particle-hole conjugate) Laughlin state, i.e. a $\nu=1/3$ or 2/3 state, residing on top of a completely filled LL. The wavefunction is the well-known Laughlin wavefunction (3.17). Numerical studies have indicated that $\nu=7/3$ and 8/3 might not be well described by this Laughlin wavefunction [45–48].

3.6.2.2 Bonderson-Slingerland States

The Haldane-Halperin hierarchy [14, 15] is used to construct hierarchical FQH states in the lowest Landau level. Here, the fundamental quasielectrons and quasiholes of a FQH state in the first Landau level themselves form a new FQH state. In a gen-

¹It should be noted that it is not clear whether this hierarchy is actually implemented in reality, as there are inconsistencies with experiment and theory, see for example [5].

eralized approach, Bonderson and Slingerland [49] showed that hierarchical states that are constructed over the Moore-Read Pfaffian state can reproduce all important filling factors of the second Landau level, hence creating a closed scheme that might comprise all the physics of the second Landau level. The Bonderson-Slingerland states are expected to be $p_x - ip_y$ paired and non-Abelian, like the MR Pf state. The most simple hierarchy wavefunctions are found by building on the I (vacuum) fusion channel of the fundamental quasielectrons and quasiholes of the Moore-Read Pfaffian state. Here, the wavefunctions can be written as composite Fermion construction [49]:

$$\psi_{\text{BS}_{\nu}} = \mathcal{P}_{\text{LLL}} \left[\text{Pf} \left(\frac{1}{z_i - z_i} \right) \chi_1^{2p+1} \chi_{\pm n} \right]$$
 (3.31)

where χ_n is the wave function of n filled Landau levels and \mathcal{P}_{LLL} is the projection onto the lowest LL. This can be written in good approximation as [49, 50]:

$$\psi_{\mathrm{BS}_{\nu}} = \psi_{1}^{\mathrm{(MR)}} \psi_{\frac{n}{2pn\pm 1}}^{\mathrm{(CF)}} \tag{3.32}$$

where $\psi_1^{(MR)}$ is the Bosonic $\nu=1$ MR Pf wavefunction and $\psi_{\frac{n}{2pn\pm 1}}^{(CF)}$ is the CF wavefunction at $\nu=\frac{n}{2pn\pm 1}$. The states $\overline{BS}_{2/3}$ and $BS_{2/3}$ are hence the respective candidates for $\nu=7/3$ and $\nu=8/3$.

Building on a fundamental quasihole and quasielectron gas with the ψ (Majorana Fermion) fusion channel, other hierarchical states (denoted as BS_{ν}^{ψ}) can be constructed [49]. Here, the candidate states for $\nu = 7/3$ and 8/3 are $BS_{1/3}^{\psi}$ and $\overline{BS}_{1/3}^{\psi}$.

3.6.2.3 Read-Rezayi State

In the k-clustered Read-Rezayi states (RR_k), clusters of k Anyons are expected to form effective Bosons and to condense in a liquid of filling factor $\nu = k/(k+2)$ [30, 51]. The k=2 Read-Rezayi state is identical to the Moore-Read Pfaffian state. The interest in this state is particularly large, as universal quantum computation might be possible here (for k=3) [52].

The RR_{k=4}-state and its particle-hole conjugate, the $\overline{RR}_{k=4}$ -state are potential candidates for the wavefunctions at $\nu=7/3$ and 8/3. Here we expect $e^*/e=1/6$ quasiparticle excitations to show up in a tunneling experiment.

3.6.3 Candidate States for $\nu = 12/5$

The $\nu=12/5$ state is even more fragile than the $\nu=5/2$ state [53–55] and has not been investigated by us. A measurement where the $\nu=12/5$ state is slightly visible in one of our samples is shown in Fig. 3.7. Due to the potentially interesting physics

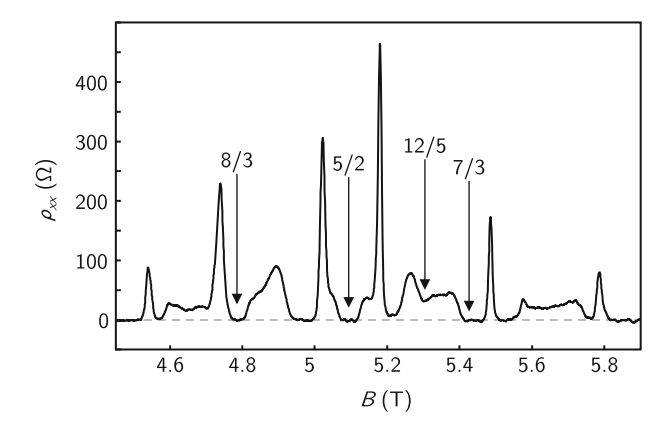


Fig. 3.7 Longitudinal resistivity of a high-mobility Hall-bar, measured at an electronic temperature $T_{\rm el} \approx 12$ –13 mK. The $\nu = 12/5$ state (identified by the *B*-field position) is weakly visible as a dip in ρ_{xx}

involved, we nevertheless would like to discuss possible ground states. At $\nu=12/5$, numerical calculations indicate that a non-Abelian Read-Rezayi state [30, 56] or a Bonderson-Slingerland state [50] might be realized at this filling factor, making it even more interesting for topological quantum computing than $\nu=5/2$ due to the potential possibility of universal quantum computation.

Potential candidates for $\nu=12/5$ are an Abelian, hierarchical Haldane-Halperinstate (HH_{2/5}) [14, 15], two different non-Abelian Bonderson-Slingerland states BS_{2/5} and $\overline{\rm BS}_{3/5}^{\psi}$, and the non-Abelian particle-hole conjugate Read-Rezayi 3-clustered state ($\overline{\rm RR}_{k=3}$). The respective quasiparticle excitations and their parameters are cited in Table 3.4.

Table 3.4 Overview of the theoretically proposed parameter pairs g and e^*/e for different states	ates
at $\nu = 12/5$ ('n-A' non-Abelian; taken from [35])	

FF	State	e^*/e	g	n-A?
$\nu = 12/5$	HH _{2/5}	1/5	3/5	No
		2/5	2/5	No
	BS _{2/5}	1/5	9/40	Yes
		1/5	3/5	No
		2/5	2/5	No
	$\overline{\mathrm{BS}}_{3/5}^{\psi}$	1/5	19/40	Yes
		1/5	3/5	No
		2/5	2/5	No
	$\overline{RR}_{k=3}$	1/5	2/5	Yes
		2/5	2/5	No

3.7 Conclusion 43

3.7 Conclusion

In this chapter, we have given a review of the basics of quantum Hall physics. We have discussed the properties of the FQH states in the second LL, especially their interaction parameters that become important in tunneling experiments, their edge modes and their spin-polarization. These are the most important characteristics that allow a comparison with experiments. In Chap. 6 we will give an overview of experiments at $\nu=5/2$ by other authors. There, we will compare the experimental outcomes to the properties that we have discussed here. In Chap. 11, we will discuss quasiparticle tunneling experiments performed by us, which then are compared to the candidate states reviewed in the present chapter.

References

- 1. E.H. Hall, Am. J. Math. 2, 287 (1879). doi:10.2307/2369245
- K.v. Klitzing, G. Dorda, M. Pepper, Phys. Rev. Lett. 45, 494 (1980). doi:10.1103/PhysRevLett. 45.494
- D.C. Tsui, H.L. Stormer, A.C. Gossard, Phys. Rev. Lett. 48, 1559 (1982). doi:10.1103/ PhysRevLett.48.1559
- T. Ihn, Semiconductor Nanostructures: Quantum States and Electronic Transport (OUP, Oxford, 2010)
- 5. J.K. Jain, *Composite Fermions* (Cambridge University Press, Cambridge, 2007)
- 6. Z.F. Ezawa, Quantum Hall Effects: Field Theoretical Approach and Related Topics (World Scientific, Singapore, 2008)
- 7. M. Furlan, Phys. Rev. B 57, 14818 (1998). doi:10.1103/PhysRevB.57.14818
- 8. B.I. Halperin, Phys. Rev. B 25, 2185 (1982). doi:10.1103/PhysRevB.25.2185
- 9. M. Buttiker, IBM J. Res. Dev. 32, 317 (1988). doi:10.1147/rd.323.0317
- 10. R. Landauer, IBM J. Res. Dev. **32**, 306 (1988). doi:10.1147/rd.323.0306
- 11. A.D. Stone, A. Szafer, IBM J. Res. Dev. 32, 384 (1988). doi:10.1147/rd.323.0384
- W. Pan, H.L. Stormer, D.C. Tsui, L.N. Pfeiffer, K.W. Baldwin, K.W. West, Phys. Rev. Lett. 88, 176802 (2002). doi:10.1103/PhysRevLett.88.176802
- 13. R.B. Laughlin, Phys. Rev. Lett. **50**, 1395 (1983). doi:10.1103/PhysRevLett.50.1395
- 14. F.D.M. Haldane, Phys. Rev. Lett. **51**, 605 (1983). doi:10.1103/PhysRevLett.51.605
- 15. B.I. Halperin, Phys. Rev. Lett. **52**, 1583 (1984). doi:10.1103/PhysRevLett.52.1583
- 16. J.K. Jain, Lecture Notes (International Summer School, Bangalore, 2011)
- 17. J.K. Jain, Phys. Rev. Lett. 63, 199 (1989). doi:10.1103/PhysRevLett.63.199
- W. Pan, H.L. Stormer, D.C. Tsui, L.N. Pfeiffer, K.W. Baldwin, K.W. West, Phys. Rev. Lett. 90, 016801 (2003). doi:10.1103/PhysRevLett.90.016801
- W. Pan, H.L. Stormer, D.C. Tsui, L.N. Pfeiffer, K.W. Baldwin, K.W. West, Int. J. Mod. Phys. B 16, 2940 (2002). doi:10.1142/S0217979202013250
- N. Deng, A. Kumar, M.J. Manfra, L.N. Pfeiffer, K.W. West, G.A. Csáthy, Phys. Rev. Lett. 108, 086803 (2012). doi:10.1103/PhysRevLett.108.086803
- M.M. Fogler, arXiv:cond-mat/0111001 (2001), pp. 98–138, in *High Magnetic Fields: Applications in Condensed Matter Physics and Spectroscopy*, eds. by C. Berthier, L.-P. Levy, G. Martinez (Springer, Berlin, 2002)
- A.A. Koulakov, M.M. Fogler, B.I. Shklovskii, Phys. Rev. Lett. 76, 499 (1996). doi:10.1103/ PhysRevLett.76.499
- M.M. Fogler, A.A. Koulakov, B.I. Shklovskii, Phys. Rev. B 54, 1853 (1996). doi:10.1103/ PhysRevB.54.1853

- 24. M.M. Fogler, A.A. Koulakov, Phys. Rev. B 55, 9326 (1997). doi:10.1103/PhysRevB.55.9326
- M.O. Goerbig, P. Lederer, C.M. Smith, Phys. Rev. B 69, 115327 (2004). doi:10.1103/ PhysRevB.69.115327
- M.O. Goerbig, P. Lederer, C.M. Smith, Phys. Rev. B 68, 241302 (2003). doi:10.1103/ PhysRevB.68.241302
- 27. E. Fradkin, S.A. Kivelson, Phys. Rev. B **59**, 8065 (1999). doi:10.1103/PhysRevB.59.8065
- R. Willett, J.P. Eisenstein, H.L. Störmer, D.C. Tsui, A.C. Gossard, J.H. English, Phys. Rev. Lett. 59, 1776 (1987). doi:10.1103/PhysRevLett.59.1776
- 29. G. Moore, N. Read, Nucl. Phys. B 360, 362 (1991). doi:10.1016/0550-3213(91)90407-O
- 30. N. Read, E. Rezayi, Phys. Rev. B 59, 8084 (1999). doi:10.1103/PhysRevB.59.8084
- C. Nayak, S.H. Simon, A. Stern, M. Freedman, S.D. Sarma, Rev. Mod. Phys. 80, 1083 (2008). doi:10.1103/RevModPhys.80.1083
- 32. B.J. Overbosch, X.G. Wen. arXiv:0804.2087 [cond-mat] (2008)
- 33. D.E. Feldman, F. Li, Phys. Rev. B 78, 161304 (2008). doi:10.1103/PhysRevB.78.161304
- 34. G. Yang, D.E. Feldman. arXiv:1406.2263 [cond-mat] (2014)
- W. Bishara, P. Bonderson, C. Nayak, K. Shtengel, J.K. Slingerland, Phys. Rev. B 80, 155303 (2009). doi:10.1103/PhysRevB.80.155303
- 36. G. Yang, D.E. Feldman, Phys. Rev. B 88, 085317 (2013). doi:10.1103/PhysRevB.88.085317
- 37. X.G. Wen, A. Zee, Phys. Rev. B 46, 2290 (1992). doi:10.1103/PhysRevB.46.2290
- M. Levin, B.I. Halperin, B. Rosenow, Phys. Rev. Lett. 99, 236806 (2007). doi:10.1103/ PhysRevLett.99.236806
- S.-S. Lee, S. Ryu, C. Nayak, M.P.A. Fisher, Phys. Rev. Lett. 99, 236807 (2007). doi:10.1103/ PhysRevLett.99.236807
- C. d. C. Chamon and X. G. Wen, Phys. Rev. B 49, 8227 (1994). doi:10.1103/PhysRevB.49.
 8227
- 41. B.I. Halperin, Helv. Phys. Acta **56**, 75 (1983). doi:10.5169/seals-115362
- I.A. McDonald, F.D.M. Haldane, Phys. Rev. B 53, 15845 (1996). doi:10.1103/PhysRevB.53.
 15845
- 43. X.G. Wen, Phys. Rev. Lett. 66, 802 (1991). doi:10.1103/PhysRevLett.66.802
- 44. B. Blok, X. Wen, Nucl. Phys. B 374, 615 (1992). doi:10.1016/0550-3213(92)90402-W
- 45. A. Wójs, Phys. Rev. B **63**, 125312 (2001). doi:10.1103/PhysRevB.63.125312
- A.C. Balram, Y.-H. Wu, G.J. Sreejith, A. Wójs, J.K. Jain, Phys. Rev. Lett. 110, 186801 (2013). doi:10.1103/PhysRevLett.110.186801
- A.H. MacDonald, S.M. Girvin, Phys. Rev. B 33, 4009 (1986). doi:10.1103/PhysRevB.33.
 4009
- 48. N. d'Ambrumenil, A.M. Reynolds, J. Phys. C: Solid State Phys. **21**, 119 (1988). doi:10.1088/0022-3719/21/1/010
- P. Bonderson, J.K. Slingerland, Phys. Rev. B 78, 125323 (2008). doi:10.1103/PhysRevB.78.
 125323
- P. Bonderson, A.E. Feiguin, G. Möller, J.K. Slingerland, Phys. Rev. Lett. 108, 036806 (2012). doi:10.1103/PhysRevLett.108.036806
- 51. A. Stern, Ann. Phys. **323**, 204 (2008). doi:10.1016/j.aop.2007.10.008
- 52. M. Freedman, A. Kitaev, M. Larsen, Z. Wang, Bull. Am. Math. Soc. **40**, 31 (2003). doi:10. 1090/S0273-0979-02-00964-3
- J.S. Xia, W. Pan, C.L. Vicente, E.D. Adams, N.S. Sullivan, H.L. Stormer, D.C. Tsui, L.N. Pfeiffer, K.W. Baldwin, K.W. West, Phys. Rev. Lett. 93, 176809 (2004). doi:10.1103/PhysRevLett. 93.176809

References 45

 W. Pan, J.S. Xia, H.L. Stormer, D.C. Tsui, C. Vicente, E.D. Adams, N.S. Sullivan, L.N. Pfeiffer, K.W. Baldwin, K.W. West, Phys. Rev. B 77, 075307 (2008). doi:10.1103/PhysRevB. 77.075307

- A. Kumar, G.A. Csáthy, M.J. Manfra, L.N. Pfeiffer, K.W. West, Phys. Rev. Lett. 105, 246808 (2010). doi:10.1103/PhysRevLett.105.246808
- 56. E.H. Rezayi, N. Read, Phys. Rev. B 79, 075306 (2009). doi:10.1103/PhysRevB.79.075306

Chapter 4 Physics at the Edge

Abstract We review the most important theoretical findings about edge states in the IQH and FQH regime. In the first part of this chapter, we discuss the spatial structure of edge states, which is strongly influenced by interaction effects at the edge. Then we discuss a theoretical approach developed by Wen, which describes excitations of a FQH edge as a chiral Luttinger liquid. Finally we discuss the experimental signatures of tunneling across a QPC in a chiral Luttinger liquid.

4.1 Introduction

God made the bulk; surfaces were invented by the devil.

Wolfgang Pauli

The behavior of most physical systems can be understood more easily, if the system is assumed to be infinitely large and if edge or surface effects are neglected. In contrast, edge effects are crucial for our understanding of the quantum Hall effect. Furthermore, edges reflect the properties of the bulk FQH state and allow us to probe its properties in transport measurements. In the following, we will give a short review about edge properties of quantum Hall systems. We start by theories which discuss the spatial behavior of density distribution and energy levels, which we refer to as "spatial edge state picture". Then we discuss the theory of the chiral Luttinger liquid by Wen. This picture tells us something about the dynamical properties of the edge, which will become especially important for the quasiparticle tunneling experiments performed by us (Chap. 11). We refer to those theories as "energetic edge state picture".

4.2 Spatial Edge State Picture

Top-gate defined structures on 2DEGs provide a smooth confinement potential which defines the edge of a FQH liquid. In a realistic system, interactions at the edge strongly change the properties of the edge, compared to the properties of the bulk.

In this section, we discuss the spatial structure of edge states in the IQH and FQH regimes. This structure will be of importance for the experimental results discussed later in this book, especially Chap. 10. For further details we refer the reader to the comprehensive review article by Deviatov [1].

4.2.1 Self-consistency at the Edge

The Landauer-Büttiker edge state picture which we have discussed in the preceding chapter does not take electron-electron interaction into account and is hence not sufficient for describing the edge structure of a realistic sample. In this picture, LL energies are lifted adiabatically towards the edge (Fig. 4.1a). Each LL hosts $n_{\rm L} = 2 \frac{|\vec{e}|B}{h}$ electrons, resulting in jumps of the density by $n_{\rm L}$ whenever a LL intersects the Fermi energy (Fig. 4.1b). Such discontinuities in the density are energetically very unfavorable in reality, where electron-electron interaction leads to screening and a self-consistent potential and density distribution at the edge. The self-consistent picture has been pioneered by Chklovskii et al. [2]. They investigated the problem in a mean-field approximation, including electron-electron interaction. Instead of the one-dimensional intersections of the LL energies with the Fermi energy as in Fig. 4.1a, they found strips of finite width where the Landau level is pinned to the Fermi energy (Fig. 4.1d). In those strips, the potential gradient is well screened by the extended states [3] and the density increases smoothly towards the center of the sample (Fig. 4.1e). We refer to those regions as "compressible", as unoccupied extended states exist at the Fermi energy. In contrast, in the incompressible regions, no extended states lie at the Fermi energy. As a result, potential fluctuations are no longer screened here, leading to a varying confinement potential, but constant electron density (Fig. 4.1e). In this picture, the density distribution in the QH regime is only slightly changed compared to the density distribution at zero magnetic field (dashed line in Fig. 4.1e).

Let us now turn to the question of the current distribution at the edge. For a self-consistent edge channel picture in equilibrium, there are two contributions to the current [4]. The first contribution arises due to regions with a finite potential gradient, like incompressible stripes at the edge and around localized states [1]. Due to the finite electron group velocity, this leads to dissipation-free paramagnetic currents [1]. A second contribution arises from the density gradient in the compressible stripes, leading to diamagnetic currents that flow in the opposite direction (Fig. 4.1f) [4]. In an equilibrium situation where no bias is applied to the system, the equilibrium currents at both edges of the sample exactly cancel out, due to the different sign of density and potential gradients [1, 5]. When a bias is applied to either source or drain of a Hall-bar, the electrochemical potential of one edge is lifted with respect to the electrochemical potential of the other edge. When the electrochemical potential on one side is lifted by $\Delta\mu$, the width of compressible regions decreases, while incompressible regions become wider [1] (see Fig. 4.2a, b). By changing the relative width of these both regions with inverse current directions (see Fig. 4.2c), the total current on both sides

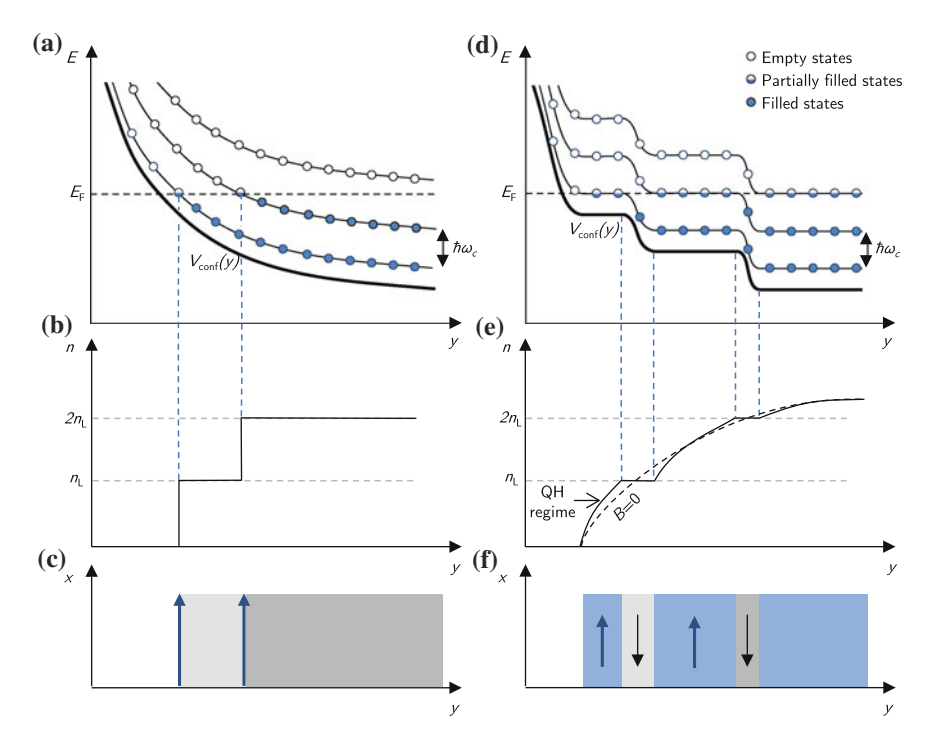


Fig. 4.1 LL energies for non-interacting electrons (**a**) and in a self-consistent picture with electronelectron interaction (**d**). In the first case, edge states are defined by intersections of the LLs with the Fermi energy. This leads to jumps in the electron density at the edge (**b**) and one-dimensional chiral edge channels with dissipationless current flow (**c**). In the second case, the system separates into compressible and incompressible regions of finite width, leading to an only slight change of the density distribution, compared to the density distribution at B = 0 (**e**). In this picture, potentialand density gradients drive equilibrium currents in both regions (**f**). Adapted from [2, 3].

of the Hall-bar is no longer equal and a net current flow ("excess current") has been induced. It turns out that the value of this current is exactly given by the difference of the electrochemical potential on both edges [1, 5], multiplied with e/h. This explains why the Landauer-Büttiker formalism can still be successfully applied. Regarding the spatial distribution of the excess current, we quote [1]: "Therefore, the "eternal" question of whether the edge current flows through compressible or incompressible strips can be answered as follows: the current flows through any area with a gradient of the potential, while the nonequilibrium ("excess") current flows along the boundary between compressible and incompressible areas and can be attributed to any of them, depending on whether the areas are considered before or after introducing nonequilibrium conditions." We note that we have only discussed edge currents and neglected possible bulk current contributions (see [6] for an overview).

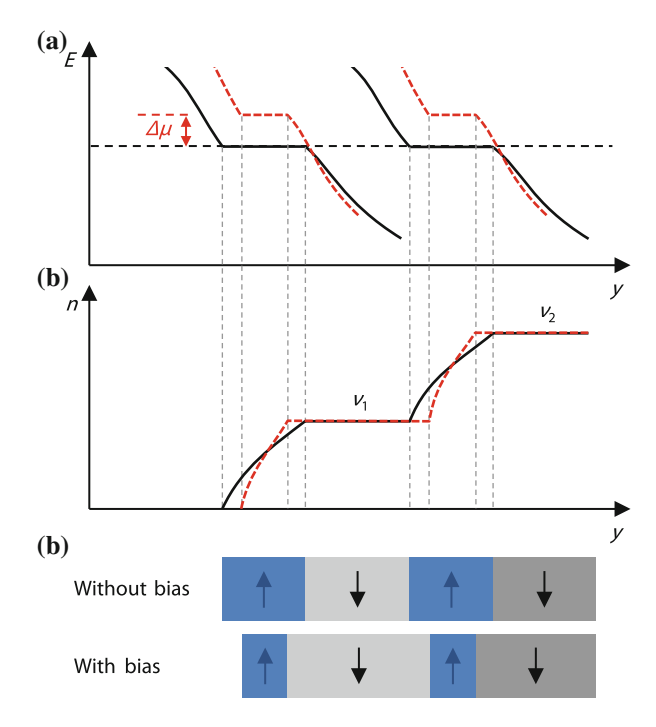


Fig. 4.2 a Schematic LL energies at the edge in equilibrium (*black*) and after varying the electrochemical potential by $\Delta\mu$ (*dashed red*). When the electrochemical potential is lifted, the width of the compressible regions decreases while the width of incompressible regions increases. This leads to a redistribution of the density at the edge (b). c Schematic distribution of the equilibrium current with and without an applied bias $\Delta\mu$. An effective "excess" current is created due to the change in the width of compressible and incompressible regions

After having clarified these details, we would like to use the following convention in the rest of this book: if we talk about an "edge state", we are referring to a compressible region.

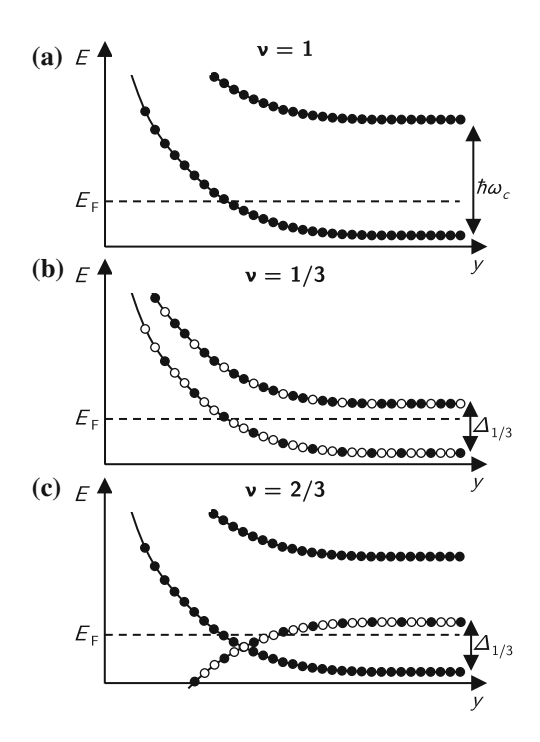
4.2.2 FQH Edge States

Many concepts which apply to the edge states in the IQH regime have been extended to the FQH regime. We will start with the simplest case, a very sharp confinement potential at the edge. As it turned out, this case is not satisfied in most realistic systems. In reality, a description by a smooth confinement potential, leading to the formation of alternating compressible and incompressible strips like in the IQH regime, is more appropriate. Finally we will discuss edge state pictures which are based on the composite Fermion theory.

4.2.2.1 Steep Confinement Potential

MacDonald has investigated edge states in the FQH regime [7] in a situation that is believed to correctly describe the system with a steep confinement potential [8]. Similar to the Landauer-Büttiker picture, an edge state is defined by the intersection of an energy level with the Fermi energy (Fig. 4.3). For the FQH states with $\nu = \frac{1}{m}$, a similar construction as in the IQH regime can be applied. While adding an electron increases the area of the QH liquid in order to enclose one additional flux quantum for $\nu = 1$, it increases in order to enclose m additional flux quanta for $\nu = \frac{1}{m}$. In analogy to a LL this can be symbolized by an energy level where (for $\nu = 1/3$) every third angular momentum state is occupied (Fig. 4.3b). Similar to the IQH case, the nonequilibrium current I in this case can be written as [1]: $I = \frac{e^*}{\hbar} \Delta \mu$ where $e^* = e/m$ and $\Delta \mu$ is the potential difference between the edges. For more complicated states, this construction is less straightforward. The example of the $\nu = 2/3$ edge is shown in Fig. 4.3c. This state is obtained by particle-hole inversion of the $\nu = 1/3$ edge state, i.e. by adding

Fig. 4.3 Edge states for v = 1, 1/3 and 2/3 for a steep confinement potential. The v = 2/3 edge state is constructed by adding a v = 1/3 droplet of holes to a filled LL spin branch of electrons. In this picture, the spin degeneracy has been neglected. Adapted from [7]



a droplet of holes with $\nu = 1/3$ to a $\nu = 1$ IQH edge state.¹ In such a construction with N branches, the Hall conductance was found to be: $G_{\rm H} = \frac{e^2}{h} \sum_{i=1}^{N} f_i$ [7] where $f_i = 1/m_i$. This approach allows the application of the Landauer-Büttiker formalism to "simple" FQH states [7].

4.2.2.2 Smooth Confinement Potential

A more realistic smooth edge potential has been considered by Beenakker [12] and Chang [13]. Here, the density towards the edge decreases slowly. Given that the change of the confinement potential over the magnetic length is small compared to the energy gaps of the FQH states [3], a sequence of alternating compressible and incompressible stripes (similar to the picture of Chklovskii et al. [18]) may form. In this case, the incompressible regions possess constant fractional filling factors ν_1, ν_2, \ldots When a bias is applied to the system and the chemical potential is changed by $\Delta \mu$, the electron density between the incompressible regions with filling factors ν_1 and ν_2 changes by Δn . Beenakker showed that the current contribution resulting from this change in density only depends on the adjacent filling factors and is independent of the details of the edge. It is given by:

$$I = -\frac{|e|}{h} \Delta \mu \Delta \nu \tag{4.1}$$

where $\Delta \nu = \nu_2 - \nu_1$ is the difference of the filling factors of two adjacent incompressible regions. This allows a generalization of the edge channel picture of Büttiker to a general situation where only the individual filling factors of the incompressible regions at the edge have to be known.

4.2.2.3 Composite Fermion Picture of Edge States

Edge states in the lowest LL can be interpreted in terms of composite Fermion models [14–19]. In the following, we will follow the argumentation of [18, 19]. Here, we discuss the system shown schematically in Fig. 4.4, where a smooth confinement potential U(y) defines the edge. For a sufficiently smooth potential, the electron density is gradually reduced towards the edge and alternating compressible and incompressible stripes are formed [12]. In a CF picture with 2p flux quanta per electron, the (fractional) bulk filling factor v_b can be written as: $v_b = \frac{v_b^*}{2pv_b^*+1}$, where v_b^* is the CF filling factor in the bulk. At the edge, multiple incompressible regions with fractional filling factors may be formed. For simplicity we consider the case,

¹This edge structure would be expected to exhibit nonuniversal conductance. Later [9–11] it was argued that the interaction between the counterpropagating edge states leads to the formation of a downstream charged mode and an upstream neutral mode, resolving the problem of non-universal conductance.

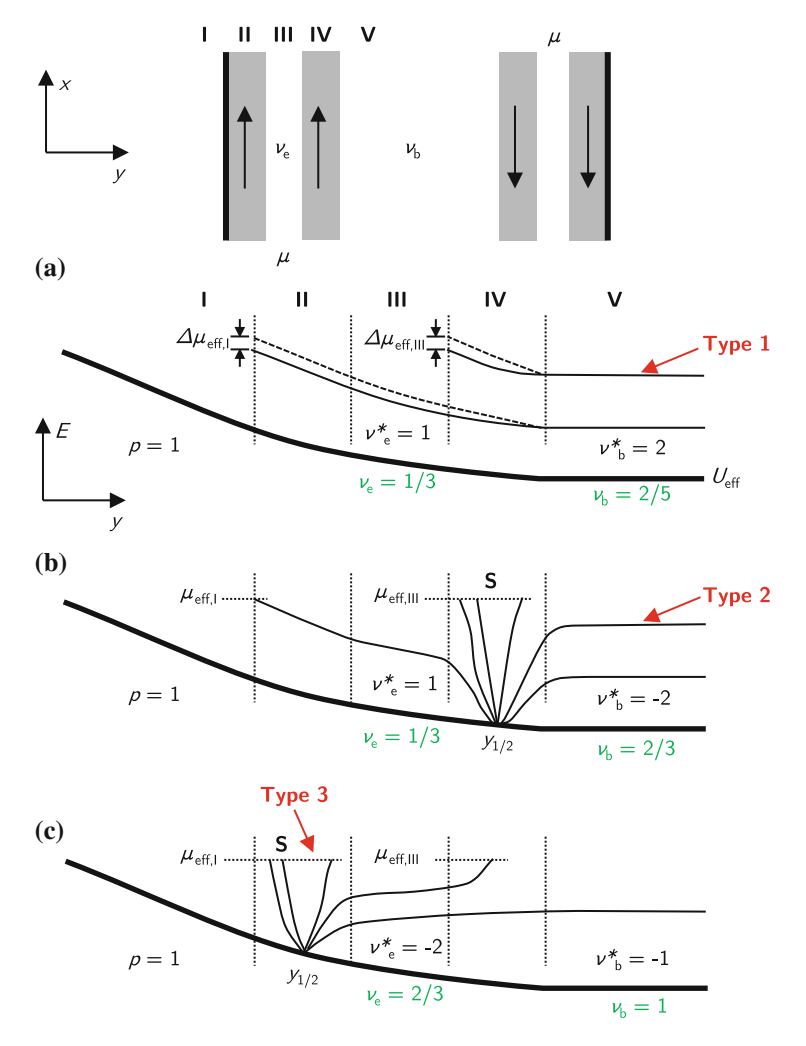


Fig. 4.4 CF energy levels for different filling factors, at the edge of the sample shown on *top*. Incompressible bulk and edge regions (III and V) are separated from each other and the edge by compressible regions (II and IV). Electron and CF filling factors in bulk (ν_b and ν_b^*) and edge (ν_e and ν_e^*) are indicated in (**a–c**). "S" denotes silent edge modes. Adapted from [18]

where only one incompressible region at the edge is defined (region III in Fig. 4.4), with a filling factor $\nu_e = \frac{\nu_e^*}{2\rho\nu_e^*+1}$, where ν_e^* is the corresponding CF filling factor. This region is separated from bulk and edge by compressible regions (regions II and IV in Fig. 4.4). Within these compressible regions, the density drops towards the edge, while the density is constant in incompressible regions.

In a mean-field theory approach, CFs experience an effective magnetic field $B^* = B - 2p\phi_0 n_s$ and an effective electric field $\mathbf{E}^* = \frac{1}{e}\nabla U + \langle \mathbf{v}\rangle \times 2p\phi_0 n_s \hat{z}$ [18], where

 $\langle \mathbf{v} \rangle$ is the average drift velocity. With this, the effective CF potential can be written as $U_{\text{eff}} = U(y) + 2p\phi_0 \int_y dI$ and the non-interacting CF energies in incompressible regions are given by Sim et al. [18]:

$$E_{\nu^*} = \left(\nu^* + \frac{1}{2}\right)\hbar\omega_c^* + U_{\text{eff}} \tag{4.2}$$

where $\omega_c^* = \frac{|eB^*|}{m_{CF}^*}$.

An example of a simple situation is shown in Fig. 4.4a. Here, bulk and edge CF filling factors are $v_b^* = 2$ and $v_e^* = 1$, corresponding to $v_b = 2/5$ and $v_e = 1/3$. Towards the edge, the effective CF potential rises until the CF energy levels intersect the effective CF electrochemical potential μ_{eff} in the compressible regions.

This picture does not hold whenever the effective magnetic field B^* changes sign, i.e. when a position $y_{1/2p}$ with a local filling factor $v = \frac{1}{2p}$ exists in a compressible region at the edge [18]. In the following, we will restrict the discussion only to cases where p=1, i.e. a CF picture with two flux quanta per electron. At $y_{1/2}$, $E_{v^*} = U_{\rm eff}$ is found due to the diverging CF effective mass [16, 17, 19]. Hence at those positions, a whole Landau fan of CF energy levels emanates from the CF potential. A situation where this occurs is shown in Fig. 4.4b. Here we have $v_b^* = -2$. Hence B^* in the bulk points in the inverse direction of the external magnetic field. Towards the edge, the density is reduced in the neighboring compressible region (IV in Fig. 4.4). Here, a position with a local filling factor v=1/2 exists, from which many CF energy levels emanate (marked by "S" in Fig. 4.4b, c). In the incompressible region III, density is again constant and v<1/2, corresponding to a positive effective magnetic field B^* . Here an example with $v_e^*=1$ is shown. This case corresponds to bulk and edge filling factors $v_b=2/3$ and $v_e=1/3$.

Overall, three different types of CF modes appear in this picture [16, 17, 19]: the first type of CF modes ("Type 1" in Fig. 4.4) corresponds to $\nu^* > 0$, i.e. a positive effective magnetic field $B^* > 0$. Towards the edge, the electron density and hence ν^* are reduced and the energy levels corresponding to the type 1 modes are bent up. In contrast, "type 2" CF modes correspond to $\nu^* < 0$, i.e. an effective magnetic field oriented antiparallel to the external field: $B^* < 0$. Here, the energy levels towards the edge are bent down, until $\nu = 1/2$, where they emanate from the effective CF potential $U_{\rm eff}$. The "type 3" modes correspond to a whole CF Landau fan emanating from $U_{\rm eff}$ at positions of the edge $y_{1/2}$, where $\nu = 1/2$. At $y_{1/2}$, $\mu_{\rm eff} - U_{\rm eff}(y)$ depends only on the local electron density [16], which is fixed. Hence we have $dU_{\rm eff}(y_{1/2}) = d\mu_{\rm eff}$ [18], which means that type 3 modes do not contribute any excess current. These modes are called "silent modes" and can be interpreted as the neutral modes that we have mentioned earlier.

Let us now look at the current carried by the CF modes in this model. It has been shown that the propagation direction of the CF edge states is equal to the propagation direction for example expected in a simple Büttiker edge state picture [16, 17]. For this, many-body effects like the divergence of the effective CF mass at $\nu = 1/2$ have to be taken into account, which has not been done in the earlier approaches of

[14, 15]. When the electrochemical potential of the system is changed by $\Delta\mu$, this leads to an effective change of the effective CF electrochemical potential $\Delta\mu_{\rm eff}$. It turns out that the current change ΔI_k , in between two incompressible regions with filling factors ν_k and ν_{k+1} , can be written as [18]:

$$\Delta I_k = -\frac{|e|}{h} \Delta \nu_k \Delta \mu \tag{4.3}$$

where $\Delta \nu_k = \nu_{k+1} - \nu_k$, in agreement with the result of Beenakker for the smooth edge (see preceding section). This allows a generalization of the Landauer-Büttiker formalism, where we can write [18]: $G = \frac{e^2}{h} \sum_k \Delta \nu_k \mathcal{T}_k$, where \mathcal{T}_k is the fraction of the current change ΔI_k that is transmitted.

4.3 Energetic Edge State Picture

In the last section, we have discussed edge state pictures that may for example explain qualitatively the substructure of the edge in a QPC. However, this description does not allow quantitative predictions about the dynamical properties of the edges, like the tunneling properties. In the following, we will give a short review of the chiral Luttinger liquid model developed by Wen [20–22] and Stone [23]. At the end of this Chapter, we will discuss the signatures of a chiral Luttinger liquid in QPC tunneling experiments. The review in this section will mainly follow references [24–28].

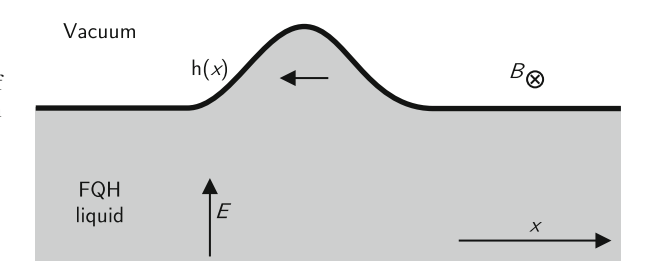
4.3.1 Hydrodynamic Theory

The dynamical properties of a FQH liquid can be found from a hydrodynamical approach developed by Wen [29]. Here, a droplet of a FQH liquid is investigated. In the bulk, low-energetic excitations are not allowed, as the FQH state is gapped. In contrast, at the edge of the droplet, the degeneracies of the LLs are lifted and excitations are possible, as the edge becomes gapless. The FQH droplet is confined by a confinement potential $V_{\rm conf}$, giving rise to an electric field E. The low-lying excitations of this liquid to not change the overall charge of the droplet and correspond to deformations of its boundary [25]. A corresponding situation is shown in Fig. 4.5. Here, the function h(x) parametrizes the edge, such that the density of the droplet can be written as: $\rho(x, y) = \Theta(h(x) - y)n_s$, leading to $\rho(x) = n_s h(x)$ by integration [26].

A density wave propagates with a velocity $v \propto \frac{E}{B}$ due to the Lorentz force and satisfies the wave equation: $\partial_t \rho(x,t) - v \partial_x \rho(x,t) = 0$.

Fig. 4.5 Edge of a FQH droplet. The function h(x) describes the displacement of the edge from its equilibrium position. Adapted from [26]

56



The classical Hamiltonian for such a situation can be written as [29]:

$$H = \int dx \frac{1}{2} eh(x)\rho(x)E = \frac{\pi\hbar v}{v} \int dx \rho^{2}(x)$$
 (4.4)

where $v = \frac{E}{B}$ and $v = \frac{n_S h}{eB}$. In Fourier space this corresponds to the classical Hamiltonian [25]:

$$H = \frac{2\pi}{\nu} \hbar \nu \sum_{k>0} \rho_k \rho_{-k} \tag{4.5}$$

The full theory of the edge excitations can be constructed by identifying the canonical coordinates and momenta: $q_k \equiv \rho_k$ and $\pi_k \equiv -\frac{2\pi i}{\nu k}\rho_{-k}$ for which the Hamiltonian equations hold: $\dot{q}_k = \frac{\partial H}{\partial \pi_k}$ and $\dot{\pi}_k = -\frac{\partial H}{\partial q}$ [25]. The canonical coordinates and momenta satisfy commutation relations $[q_k, \pi_{k'}] = i\hbar \delta_{k,k'}$ and the classical Hamiltonian can be written as: $H = iv \sum_{k>0} q_k \pi_k$ [24].

Hence the "phonon operators" ρ_k satisfy the commutation relations [25]:

$$[\rho_k, \rho_{k'}] = \frac{\nu}{2\pi} k \delta_{k+k',0} \tag{4.6}$$

With this, we have constructed a theory of electrically neutral excitations where the overall charge of the FQH droplet is not changed.

Charged excitations Now we would like to construct charged excitations of the system, for the case of the most simple FQH states at v = 1/m. Apart from electrons, we expect quasiparticles of charge $e^*/e = 1/m$ to be present. We start by looking for the electron creation and annihilation operators of the system. For the electron creation operator, we require the following property [25]:

$$\left[\rho(x), \Psi_e^{\dagger}(x')\right] = \delta(x - x')\Psi_e^{\dagger}(x') \tag{4.7}$$

which means that the operator $\Psi_e^{\dagger}(x')$ creates a charge e particle at position x'. Such operators can be constructed by a technique called "bosonization". We start by

defining a Boson field $\phi(x)$ by:

$$\rho(x) = \frac{1}{2\pi} \partial_x \phi(x) \tag{4.8}$$

The Kac-Moody Algebra defined in (4.6) reads in real space [26]:

$$\left[\rho(x), \rho(x')\right] = i\frac{\nu}{2\pi} \partial_x \delta(x - x') \tag{4.9}$$

which gives by integration:

$$\left[\rho(x), \phi(x')\right] = -i\nu\delta(x - x') \tag{4.10}$$

From (4.7) and (4.10) we see that an electron operator has to be of the following form [25]: $\Psi_e(x) \propto e^{\frac{i}{\nu}\phi(x)}$.

Now we turn to the quasiparticle creation and annihilation operators. They can be found from realizing that m QP creation operators must fuse to one electron creation operator [24]. Hence we find: $\Psi_{\text{QP}} \propto e^{i\phi(x)}$. Furthermore, we have [25]:

$$\left[\rho(x), \Psi_{\mathrm{QP}}^{\dagger}(x')\right] = \frac{1}{m}\delta(x - x')\Psi_{\mathrm{QP}}^{\dagger}(x') \tag{4.11}$$

which implies that $\Psi_{OP}^{\dagger}(x')$ creates a charge $e^*/e = 1/m$ QP at x'.

Electron and QP propagators For the tunneling properties of the FQH liquid, the propagators of the electrons and QPs will turn out to be crucial (see Sect. 4.3.3).

The electron propagator is calculated as follows [28]:

$$G_{e}(x,t) = \langle T(\Psi_{e}^{\dagger}(x,t)\Psi_{e}(0,0))\rangle \tag{4.12}$$

$$= \langle T(e^{-\frac{i}{\nu}\phi(x,t)}e^{\frac{i}{\nu}\phi(0,0)})\rangle$$
 (4.13)

$$=e^{\frac{1}{\nu^2}\langle\phi(x,t)\phi(0,0)\rangle} \tag{4.14}$$

$$\propto \frac{1}{(x - vt)^m} \tag{4.15}$$

where T denotes time-ordering and $\langle ... \rangle = \langle 0 | ... | 0 \rangle$ with $|0 \rangle$ being the ground state. Furthermore we have used the propagator of a free phonon field [25]: $\langle \phi(x,t)\phi(0,0)\rangle = -\nu \ln(x-vt) + \text{const.}$ Similarly we find for the QP operator [25]:

$$G_{\rm QP}(x,t) = \langle T(\Psi_{\rm QP}^{\dagger}(x,t)\Psi_{\rm QP}(0,0))\rangle \propto \frac{1}{(x-vt)^{1/m}}$$
 (4.16)

4.3.2 Hierarchical States and Bulk-Edge Correspondence

The above hydrodynamic approach can be extended to hierarchical FQH states. For this however, assumptions about the construction of the FQH states have to be made. A more elegant way of constructing an edge theory is the so-called bulk-edge correspondence. In the bulk, the hierarchical FQH states are described by a Chern-Simons effective theory [27]. Here the most general Abelian FQH liquids are classified by a symmetric matrix K with integer elements and odd diagonal elements. It was shown that the bulk topological order, described by K, is directly related to the physics at the edge [20, 22] and that the behavior of the edge reflects the topological order in the bulk. This does not require a specific construction of the edge but only relies on bulk properties. All physical quantities of the edge, like the charge and statistics of the possible QP excitations and their propagators can be calculated from K. A detailed discussion of this construction is beyond the scope of this book and we refer the interested reader to [24, 25].

4.3.3 Tunneling in a QPC

Qualitative discussion With the help of the formalism developed so far, we are now able to investigate the tunneling properties of a FQH edge at a QPC. In order to allow a perturbative treatment of the situation, we will investigate the system in a weak tunneling situation. Here we will look at two different configurations: first, we consider the tunneling between two FQH edges, separated by vacuum (Fig. 4.6a), i.e. across a pinched-off QPC. In this situation only electrons tunnel. Assuming a point-like interaction between lower and upper edge at x=0, the tunneling Hamiltonian will consist of terms of the form $\Psi_{e,L}^{\dagger}(0,t)\Psi_{e,U}(0,t)+\text{h.c.}$, where $\Psi_{e,L/U}^{\dagger}$ or $\Psi_{e,U/L}$ are the electron creation or annihilation operators on the lower or upper edge. These terms hence annihilate an electron on one edge, while creating an electron on the other edge.

The second situation we consider is depicted in Fig. 4.6b. Here, left- and right-moving edge states are weakly backscattered at a QPC. In this situation, quasiparticles tunnel between left and right edge and the tunneling Hamiltonian consists of terms of the form $\Psi_{\text{QP,L}}^{\dagger}(0,t)\Psi_{\text{QP,R}}(0,t) + \text{h.c.}$, where $\Psi_{\text{QP,L/R}}^{\dagger}$ or $\Psi_{\text{QP,R/L}}$ are the quasiparticle creation or annihilation operators on the left or right edge.

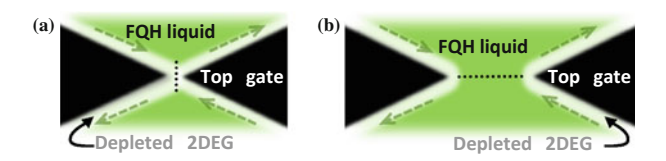


Fig. 4.6 a Weak electron tunneling. b Weak quasiparticle tunneling

Calculation of the tunneling conductance at v = 1/m Let us look at the specific situation at v = 1/m, where we have calculated the electron and quasiparticle propagators. The tunneling density of states (TDOS) for quasiparticles, $N_{\rm QP}(\omega)$, evaluated at $\omega = \frac{eV}{\hbar}$ is found from the imaginary part of the Fourier transform of the propagator [30], which yields [24]:

$$N_{\rm QP}(\omega) \propto {\rm Im} \lim_{x \to 0^+} \int_{-\infty}^{\infty} dt G_{\rm QP}(x,t) e^{i\omega t} \propto |\omega|^{1/m-1}$$
 (4.17)

Similarly we find for the electron TDOS: $N_e(\omega) \propto |\omega|^{m-1}$.

The full Hamiltonian of the QP tunneling system (Fig. 4.6b) can be written as [24]:

$$H = H_R + H_L + \Gamma e^{i\omega_0^* t} \Psi_{\text{OPL}}^{\dagger}(0, t) \Psi_{\text{QP,R}}(0, t) + h.c.$$
 (4.18)

where H_R and H_L are the Hamiltonians of the left and right edge, Γ is the tunneling matrix element and $\omega_0^* = (e^*/e)V/\hbar$. The term $e^{i\omega_0^*t}$ arises from the potential difference V between left and right edge. Using Fermi's golden rule, the QP tunneling current can be written in the following form [24]:

$$I_{\text{QP}}(V) = 2\pi \frac{e}{m\hbar} |\Gamma|^2 \int_{-eV}^{0} dE N_{\text{QP}}(E, T) N_{\text{QP}}(E + eV, T) \propto V^{2/m - 1}$$
 (4.19)

From this we see that the quasiparticle tunneling current diverges for $V \to 0$ (at zero temperature). Similarly we find for electron tunneling: $I_e(V) \propto V^{2m-1}$, which means that electron tunneling is suppressed at low biases.

In experiments the QP tunneling conductance $g_{\rm tun}$ is typically measured. It also exhibits a characteristic power-law scaling at zero temperature: $g_{\rm tun}(V)=\frac{dI_{\rm QP}}{dV}\propto V^{2/m-2}$

General case For FQH states which are not described by v = 1/m, the tunneling conductance is related to the scaling behavior of the QP creation and annihilation operators in a similar way. Here we assume a scaling with an exponent g [25]:

$$\langle T(\Psi_{\mathrm{OP}}^{\dagger}(t, x = 0)\Psi_{\mathrm{OP}}(0, 0))\rangle \propto t^{-g} \tag{4.20}$$

Here g is called Coulomb interaction parameter. For the most general Abelian FQH states, g can be directly calculated from the K-matrix describing the topological order in the bulk. Edge theories for the most important non-Abelian FQH states have been developed in literature (see for example [31, 32] for an overview). Here, QP operators can be constructed and g is then obtained from their scaling properties. A summary of the different g for the edge modes of the FQH states in the second LL is given in Tables 3.2, 3.3 and 3.4.

From the scaling of the QP propagator (4.20), we find for the QP TDOS: $N_{\rm QP}(\omega) \propto |\omega|^{g-1}$ and for the QP tunneling current: $I_{\rm QP}(V) \propto V^{2g-1}$, which leads to $g_{\rm tun}(V) \propto V^{2g-2}$ at zero temperature.

Performing the above calculation for finite T and V, the following expression was found for the tunneling conductance [33, 34]:

$$g_{\text{tun}}(V,T) \propto |\Gamma|^2 \times T^{(2g-2)} \times F\left(g, \frac{e^*/e \ V}{k_B T}\right)$$
 (4.21)

where F is a function of g and $(e^*/e\ V)/(k_BT)$:

$$F\left(g,x\right) = \mathrm{B}\left(g + i\frac{x}{2\pi}, g - i\frac{x}{2\pi}\right) \times \left\{\pi\cosh\left(\frac{x}{2}\right) - 2\sinh\left(\frac{x}{2}\right)\operatorname{Im}\left[\Psi\left(g + i\frac{x}{2\pi}\right)\right]\right\} \tag{4.22}$$

Here, B(x, y) is the Euler beta function and $\Psi(x)$ is the digamma function. This expression will be used to investigate the properties of the FQH states in the second Landau level in Chap. 11 and allows the extraction of the characteristic parameters g and e^* . From the power-law temperature dependence $g_{tun}(V,T) \propto T^{(2g-2)}$, we see that the edge modes with the smallest g dominate the QP tunneling at the lowest temperatures. We note that for edge states with counterpropagating modes, g can be non-universal and depend on the strength of the interactions between the modes.

Physical meaning of g The Coulomb interaction parameter g can be seen as analog to the Luttinger liquid coupling constant: two chiral Luttinger liquid edges coupled with an interaction parameter g are equivalent to having one non-chiral Luttinger liquid with coupling constant $g_{\text{Lutt}} = g$ [30], called "Luttinger parameter".²

The coupling constant can be written as [35]: $g = \pi \hbar \sqrt{\rho \kappa/m^*}$ where $\kappa = \partial \rho/\partial \mu$ is the compressibility. A more simple interpretation of g can be found from the ratio of the Coulomb interaction energy in the edge U to the Fermi energy of the non-interacting system [36]:

$$g \approx \left(1 + \frac{U}{2E_{\rm F}}\right)^{-1/2} \tag{4.24}$$

Hence g = 1 corresponds to the non-interacting Fermi liquid, while g < 1 or g > 1 indicate a repulsive of attractive interaction in the edge [37].

$$H = \frac{\hbar v_F}{2\pi} \int_0^L \left[g_{\text{Lutt}} \left(\frac{\partial \varphi(x)}{\partial x} \right)^2 + \frac{1}{g_{\text{Lutt}}} \left(\frac{\partial \theta(x)}{\partial x} \right)^2 \right] dx \tag{4.23}$$

where $\varphi(x)$ is the phase field and $\theta(x)$ is the phonon displacement field.

²The Luttinger liquid Hamiltonian can be written as [30]:

References 61

References

- E.V. Devyatov, Physics-Uspekhi 50, 197 (2007). doi:10.1070/PU2007v050n02ABEH006244
- D.B. Chklovskii, B.I. Shklovskii, L.I. Glazman, Phys. Rev. B 46, 4026 (1992). doi:10.1103/ PhysRevB.46.4026
- 3. T. Ihn, Semiconductor Nanostructures: Quantum States and Electronic Transport (Oxford University Press, Oxford, 2010)
- 4. M.R. Geller, G. Vignale, Phys. Rev. B 52, 14137 (1995). doi:10.1103/PhysRevB.52.14137
- 5. D.J. Thouless, Phys. Rev. Lett. **71**, 1879 (1993). doi:10.1103/PhysRevLett.71.1879
- S. Komiyama, NanoScience and Technology, in *Mesoscopic Physics and Electronics*, ed. by P.T. Ando, P.Y. Arakawa, P.K. Furuya, P.S. Komiyama, P.H. Nakashima (Springer, Berlin, 1998), pp. 120–131
- 7. A.H. MacDonald, Phys. Rev. Lett. 64, 220 (1990). doi:10.1103/PhysRevLett.64.220
- 8. Y. Meir, Phys. Rev. Lett. 72, 2624 (1994). doi:10.1103/PhysRevLett.72.2624
- C.L. Kane, M.P.A. Fisher, J. Polchinski, Phys. Rev. Lett. 72, 4129 (1994). doi:10.1103/ PhysRevLett.72.4129
- 10. C.L. Kane, M.P.A. Fisher, Phys. Rev. B 51, 13449 (1995). doi:10.1103/PhysRevB.51.13449
- 11. C.L. Kane, M.P.A. Fisher, Phys. Rev. B 55, 15832 (1997). doi:10.1103/PhysRevB.55.15832
- 12. C.W.J. Beenakker, Phys. Rev. Lett. 64, 216 (1990). doi:10.1103/PhysRevLett.64.216
- 13. A.M. Chang, Solid State Commun. 74, 871 (1990). doi:10.1016/0038-1098(90)90447-J
- 14. L. Brey, Phys. Rev. B 50, 11861 (1994). doi:10.1103/PhysRevB.50.11861
- 15. D.B. Chklovskii, Phys. Rev. B 51, 9895 (1995). doi:10.1103/PhysRevB.51.9895
- 16. G. Kirczenow, B.L. Johnson, Phys. Rev. B 51, 17579 (1995). doi:10.1103/PhysRevB.51.17579
- 17. G. Kirczenow, Phys. Rev. B 53, 15767 (1996). doi:10.1103/PhysRevB.53.15767
- H.-S. Sim, K.J. Chang, G. Ihm, Phys. Rev. Lett. 82, 596 (1999). doi:10.1103/PhysRevLett.82.
- B.L. Johnson, G. Kirczenow, Rep. Prog. Phys. 60, 889 (1997). doi:10.1088/0034-4885/60/9/ 002
- 20. X.-G. Wen, Phys. Rev. B 41, 12838 (1990). doi:10.1103/PhysRevB.41.12838
- 21. X.-G. Wen, Phys. Rev. Lett. 64, 2206 (1990). doi:10.1103/PhysRevLett.64.2206
- 22. X.-G. Wen, Phys. Rev. B 44, 5708 (1991). doi:10.1103/PhysRevB.44.5708
- 23. M. Stone, Int. J. Mod. Phys. B 05, 509 (1991). doi:10.1142/S0217979291000316
- E. Fradkin, Field Theories of Condensed Matter Physics (Cambridge University Press, Cambridge, 2013)
- 25. X.-G. Wen, Quantum Field Theory of Many-Body Systems: From the Origin of Sound to an Origin of Light and Electrons (Oxford University Press, Oxford, 2007)
- 26. Z.F. Ezawa, *Quantum Hall Effects: Field Theoretical Approach and Related Topics* (World Scientific, Singapore, 2008)
- 27. X.-G. Wen, Adv. Phys. 44, 405 (1995). doi:10.1080/00018739500101566
- 28. A.M. Chang, Rev. Mod. Phys. 75, 1449 (2003). doi:10.1103/RevModPhys.75.1449
- 29. X.-G. Wen, Int. J. Mod. Phys. B **06**, 1711 (1992). doi:10.1142/S0217979292000840
- 30. G. Giuliani, G. Vignale, *Quantum Theory of the Electron Liquid* (Cambridge University Press, Cambridge, 2005)
- 31. G. Yang, D.E. Feldman, Phys. Rev. B 88, 085317 (2013). doi:10.1103/PhysRevB.88.085317
- 32. B.J. Overbosch, X.-G. Wen. arXiv:0804.2087 [cond-mat] (2008)
- 33. C.C. de Chamon, D.E. Freed, S.A. Kivelson, S.L. Sondhi, X.G. Wen, Phys. Rev. B **55**, 2331 (1997). doi:10.1103/PhysRevB.55.2331
- 34. B.J. Overbosch, *Edge tunneling and transport in non-abelian fractional quantum Hall systems*, Ph.D. thesis, Massachusetts Institute of Technology, 2008
- 35. F.D.M. Haldane, Phys. Rev. Lett. 48, 569 (1982). doi:10.1103/PhysRevLett.48.569.2
- 36. C.L. Kane, M.P.A. Fisher, Phys. Rev. B 46, 15233 (1992). doi:10.1103/PhysRevB.46.15233
- 37. C.L. Kane, M.P.A. Fisher, Phys. Rev. Lett. 68, 1220 (1992). doi:10.1103/PhysRevLett.68.1220

Chapter 5 Non-Abelian Statistics and Its Signatures in Interference Experiments

Abstract We review the concept of anyon statistics and how non-Abelian anyons arise in the Moore-Read Pfaffian state at $\nu = 5/2$. Furthermore, we give a short overview of complications that arise in real systems due to Coulomb blockade physics and the expected signatures of non-Abelian physics in an interference experiment.

5.1 From Fermions to Anyons

Fermi and Bose statistics are the two fundamental cases that describe the equilibrium properties of quantum mechanical particles. Exchanging two particles multiplies the wavefunction with a phase factor $\exp(i\delta)$, while it is multiplied with $\exp(2i\delta)$ for a closed loop of one particle around the other [1]. For Bosons and Fermions ($\delta_B = 2n\pi$ and $\delta_F = (2n+1)\pi$, $n \in \mathbb{Z}$), this phase just multiplies the wavefunction by ± 1 upon exchange.

An exchange of particles in two dimensions is distinct from the exchange in three dimensions. While in the latter any exchange trajectory can be continuously transformed into an infinitesimally small loop, this is not possible in two dimensions, where loops encircling different numbers of other particles are topologically distinct (Fig. 5.1). It was soon realized that this opens the possibility for Anyonic statistics, where other values of δ are allowed than for Fermions and Boson [2–4]. A system where Anyonic statistics is realized is the FQH effect. Arovas et al. [5] have investigated the statistical phases arising here, by calculating the Berry phase of an e/m quasiparticle (for a filling factor $\nu=1/m$), encircling another quasiparticle on a closed loop $\mathcal C$. This consideration can be described in the following simplified way [6]: we start with a Laughlin state $\psi_{1/m}$ and add a charge e/m quasihole (QH) to the system while the external magnetic field is fixed. Then we move the QH clockwise around a closed loop $\mathcal C$. By this, an Aharonov-Bohm phase γ arises [6]:

$$\gamma = -\frac{e^*}{\hbar} \oint_C \mathbf{A} \cdot d\mathbf{r} = -2\pi \frac{e^*}{e} \frac{\phi}{\phi_0}$$
 (5.1)

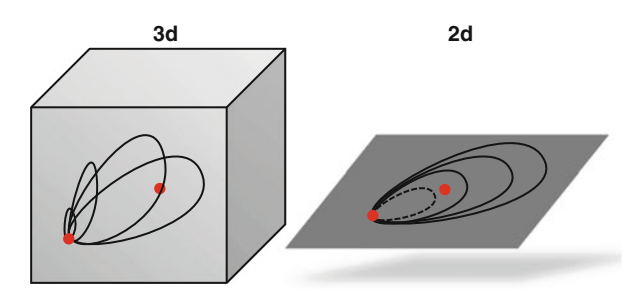


Fig. 5.1 Trajectories for a closed loop of a single particle around another particle in three and two spatial dimensions. The *dashed line* in two dimensions is topologically distinct from the *solid lines*

where $\phi = -2\pi m N_{\rm encl}$ is the total flux enclosed by $\mathcal C$ and $N_{\rm encl}$ is the number of enclosed electrons. Adding an e/m QH in the interior of the contour, the net charge encircled changes to $-eN_{\rm encl} + e/m$ with a total Aharonov-Bohm phase of $\gamma' = -2\pi (N_{\rm encl} - 1/m)$ [6]. From this we find that the statistical phase of one quasiparticle encircling the other quasiparticle is given as:

$$\delta_{\frac{1}{m}} = \pm \frac{\pi}{m} \tag{5.2}$$

For general FQH states at $\nu = \frac{\nu^*}{2\nu\nu^*+1}$, the statistical phase is found to be [7]:

$$\delta_{\frac{\nu^*}{2p\nu^*+1}} = \pm \left(\frac{2p(\nu^*-1)+1}{2p\nu^*+1}\right)\pi \pmod{2\pi}$$
 (5.3)

5.2 Non-Abelian Anyons in the Moore-Read Pfaffian State

We have seen in the last section that the correlations in the FQH effect can change the particle statistics and hence change the phase of a wavefunction upon QP exchange. With the discovery of the Moore-Read Pfaffian (MR Pf) wavefunction, it was realized that this wavefunction might allow quasiparticles which behave as non-Abelian Anyons [8]. When two QPs are exchanged here, not only the phase of the wavefunction changes, but a unitary transformation acts on the wavefunction itself [9]. If these transformations do not commute, the system is said to be non-Abelian. Performing a particular sequence of QP exchanges might transform the wavefunction of the system into a desired final state, which might be exploited for quantum computation.

The MR Pf state can be seen as a BCS-like condensate of Cooper-paired composite Fermions. In the following, we will motivate how non-Abelian statistics can arise in such a system, following [10, 11]. The situation of the MR Pfaffian state can be analyzed starting from a common BCS mean-field Hamiltonian (see for example

[12]). This Hamiltonian can be diagonalized by a Bogoliubov transformation, leading to the BCS Hamiltonian [12]:

$$H_{\rm BCS} = E_{\rm BCS} + \sum_{\mathbf{k}\sigma} E_{\mathbf{k}} \Gamma_{\mathbf{k}\sigma}^{\dagger} \Gamma_{\mathbf{k}\sigma}$$
 (5.4)

Here $\Gamma^{\dagger}_{{\bf k}\sigma}$ and $\Gamma_{{\bf k}\sigma}$ define the Bogoliubov quasiparticles with positive energy eigenvalues. They are a superposition of electrons and holes and are electrically neutral at the Fermi Energy [12]. Let us turn to the p-wave pairing case: here the angular momentum eigenvalues L=-1 break the spin- and spatial rotation symmetries [10]. When vortices are present in the superconductor (i.e. when the filling factor deviates slightly from $\nu=5/2$), the mean field Hamiltonian has zero-energy eigenvalues and its ground state becomes degenerate [10]. These vortices can be identified with the zero-energy modes γ_i which define the non-Abelian quasielectrons and quasiholes at $\nu=5/2$. The zero energy solutions can be written in the following form [11]:

$$\gamma_i = \frac{1}{\sqrt{2}} \int d\mathbf{r} \left[F(\mathbf{r}) e^{-\frac{i}{2}\Omega_i} \psi(\mathbf{r}) + F^*(\mathbf{r}) e^{\frac{i}{2}\Omega_i} \psi^{\dagger}(\mathbf{r}) \right]$$
 (5.5)

where $\psi(\mathbf{r})$ and $\psi^{\dagger}(\mathbf{r})$ are the (composite) Fermion field operators, $F(\mathbf{r})$ is a decaying function for large r and $\Omega_i = \sum_{j \neq i} \arg(\mathbf{R}_j - \mathbf{R}_i)$. Each solution γ_i corresponds to a

single vortex and is localized near the core of the vortex at \mathbf{R}_i [11]. These zero energy solutions possess two important properties: they satisfy Fermionic anti-commutation relations and can be seen as their own anti-particles:

$$\left\{\gamma_i, \gamma_j\right\} = 2\delta_{ij} \tag{5.6}$$

$$\gamma_i = \gamma_i^{\dagger} \tag{5.7}$$

Here $\{\gamma_i, \gamma_j\}$ denotes the anti-commutator of γ_i and γ_j . These properties make them Majorana Fermions.

Let us turn to the exchange statistics of the Majorana Fermions: when vortex i encircles vortex j, $\arg(\mathbf{R}_j - \mathbf{R}_i)$ changes by 2π and we have: $\gamma_i \to -\gamma_i$ and $\gamma_j \to -\gamma_j$ (see 5.5). This corresponds to a unitary transformation of the groundstate of the system, which transforms the operators (up to a phase) according to [11]:

$$\gamma_k \to U_{ii}^{\dagger} \gamma_k U_{ij}$$
 (5.8)

where $U_{ij} = \gamma_i \gamma_j = \exp(\pi \gamma_i \gamma_j / 2)$. These transformations do not necessarily commute, giving rise to non-Abelian exchange statistics.

5.3 Interferometry with Non-Abelian Anyons

The implications of non-Abelian statistics for interference experiments have been studied intensively in theory [13–22]. The basic prediction of these studies is that the interference pattern depends critically on the parity of the number of charge e/4QPs that is enlosed in the interference path, denoted by N_{encl} .

Following [15] we discuss the expected outcome for the situation that is depicted schematically in Fig. 5.2a. Here a quasiparticle moves from left to right along the lower edge of the system. The OP is either reflected at the left or right OPC of the Fabry-Pérot interferometer (with tunneling amplitudes t_L and t_R) or is transmitted through the interferometer. The partial waves reflected at the left or right QPC apply unitary transformations $U_{\rm L}$ or $U_{\rm R}$ to the initial ground state of the system $|\psi_i\rangle$ [15]. To lowest order, the backscattered current of this situation can be written as [15]:

$$I^{e/4} \propto 2 \operatorname{Re} \left[t_{\mathrm{L}}^* t_{\mathrm{R}} e^{2\pi i \Omega} \langle \psi_i | U_{\mathrm{L}}^{-1} U_{\mathrm{R}} | \psi_i \rangle \right]$$
 (5.9)

where Ω denotes the relative phase of the interfering partial waves and satisfies $\frac{\partial \Omega}{\partial A} = B/4\phi_0$ with A being the area of the interferometer.

The unitary transformation acting on the system depends on the Majorana mode γ_a of the charge e/4 quasiparticle that is moving along the edge of the interferometer and the Majorana modes γ_i of the N_{encl} charge e/4 QPs that are localized within the interference path [15]:

$$U_a = U_{\rm I}^{-1} U_{\rm R} = \gamma_a^{N_{\rm encl}} \gamma_{\rm int} \tag{5.10}$$

where $\gamma_{\mathrm{int}} = \prod_{j=1}^{N_{\mathrm{encl}}} \gamma_j$ and U_a has eigenvalues ± 1 or $\pm i$. The fact that γ_a is a Majorana operator leads to two distinct behaviors, depending on if N_{encl} is even or odd. If N_{encl} is even, $\gamma_a^{N_{\mathrm{encl}}} = 1$ and U_a does not depend on the Majorana operator γ_a . Hence an interference (5.9) characteristic for e/4 charge quasiparticles is observed, as the operators $U_a, U_b, ...$ are identical for all incident QPs

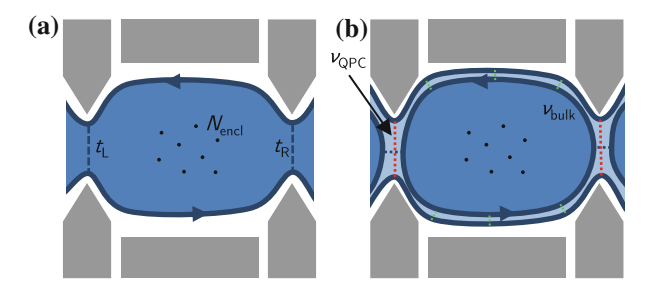


Fig. 5.2 Schematic interferometers in an idealized Aharonov-Bohm regime (a adapted from [20]) or in a Coulomb-dominated regime (b) where QPCs and bulk possess different filling factors

with Majorana modes $\gamma_a, \gamma_b, \dots$. The two different eigenvalues of γ_{int} correspond to two different interference patterns shifted by π .

If N_{encl} is odd, $\gamma_a^{N_{\text{encl}}} = \gamma_a$ and the unitary transformations U_a , U_b for two different incoming QPs are different and do not necessarily commute. For a large number of QPs, this randomizes the interference phase (5.9) and hence no interference is observed [15].

To summarize, to lowest order the backscattered current can be written as [23]:

$$I^{e/4} \propto \begin{cases} \cos\left(2\pi \frac{\phi}{4\phi_0} \mp \frac{N_{\text{encl}}\pi}{4} + N_{\psi}\pi\right) & N_{\text{encl}} \text{ even} \\ 0 & N_{\text{encl}} \text{ odd} \end{cases}$$
 (5.11)

where ϕ is the magnetic flux penetrating the interferometer. Here only the lowest-order interference terms have been considered and $N_{\psi}=0$ or 1, depending on whether the eigenvalue of $\gamma_{\rm int}$ is $\pm i$ or ± 1 . The minus in (5.11) corresponds to the case of the MR Pf and SU(2)₂ states, whereas the plus corresponds to the anti-Pfaffian state. For the analysis, it was furthermore assumed that the $N_{\rm encl}$ localized QPs in the interferometer are sufficiently far away from the edge, such that their coupling to the edge is weak [15].

The "even-odd effect" captured in (5.11) opens a way to probe the non-Abelian statistics experimentally. If the side-gate voltage of an Aharonov-Bohm interferometer is changed, the area of the interference loop varies. Hence we either observe oscillations with a periodicity characteristic for e/4 quasiparticles, or no oscillations (in lowest order), depending on the parity of $N_{\rm encl}$. For a sufficient variation of the side-gate voltage, changes in $N_{\rm encl}$ may appear, leading to a characteristic on/off-switching of the interference. Such a behavior is only expected for non-Abelian states and is a strong indication for non-Abelian statistics. In a system where the bulk-edge coupling of QPs is not weak, the experimental signatures might be more complicated and (5.11) no longer holds. We furthermore note that certain two-component states, like the (3,3,1)-state might mimic the signatures of the even-odd effect (see discussion in the last paragraph of this chapter).

5.4 Aharonov-Bohm Versus Coulomb-Dominated Physics

In the above considerations, the system has been examined in a perfect Aharonov-Bohm case, where weak backscattering only occurs at the entrance and exit of an interferometer and one-dimensional edge channels define the interference paths. However in a realistic system, the situation can be much more difficult. Here, regions of different filling factors may form throughout the interferometer, for example a filling factor $\nu_{\rm QPC}$ in the QPCs, smaller than the bulk filling factor $\nu_{\rm bulk}$ (which is assumed to be the same in the bulk of the sample and in the center of the interferometer, see Fig. 5.2b). In such a situation different tunneling paths may connect the isolated puddle in the

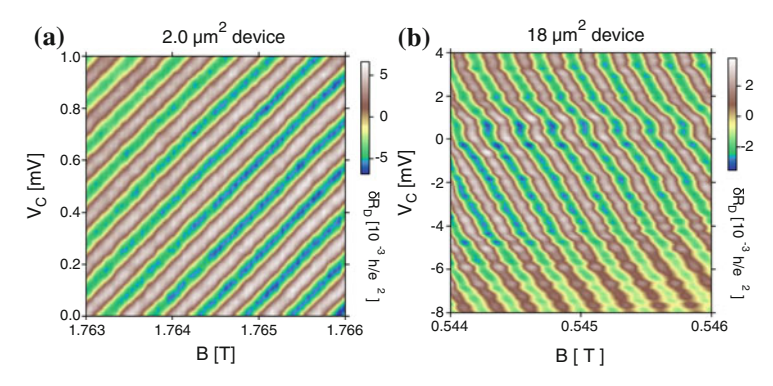


Fig. 5.3 a Conductance oscillations as a function of the magnetic field and a side-gate voltage of an interferometer. Oscillations in the Coulomb-dominated (a) and Aharonov-Bohm case (b) exhibit a different dependence on both parameters. (Reprinted figure with permission from [25]. Copyright 2009 by the American Physical Society)

center of the interferometer to the bulk and the surrounding compressible region [24] (blue, red and green dashed lines in Fig. 5.2b). Here the lowest-order interference picture discussed above no longer holds. Transport through the isolated puddle in the interferometer can lead to Aharonov-Bohm like oscillations, which however arise due to Coulomb-blockade physics. In the IQH regime, a distinct behavior of Aharonov-Bohm (AB) and Coulomb-dominated cases appears [25, 26]. In the pure AB case, conductance oscillations arise at a fixed magnetic flux enclosed by the interfering paths. When the magnetic field strength is increased, a side-gate voltage of the interferometer has to be biased more negatively in order to decrease the area of the enclosed path and in order to stay on resonance. This is exactly the behavior that has been observed in large Fabry-Pérot type interferometers [25] (see Fig. 5.3b). For small interferometers (Fig. 5.3a), a contrary behavior has been observed. Here, the number of electrons on the isolated puddle in the interferometer is quantized, hence this case is called "Coulomb-dominated". A conductance resonance occurs whenever configurations with N and N+1 electrons are energetically degenerate. Adding a single flux quantum to the interferometer area increases the total degeneracy of the LLs underlying the isolated puddle in the interferometer. Hence an increase of the B-field transfers electrons from the island to the lower LLs, which can be compensated by applying a more positive voltage to the side-gate of the interferometer. This explains the slope observed in Fig. 5.2a. For the AB case, the B-field periodicity ΔB is independent of the filling factor in the IQH regime. However, for the Coulombdominated case, $\Delta B \propto \frac{1}{\nu_{\rm OPC}}$ is expected [24–26]. The reason lies in the fact that adding a single flux quantum to the interferometer region enhances the degeneracy of each LL underlying the island by two and hence expels ν_{OPC} electrons from the OD.

Similar systems have been studied experimentally in the FQH regime [27–29], where periodicities depend on QP charges and on the edge structure.

Signatures of non-Abelian statistics in Coulomb blockade experiments

Several authors have investigated signatures of non-Abelian statistics that arise in Coulomb blockade experiments [15, 19, 20, 30–32] and might allow to determine the nature of the QP excitations at $\nu = 5/2$ (and at other FQH states, like the $\nu = 12/5$ state).

The general idea behind these proposals is the following: in a large QD, we expect to add or remove one electron whenever the area changes by $\Delta A \propto \frac{e}{n_0}$, where n_0 is the average electron density in the dot. When a paired state is formed in the bulk of the QD, transport signatures again depend on the parity of N_{encl} . When N_{encl} is even, we expect that a lower energy is needed to add an electron whenever the electron number on the dot is odd compared to an even number of electrons occupying the dot [15], as the total energy is minimized by forming a paired state. Thus the peak spacing is expected to vary between alternating values. When N_{encl} is odd, electrons tunnel to the dot via the zero energy mode on the edge and an alternation of the periodicity is absent [11]. In this consideration it was assumed that the coupling between the edge and the QPs localized in the bulk is weak [32] (such that no relaxation between bulk and edge zero energy modes occurs on the timescale of the measurement). For $\nu = 5/2$, the Coulomb blockade signal was found to be identical for most important candidate states [32]: the non-Abelian MR Pf, anti-Pfaffian, SU(2)₂ states and the Abelian (3,3,1)-state are expected to show alternating CB peak spacings that vary between the following values:

$$\Delta A = \frac{e}{n_0} \left(1 \pm \frac{v_n}{2v_c} \right) \tag{5.12}$$

where v_c and v_n are the velocities of charge and neutral modes. Typically v_c is approximately one order of magnitude larger than v_n [33, 34], thus a good experimental resolution is required to unambiguously identify the alternation. For sufficiently strong bulk-edge relaxation, the alternation disappears and the original $\Delta A = \frac{e}{n_0}$ is found again [32]. Coulomb blockade signatures that are expected for other candidate states and other filling factors in the second LL have been discussed in literature. An overview of the expected peak spacings can be found in [32].

Coulomb blockade and interference "doppelgänger" states Following the argumentation of Bonderson et al. [32], the identical outcomes for different candidate states might indicate that a Coulomb blockade experiment is not suitable to distinguish between the candidate states at $\nu = 5/2$ (and similarly for other filling factors) and might not even allow to distinguish between an Abelian and a non-Abelian state. However, Stern et al. have pointed out [20] that although Abelian and non-Abelian states might show similar experimental signatures in some cases, Abelian states are sensitive to local perturbations, which is not true for the non-Abelian states which are of topological origin. This might hence enable to distinguish between both cases. The same argumentation holds for a lowest-order interference experiment, where the Abelian (3,3,1)-state might mimic the even-odd signatures of a non-Abelian state [20], at the point of symmetry between the two different electron flavors. Stern

et al. showed that lowest-order interference experiments and Coulomb blockade experiments contain the same information about the quasi-particle statistics of the system and hence both regimes offer a promising approach for testing non-Abelian statistics experimentally.

References

- F.E. Camino, W. Zhou, V.J. Goldman, Phys. Rev. B 72, 075342 (2005). doi:10.1103/PhysRevB. 72.075342
- 2. J.M. Leinaas, J. Myrheim, Il Nuovo Cimento B Ser. 11(37), 1 (1977). doi:10.1007/BF02727953
- 3. F. Wilczek, Phys. Rev. Lett. 48, 1144 (1982). doi:10.1103/PhysRevLett.48.1144
- 4. F. Wilczek, Phys. Rev. Lett. 49, 957 (1982). doi:10.1103/PhysRevLett.49.957
- D. Arovas, J.R. Schrieffer, F. Wilczek, Phys. Rev. Lett. 53, 722 (1984). doi:10.1103/ PhysRevLett.53.722
- P. L. Taylor, O. Heinonen, A Quantum Approach to Condensed Matter Physics (Cambridge University Press, Cambridge, 2002)
- E. Fradkin, Field Theories of Condensed Matter Physics (Cambridge University Press, Cambridge, 2013)
- 8. G. Moore, N. Read, Nucl. Phys. B 360, 362 (1991). doi:10.1016/0550-3213(91)90407-0
- 9. S.D. Sarma, M. Freedman, C. Nayak, Phys. Today **59**, 32 (2006). doi:10.1063/1.2337825
- 10. N. Read, D. Green, Phys. Rev. B 61, 10267 (2000). doi:10.1103/PhysRevB.61.10267
- A. Stern, Ann. Phys. (Series January Special Issue) 323, 204 (2008). doi:10.1016/j.aop.2007. 10.008
- M. Tinkham, Introduction to Superconductivity (Dover Publications Incorporated, New York, 2012)
- E. Fradkin, C. Nayak, A. Tsvelik, F. Wilczek, Nucl. Phys. B 516, 704 (1998). doi:10.1016/ S0550-3213(98)00111-4
- S. Das Sarma, M. Freedman, C. Nayak, Phys. Rev. Lett. 94, 166802 (2005). doi:10.1103/ PhysRevLett.94.166802
- A. Stern, B.I. Halperin, Phys. Rev. Lett. 96, 016802 (2006). doi:10.1103/PhysRevLett.96. 016802
- P. Bonderson, A. Kitaev, K. Shtengel, Phys. Rev. Lett. 96, 016803 (2006). doi:10.1103/ PhysRevLett.96.016803
- P. Bonderson, K. Shtengel, J.K. Slingerland, Phys. Rev. Lett. 97, 016401 (2006). doi:10.1103/ PhysRevLett.97.016401
- 18. S.B. Chung, M. Stone, Phys. Rev. B 73, 245311 (2006). doi:10.1103/PhysRevB.73.245311
- R. Ilan, E. Grosfeld, K. Schoutens, A. Stern, Phys. Rev. B 79, 245305 (2009). doi:10.1103/ PhysRevB.79.245305
- A. Stern, B. Rosenow, R. Ilan, B.I. Halperin, Phys. Rev. B 82, 085321 (2010). doi:10.1103/ PhysRevB.82.085321
- D.E. Feldman, A. Kitaev, Phys. Rev. Lett. 97, 186803 (2006). doi:10.1103/PhysRevLett.97. 186803
- D.E. Feldman, Y. Gefen, A. Kitaev, K.T. Law, A. Stern, Phys. Rev. B 76, 085333 (2007). doi:10. 1103/PhysRevB.76.085333
- W. Bishara, P. Bonderson, C. Nayak, K. Shtengel, J.K. Slingerland, Phys. Rev. B 80, 155303 (2009). doi:10.1103/PhysRevB.80.155303
- B. Rosenow, B.I. Halperin, Phys. Rev. Lett. 98, 106801 (2007). doi:10.1103/PhysRevLett.98. 106801
- Y. Zhang, D.T. McClure, E.M. Levenson-Falk, C.M. Marcus, L.N. Pfeiffer, K.W. West, Phys. Rev. B 79, 241304 (2009). doi:10.1103/PhysRevB.79.241304

References 71

 B.I. Halperin, A. Stern, I. Neder, B. Rosenow, Phys. Rev. B 83, 155440 (2011). doi:10.1103/ PhysRevB.83.155440

- A. Kou, C.M. Marcus, L.N. Pfeiffer, K.W. West, Phys. Rev. Lett. 108, 256803 (2012). doi:10. 1103/PhysRevLett.108.256803
- D.T. McClure, W. Chang, C.M. Marcus, L.N. Pfeiffer, K.W. West, Phys. Rev. Lett. 108, 256804 (2012). doi:10.1103/PhysRevLett.108.256804
- N. Ofek, A. Bid, M. Heiblum, A. Stern, V. Umansky, D. Mahalu, Proc. Nat. Acad. Sci. 107, 5276 (2010). doi:10.1073/pnas.0912624107
- R. Ilan, E. Grosfeld, A. Stern, Phys. Rev. Lett. 100, 086803 (2008). doi:10.1103/PhysRevLett. 100.086803
- R. Ilan, B. Rosenow, A. Stern, Phys. Rev. Lett. 106, 136801 (2011). doi:10.1103/PhysRevLett. 106.136801
- P. Bonderson, C. Nayak, K. Shtengel, Phys. Rev. B 81, 165308 (2010). doi:10.1103/PhysRevB. 81,165308
- X. Wan, Z.-X. Hu, E.H. Rezayi, K. Yang, Phys. Rev. B 77, 165316 (2008). doi:10.1103/ PhysRevB.77.165316
- Z.-X. Hu, E.H. Rezayi, X. Wan, K. Yang, Phys. Rev. B 80, 235330 (2009). doi:10.1103/ PhysRevB.80.235330

Chapter 6 Overview of Experiments Probing the Properties of the $\nu = 5/2$ State

Abstract We give an overview of methods that try to probe the properties of the $\nu = 5/2$ state, with emphasis on experiments that probe directly or indirectly the quasiparticle statistics. The different implications of the experiments and their relevance for the work presented in this book are discussed.

6.1 Introduction

The potential realization of a non-Abelian state at $\nu = 5/2$ has raised a great interest in this state, experimentally as well as theoretically. In this section, we will review some important experiments and numerical calculations that might shed light on the question weather a non-Abelian state is realized at $\nu = 5/2$.

We begin by giving an overview of numerical studies. Experiments trying to measure the quasiparticle charge are mostly in agreement with $e^*/e = 1/4$. We then proceed to discuss experiments that investigate the spin polarization. Here, contradictory results were found, though most experiments support a full spin polarization. Properties which are related to the edge have also been studied experimentally. Here, we emphasize neutral mode spectroscopy and quasiparticle tunneling experiments. Finally, we discuss implementations of interferometry experiments which might allow to directly investigate the quasiparticle statistics.

Other approaches which we will not discuss investigate for example thermodynamic properties of the bulk. The large degeneracy of non-Abelian FQH states, which is exponential in the number of quasiparticles, has an effect on the low temperature entropy of the system. Theoretical predictions for probing this effect by thermopower measurements [1] or by measuring the magnetization density and the electrochemical potential [2] exist.

For a more detailed discussion of experiments at $\nu = 5/2$, we refer the reader to the review paper of Willett [3].

6.2 Numerical Studies

Numerical calculations in the FQH regime make use of the fact that in the limit $B \to \infty$ where only the lowest Landau level is occupied, finite systems have a finite number of many-body ground-states [4]. The exact solution can be found by numerical diagonalization of the Hamiltonian, taking Coulomb interaction into account. Typically, experimental complications like finite thickness effects, Landau level mixing and disorder are neglected. In contrast to experiments where only single observables are accessible, the numerical approach offers the advantage of being able to calculate the overlap of the numerical solution with explicitly known candidate wavefunctions and hence verifying all observables at once [4].

One of the first numerical treatments of the physics at $\nu = 5/2$ has been presented by Morf [5]. He investigated spin-polarized and spin-unpolarized ground-states in systems with $N \le 18$ electrons by numerical diagonalization. The system was treated in a spherical geometry [6] and Landau level mixing was neglected. It was found that the ground-state is spin-polarized and incompressible and has a large overlap (approximately 0.8–0.9) with paired FQH states like the Moore-Read Pfaffian state [5]. Evidence for a spin-polarized, paired ground-state leading to an energy gap has been found by a number of other authors [7–16].

However, these numerical studies have certain limitations, for example because they often neglect Landau level mixing or disorder. This might explain why the calculated energy gaps are much larger than the actually measured energy gaps [8, 12, 17, 18].

The question whether the ground state is better described by the Moore-Read Pfaffian state or the Anti-Pfaffian state has recently raised interest. Both states cannot be distinguished when particle-hole symmetry is assumed [19, 20]. Particle-hole symmetry breaking by Landau level mixing was taken into account in different numerical studies, and was found to substantially complicate the problem. The MR Pf state [21], as well as the Anti-Pfaffian state [22] have found support in studies employing different numerical approaches. Finite thickness effects, which might also have to be taken into account for a correct description of the ground state, have been found to stabilize the Pfaffian ground state [23–25] and to significantly enhance the overlap with the numerical solution. To our knowledge, only the spin-unpolarized version of the (3,3,1)-state has been investigated in numerical studies. We are not aware whether a description of the $\nu = 5/2$ state by this Abelian state is physically favorable.

An interesting recent development that we would like to mention are numerical studies of bilayer FQH systems. At a total filling factor $\nu_{\text{total}} = 1/2$, the FQH state for weak tunneling and an intermediate layer separation d is thought to be well described by the Abelian Halperin (3,3,1)-state [26]. For this system, it was found that a sizable energy gap only occurs for the (3,3,1)-state but not for the MR Pf state [27] which is expected for a smaller layer separation and stronger inter-layer

6.2 Numerical Studies 75

tunneling. In contrast, at $\nu_{\rm total} = 5/2$ results suggest that both the (3,3,1)-state (at weak inter-layer tunneling and large d) and the MR Pf state (at strong inter-layer tunneling and small d) might be gapped [27], which might lead to a quantum phase transition that could be probed in experiments.

6.3 Detecting the Quasiparticle Charge

The quasiparticle charge alone does not tell us anything about the statistics of the underlying FQH state and all candidate wavefunctions have edge excitations with an expected quasiparticle charge of $e^*/e = 1/4$ (see Table 3.2). Nevertheless, the verification of the $e^*/e = 1/4$ quasiparticle charge is important as verification and for the interpretation of other experiments. We will mainly discuss two approaches here: shot noise measurements and local compressibility measurements.

6.3.1 Shot Noise Measurements

In these experiments, shot noise generated by partitioning of electrons or quasiparticles at a QPC is measured. The zero frequency spectral density of the current fluctuations S, which is generated in this process, depends on the driving current I, the charge of the partitioned charge carriers q and the transmission t of the QPC (at T=0):

$$S \propto 2qI \times t(1-t) \tag{6.1}$$

Hence, measuring S as a function of I gives access to q. Taking finite temperature effects and transmission of underlying edge states into account, a more complicated expression is found [28], but the principle of the determination of q is the same. Using this shot noise approach, $e^*/e = 1/3$ has been found at $\nu = 1/3$ [29, 30]. In the second Landau level, quasiparticle charges of $e^*/e = 1/4$ for $\nu = 5/2$ and $e^*/e = 1/3$ for $\nu = 8/3$ have been found by Dolev et al. [31].

Subsequent experiments revealed that extracted quasiparticle charges depend significantly on the transmission of the QPC [32]. The quasiparticle charge at $\nu=5/2$ is shown in Fig. 6.1 for different average transmission of the QPC. The expected quasiparticle charge $e^*/e=1/4$ is only found in a range of transmissions from approximately 0.4 to approximately 0.6, but is much larger otherwise. The reason for this effect and the implications for the underlying physics are not understood, but might be of great importance for tunneling and interference experiments where QPC transmission is typically very small or close to one.

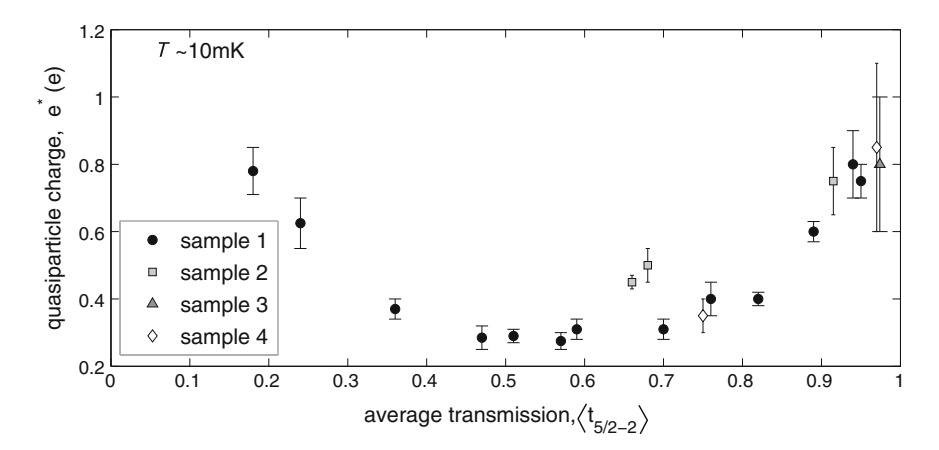


Fig. 6.1 Extracted quasiparticle charge at $\nu=5/2$ for different average transmission of the QPC. At high or low transmission, e^*/e clearly deviates from the expected value of 0.25. (Reprinted figure with permission from [32]. Copyright 2010 by the American Physical Society.)

6.3.2 Local Compressibility Measurements

Scanning SET experiments have been used to investigate localization in the quantum Hall regime [33, 34]. When the bulk is tuned to an incompressible state, charge is localized in puddles which arise from the disorder potential in the sample [33]. The occupation of these localized states is governed by Coulomb blockade physics, when the disorder broadening is small compared to the energy gap of the FQH state [33]. Using a scanning SET, jumps of the local chemical potential, associated with adding or removing charge from the compressible puddles, can be detected. Venkatachalam et al. have used a SET, fabricated on the surface of a high mobility 2DEG, to detect these discontinuities in the chemical potential [35]. Varying the density, jumps in the local chemical potential are observed. The periodicity is expected to scale with the quasiparticle charge, which is associated with the incompressible FQH state surrounding the compressible puddle (i.e. the bulk FQH state).

Venkatachalam et al. have used a comparison of the FQH states at $\nu=7/3$ and $\nu=5/2$ to estimate the quasiparticle charge at $\nu=5/2$. From the periodicity of the jumps of the electrochemical potential when the backgate is varied, they found: $e_{7/3}^*/e_{5/2}^*=1.31$. Assuming $e_{7/3}^*=e/3$, this corresponds to $e_{5/2}^*=0.254$ e.

6.4 Bulk Experiments: Probing the Spin Polarization

The spin-polarization of the $\nu = 5/2$ state has been investigated with different techniques. Transport methods employ a density variation or in-plane fields and try to find signatures of the spin-polarization by its influence on the energy gap of

the $\nu = 5/2$ state. We will also discuss experiments that have used optical or nuclear magnetic resonance methods to probe the spin-polarization in a more direct way.

6.4.1 Transport: Density Dependence of the Gap

Many authors have reported studies investigating the density dependence of the energy gap at $\nu=5/2$. A fundamental experimental challenge faced by these studies lies in the fact that the density of conventionally doped heterostructures can only be tuned over a relatively small range. Furthermore the mechanism limiting the energy gap of the $\nu=5/2$ state is not fully understood. A change of the gap as a function of the density might arise from a combination of several effects, especially also due to the contribution of different scattering mechanisms at different densities. Though the density dependence of the energy gap is not directly connected to the nature of the ground state at $\nu=5/2$, such studies potentially give important information about phase transitions and mechanisms limiting the gap.

An example of such a measurement is shown in Fig. 6.2a. Here the energy gaps at $\nu = 5/2$ and $\nu = 8/5$ obtained by Pan et al. [36] is shown for a large range of electron densities. They have used a heterojunction insulated gate field-effect transistor (HIGFET), i.e. a structure without intrinsic doping, where the 2DEG is only induced via a biased gate. With this structure, density could be changed over a large range and a surprisingly pronounced $\nu = 5/2$ state was observed given a mobility of $\mu < 5.5 \times 10^6 \text{ cm}^2/\text{Vs}$.

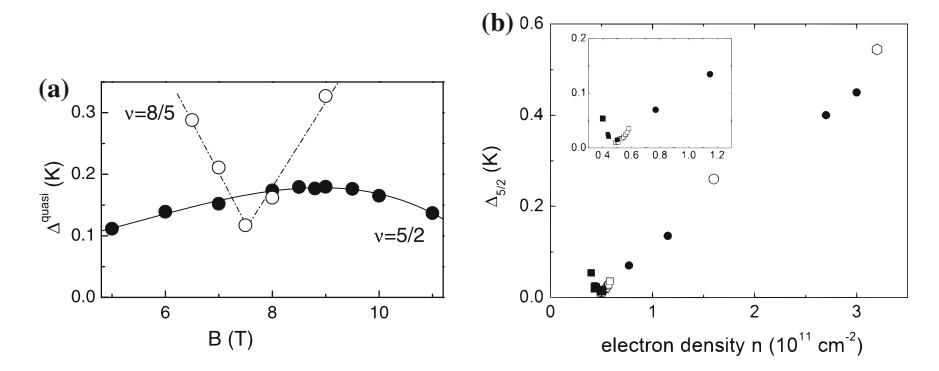


Fig. 6.2 a Energy gaps at $\nu = 5/2$ and $\nu = 8/5$ versus perpendicular magnetic field. The energy gap at $\nu = 8/5$ shows a non-monotonicity due to a spin transition at $B \approx 7.5$ T. In contrast, the energy gap of $\nu = 5/2$ only shows a weak variation over the whole density range. (Reprinted from [36] with permission from Elsevier.) **b** Energy gap at $\nu = 5/2$ versus electron density. A non-monotonicity in the energy gap, which might be interpreted as a spin transition, was found at very low densities of $n \approx 0.5 \times 10^{11}$ cm⁻². (Reprinted figure with permission from [37]. Copyright 2014 by the American Physical Society.)

The FQH state at $\nu=8/5$ is thought to be spin-unpolarized [38, 39]. The strength of the external magnetic field changes the Zeeman energy of the $\nu=8/5$ state, which might lead to a phase transition and hence a non-monotonic dependence of the energy gap on density. The kink observed in Fig. 6.2a has been interpreted as such a spin transition. The comparably weak dependence of the energy gap of $\nu=5/2$ on the density was interpreted as evidence for spin polarization, as here a linear or negligible dependence on magnetic field is expected.

Other experiments that report systematic investigations of the energy gap as a function of density include for example the data of Nuebler et al. [40]. Compared to the experiment of Pan et al. [36], their sample showed much higher energy gaps and mobilities. They found a roughly linear increase of the $\nu = 5/2$ energy gap with density, with no non-monotonicity that could be interpreted as phase transition in the sense of a spin-unpolarized ground state.

Though most of the experiments investigating the density dependence of the energy gap have been interpreted as to support spin-polarization [36, 41], Das Sarma et al. have argued in their work [42] that a spin-unpolarized ground-state cannot be ruled out from the experimental data. They argue that the energy gap of a spin-unpolarized state should show a maximum at perpendicular magnetic fields $B_{\perp} \approx 4.5$ T. The reason for this is that for the spin-unpolarized case, Coulomb energy increases with $\sqrt{B_{\perp}}$, which increases the energy gap. On the other hand, the Zeeman term ($\propto B_{\rm tot}$) decreases the energy gap.

Figure 6.3 shows a collection of energy gap values for $\nu = 5/2$, reported by different authors (filled symbols), versus the respective magnetic field B_{\perp} where $\nu = 5/2$ occurs. Bent curves represent fits of a gap model which assumes a spin-unpolarized ground state, while the red dotted-dashed line with a roughly linear slope corresponds to the spin-polarized case. The authors argue that the increase of energy gaps with density was only observed in a too limited density range to be fully conclusive. Furthermore, some experiments are in agreement with a maximum of the energy gap at intermediate densities [36, 41]. Hence, the conclusion that the groundstate at $\nu = 5/2$ is spin-polarized cannot be drawn from these experiments. The inset shows a comparison of energy gaps versus magnetic field (i.e. density) for the spin-polarized state at $\nu = 1/3$. Here, experiments (empty symbols) and gap models for a spin-polarized ground-state (solid lines) agree well.

Very recently, Pan et al. have reported an increase of the energy gap at $\nu=5/2$ when lowering the electron density in a very low density regime [37]. The energy gap as a function of the electron density is shown in Fig. 6.2b. This non-monotonicity could be interpreted as a spin transition occurring at low densities. The data points have only been reported after the study of Das Sarma et al. (Fig. 6.3) and might change the overall interpretation.

To summarize, studies investigating the density dependence of the energy gap might potentially shed light on spin transitions at $\nu = 5/2$. However, the problem that the degree of spin-polarization is only non-trivially connected to the energy gap remains. A more direct probe of the spin polarization is desirable. We will discuss later, how this can be implemented using NMR or optical experiments.

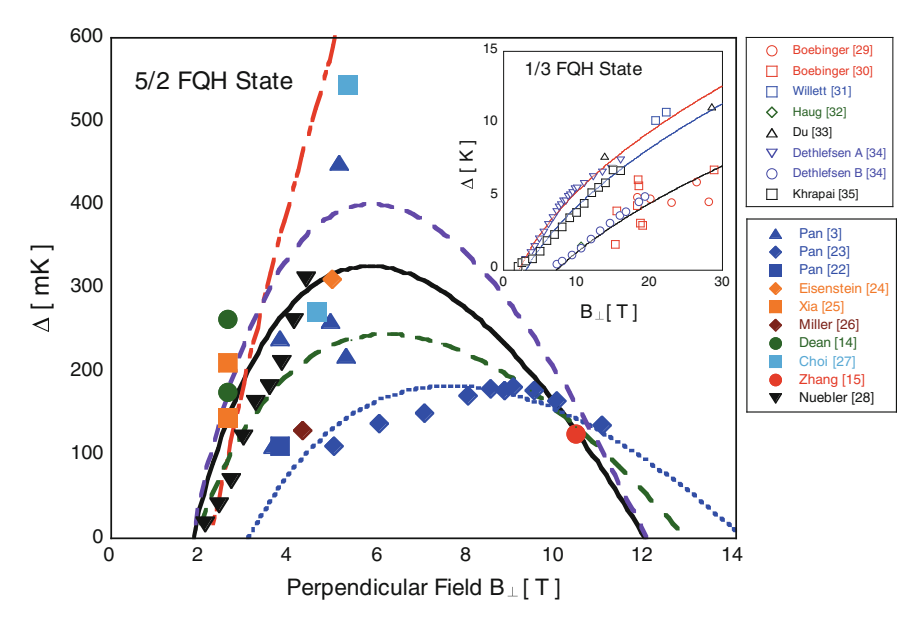


Fig. 6.3 Energy gap of the $\nu = 5/2$ FQH state versus perpendicular magnetic field B_{\perp} . Filled symbols are energy gap values reported in the literature (in [42]). The red dotted-dashed line represents a fit of a spin-polarized gap model, while the bent curves are a fit of spin-unpolarized gap models. A definite agreement with neither case is not found. The inset shows the situation for the spin-polarized state at $\nu = 1/3$, where energy gap values from literature (empty symbols, in [36, 41]) are plotted versus the perpendicular magnetic field B_{\perp} and are compared with spin-polarized gap models (solid lines). Here, a good agreement between model and experiment is found. (Reprinted figure with permission from [42]. Copyright 2010 by the American Physical Society.)

6.4.2 Transport: In-Plane Magnetic Fields

Transport measurements in tilted magnetic fields rely on the fact that the Zeeman energy gap depends on the total magnetic field applied, while the filling factor of the 2DEG is only determined by the carrier sheet density and the perpendicular magnetic field B_{\perp} . For a spin-unpolarized state, the energy gap is expected to decrease monotonically with the Zeeman energy splitting, while the energy gap of a spin-polarized state should either increase with Zeeman energy splitting or not show any dependence at all [42].

Experiments investigating transport in the second Landau level in tilted magnetic fields have shown many stunning results which are not fully understood yet. Adding an in-plane field creates a large transport anisotropy in the second Landau level (Fig. 6.4c, 45° tilt) and reduces the energy gap of the ν = 5/2 state [43–47] (Fig. 6.4a). In contrast, the energy gap of the ν = 7/3 state was found to increase with moderate tilt angles (Fig. 6.4b) [44, 45], which was very surprising, as a similar behavior of ν = 5/2 and 7/3 would be expected if they both are spin-polarized.

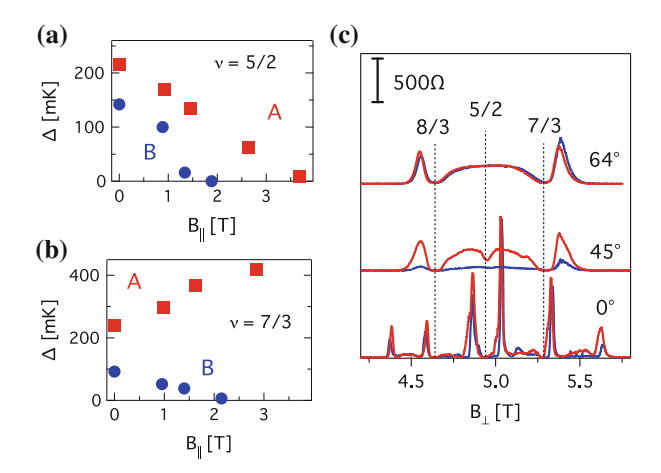


Fig. 6.4 Energy gap at $\nu = 5/2$ as a function of the in-plane magnetic field B_{\parallel} for samples A and B of [45]. The energy gap is substantially reduced by an in-plane component of the magnetic field. **b** Energy gap at $\nu = 7/3$ as a function of the in-plane magnetic field B_{\parallel} for samples A and B of [45]. Sample A shows a surprising increase of the energy gap with increasing B_{\parallel} , similar to earlier observations [44]. In sample B, the energy gap of $\nu = 7/3$ is reduced with increasing B_{\parallel} , \mathbf{c} R_{xx} and R_{yy} between $\nu = 3$ and $\nu = 2$ for three different tilt angles. The initially isotropic incompressible phase at $\nu = 5/2$ is transformed to an anisotropic incompressible phase (45°). When the tilt angle is further increased, a reentrant isotropic compressible phase occurs (64°) [45]. (Reprinted figure with permission from [45]. Copyright 2010 by the American Physical Society.)

As the in-plane component of the magnetic field is further enhanced (Fig. 6.4c, 64° tilt), a transition back to an isotropic phase was found. Here, $\nu = 5/2$ is completely absent, while $\nu = 7/3$ and 8/3 are still visible [45]. Overall, the structure of this "reentrant isotropic compressible (RIC) phase" is very similar to that of the lowest Landau level.

Generally, the decrease of the energy gap of the $\nu=5/2$ state for larger in-plane fields cannot be seen as proof for a spin-unpolarized ground state. Also other FQH states which are generally believed to be spin-polarized, like the $\nu=1/3$ and 2/5 states disappear as the in-plane field strength is increased [42]. Das Sarma et al. proposed that the reason for the disappearance of the gap is not a proof for a spin-polarized ground state, but is rather due to an increase of the effective disorder broadening because of magneto-orbital coupling [42]. Also a competing stripe phase at increasing tilt angles might be responsible for the breakdown of the energy gap [48].

6.4.3 *Optics*

Recent optical approaches to measure the electron spin polarization at $\nu = 5/2$ include polarization resolved photoluminescence spectroscopy experiments by Stern et al. [49] and resonant inelastic light scattering experiments by Wurstbauer et al. [50].

Stern et al. measured the energy splitting between the σ^+ and σ^- emission lines, which depends on the sum of Zeeman energies of conduction band electrons and valence band holes and an interaction term that is proportional to the electron spin polarization [49]. Close to $\nu = 5/2$, this interaction term disappears from which the authors concluded the absence of spin polarization. It was later pointed out by Jain [48] that skyrmion-like excitations due to valence band holes (as proposed by Wójs et al. [51]) might lead to a local spin depolarization, which might influence the outcomes of the experiment.

Wurstbauer et al. have found evidence for gapped low-lying excitations at $\nu = 5/2$ by resonant inelastic light scattering. The intensity of spin-wave modes at $\nu = 5/2$ and 7/3 (but not 8/3) was found to depend on the population of the spin-up branch of the N=1 Landau level, which might indicate a full spin polarization at these filling factors.

6.4.4 Nuclear Magnetic Resonance Techniques

Recent experiments have made use of nuclear magnetic resonance (NMR) techniques for the detection of the electron spin polarization [52, 53]. A non-zero electron spin-polarization represents an effective local magnetic field, which reduces the nuclear resonance frequency, the "Knight shift".

In the work by Tiemann et al. [52], the Knight shift was detected by using a resistively detected nuclear magnetic resonance technique [54]. This technique makes use of the fact that resonant absorption of radio frequency (rf) magnetic fields leads to a detectable change in R_{xx} , as hyperfine interaction couples the nuclear spin bath and the electron Zeeman energy. Here, a backgate was used to switch to a filling factor where R_{xx} is finite and the rf absorption can be seen as a change in R_{xx} . Figure 6.5b shows the degree of nuclear spin polarization P that has been obtained

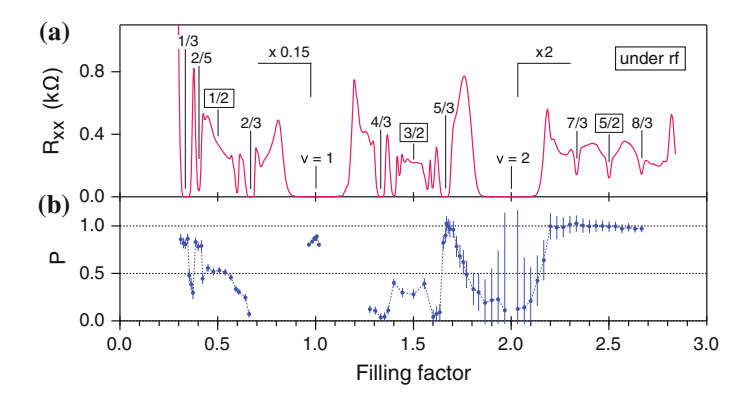


Fig. 6.5 a R_{xx} versus the filling factor under rf exposure. **b** Degree of spin polarization P for various filling factors. Here $\nu = 5/3$ was chosen as fully spin-polarized reference. (Taken from [52]. Reprinted with permission from AAAS.)

by Tiemann et al. for the different FQH states shown in Fig. 6.5a, as a function of the filling factor. The FQH state at $\nu = 5/3$ was chosen as fully polarized reference state for the calculation of P. The results suggest that the second Landau level and especially the $\nu = 5/2$ state is fully spin-polarized. Similar conclusions have been found by Stern et al. [53].

6.4.5 Conclusion

We have discussed several experiments, trying to investigate the spin polarization at $\nu=5/2$ with different approaches. While some experiments find indications for spin polarization [41, 50, 52, 53], others interpret $\nu=5/2$ as spin-unpolarized [49, 55]. Apart from the experimental complication that all experiments slightly disturb the $\nu=5/2$ state and hence might not probe the equilibrium spin polarization, the possibility that different spin phases of the $\nu=5/2$ state exist has to be considered [48].

6.5 Probing the Edge Properties

We have seen that the spin polarization, a bulk property of the FQH states, can be probed in experiments with different techniques. However, most of the candidate wavefunctions possess a full spin polarization, thus other methods have to be employed in order to discriminate between them. One possibility is to probe the edge properties, which are a more unique signature of the underlying FQH state. Different edge mode parameters for the different FQH states have been worked out theoretically (see Table 3.2), which allows a comparison with experiments.

6.5.1 Quasiparticle Tunneling

Quasiparticle tunneling experiments investigate a system where edge states are weakly backscattered at a nearly completely open quantum point contact. As we have seen in Sect. 4.3.3, quasiparticles tunnel between the counterpropagating edge states in this case, giving rise to a tunneling conductance g_{tun} . Scaling parameters for this tunneling conductance can be extracted from the edge models that have been proposed by theory. The Coulomb interaction parameter g (see Table 3.2) describes the temperature dependence of the tunneling conductance via $g_{\text{tun}} \propto T^{2g-2}$, where T is the temperature. Hence measuring g_{tun} in a weak tunneling situation as a function of the temperature allows extracting g. A finite bias measurement furthermore gives access to the quasiparticle charge e^*/e . The application of this method will be

discussed in much more detail later (see Chap. 11), hence we will restrict ourselves to a discussion of the results of related experiments.

In the first work applying this method to $\nu = 5/2$ by Radu et al. [56], the authors found that the measured tunneling conductance at $\nu = 5/2$ can be very well fitted by the theoretical Luttinger liquid tunneling conductance (4.21) that depends on g and e^*/e (see Fig. 6.6a). The parameters that are extracted from the fit were g = 0.35 and $e^*/e = 0.17$. When the fit error is plotted versus g and e^*/e (Fig. 6.6b), a comparison with the parameters cited in Table 3.2 becomes possible. Agreement with the candidate wavefunctions that share g = 0.5, i.e. the anti-Pfaffian, the SU(2)₂ state and the Majorana-gapped edge-reconstructed Pfaffian, is best. For the experiments of Radu et al., a QPC with a short channel geometry has been used (Fig. 6.6c, Device 1).

Subsequent experiments by Lin et al. [57] have investigated two QPCs of different geometry, fabricated on the identical sample as used by Radu et al. The two QPCs are defined by either biasing the gates A1, G3, and G4 (Fig. 6.6c, Device 2, geometry A) or the gates G1, G2, G3, and G4 (geometry B). For the geometries A/B, best fit parameters g = 0.42/0.34 and $e^*/e = 0.25/0.22$ were found, thus favoring the Abelian (3,3,1)-state and no longer the non-Abelian states that were the favorite candidates for the experiment of Radu et al.

The seemingly contradictory results of the experiments of Radu et al. and Lin et al. were later addressed by Yang and Feldman [58]. They investigated theoretically the influence of Coulomb interaction across the QPC gate on the scaling of the tunneling conductance. They found that an unscreened Coulomb interaction enhances the effective parameter g that is probed in a tunneling experiment. While in an experiment with a long QPC channel Coulomb interaction across the QPC gate has a negligible influence, it was found to enhance g by 0.04 for geometry A and by

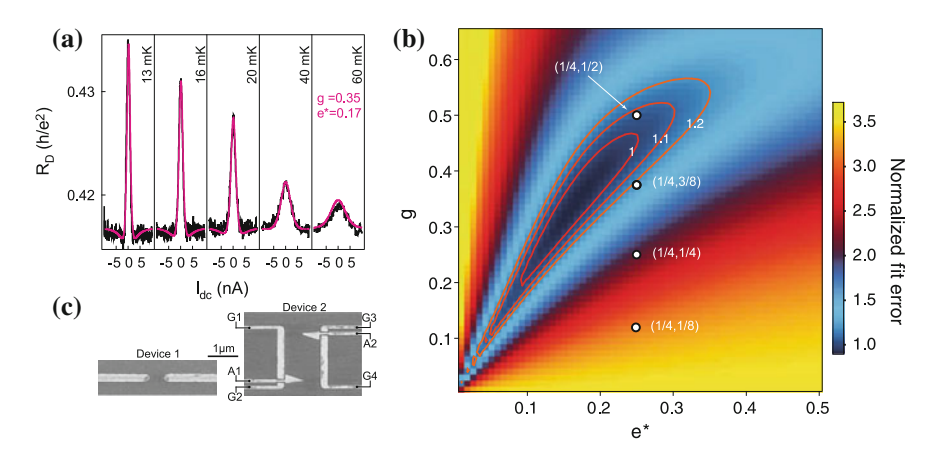


Fig. 6.6 a Measured diagonal resistance $R_{\rm D}$ versus the DC current at $\nu=5/2$ for different temperatures (*black*). A fit of the theoretical weak-tunneling expression (*pink*) fits well the data for the parameters g=0.35 and $e^*/e=0.17$. b Normalized fit error versus g and e^*/e . c Different device geometries for the experiments. (Taken from [56]. Reprinted with permission from AAAS.)

0.08 for the short QPC (device 1 used by Radu et al.). Taking this into account, Yang et al. argue that both experiments by Radu et al. and Lin et al. agree best with an Abelian (3,3,1)-state. Later, it was argued that the Abelian (1,1,3)-state might also be a viable candidate for $\nu = 5/2$ [59]. The quasiparticle tunneling signatures of this state are expected to be identical with those of the (3,3,1)-state [59]. Hence also the (1,1,3)-state is in agreement with the described experiments.

The discussed weak tunneling experiments at $\nu = 5/2$ give important insight in the physics at $\nu = 5/2$. Especially the fact that the weak tunneling conductance can be so well reproduced by a theoretical expression gives confidence about the significance of the weak tunneling theory.

However, there are certain open questions that need to be addressed in order to make a clear statement about the validity of these experiments. The weak tunneling approximation itself is a strong assumption and needs justification. The influence of the tunneling strength on the fit parameters should be investigated. This can for example be done by varying the backscattering strength of the QPC with a gate voltage. Furthermore, the reentrant integer quantum Hall states have a very strong temperature dependence that could strongly influence the extracted parameters. Hence, repeating the tunneling experiments at different magnetic field strengths would be an important validity check. Lastly, a comparison to other FQH states of the second Landau level would be desirable. Though the nature of the most prominent states in the second Landau level, the $\nu=7/3$ and 8/3 states, is not fully clear, they are an important comparison in order to assess the general applicability of the weak tunneling approximation. We will address these open questions in Chap. 11.

6.5.2 Neutral Mode Experiments

The edge properties of the $\nu=2/3$ state have been studied theoretically for a long time. For a steep edge potential, the $\nu=2/3$ edge was predicted to consist of a $\nu=1$ IQH edge state and a counterpropagating hole edge state with filling factor $\nu=1/3$ [60, 61]. However, under such circumstances the two-terminal conductance of the $\nu=2/3$ edge would be non-universal, which was not observed in the experiments. It was then realized that electron interactions and disorder mix these modes, resulting in a collective charge mode and a neutral mode which propagates in the inverse direction [62–64]. In this configuration, the correct two-terminal conductance of $2/3 \times e^2/h$ is found. The neutral mode does not carry any charge, but noise which could eventually be detected in an experiment.

The detection of a neutral mode would be a worthy goal alone, but there are even more reasons why we are interested in it: among the candidate wavefunctions at $\nu = 5/2$, only the Anti-Pfaffian (with and without edge reconstruction) and the Pfaffian (with edge reconstruction) were initially believed to allow a counterpropagating neutral mode [19, 20, 65, 66] (see Table 3.2). Hence an observation of a neutral mode at $\nu = 5/2$ would be a strong (indirect) sign for a non-Abelian state. Later it was recognized [58, 59] that also the Abelian anti-(3,3,1) and (1,1,3)-states and the

non-Abelian anti-SU₂(2) state allow a counterpropagating neutral mode. Hence, also the detection of a neutral mode is not sufficient as proof for a non-Abelian state.

An experiment trying to detect neutral modes has been performed by Bid et al. [67]. The authors have used a measurement scheme where the counterpropagating neutral mode is partially reflected at a QPC and fragmented in charge carriers, which then are detected in a shot noise measurement.

Similar as in the shot noise experiments discussed before, a current bias is used to drive the neutral mode through the partially transmitting QPC (called neutral current). The charged mode (which carries the current) is sent to ground via an additional Ohmic contact and hence is not expected to influence the noise. If no neutral mode is present, no excess noise should be observed, even as the neutral current is increased. However, if a neutral mode is present, excess noise is expected to increase with neutral current. (The peculiar dependence of the current depends on the quasiparticle charge, the temperature and the QPC transmission, for details see [67].)

The latter was exactly what was observed in the experiments of Bid et al. Fig. 6.7 shows the excess noise as a function of the neutral current for two different filling factors—the conventional $\nu=2/5$, where no neutral mode is expected and $\nu=5/2$. For $\nu=5/2$ and for $\nu=2/3$, the excess noise was found to increase with neutral current, which is a strong indication for the presence of a neutral mode. No such behavior was found for $\nu=2/5$, where increasing the neutral current did not generate excess noise.

Later experiments could confirm the presence of neutral modes at $\nu = 5/2$ and also found a neutral mode at $\nu = 8/3$ while it was absent at $\nu = 7/3$ [68]. This would exclude the non-Abelian Read-Rezayi state for $\nu = 7/3$. Furthermore, it was argued that the $\nu = 7/3$ state is not edge reconstructed (as the neutral mode is absent), hence edge reconstruction could also be expected to be absent for $\nu = 5/2$. In this case, the only valid candidate wavefunctions for $\nu = 5/2$ would be the anti-Pfaffian, together with

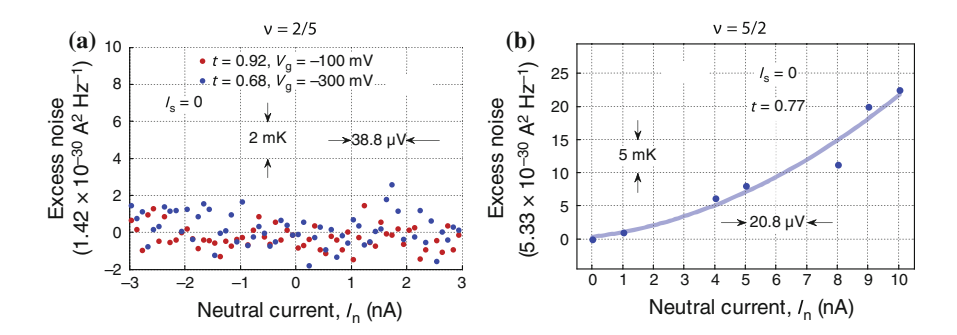


Fig. 6.7 Excess noise as a function of the neutral current for $\nu = 2/5$ (**a**) and $\nu = 5/2$ (**b**). While the neutral current does not induce excess noise for the conventional $\nu = 2/5$ state, an increased excess noise for increased neutral current at $\nu = 5/2$ is an indication for the presence of a neutral mode. (Taken from [67]. Reprinted by permission from Macmillan Publishers Ltd: Nature 466, 585, copyright 2010)

the only later described Abelian anti-(3,3,1)- and (1,1,3)-states and the non-Abelian anti- $SU_2(2)$ state [58, 59].

Overall, the neutral mode experiments seem to give convincing evidence for the presence of a counterpropagating neutral mode at $\nu=5/2$ and rule out some candidate wavefunctions. However, recent experiments [69] have shown some puzzling results that put our understanding of the neutral modes into question. It was found that also ordinary, non-particle-hole conjugate FQH states, like the $\nu=1/3$ state, show neutral modes. Even more surprising, neutral modes were found to propagate through the incompressible bulk of the sample. These findings possibly suggest that edge reconstruction, even for "simple" FQH states, is much more complex than anticipated. Furthermore, unknown mechanisms coupling the bulk and edge might exist.

Given the current lack of knowledge of these processes and neutral modes in general, the observation of a neutral mode alone seems not to be sufficient evidence for definitively demonstrating that one particular candidate wavefunction for $\nu = 5/2$ is correct. Further experiments which probe other aspects of the $\nu = 5/2$ FQH state are needed. Furthermore, Yang et al. have argued very recently that the Abelian (1,1,3)-state is a candidate for $\nu = 5/2$, which similar to the non-Abelian states, exhibits a counterpropagating neutral mode [59].

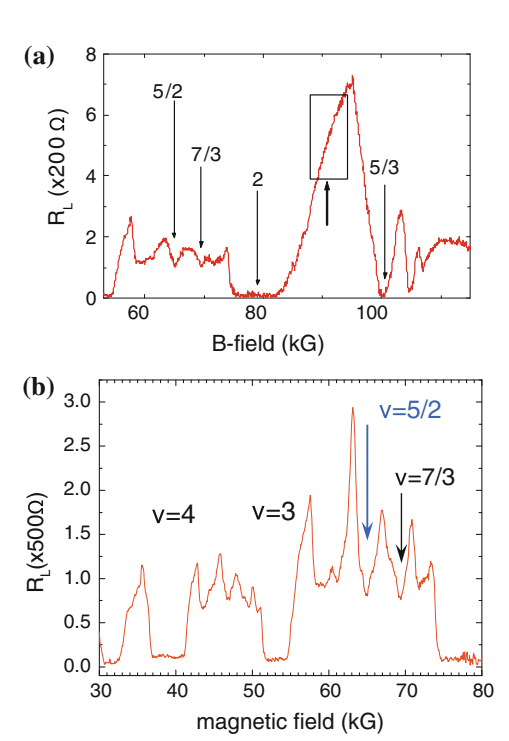
6.6 Interference Experiments at $\nu = 5/2$

We have discussed the basic principle of examining the statistic of the $\nu=5/2$ state with interferometry in Sect. 5.3. A number of experiments [70–73] have tried to implement the theoretical proposals. In the following, we will give a short overview of the experiments of Willett et al., which have attracted most attention. Willett et al. have investigated transport through top-gate defined interferometers [70–72]. These interferometers (see Fig. 6.9a) are approximately 2 μ m long with 1 μ m wide QPCs. In a configuration where a negative top-gate voltage is applied to the 2DEG, the resistance longitudinally across the interferometer, $R_{\rm long}$, is measured. Figure 6.8a, b shows the longitudinal resistance for two different sets of measurements as a function of the magnetic field. While $R_{\rm long}$ drops to zero for IQH filling factors, $R_{\rm long} \approx 200~\Omega$ (Fig. 6.8a) and $R_{\rm long} \approx 380~\Omega$ (Fig. 6.8b) is observed at $\nu=5/2$.

In this configuration, the magnetic field has been set to a certain bulk filling factor and the longitudinal resistance has been measured as a function of the voltage applied to the side-gate of the interferometer (large gates in Fig. 6.9a). For this, side-gate voltages have been swept very slowly (400 mV/24 h) and measurement signals have been integrated using very long lock-in time constants (30–100 s) [71]. Exemplary traces of the longitudinal resistance versus the side-gate voltage are shown in Fig. 6.9c–e. Insets show the Fourier spectra of the individual traces.

Close to a bulk filling factor $\nu = 2$, a side-gate period of 2.5 mV is observed. At $\nu = 7/3$ and 5/2, 9.4 and 12 mV are found for the side-gate period. At $\nu = 5/2$, also a smaller periodicity is observed for a certain side-gate voltage interval (Fig. 6.9e). Looking at the Fourier spectra of the two different side-gate voltage regions (Fig. 6.9f, g) one

Fig. 6.8 Resistance measured longitudinally across the interferometers of [70] (a) and [71] (b) as a function of the magnetic field. While $R_{\rm long}$ drops to zero for IQH states, a finite $R_{\rm long}$ is observed for $\nu = 5/2$. (a From [70]. Copyright 2009 by the National Academy of Sciences, USA. b Reprinted figure with permission from [71]. Copyright 2010 by the American Physical Society.)



can see that their frequencies differ by a factor of approximately two. Willett et al. have argued that the periodicities observed are compatible with an Aharonov-Bohm behavior. A change of the side-gate voltage ΔV_s is expected to lead to a variation of the area of the interferometer, ΔA . Willett et al. argue that in such an Aharonov-Bohm situation, ΔV_s is expected to be proportional to the inverse of the quasiparticle charge e^* : $\Delta V_s \propto \Delta A \propto (h/e^*B)$. A plot of $\Delta V_s \times B$ is shown in Fig. 6.9b. When $e^* = e$ is fixed at $\nu = 2$, the periodicities are compatible with $e^*/e = 1/3$ at $\nu = 7/3$ and $e^*/e = 1/4$ or 1/2 at $\nu = 5/2$.

Another exemplary measurement of the longitudinal resistance versus the side-gate voltage of Willett et al. is shown in Fig. 6.10a [71]. Over a larger voltage range, different regimes, with oscillation amplitudes either corresponding to $e^* = e/4$ or $e^* = e/2$ are observed. The Fourier components for periodicities corresponding to $e^* = e/4$ and $e^* = e/2$ are shown in Fig. 6.10b. Here, an alternation between $e^* = e/4$ and $e^* = e/2$ dominated behavior is observed for different side-gate intervals. In the peak-to-peak spacing of maxima in $R_{\rm long}$ (Fig. 6.10c), a similar alternation is observed.

As we have discussed in Sect. 5.3, theoretical predictions for lowest-order interference processes of FQH states with non-Abelian statistics propose an even-odd pattern for the conductance through an interferometer. For a non-Abelian state at $\nu = 5/2$, periodic conductance oscillations with a side-gate period corresponding to a quasiparticle charge $e^* = e/4$ are expected when an even number of e/4 quasiparticles

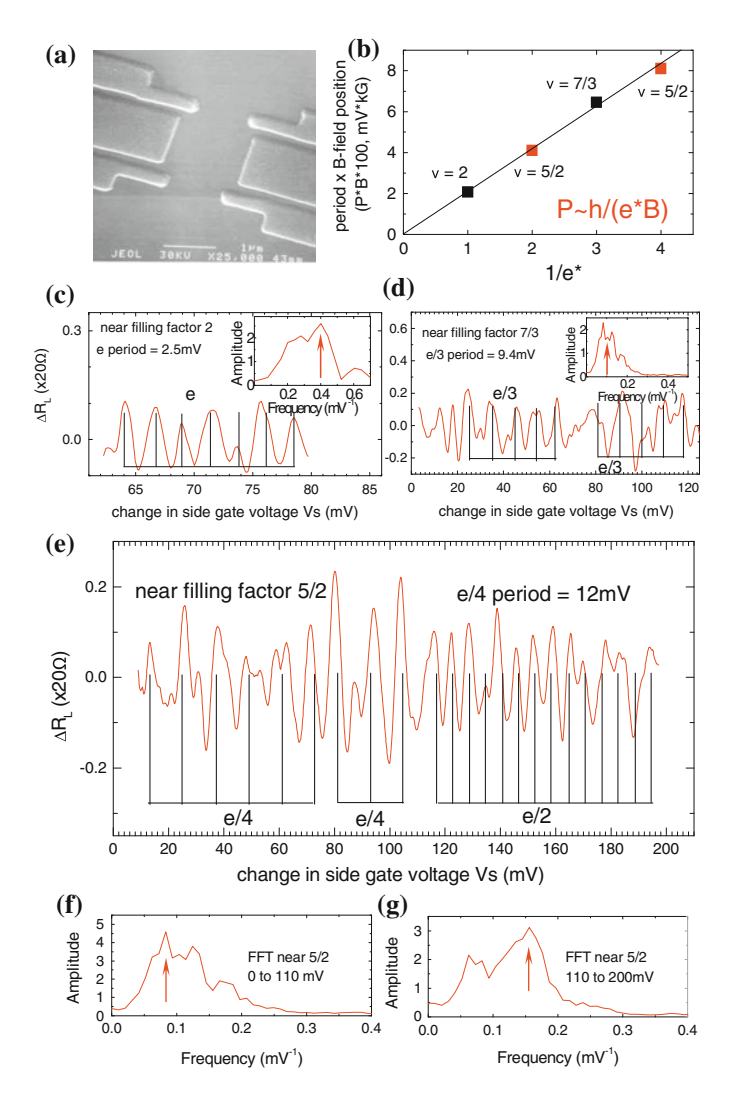


Fig. 6.9 a Interferometer used for the experiments by Willett et al. (c-e): Resistance measured longitudinally across the interferometer as a function of the side-gate voltage for filling factors 2 (c), 7/3 (d) and 5/2 (e). Side-gate voltage periodicities $\Delta V_{\rm s}$ of (c-e), multiplied by the magnetic field are shown in (b). The behavior is consistent with an Aharonov-Bohm behavior with $\Delta V_{\rm s} \propto \Delta A \propto (h/e^*B)$, where ΔA is the induced interferometer area change and e^* is the quasiparticle charge. *Insets* show the Fourier spectra of the *curves*. (Reprinted figure with permission from [71]. Copyright 2010 by the American Physical Society.)

is localized within the interference path [74–78]. For an odd number of *e*/4 quasi-particles localized within the interference path, the interference pattern is expected to vanish.

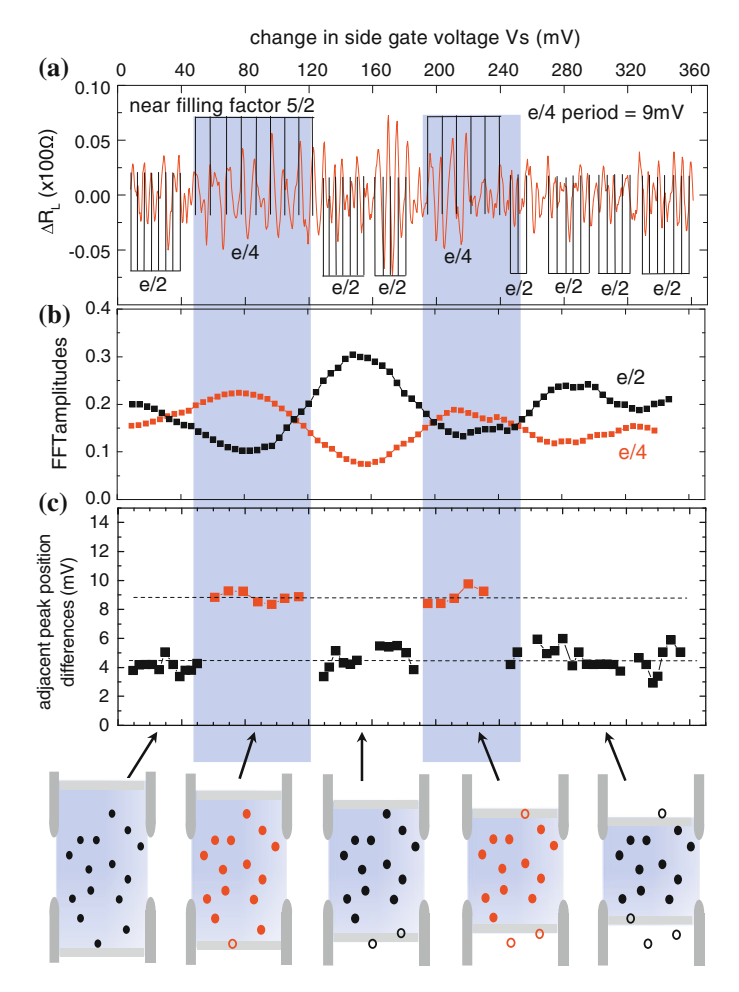


Fig. 6.10 a Longitudinal resistance close to $\nu = 5/2$ as a function of the side-gate voltage. White and shaded blue regions indicate two different regimes. The supposed periodicities corresponding to $e^* = e/4$ and $e^* = e/2$ are indicated. The Fourier components for periodicities corresponding to $e^* = e/4$ and $e^* = e/2$ are shown in (b). Here, an alternation between $e^* = e/4$ and $e^* = e/2$ is observed. In the peak-to-peak spacing of maxima in R_{long} (c), a similar alternation is observed. (Reprinted figure with permission from [71]. Copyright 2010 by the American Physical Society.)

The observation of the alternation between $e^* = e/4$ and $e^* = e/2$ side-gate voltage periodicities has been interpreted by Willett et al. as support for non-Abelian statistics [70, 71]. The authors argue that the disappearance of the e/4 oscillations could be understood as a result of the even-odd behavior predicted by theory. A change between the e/4 and e/2 periodic oscillations then would occur whenever the side-gate voltage has been sufficiently varied to change the number of localized e/4 quasiparticles within the interferometer by one. The appearance of the e/2-periodic

oscillations is not completely understood. They might arise from processes, where a quasiparticles makes two loops around the interferometer [71]. Another possibility might be that they arise from the e/2 Laughlin-type edge excitations that exist for all proposed wavefunctions at $\nu = 5/2$ [74].

Though the results of Willett et al. might constitute the first demonstration of non-Abelian statistics, open questions about the validity of the implementation and the interpretation remain. For example, Abelian states like the (3,3,1)- and (1,1,3)-states might produce a similar even-odd interference pattern as expected for non-Abelian FQH states [59, 79].

6.7 Summary

We have discussed experiments, numerical simulations and theoretical proposals that investigate the properties of the $\nu = 5/2$ state. Numerical studies largely agree on a fully spin-polarized ground state which is closely related to the Moore-Read Pfaffian state [42].

Shot noise, local compressibility and quasiparticle tunneling experiments agree on a quasiparticle charge of $e^*/e = 1/4$. However, this alone does not allow to discriminate between the candidate wavefunctions, as they all are expected to possess $e^*/e = 1/4$ quasiparticle excitations.

The spin polarization is not directly connected to the Abelian or non-Abelian nature of the $\nu = 5/2$ state, but might help to exclude certain candidate states. Experiments have yielded inconsistent results for the spin polarization, though a spin-polarized state seems to be more likely, especially given the recent experiments of [37, 50, 52].

A better discrimination of the different states proposed can be achieved, at least in principle, by probing certain properties of the edge. Tunneling experiments employing QPCs allow extracting interaction parameters that reflect the topological order of the bulk and can be directly compared to expectations for the candidate wavefunctions. Here, experiments agreed closest with the non-Abelian anti-Pfaffian and $SU_2(2)$ FQH states [56] or the Abelian (3,3,1)-state [57]. When intra-edge Coulomb interaction is taken into account, all experiments favor the Abelian (3,3,1)-state. Later, it was argued that the Abelian (1,1,3)-state might also be a viable candidate for $\nu = 5/2$, consistent with quasiparticle tunneling experiments [59]. However, certain points of the tunneling experiments remain unclear. Especially the validity of the weak tunneling assumption and influence of density-modulated phases, backscattering, etc., should be carefully checked. A comparison to presumably better understood FQH states of the second Landau level is highly desirable. We will address these points experimentally in Chap. 11.

Another possibility to probe the edge properties is to probe the presence of a neutral mode. Such a neutral mode is only supported by certain candidate wavefunctions and was found for $\nu = 5/2$ and $\nu = 8/3$, but not for $\nu = 7/3$. This might suggest that $\nu = 5/2$ indeed is a non-Abelian state, though also the Abelian anti-(3,3,1) and

6.7 Summary 91

(1,1,3)-states cannot be ruled out. However, recent experimental observations challenge our general understanding of neutral modes. With this lack of understanding, it might not be possible to draw strong conclusions from the presence of a neutral mode. Furthermore, the Abelian (1,1,3)-state [59], which agrees well with the quasiparticle tunneling experiments, also is expected to possess a neutral mode.

The most direct and most convincing demonstration of a non-Abelian state would be the realization of quasiparticle braiding in an interferometer. We have given an overview of experiments trying to accomplish this. Though the results might indicate non-Abelian statistics, many open questions remain. For example, similar interference patterns as observed might be caused by the Abelian (3,3,1)- and (1,1,3)-states [59, 79]. Further experiments are needed to definitely clarify the question of the nature of the $\nu = 5/2$ state.

References

- 1. K. Yang, B.I. Halperin, Phys. Rev. B 79, 115317 (2009). doi:10.1103/PhysRevB.79.115317
- N.R. Cooper, A. Stern, Phys. Rev. Lett. 102, 176807 (2009). doi:10.1103/PhysRevLett.102. 176807
- 3. R.L. Willett, Rep. Prog. Phys. 76, 076501 (2013). doi:10.1088/0034-4885/76/7/076501
- 4. J.K. Jain, Composite Fermions (Cambridge University Press, Cambridge, 2007)
- 5. R.H. Morf, Phys. Rev. Lett. **80**, 1505 (1998). doi:10.1103/PhysRevLett.80.1505
- 6. F.D.M. Haldane, Phys. Rev. Lett. 51, 605 (1983). doi:10.1103/PhysRevLett.51.605
- E.H. Rezayi, F.D.M. Haldane, Phys. Rev. Lett. 84, 4685 (2000). doi:10.1103/PhysRevLett.84. 4685
- A.E. Feiguin, E. Rezayi, C. Nayak, S.D. Sarma, Phys. Rev. Lett. 100, 166803 (2008). doi:10. 1103/PhysRevLett.100.166803
- 9. G. Möller, S.H. Simon, Phys. Rev. B 77, 075319 (2008). doi:10.1103/PhysRevB.77.075319
- A.E. Feiguin, E. Rezayi, K. Yang, C. Nayak, S.D. Sarma, Phys. Rev. B 79, 115322 (2009). doi:10.1103/PhysRevB.79.115322
- O.S. Zozulya, M. Haque, N. Regnault, Phys. Rev. B 79, 045409 (2009). doi:10.1103/PhysRevB. 79.045409
- M. Storni, R.H. Morf, S.D. Sarma, Phys. Rev. Lett. 104, 076803 (2010). doi:10.1103/ PhysRevLett.104.076803
- G. Möller, A. Wójs, N.R. Cooper, Phys. Rev. Lett. 107, 036803 (2011). doi:10.1103/ PhysRevLett.107.036803
- X. Wan, K. Yang, E.H. Rezayi, Phys. Rev. Lett. 97, 256804 (2006). doi:10.1103/PhysRevLett. 97.256804
- X. Wan, Z.-X. Hu, E.H. Rezayi, K. Yang, Phys. Rev. B 77, 165316 (2008). doi:10.1103/ PhysRevB.77.165316
- I. Dimov, B.I. Halperin, C. Nayak, Phys. Rev. Lett. 100, 126804 (2008). doi:10.1103/ PhysRevLett.100.126804
- R.H. Morf, N. d'Ambrumenil, S.D. Sarma, Phys. Rev. B 66, 075408 (2002). doi:10.1103/ PhysRevB.66.075408
- R. Morf, N. d'Ambrumenil, Phys. Rev. B 68, 113309 (2003). doi:10.1103/PhysRevB.68.
 113309
- M. Levin, B.I. Halperin, B. Rosenow, Phys. Rev. Lett. 99, 236806 (2007). doi:10.1103/ PhysRevLett.99.236806
- S.-S. Lee, S. Ryu, C. Nayak, M.P.A. Fisher, Phys. Rev. Lett. 99, 236807 (2007). doi:10.1103/ PhysRevLett.99.236807

- A. Wójs, C. Tőke, J.K. Jain, Phys. Rev. Lett. 105, 096802 (2010).doi:10.1103/PhysRevLett. 105.096802
- E.H. Rezayi, S.H. Simon, Phys. Rev. Lett. 106, 116801 (2011). doi:10.1103/PhysRevLett.106. 116801
- M.R. Peterson, T. Jolicoeur, S.D. Sarma, Phys. Rev. Lett. 101, 016807 (2008). doi:10.1103/ PhysRevLett.101.016807
- M.R. Peterson, T. Jolicoeur, S.D. Sarma, Phys. Rev. Lett. 78, 155308 (2008). doi:10.1103/ PhysRevB.78.155308
- J. Biddle, M.R. Peterson, S.D. Sarma, Phys. Rev. Lett. 84, 125141 (2011). doi:10.1103/ PhysRevB.84.125141
- M.R. Peterson, J. Phys. Confer. Ser. 402, 012021 (2012). doi:10.1088/1742-6596/402/1/ 012021
- M.R. Peterson, S.D. Sarma, Phys. Rev. B 81, 165304 (2010). doi:10.1103/PhysRevB.81. 165304
- 28. T. Martin, R. Landauer, Phys. Rev. B 45, 1742 (1992). doi:10.1103/PhysRevB.45.1742
- L. Saminadayar, D.C. Glattli, Y. Jin, B. Etienne, Phys. Rev. Lett. 79, 2526 (1997). doi:10.1103/ PhysRevLett.79.2526
- R. de Picciotto, M. Reznikov, M. Heiblum, V. Umansky, G. Bunin, D. Mahalu, Nature 389, 162 (1997). doi:10.1038/38241
- M. Dolev, M. Heiblum, V. Umansky, A. Stern, D. Mahalu, Nature 452, 829 (2008). doi:10. 1038/nature06855
- M. Dolev, Y. Gross, Y.C. Chung, M. Heiblum, V. Umansky, D. Mahalu, Phys. Rev. B 81, 161303 (2010). doi:10.1103/PhysRevB.81.161303
- S. Ilani, J. Martin, E. Teitelbaum, J.H. Smet, D. Mahalu, V. Umansky, A. Yacoby, Nature 427, 328 (2004). doi:10.1038/nature02230
- J. Martin, S. Ilani, B. Verdene, J. Smet, V. Umansky, D. Mahalu, D. Schuh, G. Abstreiter, A. Yacoby, Science 305, 980 (2004). doi:10.1126/science.1099950
- V. Venkatachalam, A. Yacoby, L. Pfeiffer, K. West, Nature 469, 185 (2011). doi:10.1038/ nature09680
- 36. W. Pan, H.L. Stormer, D.C. Tsui, L.N. Pfeiffer, K.W. Baldwin, K.W. West, Solid State Commun. **119**, 641 (2001). doi:10.1016/S0038-1098(01)00311-8
- W. Pan, A. Serafin, J.S. Xia, L. Yin, N.S. Sullivan, K.W. Baldwin, K.W. West, L.N. Pfeiffer,
 D.C. Tsui, Phys. Rev. B 89, 241302 (2014). doi:10.1103/PhysRevB.89.241302
- 38. J.P. Eisenstein, H.L. Stormer, L. Pfeiffer, K.W. West, Phys. Rev. Lett. **62**, 1540 (1989). doi:10. 1103/PhysRevLett.62.1540
- J.P. Eisenstein, H.L. Stormer, L.N. Pfeiffer, K.W. West, Phys. Rev. B 41, 7910 (1990). doi:10. 1103/PhysRevB.41.7910
- J. Nuebler, V. Umansky, R. Morf, M. Heiblum, K. von Klitzing, J. Smet, Phys. Rev. B 81, 035316 (2010). doi:10.1103/PhysRevB.81.035316
- 41. C. Zhang, T. Knuuttila, Y. Dai, R.R. Du, L.N. Pfeiffer, K.W. West, Phys. Rev. Lett. **104**, 166801 (2010). doi:10.1103/PhysRevLett.104.166801
- S. Das Sarma, G. Gervais, X. Zhou, Phys. Rev. B 82, 115330 (2010). doi:10.1103/PhysRevB. 82.115330
- 43. M.P. Lilly, K.B. Cooper, J.P. Eisenstein, L.N. Pfeiffer, K.W. West, Phys. Rev. Lett. 83, 824 (1999). doi:10.1103/PhysRevLett.83.824
- C.R. Dean, B.A. Piot, P. Hayden, S.D. Sarma, G. Gervais, L.N. Pfeiffer, K.W. West, Phys. Rev. Lett. 101, 186806 (2008). doi:10.1103/PhysRevLett.101.186806
- J. Xia, V. Cvicek, J.P. Eisenstein, L.N. Pfeiffer, K.W. West, Phys. Rev. Lett. 105, 176807 (2010). doi:10.1103/PhysRevLett.105.176807
- J.P. Eisenstein, R.L. Willett, H.L. Stormer, L.N. Pfeiffer, K.W. West, Surf. Sci. 229, 31 (1990). doi:10.1016/0039-6028(90)90824-R
- 47. J.P. Eisenstein, R. Willett, H.L. Stormer, D.C. Tsui, A.C. Gossard, J.H. English, Phys. Rev. Lett. 61, 997 (1988). doi:10.1103/PhysRevLett.61.997
- 48. J.K. Jain, Physics 3, 71 (2010). doi:10.1103/Physics.3.71

References 93

 M. Stern, P. Plochocka, V. Umansky, D.K. Maude, M. Potemski, I. Bar-Joseph, Phys. Rev. Lett. 105, 096801 (2010). doi:10.1103/PhysRevLett.105.096801

- U. Wurstbauer, K.W. West, L.N. Pfeiffer, A. Pinczuk, Phys. Rev. Lett. 110, 026801 (2013). doi:10.1103/PhysRevLett.110.026801
- A. Wójs, G. Möller, S.H. Simon, N.R. Cooper, Phys. Rev. Lett. 104, 086801 (2010). doi:10. 1103/PhysRevLett.104.086801
- L. Tiemann, G. Gamez, N. Kumada, K. Muraki, Science 335, 828 (2012). doi:10.1126/science. 1216697
- M. Stern, B.A. Piot, Y. Vardi, V. Umansky, P. Plochocka, D.K. Maude, I. Bar-Joseph, Phys. Rev. Lett. 108, 066810 (2012). doi:10.1103/PhysRevLett.108.066810
- W. Desrat, D.K. Maude, M. Potemski, J.C. Portal, Z.R. Wasilewski, G. Hill, Phys. Rev. Lett. 88, 256807 (2002). doi:10.1103/PhysRevLett.88.256807
- T.D. Rhone, J. Yan, Y. Gallais, A. Pinczuk, L. Pfeiffer, K. West, Phys. Rev. Lett. 106, 196805 (2011). doi:10.1103/PhysRevLett.106.196805
- I.P. Radu, J.B. Miller, C.M. Marcus, M.A. Kastner, L.N. Pfeiffer, K.W. West, Science 320, 899 (2008). doi:10.1126/science.1157560
- X. Lin, C. Dillard, M.A. Kastner, L.N. Pfeiffer, K.W. West, Phys. Rev. B 85, 165321 (2012). doi:10.1103/PhysRevB.85.165321
- 58. G. Yang, D.E. Feldman, Phys. Rev. B 88, 085317 (2013). doi:10.1103/PhysRevB.88.085317
- 59. G. Yang, D.E. Feldman, Phys. Rev. B **90**, 161306(R) (2014). doi:10.1103/PhysRevB.90.161306
- 60. A.H. MacDonald, Phys. Rev. Lett. **64**, 220 (1990). doi:10.1103/PhysRevLett.64.220
- M.D. Johnson, A.H. MacDonald, Phys. Rev. Lett. 67, 2060 (1991). doi:10.1103/PhysRevLett. 67.2060
- C.L. Kane, M.P.A. Fisher, J. Polchinski, Phys. Rev. Lett. 72, 4129 (1994). doi:10.1103/ PhysRevLett.72.4129
- 63. C.L. Kane, M.P.A. Fisher, Phys. Rev. B 51, 13449 (1995). doi:10.1103/PhysRevB.51.13449
- 64. C.L. Kane, M.P.A. Fisher, Phys. Rev. B 55, 15832 (1997). doi:10.1103/PhysRevB.55.15832
- 65. B.J. Overbosch, X.-G. Wen. arXiv:0804.2087 [cond-mat] (2008)
- 66. M. Milovanović, N. Read, Phys. Rev. B 53, 13559 (1996). doi:10.1103/PhysRevB.53.13559
- A. Bid, N. Ofek, H. Inoue, M. Heiblum, C.L. Kane, V. Umansky, D. Mahalu, Nature 466, 585 (2010). doi:10.1038/nature09277
- M. Dolev, Y. Gross, R. Sabo, I. Gurman, M. Heiblum, V. Umansky, D. Mahalu, Phys. Rev. Lett. 107, 036805 (2011). doi:10.1103/PhysRevLett.107.036805
- 69. H. Inoue, A. Grivnin, Y. Ronen, M. Heiblum, V. Umansky, D. Mahalu, Nature Commun. 5 (2014). doi:10.1038/ncomms5067
- R.L. Willett, L.N. Pfeiffer, K.W. West, Proc. Nat. Acad. Sci. 106, 8853 (2009). doi:10.1073/pnas.0812599106
- 71. R.L. Willett, L.N. Pfeiffer, K.W. West, Phys. Rev. B **82**, 205301 (2010). doi:10.1103/PhysRevB. 82.205301
- 72. R.L. Willett, C. Nayak, K. Shtengel, L.N. Pfeiffer, K.W. West, Phys. Rev. Lett. 111, 186401 (2013). doi:10.1103/PhysRevLett.111.186401
- 73. S. An, P. Jiang, H. Choi, W. Kang, S.H. Simon, L.N. Pfeiffer, K.W. West, K.W. Baldwin, *Braiding of Abelian and Non-Abelian Anyons in the Fractional Quantum Hall Effect*. arXiv:1112.3400 (2011)
- 74. W. Bishara, P. Bonderson, C. Nayak, K. Shtengel, J.K. Slingerland, Phys. Rev. B **80**, 155303 (2009). doi:10.1103/PhysRevB.80.155303
- A. Stern, B.I. Halperin, Phys. Rev. Lett. 96, 016802 (2006). doi:10.1103/PhysRevLett.96. 016802
- P. Bonderson, A. Kitaev, K. Shtengel, Phys. Rev. Lett. 96, 016803 (2006). doi:10.1103/ PhysRevLett.96.016803
- P. Bonderson, K. Shtengel, J.K. Slingerland, Phys. Rev. Lett. 97, 016401 (2006). doi:10.1103/ PhysRevLett.97.016401
- R. Ilan, E. Grosfeld, K. Schoutens, A. Stern, Phys. Rev. B 79, 245305 (2009). doi:10.1103/ PhysRevB.79.245305
- A. Stern, B. Rosenow, R. Ilan, B.I. Halperin, Phys. Rev. B 82, 085321 (2010). doi:10.1103/ PhysRevB.82.085321

Part II Setup and Sample Optimization

Chapter 7 Measurement Setup Optimization for Low Electron Temperatures

Abstract The main steps for improving a dry dilution refrigerator setup for low electron temperatures are discussed. The pulse tube refrigerator (PTR) and the still turbo-pump are the main sources of vibrations, which couple to the sample via the magnetic field and cause heating. This effect was minimized by decoupling the PTR from the cryostat top-plate, 77 K and 4 K plates. The still turbo-pump could efficiently be decoupled via a T-bellows construction. A customized frame has been constructed to avoid vibrations caused by the experimentalist. Using a well-considered grounding scheme and insulation transformers, low electronic noise levels, necessary for low electron temperatures, are achieved. To be able to reach the lowest electron temperatures, advanced filtering and thermal anchoring are necessary. We describe how this is accomplished in our setup, using different filtering and thermalization elements.

7.1 Introduction

Experiments that probe the $\nu=5/2$ state and other FQH states in the second LL require extremely low electronic temperatures. Activation energies of these states of as low as approximately $100-150\,\mathrm{mK}$ are found in even the best high mobility quantum wells grown at ETH Zürich [1]. The proposed interference experiments for the $\nu=5/2$ state require electronic temperatures of below $20\,\mathrm{mK}$, because of the short and temperature-dependent quasiparticle coherence lengths [2] (see Sect. 14.2). Though dilution refrigerators with base temperatures below $10\,\mathrm{mK}$ are commercially available, cooling 2DEG electrons still is experimentally challenging.

Phonon-mediated heat transfer across an interface between two solids is described by the Kapitza thermal resistance $R_{\rm K}$ [3]. The Kapitza resistance occurs due to an acoustic mismatch at an interface between two solids. Here, an incident phonon has a finite probability of being reflected, because of a discontinuity of the refractive index at the interface [4]. Overall, this leads to a large thermal boundary resistance $R_{\rm K} \propto T^{-3}$ [5]. The electron-lattice thermal resistance $R_{\rm ep}$ is even larger at low temperatures. Here, $R_{\rm ep} \propto T^{-4}$ [6] or $R_{\rm ep} \propto T^{-5}$ [7] is found for pure or dirty metals. Thus the cold phonon bath is only extremely weakly coupled to the electron bath at these low temperatures, which results in a very small cooling power that

reaches the sample 2DEG. Even small heat sources lead to an electronic temperature that is significantly larger than the phonon (bath) temperature. The sample cabling, which necessarily forms an electric connection to the room temperature environment, is one of the main heat sources. It transmits high frequency radiation from the room temperature side to the sample, which results in electronic temperatures of $T_{\rm el} > 60\,{\rm mK}$ for typical cryostat cablings.

For the work presented in this book, a new cryostat filtering setup had to be designed and built and the existing dilution refrigerator had to be modified to allow for low-noise measurements at low electronic temperatures. To accomplish this, first heating sources as electronic noise or vibrations had to be minimized. The experiments were conducted in a dry dilution refrigerator, which is pre-cooled to temperatures below 4 K with a pulse-tube refrigerator [8]. The mechanical vibrations caused by the expanding gas in the cold head and vibrations of the rotary valve set an experimental challenge compared to traditional wet dilution refrigerators.

The second step towards decreasing the electronic temperature is done by heavily filtering the DC lines that connect the sample. High-frequency radiation in the GHz and THz range has to be efficiently blocked. As every filtering element emits thermal noise by itself, this filtering has to be done at different temperature stages and especially at the lowest temperature. Lastly, the thermal contact of the sample to the mixing chamber has to be optimized, to allow for efficient cooling of the electron gas. This has been accomplished by integrating a cold-finger made of high-purity, thermally annealed silver, providing an extremely high thermal conductivity. Heat sinks ensure thermalization of the cables, which are directly coupled to the electron bath of the 2DEG. Contact resistances are another bottleneck for the thermal coupling between the mixing chamber and the electron gas. In Chap. 8, we will discuss how contacts of mesa-defined structures were optimized in this respect. An overview of the experimental problems that prevent low electron temperatures and possible solutions is given in Table 7.1.

7.2 Dilution Refrigerator Setup

Most experiments presented in this work have been performed in a dry VeriCold¹ dilution refrigerator, with a base temperature of approximately 9–10 mK. The cryostat and the setup frame are shown in Fig. 7.1a. An overview of the mixing chamber plate, seen from below is shown in Fig. 7.1b. Different filtering components are arranged around the silver cold-finger, which points in the bore of a superconducting 5 T magnet. On top of the base-plate, cold-plate ($T \approx 80 \, \text{mK}$) and still-plate ($T \approx 800 \, \text{mK}$) are visible.

¹Now part of Oxford Instruments.

Table 7.1 Overview of different problems that prevent us from reaching low electron temperatures, their effect on the sample and possible solutions

Problem	Effects on sample	Solution
Mechanical vibrations from:		
• Pulse tube head and rotary valve	Heating of the mixing chamber by friction	• PT head has been decoupled from 4 K plate
Turbo molecular pump	• Induces noise and currents in the sample cabling by vibrations in the magnetic field, and hence sample heating	Rotary valve as been mounted to ceiling
• Experimentalists, etc.		• Turbo molecular pump is decoupled via bellows construction
		More stable cryostat frame has been installed
Environment noise:		
• Electric and magnetic noise from pumps, power supplies, etc. (mainly 50 Hz and higher order)	Sample heating, noisy measurement signals	• High frequency radiation (f > 1 kHz) is removed by several filtering stages in the cabling
• High frequency noise from screens, radio transmitters, etc.		• Low frequency noise is hard to filter out. Noise is reduced by using insulation transformers, opto-couplers and keeping power supplies etc. far away from the cryostat
Thermal radiation		
	Sample heating by absorption of high frequency radiation	• Filtered out by several cold filtering stages in the cabling. For very high frequencies Thermocoax cables are highly efficient
		Sample and cabling on the mixing chamber are double shielded by massive high thermal conductivity silver shields
Weak thermal coupling of the sample		
	• Equilibrium temperature of the sample is higher for a given heat leak	• Coupling is optimized by using quartz heat sinks and by thermalizing copper cables on the silver cold finger
		• Optimized thermal coupling by high thermal conductivity silver cold finger

(continued)

Table 7.1 (continued)

Problem	Effects on sample	Solution
		Contact resistances of the samples are minimized with an optimized contact recipe
		• Cold ground may contribute additional thermal coupling
Heating by eddy currents and adiabatic magnetization		
	• Electron temperature is enhanced after and during sweeps of the <i>B</i> -field	Adiabatic (de-) magnetization is minimized by using a silver cold finger
		 Eddy current heating only depends on the geometry of the cold finger. We have favored optimized shielding over geometry optimized for small eddy currents → B-field has to be swept sufficiently slow

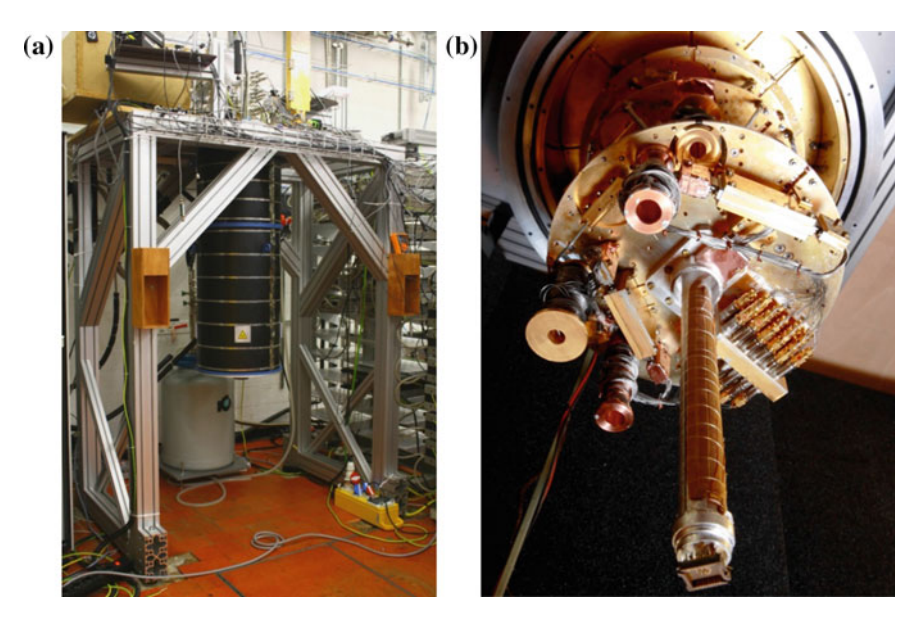


Fig. 7.1 a Overview of the dilution refrigerator setup and the setup frame. The cryostat OVC is wrapped in thick neoprene mats for vibration damping. **b** View on the mixing chamber plate of the cryostat from *below*. The individual components of the filtering setup are described later

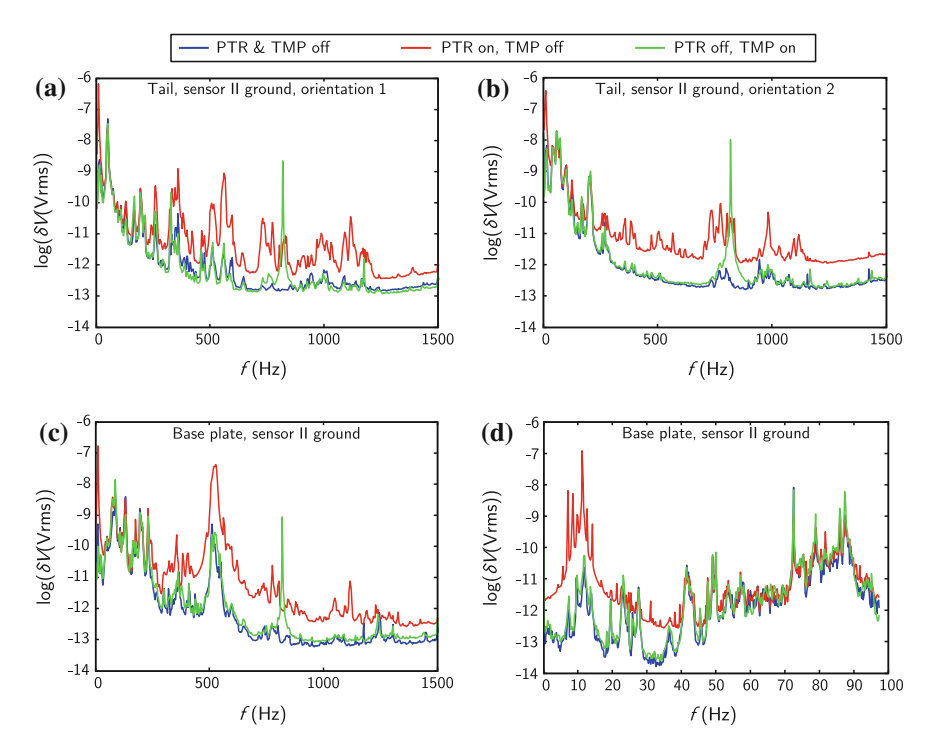


Fig. 7.2 Vibration spectra for different orientations of a piezo acceleration sensor on the tail and the base-plate. Compared to the reference measurements (*blue*), where PTR and TMP are switched off, substantial additional noise sets in, as PTR (*red*) or TMP (*green*) are switched on

7.2.1 Vibration Minimization and Insulation

The advantage of not having to refill liquid Helium comes for a price—significantly increased vibrations, compared to a traditional wet system. Figure 7.2 shows vibration measurements before the decoupling of the PT head. These measurements were done with a piezo acceleration sensor for different orientations on the cold-finger and on the base-plate. Here, the amplitude δV is linearly proportional to the acceleration for the displayed frequency range. Comparing measurements where PTR and TMP are running with the reference measurement (blue) reveals strongly enhanced vibrations due to the PTR and the TMP. The TMP mainly causes vibrations at its operation frequency of 820 Hz, whereas the PTR induces a whole range of vibrations from 1.4 Hz to more than 1 kHz.

Figure 7.3 shows the power spectral density of the current through a QPC ($R \approx 22$ k Ω and $R \approx 40$ k Ω for B = 4.4 T), measured with an IV converter with a feedback resistance of 10 M Ω . As a finite magnetic field is applied, PTR and TMP vibrations are translated into substantial electronic noise, which might cause significant heating of the sample.

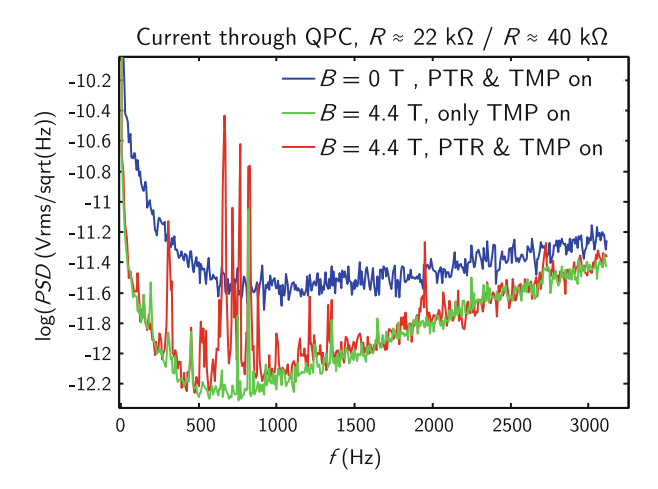


Fig. 7.3 Power spectral density of the voltage output of an IV-Converter ($R_F = 10 \,\mathrm{M}\Omega$), connected to a cold QPC. As the magnetic field is switched on, TMP and PTR vibrations are visible as pronounced electronic noise

The components which are responsible for the biggest part of the vibrations are discussed in the following.

7.2.1.1 Pulse Tube Cryocooler

The pulse tube cryocooler itself is integrated in the OVC of the dilution refrigerator. In the initial configuration, the room temperature side of the head was fixed to the top-plate of the cryostat. Both cold stages were decoupled from their respective plates by short and stiff copper braids. For vibration reduction, the fixed connection on the room temperature side has been replaced by a flexible bellows-ring (Fig. 7.4b). For this, it was necessary to completely open the mixing circuit which is soldered to the cold head for pre-cooling.

The thermal anchoring to 4 K and 70 K plates has been replaced by much longer and more flexible copper braids. In Fig. 7.4a, the two cold head stages with the new thermal anchoring can be seen. A comparison of the initial and the new, self-made copper braids is shown in Fig. 7.5.

The effect of the decoupling of the PTR head is shown in Fig. 7.6. Here, vibration spectra, measured with a piezoelectric vibration sensor on the base-plate, before and after decoupling are shown. After decoupling, the overall background is reduced and the wide dominant peak at approx. 12 Hz is less visible. It should be noted that a quantitative comparison is difficult, as the recorded vibration spectrum depends strongly on the exact position of the piezo sensor and how it is fixed, which is not necessarily comparable for two different measurements. However, the overall flatter vibration spectrum after decoupling suggests that this measure was highly efficient.

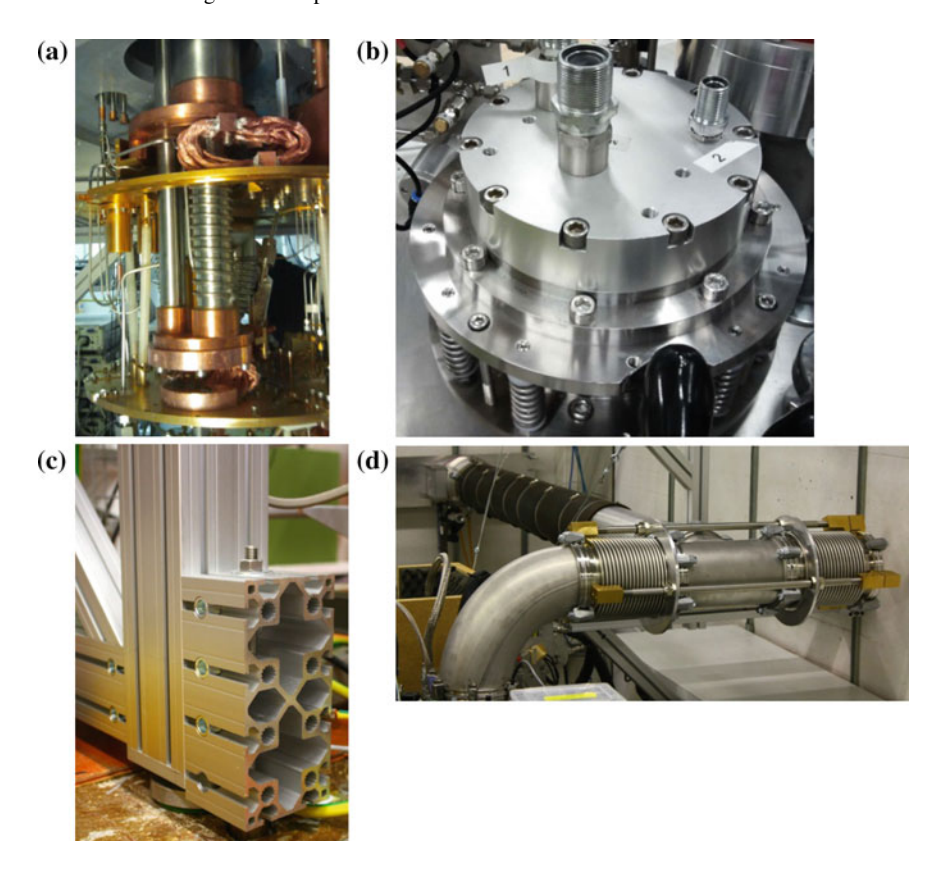


Fig. 7.4 a The pulse tube cryorefrigerator, installed in the dilution refrigerator system with improved thermal anchoring. b A newly installed bellows-ring reduces vibration transfer from the cold head to the cryostat. c A very stiff Kanya frame has been chosen for mounting the cryostat. For minimal vibration sensitivity, the frame is anchor bolted to the concrete bottom plate of the building. d The still turbo-pump is anchor bolted to the building wall (left). The still line is connected to the cryostat via a T-bellows construction which efficiently avoids vibration transfer. The still line is also wrapped with thick neoprene mats (black)

7.2.1.2 Pulse Tube Rotary Valve

The rotary valve of the pulse tube cooler is connected to the cold head by an approximately 0.7 m long high pressure tube, which is contracting and expanding. The rotary valve has been placed in a noise insulating box, which is flexibly mounted to the lab ceiling. This step strongly reduced low frequency vibrations which were visible in the measurements when the rotary valve was fixed on top of the cryostat frame. Compared to the initial configuration of the system, the motor driver of the rotary valve has been replaced. Initially, the rotary valve was controlled by the Cryomech pulse tube compressor, which applied a sinusoidal voltage pulse to drive the rotary valve. The resolution of the voltage output of the compressor was found to have a very poor



Fig. 7.5 The standard thermal anchoring of the PTR (*upper column*) was very stiff and also too short after the installation of the PTR head bellows ring. The self-made replacement of the thermal anchoring is shown *below*. By using longer and more flexible copper braids, the vibration transfer could be significantly reduced

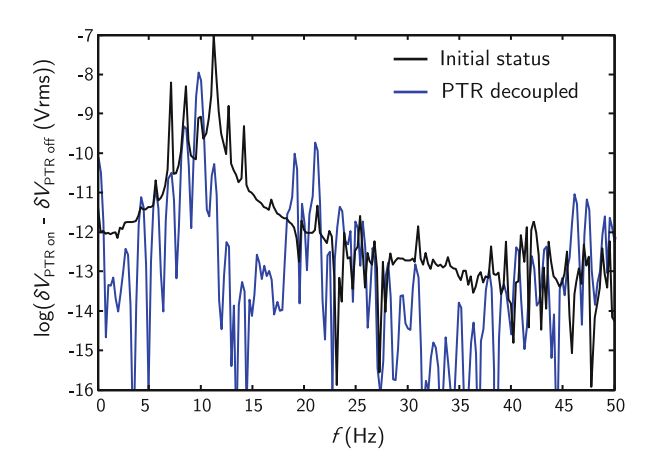


Fig. 7.6 Vibration spectra on base-plate, before and after decoupling of the PTR head

resolution, which "chops" the sinus pulse in coarse rectangular pulses and with this generates significant electronic noise and also mechanical vibrations. We have added an external driver (Precision Motion Controls LNX-G) to our setup, which resolves this problem by applying a much smoother voltage signal. The new driver was found by other groups² to significantly reduce vibrations and electromagnetic emission.

²C.L. Degen, private communication.

7.2.1.3 Turbomolecular Pump

As discussed earlier, the TMP mainly causes vibrations at its operation frequency of 820 Hz. In order to get rid of these vibrations, a T-bellows construction (Fig. 7.4d) has been implemented. This construction avoids an asymmetric contraction under vacuum and insulates the cryostat from the transversal still line vibrations at the same time. After the installation of the T-bellows, no 820 Hz noise could further be observed in any measurement.

7.2.1.4 Forepump

The rotary forepump and the compressor are kept outside of the laboratory, mainly for noise reasons. The forepump is connected to the still TMP via a long vacuum tube. In order to prevent vibration transmission from the forepump to the TMP and hence to the cryostat, the long vacuum tube is partially buried in a sand box, which efficiently damps the low-frequency vibrations (see Fig. 7.7).

7.2.1.5 Cryostat Frame

The initially used frame of the cryostat turned out not to be stable enough against vibrations caused by the experimentalists and had to be scaled down for space reasons. The final frame, built out of Kanya profiles with multiple connections to stiffen the

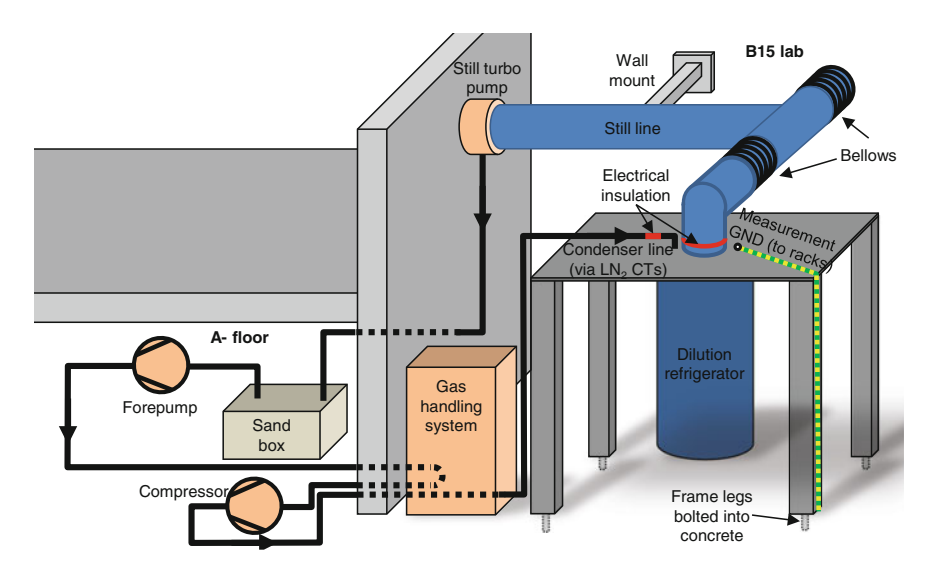


Fig. 7.7 Schematic overview of the pumping circuit of the dilution refrigerator setup

construction can be seen in Fig. 7.1a. The frame itself is not free-standing any more, but is anchor bolted to the 3 m thick concrete bottom plate of the building (Fig. 7.4c). With this frame it is possible to work on the devices and cabling on the top-plate of the cryostat, without heating the mixing chamber and the sample by vibrations.

Figure 7.7 shows an overview of the most important components of the vibration optimized dilution refrigerator setup, including the decoupled still pumping line and the dilution circuit connections.

7.2.2 Electronic Noise

As low electron temperatures require low electronic noise, a large emphasis has been put on the electronic noise reduction of the setup. Noise mainly couples in the system via AC electric and magnetic fields. In our labs, typical background AC magnetic fields of some 10^{-9} T were observed. The shielding of these magnetic fields is very difficult. Tries to shield the OVC of our cryostat with mu-metals have not improved the noise level. Thus the only possibility is to keep the area of the cabling as small as possible, for example by winding the Thermocoax cables non-inductively and keeping their cross-section small. Furthermore, possible electric and magnetic noise sources, as power supplies, are kept away from the cryostat as far as possible. In contrast, shielding (low frequency) electric fields is much easier by using grounded metal shields. (A good overview of grounding concepts and noise can be found in [9]). For this, the grounding concept of the cryostat has been optimized, in order to connect all vital parts of the measurement setup to a well-defined measurement ground (see Fig. 7.8). For all measurement devices, a low-impedance connection

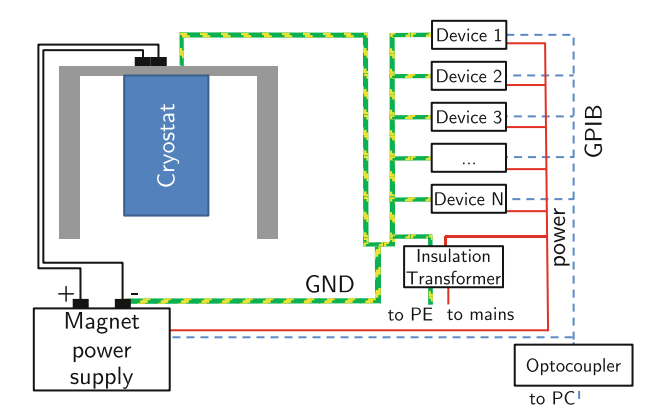


Fig. 7.8 Schematics of the grounding connections of the setup. Pumping and measurement lines from the cryostat to the gas handling system are insulated, the cryostat top-plate is connected to a well-defined grounding plate in the racks



Fig. 7.9 New rack design with low-impedance ground connections for all measurement devices

to the measurement ground is supplied via newly designed racks (Fig. 7.9). The setup power is supplied via an insulation transformer that decouples the system from possible high-frequency noise on the mains. Measurement device GPIB ports are only contacted via opto-couplers, to avoid the transmission of high frequency noise from the PC switching power supplies to the setup. Ground loops in the setup, in the gas-handling system and in the pumping circuits were removed by introducing insulating elements. Compared to the initial status of the setup, a big improvement of the noise level could be achieved by removing all ground-loops in the pumping lines. Large circular currents were found to build up in a network of interconnected pumping lines. Though these lines were not directly connected to the cryostat, noise cross-talk was sufficient to be noticeable in the measurement setup.

As a qualitative criterion for the noise of the setup, we have investigated the strength of rectification via noise in a single quantum dot. Figure 7.10 shows the current through the QD as a function of the plunger gate voltage, for different applied DC voltages. Rectification is only visible for $|V_{\text{SD,DC}}| \leq 1 \,\mu\text{V}$. In typical dilution refrigerator setups, this noise-induced effect is visible for biases $|V_{\text{SD,DC}}|$ of up to approximately $10-20\,\mu\text{V}$ [10], indicating an excellent noise level of our setup.

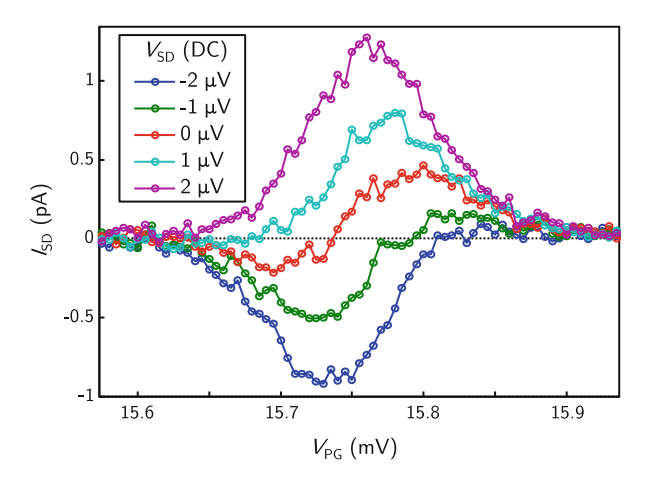


Fig. 7.10 Rectification via noise of a single quantum dot, for different applied DC voltages

7.3 Cryostat Cabling and Cold Filtering

Many research groups have successfully reached low electron temperatures, using various different filtering techniques. The interested reader is referred to the literature [11, 13–15, 17–26] for an overview of different filtering techniques. The filtering setup used by us is shown in Fig. 7.11. The cabling is set up in a modular way, where different filtering components filter out different parts of the noise spectrum. Cabling down to the cold-plate ($T \approx 80\,\mathrm{mK}$) is done using standard Loom wire. On the cold-plate, wires are thermally anchored with a quartz heat sink. From the cold-plate to the silver cold-finger, cabling is done using Thermocoax cables. On the bottom of the base-plate, additional RC filters, Pi filters and heat sinks (Fig. 7.11) are installed.

7.3.1 General Remarks

For a low temperature setup, materials and joining techniques have to be well chosen. References [27–29] are excellent references for this purpose. Thermal conductivities at millikelvin temperatures are extremely small for many insulators (Fig. 7.12). Thus insulators should be avoided wherever possible, especially ceramic and glass components which have a large heat capacity in addition to the poor thermal conductivity. Cases of our home-made filters and heat sinks were designed from oxygen free copper, which offers a high thermal conductivity even at low temperatures. The filters were screwed on the base-plate. At low temperatures, the thermal conductance of screwed solid-solid joints depends roughly linearly on the force that is applied at the joint. Furthermore, the heat transfer across gold-plated interfaces works much better than across two copper surfaces (see Fig. 7.13). Thus filter cases were gold-plated and

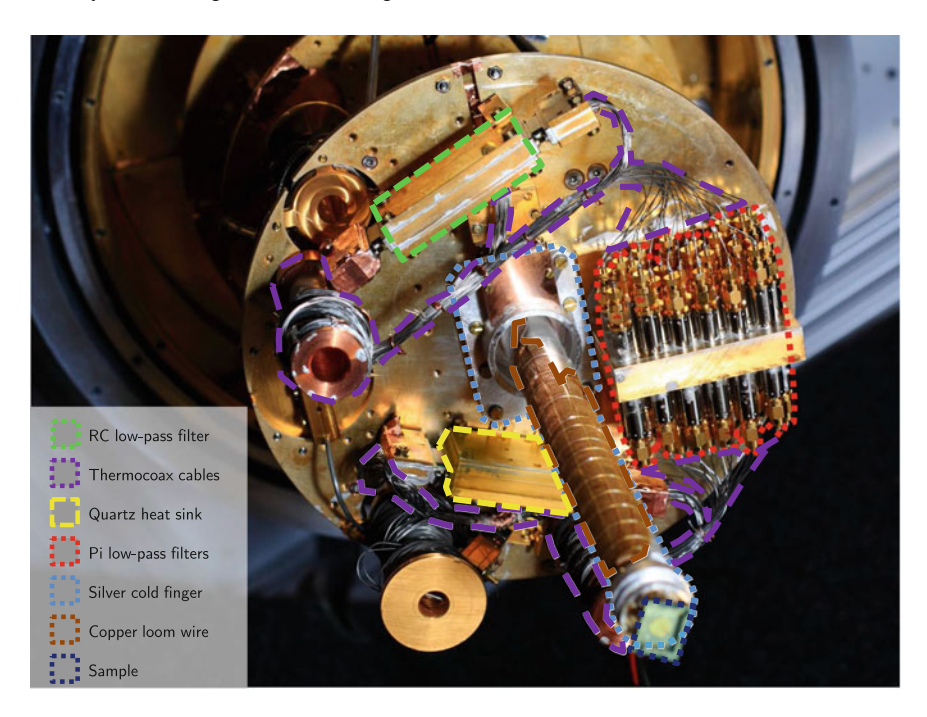


Fig. 7.11 Overview *bottom side* of the mixing chamber plate. Different components of the cabling are indicated

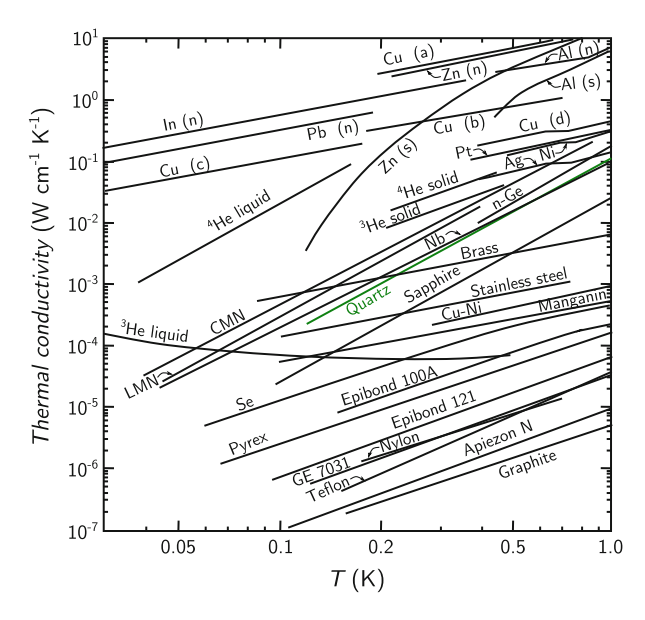


Fig. 7.12 Thermal conductivity of different materials at temperatures below 1 K. Quartz (*green curve*) is the thermally best conducting, electrically insulating solid at these temperatures, nearly one order of magnitude better than sapphire. Adapted from [28]

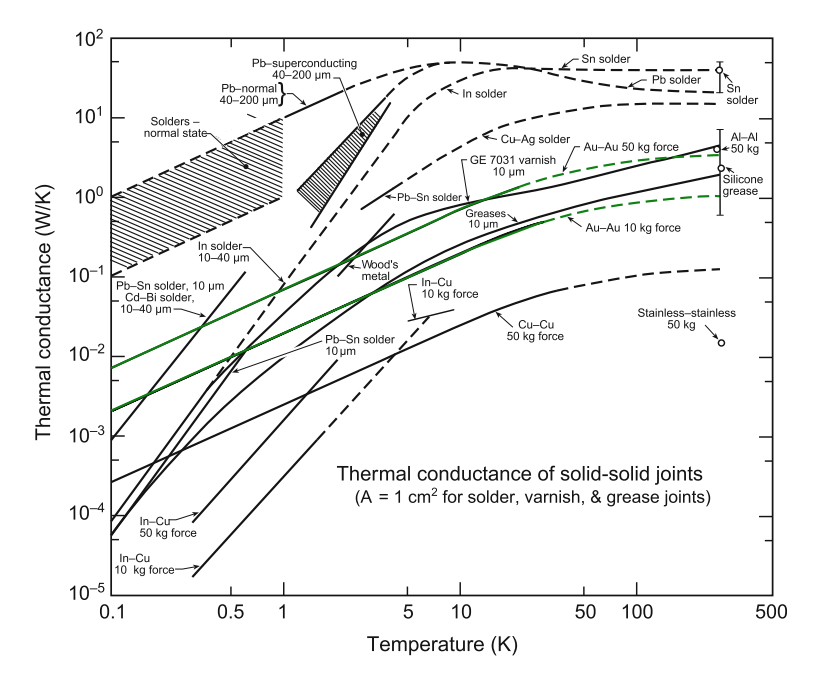


Fig. 7.13 Overview of the thermal conductance of different joints between solids at different temperatures. (Taken from [27]. By permission of Oxford University Press)

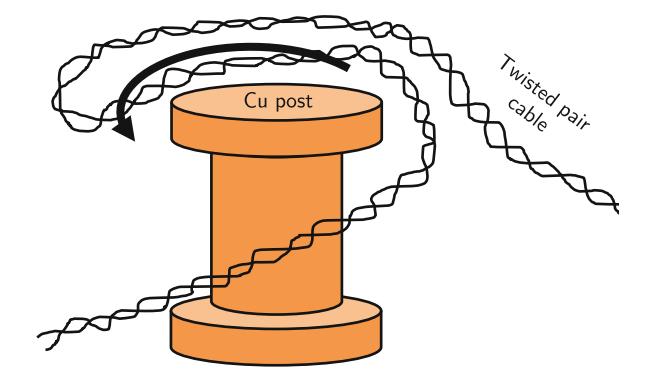
fixed to the mixing chamber plate using stainless steel screws.³ These connections used in our setup provide a good thermal conductance, even at the lowest temperatures (see green curves in Fig. 7.13). In addition to the mechanical connections, electrical connections of cables have to be made. Unfortunately for this we have to cope with the problem that all common soft solders become superconducting at millikelvin temperatures [30].⁴

Presumably, the thermal conductivity of a superconducting solder joint still is sufficiently high for the use in our cabling (Fig. 7.13). Still, superconducting junctions have been avoided by wrapping cables around each other or around contacts before soldering. Due to the small critical field ($H_c = 80 \text{ mT}$ at 1.3 K for 60Sn/40Pb [27]), most of the solder joints will be normally conducting as soon as a magnetic field is applied. When installing the cables, we want to avoid noise coupling in via AC electric and magnetic fields. Electric fields can be shielded. This is accomplished by using shielded Thermocoax cables from the cold-plate to the silver cold-finger. Inside the cold-finger, cables are shielded by an additionally mountable cover. All

³Note that if no sufficient force can be applied to a screwed connection, the thermal conductivity can be enhanced by adding a thin film of vacuum grease in between.

⁴Bismuth solder is the only soft solder that does not become superconducting [31] but has been disregarded because of its bad mechanical stability.

Fig. 7.14 Non-inductive winding of measurement cables. Adapted from [27]



filtering and heat sinking cases are designed to be high frequency radiation tight, by the use of notched covers and additional sealing with conductive silver.

Magnetic fields cannot be easily shielded. However, cabling can be installed such that areas for inductive coupling are minimized. This is accomplished by keeping cables tightly together and winding them non-inductively (see Fig. 7.14).

7.3.2 Thermocoax Cables

Thermocoax cables are coaxial cables made of NiCr, filled with compacted MgO powder. Due to the large surface of the MgO powder, high frequency radiation, up to the THz range, is efficiently filtered out due to skin effect damping [18]. The main advantage of these cables is that they are relatively compact and already have a strong filter integrated. However, they are difficult to handle and soldering of these cables is a real pain. In our setup, we have integrated 24 DC lines, with approx. 3 m long Thermocoax segments for each line, from the cold-plate down to the mixing chamber plate. The soldered cables have to be sealed, in order to prevent the MgO filling to absorb water vapor. This leads to a leakage current between inner and outer conductor, which however freezes out at low temperatures. The sealing is done, by heating the cable for approx. 20 min to 120 °C. Then, the ends of the cable are sealed with Stycast 2850 FT epoxy, which hardens over night.

7.3.3 π -Filters

In addition to the Thermocoax cables, commercial Minicircuits VLFX-80 π -low-pass filters have been integrated. These filters work at low temperatures and provide 40 dB insertion loss from approximately 200 MHz up to frequencies of 20 GHz. The complete array of 24 of these filters can be seen in Fig. 7.15. These components provide additional filtering at the lowest temperature stage.

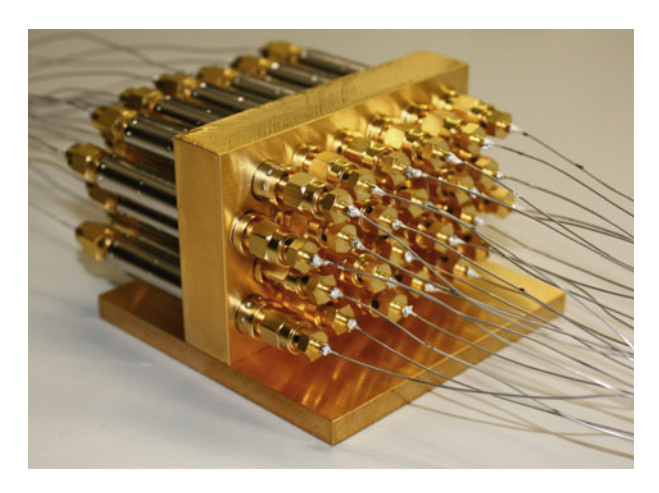


Fig. 7.15 Array of 24 Minicircuits VLFX-80 Pi-filters. In- and output are connected via Thermocoax cables

7.3.4 Quartz Heat Sinks

For the thermalization of the inner conductor, heat sinking elements, using quartz single crystal wafers have been built. Similar designs have been described in [11, 12]. Quartz is the best thermally conducting insulator at low temperatures, nearly one order of magnitude better than sapphire (see Fig. 7.12). Quartz wafers have been gold-coated on the back. Then, meandering gold lines ($R \approx 50~\Omega$) were defined on the front, using a photolithography step, metal evaporation and lift-off. The quartz wafer then is integrated in a casing (see Fig. 7.16) and inner conductors are soldered to the meandering gold lines. It is important to know that standard Pb/Sn solder rapidly dissolves thin gold films, thus a lot of caution or soldering with indium is advised. Using small amounts of lead-free solder, we could successfully connect



Fig. 7.16 Quartz heat sinks for thermally equilibrating the Thermocoax inner conductor. Meandering gold lines are evaporated on a quartz wafer with a gold-plated backside

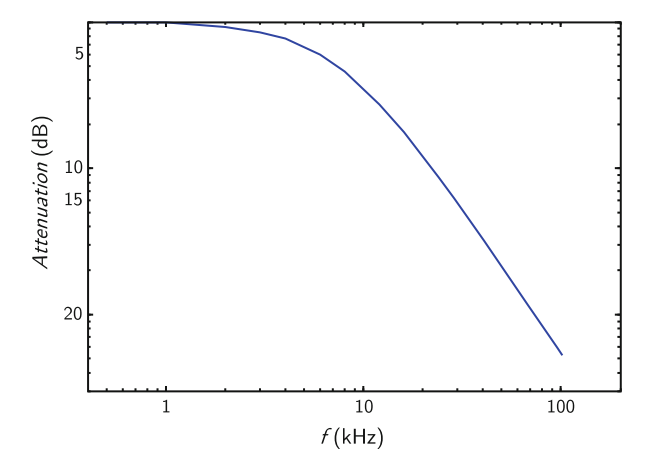


Fig. 7.17 Measured attenuation of the standard RC filter at room temperature

the gold lines. Two of these thermalization elements were used in the final setup: one on the cold-plate, one on the mixing chamber plate.

7.3.5 RC Low-Pass Filters

To filter out noise in the kHz range, a simple home-built RC low-pass filter has been added to the cold part of the wiring, realized with SMD components on a printed circuit board. This filter is expected to attenuate effectively in the kHz range, while high-frequency MHz and GHz radiation is not attenuated effectively, due to stray capacitances and resistances of the components. The measured attenuation for a capacitance of 10 nF (Kemet C0805 X103J5GACTU Ceramics MLCC SMD, flexible termination) and a resistance of 1 k Ω (Sumusu RR 122OP-102-D thin-film SMD) is shown in Fig. 7.17. An attenuation of more than 20 dB is reached at f=100 kHz. The components in use have been characterized at T=4 K, where their characteristics are only minimally changed compared to room temperature. It should be noted that only thin-film resistors are suitable for low temperature applications, as the characteristics of other resistor types vary strongly for T<77 K. Capacitors, other than the component in use, have been found to vary in capacitance up to a factor of two when cooled down to T=4 K.

7.3.6 Silver Cold-Finger

The cold-finger in the setup should provide good thermal contact between the sample, situated in the bore of the magnet, and the mixing chamber plate. Additionally, it should be stable against vibration and be designed such that heating via eddy

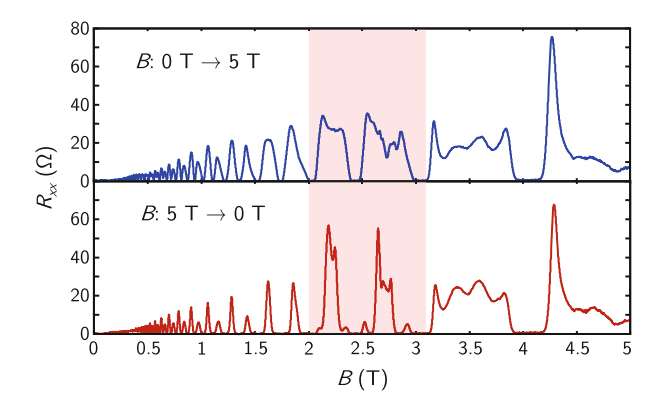
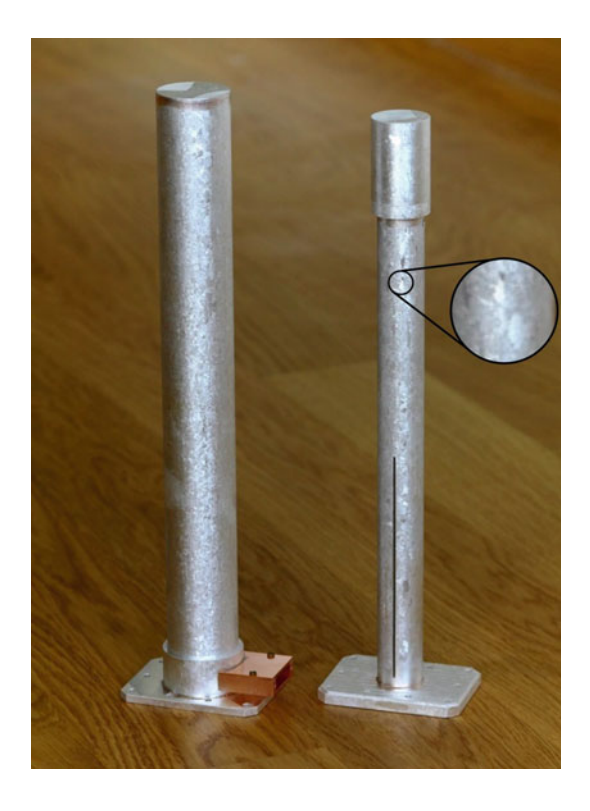


Fig. 7.18 Longitudinal resistance of a high-mobility 2DEG for two subsequent magnetic field sweeps (copper cold-finger installed in the system). In both cases, the sweep rate is identical, only the direction is reversed. In the filling factor region between $\nu = 6$ and $\nu = 8$ (shaded region), the longitudinal resistance looks qualitatively different. As the magnetic field is lowered, characteristic signatures of the RIQH state are observed, indicating a lower electronic temperature

currents and adiabatic magnetization effects is minimal. For this, a customized silver cold-finger has been designed. It then has been built in the D-PHYS workshop, using high-purity silver (99.97 % Ag). Compared to the original Cu cold-finger used in the setup, heating via adiabatic magnetization could be reduced. Adiabatic magnetization means that the (J = 3/2 for Cu) nuclear spins are polarized when the magnetic field is increased, thus heating the system via a decrease of the entropy. The effect of this process is shown in Fig. 7.18 for the Cu cold-finger, where the magnetic field is swept in different directions. Temperature-sensitive features, associated with the RIQH effect in higher Landau levels are much more pronounced when the magnetic field strength is lowered (red shaded regions in Fig. 7.18), indicating a lower electron temperature in this case (but still higher than the steady-state electron temperature, due to eddy current heating). For the new Ag cold-finger, this asymmetry is strongly reduced, due to the lower (J = 1/2) nuclear spin of the silver. Heating due to eddy currents cannot be circumvented, as long as an electrically conducting cold-finger material is used. To minimize this heating, singly-connected metal cross-sections in the bore of the magnet should be as small as possible. This has been achieved by slicing the pole of the cold-finger (see Fig. 7.19). In this aspect, a trade-off between mechanical stability and high thermal conductivity, and a small cross-section has to be made. The design of our silver cold-finger (Fig. 7.19) has been optimized for mechanical stability and high thermal conductivity. The sample is doubly shielded by massive silver shields. This design has the drawback of strong eddy current heating, which is not a big issue for us, as most experiments are conducted in a small B-field interval and excessive B-field sweeps are only needed for sample characterization. The cabling from the mixing chamber plate down to the sample is done using copper wire, which has a thermal conductivity nearly three orders of magnitude larger than Manganin wire [27]. The wire is glued on the inner part of the cold-finger using GE varnish to allow for ideal thermalization (see Fig. 7.11). To achieve a good

Fig. 7.19 High-purity, thermally annealed silver cold-finger, before the installation in the system. The sample chamber is double-shielded and extremely well thermally anchored to the mixing chamber plate due to the high thermal conductivity of the annealed silver



thermalization with the chip carrier (mounted on the tip of the silver cold-finger in an additional shield), all free pins of the socket were electrically connected to the silver cold-finger by 99.999 % Ag wire. These grounded pins were then bonded to the gold-plated chip carrier bottom, using multiple bonds. The samples were glued in the chip carrier with conductive silver. The thermal conductivity of the silver cold-finger has been increased by thermally annealing the material, after brazing the individual parts with non-superconducting solder. The annealing process which is conducted in an oxygen atmosphere (for details see Appendix E) leads to a clustering of impurities in the silver solid. This can be seen by eye as millimeter-sized glittering grains (see Fig. 7.19). By use of this method, [32] reports an increase of the residual resistivity ratio (RRR) of a silver specimen from 140 before annealing to 9500 after repeated treatment.

7.3.7 Filter Attenuation

The filter attenuation in the frequency range from 10 MHz to 40 GHz has been measured with a Rohde & Schwarz Vector Network Analyzer. The results for different filtering components are shown in Fig. 7.20a. 1 m of Thermocoax cables (blue curve)

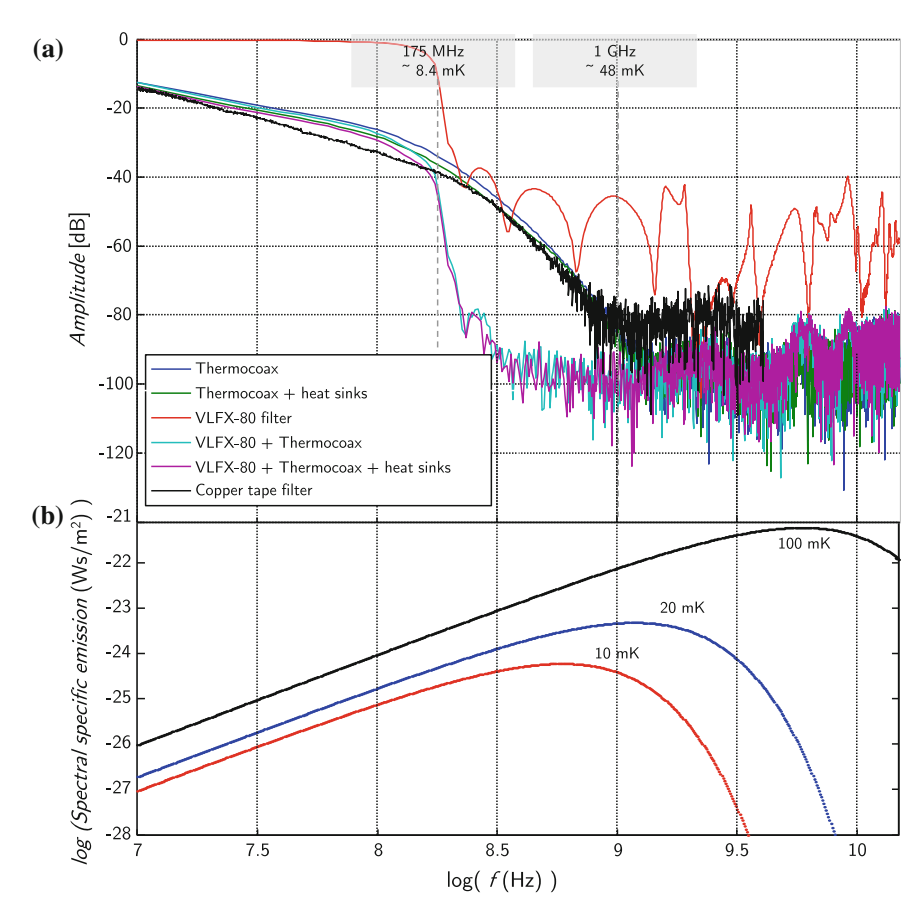


Fig. 7.20 a Attenuation of different components of the cold filtering setup. As all components (without RC low-pass-filter) are combined, the noise floor is reached at a frequency of approx. 200 MHz. **b** Spectral specific blackbody emission at different temperatures

leads to a strong attenuation at high frequencies, reaching the noise floor attenuation >90 dB at approximately 1 GHz. Adding the heat sinks does not change the attenuation performance (green curve). Thermocoax cables are slightly more efficient in blocking high frequency radiation than copper tape filters [13, 15] (black curve), which we found to be less robust and less suitable for our applications. The commercially available VLFX-80 filters (red curve) show an attenuation >40 dB for frequencies larger than approximately 200 MHz. The combination of all those elements (purple curve) leads to an attenuation reaching the noise floor at approximately 200 MHz. With this, thermal radiation (compare to spectral specific blackbody emission, Fig. 7.20b), even from low temperature stages is efficiently blocked. In combination with the simple RC filter (Sect. 7.3.5), noise from several tens of kHz up to THz is efficiently blocked from entering the sample.

7.4 Estimation of the Electronic Temperature

Measuring temperature in the millikelvin range is a difficult business. Resistive thermometers generally need to be calibrated and suffer from heating from the necessary electric connections made to read them out. Nuclear orientation thermometers [16] are reliable, but less practical due to the use of radioactive materials and the involved export restrictions and safety regulations. In our setup, the temperature of the mixing chamber plate is measured by a SQUID-based noise thermometer, which gives reliable results down to temperatures below 10 mK and is based on the linear characteristics of the Nyquist theorem [33, 34]. After the noise spectrum has been calibrated at approximately 100 mK, it reflects reliably the mixing chamber plate temperature of the cryostat.

However, we are interested in the electronic temperature of our sample, which is yet more difficult to estimate. One possibility is measuring the FWHM of a (only temperature broadened) Coulomb blockade peak [24, 25, 35, 36], which scales linearly with electron temperature and serves as a primary thermometer without the necessity to calibrate. The drawback of this method is that a very high wafer stability is crucial, in order to avoid peak broadening. Furthermore, there is always a contribution of tunneling broadening, thus only an upper bound of the temperature can be given. Lastly, the impedance of a Coulomb blockaded quantum dot strongly differs from the impedance of a quantum Hall interferometer. Thus, electronic temperatures might be different in both cases.

Due to the strong temperature dependence of the electron-lattice thermal resistance, the electron gas is expected to be warmer than the phonon bath at the lowest temperatures. At slightly higher temperatures, their coupling grows rapidly and temperatures are expected to equilibrate. A schematic dependence of the electronic temperature on the bath temperature of the cryostat is shown in Fig. 7.21. Hence, measuring the known temperature dependence of a physical effect at temperatures where bath and electron temperatures are equal allows the interpolation to the lowest electron temperature. In our experiment, we use the temperature evolution of several temperature-sensitive (fractional) quantum Hall features to give an estimate of the electronic temperature, similar to [24, 37]. Figure 7.22 shows the temperature dependence of R_{xy} (Fig. 7.22a) and R_{long} (Fig. 7.22b) measured in a high mobility quantum well in a van der Pauw geometry, with Ge/Au/Ni ohmic contacts. The most temperature-sensitive features are the reentrant integer quantum Hall states. Here, even heating the mixing chamber from 9.4 to 13.2 mK leads to a visible change in R_{xy} . This is already an indication that the electronic temperature is not fully saturated and is relatively close to the bath temperature. Due to the complicated temperature dependence of the RIQH states [38], a more quantitative statement cannot be made. Other temperature-sensitive features in the measurement are the FQH states at $\nu = 11/5$ and 14/5, with small activation gaps of 37 and 48 mK (compared to approx. 130 mK at $\nu = 5/2$).

When an activated behavior for $R_{\rm long}$ is assumed at these fillings, we expect $R_{\rm long} \propto e^{-\frac{E_{\rm gap}}{2k_BT}}$. Hence a linear slope is expected in an Arrhenius plot, as long as

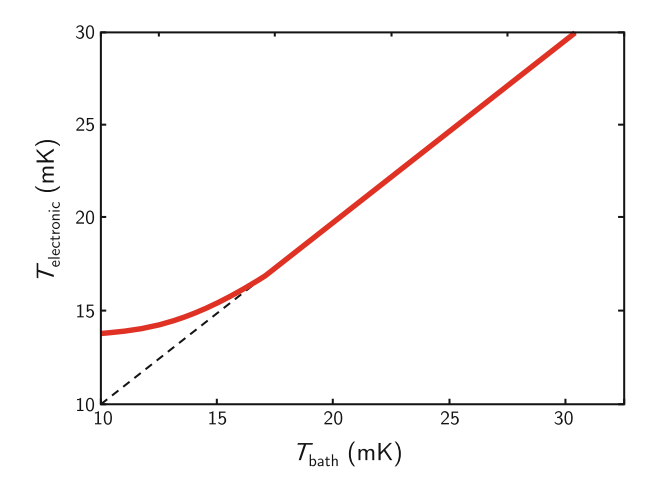
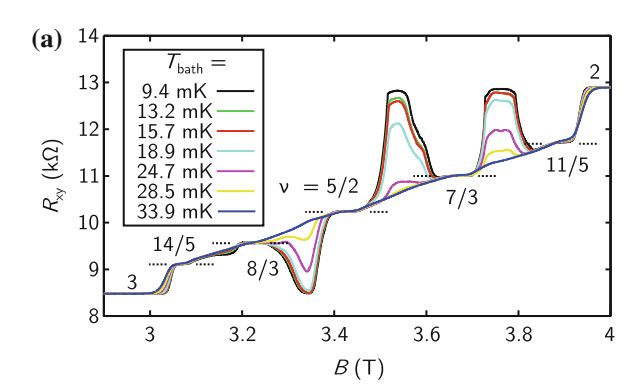
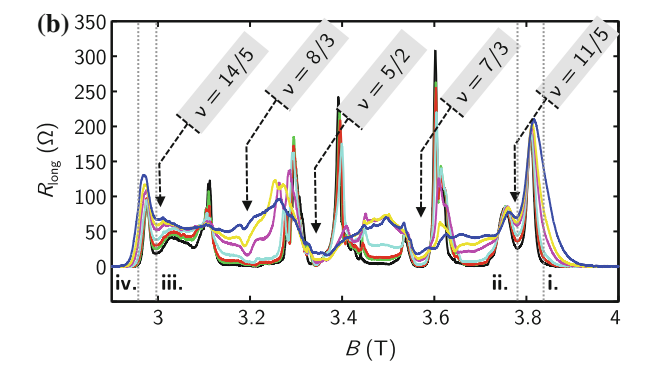


Fig. 7.21 Schematic dependence of the electronic temperature on the bath temperature of the cryostat

Fig. 7.22 Temperature dependence of R_{xy} (a) and R_{long} (b) measured in a high mobility quantum well in a van der Pauw geometry. The B-field range for filling factors between 2 and 3 is shown. Different FQH states are indicated and show a strong temperature dependence in the plotted temperature range





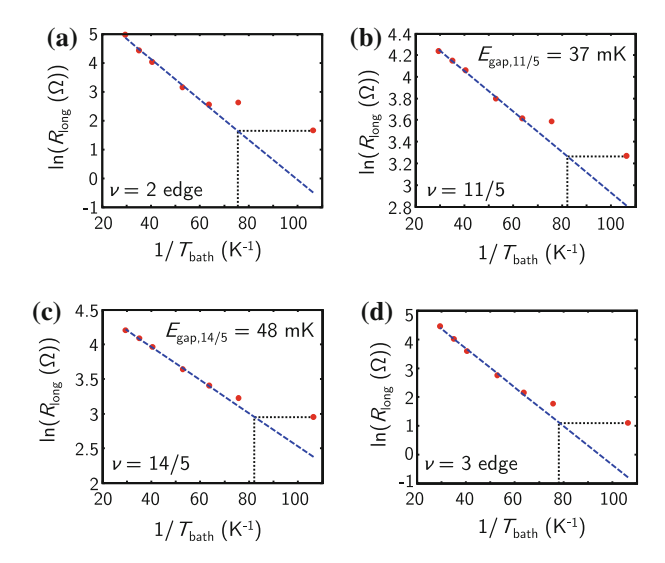


Fig. 7.23 Arrhenius plots for $\nu = 11/5$ (b), $\nu = 14/5$ (c) and of the edges of $\nu = 2$ (a) and $\nu = 3$ (d). The respective *B*-field positions where the temperature dependence is plotted are indicated in Fig. 7.22 as *dashed lines*

electron and bath temperature are identical and the activated behavior is not violated. This is observed for temperatures down to 15 mK (see Fig. 7.23), indicating closely similar electron and phonon temperatures. As the phonon temperature is further decreased, $T_{\rm el}$ and hence $R_{\rm long}$ saturate. Interpolating the minimum of $R_{\rm long}$ on the fitted activated behavior (Fig. 7.23b, c), an estimate of the electron temperature at the lowest phonon temperature can be found. The same method can be applied to the edges of $\nu = 2$ and 3, where $R_{\rm long}$ nearly vanishes at the lowest temperatures (Fig. 7.23a, d). For all cases, an electron temperature of approximately 12–13 mK has been extrapolated. Consistent results have been obtained with other samples, where the electron temperature was also equal the phonon temperature above approximately 15 mK.

Unfortunately, this method of estimating the electronic temperature requires certain assumptions which are not necessarily true. As argued in [39], dominant contributions of variable range hopping may violate the assumption of an activated behavior. Different mechanisms of hopping transport generally contribute to the conductivity via an expression of the following form [40]:

$$\sigma_{xx} = \sigma_{xx}^0 \exp\left[-\left(\frac{T_0}{T}\right)^p\right],\tag{7.1}$$

where p = 1 for thermally activated hopping, p = 1/3 for variable range hopping in 2 dimensions [40] and p = 1/2 for variable range hopping in the presence of Coulomb interaction [41, 42]. This transport regime describes the transport in the conductivity

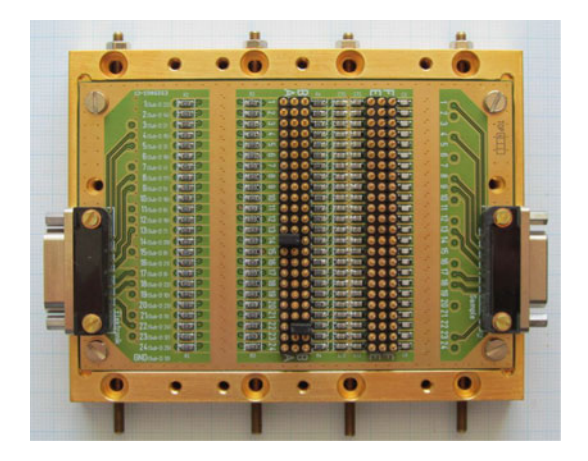
minima of the quantum Hall regime [40], when σ_{xx} is much smaller than the value of σ_{xx} when the thermal energy exceeds the gap energy. Due to the small gap of the $\nu = 11/5$ and 14/5 states, we do not reach a temperature regime where states in the bulk are completely localized and thus expect an activated behavior to be valid. Similarly, at the $\nu = 2$ and 3 edges, the extracted electron temperature does not depend on the exact *B*-field position and hence the value of R_{long} at the lowest temperature.

To summarize, we conclude that the electronic temperature achieved with the filtering setup is approximately 12–13 mK, at a bath temperature of 9–10 mK. As the bath temperature is increased to more than approximately 15 mK, bath and electronic temperatures coincide. Limitations in the method used for estimating the electron temperature exist, thus an uncertainty, especially at the lowest temperatures, remains.

7.5 Outlook

To allow for a more simple and more reliable setup, a new low temperature filter has been designed by P. Märki (Fig. 7.24). Here, RC-filters, Pi-filters and Thermocoax cables have been replaced by several stages of conventional RC and LC filters, integrated in a radiation sealed casing. Components used are standard SMD resistors (Panasonic Metal Film Thin Film Chip Resistors, type ERA 6A), inductors (WE-CBF SMD EMI Suppression Ferrite Bead) and capacitances (Kemet C0805X223J5GACTU). Attenuation measurements suggest that the performance of the filter is similar or superior to the filtering setup described earlier, however in a much smaller package.

Fig. 7.24 Prototype of a new cold filter which includes all different filter components in one device



7.6 Conclusion 121

7.6 Conclusion

We have investigated mechanical and electronic noise that affects low temperature measurements in a dry dilution refrigerator. Mechanical noise could be significantly reduced by decoupling moving parts, like the pulse tube head or the turbomolecular pump, from the sample stage and by making the cryostat frame very stiff. Electronic noise was mainly improved by an optimized grounding scheme for cryostat and pumping lines.

Components of our self-built filtering setup have been discussed and characterized. The final setup blocks efficiently high-frequency radiation from entering into the sample. Utilizing the optimized setup, an electronic base temperatures of approximately 12–13 mK could be reached.

References

- C. Reichl, J. Chen, S. Baer, C. Rössler, T. Ihn, K. Ensslin, W. Dietsche, W. Wegscheider, New J. Phys. 16, 023014 (2014). doi:10.1088/1367-2630/16/2/023014
- W. Bishara, P. Bonderson, C. Nayak, K. Shtengel, J.K. Slingerland, Phys. Rev. B 80, 155303 (2009). doi:10.1103/PhysRevB.80.155303
- 3. P.L. Kapitza, J. Phys. USSR 4, 4 (1941)
- 4. R.E. Peterson, A.C. Anderson, J. Low Temp. Phys. 11, 639 (1973). doi:10.1007/BF00654451
- 5. E.T. Swartz, R.O. Pohl, Rev. Mod. Phys. 61, 605 (1989). doi:10.1103/RevModPhys.61.605
- M.L. Roukes, M.R. Freeman, R.S. Germain, R.C. Richardson, M.B. Ketchen, Phys. Rev. Lett. 55, 422 (1985). doi:10.1103/PhysRevLett.55.422
- A.K.M. Wennberg, S.N. Ytterboe, C.M. Gould, H.M. Bozler, J. Klem, H. Morkoç, Phys. Rev. B 34, 4409 (1986). doi:10.1103/PhysRevB.34.4409
- R. Radebaugh, in Low Temperature and Cryogenic Refrigeration, NATO Science Series No. 99, ed. by S. Kakaç, H.F. Smirnov, M.R. Avelino (Springer Netherlands, 2003), pp. 415–434. doi:10.1007/978-94-010-0099-4_24
- 9. R. Morrison, Grounding and Shielding: Circuits and Interference (Wiley, 2006)
- C. Rössler, Elektronische und optische Eigenschaften freitragender Nanostrukturen, Ph.D. thesis, Ludwig-Maximilians-Universität München, Munich (2008)
- 11. Y. Zhang, Waves, particles, and interactions in reduced dimensions, Ph.D. thesis, Harvard University, Cambridge, Massachusetts (2009)
- 12. D. Templeton McClure III, Interferometer-based studies of quantum hall phenomena, Ph.D. thesis, Harvard University, Cambridge, Massachusetts (2012)
- 13. L. Spietz, J. Teufel, R.J. Schoelkopf, arXiv:cond-mat/0601316 (2006)
- 14. H.l. Sueur, P. Joyez, Rev. Sci. Instrum. 77, 115102 (2006). doi:10.1063/1.2370744
- 15. H. Bluhm, K.A. Moler, Rev. Sci. Instrum. 79, 014703 (2008). doi:10.1063/1.2835716
- 16. C. Enss, S. Hunklinger, Low-Temperature Physics (Springer, 2005)
- 17. A. Lukashenko, A.V. Ustinov, Rev. Sci. Instrum. 79, 014701 (2008). doi:10.1063/1.2827515
- 18. A.B. Zorin, Rev. Sci. Instrum. 66, 4296 (1995). doi:10.1063/1.1145385
- P.L. Gammel, D.J. Bishop, J.P. Eisenstein, J.H. English, A.C. Gossard, R. Ruel, H.L. Stormer, Phys. Rev. B 38, 10128 (1988). doi:10.1103/PhysRevB.38.10128
- W. Pan, J.-S. Xia, V. Shvarts, D.E. Adams, H.L. Stormer, D.C. Tsui, L.N. Pfeiffer, K.W. Baldwin, K.W. West, Phys. Rev. Lett. 83, 3530 (1999). doi:10.1103/PhysRevLett.83.3530
- J.S. Xia, E.D. Adams, V. Shvarts, W. Pan, H.L. Stormer, D.C. Tsui, Phys. B: Condens. Matter 280, 491 (2000). doi:10.1016/S0921-4526(99)01843-8

- L. Spietz, R.J. Schoelkopf, P. Pari, Appl. Phys. Lett. 89, 183123 (2006). doi:10.1063/1. 2382736
- L. Spietz, K.W. Lehnert, I. Siddiqi, R.J. Schoelkopf, Science 300, 1929 (2003). doi:10.1126/ science.1084647
- I.P. Radu, J.B. Miller, C.M. Marcus, M.A. Kastner, L.N. Pfeiffer, K.W. West, Science 320, 899 (2008). doi:10.1126/science.1157560
- 25. C.P. Scheller, S. Heizmann, K. Bedner, D. Giss, M. Meschke, D.M. Zumbühl, J.D. Zimmerman, A.C. Gossard, arXiv:1403.6205 [cond-mat] (2014)
- K. Bladh, D. Gunnarsson, E. Hürfeld, S. Devi, C. Kristoffersson, B. Smålander, S. Pehrson, T. Claeson, P. Delsing, M. Taslakov, Rev. Sci. Instrum. 74, 1323 (2003). doi:10.1063/1.1540721
- J. Ekin, Experimental Techniques for Low-Temperature Measurements: Cryostat Design, Material Properties and Superconductor Critical-Current Testing (Oxford University Press, 2006)
- 28. O.V. Lounasmaa, Experimental Principles and Methods Below 1 K (Academic Press, 1974)
- 29. F. Pobell, Matter and Methods at Low Temperatures (Springer, 2007)
- 30. W.H. Warren Jr, W.G. Bader, Rev. Sci. Instrum. 40, 180 (1969). doi:10.1063/1.1683729
- 31. H.C. Meijer, C. Beduz, F. Mathu, J. Phys. E: Sci. Instrum. **7**, 424 (1974). doi:10.1088/0022-3735/7/6/004
- 32. A.C. Ehrlich, J. Mater. Sci. 9, 1064 (1974). doi:10.1007/BF00552819
- J. Engert, D. Heyer, J. Beyer, H.-J. Barthelmess, J. Phys.: Conf. Ser. 400, 052003 (2012). doi:10.1088/1742-6596/400/5/052003
- J. Engert, J. Beyer, D. Drung, A. Kirste, D. Heyer, A. Fleischmann, C. Enss, H.-J. Barthelmess,
 J. Phys.: Conf. Ser. 150, 012012 (2009). doi:10.1088/1742-6596/150/1/012012
- R.M. Potok, I.G. Rau, H. Shtrikman, Y. Oreg, D. Goldhaber-Gordon, Nature 446, 167 (2007). doi:10.1038/nature05556
- V. Venkatachalam, S. Hart, L. Pfeiffer, K. West, A. Yacoby, Nature Physics 8, 676 (2012). doi:10.1038/nphys2384
- I. Radu, Electron transport in confined structures in very high mobility GaAs in perpendicular magnetic fields, Ph.D. thesis, Massachusetts Institute of Technology, Cambridge, Massachusetts (2009)
- 38. N. Deng, A. Kumar, M.J. Manfra, L.N. Pfeiffer, K.W. West, G.A. Csáthy, Phys. Rev. Lett. **108**, 086803 (2012). doi:10.1103/PhysRevLett.108.086803
- 39. J.B. Miller, Electron transport in GaAs heterostructures at various magnetic field strengths, Ph.D. thesis, Harvard University, Cambridge, Massachusetts (2007)
- 40. M. Weiss, Quantum hall effect in a strongly disordered system, Ph.D. thesis, Universität Konstanz, Konstanz (2004)
- A.L. Efros, B.I. Shklovskii, J. Phys. C: Solid State Phys. 8, L49 (1975). doi:10.1088/0022-3719/8/4/003
- D.G. Polyakov, B.I. Shklovskii, Phys. Rev. B 48, 11167 (1993). doi:10.1103/PhysRevB.48.
 11167

Chapter 8 Optimization of Samples and Sample Fabrication

Abstract In this section, we describe how our sample fabrication processes are checked for non-invasiveness, by measuring densities, mobilities and the energy gap of (integer) quantum Hall states. We describe an optimized mesa geometry and contact annealing process, which results in samples with a consistently quantized $\nu = 5/2$ state for all contact pairs.

8.1 Introduction

For the experiments presented in this book, the observation of fragile FQH states in fully processed Hall-bar samples with contacts defined by optical lithography is required. Thus a fabrication process which does not degrade the 2DEG quality is required. In the fabrication process, the Ohmic Au/Ge/Ni contacts play a crucial role. The contact and mesa geometry have to be well chosen to allow for the observation of the most fragile FQH states. Furthermore, the contact resistance which depends on the geometry of the contact and the annealing process used, is a bottleneck for efficiently cooling the electrons in the 2DEG and should be as small as possible.

8.2 Non-invasive Processing

To exclude any negative influence of the individual photolithography processing steps on the 2DEG quality, several samples, treated with different processing steps, have been measured. These steps are (for the full recipe see Appendix D):

- Spin-coating with photolithography resist (AZ5214E) and subsequent removal with acetone and isopropanole
- Spin-coating with photolithography resist, illumination, development (MF319) and subsequent resist removal
- Etching of a photolithographically defined Mesa (Piranha: H₂O:H₂O₂:H₂SO₄ = 100:3:3)

- Deposition of a photolithographically defined Au top-gate
- Contacting with photolithographically defined Au/Ge/Ni contacts

If not stated otherwise, samples and reference samples are contacted via Indium soldering and are measured in a van der Pauw geometry. Densities and mobilities of the processed samples and unprocessed reference samples show a large variation (Fig. 8.1), in the dark, as well as under illumination (T = 1 K). For the samples in study, higher mobility is correlated with lower carrier sheet density. This comes from the fact that growth is optimized for the central part of the wafer. Towards the corners of the wafer, all layer thicknesses decrease and density increases. Mobility depends sensitively on the layer thicknesses and decreases towards the edge where they are no longer in the optimal range.

Figure 8.2 shows the normalized energy gaps (left) and onset-field of the Shubnikov-de Haas oscillations (right) for samples treated with different processing steps. Overall, the large sample-to-sample variation makes it hard to identify potentially harmful processing steps, which could affect the energy gaps, carrier density or mobility of the electron gas (the onset of the SdH oscillations is mostly limited by temperature in this regime). However, the properties of all processed samples lie within the variance of the reference samples (the standard deviation is indicated in Fig. 8.2), excluding at least a massive degrading of the 2DEG by the processing. Later performed transport measurements on fully processed Hall-bar structures at millikelvin temperatures have revealed energy gaps of the $\nu = 5/2$ state which are of similar size as energy gaps obtained with bare In contacted wafer pieces. We conclude that the processing steps presented in Appendix D do not degrade the 2DEG quality within our sample-to-sample variation.

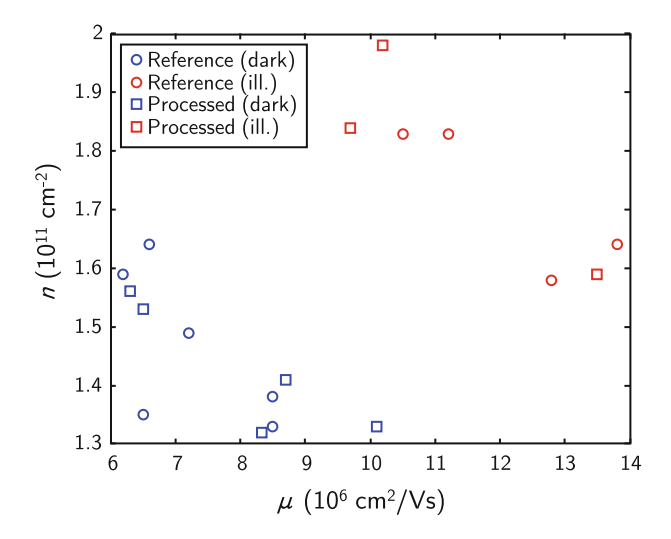


Fig. 8.1 Densities and mobilities for processed and reference samples, before (*blue*) and after illumination with a red LED (*red*)

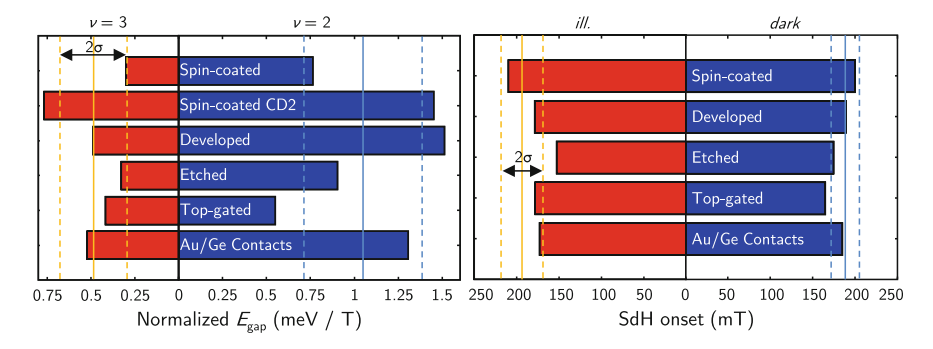


Fig. 8.2 Normalized energy gaps (*left*) and onset-field of the Shubnikov-de Haas oscillations (*right*) for samples treated with different processing steps. The average reference value from several cooldowns is indicated with *solid lines*. *Dashed lines* indicate the average, plus or minus the standard deviation

8.3 Mesa and Contact Geometry

When designing the mesa and contact geometry, certain guidelines have to be followed to allow for low contact resistances and the observation of fragile FQH states. Two common contact geometry problems that should be avoided are shown in Fig. 8.3. In the first case, the cross-section between mesa and contact is too small, resulting in weak coupling of contact and 2DEG. Experimentally, the contact resistance was observed to scale inversely with the cross-section length w [1]. Another common problem is denoted as Corbino contact: here, the contact does not overlap with the edge of the 2DEG. As the magnetic field strength is increased and a

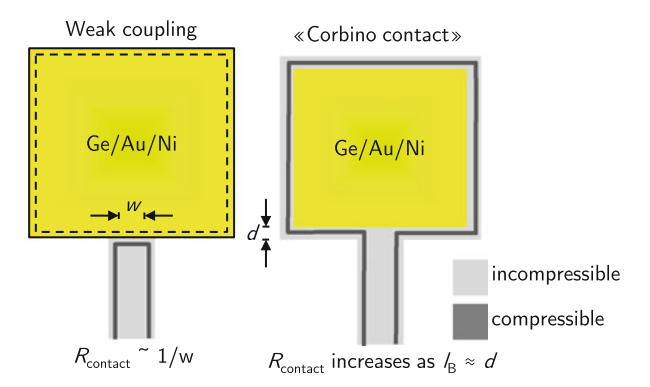


Fig. 8.3 Two examples of unsuitable contact geometries. A small cross-section between contact and 2DEG (*left*) leads to a high contact resistance due to unsufficient coupling of the edge to the contact. In a Corbino geometry (*right*), the contact resistance increases drastically in high magnetic fields, as the edge is no longer connected to the contact

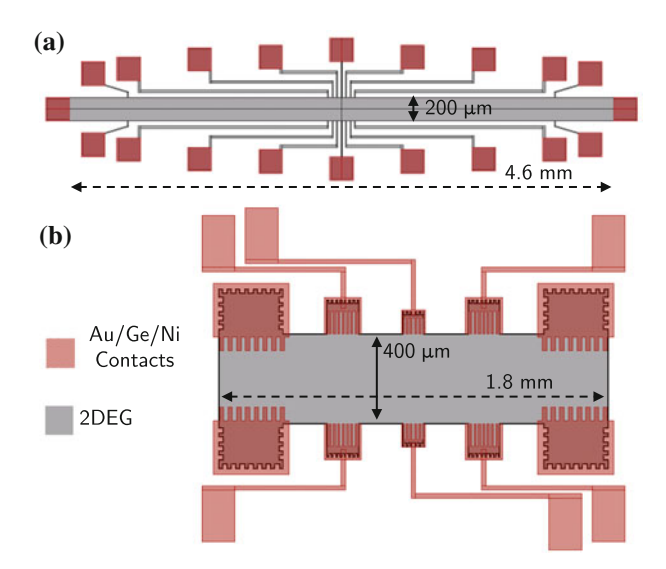


Fig. 8.4 a Traditional Hall-bar geometry used in the Ensslin group. **b** Optimized geometry for experiments at $\nu = 5/2$. Contacts possess a large linear cross-section with the 2DEG and overlapping edges. Furthermore, contacts are placed directly at the edge of the wide bulk of the Hall-bar, minimizing the influence of density in homogeneities

compressible region, separated by an incompressible region from the contact, is running around and the contact resistance increases drastically.

Thus, we have chosen the contact geometry such, that there is a large overlap between contact and 2DEG and a maximized linear cross-section (see Fig. 8.4b) by a meandering contact boundary. Another reason for the meandering contact boundary is that the contact resistance is anisotropic regarding the orientation of the cross-section line and the GaAs crystal [2]. Another important influence on the mesa and contact design comes from the fact that there are density in homogeneities and density gradients in the employed 2DEGs, of the order of several percent. Fragile FQH states like the $\nu = 5/2$ state exist only in a very narrow density range Δn at a given magnetic field. Thus, the experimental observation of a fully gapped $\nu = 5/2$ state requires that the contacts used for the measurement are connected via a percolating path of equal density (and a width $\leq \Delta n$). Experimentally, this effect was found to be relevant in large van der Pauw samples. There, nicely quantized FQH states could be observed using contacts in close proximity (approx. 500 μ m apart), but not when using contacts several mm apart from each other.

Figure 8.5 shows the two-terminal resistance (minus the Hall resistance) of two different contact pairs of the Hall-bar shown in Fig. 8.4a. The total cable resistances are of the order of 2 k Ω , thus contact resistances at B=0 are small in both cases. When the two-terminal resistance is measured through two 10 μ m narrow arms

¹C. Reichl, private communication.

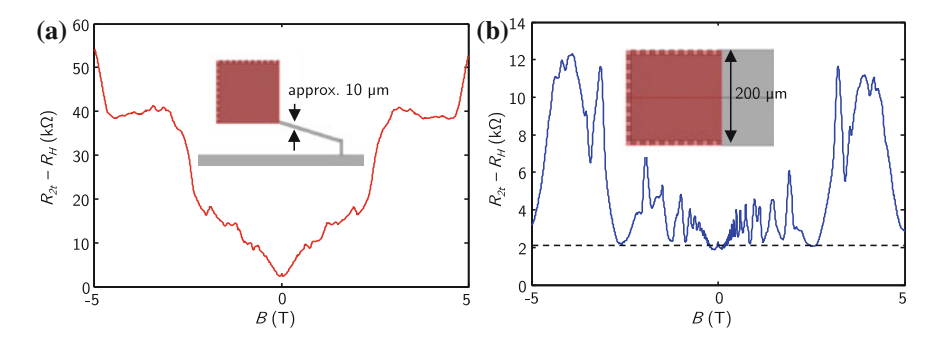


Fig. 8.5 Two-terminal resistance between contacts of different geometry (the Hall resistance has been subtracted). The two-terminal resistance of contacts connected via thin mesa arms increases drastically as the magnetic field strength is increased (*left*). In contrast, large contacts connected via wide 2DEG regions (*right*) do not exhibit such a monotonous increase

(Fig. 8.5a), it increases with the magnetic field. In contrast, a two-terminal measurement through the wide bulk of the Hall-bar does not show this increase, apart from the B-field dependence of $R_{\rm xx}$ which results in variations of the two-terminal resistance. In the geometry of Fig. 8.5a, even a small density inhomogeneity on a micron lengthscale can induce backscattering of an edge state, whereas this would not influence measurements in the geometry of Fig. 8.5b. This observation suggests that the cross-section of contact and 2DEG should be as long as possible to enhance coupling and placed at a wide section of the Hall-bar, to avoid an influence of density inhomogeneities in mesa arms. In the final mesa geometry shown in Fig. 8.4b, contacts are directly placed at the 400 μ m wide bulk of the Hall-bar.

8.4 Ohmic Contacts and Contact Resistance

Fabricating Ohmic contacts with low contact resistance is more tricky than one might expect and gets increasingly difficult with increasing 2DEG depth and decreasing carrier sheet densities. Since the first description of Au/Ge/Ni ohmic contacts [3], several groups have investigated and improved different recipes (see for example [1, 2, 4–7] for further information). An eutectic mixture of Au and Ge (88 % Au, 12 % Ge by weight [3]) melts at a temperature of 360 °C [8], substantially smaller than the melting points of the individual alloy components. Above the melting point, the eutectic mixture diffuses in the GaAs crystal and contacts the electron gas. The addition of Ni is crucial, as it improves diffusion of Ge into GaAs [7]. The recipe used by us is based on a recipe reported in [1, 7], which has been optimized for a 320 nm deep 2DEG with an electron density of approximately 1.5×10^{11} cm⁻². For an eutectic mixture, Ge and Au with a thickness ratio 1 : 2.03 are evaporated in high vacuum on the sample surface. Before this, the surface oxide has been removed by a dip-etch in HCl. The sequence of evaporated metals reads Ge/Au/Ge/Au/Ni/Au

with thicknesses 52.8/107.2/52.8/107.2/80/100 nm. The topmost Au layer is added to allow for easier wire bonding of the contacts. After lift-off, the samples are thoroughly cleaned in warm acetone and isopropanole and with UV ozone cleaning (see Appendix D), in order to remove resist residues which might burn or damage the substrate during annealing. The sample finally is heated in order to melt the eutectic mixture and to allow for diffusion in the GaAs crystal. We have found that contact is reliably made for temperatures of >500 °C, whereas single contacts may fail for temperatures of 475 °C or lower. Thus, samples are annealed at 500 °C, using a 200 sccm H₂/N₂ (5%) flow ($p \approx 10$ mbar). Measured contact resistances (at T =4 K) for different samples, annealed for different times at T = 500 °C are shown in Fig. 8.6. For short annealing times, contact resistances and contact resistance variations are large, as the eutectic mixture has not diffused sufficiently in the crystal. For long annealing times ($t_{anneal} > 8 \text{ min}$), diffusion is sufficient but the metal reservoir on the surface is used up, hence the doping concentration in the crystal decreases. Smallest contact resistances with a small standard deviation were found for t_{anneal} = 4 and 6 min. The high-mobility quantum wells used for the experiments at v = 5/2are typically approximately 200 nm below the surface. For these samples, contact resistances $< 200 \Omega$ were consistently achieved with the described recipe and an annealing time of 5 min.

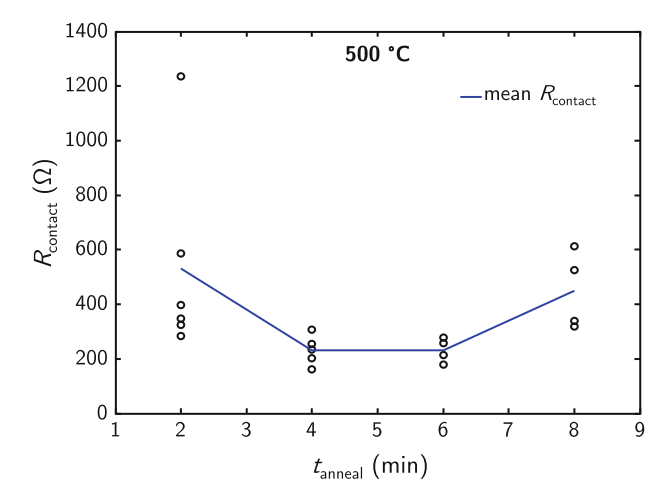


Fig. 8.6 Measured contact resistances for different annealing times at T = 500 °C. Contact resistances and their variance are minimal for annealing times between 4 and 6 min

8.5 Conclusion 129

8.5 Conclusion

The non-invasiveness of the photo-lithography fabrication steps used by us has been verified. It was found that initially poorly quantized quantum Hall states were related to the contact and mesa geometry. We have discussed an optimized geometry, suitable for experiments with the most fragile fractional quantum Hall states. Finally, we have optimized a recipe for Au/Ge/Ni ohmic contacts on deep high mobility heterostructures. Using this recipe, we could reproducibly achieve contact resistances of around $200~\Omega$ or lower.

References

- O. Göktaş, J. Weber, J. Weis, K. von Klitzing, Physica E 40, 1579 (2008). http://dx.doi.org/10. 1016/j.physe.2007.09.115
- M. Kamada, T. Suzuki, F. Nakamura, Y. Mori, M. Arai, Appl. Phys. Lett. 49, 1263 (1986). http://dx.doi.org/10.1063/1.97381
- N. Braslau, J.B. Gunn, J.L. Staples, Solid-State Electron. 10, 381 (1967). http://dx.doi.org/10. 1016/0038-1101(67)90037-8
- R.P. Taylor, P.T. Coleridge, M. Davies, Y. Feng, J.P. McCaffrey, P.A. Marshall, J. Appl. Phys. 76, 7966 (1994). http://dx.doi.org/10.1063/1.357908
- H.J. Bühlmann, M. Ilegems, J. Electrochem. Soc. 138, 2795 (1991). http://dx.doi.org/10.1149/ 1.2086058
- A. Valeille, K. Muraki, Y. Hirayama, Appl. Phys. Lett. 92, 152106 (2008). http://dx.doi.org/10. 1063/1.2912034
- O. Göktas, Small alloyed ohmic contacts to 2DES and submicron scale corbino devices in strong
 magnetic fields: observation of a zero bias anomaly and single electron charging, Ph.D. thesis,
 Max-Planck-Institut für Festkörperforschung, Stuttgart (2009)
- G.Y. Robinson, Solid-State Electron. 18, 331 (1975). http://dx.doi.org/10.1016/0038-1101(75)90088-X

Part III Quantum Point Contact Experiments

Chapter 9 Quantum Point Contacts

Abstract Quantum point contacts (QPCs) are a basic building block for many experiments in mesoscopic physics. Interference and tunneling experiments in the quantum Hall regime require detailed control and understanding of QPC confinement and transmission properties. A short review of the basic properties of QPCs is given. Optimized growth techniques allow the gating and study of QPCs on high-mobility two-dimensional electron gases, where the influence of disorder is strongly reduced. In these clean systems, the energy spectrum can be accessed via finite-bias transport, which allows us to characterize the shape of the confinement potential of the QPC. As the formation of compressible and incompressible stripes in the (fractional) quantum Hall regime depends sensitively on the steepness of the edge potential, understanding the confinement parameters is crucial for a further investigation of QPCs in finite magnetic fields.

9.1 Introduction

For the "birth" of mesoscopic physics, two-dimensional electron gases defined in GaAs/AlGaAs heterostructures played a crucial role. Here, the Fermi wavelength is of the order of 10–100 nm, two orders of magnitude larger than in a metal. Furthermore, these structures are available in such high purity that electron transport at the Fermi energy is ballistic on even much longer length scales. Using state-of-the-art nanofabrication procedures, van Wees and co-workers and Wharam and co-workers were able to implement what is known as quantum point contact (QPC) [2, 3]. The device is shown schematically in Fig. 9.1. By applying a negative voltage to metallic top-gates, the electron gas underneath the gates is depleted. A current passed in between the two contacts therefore has to travel through the narrow constriction with a width comparable to the Fermi wavelength. It was found that the conductance exhibited pronounced steps described by

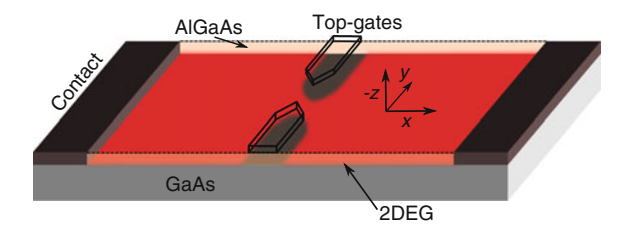


Fig. 9.1 Schematic illustration of a QPC on GaAs/AlGaAs heterostructure. Adapted from [4]

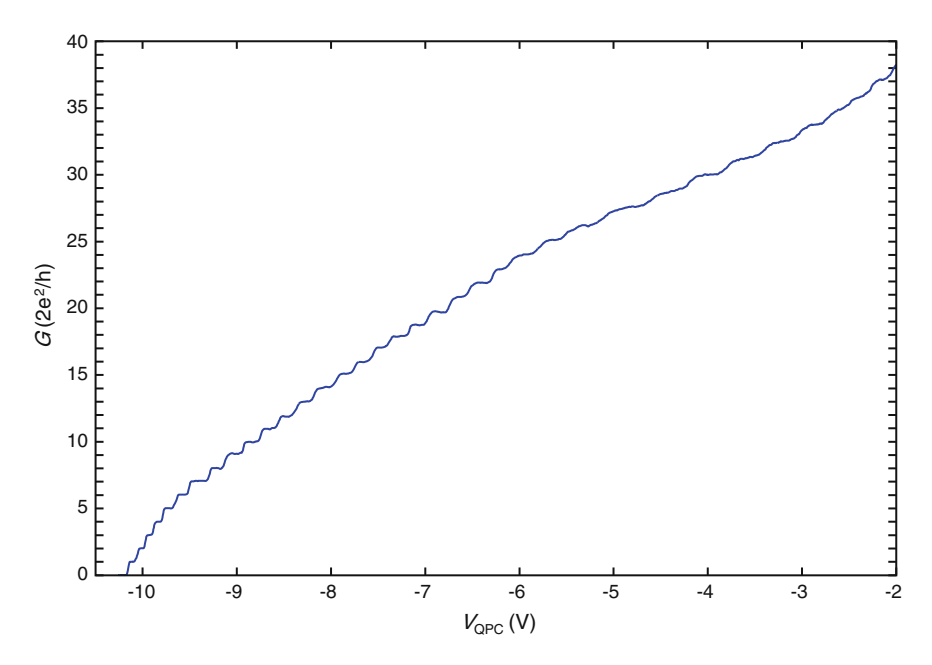


Fig. 9.2 Conductance of a QPC on a high mobility quantum well. Conductance plateaus are visible up to more than $35\times 2e^2/h$

$$G = \frac{2e^2}{h}N\tag{9.1}$$

where N is an integer number and depends on the QPC gate voltage. Experiments were carried out at cryogenic temperatures, where the thermal energy does not wash out the quantization of the energy levels due to the lateral confinement. A similar measurement with a QPC fabricated on a state-of-the-art high mobility wafer is shown in Fig. 9.2. In this structure, influence of disorder is minimal and conductance quantization up to more than $35 \times 2e^2/h$ is observed.

Despite more than 25 years have passed since the first realization, QPCs are still widely studied and used in experiments. They are for example employed to realize tunneling barriers in quantum dots or as charge detectors [5–8]. Interesting

9.1 Introduction 135

many-body phenomena in QPCs, like tunneling in the quantum Hall regime [9–12], the 0.7 anomaly [13–18] and spin-orbit interaction effects [19] are current research topics of great interest.

9.2 Conductance of Ideal and Non-ideal QPCs

In the following, we will discuss how quantized conductance arises in a two-dimensional system, where electron energies are quantized due to a confinement in one dimension. After a discussion of the simplest case, an ideal one-dimensional wire, we will progress to a more general case and sketch how the Landauer formula can be obtained. Finally, the particular case of a saddle-point potential and the resulting conductance curve will be discussed.

9.2.1 Transmission of an Ideal Quantum Wire

The simplest model to study the quantized conductance of a QPC is an ideal quantum wire (Fig. 9.3a). In the following discussion we will use the coordinate system sketched in Fig. 9.1, where x points along the QPC channel and y points perpendicularly to the QPC channel. The origin x = y = 0 resides in the center of the QPC channel.

For simplicity we first assume the wire to be infinitely long in x-direction, such that energy quantization is only important in y-direction. The wave functions in the wire can be written as [20]:

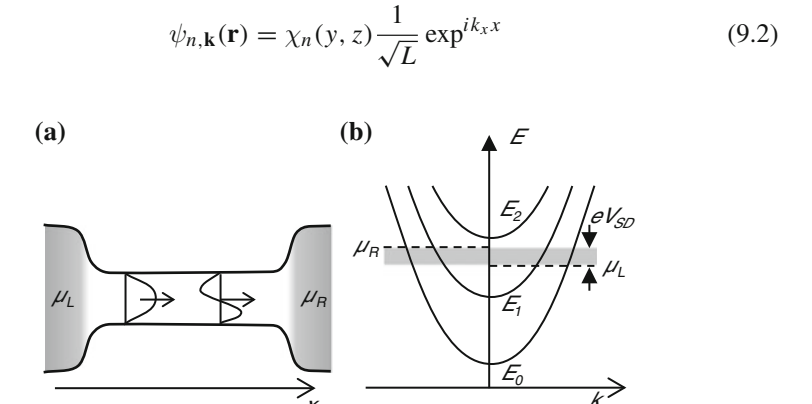


Fig. 9.3 a Schematic sketch of the ideal quantum wire connecting two reservoirs with electrochemical potentials μ_L and μ_R . b Subband energy versus wavevector for the parabolic dispersion relation. All subbands below μ_R contribute to the *left*-moving current, while subbands below μ_L contribute to the *right*-moving current. Adapted from [20]

where the transverse modes of the wire $\chi_n(y, z)$ are assumed to be normalized. The energy dispersion along the *x*-direction is assumed to be parabolic, $E_n(k_x) = E_n + \frac{\hbar^2 k_x^2}{2m^*}$ (Fig. 9.3b). Here, E_n is the energy of the *n*th subband due to the transversal confinement.

With this, the differential current density of the mode n and wave vector k_x can be written as [20]:

$$d\mathbf{j}_{n,k_x}(\mathbf{r}) = -\mathbf{e}_x g_s \frac{|e|}{h} |\chi_n(y,z)|^2 \frac{\partial E_n(k_x)}{\partial k_x} dk_x$$
(9.3)

Here g_s denotes the spin degeneracy. We are now interested in the total current through the wire, depending on the electrochemical potentials μ_L and μ_R at the entrance and exit of the wire (Fig. 9.3a). The total current is found by summing over all occupied modes n and integrating over the wavevectors k_x :

$$I_{\text{tot}} = \left(\sum_{n} \int_{k_x > 0, occ.} dj_{n, k_x}\right) - \left(\sum_{n} \int_{k_x < 0, occ.} dj_{n, k_x}\right)$$
(9.4)

Hence all subbands below μ_R contribute to the left-moving current, while subbands below μ_L contribute to the right-moving current (Fig. 9.3b).

Left-moving (second term) and right-moving (first term) charge carriers contribute with a different sign to the net current, hence the total current cancels out in an equilibrium situation. Using the fact that left- and right-moving states are occupied with the Fermi-Dirac distribution of the right or left reservoir, f_R or f_L , the expression can be rewritten in terms of an energy integral [20]:

$$I_{\text{tot}} = g_s \frac{|e|}{h} \left(\sum_{n} \int_{E_n}^{\infty} dE \left[f_L(E - \mu_L) - f_R(E - \mu_R) \right] \right)$$
(9.5)

In the linear response regime where the applied voltage is small, ¹ the integrand can be expanded:

$$f_L(E-\mu_L) - f_R(E-\mu_R) \approx -\frac{\partial f_L(E-E_F)}{\partial E} |e|V_{SD} \xrightarrow{T\to 0} |e|V_{SD}\delta(E-E_F)$$
 (9.6)

where $\mu_L - \mu_R = |e|V_{\text{SD}}$. We find [20]:

$$G = \frac{I_{tot}}{V_{SD}} \approx \begin{cases} g_s \frac{e^2}{h} \sum_n f_L(E_n - E_F), & T > 0\\ g_s \frac{e^2}{h} N, & T \to 0 \end{cases}$$
(9.7)

 $^{^{1}|}e|V_{SD} \ll k_{B}T$.

where T is the temperature. For a spin degeneracy of two the conductance is quantized in multiples of $2e^2/h$ for $T \to 0$.

9.2.2 Non-ideal QPC

In the previous section, the transmission through an ideal quantum wire was discussed. Due to the simplifying assumptions, the energy eigenvalues E_n were not dependent on the spatial position in the wire. In a more realistic QPC geometry, both the width of the channel and the confinement potential change as a function of position. Hence the Schrödinger equation is no longer separable and finding a solution becomes more difficult. Nevertheless, more realistic systems were investigated successfully in what is called the "adiabatic approximation". Here, the length scale on which the confinement potential changes is much longer than the relevant dimensions for the energy quantization, i.e. the Fermi wavelength [21]. Under those simplifying conditions, it was shown that the wave functions are locally separable [22] and a position dependent $E_n(x)$, which takes the function of an effective potential, can be found. Similar to before, the total current can be expressed as:

$$I_{tot} = g_s |e| \sum_{n} \int_{-\infty}^{\infty} \frac{dk_x}{2\pi} v_x(k_x) f_n(k_x)$$
 (9.8)

where $v_x(k_x) = \hbar k_x/m^*$ is the group velocity of the charge carriers. Here, $f_n(k_x)$ is a function that describes the contribution of mode n at wave vector k_x to the current density and hence depends on the transmission. This can be applied to calculate the current transmitted through a QPC with a finite reflection probability. Right-moving electrons ($k_x > 0$) originate from the left contact and are thus occupied with the Fermi-Dirac distribution of the left lead, $f_L(E)$. Left-moving electrons ($k_x < 0$) are either reflected (with a probability $1 - T_n(E)$) and thus are occupied with the Fermi-Dirac distribution of the left lead or are transmitted from the right lead (with a probability $T_n(E)$) and are occupied with the Fermi-Dirac distribution of the right lead. Thus we can write [21]:

$$I_{tot} = g_s|e| \sum_{n} \left[\int_{0}^{\infty} \frac{dk_x}{2\pi} v_x(k_x) f_L(E) \right]$$
 (9.9)

$$+\int_{-\infty}^{0} \frac{dk_{x}}{2\pi} v_{x}(k_{x}) \left[(1 - T_{n}(E)) f_{L}(E) + T_{n}(E) f_{R}(E) \right]$$
(9.10)

$$= g_s|e| \sum_{n=0}^{\infty} \int_{0}^{\infty} \frac{dk_x}{2\pi} v_x(k_x) T_n(E) \left[f_L(E) - f_R(E) \right]$$
 (9.11)

Here $T_n(E) = \sum_m |t_{mn}(E)|^2$ is the probability of transmitting through channel n from all possible channels m at energy E. When modes are decoupled in an adiabatic system, this is simplified to: $T_n(E) = |t_{nn}(E)|^2$. Changing the integration variable to energy, one obtains:

$$I_{tot} = \frac{g_s|e|}{2\pi} \int_{0}^{\infty} dE \sum_{n} T_n(E) \left[f_L(E) - f_R(E) \right]$$
 (9.12)

Expanding again in the linear response regime gives [20]:

$$G = \frac{I_{tot}}{V_{SD}} = \begin{cases} g_s \frac{e^2}{h} \int_{-\infty}^{\infty} dE \sum_n T_n(E) \left(-\frac{\partial f_L(E)}{\partial E} \right), & T > 0 \\ g_s \frac{e^2}{h} \sum_n T_n(E_F), & T \to 0 \end{cases}$$
(9.13)

This is the famous Landauer formula, which is the foundation of the Landauer-Büttiker theory.

9.2.3 Saddle-Point Potential

In order to work out the conductance through an arbitrary QPC potential, solutions to (9.13) have to be found. However in most cases, exactly calculating the transmission probabilities $T_n(E)$ is not possible. A simple QPC potential, where transmission probabilities can be calculated is the saddle-point model [23, 24]:

$$V(x, y) = -\frac{1}{2}m^*\omega_x^2 x^2 + \frac{1}{2}m^*\omega_y^2 y^2 + V_0$$
 (9.14)

Here, the QPC potential is modeled as a saddle point, with parabolic confinement in the y-direction and a parabolic drop-off in the x-direction. As before, x = y = 0 lies in the center of the QPC channel and x and y have the direction indicated in Fig. 9.1.

We will see later that this model potential is a good description of a realistic QPC in most cases. The saddle point potential leads to a separable Hamiltonian, where the y-confinement leads to equidistant energy eigenstates: $E_n = \hbar \omega_y (n + \frac{1}{2})$, where n = 0, 1, 2, ... is the mode number. The transmission probability for the mode n at energy E can be calculated [23, 24]:

$$T_n(E) = \frac{1}{1 + e^{\frac{-2\pi}{\hbar\omega_x}\epsilon_n}}, \ n = 0, 1, 2, \dots$$
 (9.15)

with an energy parameter:

$$\epsilon_n = E - \hbar \omega_{\nu} (n + 1/2) - V_0, \ n = 0, 1, 2, \dots$$
 (9.16)

Using (9.13) and (9.15), the conductance through the saddle point potential can be calculated once ω_x , ω_y and V_0 are known. Typical conductance steps are found if $\omega_y/\omega_x \ge 1$ and steps become more pronounced when the ratio increases.

9.2.4 Magneto-Electric Depopulation

The saddle-point potential also leads to an analytically solvable transmission in an external magnetic field. Here, the transmission takes a similar form:

$$T_n(E) = \frac{1}{1 + e^{-\pi \tilde{\epsilon}_n}}, \ n = 0, 1, 2, \dots$$
 (9.17)

with a changed energy parameter that takes the effects of the magnetic field into account [24]:

$$\tilde{\epsilon}_n = \frac{E - E_2(n+1/2) - V_0}{E_1}, \ n = 0, 1, 2, \dots$$
 (9.18)

The parameters E_1 and E_2 now play the role of $\hbar\omega_x/2$ and $\hbar\omega_y$ at zero *B*-field and are given as [24]:

$$E_1 = \frac{\hbar}{2\sqrt{2}} \left[\left(\Omega^4 + 4\omega_x^2 \omega_y^2 \right)^{1/2} - \Omega^2 \right]^{1/2}$$
 (9.19)

$$E_2 = \frac{\hbar}{\sqrt{2}} \left[\left(\Omega^4 + 4\omega_x^2 \omega_y^2 \right)^{1/2} + \Omega^2 \right]^{1/2}$$
 (9.20)

where $\Omega = \omega_c^2 + \omega_y^2 - \omega_x^2$ and $\omega_c = |e|B/m^*$ is the cyclotron frequency. The effect of an increasing *B*-field can be seen in Fig. 9.4: conductance steps become more pronounced while they are lifted to higher energies. This effect is referred to as magneto-electric depopulation.

9.3 QPC Simulations

To gain insight in a reasonably realistic density distribution and potential profile of the QPCs investigated by us, we have conducted numerical simulations using the software package "nextnano3". Here, the Poisson and Schrödinger equations

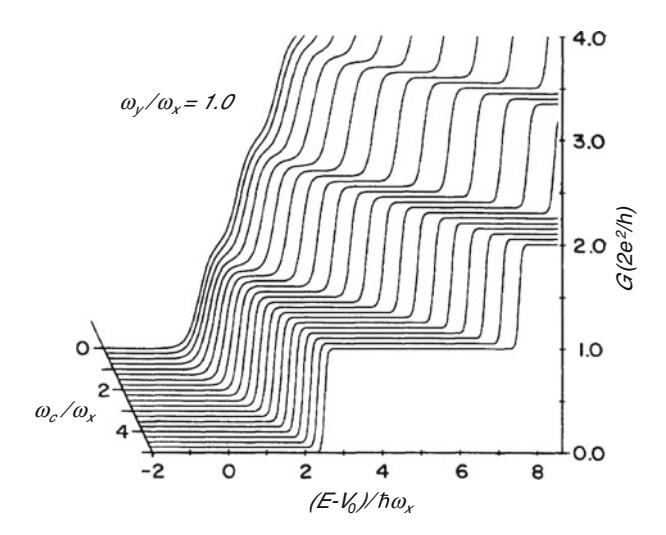


Fig. 9.4 Evolution of the saddle point conductance for a change in the cyclotron frequency ω_c . In stronger magnetic fields, subbands are lifted in energy and conductance steps become more pronounced. (Reprinted figure with permission from [24]. Copyright 1990 by the American Physical Society.)

were solved self-consistently in two dimensions for $T=1\,\mathrm{K}$, for a GaAs/AlGaAs (x=0.24) heterostructure with a 320 nm deep 2DEG (wafer D110504A). For simplicity, the 700 nm wide QPC was assumed to be infinitely long in x-direction. The doping concentrations were adjusted to compensate for surface charges and to reproduce the gate depletion voltages correctly. Figure 9.5a shows the eigenfunctions that were obtained for a relatively open QPC, when a voltage of $-1.94\,\mathrm{V}$ is applied to the top-gates. Here, the square of the electron wavefunction is plotted as a function of the transversal direction y and the growth direction -z. Higher energy modes are off-set in -z direction by multiples of 50 nm.

The resulting electron volume density is shown in Fig. 9.5b. The interface between GaAs and AlGaAs at $z=320\,\mathrm{nm}$ is indicated by the white dashed line. A finite density is found over a width of approximately 200 nm. The electron density spreads approximately 15–20 nm in z-direction and only the lowest subband for quantization in z-direction is occupied. The integrated sheet electron density is shown in Fig. 9.5c for different voltages applied to the top-gates. For a QPC voltage of $-1.94\,\mathrm{V}$, the maximum density in the center of the channel is already reduced compared to the bulk electron density of approximately $1.5\times10^{11}\,\mathrm{cm}^{-2}$. The fine-structure in the density distribution originates from contributions of different subbands with different spatial probability density [25].

In addition to the density distribution, the electrostatic potential has been calculated. Results are shown in Fig. 9.6a. Here, the electrostatic potential (at $z=320 \,\mathrm{nm}$) is plotted versus the spatial coordinate y. The potential energy is flat in the central region of the QPC when the QPC is open and is not well described by a parabolic

9.3 QPC Simulations 141

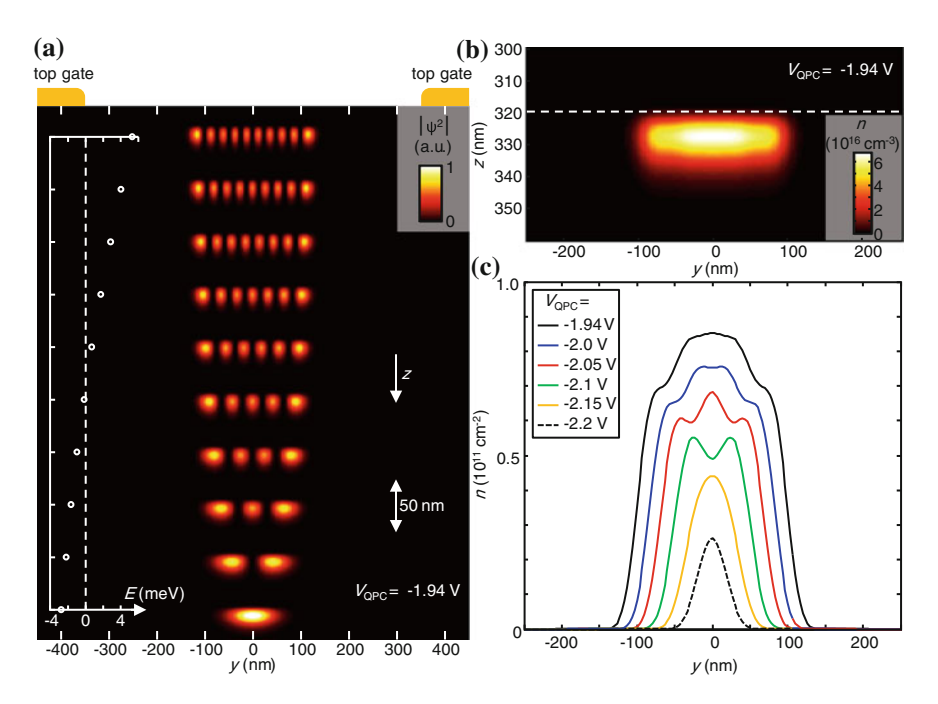


Fig. 9.5 a Calculated square of the electron wavefunction for eigenmodes of a 700 nm wide QPC. y denotes the transverse direction, while -z is the growth direction. Higher modes are offset in -z direction by multiples of 50 nm. Top-gates of the 700 nm wide QPC are shown schematically. The energy eigenvalues of the corresponding mode are shown in the *left inset*. **b** Calculated electron volume density in a QPC as a function of transverse (y) and growth direction (-z). **c** Carrier sheet density as a function of transverse (y) direction

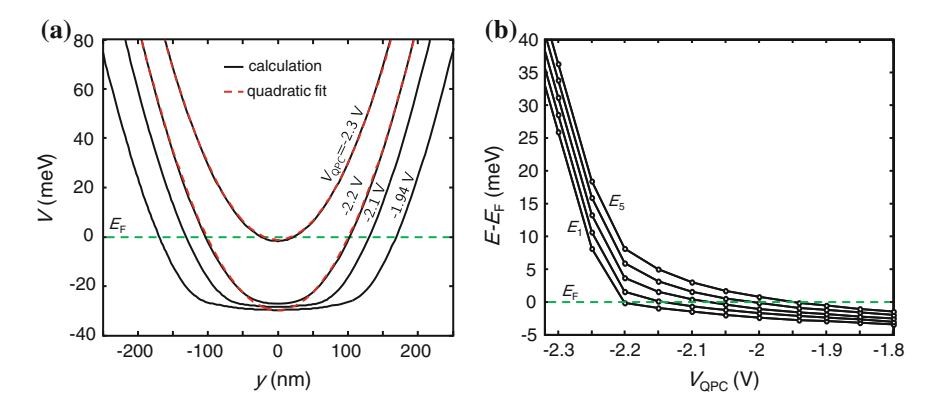


Fig. 9.6 a Calculated electrostatic potential (*black*). Close to pinch-off, a quadratic fit (*red*) is a good approximation to the confinement potential. **b** Energies of the five lowest subbands with respect to the Fermi energy versus the QPC voltage

potential. Closer to pinch-off, when only a small number of modes is occupied, the conduction band gets lifted and a quadratic fit agrees well with our calculations. The energies of the five lowest subbands relative to the Fermi energy are shown in Fig. 9.6b, as a function of the voltage applied to the QPC. Subband energies increase towards pinch-off. As soon as subbands lie above the Fermi energy, they are rapidly lifted in energy when the gate voltage decreases, while the subband spacing then changes only by little. Similar results have been found by Laux et al. [25].

9.4 Transport Properties of Clean QPCs

Tunneling and interference experiments in the quantum Hall regime require a detailed understanding of the transmission properties of QPCs. Thus, understanding and controlling the confinement and disorder potential is crucial. Here we present measurements that try to address these points. By shifting the QPC channel, we can show that disorder does not affect transport at B=0 T. Applying a finite source-drain voltage to the QPC, we observe half-plateaus in the conductance and are able to characterize the QPC confinement potential. We furthermore study two QPC geometries, where the confinement potential can be varied by using gate voltages. After characterizing the confinement potential, we investigate its effect on the QPC transmission in the quantum Hall regime.

9.4.1 Lateral Shifting of the QPC Channel

Figure 9.7a shows the transconductance of a 250 nm wide QPC, when the voltages applied to each of the two top-gates defining the QPC are varied individually. Black regions denote pinch-off or regions of quantized conductance with conductance values of $G = 2, 4, 6, \dots e^2/h$. Bright regions of increasing conductance bend around the pinch-off region. As soon as the electron gas under either of the gates is no longer depleted (at approximately $-1.3 \,\mathrm{V}$), the conductance strongly increases (white borders in Fig. 9.7a). By varying the ratio of the voltages applied to right or left QPC gate, the potential minimum of the channel is shifted in the lithographically defined channel. Thus by moving along a conductance plateau in Fig. 9.7a, spatial variations of the QPC background potential are mapped out [26]. A static disorder potential, for example created by dopants, is fixed in space and influences the transmission of the QPC channel, when the channel is moved across the static scattering center. Thus, localizations are expected to show up as lines intersecting the conductance steps. No such behavior is visible in Fig. 9.7a, apart from charge-rearrangements which create shifts parallel to the V_1 axis. This confirms the cleanliness of the samples studied, where the gate-defined confinement potential is expected to be mainly responsible for the transmission properties, with negligible influence of disorder. An example of

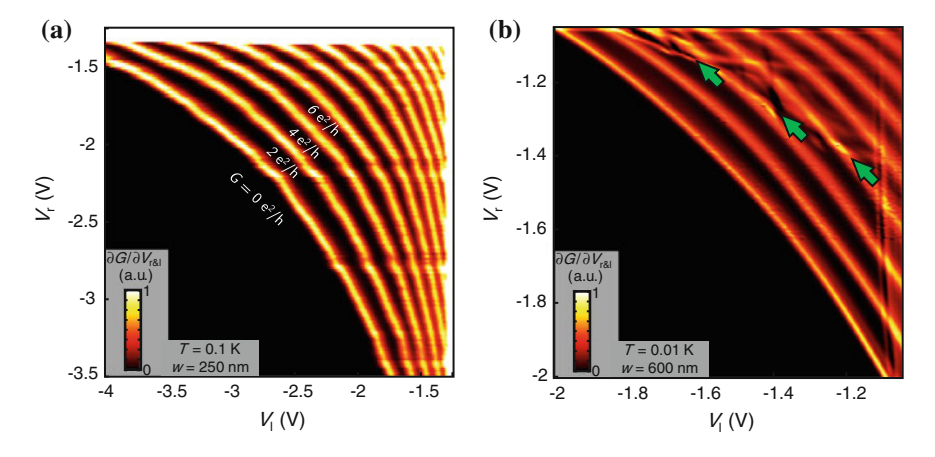


Fig. 9.7 a Transconductance of a 250 nm wide QPC, as a function of the voltages V_l and V_r applied to the *left* and *right* finger gates of the QPC. Conductance is quantized in values of $G = 0, 2, 4, \ldots \times e^2/h$ (*black* regions). Regions where the conductance increases (*bright*) bend around the pinch-off region. The *white* borders arise when the electron gas under either of the gates is no longer depleted (at approximately $-1.3\,\mathrm{V}$) and thus the conductance strongly increases. **b** Transconductance of a 600 nm wide QPC with clear signs of localizations in the constriction (*green arrows*)

a QPC with clear signs of localizations is shown in Fig. 9.7b. Here, disorder-induced resonances (marked by green arrows) modulate the QPC conductance.

The magnitude of the spatial shift can be estimated from the number of conductance plateaus $n_{\rm l}$ and $n_{\rm r}$ that are observed when the gate voltages $V_{\rm l}$ or $V_{\rm r}$ are varied: $\Delta y \approx \lambda_{\rm F}/2 \times (n_{\rm l}-n_{\rm r})/2$ [1, 27] where $\lambda_{\rm F} = \sqrt{2\pi/n_{\rm s}}$ is the Fermi wavelength. In Fig. 9.7a, the largest shift of Δy corresponds to: $\Delta y \approx 21$ nm $\times (11-1)/2=105$ nm, which roughly corresponds to a shift from the center to the edge of the lithographically defined channel.

9.4.2 Finite Bias Transmission

In order to characterize the confinement potential of a QPC, the knowledge of its energy spectrum is essential. By applying a finite source-drain voltage $V_{\rm SD}$, we can access the QPC's subband spacing $\Delta_{\rm SB}$ which arises due to the transversal confinement [28–31] (see Sect. 9.2.3).

Figure 9.8b shows the conductance of the 250 nm wide QPC in the linear response regime, with $V_{\rm SD}\approx 0$ mV. The schematic image on the right-hand side depicts the situation that applies here. Source and drain electrochemical potentials are aligned. The dispersion relation in the QPC is parabolic and different subbands are energetically separated by the subband spacing $\Delta_{\rm SB}$. On the first conductance plateau, the bottom of the lowest (spin degenerate) subband lies below source and drain

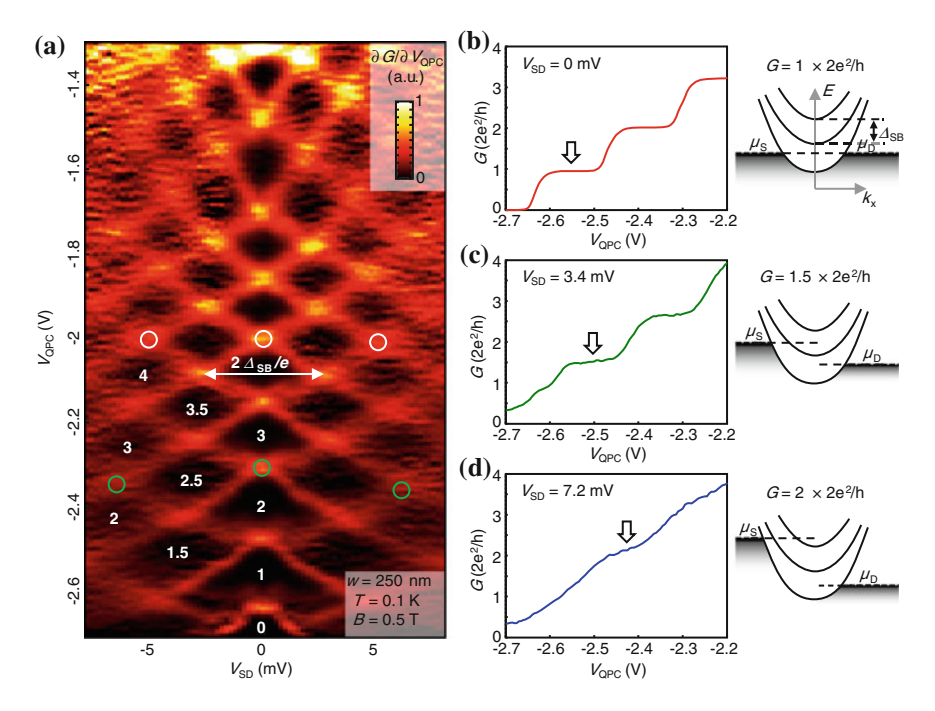


Fig. 9.8 a Numerical transconductance $\partial G/\partial V_{QPC}$ as a function of the source-drain bias V_{SD} and the QPC voltage V_{QPC} . **b** At zero source-drain bias, a conductance quantized in multiples of $2e^2/h$ is found in *diamond-shaped* regions (*black*). The width of the regions is determined by the subband spacing Δ_{SB} . **c** As the source-drain bias is increased, half-plateaus at 1.5, 2.5, 3.5, ... × $2e^2/h$ are found. At even higher bias where two subbands fit in the bias window, conductance plateaus at 2, 3, 4, ... × $2e^2/h$ are found again (**d**)

electrochemical potentials and contributes $2e^2/h$ to the conductance. Transport via higher subbands is suppressed, as the thermal energy k_BT is small compared to Δ_{SB} .

For a source-drain bias $V_{\rm SD}=3.4\,\mathrm{mV}$, conductance plateaus at $G=1.5, 2.5, \ldots \times 2e^2/h$ are observed (Fig. 9.8c). The scheme on the right-hand side reflects a situation with a conductance $G=1.5\times 2e^2/h$. Here, the bottom of the lowest subband lies below source and drain electrochemical potentials, and thus contributes $2e^2/h$ to the conductance. In contrast, the bottom of the second subband falls in the bias window and thus only contributes $0.5\times 2e^2/h$ to the conductance.

Similarly, at even higher source-drain biases ($V_{\rm SD}=7.2\,\mathrm{mV}$ in Fig. 9.8d), two subbands fit in the bias window and a quantization in integer multiples of $2e^2/h$ is found again.

The full dependence of the conductance on source-drain bias and QPC voltage is shown in Fig. 9.8a. Here, the transconductance is plotted, with dark diamond shaped regions corresponding to conductance plateaus. The conductance values are indicated (white) as multiples of $2e^2/h$.

9.4.2.1 Interpreting the Confinement Potential

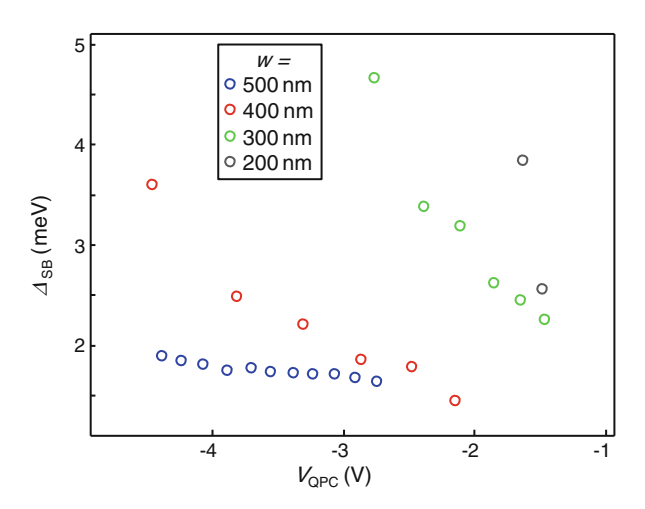
Conductance plateaus and steps span a regular pattern in the $V_{\rm SD}-V_{\rm QPC}$ plane. Close to pinch-off, applying a large source-drain bias across the QPC leads to a deformation of the confinement potential. This self-gating is responsible for the finite slope of the pinch-off line and a deviation from a regular chessboard pattern of conductance steps [1, 14]. In contrast, far away from pinch-off, self-gating is not expected to play a role. Here, higher-order conductance steps appear at the same QPC voltage as the lowest order steps (white circles in Fig. 9.8a).

At the lowest order conductance step of the QPC, the nth subband is aligned with source and drain electrochemical potentials when $V_{\rm SD} = 0\,\mathrm{mV}$. As the bias is increased symmetrically to $V_{\rm SD} > \Delta_{\rm SB}/e$, a second order conductance step is observed. Here, the nth subband lies in the bias window, while (n+1)th and (n-1)th subbands are aligned with $\mu_{\rm S}$ or $\mu_{\rm D}$. Thus, the subband spacing between (n-1)th and nth subband equals the subband spacing between nth and (n+1)th subband. Such an equidistant energy spectrum is characteristic for a harmonic potential. This configuration is exactly valid for the situation marked by white circles in Fig. 9.8a.

Closer to pinch-off, the pattern of conductance steps is distorted (green circles, Fig. 9.8a). Here, Δ_{SB} seems to increase with the subband index n, which is characteristic for a confinement potential which is steeper than a harmonic potential.

We now would like to extract characteristic parameters for the shape of the confinement potential from a finite-bias measurement (Fig. 9.8a). Due to the energet-ically equidistant subbands, the QPC potential is expected to be qualitatively well described by a harmonic confinement potential, apart from very close to pinch-off. Thus, the QPC transmission can be compared to a saddle point-model (Sect. 9.2.3). Figure 9.9 shows the subband spacing for QPCs of different width, as a function of the QPC voltage. The subband spacing is larger for QPCs of smaller width and increases towards pinch-off.

Fig. 9.9 Subband spacings for QPCs of different width w. Δ_{SB} is smaller for QPCs with larger w and increases towards pinch-off



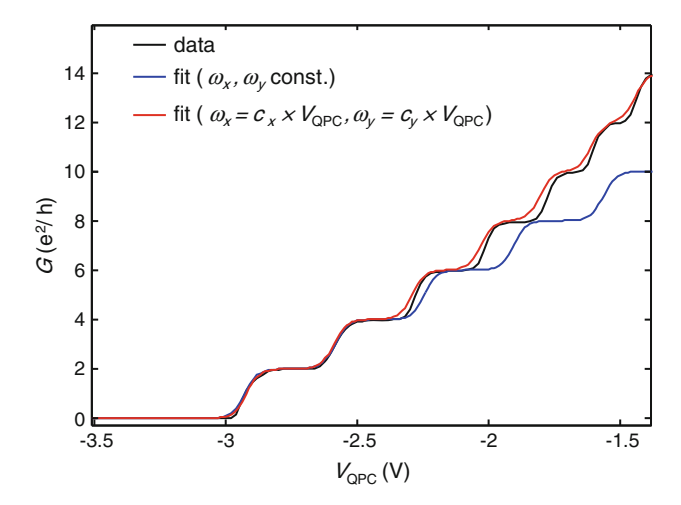


Fig. 9.10 Conductance of a 300 nm wide QPC as a function of $V_{\rm QPC}$. A fit of (9.15) with constant ω_x and ω_y is shown in *blue*. Assuming a linear dependence of ω_x and ω_y on the QPC voltage, a good fit over several conductance plateaus is achieved (*red*)

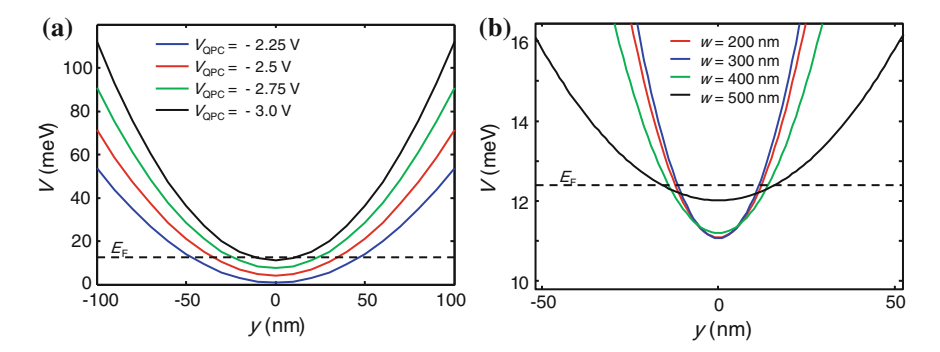


Fig. 9.11 a Transversal confinement potential of a 300 nm wide QPC as a function of the QPC voltage, obtained from a fit of (9.15). Decreasing the QPC voltage leads to a steeper lateral confinement potential. **b** Transversal confinement potential at the first conductance plateau for QPCs of different widths

By fitting the saddle-point potential transmission, we can deduce the lateral confinement potential, and the shape of the potential barrier formed by the QPC, i.e. ω_x and ω_y . Figure 9.10 shows a fit of (9.15) (blue) to a measured conductance curve (black). When a linear dependence of the confinement parameters ω_x , ω_y on the QPC voltage is assumed, a good agreement is found (red).

For investigating the formation of FQH states in strong magnetic fields, we are interested in the steepness of the confinement potential of the QPC. Due to self-consistency effects, the steepness strongly influences the formation of compressible and incompressible stripes in the quantum Hall regime. Figure 9.11a illustrates the

influence of the QPC voltage on the transversal confinement potential of a 300 nm wide QPC. The confinement potential becomes steeper towards pinch-off, which can be seen from the increase in Δ_{SB} . The effect of the QPC width on the potential steepness is illustrated in Fig. 9.11b. Here, the transversal confinement potential is plotted as a function of the spatial coordinate y when the first subband is aligned with the Fermi energy. As expected, a wider QPC results in a less steep confinement potential.

To summarize this section, finite-bias transport gave us access to the subband spectrum of a QPC. From the pattern spanned by higher-order transmission in the $V_{\rm SD}-V_{\rm QPC}$ -plane, we conclude that the QPC confinement potential is harmonic, except when many QPC modes are occupied. Close to pinch-off, the confinement potential becomes increasingly steep and subband spacing increases. Here, the regular pattern of conductance plateaus and half-plateaus becomes distorted by self-gating effects.

9.4.3 Tuning the QPC Confinement Potential

The steepness of the confinement potential influences the formation of compressible and incompressible regions in the quantum Hall regime. Thus, a tunable QPC confinement potential is desirable in order to study this effect. For this, a QPC consisting of six individually tunable gates has been investigated (see inset Fig. 9.12a). Figure 9.12a shows the conductance of the QPC as a function of voltages applied to the different gates. Four different configurations are shown: left QPC (V_L : gates 1,2), right QPC (V_R : gates 5,6), middle QPC (V_M : gates 3,4) and diagonal QPC (V_{diag} : gates 2,5). As expected, pinch-off voltages are more negative for wide QPCs (diagonal) than for narrow QPCs (middle).

Finite bias measurements have been conducted with this QPC in different gate voltage configurations:

- In the simplest case only one of the QPCs is varied $(V_L, V_M \text{ or } V_{\text{diag}})$.
- Then a QPC has been defined by mainly using right and left gate pairs $(V_L = V_R)$, while the middle gate pair was used to lower $(V_M = -0.05 \times V_R = -0.05 \times V_L)$ or increase $(V_M = 0.1 \times V_R = 0.1 \times V_L)$ or $V_M = 0.7 \times V_R = 0.7 \times V_L)$ the height of the potential barrier in the center of the QPC.
- Last, mainly the central gate pair voltage $V_{\rm M}$ is varied, while left or right gate pairs are used to lower ($V_{\rm L}=V_{\rm R}=-0.07\times V_{\rm M}$) or to lift ($V_{\rm L}=V_{\rm R}=0.7\times V_{\rm M}$) the potential at the entrance of the channel.

9.4.3.1 Saddle Point Potential Fitting Procedure

The parameters $\hbar\omega_x$ and $\hbar\omega_y$ are obtained from finite-bias measurements in this configuration and a subsequent fit of the saddle point transmission (9.15) to the

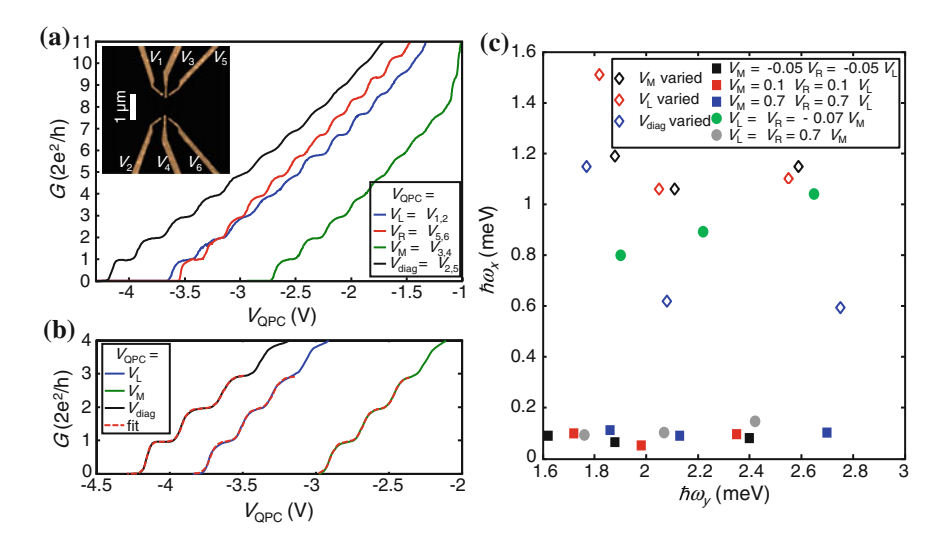


Fig. 9.12 a Conductance of a six-gate QPC (*inset*, sample D110504A-9B) as a function of voltages applied to the different gates. Four different configurations are shown: *left* QPC (gates 1,2), *right* QPC (gates 5,6), *middle* QPC (gates 3,4) and *diagonal* QPC (gates 2,5). **b** Measured QPC conductance and fitted saddle-point conductance as a function of the QPC voltage. **c** Parameters of the QPC potential for different gate voltage configurations. ω_y is extracted from finite bias measurements. ω_x is obtained from a fit of (9.15) to the QPC conductance curves

measured conductance. The method used for the fitting is described in [1]: Here, the Fermi energy is set as a reference to zero, and (9.16) then reads:

$$\epsilon_n = -\hbar\omega_y(n+1/2) - V_0, \ n = 0, 1, 2, \dots$$
 (9.21)

The conduction band bottom V_0 is assumed to depend linearly on the QPC gate voltage:

$$V_0 \left(V_{\text{QPC}} \right) = E_0 + \alpha V_{\text{QPC}} \tag{9.22}$$

The lever arm α can be found from realizing that the following equation holds for the *n*th conduction step:

$$0 = -\hbar\omega_{y}(n+1/2) - E_0 - \alpha V_{QPC}, \ n = 0, 1, 2, \dots$$
 (9.23)

Hence, the lever arm α_n in between the *n*th and (n + 1)th conductance step is given by:

$$\alpha_n = \frac{\hbar \omega_{y,n+1}(n+1/2) - \hbar \omega_{y,n}(n-1/2)}{V_{\text{OPC},n} - V_{\text{OPC},n+1}}, \ n = 1, 2, 3, \dots$$
 (9.24)

Here, $\omega_{y,n}$ is the ω_y of the *n*th conductance step (extracted from the subband spacing) and $V_{\text{QPC},n}$ is the QPC voltage at which the *n*th conductance step occurs. Now, only E_0 and $\omega_{x,n}$ remain as fitting parameters while the QPC voltage V_{QPC} is the independent variable. Measured pinch-off curves are well-fitted using this procedure (see Fig. 9.12b).

9.4.3.2 Variation of Potential Parameters

Figure 9.12c shows the parameters $\hbar\omega_x$ and $\hbar\omega_y$ that are obtained in the different gate voltage configurations for the first three conductance plateaus. $\hbar\omega_x$ changes over a large energy range, from approximately 0.05 to 1.5 meV. As expected intuitively, a longer channel, accomplished by using several gates at a time, results in a smaller $\hbar\omega_x$ and hence a smoother potential barrier in the *x*-direction.

In the configuration where the left and right QPC pairs are used to lower ($V_{\rm L} = V_{\rm R} = -0.07 \times V_{\rm M}$) or to lift ($V_{\rm L} = V_{\rm R} = 0.7 \times V_{\rm M}$) the potential at the entrance of the channel, $\hbar\omega_x$ can be changed from approximately 0.1 meV to more than 0.8 meV.

For the single QPCs (middle, left, diagonal) the obtained $\hbar\omega_x$ are larger than when multiple gates are used (approximately 0.6–1.5 meV) and of similar magnitude. In contrast, $\hbar\omega_y$ is of the same energy range (between 1.6 and 2.8 meV) for all gate configurations. Here, the dependence on the respective conductance plateau is much stronger than the geometry dependence.

We conclude that the QPC shown in the inset of Fig. 9.12a does not allow the desired tuning of the confinement potential ω_y . However, by using left and right QPC at entrance and exit of the middle QPC, ω_x and hence the adiabaticity of the QPC can be tuned.

9.4.3.3 Effect of Potential Variation in B-field Transmission

The effect of the variation of $\hbar\omega_x$ is studied by measuring the transmission of the six finger QPC when an external magnetic field has been applied, in order to set the bulk filling factor ν_{bulk} to one. Figure 9.13 shows the conductance as a function of the middle QPC pair voltage V_{M} .

Voltages on left and right QPC pairs, $V_L = V_R = \beta \times V_M$, are used to lift $(\beta > 0)$ or to lower $(\beta < 0)$ the potential at the entrance of the channel. Different conductance curves in Fig. 9.13 correspond to values of β from -0.05 to 0.86. For the situation where a steep potential barrier in x-direction is defined $(\beta = -0.05)$, conductance is smooth and a monotonic function of V_M . Conductance plateaus at $1/3 \times e^2/h$ and $2/5 \times e^2/h$ are observed. As β is increased and hence the potential barrier in x-direction is falling off less steeply, conductance curves are shifted to the right due to the mutual capacitive coupling of the QPC gates. In addition to the still observed conductance plateaus, peaks or kinks in the conductance occur (red arrows in Fig. 9.13). Qualitatively, the quantization of fractional quantum Hall states in the

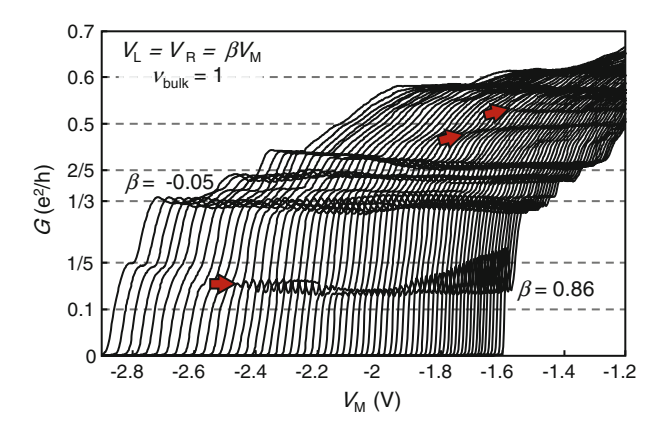


Fig. 9.13 Conductance of the six gate QPC versus voltage applied to the middle QPC gate pair. The bulk filling factor ν_{bulk} has been set to 1 by applying a perpendicular magnetic field of approximately 6.6 T. Voltages on *left* and *right* QPC pairs, $V_L = V_R = \beta \times V_M$, are used to lift $(\beta > 0)$ or to lower $(\beta < 0)$ the potential at the entrance and exit of the channel

QPC does not improve as β is increased. The strong visibility of conductance resonances for a smoother potential barrier in x-direction is contrary to what is expected when no external magnetic field is present. Here, a smooth and adiabatic potential is expected to suppress backscattering and conductance resonances. However, in strong magnetic fields, localization in compressible and incompressible regions due to the disorder potential in the channel becomes relevant. The influence of localizations on the conductance is stronger for a smoother confinement potential here. This effect will be discussed in detail in Chap. 10.

A different example of a QPC with gate-tunable confinement potential is shown in Fig. 9.14a. The 700 nm wide QPC is defined by two finger gates. In addition to that, a third top-gate resides on top of the QPC channel. With the same approach as before, we have extracted the potential parameters $\hbar\omega_x$ and $\hbar\omega_y$ for the three lowest subbands (at B = 0 T) and at different voltages of the channel top-gate V_{TG} . The resulting energies are shown in Fig. 9.14b. A similar size of $\hbar\omega_x$ is found for all configurations, while $\hbar\omega_{\nu}$ again shows a strong dependence on the subband number. In addition, $\hbar\omega_{\nu}$ shows a tendency to increase with more positive channel top-gate voltage. The effect of the channel top-gate on the QPC transmission is demonstrated in Fig. 9.14c. Here, ν_{bulk} has been set to one, while the voltage of the QPC finger gates has been varied. Different conductance curves correspond to different voltages V_{TG} applied to the channel top-gate. Here, $V_{\rm TG}$ has been varied from +100 to -545 mV. Close to pinch-off, conductance resonances are pronounced. Conductance plateaus at $1/3 \times e^2/h$ and $2/3 \times e^2/h$ are observed for all channel top-gate voltages. However, as $V_{\rm TG}$ is decreased, the plateau at $1/3 \times e^2/h$ becomes much more pronounced and conductance for $1/3 \times e^2/h < G < 2/3 \times e^2/h$ becomes smoother and less disorder is visible. As discussed in Chap. 10, applying a negative voltage to the channel topgate increases the width of the incompressible region in the center of the channel.

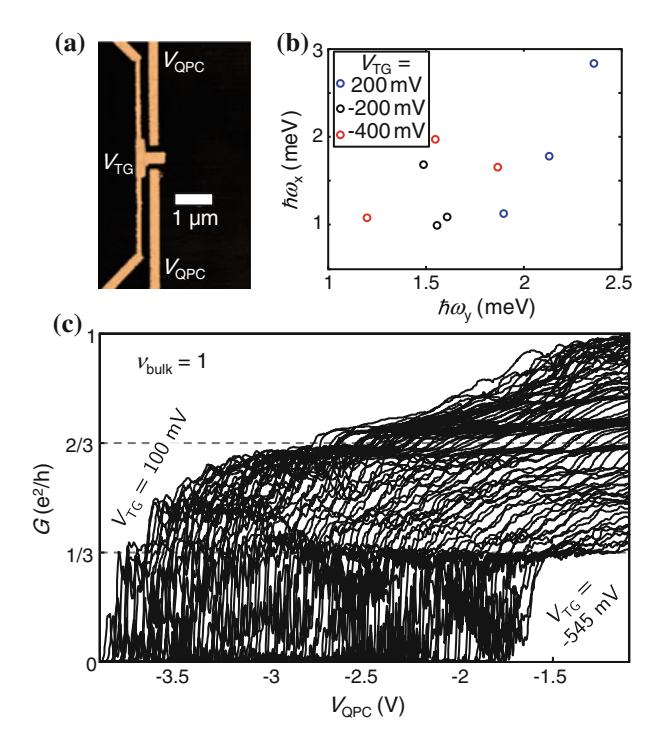


Fig. 9.14 a Finger-gate QPC with top-gate on the center of the QPC channel (D110504A_9B). b Energies $\hbar\omega_x$ and $\hbar\omega_y$ of the first three conductance plateaus (B=0 T) for different top-gate voltages V_{TG} . c Conductance of the top-gate QPC versus voltage applied to the QPC gate pair (V_{QPC}), for different voltages applied to the channel top-gate (V_{TG}). The bulk filling factor ν_{bulk} has been set to 1 by applying a perpendicular magnetic field of approximately 6.6 T

This might explain the better pronounced conductance plateau at $1/3 \times e^2/h$. The more prominent conductance oscillations at $V_{\rm TG} = +100\,{\rm mV}$ might stem from the fact that very negative voltages $V_{\rm QPC} < -3.5\,{\rm V}$ have to be applied to the QPC gates in this situation. For such voltages, sample stability is typically strongly reduced due to tunneling events between gates and doping plane or charge rearrangements close to the QPC channel.

9.4.4 Spin-Resolved Transport

Applying a perpendicular magnetic field lifts the electrons' single particle energies and thus leads to magneto-electric depopulation [24, 32] (see Sect. 9.2.4), which

²As we will see later, the visual quality of the plateau does not reflect directly the energy gap of the corresponding FQH state in the QPC, see Chap. 10.

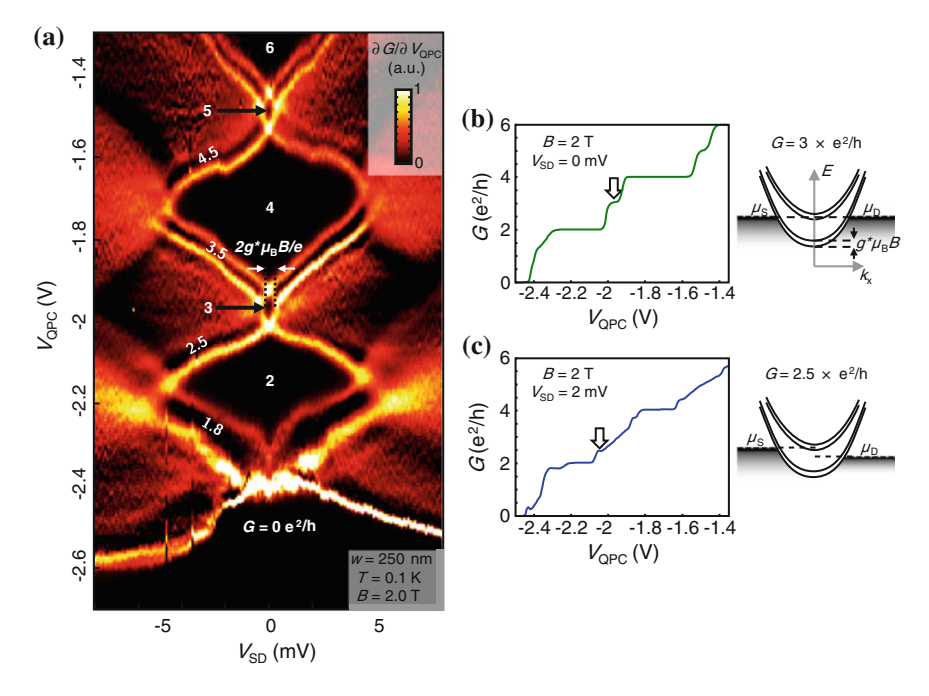


Fig. 9.15 a Transconductance of the 250 nm wide QPC as a function of the QPC voltage, when an external *B*-field of 2T is applied. Large conductance plateaus at $G=2,4,\ldots\times e^2/h$ are observed (*large black diamonds*). The spin degeneracy is lifted in this situation and leads to the observation of conductance plateaus at $G=3,5,\ldots\times e^2/h$ (*small black diamonds*). At finite biases, conductance plateaus at $G=2.5,3.5,\ldots\times e^2/h$ are observed (*black stripes*). **b** QPC conductance at $V_{\text{SD}}=0\,\text{mV}$. The configuration giving rise to $G=3\times e^2/h$ is shown schematically on the *right-hand* side. **c** QPC conductance at $V_{\text{SD}}=2\,\text{mV}$. The configuration giving rise to $G=2.5\times e^2/h$ is shown schematically on the *right-hand* side

effectively resembles an increase in the subband spacing of the QPC. Furthermore, at sufficiently strong magnetic fields the spin degeneracy of the subbands is lifted. At small magnetic fields, where the extent of the conductance plateaus in the source-drain bias is still limited by the subband spacing and not dominated by breakdown effects of the quantum Hall effect, this allows to study correlation effects in the QPC. In this configuration, we measure the resistance longitudinally across the QPC, which relates to QPC and bulk filling factors $\nu_{\rm QPC}$ and $\nu_{\rm bulk}$ via $R_{\rm long} = h/e^2 \left(1/\nu_{\rm QPC} - 1/\nu_{\rm bulk}\right)$. In Fig. 9.15b, the QPC conductance $G = e^2/h \times \nu_{\rm QPC}$ is plotted as a function of the QPC voltage $V_{\rm QPC}$ at zero source-drain bias, now in units of e^2/h . The conductance plateaus at $2e^2/h$ and $4e^2/h$ are much wider in $V_{\rm QPC}$ direction than for the measurement at B = 0 T (Fig. 9.8), due to the increased subband spacing. Furthermore, new plateaus at 3, 5, ... × e^2/h are observed.

The situation that gives rise to the conductance plateau at $3 \times e^2/h$ is shown schematically on the right-hand side. Now the subbands are no longer spin-degenerate. The two spin branches are separated in energy by $g^*\mu_B B$, where g^* is the effective g-factor and μ_B is the Bohr magneton. In this situation, the lowest subband and

the energetically lower spin-branch of the second subband lie below source and drain electrochemical potentials, each contributing e^2/h to the conductance. The energetically higher spin-branch of the second subband lies above source and drain electrochemical potentials and does not contribute to the conductance.

For a source-drain bias of 2 mV (Fig. 9.15c), additional so-called half-plateaus at 2.5, 3.5, ... × e^2/h occur. These are observed whenever a single spin branch of a subband lies in the bias window and hence contributes $0.5 \times e^2/h$ to the conductance.

Figure 9.15a shows the full bias and voltage dependence of the transconductance of the 250 nm wide QPC. Large black diamonds indicate regions where the conductance is quantized in $G=2,4,\ldots\times e^2/h$. Spin-split plateaus show up as much smaller black diamonds with conductance values of $G=3,5,\ldots\times e^2/h$. A plateau at $G=1\times e^2/h$ is obscured by the presence of the 0.7 anomaly. Higher-order plateaus appear as dark regions neighboring the large conductance plateaus, with conductance values $G=2.5,3.5,\ldots\times e^2/h$. Close to pinch-off, a conductance half-plateau related to the 0.7 anomaly is observed at $G=1.8\times e^2/h$.

The extent $\Delta V_{\rm SD}$ of the spin-split conductance plateaus allows for an extraction of the effective g-factor g^* in the QPC via $\Delta V_{\rm SD}=2g^*\mu_{\rm B}B/e$. From this, we find $g^*=4.4$ for $G=3\times e^2/h$ and $g^*=3.8$ for $G=5\times e^2/h$. Compared to the bulk GaAs value of g=-0.44, the effective g-factor is strongly enhanced. Increases of the effective g^* -factor towards lower subbands have for example been reported in [13]. Here, $g^*\approx1.3$ has been found for an in-plane g-field in a QPC at the first conductance plateau. As argued in [1], disorder might reduce the spin enhancement and hence explain the stronger effect observed in our high-mobility samples.

9.4.5 Bias Dependence in the Quantum Hall Regime

Transmission through the QPC is no longer governed by the subband spacing when a strong perpendicular magnetic field is applied and the cyclotron radius becomes much shorter than the QPC width. When a source-drain bias is applied in this situation, transmission does not vary due to shifting source and drain electrochemical potentials with respect to the subbands, but due to a breakdown of the quantum Hall effect in the constriction. Here, the critical current is much smaller than in the bulk due to the smaller width [33]. The microscopic origin of the breakdown in the QPC is not understood and might depend on the details of the current distribution and Hall potential drop across the channel.

Figure 9.16a shows the transconductance of a 800 nm wide QPC, where the QPC voltage and the source-drain voltage have been varied. The bulk filling factor has been tuned to two by the application of an external magnetic field (B = 3.45 T). Pinch-off and a conductance plateau at e^2/h show up as black regions. Conductance curves at three different biases are shown in Fig. 9.16b. Close to pinch-off, the conductance is strongly modulated by resonances and no further conductance plateaus are visible.

The conductance plateau at e^2/h (Fig. 9.16a) shrinks slightly in width as soon as the source-drain bias is increased. At $V_{\rm SD} \approx 1\,\mathrm{mV}$, it then suddenly disappears.

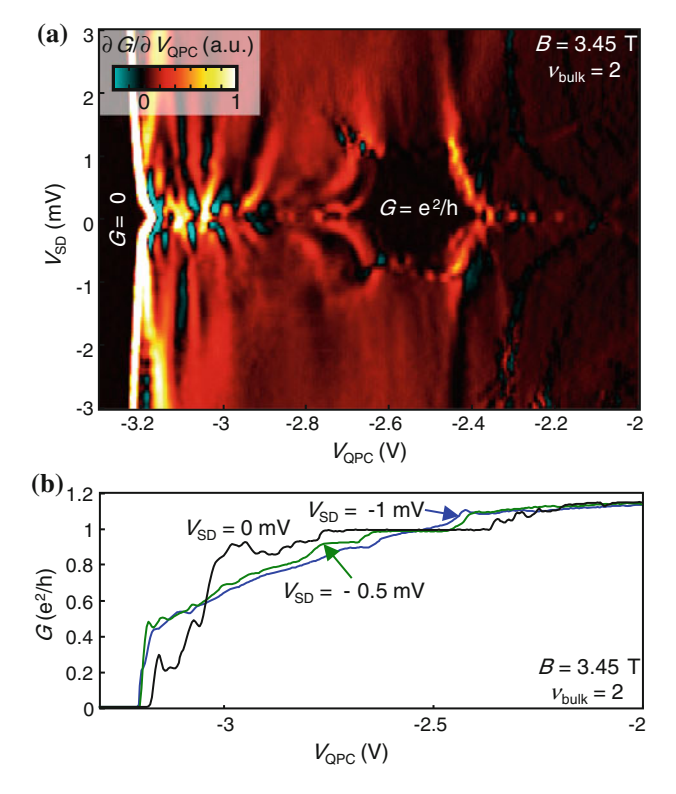


Fig. 9.16 a Transconductance of a 800 nm wide QPC as a function of the QPC voltage and the source-drain bias. The bulk filling factor has been set to $\nu_{\text{bulk}} = 2$. A pronounced conductance plateau at e^2/h is found, but disappears rapidly for source-drain biases of more than 1 mV. At more negative gate voltages, disorder becomes more pronounced and no additional conductance plateaus are observed. b Conductance curves at $V_{\text{SD}} = 0 \, \text{mV}$, $V_{\text{SD}} = -0.5 \, \text{mV}$ and at $V_{\text{SD}} = -1 \, \text{mV}$

A similar situation is shown in Fig. 9.17a for $\nu_{\rm bulk}=2/3$. The transconductance is plotted as a function of the QPC voltage and the source-drain bias. Black regions indicate the conductance plateaus at $1/3 \times e^2/h$ and $2/5 \times e^2/h$, while conductance is dominated by disorder for $G < 1/3 \times e^2/h$ and exhibits various conductance resonances. The QPC conductance has been plotted in Fig. 9.17b as a function of $V_{\rm QPC}$ and for three different values of $V_{\rm SD}$. As the source-drain bias is increased, conductance plateaus at $G = 1/3 \times e^2/h$ and $G = 2/5 \times e^2/h$ continuously disappear. Close to pinch-off, we are in the weak electron tunneling regime between two $\nu = 2/3$ FQH liquids (see Chap. 4). In this regime, a bias dependence $G \propto V_{\rm SD}^{2g_e-2}$ is expected, where $g_e = 3$ for $\nu = 1/3$ and $g_e = 2$ for $\nu = 2/3$ [34]. The dependence of the conductance on $V_{\rm SD}$ is shown in Fig. 9.17c for different QPC voltages. The corresponding voltages are indicated in Fig. 9.17a, b as dashed red lines. Conductance is minimal at $V_{\rm SD} = 0$ mV and increases sharply, as the source-drain bias is increased. The conductance $\Delta G(V_{\rm SD}) = G(V_{\rm SD}) - G(V_{\rm SD} = 0)$ is shown in a log-log plot

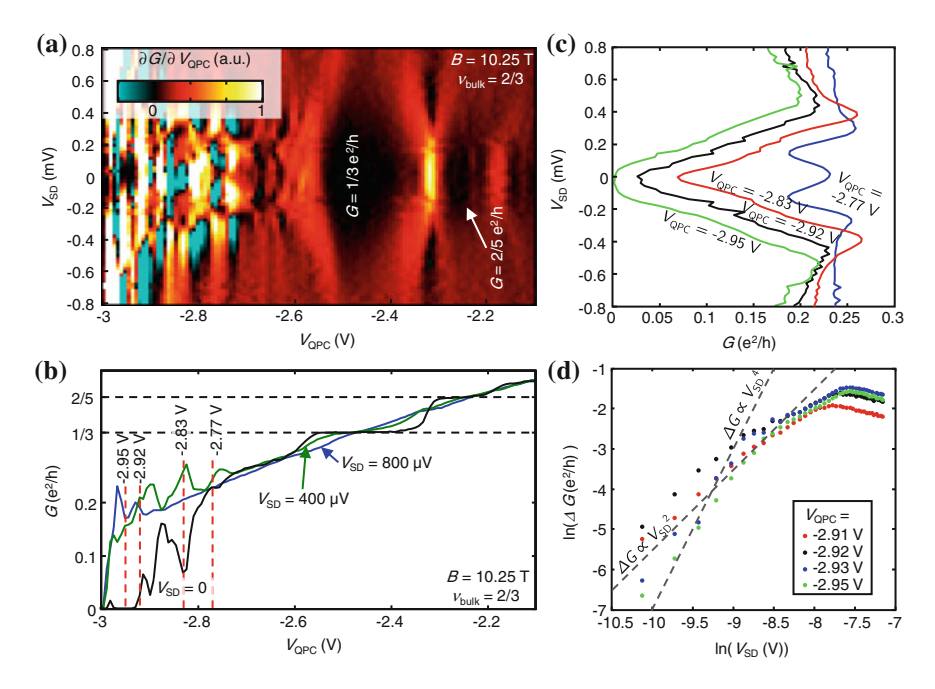


Fig. 9.17 a Transconductance of a 700 nm wide QPC as a function of the QPC voltage and the source-drain bias. The bulk filling factor has been set to $\nu_{\rm bulk} = 2/3$. Plateaus at $G = 1/3 \times e^2/h$ and $G = 2/5 \times e^2/h$ are observed in the conductance, but disappear as the source-drain bias is increased. **b** Conductance versus $V_{\rm QPC}$ for three different source-drain biases. *Red dashed lines* indicate the position of the cuts shown in **c**. **c** Bias dependence of the conductance close to pinch-off. Corresponding values of the gate voltage are indicated. **d** Log-log plot of ΔG versus the source-drain bias. $\Delta G \propto V_{\rm SD}^2$ and $\Delta G \propto V_{\rm SD}^4$ are indicated as *gray dashed lines*

in Fig. 9.17d. Neither $\Delta G \propto V_{\rm SD}^4$ ($g_e=3$) nor $\Delta G \propto V_{\rm SD}^2$ ($g_e=2$) fit the data over a large voltage range. Due to the apparent disorder close to pinch-off, resonant tunneling processes which involve different filling factor regions might contribute to the tunneling, thus making an interpretation in terms of weak tunneling theory impossible.

9.5 Conclusion

We have reviewed basic properties of quantum point contacts. Numerical calculations for one of our samples have allowed us to extract a realistic density and potential profile in the channel. By spatially shifting the QPC channel, we could show that static localizations do generally not influence transport in the high-mobility samples used by us. Finite bias measurements revealed a regular pattern of conductance plateaus and half-plateaus and indicate that the QPC confinement potential is harmonic. From finite-bias measurements, we were able to extract parameters that describe the QPC

confinement potential. We demonstrate how the confinement potential can be varied in gate-tunable geometries and the resulting effect on the QPC transmission in the quantum Hall regime. We have investigated the bias dependence of the transmission for a QPC filling factor $\nu_{\rm QPC} < 1/3$. We find that a comparison to the expected power-law scaling of the conductance is difficult, presumably due to the influence of disorder in the channel.

References

- C. Rössler, S. Baer, E. de Wiljes, P.-L. Ardelt, T. Ihn, K. Ensslin, C. Reichl, W. Wegscheider, New J. Phys. 13, 113006 (2011). doi:10.1088/1367-2630/13/11/113006
- D.A. Wharam, T.J. Thornton, R. Newbury, M. Pepper, H. Ahmed, J.E.F. Frost, D.G. Hasko, D.C. Peacock, D.A. Ritchie, G.A.C. Jones, J. Phys. C: Solid State Phys. 21, L209 (1988). doi:10.1088/0022-3719/21/8/002
- 3. B.J. van Wees, H. van Houten, C.W.J. Beenakker, J.G. Williamson, L.P. Kouwenhoven, D. van der Marel, C.T. Foxon, Phys. Rev. Lett. 60, 848 (1988). doi:10.1103/PhysRevLett.60.848
- 4. H.v. Houten, C. Beenakker, Phys. Today 49, 22 (1996). doi:10.1063/1.881503
- S. Gustavsson, R. Leturcq, B. Simovič, R. Schleser, T. Ihn, P. Studerus, K. Ensslin, D.C. Driscoll, A.C. Gossard, Phys. Rev. Lett. 96, 076605 (2006). doi:10.1103/PhysRevLett.96. 076605
- S. Gustavsson, M. Studer, R. Leturcq, T. Ihn, K. Ensslin, D.C. Driscoll, A.C. Gossard, Phys. Rev. Lett. 99, 206804 (2007). doi:10.1103/PhysRevLett.99.206804
- C. Rössler, T. Krähenmann, S. Baer, T. Ihn, K. Ensslin, C. Reichl, W. Wegscheider, New J. Phys. 15, 033011 (2013). doi:10.1088/1367-2630/15/3/033011
- S. Baer, C. Rössler, T. Ihn, K. Ensslin, C. Reichl, W. Wegscheider, New J. Phys. 15, 023035 (2013). doi:10.1088/1367-2630/15/2/023035
- F. Milliken, C. Umbach, R. Webb, Solid State Commun. 97, 309 (1996). doi:10.1016/0038-1098(95)00181-6
- A.M. Chang, L.N. Pfeiffer, K.W. West, Phys. Rev. Lett. 77, 2538 (1996). doi:10.1103/ PhysRevLett.77.2538
- S. Roddaro, V. Pellegrini, F. Beltram, G. Biasiol, L. Sorba, Phys. Rev. Lett. 93, 046801 (2004). doi:10.1103/PhysRevLett.93.046801
- I.P. Radu, J.B. Miller, C.M. Marcus, M.A. Kastner, L.N. Pfeiffer, K.W. West, Science 320, 899 (2008). doi:10.1126/science.1157560
- 13. K.J. Thomas, J.T. Nicholls, M.Y. Simmons, M. Pepper, D.R. Mace, D.A. Ritchie, Phys. Rev. Lett. 77, 135 (1996). doi:10.1103/PhysRevLett.77.135
- A. Kristensen, H. Bruus, A.E. Hansen, J.B. Jensen, P.E. Lindelof, C.J. Marckmann, J. Nygård,
 C.B. Sørensen, F. Beuscher, A. Forchel, M. Michel, Phys. Rev. B 62, 10950 (2000). doi:10. 1103/PhysRevB.62.10950
- S.M. Cronenwett, H.J. Lynch, D. Goldhaber-Gordon, L.P. Kouwenhoven, C.M. Marcus, K. Hirose, N.S. Wingreen, V. Umansky, Phys. Rev. Lett. 88, 226805 (2002). doi:10.1103/ PhysRevLett.88.226805
- Y. Komijani, M. Csontos, I. Shorubalko, T. Ihn, K. Ensslin, Y. Meir, D. Reuter, A.D. Wieck, EPL (Europhys. Lett.) 91, 67010 (2010). doi:10.1209/0295-5075/91/67010
- A.P. Micolich, J. Phys.: Condens. Matter 23, 443201 (2011). doi:10.1088/0953-8984/23/44/ 443201
- Y. Komijani, M. Csontos, T. Ihn, K. Ensslin, Y. Meir, D. Reuter, A.D. Wieck, Phys. Rev. B 87, 245406 (2013). doi:10.1103/PhysRevB.87.245406
- F. Nichele, S. Chesi, S. Hennel, A. Wittmann, C. Gerl, W. Wegscheider, D. Loss, T. Ihn, K. Ensslin, Phys. Rev. Lett. 113, 046801 (2014). doi:10.1103/PhysRevLett.113.046801

References 157

 T. Ihn, Semiconductor Nanostructures: Quantum States and Electronic Transport (OUP, Oxford, 2010)

- Y.V. Nazarov, Y.M. Blanter, Quantum Transport: Introduction to Nanoscience (Cambridge University Press, 2009)
- 22. A. Yacoby, Y. Imry, Phys. Rev. B 41, 5341 (1990). doi:10.1103/PhysRevB.41.5341
- 23. H.A. Fertig, B.I. Halperin, Phys. Rev. B 36, 7969 (1987). doi:10.1103/PhysRevB.36.7969
- 24. M. Büttiker, Phys. Rev. B 41, 7906 (1990). doi:10.1103/PhysRevB.41.7906
- 25. S. Laux, D. Frank, F. Stern, Surf. Sci. 196, 101 (1988). doi:10.1016/0039-6028(88)90671-1
- J.G. Williamson, C.E. Timmering, C.J.P.M. Harmans, J.J. Harris, C.T. Foxon, Phys. Rev. B 42, 7675 (1990). doi:10.1103/PhysRevB.42.7675
- S. Schnez, C. Rössler, T. Ihn, K. Ensslin, C. Reichl, W. Wegscheider, Phys. Rev. B 84, 195322 (2011). doi:10.1103/PhysRevB.84.195322
- L.I. Glazman, A.V. Khaetskii, EPL (Europhys. Lett.) 9, 263 (1989). doi:10.1209/0295-5075/9/3/013
- N.K. Patel, L. Martin-Moreno, M. Pepper, R. Newbury, J.E.F. Frost, D.A. Ritchie, G.A.C. Jones, J.T.M.B. Janssen, J. Singleton, J.A.A.J. Perenboom, J. Phys.: Condens. Matter 2, 7247 (1990). doi:10.1088/0953-8984/2/34/018
- N.K. Patel, J.T. Nicholls, L. Martn-Moreno, M. Pepper, J.E.F. Frost, D.A. Ritchie, G.A.C. Jones, Phys. Rev. B 44, 13549 (1991). doi:10.1103/PhysRevB.44.13549
- K.J. Thomas, M.Y. Simmons, J.T. Nicholls, D.R. Mace, M. Pepper, D.A. Ritchie, Appl. Phys. Lett. 67, 109 (1995). doi:10.1063/1.115498
- C.W.J. Beenakker, H. van Houten, arXiv:cond-mat/0412664 (2004), Solid State Phys. 44, 1 (1991)
- 33. G. Nachtwei, Phys. E: Low-dimens. Syst. Nanostruct. **4**, 79 (1999). doi:10.1016/S1386-9477(98)00251-3
- 34. X.-G. Wen, Adv. Phys. 44, 405 (1995). doi:10.1080/00018739500101566

Chapter 10 Integer and Fractional Quantum Hall States in QPCs

Abstract We investigate integer and fractional quantum Hall states in quantum point contacts (QPCs) of different geometries, defined in AlGaAs/GaAs heterostructures employing different doping and screening techniques. We find that, even in the highest mobility samples, interference and localization strongly influence the transport properties. We propose microscopic models for these effects, based on single- and many-electron physics. For integer quantum Hall states, transport is modulated due to the self-consistent formation of compressible regions of enhanced or reduced density in the incompressible region of the constriction. In the fractional quantum Hall regime, we observe the localization of fractionally charged quasiparticles in the constriction and an interplay of single- and many-electron physics. At low electron densities and in comparatively weak magnetic fields, single-electron interference dominates transport. Utilizing optimized growth and gating techniques, the $\nu = 5/2$ state can be observed in a OPC, conserving the bulk properties in an unprecedented quality. Our results might improve the understanding of the influence of localization on the transmission properties of QPCs, which is necessary for the interpretation of interference experiments employing QPCs, especially at $\nu = 5/2$.

10.1 Introduction

Localization plays a crucial role for understanding the exact quantization of the quantum Hall effect. In strong magnetic fields, electronic transport can be described in terms of narrow edge channels, leading to the well-known observations of $R_{xx} \approx 0$ and $R_{xy} = h/(e^2 \nu_{\text{bulk}})$. In this case, varying the magnetic field only (de)populates localized states in the bulk, which do not affect transport because backscattering of the chiral edge states across the wide bulk region is negligible. Alternative pictures, where the current is believed to flow in the bulk, exist (see for example [2] for an overview). Also in this case, the (de)population of localized states plays the key role for the conductance quantization. These theoretically predicted localized states have been investigated in various experiments using spatially resolved imaging techniques

[©] Springer International Publishing Switzerland 2015

¹⁵⁹

[3, 4, 6–8] or single-electron transistors fabricated on top of a two-dimensional electron gas (2DEG) [9]. In a pioneering work by Ilani et al. [4], the equilibrium properties of such localized states have been investigated in the bulk of a 2DEG with scanning single-electron transistor (SET) techniques. The behavior of the bulk localizations was shown to be dominated by Coulomb blockade physics. This picture cannot be explained as a single-electron effect, but requires the formation of compressible and incompressible regions in the bulk, in analogy to an edge state picture that takes self-consistent screening into account [10–12]. Here, the system is decomposed into compressible regions, in which potential fluctuations are screened and the density varies, and incompressible regions of constant density but varying background potential. Apart from the aforementioned experiments which probe localizations on a very local scale in the bulk, conductance fluctuations in the quantum Hall regime, believed to be related to localized states, have been studied in direct transport experiments [13–21]. They have been investigated for example in Si-MOSFETs [15], Graphene [22–24], InGaAs quantum wells [25] and in narrow AlGaAs/GaAs heterostructures [13, 14], where localized states couple to the edge and thus become accessible. In the latter experiments [13, 14], resistance fluctuations have been interpreted as magnetically bound states. As pointed out later [26-28], Coulomb blockade effects are of great importance for such experiments and have to be taken into account for the interpretation of B-field and gate-voltage periodicities. In the work of Cobden et al. [15], conductance fluctuations in the quantum Hall regime span a distinct pattern in the density versus magnetic field plane, with resonances parallel to neighboring conductance plateaus, similar to the phase diagram obtained by Ilani et al. This has been interpreted as Coulomb charging of localized states in the bulk of the employed small structures. The absence of a clear periodicity suggests either the contribution of many localized states or the validity of other interpretations [16], which are based on the presence of a network of compressible stripes.

More recently, scanning gate experiments have tried to combine spatial resolution with transport [29–31]. Hackens et al. have investigated Coulomb-dominated islands inside quantum Hall interferometers [29]. Modulations of transport, due to the coupling of the localized islands to the edge states were found. In contrast to this behavior dominated by Coulomb charging, recent experiments [31] report phase coherent tunneling across constrictions in the quantum Hall regime.

Quantum point contacts are one of the conceptually most simple, though interesting systems studied in mesoscopic physics. The possibility to locally probe transport allows us to employ QPCs in the quantum Hall regime for investigating the influence of disorder-induced localizations on transport. The influence of localized states on (fractional) quantum Hall states confined in QPCs is not fully understood. Furthermore, the influence of individual localizations on non-equilibrium transport was not accessible in the mentioned transport experiments. In contrast, scanning SET experiments provided information about individual localizations, but not about their influence on transport. For the interpretation of interference experiments in the quantum Hall regime [32–36], a detailed understanding of the transmission properties of single QPCs is necessary. Even in 2DEGs with the highest mobilities technologically achievable at the moment, disorder significantly influences transport through

10.1 Introduction 161

the QPC, as soon as a perpendicular magnetic field is applied. We show that even in simple QPCs complicated behavior can be observed, which is interpreted in terms of single- and many-electron physics of individual disorder-induced localizations. We argue that the influence of localizations can be minimized by employing growth and gating techniques, which result in a very steep QPC confinement potential (perpendicular to transport direction) and low disorder in the channel. By this, the $\nu=5/2$ state can be confined to a QPC without noticeable backscattering and preserving the bulk properties in an unprecedented quality, giving a good starting position for tunneling- and interference experiments in the second Landau level.

10.2 Experimental Details

The QPCs used in this chapter are defined by electron-beam lithography and subsequent Ti/Au evaporation on photolithographically patterned high-mobility wafers. Constrictions with different geometries have been studied here (see Table. 10.1 for an overview). For the 250 nm wide QPC I.a and the 500 nm wide QPC I.b, a 30 nm wide quantum well with a carrier sheet density $n_s \approx 3.04 \times 10^{11} \text{ cm}^{-2}$ and a mobility $\mu \approx 13 \times 10^6 \, \mathrm{cm}^2/\mathrm{Vs}$ has been used. In this structure the 165 nm deep quantum well is neighbored by two δ -Si doped GaAs layers, enclosed in 2 nm thick layers of AlAs. These screening layers reside 70 nm below and above the 2DEG. The electrons in the AlAs wells populate the X-band and provide additional low-mobility electron layers, which screen the Γ -electrons in the 2DEG from remote ionized impurities. Due to the screening layers, hysteretic and time-dependent processes make gating difficult. The gating properties of these wafers have been studied earlier [38]. The 1.2 µm wide QPC III.a has been fabricated on a wafer which employs a similar growth technique $(\mu \approx 17.8 \times 10^6 \text{ cm}^2/\text{Vs}, n_s \approx 2.13 \times 10^{11} \text{ cm}^{-2}, 250 \text{ nm deep}, 30 \text{ nm wide quantum})$ well, screening layers 100 nm below and above the 2DEG). The high mobility structures used for QPCs I.a,b and III.a,b,c are optimized for the $\nu = 5/2$ state without

Table 10.1	Overview of the	ne different samples used	d in this chapter
			11

QPC	w (nm)	Heterostructure	$n_s (10^{11} \text{ cm}^{-2})$	$\mu (10^6 \text{cm}^2/\text{Vs})$
QPCI.a	250	30 nm QW, δ-Si screening	3.0	13.0
QPCI.b	500			
QPCII.a	700	Single-side doped	1.5	8.0
QPCII.b	700	GaAs/Al _{0.24} Ga _{0.76} As		
QPCII.c	900	heterostructure		
QPCII.d	800			
QPCIII.a	1200	30 nm QW, δ-Si screening	2.1	17.8
QPCIII.b	1000			
QPCIII.c	1700			

Channel width w, electron sheet density n_s and mobility μ are indicated for the different QPCs

the requirement of prior LED illumination [40], OPC II.a, OPC II.b (both 700 nm wide), OPC II.c (900 nm wide) and OPC II.d (800 nm wide) were fabricated on a single side doped GaAs/Al_xGa_{1-x}As heterostructure with a mobility of approximately 8×10^6 cm²/Vs and a 320 nm deep 2DEG with an electron density of approximately $1.5 \times 10^{11} \,\mathrm{cm}^{-2}$. Hysteresis effects are much less pronounced in these structures which employ a reduced proportion of Al in the spacer layer between the doping plane and the 2DEG (x = 0.24 compared to typically x = 0.30-0.33). Long-range scattering is therefore reduced, thus facilitating the formation of the $\nu = 5/2$ state and other fragile FQH states [41, 42]. The measurements have been conducted in a dilution refrigerator at a base temperature of approximately 85 mK and in magnetic fields up to 13 T. Measurements of QPC III.a have been performed in a dry dilution refrigerator with an electronic temperature of approximately 12-13 mK, achieved by massive filtering and thermal anchoring at every temperature stage. Standard fourterminal lock-in measurement techniques have been used to measure R_{xx} and R_{xy} of the bulk 2DEG and the differential conductance the QPC, $G = \partial I_{\rm AC}/\partial V_{\rm diag}$, which gives access to the effective QPC filling factor $\nu_{\rm OPC}$ [43]. Here, the voltage drop $V_{\rm diag}$ is measured diagonally across the QPC.

10.3 Results and Discussion

The main part of this chapter will be organized as follows: First, an exemplary quantum Hall phase diagram will be discussed (Sect. 10.3.1). The influence of different QPC geometries on the width of the incompressible region separating the edge states and the density distribution is discussed in Sect. 10.3.2. In the main part of this chapter, Sect. 10.3.3, QPC resonances are characterized and explained via a microscopic model. A short summary of this central Section is given afterwards. The resonances' dependence on the spatial position of the conducting channel inside the QPC is investigated in the following (Sect. 10.3.4). At the end, methods for confining the most fragile fractional quantum Hall states are discussed (Sect. 10.3.5).

10.3.1 Quantum Hall Phase Diagram of a QPC

Figure 10.1a shows the differential conductance G (plotted: numerical derivative $\partial G/\partial V_{\rm QPC}$ in colorscale) of QPC I.a as a function of the voltage applied to the QPC gates ($V_{\rm QPC}$) and a perpendicular magnetic field B. At zero magnetic field, the well-known QPC conductance quantization in multiples of $2 \times e^2/h$ is found. As the magnetic field is increased, conductance steps (or plateaus), seen as maxima (or black areas) of $\partial G/\partial V_{\rm QPC}$, bend to more positive QPC voltages, due to magneto-electric depopulation of the QPC channel [43, 46]. The quantized conductance plateaus successively develop into regions of constant effective filling factor of the QPC ($\nu_{\rm QPC}$) with a diagonal resistance $R_{\rm diag} = h/(e^2\nu_{\rm QPC})$. In this regime the spin splitting

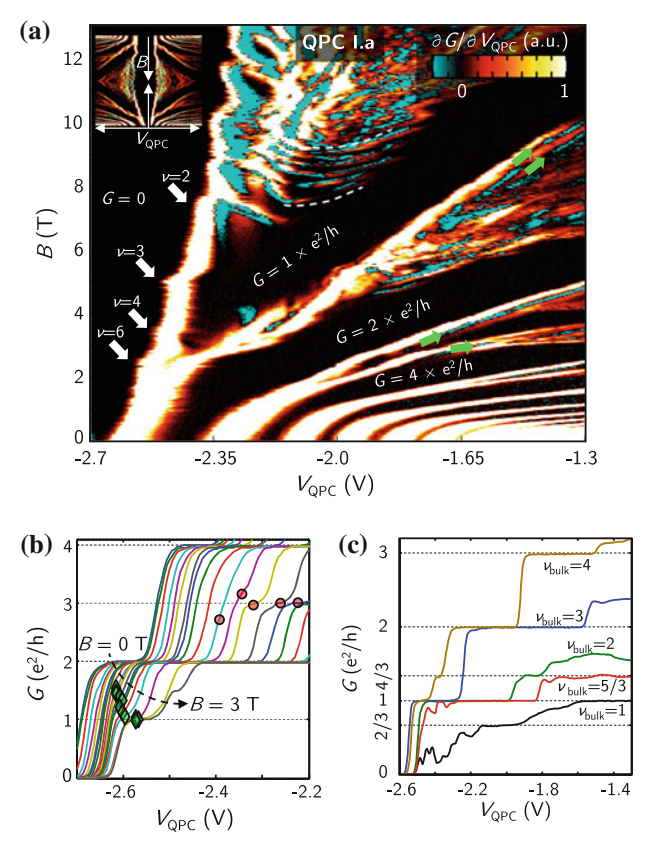


Fig. 10.1 a Transconductance of QPC I.a as a function of the QPC voltage and the magnetic field. Conductance plateaus at multiples of e^2/h can be seen as *black regions*. Resonances, bending in the $B-V_{\rm QPC}$ -plane are indicated by *white dashed lines*. The 1/B periodic kinks (*white arrows*) are believed to originate from a change of the filling factor in the bulk. A possible combination of bulk filling factors is indicated. *Inset* full B-field and voltage dependence of the system. Here, the voltage was swept from $-1.3~{\rm V} \rightarrow -2.7~{\rm V} \rightarrow -1.3~{\rm V}$ repeatedly and the *B*-field was stepped from $0~{\rm T} \rightarrow 13~{\rm T} \rightarrow 0~{\rm T}$. **b** The $B=0~{\rm QPC}$ conductance plateaus at multiples of $2\times e^2/h$ spin-split for increasing magnetic fields (magnetic field from $0~{\rm to}~3~{\rm T}$). For $0< G< 2\times e^2/h$ and $2\times e^2/h < G< 4\times e^2/h$, local minima in the slope of the conductance are marked by *green diamonds* or *red circles*. In contrast to the second and third subband, the spin-splitting of the lowest subband starts at conductance values of approx. $0.7\times 2\times e^2/h$ and approaches $1\times e^2/h$ as the magnetic field strength is increased [44, 45]. **c** At strong magnetic fields (with bulk filling factors $\nu_{\rm bulk}$), conductance plateaus corresponding to different integer and fractional filling factors can be observed in the QPC. (Reprinted figure with permission from [1]. Copyright 2014 by the American Physical Society.)

is sufficiently strong to also observe conductance plateaus at $G=1,3,5,\ldots \times e^2/h$ [44, 45]. The low-field behavior of the spin-splitting is shown in Fig. 10.1b. Numerically extracted local minima of the slope of the conductance curve have been marked with green diamonds/red circles. As $B\to 0$, the $G=1\times e^2/h$

plateau seems to join the $0.7 \times 2 \times e^2/h$ anomaly [47]. No similar behavior can be observed at $G=3\times e^2/h$ and $G=5\times e^2/h$ (data not shown). In the quantum Hall regime, conductance curves of the QPC (Fig. 10.1c) show fractional effective filling factors at $\nu_{\rm QPC}=2/3$ and $\nu_{\rm QPC}=4/3$ for different integer and fractional filling factors of the bulk ($\nu_{\rm bulk}$). The shape of the boundary of the G=0 region of Fig. 10.1a is determined by different effects: first, an increasing magnetic field leads to magneto-electric depopulation due to an increase of the single-particle electron energy, thus moving the pinch-off region to less negative gate voltages. In addition, time-dependent and hysteretic processes of the X-electron screening layers lead to an additional drift of the pinch-off line towards less negative QPC voltages. Figure 10.2 shows the full time- and voltage dependence of the system. Here, the voltage was swept from $-1.3 \text{ V} \rightarrow -2.7 \text{ V} \rightarrow -1.3 \text{ V}$ repeatedly (horizontal axis) and the

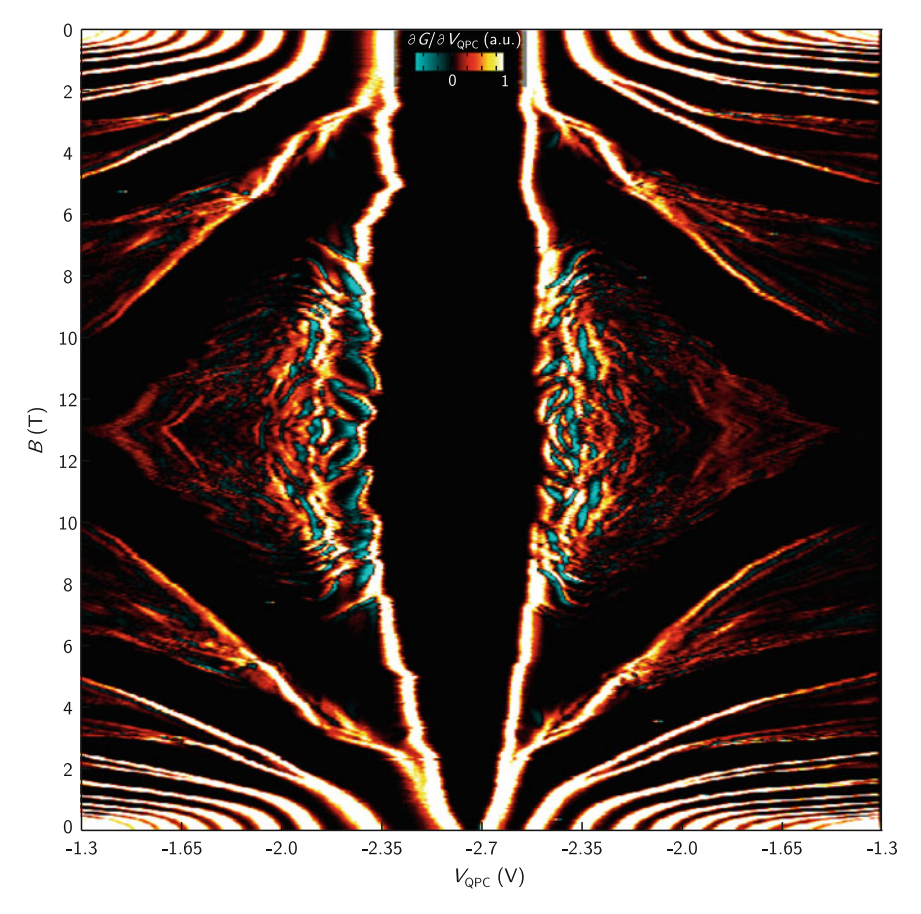


Fig. 10.2 Transconductance of QPC I.a as a function of the QPC voltage and the magnetic field, for changing the QPC voltage from $-2.7~V \rightarrow -1.3~V \rightarrow -2.7~V$ and the *B*-field from $0~T \rightarrow 13~T \rightarrow 0~T$

B-field was stepped from $0 \text{ T} \rightarrow 13 \text{ T} \rightarrow 0 \text{ T}$ (vertical axis). Upper and lower part of the figure are not mirror symmetric—over the time of the measurement, the pinch-off-line drifts towards less negative voltages, indicating a time-dependence of the system. Furthermore, changes of the filling factor in the bulk can lead to an abrupt decrease of the Fermi energy of the system as observed in quantum dots (QDs) [48]. This effect is believed to cause the 1/B-periodic kinks in the pinch-off line. When increasing the B-field across the kinks, the pinch-off line suddenly moves towards more positive QPC voltages (marked by white arrows in Fig. 10.1a), though an assignment to the individual filling factors in the bulk is not uniquely possible, probably due to a reduced density in the bulk near the QPC, which governs the local coupling of bulk states into the QPC.

In the regions of Fig. 10.1a where the QPC filling factor changes, the QPC conductance does not vary monotonically. For $G > 1 \times e^2/h$, resonances which are parallel to the boundary of one of the neighboring conductance plateaus are observed (green arrows). In contrast, the region $G < 1 \times e^2/h$ shows resonant features without any preferred slope, or even with varying slope at different B-fields (a set of bending resonances is indicated by the white dashed line). Very similar resonances have been found in several QPCs in different cooldowns. The origin of these resonances will be discussed later in the framework of single- and many-electron physics.

10.3.2 Influence of QPC Geometry on Incompressible Separating Region and Density Distribution

To be able to understand the mechanisms behind the resonances in more detail, we have investigated two different QPC designs, fabricated on a 2DEG of lower density. QPC II.a is 700 nm wide with a top-gate above the conducting channel (see inset Fig. 10.3a). QPCs II.b (inset Fig. 10.3b) and II.c are standard 700/800 nm wide QPCs. Density profiles in the y-direction (along the lateral confinement potential) for the two QPC designs (at B = 0) have been obtained from a self-consistent bandstructure calculation using nextnano. The doping concentration was adjusted to account for surface charges and to reproduce the gate pinch-off voltages correctly. The applied voltages to the gates were chosen such that the calculated density at B = 0 corresponds to the density necessary for $\nu_{OPC} = 2$ at B = 1.71 T, as in the measurements. Using the calculated density profile at B = 0, we have calculated the altered density profile when a compressible region is formed in the center of the QPC (Fig. 10.3) and the width Δa of the incompressible region for different QPC filling factors, using the electrostatic model of Chklovskii et al. [49]. In this model, perfect metallic screening in the compressible regions is assumed. For the gap energies, $\hbar\omega_c$ and $g^*\mu_B B$ with an exchange enhanced $q^* \approx 4$ (see Sect. 9.4.4) have been used as estimates for $\nu = 2$ and $\nu = 1$. The energy gap at $\nu = 1/3$ has been measured (see Sect. 10.3.6). In Fig. 10.3, the resulting self-consistent densities (for $\nu_{OPC} = 2$) are shown as solid lines. The original density at B = 0 (dashed blue line, second row) is modified

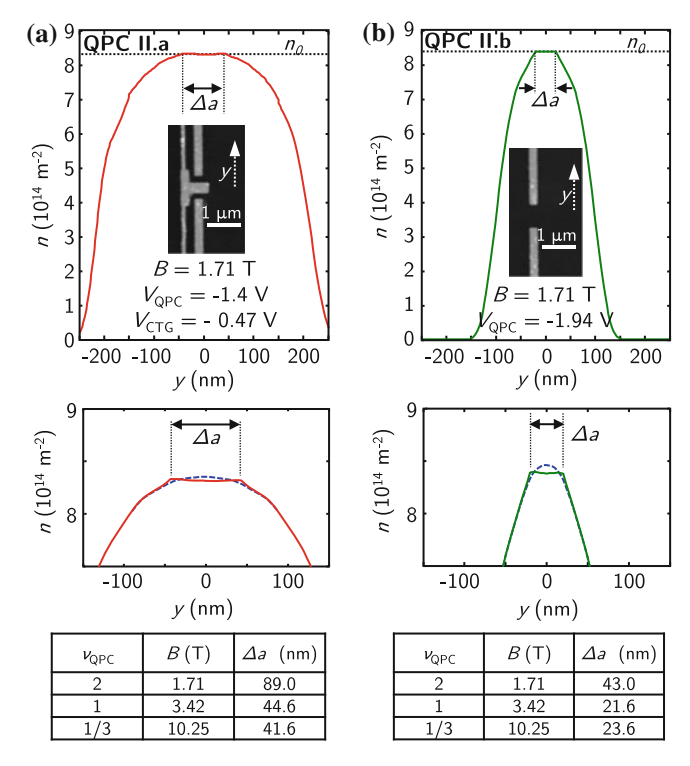


Fig. 10.3 Calculated density distributions in the channels of QPCII.a (a) and QPCII.b (b). The original zero magnetic field density distribution (dashed(blue)), blow-up in second row) has been altered by the formation of an incompressible region in the center of the constriction at $B=1.71\,\mathrm{T}$ ($v_{\mathrm{QPC}}=2$), resulting in a region of constant density n_0 . The width Δa of the incompressible region is indicated for different filling factors v_{QPC} in both QPCs. (Reprinted figure with permission from [1]. Copyright 2014 by the American Physical Society.)

by the formation of an incompressible stripe (constant density n_0) in the center of the channel. When a negative voltage is applied to the channel top-gate (CTG) of QPC II.a, the subband minimum is lifted. In this situation, the curvature of the electron density in the center of the constriction is small. When QPC II.b is tuned to a similar density in the constriction, the density curvature in the center is much greater, leading to a narrower compressible region (Fig.10.3b). Comparing Δa of the two QPCs, we conclude that for QPC II.a, a significantly wider incompressible region is expected according to the model of Chklovskii et al. [49]. The widths Δa range from approximately 20–90 nm. Disorder potential fluctuations have typical length scales of the order of 100 nm [4, 50]. If the amplitude of such a disorder potential fluctuation in the incompressible region in the center of the QPC is large enough to create an intersection of the Landau level with the Fermi energy (Fig. 10.6b, c, left column), compressible regions of enhanced or reduced density (Fig. 10.6b, c, middle column) are formed. Thus, the small width of the incompressible region in QPCII.b

(and hence in the QPCII.c with similar geometry) makes it less likely that a disorder potential fluctuation leads to the formation of a localization in the constriction (see also Fig. 10.4). Furthermore, the coupling to such a localization is strongly varied as the width of the separating incompressible region changes, making the observation of periodic charging of a single localization impossible. To observe periodicities and study resonances in more detail, we now investigate electronic transport in QPC II.a, where a much stronger influence of disorder-induced localizations is expected. Here, a periodic behavior is expected over a larger parameter range, as the width of the incompressible regions separating edge and localizations is sufficiently wide.

10.3.3 Characterization of QPC Resonances and Microscopic Model

10.3.3.1 Periodic Conductance Oscillations in QPCs of Different Geometries

The filling factor spectra of QPC II.a and QPC II.c are investigated similarly to the measurement of Fig. 10.1a, by varying the QPC gate voltage versus the magnetic field B. First, the channel top-gate voltage $V_{\rm CTG}$ has been varied (Fig. 10.5a). This gate varies the density of the channel roughly linearly with applied voltage (neglecting filling-factor dependent capacitances), as seen from the slope $dB/dV_{\rm CTG} \propto 1/\nu_{\rm QPC}$ of the conductance plateaus, which show up as black areas of quantized conductance. In addition to the full series of integer filling factors, fractional states at $\nu_{\rm QPC} = 1/3$, 2/3, 4/3 and 5/3 can be observed. Close to the low- and high density edges of the conductance plateaus, sets of conductance oscillations with a slope parallel to the boundaries are observed, similar to the ones observed in small Hall-bars [15, 16]. The slope and number of these resonances are independent of density and magnetic field strength.

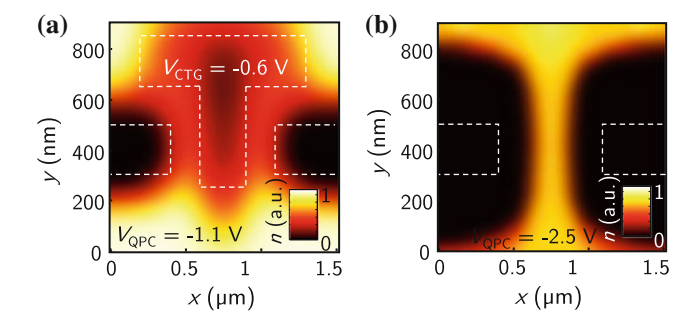


Fig. 10.4 Calculated density distributions in the channels of QPCII.a (a) and QPCII.b (b). While the density increases slowly towards the channel center for QPCII.a, a sharp increase is found for QPCII.b.

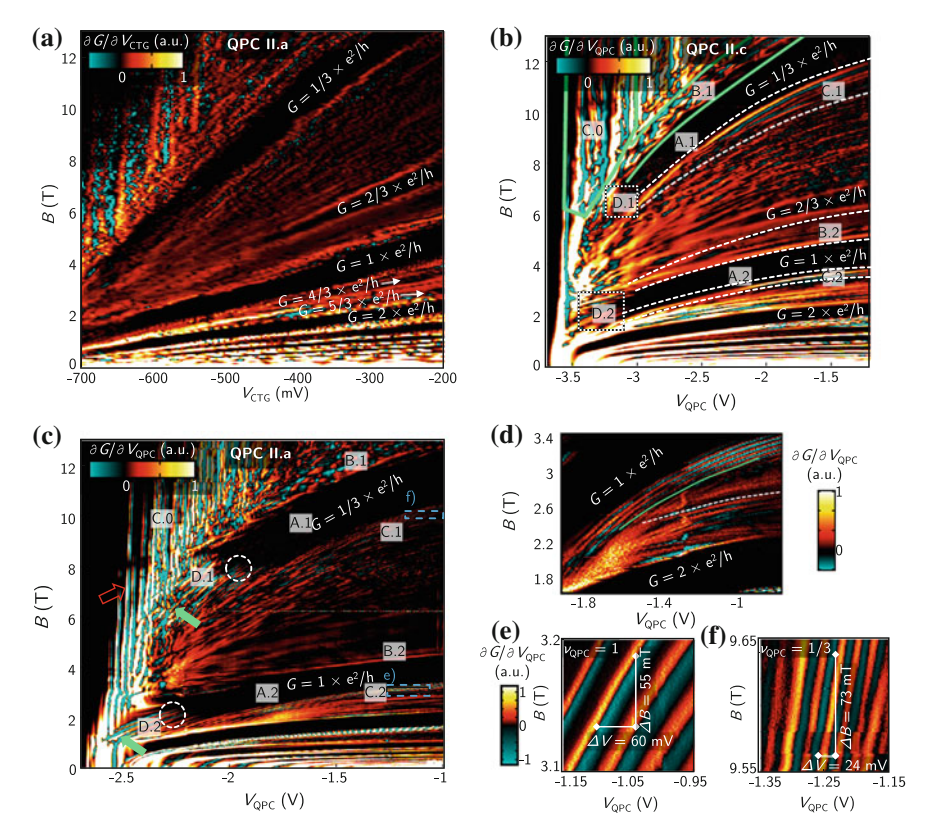


Fig. 10.5 a Transconductance of QPC II.a as a function of the voltage $V_{\rm CTG}$ and magnetic field B. Here, the density is tuned roughly linearly by the gate voltage. **b** Transconductance of QPC II.c as a function of $V_{\rm QPC}$. Pronounced fractional and integer filling factors are observed (black regions A.1, A.2, etc.). Apart from these regions of nearly-perfect transmission, disorder modulates transport in other regions: for small transmission (C.0, C.1), small backscattering (B.1) and at the low density, low B-field end of the conductance plateaus (D.1). A similar behavior is found when one underlying edge state is perfectly transmitted (regions B.2–D.2). **c** Transconductance of QPC II.a, when -400 mV are applied to the CTG. **d** Zoom of Fig. 10.5c: transition from $\nu_{\rm QPC}=2$ to $\nu_{\rm QPC}=1$. Two distinct slopes (green solid/white dashed lines), parallel to the boundary of the neighboring conductance plateaus, are observed. **e**, **f** Close-ups of the conductance oscillations for $\nu_{\rm QPC}=1$ and $\nu_{\rm QPC}=1/3$ (enframed areas in **c**). (Reprinted figure with permission from [1]. Copyright 2014 by the American Physical Society.)

A qualitatively similar behavior can be found for QPC II.c as $V_{\rm QPC}$ is varied (Fig. 10.5b). Here, regions of perfect transmission have been marked (A.1). Modulations occur at the low-density side (B.1) and high-density side of the conductance plateaus (C.1) or pinch-off (C.0). Furthermore, resonances at the low-density and low-B-field end of conductance plateaus are observed (D.1). These resonances disappear as the density and B-field strength increase. Similar regions can be attributed to higher filling factors, for which underlying edge states are perfectly transmitted (A.2–D.2).

As mentioned above, a much stronger influence of a disorder-induced localization is expected for OPC II.a, as the wider incompressible region is much more likely to accommodate one or several extrema of the disorder potential. Here, quasiperiodic conductance modulations should occur over a larger parameter range, as the width of the incompressible regions separating edge and localizations is sufficiently wide. In order to verify this expectation, Fig. 10.5c shows the transconductance of QPC II.a, obtained by keeping V_{CTG} fixed while varying V_{OPC} and B. Compared to Fig. 10.5b, more pronounced conductance oscillations are observed (red empty arrow). Especially gate voltage regions close to pinch-off are now dominated by equidistant conductance peaks parallel to the magnetic field axis. Regions C and D overlap, which can be seen from the coexistence of two different distinguishable slopes (indicated by green solid arrows). In the integer quantum Hall regime (for example in Fig. 10.5d), conductance oscillations with distinct slopes are observed between neighboring conductance plateaus. The resonances are parallel to either of the two neighboring plateau boundaries (Fig. 10.5d, green solid/white dashed line). Close to $\nu_{\rm OPC} = 1/3$, strong resonances, parallel to the conductance plateau occur (Fig. 10.5f). At lower B-fields, between $\nu_{OPC} = 1/3$ and $\nu_{OPC} = 1$, weak modulations with an intermediate slope are observed.

10.3.3.2 Screening and Localization Model

The mechanism which gives rise to the different resonances in regions A-D can be understood in terms of an edge-state picture which takes non-linear screening of potential fluctuations into account (Fig. 10.6). Similar models have been employed to understand bulk localizations in scanning SET and scanning capacitance experiments [4, 6, 7, 51]. Regions of locally enhanced or reduced density are formed on top of the background density, associated with different extended quantum Hall states. These localizations in the constriction couple to the edge states and give rise to conductance oscillations. In Fig. 10.6, the guiding center energies of two extended quantum Hall states are shown as a function of the spatial direction y, intersecting the QPC channel (Fig. 10.6a, left column). Empty/filled circles symbolize empty or occupied states. The extended states could for example be associated with Landau levels (in this case $\Delta_{\rm ext} = \hbar \omega_c$), spin-split Landau levels ($\Delta_{\rm ext} = g^* \mu_B B$ with an exchange enhanced g^*), or Λ -levels of composite Fermions, corresponding to a FQH state at $\nu = 1/m$ $[52, 54, 55](\Delta_{\text{ext}} = \Delta_{1/m} \text{ is the energy gap of the FQH state})$. For simplicity, we will constrain the discussion in the following to the situation, where extended states arise from a Landau level splitting. If spin-split Landau levels or Λ -levels are considered, an analog picture can be constructed.

In Fig. 10.6a, energies of the second Landau level are far above the Fermi energy. In the most simple edge state picture [56, 57], Landau level energies are bent up by the confinement potential of the QPC, giving rise to chiral edge states at the intersections with the Fermi energy, thus leading to a step-wise density increase towards the bulk of the sample. However, self-consistency of the Poisson and Schrödinger equations at a smooth, electrostatically defined edge [10] leads to a screened potential and

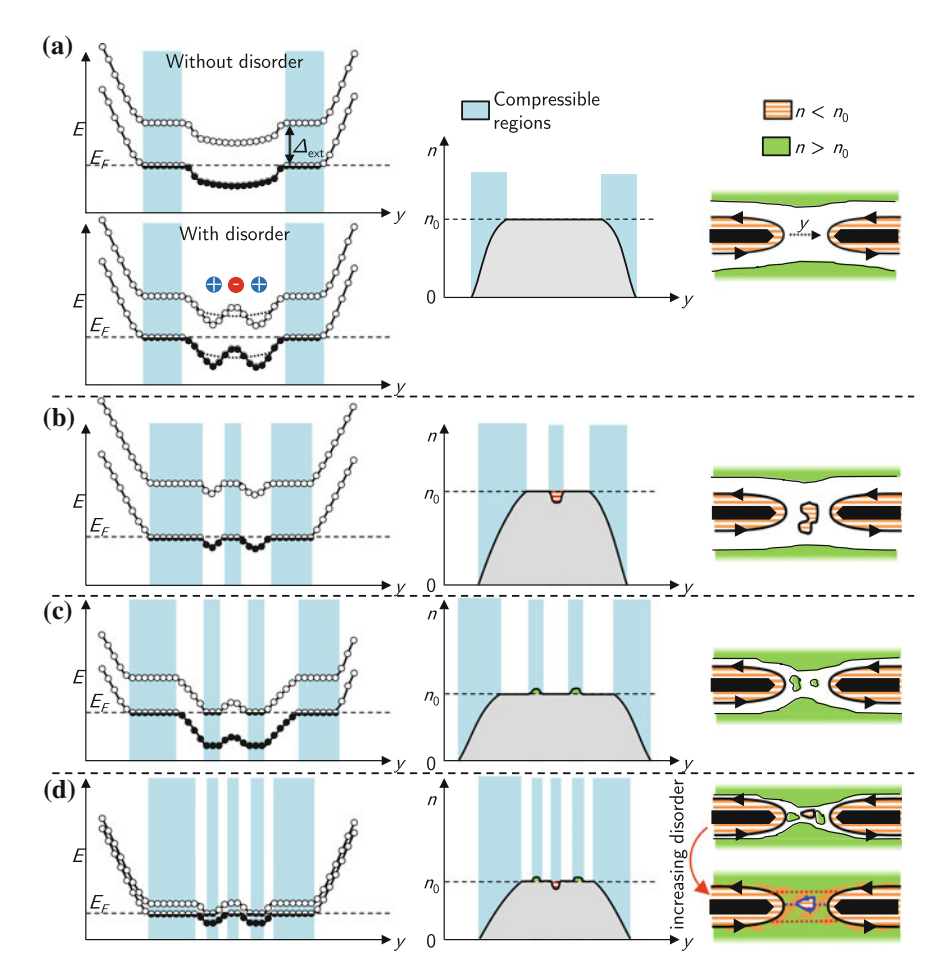


Fig. 10.6 Schematic guiding center energies of extended states and densities within a QPC. a-d correspond to the different transmission situations A-D, as indicated in Fig. 10.5b. Empty/filled circles symbolize empty or occupied states. In the case of perfect transmission (a), adding an exemplary disorder potential does not alter the density distribution within the channel. As density fluctuations in the transmitted (b) or energetically lowest reflected (c) Landau level lead to partially occupied states at the Fermi energy, compressible regions of enhanced (c, green area) or reduced density (b, red striped area) are formed within the incompressible region. This gives rise to a quantized charge on the compressible regions of enhanced or reduced density formed in the incompressible region which separates the edge states. For smaller magnetic fields or stronger disorder fluctuations, wide compressible regions are absent and only states below the Fermi energy are occupied. Here, compressible regions of enhanced and reduced density modulate the transport in the constriction at the same time (d). As wide incompressible regions are absent, the compressible regions of enhanced or reduced density are no longer governed by Coulomb-dominated physics. Here, singleelectron resonances arise from localized states, encircling a certain number of magnetic flux quanta. In contrast to the Coulomb-dominated mechanism, such single-electron resonances give rise to a dependence in the $B - V_{\rm OPC}$ plane which may differ from the slope of the conductance plateaus. (Reprinted figure with permission from [1]. Copyright 2014 by the American Physical Society.)

smooth density variations in compressible regions of finite width (Fig. 10.6a, middle column). In this compressible region, partially filled states (half-filled circles) reside at the Fermi energy. The density of electrons in the lowest Landau level is constrained via $n < n_0 = 2eB/h$, due to its finite degeneracy. Where the Landau level energy lies below the Fermi energy, all states are occupied (filled circles) and this maximum density is reached. Potential fluctuations can no longer be screened, in contrast to the ideally perfect screening in compressible regions where the potential is flat. In this picture, compressible regions in between regions of constant filling factors ν_1 and ν_2 contribute $G = e^2/h \times \Delta \nu$ to the conductance, where $\Delta \nu = \nu_2 - \nu_1$ [58]. Alternate models exist, where the current is flowing in the bulk (see for example [2] for an overview). In our case however, the details of the current distribution in the QPC are not important, as only the total conductance through the QPC can be measured. A schematic spatial density distribution within the QPC is shown in the right column of Fig. 10.6a. Here, the boundaries between compressible and incompressible regions are indicated as black arrows. For simplicity, these will be referred to as "edge states" from now on. In this picture, the edge state is perfectly transmitted through the OPC constriction (between black polygons) and both counterpropagating directions are separated by a wide incompressible region [49] (white), yielding a quantized QPC conductance. Far away from the QPC, additional Landau levels eventually fall below the Fermi energy, leading to additional compressible regions where the density increases towards its bulk value (green area). Adding schematic potential fluctuations (Fig. 10.6a, left column) does not change the overall situation, as long as no states in the second Landau level become occupied. This is the analog situation to the regions A.1 and A.2 of Fig. 10.5b. As the magnetic field strength is increased, Landau levels are lifted in energy, leading to a narrower incompressible region in the center of the QPC between the edge states. The density is locally reduced (Fig. 10.6b, middle column) where maxima of the potential fluctuations intersect the Fermi energy (Fig. 10.6b, left column). This leads to the formation of a compressible region of reduced density (red striped) that is separated from the edge states via incompressible stripes.

For an increasing disorder amplitude or decreasing Landau level splitting, compressible regions of enhanced or reduced density can occur in the constriction at the same time, explaining the simultaneous visibility of resonances with a different slope in Fig. 10.5c (indicated by solid green arrows). When disorder dominates over the Landau level splitting, i.e. when the gradient of the background potential $\partial V/\partial y$ becomes comparable to $E_{\rm gap}/l_{\rm B}$ [59], where $l_{\rm B}$ is the magnetic length, the system is no longer described by a many-electron picture with screening via compressible and incompressible regions (Fig. 10.6d). In that confinement-dominated case, single-electron states localized around a potential minimum or maximum in the constriction enclose a fixed number of flux quanta [60] (Fig. 10.6d, solid blue line). As the area of the localized state is tuned non-linearly with the QPC gate voltage, resonances with varying slope in the $B-V_{\rm QPC}$ plane are expected [4].

Different tunneling paths that lead to a qualitatively similar behavior have been proposed [5]. Here, non-adiabaticity of the QPC potential leads to enhanced tunneling between the edge channels at the entrance and exit of the constriction (Fig. 10.6d,

red dashed lines). In contrast, the situation of Fig. 10.6b is described by Coulombdominated physics of the compressible region of reduced density inside the constriction. Here, electron-electron interactions lead to a potential with compressible and incompressible regions. The charge of the compressible region of reduced density is quantized, leading to resonances with a certain slope in the $B - V_{OPC}$ plane [4], whenever an electron is added or removed from the compressible region of reduced density. The slope is uniquely determined by the filling factor of the incompressible region in which the compressible region of enhanced or reduced density is formed and equals the slope of the corresponding conductance plateaus in the $V_{\rm OPC}$ -B-field plane. This explains why resonances only occur with one of the slopes of the neighboring conductance plateaus (Fig. 10.5d). Conductance resonances are only visible in the transport data when the incompressible region between the edge states and the compressible region of reduced density is sufficiently small, allowing for resonant backscattering across the constriction. This is the case as the conductance starts to decrease below the plateau value, as in Fig. 10.5b B.1 and B.2. Similarly, potential minima of the second Landau level fall below the Fermi energy, as the magnetic field strength is decreased (Fig. 10.6c, left column), leading to compressible region of enhanced density within the incompressible region separating the edge states. As additional transmission sets in (Fig. 10.5b, C.1 and C.2), the coupling of these compressible region of enhanced density leads to a periodic modulation of the transmission.

In this discussion, the additional complication of possible edge reconstruction of integer quantum Hall (IQH) edge states [61] has not been taken into account. Furthermore, we observe faint conductance plateaus at $G = 2/3 \times e^2/h$ in the OPC. This state is clearly visible in the QPCII.c (Fig. 10.5b) and in QPCII.a when the voltage applied to the CTG is swept (Fig. 10.5a). Surprisingly, the $\nu = 2/3$ state is not observed, when the QPC voltage of QPCII.a is swept while a constant voltage is applied to the CTG (Fig. 10.5c). The edge structure of the $\nu=2/3$ state is still not understood in detail. Theory and experimental findings suggest that this state may consist of a $\delta \nu = 1$ IQH edge state and a counterpropagating $\delta \nu = -1/3$ edge state of holes which are equilibrated by interaction, resulting in a single chiral charged mode and a counterpropagating neutral mode [52, 53, 62, 63]. Even more advanced theoretical proposals exist [64], which can explain the experimental findings of these states. How to interpret localizations in the case of such a complicated edge structure remains an open question. The weak visibility of the $\nu = 2/3$ state could be due to this complicated edge structure and suggests a smaller energy gap than observed for the $\nu = 1/3$ state.

As mentioned before, resonances with bending slopes in the B-field— $V_{\rm QPC}$ plane are expected for single-electron resonances [4, 60]. The detailed behavior of the slope depends on the disorder potential intersecting the Fermi energy. This suggests that the resonances in the FQH regime of Fig. 10.1a (marked by white dashed line) could be interpreted as single-electron effects. In [14], a model for a disorder potential maximum in a constriction is proposed, leading to magnetically bound states which could qualitatively reproduce the bending of the resonances. In this situation, disorder dominates over the smaller FQH gaps and the formation of wide compressible and incompressible regions in the constriction is no longer possible (Fig. 10.6d). Thus,

the slope in the B-field - V_{QPC} plane depends on the influence of the QPC voltage on the enclosed area, which depends on the shape of the disorder potential maximum.

10.3.3.3 *B*-field and Voltage Periodicities

Within this framework, we may now investigate the periodicities of the resonances in Fig. 10.5c-f. For a Coulomb-dominated quantum dot, a distinct behavior of the periodicities $\Delta B(\nu_{\rm OPC})$ and $\Delta V_{\rm OPC}(\nu_{\rm OPC})$ is expected. These periodicities depend on the filling factor of the incompressible region, in which the Coulomb-dominated region is formed, in our case this is ν_{OPC} . From theoretical models [27, 28] for Coulomb-dominated Fabry-Pérot interferometers it is expected that $\Delta B(\nu_{\rm OPC}=1)\approx 2\Delta B(\nu_{\rm OPC}=2)\approx \Delta B(\nu_{\rm OPC}=1/3)$ and $\Delta V_{\rm OPC}(\nu_{\rm OPC}=1) \approx \Delta V_{\rm OPC}(\nu_{\rm OPC}=2) \approx 3\Delta V_{\rm OPC}(\nu_{\rm OPC}=1/3)$, which has been observed in lithographically defined quantum dots [35]. In the IOH regime, our periodicities for $\nu_{\rm OPC} = 2 \; (\Delta B \approx 30 \; {\rm mT}, \; \Delta V_{\rm OPC} \approx 62 \; {\rm mV})$ and $\nu_{\rm OPC} = 1$ $(\Delta B \approx 55 \text{ mT}, \ \Delta V_{OPC} \approx 60 \text{ mV})$ are in good agreement with these predictions. Periodicities for $\nu_{\rm OPC} = 1/3~(\Delta B \approx 73~{\rm mT},~\Delta V_{\rm OPC} \approx 24~{\rm mV})$ are at least compatible with a Coulomb-dominated localization of fractional e/3 charges. The area which can be extracted from these periodicities ($A \approx 0.075 \,\mu\text{m}^2$) is compatible with a localization in the channel of the QPC. However, it should be noted that the geometry of the compressible region of enhanced or reduced density within the constriction might change as the B-field is varied, because it is not lithographically defined but might change self-consistently. A different behavior is observed in the low-n/low-Bfield end of conductance plateaus ("D" in Fig. 10.6), where single-electron physics is expected to dominate. In the measurement of Fig. 10.5c (regions encircled by white dashed line), periodicities for $\nu_{\rm OPC} = 1 \ (\Delta B \approx 200 \ {\rm mT}, \ \Delta V_{\rm OPC} \approx 53$ mV) and $\nu_{\rm OPC} = 1/3$ ($\Delta B \approx 360$ mT, $\Delta V_{\rm OPC} \approx 48$ mV) are incompatible with a Coulomb-dominated mechanism and indicate single-electron behavior. Similar enhancements of ΔB for $\nu = 1/3$ have been interpreted as magnetically bound states in earlier experiments [13]. However in this interpretation, finite temperature effects or an interplay with Coulomb blockade mechanisms might have to be taken into account [26].

10.3.3.4 Summary

To summarize, the most important findings of this section are: periodic conductance oscillations with a slope, parallel to either of the neighboring conductance plateaus were observed. They were interpreted to originate from the Coulomb-dominated charging of compressible region of enhanced or reduced density, formed in a

¹For the voltage periodicity at $\nu_{\rm QPC}=1/3$, the gating effect of the background electrons has to be taken into account, as described in [35]. In our case however, this only gives a negligible correction from $\Delta V_{\rm QPC}(\nu_{\rm QPC}=1)\approx 3\Delta V_{\rm QPC}(\nu_{\rm QPC}=1/3)$.

constant filling factor background. This filling factor determines the slope. B-field and gate voltage periodicities agree with expectations for a Coulomb-dominated Fabry-Pérot interferometer. At low densities and in weak magnetic fields, disorder prevents the formation of compressible and incompressible regions. Here, resonances are interpreted as single-electron effects, where electronic states are dominated by confinement and encircle a local potential maximum and enclose a certain number of flux quanta. In the fractional quantum Hall regime where energy gaps are smaller than in the integer quantum Hall regime, an influence of both mechanisms can be seen. At the plateau boundaries of the $\nu_{OPC} = 1/3$ state, conductance oscillations, compatible with Coulomb-dominated charging of fractionally charged quasiparticles, are observed. For $1/3 < \nu_{OPC} < 1$, modulations of the conductance with an intermediate slope (in-between slopes of the $\nu_{OPC} = 1$ and $\nu_{OPC} = 1/3$ plateaus) are observed. These slopes move with the local filling factor of the QPC, i.e. correspond to a certain number of flux quanta per electron. This indicates the importance of single-electron interference, where resonances are expected to emanate from the B = 0, n = 0 origin of the Landau fan [50].

10.3.4 Spatial Dependence of QPC Resonances

By applying different voltages to the two different OPC gates, it is possible to laterally shift the QPC channel in the lithographically defined constriction (this technique was for example used in [65–67]). For OPCs similar to OPC I.a, this shift was found to be of the order of the lithographic QPC width [65, 68]. Figure 10.7 shows the numerical derivative of G in diagonal direction (transconductance $\partial G/\partial V_{l\&r}$), as the voltages V_1 and V_r of the left and right QPC gate are varied. In these measurements, the 2DEG far away from the QPC (bulk) is tuned to a fixed filling factor ν_{bulk} with $R_{\text{xx}} \approx 0$. Regions of constant conductance and pinch-off show up as black areas, bright regions of increasing conductance bend around the pinch-off region. Figure 10.7a, c shows the asymmetry-dependence of resonances (the diagonal of Fig. 10.7a is a cut across the resonances of Fig. 10.1a indicated by the dashed line) in the low-density low-Bfield end of the $\nu_{\rm OPC} = 1$ plateau for three different QPCs (Fig. 10.7a, b: QPC I.a, Fig. 10.7c: QPC II.d, Fig. 10.7d: QPC II.a) on 2DEGs of different density. Resonances believed to originate from single-electron effects (indicated by white arrows), are observed at the low-density end of the $G = 1 \times e^2/h$ conductance plateau. The resonances show up as two or three parallel lines with a varying slope clearly different from the conductance plateaus' slope and sit deep in the $G = 1 \times e^2/h$ conductance plateau. Such resonances, occurring mainly in symmetric configurations, have been observed in most of the QPCs in study. Additional modulations of the conductance can be observed between the conductance plateaus. These many-electron resonances bend roughly in the same way as the pinch-off line but vary in intensity, as the asymmetry is varied.

Figure 10.7b, d shows the asymmetry behavior in strong magnetic fields. For a bulk filling factor $\nu_{\text{bulk}} = 1$, conductance plateaus in the QPC at $G = 1/3 \times e^2/h$

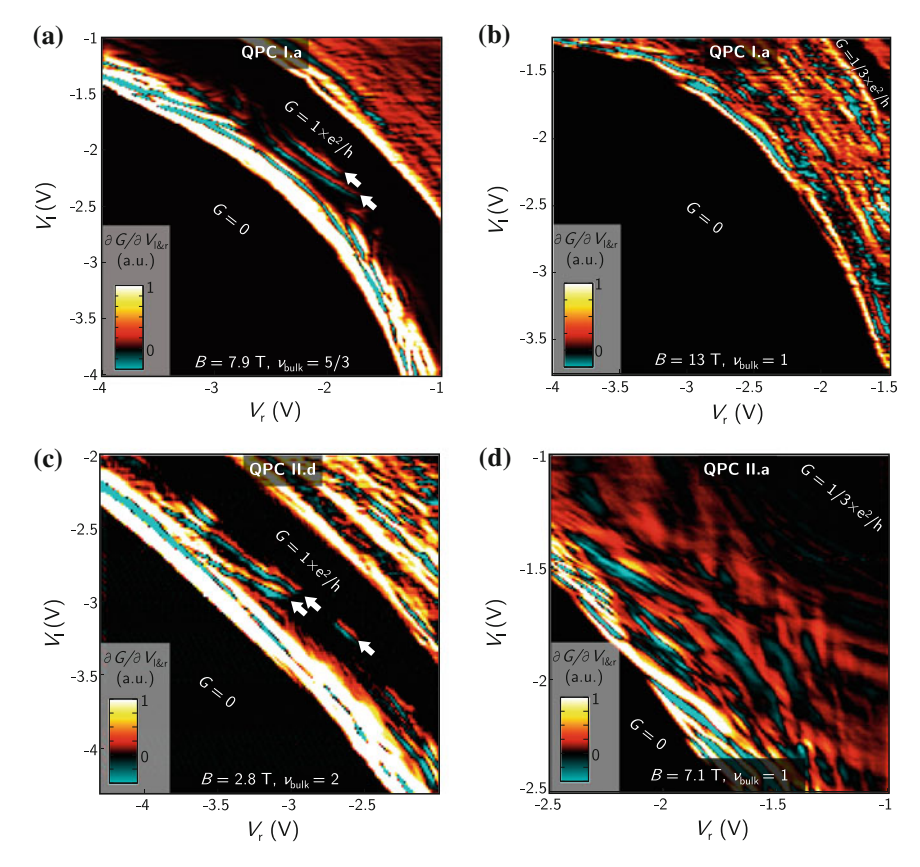


Fig. 10.7 a-d Transconductance (numerical derivative in diagonal direction) of QPCs on a high-density sample (QPC I.a, a, b) and a low-density sample (QPC II.d, c, QPC II.a, d) as the voltages of left and right QPC gates V_1 and V_r are varied. White arrows mark resonances that are believed to be due to single-electron interference. These resonances move with a more complicated dependence as the asymmetry is varied, in contrast to many-electron resonances which bend parallel to the conductance plateaus. (Reprinted figure with permission from [1]. Copyright 2014 by the American Physical Society.)

are observed. In Fig. 10.7b, mainly resonances bending with the pinch-off line are observed. In contrast, in Fig. 10.7d, non-regular resonances without any preferred slope are observed.

With our model (Fig. 10.6) we can now try to distinguish the asymmetry-behavior of the two different types of resonances: on the one hand, the confinement dominated resonances (Fig. 10.6d) for the situation where compressible and incompressible regions are absent and the system is described by single-electron physics, on the other hand the many-electron resonances (Fig. 10.6b, c) where a compressible region of enhanced or reduced density, situated in an incompressible region, is charged.

Confinement-dominated single-electron resonances are expected to occur as a result of a localized state at a certain position in the channel, to which both edges couple. As the asymmetry and thus the background potential is varied, single-particle energy levels are shifted in energy, which changes the position in gate voltages of the resonance relative to pinch-off. Thus, single-electron resonances are expected to possess a dependence on gate voltage which is not parallel to the respective conductance plateau as the asymmetry is varied. They should disappear, as soon as the coupling to one of the edges is lost. Here, the gate voltage dependence is influenced by the details of the confinement and disorder potential. The proposed gate voltage dependence of the single-electron resonances (which causes a bending not necessarily parallel to the pinch-off line) and the disappearance of the resonances with increasing asymmetry are indeed observed (Fig. 10.7a, b, white arrows). A similar behavior might be expected from an Aharonov-Bohm mechanism, where non-adiabaticity of the QPC saddle-point potential leads to enhanced tunneling between the edge channels at the entrance and exit of the constriction and thus defines a QPC-voltage dependent area [5].

In the ideal model of many-electron resonances, the charge of the compressible island of reduced or enhanced density is quantized and changes when the total density in the constriction is varied (i.e. when moving perpendicular to pinch-off in the $V_l - V_r$ plane). When the asymmetry is varied parallel to pinch-off, we expect to change mainly the width of the incompressible regions separating the compressible island of reduced or enhanced density from the edge. Thereby the resonance amplitude which highly depends on the width of the incompressible region [69] is changed. At the same time, the occupation of the compressible region of reduced or enhanced density is expected to be approximately constant, as long as the picture of compressible and incompressible regions does not break down. In this scenario, resonances are thus expected to run parallel to the conductance plateau edges, as observed in the measurements (Figs. 10.7a–c).

Because the conductance varies strongly in-between the plateaus, resonances cannot be attributed to individual localizations as it was possible for example in Fig. 10.5c. Thus, in a yet different scenario, conductance oscillations could also originate from single-electron effects, where we only probe localizations that couple to both edges for a given voltage asymmetry. At this asymmetry, they possess a local gate voltage dependence, shifting them parallel to the conductance plateaus. The overall behavior of the resonances could result from averaging the contributions of many single-electron resonances.

Summarizing, we may state that the bending resonances of Fig. 10.7a, c (marked by white arrows) are compatible with a confinement dominated single-electron effect, whereas resonances parallel to the conductance plateaus (Fig. 10.7a–c) are compatible with a many-electron effect. However, other mechanisms leading to similar observations cannot be excluded. The fact that in Fig. 10.7d no resonances bending with the conductance plateaus are observed may indicate that in Fig. 10.7d transport is dominated by single-electron physics, while many-electron effects dominate in Fig. 10.7b, where the applied magnetic field is much stronger and the disorder potential is smaller due to a higher mobility 2DEG.

10.3.5 Fragile Fractional Quantum Hall States in QPCs

Figure 10.8a shows the transmission of QPC I.b (light/dark blue) and QPC II.d (red) as a function of applied QPC voltage. The conductance of QPC II.d as a function of $V_{\rm QPC}$ (red) shows conductance oscillations on the low-density side of the $\nu_{\rm QPC}=1$ plateau. These are those resonances of Fig.10.7c, which were interpreted as single-electron effects.

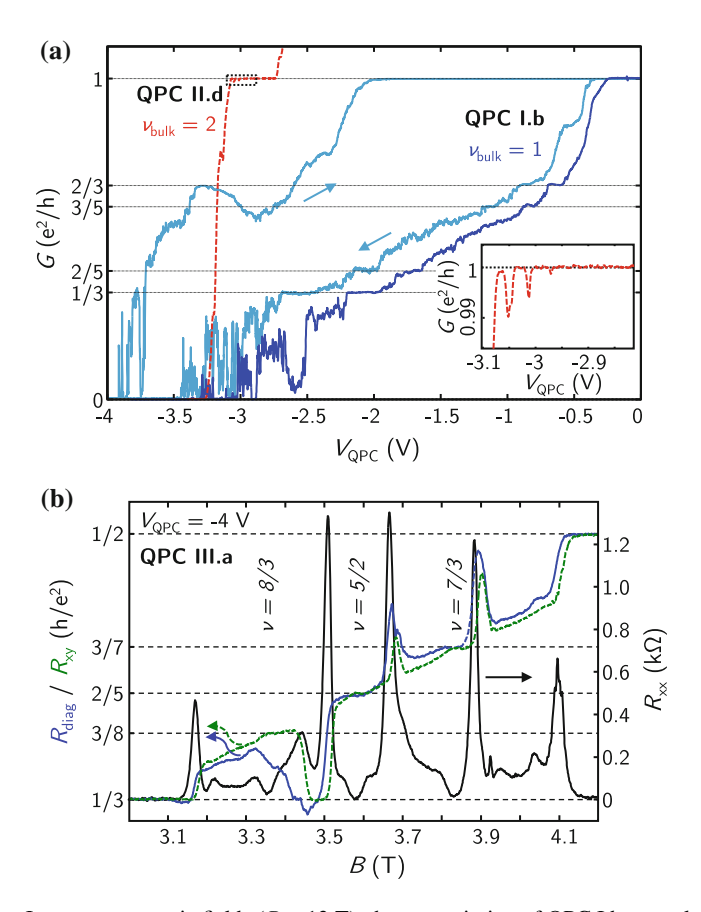


Fig. 10.8 a In strong magnetic fields (B=13 T), the transmission of QPC I.b strongly fluctuates close to pinch-off ($light/dark\ blue$). The $dashed\ red\ curve$ depicts a situation in which a transmitted edge state is weakly backscattered in QPC II.d (see inset). **b** Transmission of QPC III.a for $2 \le \nu_{bulk} \le 3$. In the bulk, $\nu_{bulk} = 7/3$, 8/3 and 5/2 are fully quantized with a strong minimum in R_{xx} ($solid\ black\ line$) and a plateau in R_{xy} ($dashed\ green\ line$). In addition, pronounced reentrant integer quantum Hall (RIQH) states are observed. The diagonal resistance across the QPC, R_{diag} ($solid\ blue\ line$), shows a plateau at $\nu = 5/2$, indicating nearly perfect transmission through the QPC. The density within the constriction is very similar to the bulk density. (Reprinted figure with permission from [1]. Copyright 2014 by the American Physical Society.)

QPC I.b exhibits conductance plateaus at 2/3, 3/5, 2/5 and $1/3 \times e^2/h$ in strong magnetic fields (B = 13 T, $\nu_{\text{bulk}} = 1$). Close to pinch-off, the conductance strongly fluctuates. Unfortunately the observation of $\nu_{OPC} = 2/3$, 3/5, 2/5 and 1/3 does not allow to draw conclusions about the edge reconstruction of the $\nu_{\text{bulk}} = 1$ edge state. Over the whole OPC voltage range, not only the transmission, but also the channel density and the shape of the OPC confinement potential strongly vary [65]. The measurement in dark blue shows the first $V_{\rm OPC}$ sweep after the cool-down. When closing the channel for a second time (light blue), fractional filling factors are still visible, but a more negative gate voltage has to be applied to pinch off the channel. As the QPC is subsequently opened again, a pronounced hysteresis is visible and the more fragile conductance plateaus at $G = 2/5 \times e^2/h$, $G = 3/5 \times e^2/h$, $G = 1/3 \times e^2/h$ and $G = 2/3 \times e^2/h$ disappear. This behavior can be understood considering the time- and voltage-dependent density in the X-electron screening layers. After the screening layers have been depleted, the density only relaxes with long time constants. The electron density of the 2DEG is inversely proportional to the charge carrier density in the X-electron bands due to capacitive coupling. Thus, depleted screening layers lead to a increased 2DEG electron density at the same OPC voltage, explaining why the QPC conductance is higher for opening the QPC than for closing it. A measurement of the time-dependence of the channel density is shown in Fig. 10.9, where the QPC voltage is changed starting at t = 0. When voltages are applied at $T \approx 1.3$ K, density relaxes back to the bulk density over time constants of several minutes. This process is much faster at $T \approx 3.6$ K.

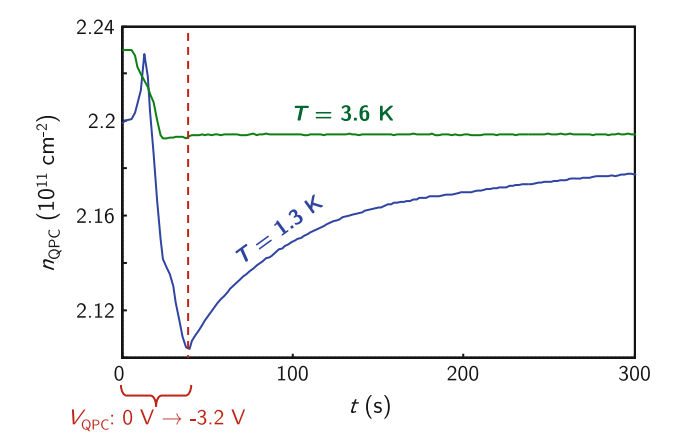


Fig. 10.9 Time dependence of the density in the QPC constriction of QPC III.b, extracted from the slope of $R_{\rm diag}$ at $B\approx 0.1$ T. Starting at t=0, the QPC voltage is swept from 0 to -3.2 V. After that, the QPC voltage is kept fixed. At T=1.3 K, the density drops until the QPC voltage remains constant. After that, density relaxes back towards the bulk density over several minutes. At T=3.6 K, the density is nearly already saturated after the sweeping of the gate voltage has been finished. Here, relaxation processes are much faster. (Sample D120427C-1D)

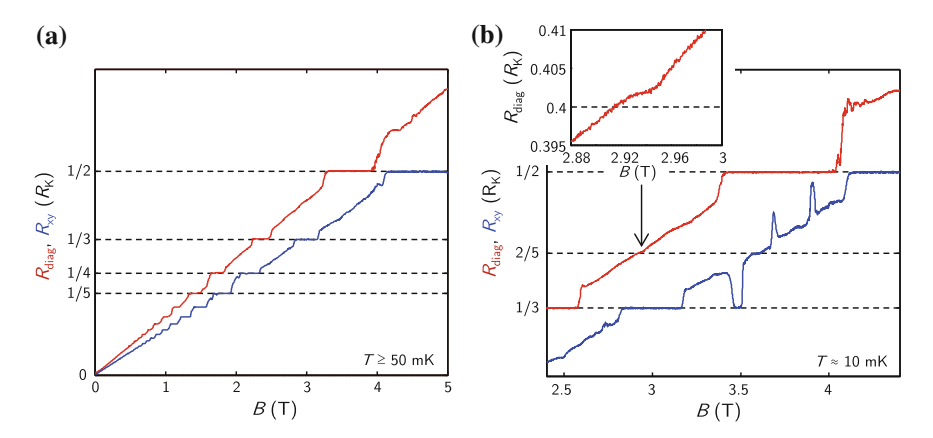


Fig. 10.10 a Bulk Hall resistance R_{xy} and $R_{\rm diag}$ measured diagonally across QPC III.c versus magnetic field (at $T \geq 50$ mK). QPC III.c is a 1700 nm wide and 1500 nm long channel, formed by two plunger gates. Here, top-gate voltages of -2.3 V have been applied to the QPC at T < 100 mK. The density in the QPC channel is reduced compared to the bulk density, as seen from the shift of the plateaus in $R_{\rm diag}$ towards smaller magnetic fields. b At $T \approx 10$ mK, pronounced RIQH states and a plateau corresponding to $\nu = 5/2$ are observed in R_{xy} (here: $V_{\rm QPC} = -2.2$ V). While RIQH states are completely absent in $R_{\rm diag}$, a weakly pronounced resistance plateau is found at $R_{\rm diag} = \frac{2}{5}h/e^2$ (see *inset*), while $\nu_{\rm bulk} = 3$ at the same magnetic field. (Sample D120427C-1C)

At millikelvin temperatures, a saturation of the QPC density does not set in within realistic time scales of an experiment. The effect of biasing a QPC top-gate at T < 100 mK is shown in Fig. 10.10. Here, the density in the QPC channel is reduced compared to the bulk density. Quantization of the FQH states is nearly completely lost in the QPC, apart from a weakly pronounced resistance plateau at $R_{\rm diag} = \frac{2}{5}h/e^2$ corresponding to $\nu = 5/2$ (see inset), while $\nu_{\rm bulk} = 3$ at the same magnetic field.

Figure 10.8a demonstrates that many different fractional filling factors ν_{QPC} can be transmitted by applying an appropriate QPC voltage and keeping the magnetic field fixed. However, relaxation of the barely mobile X-band screening layer electrons makes the observation of the most fragile fractional quantum Hall states difficult. To overcome this limitation, the fact that the X-band screening layers become mobile for temperatures above approximately 1 K can be used [38, 39]. By applying top-gate voltages at higher temperatures, the screening layer density can relax in a steady state and density fluctuations in the constriction are avoided (see Fig. 10.9). By this relaxation, additional screening is provided, which is believed to result in a much steeper QPC confinement potential. To allow a full relaxation of the screening layers, the system is kept at $T\approx 4$ K for several hours.

Figure 10.8b shows the diagonal resistance of the 1.2 μ m wide QPC III.a for 2 $\leq \nu_{\text{bulk}} \leq 3$. Here, -4 V have been applied to the QPC gates at $T \approx 4$ K. The electron gas below the metallic top-gates is depleted at approx. -3.2 V. At a base temperature of 9 mK (electronic temperature ≈ 12 –13 mK), the filling factors 7/3, 8/3 and 5/2 are fully quantized in the bulk, with a strong minimum in R_{xx} and a plateau

in R_{xy} . In addition, pronounced reentrant integer quantum Hall states are observed. The density in the constriction is nearly identical to the bulk density, as seen from the overlap of different filling factors. At a magnetic field of approx. 3.6 T, the plateau in $R_{\rm diag}$ shows that the $\nu = 5/2$ state is nearly perfectly transmitted through the QPC, without significant backscattering. Here, the applied QPC voltage of -4 V has been kept fixed while cooling down to the base temperature. The deviation of $R_{\rm diag}$ and $R_{\rm xy}$ at $B \approx 3.4$ T originates from a small longitudinal component in R_{diag} due to an asymmetry of the sample geometry. The optimized growth and gating procedure allow the definition of a QPC without decreasing the density in the constriction and without destroying the quantization of the $\nu = 5/2$ state, which is otherwise not possible. Interference experiments at $\nu = 5/2$ [36, 37, 70–74] require a filling factor $\nu = 5/2$ in the center of the employed QD, while edge states are only partially transmitted. Here, the diameter of the QD is constrained to a few µm (due to the finite quasiparticle coherence length [75]), thus making the conservation of the bulk density and $\nu = 5/2$ quantization on a μ m length-scale crucial. The steep confinement potential of QPCIII.a leads to a decreased width of the compressible regions in the QPC and a wider separating incompressible region, thus reducing backscattering across. The anticipated complex edge structure of the $\nu = 5/2$ state (which was experimentally found to occur only in OPCs of rather large width [76]) might facilitate its formation in a steeper confinement potential. Furthermore, the additional screening of the disorder in the constriction via X-band electrons reduces the amplitude of the disorder potential fluctuations. Hence, the influence of conductance oscillations as discussed in Sect. 10.3.3 is expected to be reduced. The main drawback of the utilized gating method is the low tuneability of gate voltages at mK temperatures. Here, the gate voltages have to remain in very small range around the voltage that has been applied at T = 4 K. Otherwise, slow relaxation processes of the X-band screening layers destroy the quantization of the $\nu = 5/2$ state. Growth methods which utilize conventional DX-doping and a reduced Al molar fraction might help to overcome this problem, while still providing a good quantization of $\nu = 5/2$ [40–42].

Having demonstrated that we can confine a fully gapped $\nu = 5/2$ state to a QPC, we are at a good starting point for conducting tunneling and interference experiments with the fragile fractional quantum Hall states at $\nu = 7/3$ and 5/2.

10.3.6 Energy Gap of the $\nu_{\rm OPC}$ = 1/3 State

Activation measurements have been performed on the $\nu_{QPC} = 1/3$ states in the two QPCs QPCII.a and QPCII.b. The measured diagonal resistances R_{diag} of both QPCs at a magnetic field of 10.25 T are shown in Fig. 10.11a, b. Here, a two-terminal AC voltage modulation of $V_{AC} = 40 \,\mu\text{V}$, corresponding to an AC current I_{AC} of approximately

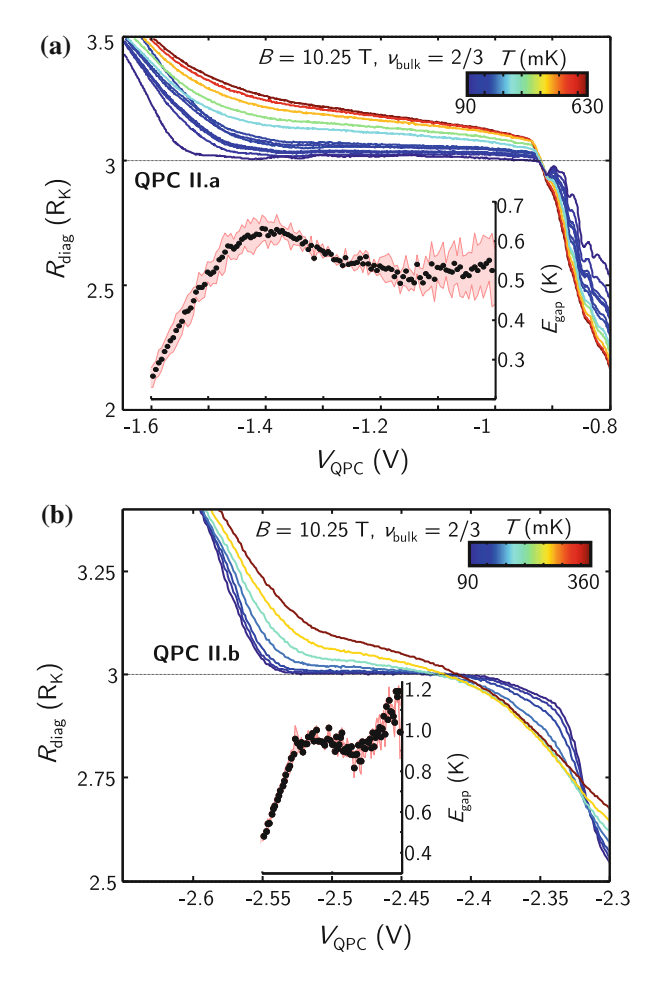


Fig. 10.11 a Diagonal resistances for different temperatures at $\nu_{\rm bulk} = 2/3$ for QPC II.a (here $V_{\rm CTG} = -0.47$ V) and QPC II.b (b). The insets show the energy gap as a function of the QPC gate voltage, which has been extracted from the activated behavior of $\Delta R_{\rm diag}$. The *shaded area* depicts an estimate of the fit error for $E_{\rm gap}$. (Reprinted figure with permission from [1]. Copyright 2014 by the American Physical Society.)

0.5 nA has been applied. The plateau at $R_{\rm diag}=3\times R_{\rm K}$ ($R_{\rm K}=h/e^2$), corresponding to $\nu_{\rm QPC}=1/3$, is much wider for QPC II.a (Fig. 10.11a). Temperature-dependent measurements reveal an activated behavior $\Delta R_{\rm diag} \propto e^{-\frac{\Delta_{\rm diag}}{k_BT}}$ of the deviation of the diagonal resistance from its plateau value, $\Delta R_{\rm diag}$. The energy gap values, extracted at different QPC voltages, are shown as insets in Fig. 10.11a, b. Extracted energy gaps ($E_{\rm gap}=2\Delta_{\rm xy}$) correspond to thermal energies between 0.6 and 1.0 K for these two QPCs, compared to an energy gap of 3.2 K for the bulk $\nu=2/3$ state at the same magnetic field (see Fig. 10.12). Thus, $R_{\rm xx}\approx 0$ has been maintained in the bulk ($\nu_{\rm bulk}=2/3$) over the whole temperature range which was used for extracting the

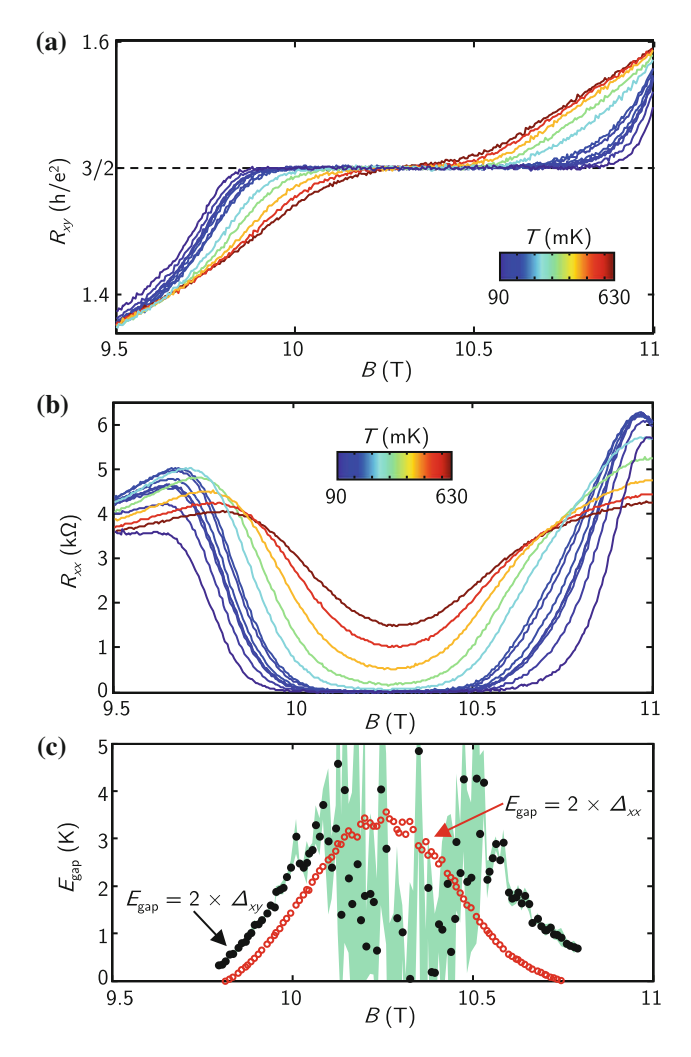


Fig. 10.12 R_{xy} (a) and R_{xx} (b) near $\nu_{\text{bulk}}=2/3$ for different temperatures. R_{xy} and R_{xx} are measured in the bulk of the sample with the QPCs II.a and II.b. The energy gaps of the $\nu_{\text{bulk}}=2/3$ state, extracted from either R_{xy} ($E_{\text{gap}}=2\Delta_{xy}$) or R_{xx} ($E_{\text{gap}}=2\Delta_{xx}$) are plotted in (c) as a function of the magnetic field. From the activated behavior of R_{xx} , an energy gap $E_{\text{gap}}\geq 3$ K is found. Close to the center of the $\nu_{\text{bulk}}=2/3$ plateau, the temperature-dependence of R_{xy} is too small to extract an energy gap. The shaded area is an estimate of the uncertainty of the fit to an activated behavior. Further away from the center of the plateau, Δ_{xy} is slightly larger than Δ_{xx}

energy gap of the $\nu_{QPC} = 1/3$ state, meaning that we probe only the temperature-dependence of the QPC. In contrast to activation measurements of R_{xy} in the bulk (see Fig. 10.12 and [77]), deviations from the quantized resistance value do not occur symmetrically around the center of the plateau. This effect, which is believed to be due to electron-electron interactions [78], is much more pronounced in the QPC with

the CTG. The similar size of these energy gaps suggests that the different widths and shapes of the $\nu_{\rm QPC}$ =1/3 plateau (as $V_{\rm QPC}$ is varied) mainly stem from different shapes of the confinement potential.

10.4 Conclusion

In conclusion, we have investigated the interplay of electronic transport and localization in quantum point contacts of different geometries and based on 2DEGs utilizing different growth techniques. In these systems, various integer and fractional quantum Hall states were observed. Using a QPC with a top-gate, we were able to investigate conductance resonances in greater detail. In this sample, edge states are separated by a wide incompressible region thus leading to a significant influence of localizations due to disorder potential fluctuations. Regions of perfect QPC transmission are surrounded by periodic conductance oscillations with an identical slope in the $V_{\rm OPC}-B$ -field plane. Within a many-electron picture, the resonances on the high (low) density end of the plateau can be interpreted as regions of enhanced or reduced density formed within incompressible regions between the counterpropagating edge states. As the charge of these regions is conserved, changing the density or magnetic field leads to periodic conductance oscillations, whenever an electron is added or removed. B-field and V_{OPC} -periodicities agree with expectations for a Coulombdominated quantum dot in strong magnetic fields and are determined by the filling factor background in which the compressible region of enhanced or reduced density is formed. At low densities and in weaker magnetic fields, resonances within the conductance plateau occur. In this regime, disorder broadening becomes comparable to the Landau level separation, thus compressible regions of reduced and enhanced density, situated in different Landau levels modulate transport at the same time. Here, the many-electron picture is not valid anymore and resonances with a dependence in the $B-V_{\rm OPC}$ plane, not necessarily equal to the conductance plateaus' dependence, are observed. These resonances are interpreted as confinement dominated single-electron interference effects. In the fractional quantum Hall regime, the behavior of the system seems to be influenced by both, single- and many-electron physics. Due to the much smaller gaps of the FQH states, disorder becomes more important. Close to perfect transmission, resonances similar to those associated with compressible regions of reduced or enhanced density in a many-electron picture can be observed. Periodicities at $\nu_{\rm OPC} = 1/3$ are compatible with the localization of fractionally charged quasiparticles in a Coulomb-dominated quantum dot. However, for intermediate transmissions, weak resonances with a slope different from the slopes of the neighboring conductance plateaus are observed, indicating the importance of single-electron physics where the formation of compressible and incompressible regions breaks down. Single-electron resonances have been studied as a function of the position of the conducting channel in the constriction. In contrast to manyelectron resonances, single-electron resonances are expected to possess slopes in the gate-voltage plane, not necessarily parallel to the conductance plateaus. Here, the

slope depends on the details of the disorder potential. Using optimized growth techniques and gating procedures, we are able to form QPC constrictions with extremely weak backscattering and a density equal to the bulk density. This allows us to observe the $\nu=5/2$ state in the QPC with a fully developed plateau. The bulk properties, like the reentrant integer quantum Hall states, are fully conserved in the QPC, making this system promising for future tunneling and interference experiments at $\nu=5/2$.

References

- S. Baer, C. Rössler, E.C. de Wiljes, P.-L. Ardelt, T. Ihn, K. Ensslin, C. Reichl, W. Wegscheider, Phys. Rev. B 89, 085424 (2014). doi:10.1103/PhysRevB.89.085424
- S. Komiyama, in *Mesoscopic Physics and Electronics*, NanoScience and Technology, ed. by P.T. Ando, P.Y. Arakawa, P.K. Furuya, P.S. Komiyama, P.H. Nakashima (Springer, Berlin, 1998), pp. 120–131
- S.H. Tessmer, P.I. Glicofridis, R.C. Ashoori, L.S. Levitov, M.R. Melloch, Nature 392, 51 (1998). doi:10.1038/32112
- S. Ilani, J. Martin, E. Teitelbaum, J.H. Smet, D. Mahalu, V. Umansky, A. Yacoby, Nature 427, 328 (2004). doi:10.1038/nature02230
- P.H.M. van Loosdrecht, C.W.J. Beenakker, H. van Houten, J.G. Williamson, B.J. van Wees, J.E. Mooij, C.T. Foxon, J.J. Harris, Phys. Rev. B 38, 10162 (1988). doi:10.1103/PhysRevB.38. 10162
- J. Martin, S. Ilani, B. Verdene, J. Smet, V. Umansky, D. Mahalu, D. Schuh, G. Abstreiter, A. Yacoby, Science 305, 980 (2004). doi:10.1126/science.1099950
- G.A. Steele, R.C. Ashoori, L.N. Pfeiffer, K.W. West, Phys. Rev. Lett. 95, 136804 (2005). doi:10. 1103/PhysRevLett.95.136804
- K. Hashimoto, C. Sohrmann, J. Wiebe, T. Inaoka, F. Meier, Y. Hirayama, R.A. Römer, R. Wiesendanger, M. Morgenstern, Phys. Rev. Lett. 101, 256802 (2008). doi:10.1103/ PhysRevLett.101.256802
- Y.Y. Wei, J. Weis, K.v. Klitzing, K. Eberl. Phys. Rev. Lett. 81, 1674 (1998). doi:10.1103/ PhysRevLett.81.1674
- D.B. Chklovskii, B.I. Shklovskii, L.I. Glazman, Phys. Rev. B 46, 4026 (1992). doi:10.1103/ PhysRevB.46.4026
- 11. A.L. Efros, Phys. Rev. B 45, 11354 (1992). doi:10.1103/PhysRevB.45.11354
- 12. N.R. Cooper, J.T. Chalker, Phys. Rev. B 48, 4530 (1993). doi:10.1103/PhysRevB.48.4530
- J.A. Simmons, H.P. Wei, L.W. Engel, D.C. Tsui, M. Shayegan, Phys. Rev. Lett. 63, 1731 (1989). doi:10.1103/PhysRevLett.63.1731
- J.A. Simmons, S.W. Hwang, D.C. Tsui, H.P. Wei, L.W. Engel, M. Shayegan, Phys. Rev. B 44, 12933 (1991). doi:10.1103/PhysRevB.44.12933
- D.H. Cobden, C.H.W. Barnes, C.J.B. Ford, Phys. Rev. Lett. 82, 4695 (1999). doi:10.1103/ PhysRevLett.82.4695
- T. Machida, S. Ishizuka, S. Komiyama, K. Muraki, Y. Hirayama, Phys. Rev. B 63, 045318 (2001). doi:10.1103/PhysRevB.63.045318
- O. Couturaud, S. Bonifacie, B. Jouault, D. Mailly, A. Raymond, C. Chaubet, Phys. Rev. B 80, 033304 (2009). doi:10.1103/PhysRevB.80.033304
- E. Peled, D. Shahar, Y. Chen, E. Diez, D.L. Sivco, A.Y. Cho, Phys. Rev. Lett. 91, 236802 (2003). doi:10.1103/PhysRevLett.91.236802
- A.A.M. Staring, H. van Houten, C.W.J. Beenakker, C.T. Foxon, Phys. Rev. B 45, 9222 (1992). doi:10.1103/PhysRevB.45.9222
- P.C. Main, A.K. Geim, H.A. Carmona, C.V. Brown, T.J. Foster, R. Taboryski, P.E. Lindelof, Phys. Rev. B 50, 4450 (1994). doi:10.1103/PhysRevB.50.4450

References 185

21. G. Timp, A.M. Chang, P. Mankiewich, R. Behringer, J.E. Cunningham, T.Y. Chang, R.E. Howard, Phys. Rev. Lett. **59**, 732 (1987). doi:10.1103/PhysRevLett.59.732

- J. Velasco, G. Liu, L. Jing, P. Kratz, H. Zhang, W. Bao, M. Bockrath, C.N. Lau, Phys. Rev. B 81, 121407 (2010). doi:10.1103/PhysRevB.81.121407
- J. Martin, N. Akerman, G. Ulbricht, T. Lohmann, K. von Klitzing, J.H. Smet, A. Yacoby, Nat. Phys. 5, 669 (2009). doi:10.1038/nphys1344
- S. Branchaud, A. Kam, P. Zawadzki, F.M. Peeters, A.S. Sachrajda, Phys. Rev. B 81, 121406 (2010). doi:10.1103/PhysRevB.81.121406
- G. Granger, S.A. Studenikin, A. Kam, A.S. Sachrajda, P.J. Poole, Appl. Phys. Lett. 98, 132107 (2011). doi:10.1063/1.3574540
- 26. P.A. Lee, Phys. Rev. Lett. 65, 2206 (1990). doi:10.1103/PhysRevLett.65.2206
- B. Rosenow, B.I. Halperin, Phys. Rev. Lett. 98, 106801 (2007). doi:10.1103/PhysRevLett.98. 106801
- B.I. Halperin, A. Stern, I. Neder, B. Rosenow, Phys. Rev. B 83, 155440 (2011). doi:10.1103/ PhysRevB.83.155440
- B. Hackens, F. Martins, S. Faniel, C.A. Dutu, H. Sellier, S. Huant, M. Pala, L. Desplanque, X. Wallart, V. Bayot, Nat. Commun. 1, 39 (2010). doi:10.1038/ncomms1038
- F. Martins, S. Faniel, B. Rosenow, M.G. Pala, H. Sellier, S. Huant, L. Desplanque, X. Wallart,
 V. Bayot, B. Hackens, New J. Phys. 15, 013049 (2013). doi:10.1088/1367-2630/15/1/013049
- F. Martins, S. Faniel, B. Rosenow, H. Sellier, S. Huant, M.G. Pala, L. Desplanque, X. Wallart, V. Bayot, B. Hackens, Sci. Rep. 3 (2013). doi:10.1038/srep01416
- 32. Y. Zhang, D.T. McClure, E.M. Levenson-Falk, C.M. Marcus, L.N. Pfeiffer, K.W. West, Phys. Rev. B **79**, 241304 (2009). doi:10.1103/PhysRevB.79.241304
- A. Kou, C.M. Marcus, L.N. Pfeiffer, K.W. West, Phys. Rev. Lett. 108, 256803 (2012). doi:10. 1103/PhysRevLett.108.256803
- F.E. Camino, W. Zhou, V.J. Goldman, Phys. Rev. B 76, 155305 (2007). doi:10.1103/PhysRevB. 76.155305
- D.T. McClure, W. Chang, C.M. Marcus, L.N. Pfeiffer, K.W. West, Phys. Rev. Lett. 108, 256804 (2012). doi:10.1103/PhysRevLett.108.256804
- R.L. Willett, L.N. Pfeiffer, K.W. West, Proc. Nat. Acad. Sci. 106, 8853 (2009). doi:10.1073/ pnas.0812599106
- R.L. Willett, C. Nayak, K. Shtengel, L.N. Pfeiffer, K.W. West, Phys. Rev. Lett. 111, 186401 (2013). doi:10.1103/PhysRevLett.111.186401
- C. Rössler, T. Feil, P. Mensch, T. Ihn, K. Ensslin, D. Schuh, W. Wegscheider, New J. Phys. 12, 043007 (2010). doi:10.1088/1367-2630/12/4/043007
- I.P. Radu, J.B. Miller, C.M. Marcus, M.A. Kastner, L.N. Pfeiffer, K.W. West, Science 320, 899 (2008). doi:10.1126/science.1157560
- C. Reichl, J. Chen, S. Baer, C. Rössler, T. Ihn, K. Ensslin, W. Dietsche, W. Wegscheider, New J. Phys. 16, 023014 (2014). doi:10.1088/1367-2630/16/2/023014
- 41. W. Pan, N. Masuhara, N.S. Sullivan, K.W. Baldwin, K.W. West, L.N. Pfeiffer, D.C. Tsui, Phys. Rev. Lett. **106**, 206806 (2011). doi:10.1103/PhysRevLett.106.206806
- 42. G. Gamez, K. Muraki, Phys. Rev. B 88, 075308 (2013). doi:10.1103/PhysRevB.88.075308
- C.W.J. Beenakker, H. van Houten, arXiv: cond-mat/0412664 (2004), Solid State Phys. 44, 1 (1991)
- D.A. Wharam, T.J. Thornton, R. Newbury, M. Pepper, H. Ahmed, J.E.F. Frost, D.G. Hasko,
 D.C. Peacock, D.A. Ritchie, G.A.C. Jones, J. Phys. C: Solid State Phys. 21, L209 (1988).
 doi:10.1088/0022-3719/21/8/002
- 45. B.J. van Wees, L.P. Kouwenhoven, H. van Houten, C.W.J. Beenakker, J.E. Mooij, C.T. Foxon, J.J. Harris, Phys. Rev. B 38, 3625 (1988). doi:10.1103/PhysRevB.38.3625
- 46. M. Büttiker, Phys. Rev. B 41, 7906 (1990). doi:10.1103/PhysRevB.41.7906
- 47. A.C. Graham, K.J. Thomas, M. Pepper, N.R. Cooper, M.Y. Simmons, D.A. Ritchie, Phys. Rev. Lett. 91, 136404 (2003). doi:10.1103/PhysRevLett.91.136404
- 48. M. Ciorga, A.S. Sachrajda, P. Hawrylak, C. Gould, P. Zawadzki, S. Jullian, Y. Feng, Z. Wasilewski, Phys. Rev. B 61, R16315 (2000). doi:10.1103/PhysRevB.61.R16315

- D.B. Chklovskii, K.A. Matveev, B.I. Shklovskii, Phys. Rev. B 47, 12605 (1993). doi:10.1103/ PhysRevB.47.12605
- 50. C. Sohrmann, R.A. Römer, New J. Phys. 9, 97 (2007). doi:10.1088/1367-2630/9/4/097
- 51. G.A. Steele, Imaging transport resonances in the quantum hall effect, Ph.D. thesis, Massachusetts Institute of Technology (2006)
- 52. A.H. MacDonald, Phys. Rev. Lett. 64, 220 (1990). doi:10.1103/PhysRevLett.64.220
- 53. S.M. Girvin, Phys. Rev. B **29**, 6012 (1984). doi:10.1103/PhysRevB.29.6012
- 54. L. Brey, Phys. Rev. B **50**, 11861 (1994). doi:10.1103/PhysRevB.50.11861
- H.-S. Sim, K.J. Chang, G. Ihm, Phys. Rev. Lett. 82, 596 (1999). doi:10.1103/PhysRevLett.82.
- 56. B.I. Halperin, Phys. Rev. B 25, 2185 (1982). doi:10.1103/PhysRevB.25.2185
- 57. M. Büttiker, Phys. Rev. B 38, 9375 (1988). doi:10.1103/PhysRevB.38.9375
- 58. C.W.J. Beenakker, Phys. Rev. B 44, 1646 (1991). doi:10.1103/PhysRevB.44.1646
- 59. C.W.J. Beenakker, Phys. Rev. Lett. 64, 216 (1990). doi:10.1103/PhysRevLett.64.216
- 60. J.K. Jain, S.A. Kivelson, Phys. Rev. Lett. 60, 1542 (1988). doi:10.1103/PhysRevLett.60.1542
- V. Venkatachalam, S. Hart, L. Pfeiffer, K. West, A. Yacoby, Nat. Phys. 8, 676 (2012). doi:10. 1038/nphys2384
- 62. X.G. Wen, Phys. Rev. Lett. 64, 2206 (1990). doi:10.1103/PhysRevLett.65.2206
- A. Bid, N. Ofek, H. Inoue, M. Heiblum, C.L. Kane, V. Umansky, D. Mahalu, Nature 466, 585 (2010), bibtex: Bid2010. doi:10.1038/nature09277
- J. Wang, Y. Meir, Y. Gefen, Phys. Rev. Lett. 111, 246803 (2013). doi:10.1103/PhysRevLett. 111.246803
- C. Rössler, S. Baer, E. de Wiljes, P.-L. Ardelt, T. Ihn, K. Ensslin, C. Reichl, W. Wegscheider, New J. Phys. 13, 113006 (2011). doi:10.1088/1367-2630/13/11/113006
- S. Sarkozy, F. Sfigakis, K. Das Gupta, I. Farrer, D.A. Ritchie, G.A.C. Jones, M. Pepper, Phys. Rev. B 79, 161307 (2009). doi:10.1103/PhysRevB.79.161307
- Y. Komijani, M. Csontos, T. Ihn, K. Ensslin, Y. Meir, D. Reuter, A.D. Wieck, Phys. Rev. B 87, 245406 (2013). doi:10.1103/PhysRevB.87.245406
- S. Schnez, C. Rössler, T. Ihn, K. Ensslin, C. Reichl, W. Wegscheider, Phys. Rev. B 84, 195322 (2011). doi:10.1103/PhysRevB.84.195322
- S. Baer, C. Rössler, T. İhn, K. Ensslin, C. Reichl, W. Wegscheider, New J. Phys. 15, 023035 (2013). doi:10.1088/1367-2630/15/2/023035
- A. Stern, B.I. Halperin, Phys. Rev. Lett. 96, 016802 (2006). doi:10.1103/PhysRevLett.96. 016802
- P. Bonderson, A. Kitaev, K. Shtengel, Phys. Rev. Lett. 96, 016803 (2006). doi:10.1103/ PhysRevLett.96.016803
- 72. P. Bonderson, K. Shtengel, J.K. Slingerland, Phys. Rev. Lett. 97, 016401 (2006). doi:10.1103/PhysRevLett.97.016401
- R. Ilan, B. Rosenow, A. Stern, Phys. Rev. Lett. 106, 136801 (2011). doi:10.1103/PhysRevLett. 106.136801
- R. Ilan, E. Grosfeld, A. Stern, Phys. Rev. Lett. 100, 086803 (2008). doi:10.1103/PhysRevLett. 108.086803
- 75. W. Bishara, P. Bonderson, C. Nayak, K. Shtengel, J.K. Slingerland, Phys. Rev. B **80**, 155303 (2009). doi:10.1103/PhysRevB.80.155303
- J.B. Miller, I.P. Radu, D.M. Zumbuhl, E.M. Levenson-Falk, M.A. Kastner, C.M. Marcus, L.N. Pfeiffer, K.W. West, Nat. Phys. 3, 561 (2007). doi:10.1038/nphys658
- H.P. Wei, A.M. Chang, D.C. Tsui, M. Razeghi, Phys. Rev. B 32, 7016 (1985). doi:10.1103/ PhysRevB.32.7016
- A. Siddiki, J. Horas, J. Moser, W. Wegscheider, S. Ludwig, EPL (Europhys. Lett.) 88, 17007 (2009). doi:10.1209/0295-5075/88/17007

Chapter 11 Quasiparticle Tunneling in the Second Landau Level

Abstract We measure weak quasiparticle tunneling across a constriction in the second Landau level. At $\nu=7/3$, 8/3 and 5/2, comparison of temperature and DC bias dependence to weak tunneling theory allows extracting parameters that describe the edges' quasiparticle excitations. At $\nu=8/3$, our results are well described by a particle-hole conjugate Laughlin state, but not compatible with proposed non-Abelian quasiparticle excitations. For $\nu=5/2$, our measurements are in good agreement with previous experiments and favor the Abelian (3,3,1) or (1,1,3)-states. At these filling factors, we further investigate the influence of the backscattering strength on the extracted scaling parameters. For $\nu=7/3$, the backscattering strength strongly affects the scaling parameters, whereas quasiparticle tunneling at $\nu=8/3$ and 5/2 appears more robust. Our results provide important additional insight about the physics in the second Landau level and contribute to the understanding of the physics underlying the fractional quantum Hall states at $\nu=7/3$, 8/3 and 5/2.

11.1 Introduction

Numerical studies of the fractional quantum Hall (FQH) states at $\nu=7/3$ and 8/3 have indicated that these states might not be well described by the Laughlin wave function [2–5]. Thus, the underlying physics which creates the energy gap might be different for $\nu=1/3$, 7/3 and 8/3. Subsequently, alternative wave functions with non-Abelian quasiparticle (QP) excitations have been proposed for $\nu=7/3$ and 8/3 [6, 7], making these states, along with the 5/2 state [8–11], potentially interesting for topologically protected quantum operations [12–14].

Most current experimental findings for both the $\nu = 7/3$ and 8/3 states are compatible with non-Abelian candidate states and a (particle-hole conjugate) Laughlin state. For instance, local electrometer [15] and shot noise measurements [16, 17] suggest

The following chapter is based on the article [1].

[©] Springer International Publishing Switzerland 2015

¹⁸⁷

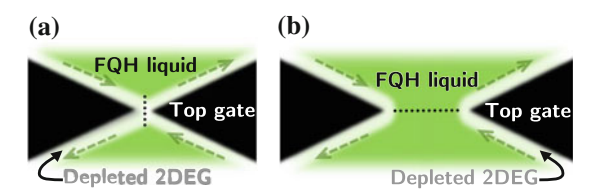


Fig. 11.1 Conceptual difference between weak and strong backscattering [19–21], in the simplest case without edge reconstruction. **a** For a quantum point contact (QPC) close to pinch-off, we have strong backscattering and weak electron tunneling (*dotted line*). **b** For an open QPC, weak backscattering and weak quasiparticle tunneling (*dotted line*) govern the transmission. (Reprinted figure with permission from [1]. Copyright 2014 by the American Physical Society.)

a QP charge $e^*/e = 1/3$. The latter experiments furthermore show that a neutral mode is present for $\nu = 8/3$ but absent for $\nu = 7/3$. From activation measurements, the $\nu = 7/3$ and 8/3 states were found to be consistent with Jain's non-interacting composite Fermion model [18], hence supporting a (particle-hole conjugate) Laughlin state. Nevertheless, further experiments are necessary, which allow a more direct discrimination of the proposed wave functions.

Tunneling experiments employing quantum point contacts (QPCs) [22] or structures made by cleaved-edge overgrowth [23] have been used to study the characteristic power-law scaling of the chiral Luttinger liquid tunneling conductance: a $\nu = 1/3$ edge was weakly tunnel-coupled to another FQH edge or to a bulk metal across vacuum. Thus measured conductances arose from the tunneling of electrons (Fig. 11.1a, dotted line), which is strongly suppressed at low temperatures. In the case where counterpropagating edge states are weakly coupled across a FQH liquid (in the simplest case without edge reconstruction, Fig. 11.1b, dotted line), QPs tunnel between the edges [19–21]. In contrast to the previous case, this process is strongly enhanced at low T. Weak OP tunneling has been used as a probe for edge properties of the $\nu = 5/2$ state [24, 25]. This situation recently also has been studied theoretically [26–29]. The DC bias and temperature dependence of the tunneling conductance across a QPC was employed to extract the QP charge e^*/e and the Coulomb interaction parameter g, which describes the strength of electron-electron interaction in a FQH edge and reflects the topological order in the bulk [30]. These parameters characterize the edge excitations of proposed wave functions for $\nu = 5/2, 7/3$ and 8/3 and hence allow probing the nature of these states experimentally.

In this chapter, we use this technique for the investigation of the most prominent filling factors of the lower spin branch of the second Landau level (LL): $\nu=7/3$, 8/3 and 5/2. To the best of our knowledge, our results constitute the first detailed experimental investigation of scaling parameters g and e^*/e for the 7/3 and 8/3 state. ¹ We provide a comparison to theoretical proposals. At $\nu=5/2$, our extracted scaling parameters are very similar to those reported earlier [24, 25], though measured in a quantum well with a different growth technique and an approximately 12 % lower

 $^{^1}$ In [31], two groups of zero bias peaks were observed for $7/3 < \nu < 8/3$. These were attributed to $\nu = 5/2$ and $\nu = 8/3$. At $\nu = 8/3$ the data was not conclusive, whereas for $\nu = 5/2$ similar conclusions as in [24] were reached.

11.1 Introduction 189

electron sheet density. Finally, we study the effect of the backscattering strength of the QPC on the QP tunneling and the extracted parameters, and investigate the breakdown of weak QP tunneling.

11.2 Experimental Details

The measured QPCs are approximately 1.1 μ m wide and are defined by electron-beam lithography and subsequent Ti/Au evaporation on photo-lithographically patterned high-mobility wafers. These high mobility structures ($n_s \approx 2.3 \times 10^{11}$ cm⁻², $\mu \approx 2.3 \times 10^7$ cm²/Vs) are optimized for the observation of the $\nu = 5/2$ state without prior LED illumination [32]. The 27 nm wide quantum well lies approximately 200 nm below the surface. A DX doping scheme has been used. Experiments have been conducted in a cryogen-free dilution refrigerator, with an electronic base temperature $T_{\rm el} \approx 12$ –13 mK, achieved by low-pass filtering and thermal anchoring at every temperature stage. The bath temperature ($T_{\rm bath} \approx 10$ mK) is measured with a SQUID-based noise thermometer, which gives reliable results down to temperatures below 10 mK [33, 34]. Top-gated structures have been cooled down from room temperature to 4 K with a positive pre-bias. Subsequently, top-gates have been negatively biased at 4 K to allow for density relaxation in the screening layers and the QPC channel [24, 35, 36]. The electron gas underneath the top-gates is depleted at a gate voltage of -1.4 V.

11.3 Measurement Results

Figure 11.2 shows the bulk Hall resistance R_{xy} measured far away from the top-gate defined QPCs and the resistance measured diagonally across one of the QPCs, R_{diag}, for filling factors in the bulk $2 \le \nu_{\text{bulk}} \le 4$ at base temperature. Here, the QPC2 gates (see inset of Fig. 11.2) are biased to -1.65 V (at the onset of weak quasiparticle tunneling), while all other gates are grounded. A constant AC current $I_{AC} = 1.0 \,\text{nA}$ is applied at f = 13.333 Hz, while $I_{DC} = 0$. R_{diag} and R_{xy} are measured in a standard 4terminal configuration (see inset of Fig. 11.2) using lock-in measurement techniques. In addition to the integer quantum Hall (IQH) states, FQH states at $\nu = 8/3$, 5/2, 7/3 and strong reentrant integer quantum Hall (RIQH) states are observed in the bulk. Whenever an IQH plateau is observed in R_{xy} , R_{diag} is quantized at exactly the same resistance value, indicating very similar bulk and QPC electronic densities. Inbetween the IQH plateaus, $R_{\text{diag}} \geq R_{\text{xy}}$, indicating reduced transmission through the QPC. In this situation, weak backscattering of edge states through the QPC occurs via weak QP tunneling between counter-propagating edge states (Fig. 11.1b). We measure the tunneling conductance across the QPC, $g_{\text{tun}} \approx (R_{\text{diag}} - R_{\text{xy}})/R_{\text{xy}}^2$ [24] for different bulk filling factors ν_{bulk} (see Appendix B). The power-law temperature dependence of the zero-bias tunneling conductance [30, 37] $g_{\text{tun}}|_{I_{\text{SD}=0}} \propto T^{2g-2}$ then

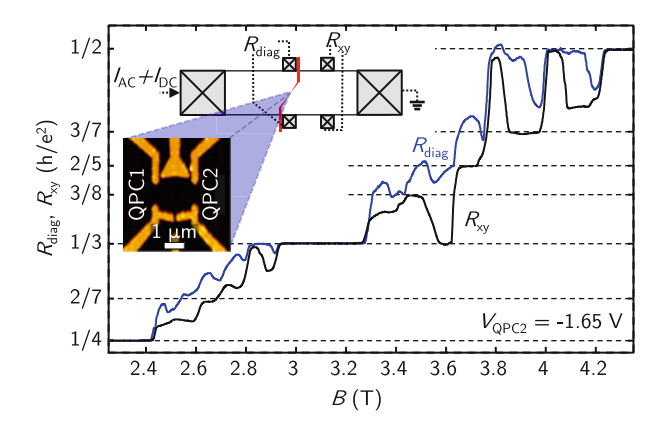


Fig. 11.2 R_{diag} (blue) and R_{xy} (black) measured in a Hall-bar geometry (upper inset) as a function of the magnetic field. Here, -1.65 V have been applied to QPC2 (left inset). In between integer filling factors, $R_{\text{diag}} \ge R_{\text{xy}}$, indicating a reduced transmission of the QPC. (Reprinted figure with permission from [1]. Copyright 2014 by the American Physical Society.)

allows extracting the Coulomb interaction parameter g, which can be compared to theoretical predictions. With an additional DC bias between the counter-propagating edges, the tunneling conductance takes the form [37–40]:

$$g_{\text{tun}} = A \times T^{(2g-2)} \times F\left(g, \frac{e^*/e I_{\text{DC}} R_{\text{xy}}}{k_B T}\right) + g_{\infty}, \tag{11.1}$$

Here, a heuristic background conductance g_{∞} has been introduced. F is a function of g and $\left(e^*/e\ I_{DC}R_{xy}\right)/(k_BT)$ [24]:

$$\begin{split} F\left(g,x\right) &= \mathrm{B}\left(g+i\frac{x}{2\pi},g-i\frac{x}{2\pi}\right) \\ &\times \left\{\pi\cosh\left(\frac{x}{2}\right) - 2\sinh\left(\frac{x}{2}\right)\mathrm{Im}\left[\Psi\left(g+i\frac{x}{2\pi}\right)\right]\right\} \end{split}$$

Here, B(x, y) is the Euler beta function and $\Psi(x)$ is the digamma function. A derivation of this formula can be found for example in [39, 40].

This formula is the result of a perturbative calculation which assumes a point-like interaction of the counter-propagating edge states in the QPC [37–40]. It relies on the scaling dimensions of the most relevant quasiparticle creation and annihilation operators of the individual edges. The exact form of these operators depends on the FQH edge modes and their interactions. Edge theories and corresponding quasiparticle operators have been developed for all the relevant candidate wavefunctions in the second LL (an overview can be found for example in [29]). As long as the interaction between the counter-propagating edge modes is weak and can be treated in a perturbative approach, we expect (11.1) to be valid.

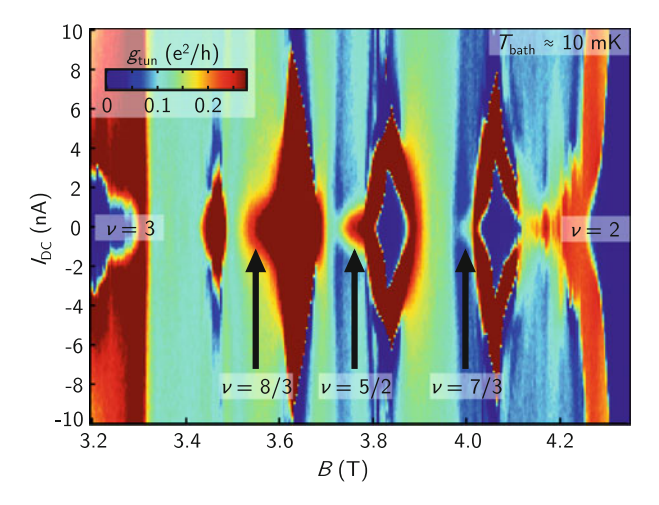


Fig. 11.3 Tunneling conductance g_{tun} as a function of B and I_{DC} . At $\nu = 7/3$, 5/2 and 8/3, QP tunneling peaks are observed at small DC biases

Measuring the full DC bias and temperature dependence of the tunneling conductance gives access to g and e^*/e via comparison to (11.1). The tunneling conductance g_{tun} is shown as a function of DC current and magnetic field B in Fig. 11.3. Here, a strong bias dependence is observed close to the RIQH phases, visible as diamond-shaped structures in the $I_{\text{DC}}-B$ -plane. This behavior is a bulk effect and will be discussed in Chap. 15. At filling factors $\nu=5/2$, 8/3 and 7/3, an enhanced tunneling conductance is observed at small biases (marked by arrows in Fig. 11.3).

In the following, this QP tunneling is studied in different configurations. First, the *B*-field is fixed to the center of the bulk filling factors and the QPC transmission is kept constant (similar to [24, 25]). In this configuration, $\nu = 5/2$ (Sect. 11.3.1) and $\nu = 8/3$ (Sect. 11.3.2) are investigated. Backscattering for $\nu = 7/3$ is much weaker than for $\nu = 5/2$ and 8/3. For the QPC voltages chosen, a reliable parameter extraction was not possible for $\nu = 7/3$ (data not shown). In Sect. 11.3.3, the influence of the magnetic field strength on the tunneling parameters is investigated. Finally, the influence of the QPC transmission is investigated (Sect. 11.3.4). In the latter two sections, also backscattering at $\nu = 7/3$ is observed in narrow parameter windows.

11.3.1 Tunneling Conductance at $\nu = 5/2$

Figure 11.4a shows the temperature dependence of the measured g_{tun} of QPC1 when V_{QPC1} is fixed to -1.8 V. At this gate voltage, backscattering is sufficiently strong to be observed up to temperatures of $\approx 65 \, \text{mK}$. A narrow peak of the tunneling conductance is observed at zero DC current. Adjacent to the QP tunneling peak, undershoots of the tunneling conductance are observed. Such undershoots of the

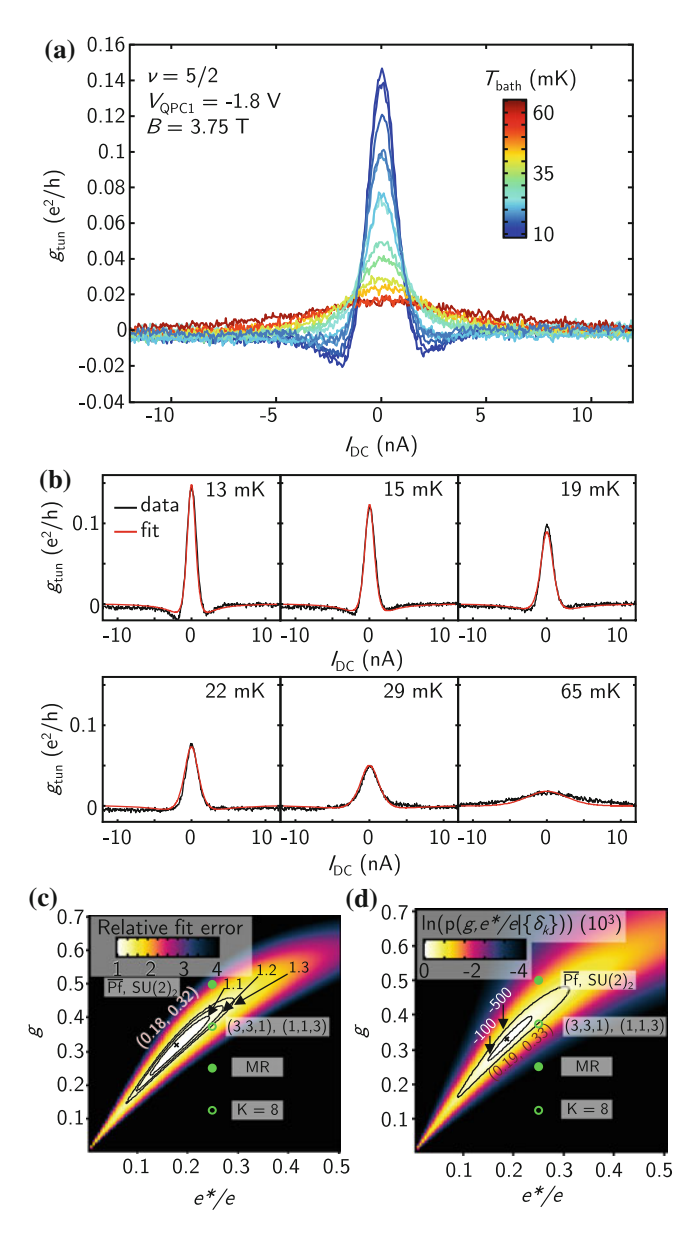


Fig. 11.4 a Zero-bias backscattering peak at $\nu=5/2$ and fixed $V_{\rm QPC1}=-1.8$ V. The peak height is strongly temperature-dependent. **b** Measured (*black*) and fitted (*red*) tunneling conductance for different electronic temperatures (fit parameters: $e^*/e=0.18$, g=0.32). **c** Normalized fit error as a function of fit parameters e^*/e and g. Parameters of Abelian (*green circles*) and non-Abelian (*green dots*) candidate wavefunctions are indicated. **d** PDF of the measured residuals $\{\delta_k\}$ as a function of e^*/e and g. The maximum probability is found for $e^*/e=0.19$, g=0.33 with $\sigma_{\rm g}=0.0026$, $\sigma_{\rm e^*/e}=0.0019$ and $\sigma_{\rm g,e^*/e}=0.0022$. (Reprinted figure with permission from [1]. Copyright 2014 by the American Physical Society.)

tunneling conductance are only expected for q < 0.5 [25, 40]. The B-field is set to the center of the bulk $\nu = 5/2$ plateau for this measurement, and an AC current $I_{AC} = 0.4 \,\mathrm{nA}$ is applied. Decreasing the AC current below this value does not narrow the g_{tun} peak, but only reduces the signal to noise ratio. A small constant background of approx. $0.1 \times e^2/h$ is removed from the data, by subtracting the saturation g_{tun} at $I_{DC} \ge 10$ nA. When the temperature is increased to approx. 65 mK, the zero-bias peak vanishes almost completely. A fit of the weak tunneling expression (11.1) to the measured g_{tun} is shown in Fig. 11.4b (six out of 13 measured temperatures are shown). The parameters g_{∞} , A, g and e^*/e are identical for all T and are fitted to the data. With $e^*/e = 0.18$ and q = 0.32, excellent agreement of experiment and QP tunneling theory is obtained. These parameters are close to those reported in [24, 25]. There, best fit parameters $e^*/e = 0.17$, g = 0.35 [24] and $e^*/e = 0.25/0.22$, g = 0.42/0.34 ([25], for two different geometries) were found. Suitable parameter ranges can be deduced from the fit residuals δ_k of the k^{th} measurement point. We plot the relative fit error, i.e. $\Sigma_{\delta} = \min_{A,g_{\infty}} \left(\sum_{k} \delta_{k}^{2}\right)$ (normalized by its minimum, $\Sigma_{\delta,\min}$), as a function of e^{*}/e and g (Fig. 11.4c), similar as it has been done in [24, 25]. With this plot, the agreement with parameters for the proposed wave functions can be assessed qualitatively. Parameters for different wave functions are cited in Table 11.1 and are indicated in Fig. 11.4c, d as green circles (Abelian modes) or green dots (non-Abelian modes). All QP excitations are expected to possess a minimum $e^*/e = 0.25$. The Abelian K = 8state [41-43] with q = 0.125 does clearly not agree well with our experimental observations. Very recently, it was shown that the (1,1,3)-state is also a viable candidate for $\nu = 5/2$ [44]. It is Abelian and is expected to possess $q \approx 0.375$ in a gate-defined geometry. Closest agreement of our data seems to be found with this (1,1,3)-state and the Abelian (3,3,1)-state [42, 43, 45] for which g = 0.375 is expected. The parameters of this state reproduce the experimental g_{tun} qualitatively well (see Appendix: "Fits for proposed parameter pairs— $\nu = 5/2$ "). The non-Abelian Moore-Read Pfaffian [46] (q = 0.25), Anti-Pfaffian [47, 48] $(\overline{Pf}, q = 0.5)$, SU(2)₂ state [49, 50] (q = 0.5)0.5) and Majorana gapped edge-reconstructed Pfaffian state [51] (g = 0.5) seem less likely and also do not fit as well qualitatively (see Appendix: "Fits for proposed parameter pairs— $\nu = 5/2$ "), though they cannot be excluded completely. For the Majorana-gapped anti-Pfaffian [51] and the particle hole conjugate states, (3, 3, 1) and $\overline{\mathrm{SU}(2)_2}$ [29], g>0.5 is expected and they hence are not indicated in Fig. 11.4c, d. For the best fit, $\chi^2=\Sigma_{\delta,\mathrm{min}}/(N\sigma_{\mathrm{meas}}^2)=2.14$ is found, where N is the number of measurement points and σ_{meas}^2 is the measurement noise (variance). This indicates a slight systematic disagreement between measurements and model function.

A more quantitative assessment can be gained from the probability distribution for g and e^*/e , p (g, $e^*/e|\{\delta_k\}$), which is calculated from the Gaussian probability density function (PDF) of our fit residuals, leading to the posterior probability p (σ , A, g_{∞} , g, $e^*/e|\{\delta_k\}$) by marginalization of the variables σ , A and g_{∞} [53] (for details see Appendix C). The maximum probability is found for $e^*/e = 0.19$ and g = 0.33 with very narrow standard deviations $\sigma_g = 0.0026$, $\sigma_{e^*/e} = 0.0019$. The positive covariance $\sigma_{g,e^*/e} = 0.0022$ indicates that we are more sensitive to the

Table 11.1 Overview of the theoretically proposed parameter pairs g and e^*/e for different states at $\nu = 5/2$ ('n-A': non-Abelian; taken from [29, 44, 51, 52]) and our results for different measurement configurations

$\nu = 5/2$			
Theory [29, 44, 51, 52	2]		
State	e^*/e	g	n-A?
K = 8	1/4	1/8	No
MR Pf	1/4	1/4	Yes
(3,3,1)	1/4	3/8	No
(1,1,3)	1/4	≈3/8 ^a	No
Pf	1/4	1/2	Yes
SU(2) ₂	1/4	1/2	Yes
(3, 3, 1)	1/4	5/8	No
<u>SU(2)</u> ₂	1/4	3/4	Yes
Majorana-gapped edge-rec. Pf	1/4	1/2	Yes
	1/2	1/2	No
Majorana-gapped Pf	1/4	0.55-0.75	Yes
	1/2	0.5-0.7	No
Experiment			
Config.	e^*/e	g	
I.	0.18	0.32	
II.	0.25	0.42	
III.	1/4	0.42	
IV.	0.15-0.21	0.24-0.32	
V.	1/4	0.37	

Only edge modes with the lowest QP charge are quoted, as they dominate the tunneling in our experiment. [Config. I.: B and $V_{\rm QPC}$ constant (see Figs. 11.4 and 11.5), II.: $V_{\rm QPC}$ varied (Fig. 11.7), III.: $V_{\rm QPC}$ varied, e^* fixed to e/4 or e/3 (Fig. 11.7), IV.: B varied (Fig. 11.6), V.: B varied, e^* fixed to e/4 or e/3 (Fig. 11.6)]

difference $g - e^*/e$ than to the individual parameters g and e^*/e . Overall, we can conclude that our measurements are well described by the weak tunneling expression of (11.1), with only a small systematic deviation. However, when comparing

^aIn a gate defined geometry [44]

the "best fit" parameters to the proposed parameter pairs, the small size of the standard deviations suggest that there is clearly a systematic deviation. Here, none of the proposed parameter pairs lie within our statistical error.

11.3.2 Tunneling Conductance at $\nu = 8/3$

A similar analysis can be conducted at a bulk filling factor $\nu_{\text{bulk}} = 8/3$. For this the B-field is set to the center of the bulk 8/3 plateau. Here, the tunneling peak has a qualitatively different shape (Fig. 11.5a) with a larger full width at half maximum (FWHM) in I_{DC} direction and absent g_{tun} undershoots. The absence of these undershoots is a sign for q > 0.5 [25, 40]. Also in this case, the weak tunneling expression (11.1) fits the data well over a large temperature range (six out of nine measured temperatures are shown in Fig. 11.5b). From the fit we obtain: $e^*/e =$ 0.22, g = 0.62. A plot of the relative fit error as a function of the parameters q and e^*/e is shown in Fig. 11.5c. For the best fit, $\chi^2 = 1.20$ is found here, thus indicating only a small systematic disagreement. Marginalization of σ , A and q_{∞} reveals that the maximum probability does not exactly coincide with the minimum relative fit error, but is slightly shifted to $e^*/e = 0.23$, g = 0.65 (Fig. 11.5d). Parameters of the candidate wave functions for $\nu = 8/3$ are cited in Table 11.2 and are indicated as (green) circles (Abelian modes) or (green) dots (non-Abelian modes) in Fig. 11.5c, d. All candidate states furthermore exhibit Abelian 2e/3 QP excitations with g = 2/3, which were not observed in the experiment. Apart from a particlehole conjugate Laughlin state $(\overline{L_{1/3}})$, two types of Bonderson-Slingerland states $(BS_{2/3} \text{ and } BS_{1/3}^{\psi})$ and a four-clustered Read-Rezayi state are possible candidates. The Bonderson-Slingerland states are constructed hierarchically over a Moore-Read Pfaffian state. This construction allows to produce the most important filling factors in the second Landau level [6]. In the four-clustered Read-Rezayi state ($RR_{k=4}$), clusters of k Anyons are expected to form effective Bosons and to condense in a liquid of filling factor $\nu = k/(k+2)$ [7, 54]. The BS_{2/3} and BS^{ψ}_{1/3} states support two e/3 edge modes with g = 2/3 and 7/24 (BS_{2/3}) and g = 2/3 and 13/24 (BS^{ψ}_{1/3}). Due to the $g_{\rm tun} \propto T^{2g-2}$ temperature dependence, we expect to probe mainly the smallest g of the edge modes. From Fig. 11.5c, d we can see that the $RR_{k=4}$ state and the non-Abelian edge modes of the BS_{2/3} state are not in agreement with our measurements. The fit parameters are closest to the particle-hole conjugate Laughlin state $(\overline{L_{1/3}})$, which fits much better than the non-Abelian edge modes of the BS $_{1/3}^{\psi}$ state. The experimental g_{tun} is qualitatively well reproduced by the $\overline{L_{1/3}}$ parameters (see Appendix: "Fits for proposed parameter pairs— $\nu = 8/3$ "). Quantitatively however, none of the candidate states lies within statistical error bars, also in this case. Similar to the previous case, "best fit" parameters can be found that lead to only a statistic deviation of theory and experiment. Again, the deviation of proposed parameter pairs and "best fit" parameters indicates a systematic deviation.

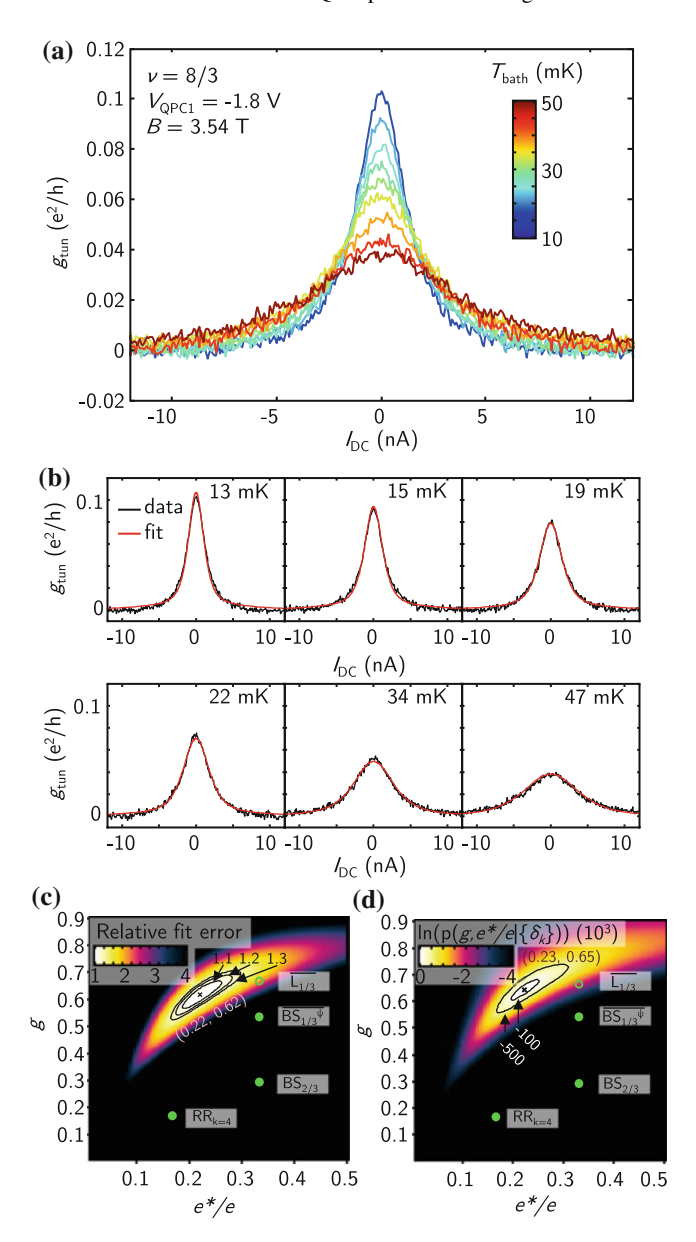


Fig. 11.5 a Zero-bias backscattering peak at $\nu=8/3$ and fixed $V_{\rm QPC1}=-1.8$ V. b Measured (black) and fitted (red) tunneling conductance for different electronic temperatures (fit parameters: $e^*/e=0.22, g=0.62$). c Relative fit error as a function of fit parameters e^*/e and g. Parameters of Abelian (green circles) and non-Abelian (green dots) candidate wave functions are indicated. d PDF of the measured residuals $\{\delta_k\}$ as a function of e^*/e and g. The maximum probability is found for $e^*/e=0.23, g=0.65$ with $\sigma_g=0.0029, \sigma_{e^*/e}=0.0028$ and $\sigma_{g,e^*/e}=0.0028$. (Reprinted figure with permission from [1]. Copyright 2014 by the American Physical Society.)

Table 11.2 Overview of the theoretically proposed parameter pairs g and e^*/e for different states at $\nu = 7/3$ and 8/3 ('n-A': non-Abelian; taken from [52]) and our results for different measurement configurations

configurations			
$\nu = 8/3$			
Theory [52]			
State	e^*/e	g	n-A?
$\overline{L_{1/3}}$	1/3	2/3	No
BS _{2/3}	1/3	7/24	Yes
	1/3	2/3	No
$\overline{{}^{}_{\mathrm{BS}^{\psi}_{1/3}}}$	1/3	13/24	Yes
	1/3	2/3	No
$RR_{k=4}$	1/6	1/6	Yes
Experiment		·	
Config.	e^*/e	g	
I.	0.22	0.62	
II.	0.21-0.25	0.55-0.72	
III.	1/3	0.67-0.82	
IV.	0.19-0.28	0.62-0.84	
V.	1/3	0.76-0.88	
$\nu = 7/3$			
Theory [52]			
State	e^*/e	g	n-A?
L _{1/3}	1/3	1/3	No
$\overline{\mathrm{BS}_{2/3}}$	1/3	23/24	Yes
	1/3	1/3	No
$\overline{\mathrm{BS}_{1/3}^\psi}$	1/3	17/24	Yes
	1/3	1/3	No
$\overline{RR}_{k=4}$	1/6	1/3	Yes
Experiment		·	·
Config.	e^*/e	g	
I.	-	_	
II.	0.21-0.29	0.34-0.45	
III.	1/3	0.47	
IV.	0.28	0.49	
V.	1/3	0.54	

Only edge modes with the lowest QP charge are quoted, as they dominate the tunneling in our experiment. [Config. I.: B and $V_{\rm QPC}$ constant (see Figs. 11.4 and 11.5), II.: $V_{\rm QPC}$ varied (Fig. 11.7), III.: $V_{\rm QPC}$ varied, e^* fixed to e/4 or e/3 (Fig. 11.7), IV.: B varied (Fig. 11.6), V.: B varied, e^* fixed to e/4 or e/3 (Fig. 11.6)]

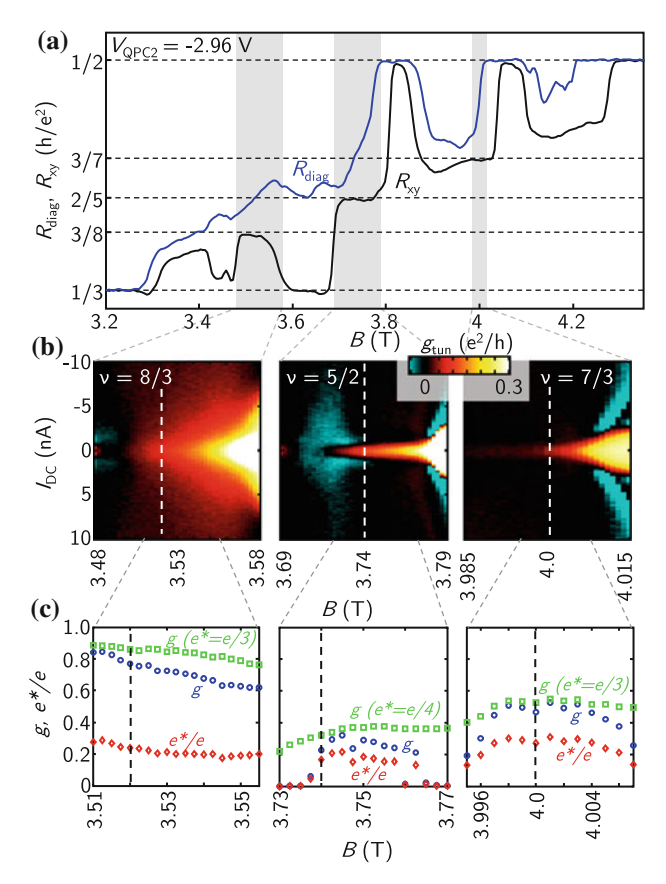


Fig. 11.6 a, b *B*-field and DC bias dependence of the tunneling conductance near $\nu = 8/3$, 5/2 and 7/3. **c** *B*-field dependence of fitting parameters e^*/e (red diamonds), g (blue circles) and g for e^*/e fixed to 1/3 or 1/4 (green squares). The vertical dashed lines in (**b**) and (**c**) indicate the center of the bulk filling factor plateaus. (Reprinted figure with permission from [1]. Copyright 2014 by the American Physical Society.)

11.3.3 Effect of Varying the Coupling via the Magnetic Field

The discussed measurements leave the question of how the extracted parameters e^*/e and g depend on the strength of QP tunneling. To investigate this, the QPC transmission has been varied by changing the B-field. The tunneling conductance g_{tun} is shown as a function of DC bias and B-field in Fig. 11.6b. The B-field has been varied in a small window around the bulk filling factors 8/3, 5/2 and 7/3 (gray shaded areas in Fig. 11.6a). Here, QPC2 instead of QPC1 was used in a different cooldown and V_{QPC2} was fixed at -2.96 V. As the magnetic field strength is increased, backscattering and hence g_{tun} continuously increase. At the same time we move out of the B-field range where the FQH states are fully gapped in the bulk. Hence the interpretation of the QP backscattering peak only makes sense in narrow B-field

regions around the bulk filling factors observed in R_{xy} . At the high magnetic field end of the graphs, reentrant integer quantum Hall (RIQH) states enter and dominate the temperature dependence of the conductance, resulting in a zero-bias peak with increased FWHM. Due to the complicated and dominant temperature-dependence of the RIQH states [55], a qualitative description via (11.1) breaks down as soon as they contribute to the conductance. Away from these states, the FWHM of g_{tun} is constant over a wide B-field interval (see Appendix: "FWHM of tunneling peaks"). The parameters g and e^*/e are extracted from temperature dependent measurements of Fig. 11.6b. They are shown in Fig. 11.6c for the B-field interval in which the peak FWHM is constant. Fits of g_{tun} (11.1) yield g (blue circles) and e^*/e (red diamonds). When e^*/e is not used as a fitting parameter but fixed at 1/3 ($\nu = 7/3$, 8/3) or 1/4 ($\nu = 5/2$), another set of g (green squares) is obtained.

11.3.3.1 $\nu = 8/3$

For $\nu=8/3$ (Fig. 11.6b, c, left column), a continuous decrease of g is observed for an increasing B-field. When the B-field moves away from the bulk 8/3 plateau (at B>3.56 T), the zero-bias peak shape changes (similar to Fig. 11.8a) and hence is not well described by weak tunneling theory any more. In the B-field range where the peak FWHM is constant and no flat peak is observed (Fig. 11.6c), g varies from 0.82 to 0.62 with g=0.77 in the center of the bulk $\nu=8/3$ plateau (indicated by dashed line, Fig. 11.6c). At the same time, e^*/e decreases from 0.28 to 0.20 where it saturates. If e^*/e is fixed to 1/3, we find slightly higher values for g in the range 0.88–0.76.

11.3.3.2 $\nu = 5/2$

For $\nu=5/2$ (Fig. 11.6b, c, middle column), a large region of negative differential tunneling conductance $g_{\rm tun}$ is observed towards the low-field end of the $\nu=5/2$ plateau. The origin of this is not clear. In this case, the undershoots of $g_{\rm tun}$ dominate the fit, yielding small values for g. Towards the center of the $\nu=5/2$ plateau, g and e^*/e take values of g=0.24–0.32 and $e^*/e=0.15$ –0.21. If e^*/e is fixed to 1/4, g saturates at approximately 0.37.

11.3.3.3 $\nu = 7/3$

For $\nu = 7/3$ (Fig. 11.6b, c, right column), a zero-bias peak with constant FWHM is only observed in a very narrow *B*-field window (Fig. 11.6c). Also the amplitude of g_{tun} is much smaller than for $\nu = 8/3$ and 5/2. At the low-field side of this window, the amplitude of the zero-bias peak is too small for a reliable fit of the data over the whole temperature range. At the high-field side, neighboring RIQH states dominate the temperature-dependence of the conductance and broaden the zero-bias peak. In

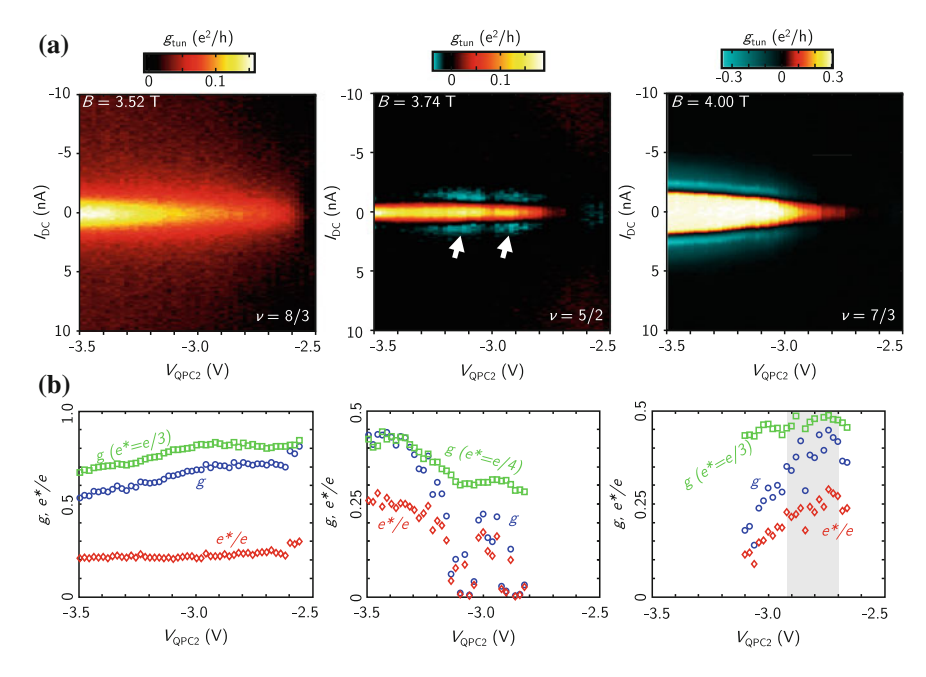


Fig. 11.7 a Dependence of the tunneling conductance at $\nu = 8/3$, 5/2 and 7/3 on the QPC voltage. **b** Fitting parameters e^*/e (red diamonds), g (blue circles) and g for e^*/e fixed to 1/3 or 1/4 (green squares) as a function of $V_{\rm QPC}$. (Reprinted figure with permission from [1]. Copyright 2014 by the American Physical Society.)

between those regimes (where also the bulk plateau center is located, dashed line Fig. 11.6c), g and e^*/e are approximately constant, with g=0.49 and $e^*/e=0.28$. Fixing e^*/e to 1/3, a plateau value of $g\approx 0.54$ is obtained.

11.3.4 Effect of Varying the Coupling via the QPC Transmission

When the magnetic field is varied, we vary the transmission but might also move out of the gap of the investigated FQH states. Instead, the transmission can be controlled by changing the QPC split-gate voltage while the *B*-field is fixed to the center of the $\nu_{\text{bulk}} = 8/3$, 5/2 and 7/3 plateaus. When the QPC is closed (Fig. 11.7a), the amplitude of g_{tun} increases. For $\nu = 5/2$ and 8/3, its FWHM is constant over the whole voltage range, whereas at $\nu = 7/3$, the FWHM increases due to the neighboring RIQH state. The voltage range in which the FWHM is constant is indicated by the gray shaded area in Fig. 11.7b. Parameters g and e^*/e , extracted from the temperature dependence of Fig. 11.7a, are shown in Fig. 11.7b.

11.3.4.1 $\nu = 8/3$

At $\nu=8/3$ (Fig. 11.7, left column), e^*/e is approximately constant at 0.21–0.25 over the whole gate voltage range. For g, constant values of approx. 0.72 are found for small $g_{\rm tun}$, which start to decrease at $V_{\rm QPC}\approx-3.0$ V down to g=0.55. If e^*/e is fixed to 1/3, a similar evolution of g, with slightly higher values (g=0.67–0.82) is found.

11.3.4.2 $\nu = 5/2$

Here (Fig. 11.7, middle column), the FWHM of g_{tun} is constant over the whole voltage range. At $V_{\text{QPC}} \approx -3.15$ V and $V_{\text{QPC}} \approx -2.9$ V (marked by white arrows), the g_{tun} peak is locally enhanced and neighbored by negative differential conductance undershoots. This behavior could be caused by resonant tunneling through a localization in the QPC. Here, the g_{tun} undershoots dominate the fit, yielding small values for e^*/e and g. Towards $V_{\text{QPC}} = -3.5$ V, e^*/e and g saturate at 0.25 and 0.42 respectively. For e^*/e fixed to 1/4, g varies from approx. 0.28 at the onset of the zero bias peak to approx. 0.42 at $V_{\text{OPC}} = -3.5$ V.

11.3.4.3 $\nu = 7/3$

For $\nu=7/3$ (Fig. 11.7, right column), $e^*/e=0.21-0.29$ are observed in the narrow region of constant FWHM (shaded gray). At the same time, we find g=0.34-0.45. Towards more negative $V_{\rm QPC}$, the RIQH temperature dependence again dominates and a reliable fit is not possible. Fixing e^*/e to 1/3, an approximately constant g=0.47 is found.

11.3.5 Breakdown of the Weak Tunneling Regime

As the QPC is pinched off further, a situation can arise in which QPC and bulk have different filling factors. This intermediate tunneling regime has been studied theoretically [56] and experimentally [57, 58] in detail. Figure 11.8a, b shows $R_{\rm diag}$ as QPC 2 is biased very negatively at bulk filling factors 8/3 and 5/2. When QPC 2 is relatively open (meaning the absence of QP tunneling at $V_{\rm QPC} = -2.5$ V), $R_{\rm diag}$ is approximately constant at a value slightly higher than expected for the respective bulk filling factor. As the QPC voltage is decreased, a QP tunneling peak at zero DC bias develops. At higher DC biases, $R_{\rm diag}$ drops close to the flat background value where it is approximately constant. For $\nu_{\rm bulk} = 8/3$, the QP tunneling peak grows, until $R_{\rm diag} \approx 0.42 \ h/e^2$, where $R_{\rm diag}$ develops a plateau in $I_{\rm DC}$ direction. The difference in diagonal resistance between those two values corresponds to $g_{\rm tun} \approx 1/6 \times e^2/h$ (Fig. 11.8a). It should be noted that this is equal to $(8/3 - 5/2) \times e^2/h$. Thus the situation of Fig. 11.8a might be interpreted as the case where the $\nu = 8/3$ edge state is partially reflected from the QPC, leaving a gapped $\nu = 5/2$ state within. As the DC

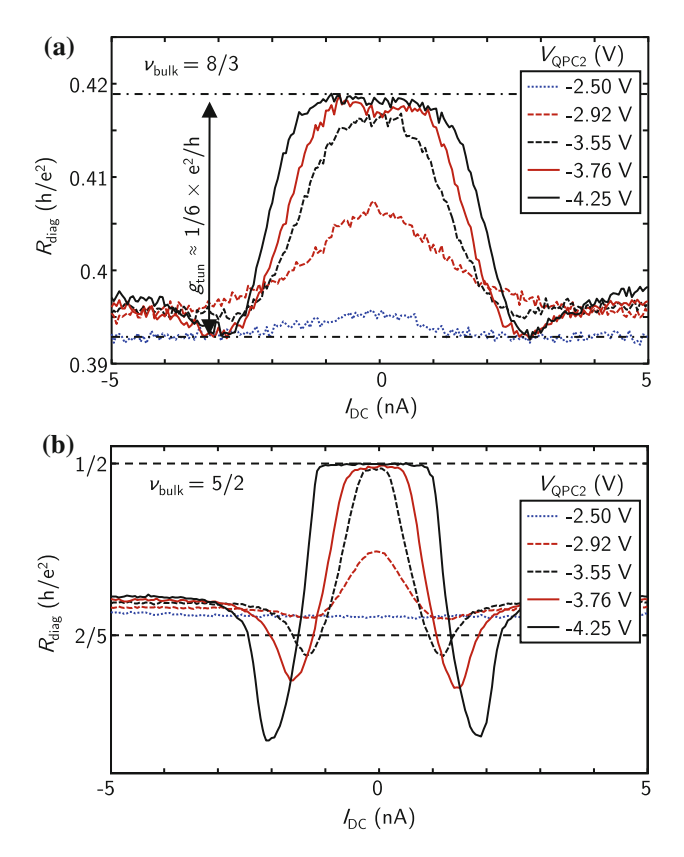


Fig. 11.8 Diagonal resistance across QPC2 (**a** $\nu_{\text{bulk}} = 8/3$, **b** $\nu_{\text{bulk}} = 5/2$) for different QPC voltages as a function of DC bias. (Reprinted figure with permission from [1]. Copyright 2014 by the American Physical Society.)

bias is increased, the gap is destroyed and the QPC filling approaches 8/3 again. At a bulk filling factor of 5/2, a transition to a RIQH state is observed (Fig. 11.8b). Here, $R_{\rm diag}$ is quantized at exactly $2 \times e^2/h$. As the DC bias is increased, strong undershoots in $R_{\rm diag}$ are observed. Then $R_{\rm diag}$ saturates again at around $R_{\rm diag} \approx 2/5 \times h/e^2$.

11.4 Interpretation and Discussion

11.4.1 $\nu = 8/3$

For $\nu=8/3$, all results (see Table 11.2 for an overview) favor the proposed parameters g=2/3 and $e^*/e=1/3$. The BS_{2/3} and $\overline{\mathrm{BS}_{1/3}^{\psi}}$ states support additional non-Abelian

e/3 edge modes with g=7/24 (BS $_{2/3}$) and g=13/24 (BS $_{1/3}^{\psi}$) which should dominate the temperature dependence. Thus the measurements agree best with an Abelian particle-hole conjugate Laughlin state ($\overline{\rm L}_{1/3}$), which qualitatively well reproduces our measurements (see Appendix: "Fits for proposed parameter pairs— $\nu=8/3$ "). In the $V_{\rm QPC}$ dependent measurement, a constant g of approximately 0.72 is observed at the onset of QP tunneling. As the tunneling strength increases, g decreases to 0.55. This might either be caused by additional coupling due to a second edge mode, or the breakdown of the weak tunneling assumptions.

11.4.2 $\nu = 5/2$

Here the interpretation of the results is less clear. If V_{OPC} and B are kept constant, we find $e^*/e = 0.18$ and g = 0.32, close to values reported earlier [24, 25]. For the case of a varying B-field, g of 0.29–0.32 and e^*/e of 0.19–0.21 are observed close to the center of the $R_{xy} = 2/5 \times h/e^2$ plateau. If e^*/e is fixed to 1/4, q saturates at around 0.37. This agrees best with the (1,1,3)- and (3,3,1)-states. As the OPC voltage is changed, an evolution of g with a saturation at $g \approx 0.42$ is observed. This would also be best described by the parameters of the (1,1,3)- and (3,3,1)-states. The origin of the strong modulation of the parameters might be the coupling to a localized state in the QPC, which can substantially influence the transmission [36]. However, at the onset of the QP tunneling peak ($V_{\rm OPC} \approx -2.9 \text{ V}$), $q \approx 0.30$ –0.31 is found. This parameter lies in-between the expectation for the Moore-Read Pfaffian (q = 0.25)and the (3,3,1) and (1,1,3)-states (q=0.375). Overall, our results agree best with the Abelian (3,3,1) and (1,1,3)-states, which qualitatively fits the measurements (see Appendix: "Fits for proposed parameter pairs— $\nu = 5/2$ "). In [24], the \overline{Pf} and $SU_2(2)$ states were found to be the states with the lowest fit error, whereas [25] also found the (3,3,1)-state to be the best fit. As argued in [29], electron-electron interaction within the edge modifies the effective Coulomb interaction parameter g. In this case, both experiments would also be best described by the (3,3,1) and (1,1,3)-states. For a geometry similar to the QPC geometry used by us, the measured g is expected to be enhanced by approximately 0.04 compared to the actual q of the FQH state [29]. Taking this into account would improve the agreement with the (3,3,1)-state in the case where e^*/e is fixed to 1/4 (Fig. 11.4c, d).

It should be noted that the (3,3,1)-state is not compatible with all results obtained by other authors, while the (1,1,3)-state seems to be compatible with all experimental observations. Numerical diagonalization studies however, favor the Moore-Read Pfaffian state or its particle-hole conjugate (\overline{Pf}) [59–69]. To our knowledge, only the spin-unpolarized version of the (3,3,1)-state has been investigated numerically. The question whether the ground state is better described by the Moore-Read Pfaffian or the Anti-Pfaffian has recently raised interest. Both states cannot be distinguished when particle-hole symmetry is assumed [47, 48]. The Pfaffian [70], as well as the Anti-Pfaffian [71] have found support in studies employing different numerical

approaches. Finite thickness effects, which might also have to be taken into account for a correct description of the ground state, have been found to stabilize the Pfaffian ground state [72–74] and to significantly enhance the overlap with the numerical solution. Recent interference experiments [75–77] might indicate non-Abelian statistics. Still, this does not rule out the Abelian (3,3,1) and (1,1,3)-states, as they might show similar signatures in the interference pattern [44, 78]. Experiments probing the spin polarization at $\nu = 5/2$ [79–84] obtained contradicting results for the polarization. Recent experiments suggest a spin transition of the $\nu = 5/2$ state at very low densities [85], similar to $\nu = 8/3$ [86]. Nevertheless, the (3,3,1)-state exists both in a spin-polarized and spin-unpolarized type [29, 51] with identical Coulomb interaction parameter q. In contrast, only the spin-polarized version of the (3, 3, 1) state is allowed for $\nu = 5/2$ [29]. The physical origin of the spin-polarized and spinunpolarized versions of the (3,3,1)-state is however different. The spin-unpolarized version can be understood as Halperin's bilayer (3,3,1)-state [87], where spin up or down electrons take the function of the two different layers [29, 51]. In contrast, the spin-polarized version arises when charge 2e/3 quasiparticles condense on top of a $\nu = 1/3$ Laughlin state [29]. Also the (1,1,3)-state might occur with and without spin polarization [44]. Shot noise experiments report the observation of a neutral mode for $\nu = 5/2$ [88]. Such a counterpropagating neutral mode is not expected for the (3,3,1)-state, but for the (1,1,3)-state. However, recent experiments [89] suggest the presence of neutral modes, even for non-particle-hole-conjugate FOH states. Thus, the existence of a neutral mode might not directly allow to draw conclusions about the wave function of the corresponding FQH liquid.

As pointed out earlier [25, 90], these inconsistencies might indicate that the $\nu = 5/2$ state might form different wave functions, depending on the physical situation.

11.4.3 $\nu = 7/3$

For $\nu=7/3$, the problem arises that $e^*/e=1/3$ and g=1/3 are proposed for the $L_{1/3}$ state and the non-Abelian edge modes of the $\overline{BS}_{2/3}$ and $BS_{1/3}^{\psi}$ states. Here, the dominant temperature dependence is expected to be due to the Abelian edge modes (smallest g), in contrast to the case at $\nu=8/3$. This makes the discrimination of these states in this experiment impossible. Experimentally, we observe g>1/3 (g saturates at approximately 0.49 when the B-field is varied and g=0.34–0.45 when changing $V_{\rm QPC}$), which might stem from a contribution of a second (non-Abelian) edge mode. The fact that the FQH state at $\nu=8/3$ is best described by a particle-hole conjugate Laughlin state ($\overline{L}_{1/3}$) does not imply that the 7/3 state must be the corresponding non-conjugate partner state ($L_{1/3}$). As argued in [52], particle-hole symmetry might for example be broken by LL mixing, or other effects.

11.4.4 Experimental Limitations and Origin of Systematic Errors

In an ideal system, density is homogeneous and edge states are brought in close proximity by the QPC, until QPs tunnel between two points of the counterpropagating edge states. However, in a realistic system, density is not perfectly homogeneous. The coexistence of different FQH states in the bulk and the constriction strongly modifies the system's behavior. For the system studied here, densities of constriction and bulk are sufficiently similar to avoid the coexistence of different FQH states in the second LL (Fig. 11.2). However, density-modulated RIQH states are observed in close proximity to $\nu = 5/2$, 7/3 and 8/3. If such states are formed within the constriction, they might strongly modify the temperature scaling of the conductance. At $\nu = 5/2$ and 8/3, a pronounced zero-bias peak is visible, sufficiently far away from the parameter ranges where a contribution of the RIQH states to the conductance becomes visible (Figs. 11.6b and 11.7a). Thus we here expect a negligible influence of the density modulated phases. However, for $\nu = 7/3$, a zero-bias peak is only visible in close proximity to the parameter ranges where the neighboring RIQH state clearly dominates the conductance (Figs. 11.6b and 11.7a). Although tunneling parameters have been extracted in the regions where the FWHM of the zero-bias peak is constant, a contribution of the neighboring RIQH state cannot be fully excluded.

Another question is the validity of the weak tunneling assumption. In the second LL, the FQH states contribute $G=2\frac{e^2}{h}+\delta G$ to the conductance. For the weak tunneling approximation to hold, $g_{\text{tun}}\ll\delta G$ is required (if edge reconstruction is present, additional complication might occur). At $\nu=8/3$ ($g_{\text{tun}}\approx0.1\times e^2/h$, $\delta G=2/3\times e^2/h$) and $\nu=7/3$ ($g_{\text{tun}}\approx0.05\times e^2/h$, $\delta G=1/3\times e^2/h$), this condition is well satisfied within the experimental possibilities. At $\nu=5/2$, we have $\delta G=0.5\times e^2/h$. As the temperature is lowered, g_{tun} increases from $g_{\text{tun}}<0.05\times e^2/h$ to $g_{\text{tun}}\approx0.15\times e^2/h$. Over the whole range, the amplitude of g_{tun} is well described by a power law T^{2g-2} . When crossing from the weak tunneling regime to the strong tunneling regime, a continuous change of the Coulomb interaction parameter g is expected [91]. This is not observed at $\nu=5/2$. Thus we conclude that also in this case we are in, or sufficiently close to the weak tunneling regime.

Other effects that might cause a systematic measurement error are for example a drift of the QPC transmission and errors in the temperature measurement. However, both of these effects are expected to have a small influence and cannot account for the systematic deviation between measurements and theoretically predicted parameters (Figs. 11.4c, d and 11.5c, d).

Furthermore, the tunneling conductance $g_{\text{tun}} \approx (R_{\text{diag}} - R_{\text{xy}})/R_{\text{xy}}^2$ is an approximation that is only valid in the weak tunneling regime when $R_{\text{diag}} \approx R_{\text{xy}}$. For extracting the bias dependence of g_{tun} , we have assumed that the current reflected at the QPC is much smaller than the current transmitted. These approximations are expected to give an error less than approximately 5% for g_{tun} .

11.5 Conclusion

In conclusion, we have measured weak quasiparticle tunneling across a QPC at $\nu =$ 8/3, 5/2 and 7/3. Comparison with theory allowed the extraction of tunneling parameters and comparison with proposed wave functions for these states. A summary of theoretical predictions [29, 51, 52] and of our findings can be found in Tables 11.1 and 11.2. Quantitatively, none of the proposed wave functions for $\nu = 5/2$, 7/3 and 8/3 lies within the statistical error. Qualitatively, the $\nu = 5/2$ state is well described by an Abelian (3,3,1) or (1,1,3)-state. However, other experimental findings pose the question of whether the $\nu = 5/2$ state can manifest in different wave functions, depending on the physical situation. Furthermore we show that the OP tunneling strength has an impact on extracted tunneling parameters, especially for $\nu = 5/2$. For $\nu = 8/3$, an ordinary particle-hole conjugate Laughlin state reproduces our data best, while proposed non-Abelian edge modes are much less likely. At $\nu = 7/3$, extracted values for g are not in agreement with the predicted parameters for non-Abelian edge modes. However, the observed parameters g are higher than expected for an ordinary Laughlin state or other Abelian edge modes, which might indicate the presence of several edge modes, in which case identical parameters for different edge modes make a discrimination of the wave functions for $\nu = 7/3$ impossible.

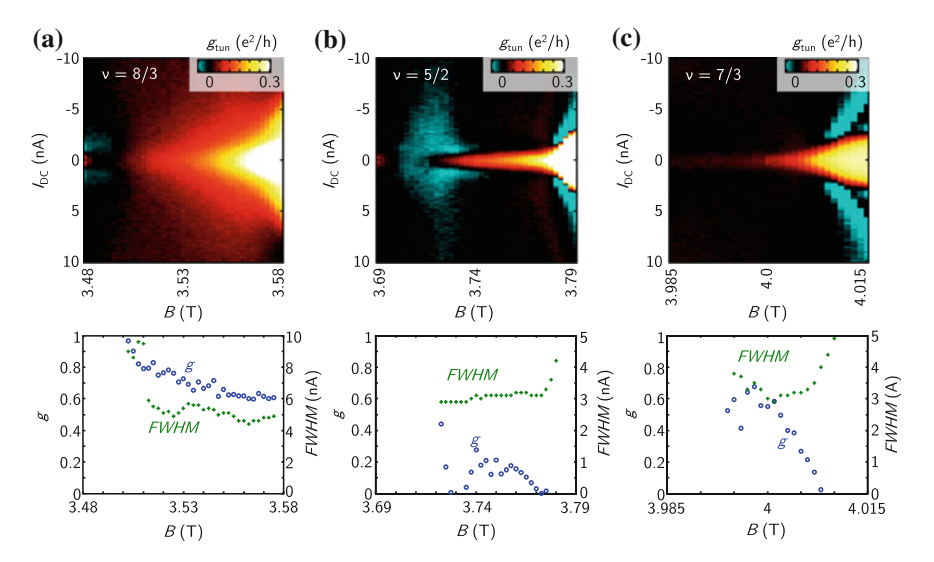


Fig. 11.9 FWHM of QP tunneling peaks (green crosses) as a function of the B-field. Parameters g, extracted only from the $I_{\rm DC}=0$ scaling of $g_{\rm tun}$ are shown as blue circles

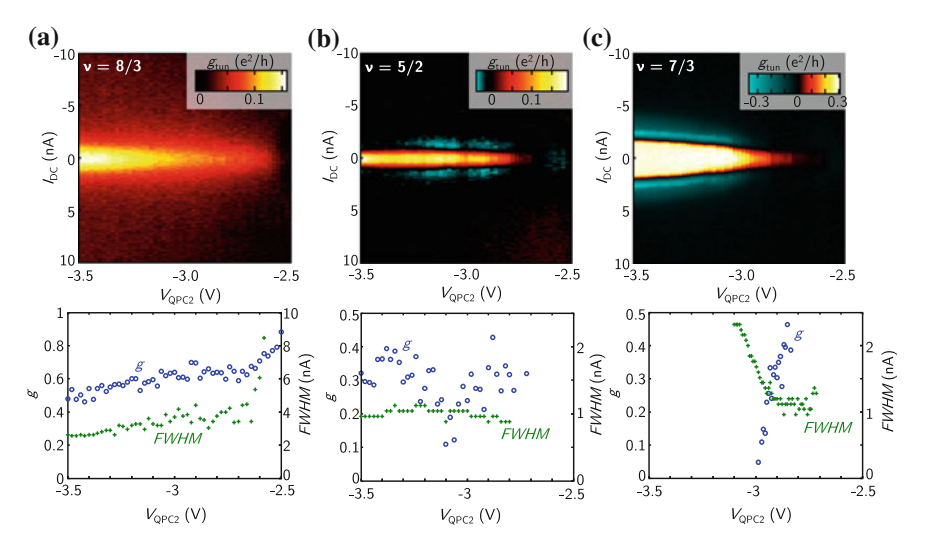


Fig. 11.10 FWHM of QP tunneling peaks (green crosses) as a function of $V_{\rm QPC}$. Parameters g, extracted only from the $I_{\rm DC}=0$ scaling of $g_{\rm tun}$ are shown as blue circles

Appendix

FWHM of Tunneling Peaks

Figures 11.9 and 11.10 show the FWHM of the zero-bias peaks at $\nu=8/3$, 5/2 and 7/3. For $\nu=7/3$, only a small parameter region with constant FWHM is found. As soon as a neighboring RIQH state contributes to the conductance, the peak FWHM is drastically increased (Figs. 11.9b, c and 11.10c). Parameters g which are indicated in Figs. 11.9 and 11.10 are extracted solely from the $g_{\text{tun}}|_{I_{\text{DC}}=0} \propto T^{2g-2}$ temperature scaling, in contrast to fits of the whole expression (11.1) used in the previous sections (Figs. 11.6 and 11.7). Resulting values for g are similar for both methods.

Fits for Proposed Parameter Pairs— $\nu = 5/2$

A qualitative evaluation of the agreement with proposed wave functions can be performed by fixing the parameters g and e^*/e to parameters proposed for different states (see Tables 11.1 and 11.2) and fitting A and g_{∞} . For $\nu = 5/2$, g = 0.375 and $e^*/e = 0.25$, corresponding to the (3,3,1)-state, produce a (qualitatively) good agreement with measurement and calculation (Figs. 11.11 and 11.12).

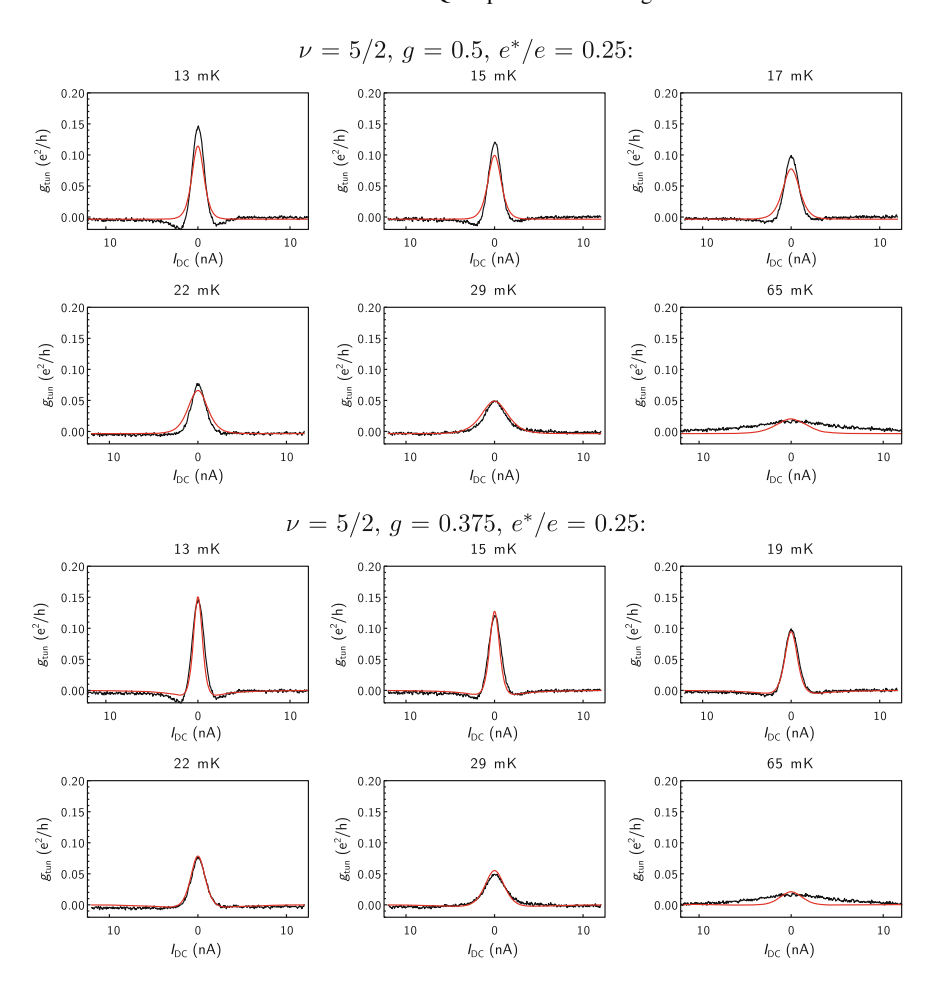


Fig. 11.11 Comparison between experimental and calculated g_{tun} for proposed parameter pairs ($\nu = 5/2$)

Fits for Proposed Parameter Pairs— $\nu = 8/3$

As before, we compare the calculated g_{tun} for theoretically proposed parameters with our measurements. For g=2/3 and $e^*/e=1/3$, a (qualitatively) good agreement is found (Figs. 11.13 and 11.14).

Appendix 209

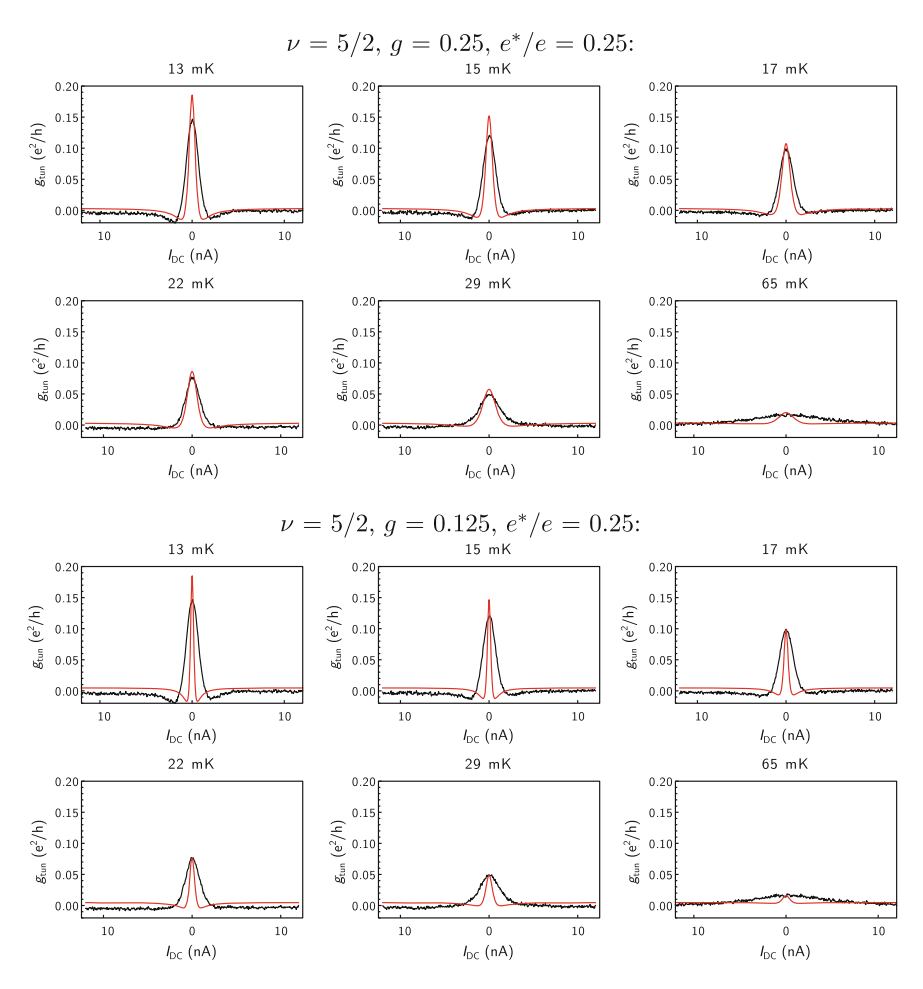


Fig. 11.12 Comparison between experimental and calculated g_{tun} for proposed parameter pairs $(\nu = 5/2)$

Additional Fits— V_{QPC} Dependence

The tunneling conductance measured at different QPC voltages (see Fig. 11.7) and fitted curves are shown in Figs. 11.15, 11.16, 11.17, 11.18, 11.19, 11.20 and 11.21 for $\nu = 8/3$, 5/2 and 7/3.

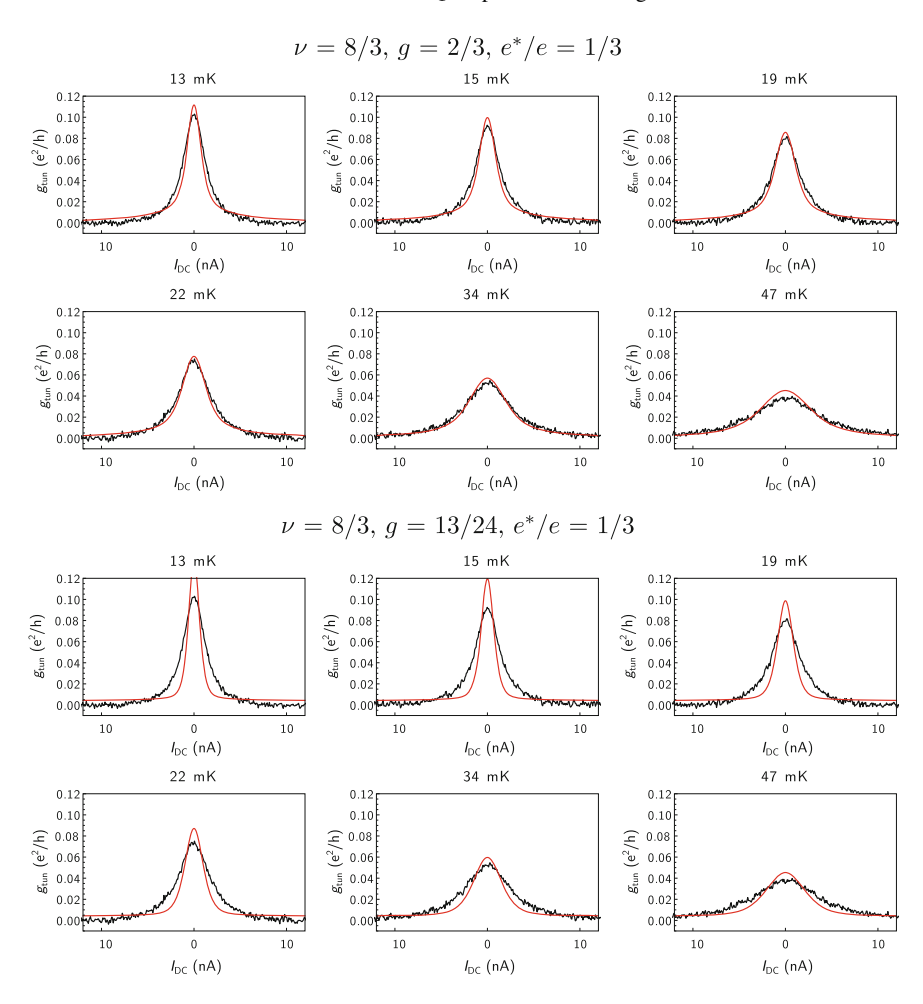


Fig. 11.13 Comparison between experimental and calculated g_{tun} for proposed parameter pairs $(\nu = 8/3)$

Appendix 211

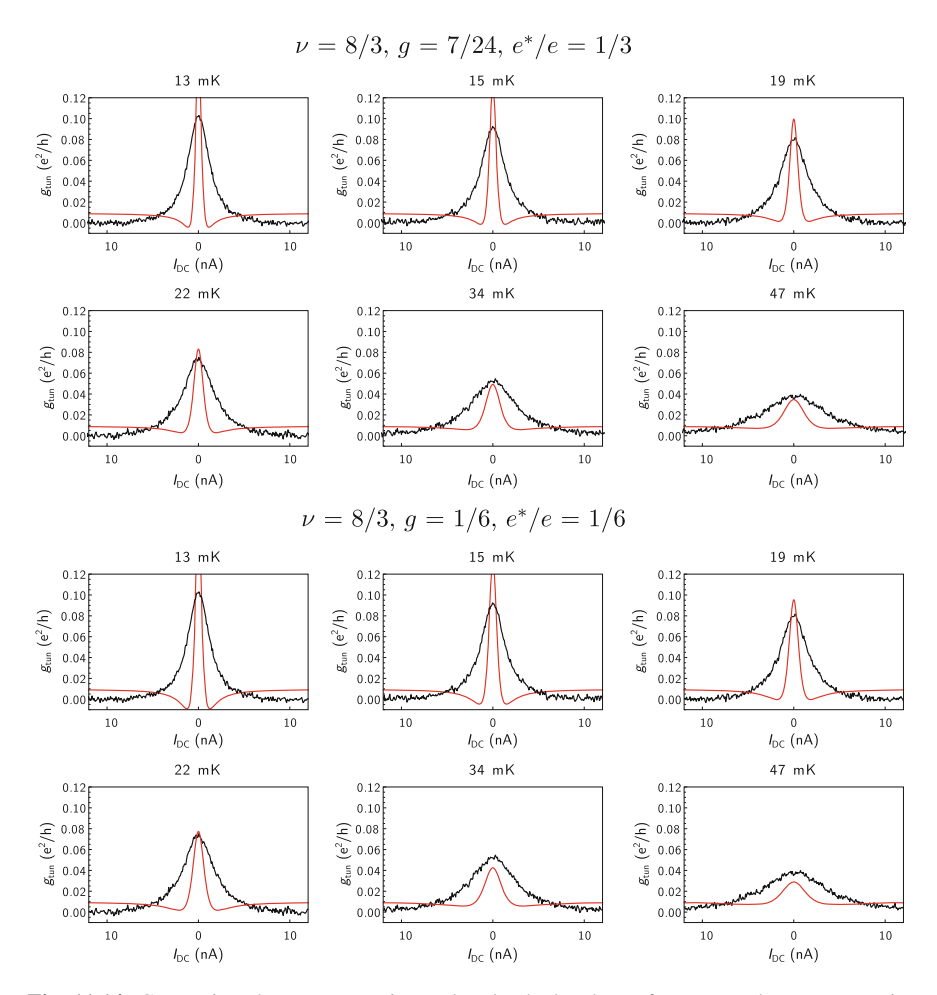


Fig. 11.14 Comparison between experimental and calculated g_{tun} for proposed parameter pairs $(\nu = 8/3)$

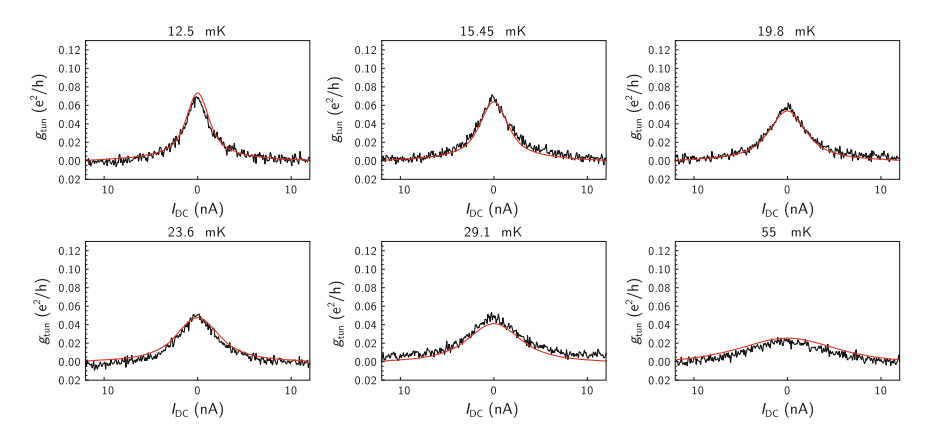


Fig. 11.15 Measurement data (*black*) and fitted weak tunneling conductance (*red*) for $\nu=8/3$ and $V_{\rm OPC}=-2.9$ V. The temperature is varied between T=12.5 mK and T=55 mK

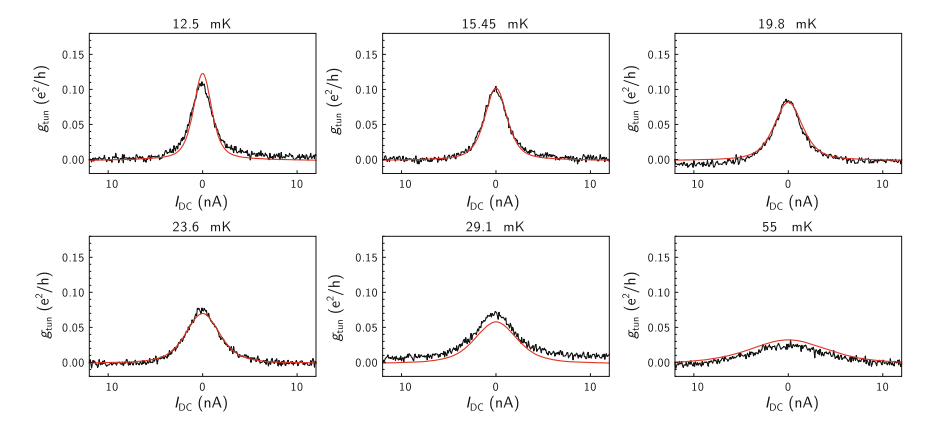


Fig. 11.16 Measurement data (*black*) and fitted weak tunneling conductance (*red*) for $\nu = 8/3$ and $V_{\rm OPC} = -3.3$ V. The temperature is varied between T = 12.5 mK and T = 55 mK

Appendix 213

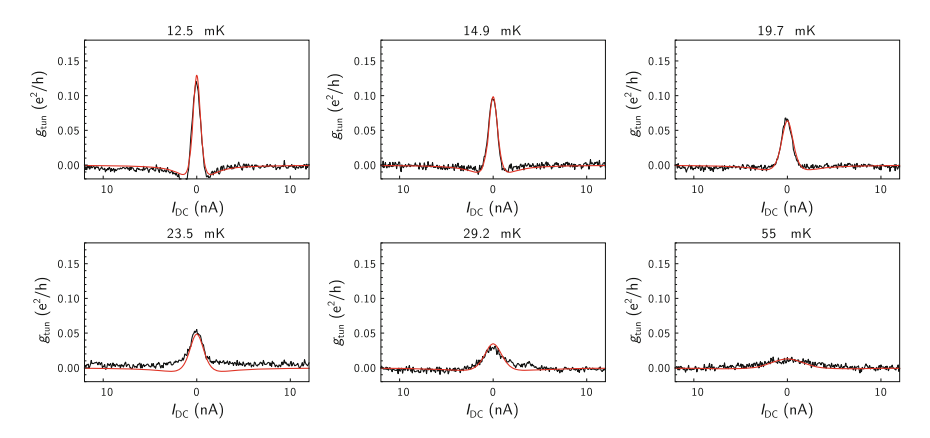


Fig. 11.17 Measurement data (*black*) and fitted weak tunneling conductance (*red*) for $\nu = 5/2$ and $V_{\rm QPC} = -3.0$ V. The temperature is varied between T = 12.5 mK and T = 55 mK

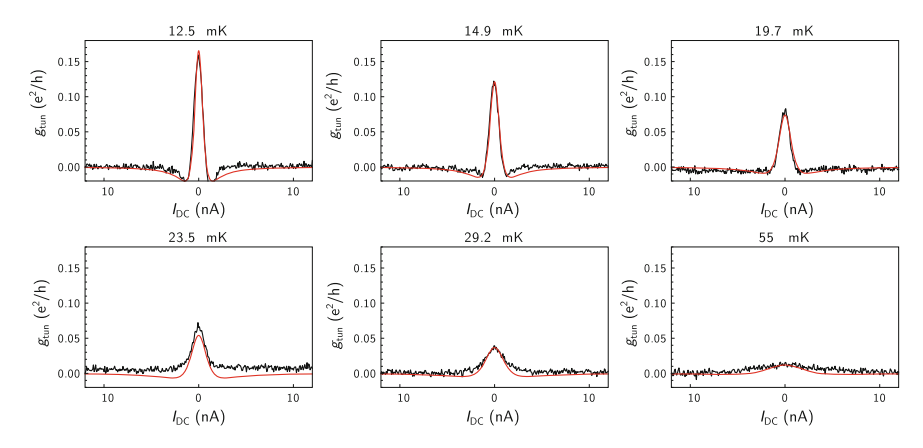


Fig. 11.18 Measurement data (*black*) and fitted weak tunneling conductance (*red*) for $\nu=5/2$ and $V_{\rm QPC}=-3.08$ V. The temperature is varied between T=12.5 mK and T=55 mK

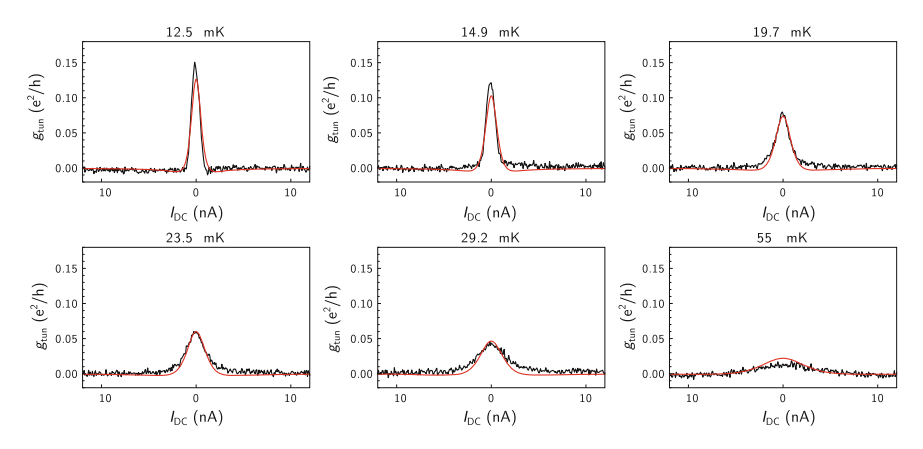


Fig. 11.19 Measurement data (*black*) and fitted weak tunneling conductance (*red*) for $\nu = 5/2$ and $V_{\rm OPC} = -3.48$ V. The temperature is varied between T = 12.5 mK and T = 55 mK

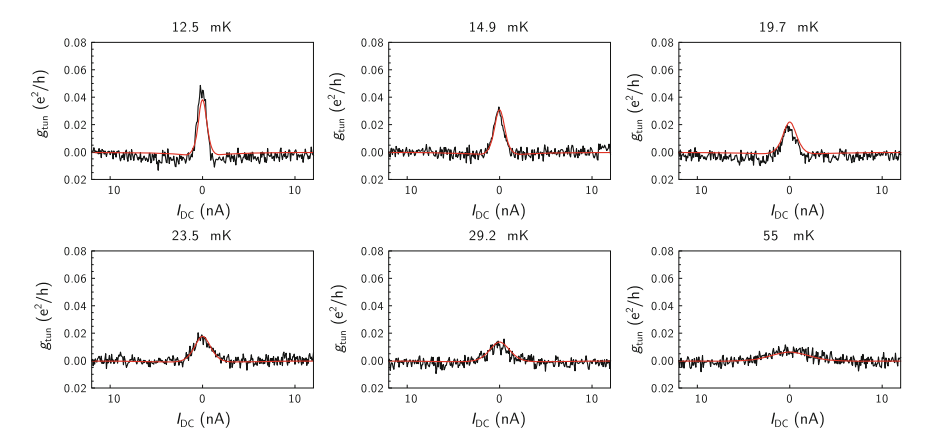


Fig. 11.20 Measurement data (*black*) and fitted weak tunneling conductance (*red*) for $\nu=7/3$ and $V_{\rm QPC}=-2.804$ V. The temperature is varied between T=12.5 mK and T=55 mK

11.5 Conclusion 215

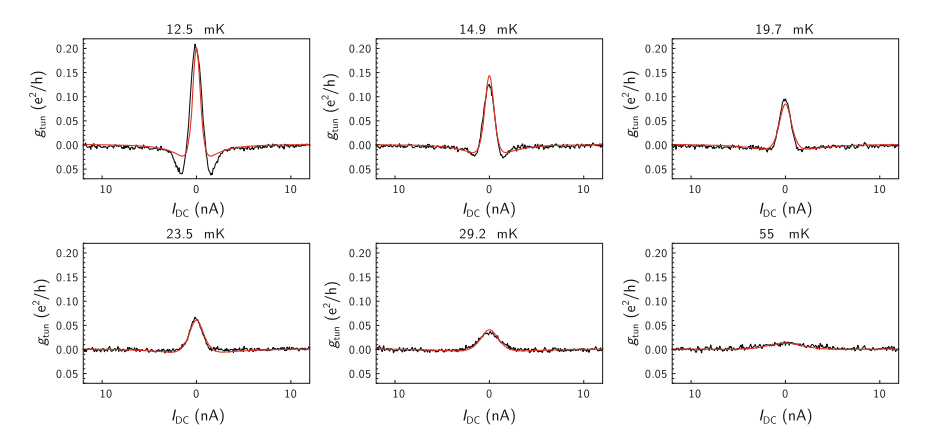


Fig. 11.21 Measurement data (*black*) and fitted weak tunneling conductance (*red*) for $\nu = 7/3$ and $V_{\rm OPC} = -2.956$ V. The temperature is varied between T = 12.5 mK and T = 55 mK

References

- S. Baer, C. Rössler, T. Ihn, K. Ensslin, C. Reichl, W. Wegscheider, Phys. Rev. B 90, 075403 (2014). doi:10.1103/PhysRevB.90.075403
- 2. A. Wójs, Phys. Rev. B 63, 125312 (2001). doi:10.1103/PhysRevB.63.125312
- A.C. Balram, Y.-H. Wu, G.J. Sreejith, A. Wójs, J.K. Jain, Phys. Rev. Lett. 110, 186801 (2013). doi:10.1103/PhysRevLett.110.186801
- A.H. MacDonald, S.M. Girvin, Phys. Rev. B 33, 4009 (1986). doi:10.1103/PhysRevB.33. 4009
- N. d'Ambrumenil, A.M. Reynolds, J. Phys. C: Solid State Phys. 21, 119 (1988). doi:10.1088/ 0022-3719/21/1/010
- P. Bonderson, J.K. Slingerland, Phys. Rev. B 78, 125323 (2008). doi:10.1103/PhysRevB.78. 125323
- 7. N. Read, E. Rezayi, Phys. Rev. B 59, 8084 (1999). doi:10.1103/PhysRevB.59.8084
- 8. R. Willett, J.P. Eisenstein, H.L. Störmer, D.C. Tsui, A.C. Gossard, J.H. English, Phys. Rev. Lett. 59, 1776 (1987). doi:10.1103/PhysRevLett.59.1776
- 9. R.L. Willett, Rep. Prog. Phys. **76**, 076501 (2013). doi:10.1088/0034-4885/76/7/076501
- W. Pan, J.-S. Xia, V. Shvarts, D.E. Adams, H.L. Stormer, D.C. Tsui, L.N. Pfeiffer, K.W. Baldwin, K.W. West, Phys. Rev. Lett. 83, 3530 (1999). doi:10.1103/PhysRevLett.83.3530
- J.P. Eisenstein, K.B. Cooper, L.N. Pfeiffer, K.W. West, Phys. Rev. Lett. 88, 076801 (2002). doi:10.1103/PhysRevLett.88.076801
- 12. M.H. Freedman, Proc. Nat. Acad. Sci. 95, 98 (1998). http://www.pnas.org/content/95/1/98
- 13. A.Y. Kitaev, Ann. Phys. **303**, 2 (2003). doi:10.1016/S0003-4916(02)00018-0
- C. Nayak, S.H. Simon, A. Stern, M. Freedman, S. Das Sarma, Rev. Modern Phys. 80, 1083 (2008). doi:10.1103/RevModPhys.80.1083
- V. Venkatachalam, A. Yacoby, L. Pfeiffer, K. West, Nature 469, 185 (2011). doi:10.1038/ nature09680
- M. Dolev, Y. Gross, R. Sabo, I. Gurman, M. Heiblum, V. Umansky, D. Mahalu, Phys. Rev. Lett. 107, 036805 (2011). doi:10.1103/PhysRevLett.107.036805

- Y. Gross, M. Dolev, M. Heiblum, V. Umansky, D. Mahalu, Phys. Rev. Lett. 108, 226801 (2012). doi:10.1103/PhysRevLett.108.226801
- A. Kumar, G.A. Csáthy, M.J. Manfra, L.N. Pfeiffer, K.W. West, Phys. Rev. Lett. 105, 246808 (2010). doi:10.1103/PhysRevLett.105.246808
- 19. A.M. Chang, Rev. Mod. Phys. 75, 1449 (2003). doi:10.1103/RevModPhys.75.1449
- 20. X.-G. Wen, Quantum Field Theory of Many-Body Systems: From the Origin of Sound to an Origin of Light and Electrons (OUP, Oxford, 2007)
- 21. E. Fradkin, Field Theories of Condensed Matter Physics (Cambridge University Press, 2013)
- F. Milliken, C. Umbach, R. Webb, Solid State Commun. 97, 309 (1996). doi:10.1103/ PhysRevB.68.113309
- A.M. Chang, L.N. Pfeiffer, K.W. West, Phys. Rev. Lett. 77, 2538 (1996). doi:10.1103/ PhysRevLett.77.2538
- I.P. Radu, J.B. Miller, C.M. Marcus, M.A. Kastner, L.N. Pfeiffer, K.W. West, Science 320, 899 (2008). doi:10.1126/science.1157560
- X. Lin, C. Dillard, M.A. Kastner, L.N. Pfeiffer, K.W. West, Phys. Rev. B 85, 165321 (2012). doi:10.1103/PhysRevB.85.165321
- P. Fendley, M.P.A. Fisher, C. Nayak, Phys. Rev. B 75, 045317 (2007). doi:10.1103/PhysRevB. 75.045317
- A. Feiguin, P. Fendley, M.P.A. Fisher, C. Nayak, Phys. Rev. Lett. 101, 236801 (2008). doi:10. 1103/PhysRevLett.101.236801
- 28. S. Das, S. Rao, D. Sen, EPL (Europhys. Lett.) **86**, 37010 (2009). doi:10.1209/0295-5075/86/37010
- 29. G. Yang, D.E. Feldman, Phys. Rev. B 88, 085317 (2013). doi:10.1103/PhysRevB.88.085317
- 30. X.-G. Wen, Int. J. Mod. Phys. B 06, 1711 (1992). doi:10.1142/S0217979292000840
- 31. Y. Zhang, Waves, particles, and interactions in reduced dimensions, Ph.D. thesis, Harvard University, Cambridge, Massachusetts (2009)
- 32. C. Reichl, J. Chen, S. Baer, C. Rössler, T. Ihn, K. Ensslin, W. Dietsche, W. Wegscheider, New J. Phys. **16**, 023014 (2014). doi:10.1088/1367-2630/16/2/023014
- J. Engert, D. Heyer, J. Beyer, H.-J. Barthelmess, J. Phys.: Conf. Ser. 400, 052003 (2012). doi:10.1088/1742-6596/400/5/052003
- J. Engert, J. Beyer, D. Drung, A. Kirste, D. Heyer, A. Fleischmann, C. Enss, H.-J. Barthelmess,
 J. Phys.: Conf. Ser. 150, 012012 (2009). doi:10.1088/1742-6596/150/1/012012
- C. Rössler, T. Feil, P. Mensch, T. Ihn, K. Ensslin, D. Schuh, W. Wegscheider, New J. Phys. 12, 043007 (2010). doi:10.1088/1367-2630/12/4/043007
- S. Baer, C. Rössler, E.C. de Wiljes, P.-L. Ardelt, T. Ihn, K. Ensslin, C. Reichl, W. Wegscheider, Phys. Rev. B 89, 085424 (2014). doi:10.1103/PhysRevB.89.085424
- 37. X.-G. Wen, Phys. Rev. B 44, 5708 (1991). doi:10.1103/PhysRevB.44.5708
- 38. C. de C. Chamon, X.G. Wen, Phys. Rev. Lett. **70**, 2605 (1993). doi:10.1103/PhysRevB.47. 12605
- C. de C. Chamon, D.E. Freed, S.A. Kivelson, S.L. Sondhi, X.G. Wen, Phys. Rev. B 55, 2331 (1997). doi:10.1103/PhysRevB.55.2331
- 40. B.J. Overbosch, Edge tunneling and transport in non-abelian fractional quantum hall systems, Ph.D. thesis, Massachusetts Institute of Technology (2008)
- 41. X.G. Wen, Q. Niu, Phys. Rev. B 41, 9377 (1990). doi:10.1103/PhysRevB.41.9377
- 42. B. Blok, X.G. Wen, Phys. Rev. B 42, 8145 (1990). doi:10.1103/PhysRevB.42.8145
- 43. X.G. Wen, A. Zee, Phys. Rev. B 46, 2290 (1992). doi:10.1103/PhysRevB.46.2290
- 44. G. Yang, D.E. Feldman, arXiv:1406.2263 [cond-mat] (2014), arXiv:1406.2263
- 45. J. Yang, W. Su, Z. Su, Mod. Phys. Lett. B 06, 119 (1992). doi:10.1088/0022-3719/21/1/010
- 46. G. Moore, N. Read, Nucl. Phys. B **360**, 362 (1991). doi:10.1016/0550-3213(91)90407-O
- M. Levin, B.I. Halperin, B. Rosenow, Phys. Rev. Lett. 99, 236806 (2007). doi:10.1103/ PhysRevLett.99.236806
- S.-S. Lee, S. Ryu, C. Nayak, M.P.A. Fisher, Phys. Rev. Lett. 99, 236807 (2007). doi:10.1103/ PhysRevLett.99.236807
- 49. X.G. Wen, Phys. Rev. Lett. 66, 802 (1991). doi:10.1103/PhysRevLett.66.802

Appendix 217

- 50. B. Blok, X. Wen, Nucl. Phys. B 374, 615 (1992). doi:10.1016/0550-3213(92)90402-W
- 51. B.J. Overbosch, X.-G. Wen, arXiv:0804.2087 [cond-mat] (2008)
- W. Bishara, P. Bonderson, C. Nayak, K. Shtengel, J.K. Slingerland, Phys. Rev. B 80, 155303 (2009). doi:10.1103/PhysRevB.80.155303
- 53. D.S. Sivia, J. Skilling, Data Analysis: A Bayesian Tutorial (Oxford University Press, 2006)
- 54. A. Stern, Ann. Phys. **323**, 204 (2008). doi:10.1016/j.aop.2007.10.008
- N. Deng, A. Kumar, M.J. Manfra, L.N. Pfeiffer, K.W. West, G.A. Csáthy, Phys. Rev. Lett. 108, 086803 (2012). doi:10.1103/PhysRevLett.108.086803
- P. Fendley, A.W.W. Ludwig, H. Saleur, Phys. Rev. B 52, 8934 (1995). doi:10.1103/PhysRevB. 52.8934
- S. Roddaro, V. Pellegrini, F. Beltram, G. Biasiol, L. Sorba, Phys. Rev. Lett. 93, 046801 (2004). doi:10.1103/PhysRevLett.93.046801
- S. Roddaro, V. Pellegrini, F. Beltram, Solid State Commun. 131, 565 (2004). doi:10.1016/j. ssc.2004.05.049
- 59. R.H. Morf, Phys. Rev. Lett. **80**, 1505 (1998). doi:10.1103/PhysRevLett.80.1505
- E.H. Rezayi, F.D.M. Haldane, Phys. Rev. Lett. 84, 4685 (2000). doi:10.1103/PhysRevLett. 84.4685
- A.E. Feiguin, E. Rezayi, C. Nayak, S. Das Sarma, Phys. Rev. Lett. 100, 166803 (2008). doi:10. 1103/PhysRevLett.100.166803
- 62. G. Möller, S.H. Simon, Phys. Rev. B 77, 075319 (2008). doi:10.1103/PhysRevB.77.075319
- A.E. Feiguin, E. Rezayi, K. Yang, C. Nayak, S. Das Sarma, Phys. Rev. B 79, 115322 (2009). doi:10.1103/PhysRevB.79.115322
- O.S. Zozulya, M. Haque, N. Regnault, Phys. Rev. B 79, 045409 (2009). doi:10.1103/ PhysRevB.79.045409
- M. Storni, R.H. Morf, S. Das Sarma, Phys. Rev. Lett. 104, 076803 (2010). doi:10.1103/ PhysRevLett.104.076803
- G. Möller, A. Wójs, N.R. Cooper, Phys. Rev. Lett. 107, 036803 (2011). doi:10.1103/ PhysRevLett.107.036803
- X. Wan, K. Yang, E.H. Rezayi, Phys. Rev. Lett. 97, 256804 (2006). doi:10.1103/PhysRevLett. 97.256804
- X. Wan, Z.-X. Hu, E.H. Rezayi, K. Yang, Phys. Rev. B 77, 165316 (2008). doi:10.1103/ PhysRevB.77.165316
- I. Dimov, B.I. Halperin, C. Nayak, Phys. Rev. Lett. 100, 126804 (2008). doi:10.1103/ PhysRevLett.100.126804
- A. Wójs, C. Tőke, J.K. Jain, Phys. Rev. Lett. 105, 096802 (2010). doi:10.1103/PhysRevLett. 105.096802
- E.H. Rezayi, S.H. Simon, Phys. Rev. Lett. 106, 116801 (2011). doi:10.1103/PhysRevLett. 106.116801
- M.R. Peterson, T. Jolicoeur, S. Das Sarma, Phys. Rev. Lett. 101, 016807 (2008). doi:10.1103/ PhysRevLett.101.016807
- M.R. Peterson, T. Jolicoeur, S. Das Sarma, Phys. Rev. B 78, 155308 (2008). doi:10.1103/ PhysRevB.78.155308
- J. Biddle, M.R. Peterson, S. Das Sarma, Phys. Rev. B 84, 125141 (2011). doi:10.1103/ PhysRevB.84.125141
- R.L. Willett, C. Nayak, K. Shtengel, L.N. Pfeiffer, K.W. West, Phys. Rev. Lett. 111, 186401 (2013). doi:10.1103/PhysRevLett.111.186401
- R.L. Willett, L.N. Pfeiffer, K.W. West, Proc. Nat. Acad. Sci. 106, 8853 (2009). doi:10.1073/pnas.0812599106
- R.L. Willett, L.N. Pfeiffer, K.W. West, Phys. Rev. B 82, 205301 (2010). doi:10.1103/ PhysRevB.82.205301
- A. Stern, B. Rosenow, R. Ilan, B.I. Halperin, Phys. Rev. B 82, 085321 (2010). doi:10.1103/ PhysRevB.82.085321
- C. Zhang, T. Knuuttila, Y. Dai, R.R. Du, L.N. Pfeiffer, K.W. West, Phys. Rev. Lett. 104, 166801 (2010). doi:10.1103/PhysRevLett.104.166801

- M. Stern, P. Plochocka, V. Umansky, D.K. Maude, M. Potemski, I. Bar-Joseph, Phys. Rev. Lett. 105, 096801 (2010). doi:10.1103/PhysRevLett.105.096801
- 81. T.D. Rhone, J. Yan, Y. Gallais, A. Pinczuk, L. Pfeiffer, K. West, Phys. Rev. Lett. **106**, 196805 (2011). doi:10.1103/PhysRevLett.106.196805
- L. Tiemann, G. Gamez, N. Kumada, K. Muraki, Science 335, 828 (2012). doi:10.1126/science. 1216697
- 83. M. Stern, B.A. Piot, Y. Vardi, V. Umansky, P. Plochocka, D.K. Maude, I. Bar-Joseph, Phys. Rev. Lett. **108**, 066810 (2012). doi:10.1103/PhysRevLett.108.066810
- U. Wurstbauer, K.W. West, L.N. Pfeiffer, A. Pinczuk, Phys. Rev. Lett. 110, 026801 (2013). doi:10.1103/PhysRevLett.110.026801
- W. Pan, A. Serafin, J.S. Xia, L. Yin, N.S. Sullivan, K.W. Baldwin, K.W. West, L.N. Pfeiffer,
 D.C. Tsui, Phys. Rev. B 89, 241302 (2014). doi:10.1103/PhysRevB.68.241302
- W. Pan, K.W. Baldwin, K.W. West, L.N. Pfeiffer, D.C. Tsui, Phys. Rev. Lett. 108, 216804 (2012). doi:10.1103/PhysRevLett.108.216804
- 87. B.I. Halperin, Helv. Phys. Acta 56, 75 (1983). doi:10.5169/seals-115362
- 88. A. Bid, N. Ofek, H. Inoue, M. Heiblum, C.L. Kane, V. Umansky, D. Mahalu, Nature **466**, 585 (2010), bibtex: Bid2010. doi:10.1038/nature09277
- H. Inoue, A. Grivnin, Y. Ronen, M. Heiblum, V. Umansky, D. Mahalu, Nature Commun. 5 (2014). doi:10.1038/ncomms5067
- 90. J.K. Jain, Physics 3, 71 (2010). doi:10.1038/srep01416
- 91. C.L. Kane, M.P.A. Fisher, in *Perspectives in Quantum Hall Effects*, ed. by S.D. Sarma, A. Pinczuk (Wiley-VCH Verlag GmbH, 2007), pp. 109–159

Part IV Quantum Dot and Interferometer Experiments

Chapter 12 **Quantum Dots and Charge Detection Techniques**

Abstract We briefly introduce the basics of quantum dots and charge detection techniques. Interferometry experiments in the quantum Hall regime rely on the use of large quantum dots that are operated as analog of a Fabry-Pérot interferometer. Charge detection techniques are a powerful tool that provides additional insight about the internal dynamics of such a system. We discuss how the sensitivity of charge detectors can be further improved by reducing screening and by inducing a localized state in the quantum point contacts' confinement potential. Exploiting these techniques, we are able to perform fast and well-resolved charge detection of a micron-sized quantum dot in the quantum Hall regime.

12.1 Introduction

In the preceding chapters, we have discussed physical effects that arise due to quantization effects in (correlated) electron liquids with many charge carriers. Quantization effects for single electrons become accessible once electrons are confined to a sufficiently small area (in the case of GaAs/AlGaAs heterostructures of the order of 1µm × 1 µm). A system where an insulated island of material (Fig. 12.1a) is capacitively and weakly tunnel-coupled to two reservoirs is called quantum dot (QD). An electron that tunnels onto the island has to overcome a certain Coulomb potential, which can be large due to the small size and hence capacitance of the quantum dot. Ground state energies of configurations with N and N+1 electrons on the QD are split by the charging energy, which is an effect of this Coulomb potential. Being able to shift the energy spectrum with a capacitively coupled plunger gate (PG, Fig. 12.1a), the occupation of the QD can be controlled one-by-one. In such systems various interesting phenomena can be studied, as for example Kondo physics [2-5], spin physics [6–11], interaction with nuclear spins [12–14], electron-phonon coupling effects [15–17] and others.

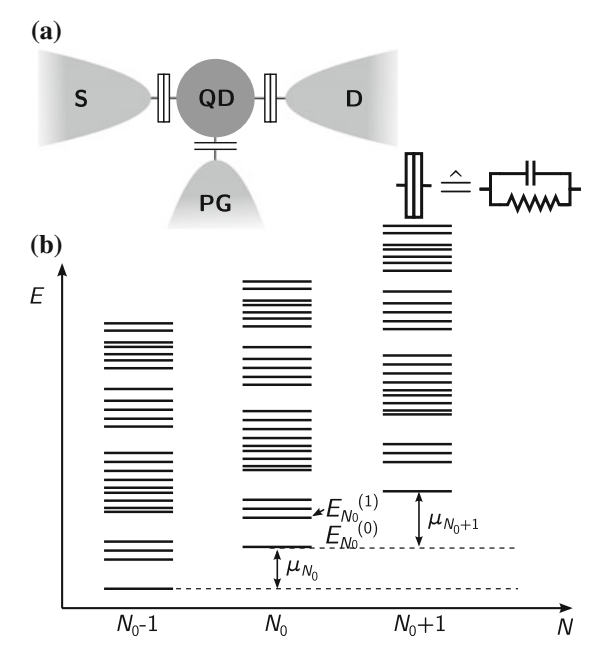


Fig. 12.1 a Schematic circuit diagram of a quantum dot (QD). The QD island is capacitively and tunnel coupled to source (S) and drain (D) reservoirs, while coupling to the plunger gate (PG) is only capacitive. Tunneling barriers are represented by a parallel circuit of a capacitor and a resistor. **b** Schematic energy levels for a QD population of $N_0 - 1$, N_0 and $N_0 + 1$ electrons. The electrochemical potential is the energy difference between the corresponding ground states, i.e., the QD's total change in energy for the addition of one electron. Adapted from [18]

12.2 Basics of Quantum Dots

In the following, basic properties of quantum dots like their energy spectrum, Coulomb blockade, Coulomb diamonds and charge detection techniques will be reviewed.

12.2.1 Energy Scales

A schematic energy spectrum of a QD is shown in Fig. 12.1b. Here, energy levels are plotted for $N_0 - 1$, N_0 , $N_0 + 1$,... electrons on the QD. Ground state energies $E_{N_0}^{(0)}$ (for N_0 electrons) lie at higher energies for a larger occupancy. Excited states ($E_{N_0}^{(1)}$,...) are labeled according to their energy eigenvalues. Mainly two different contributions determine this spectrum, the charging energy and the confinement energy.

Charging energy The energy required to add one electron to a QD populated with N_0 electrons is given by the total change in the electrostatic energy [18]:

$$E_c(N_0 + 1) = E_{\text{elstat}}(N_0 + 1) - E_{\text{elstat}}(N_0)$$
 (12.1)

Modeling the QD as a metallic disk of radius r, $E_c(N_0+1) \approx \frac{e^2}{8\varepsilon\varepsilon_0 r}N_0$ is found [18]. Here, ε_0 denotes the vacuum permittivity and ε the relative dielectric constant. The charging energy then is defined as the difference $\Delta E_c = E_c(N_0+1) - E_c(N_0) = \frac{e^2}{8\varepsilon\varepsilon_0 r}$.

Confinement energy Additionally to the charging energy, electrons need to have a certain energy to fill the quantum mechanical energy levels. In the simplest case of a two-dimensional system and a parabolic confinement potential, the total energy (without electrostatic energy) of the system is given as $E_{\rm conf}(N_0) = E_{\rm Ry}^* \left(\frac{a_{\rm B}^*}{r}\right)^2 N_0^2$ [18]. Hence, the energy required for adding an electron to the dot occupied with N_0 electrons is given as $\epsilon(N_0+1)\approx 2E_{\rm Ry}^* \left(\frac{a_{\rm B}^*}{r}\right)^2 N_0$ with a single-particle level spacing $\Delta=2E_{\rm Ry}^* \left(\frac{a_{\rm B}^*}{r}\right)^2$ [18]. In a realistic system, the structure of the single-particle level spacing can be much more complicated, due to non-harmonic confinement potentials, electron-electron interaction effects, etc.

Experimentally, we only probe relative energies for different populations of the QD. Hence the notion of the electrochemical potential makes sense. It is defined as the energy difference between ground state energies of different population: $\mu_{N_0} = E_{N_0}^{(0)} - E_{N_0-1}^{(0)}$. If an electron in source or drain reservoirs resides at an energy equal to μ_{N_0} , it provides enough energy to populate the dot which was initially filled with N_0-1 electrons. The addition energy is defined as the sum of charging and confinement energies and corresponds to the difference of the electrochemical potentials of N_0 or N_0+1 electrons on the QD: $E_{\rm add}^{(N_0)} = \mu_{N_0+1} - \mu_{N_0} = \Delta E_c + \Delta$ and is approximately independent of the electron number.

12.2.2 Coulomb Blockade

Coulomb blockade and Coulomb resonances can be understood from a simplistic picture illustrated in Fig. 12.3a, b. Here, source and drain reservoirs are labeled with their electrochemical potentials μ_S and μ_D . Electronic states in these reservoirs are filled from the conduction band bottom up to roughly μ_S and μ_D with an occupation described by the Fermi-Dirac distribution. The QD (middle) is weakly tunnel-coupled to source and drain. Vertical bars illustrate the tunneling barriers between QD and source or drain. The tunneling conductance G_{tun} is much smaller than e^2/h such that the charge on the island is quantized.

The occupation of the QD is determined by the position of the energy levels in the dot. In Fig. 12.3a, μ_{N-1} lies below μ_S and μ_D while μ_N lies above. Hence the QD is

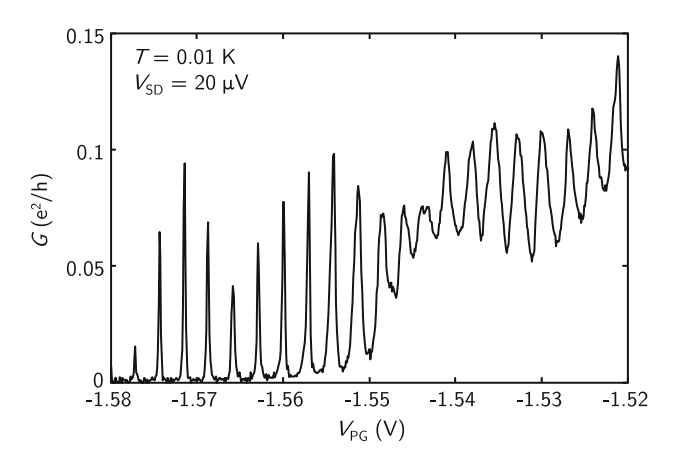


Fig. 12.2 Conductance of a laterally defined QD as a function of the plunger gate voltage. Sharp conductance peaks and Coulomb blockade become visible once the QD tunneling barriers are sufficciently closed (at $V_{PG}<-1.55~V$)

occupied with N-1 electrons, given the broadening of the Fermi-Dirac distribution in the leads is much smaller than $\mu_N-\mu_{N-1}$. Tunneling in the energy level μ_N is not possible, as it lies above μ_S and μ_D in energy. Furthermore, electrons occupying the QD cannot leave it, as all electronic states in the leads are occupied at energies below μ_S and μ_D . This situation is referred to as Coulomb blockade.

By applying a voltage to the PG, energy levels of the QD can be shifted in energy due to the mutual capacitive coupling between QD and PG. In the simplest case, a linear relation is assumed and changing the PG voltage by ΔV_{PG} shifts energy levels on the QD (relative to source and drain electrochemical potentials) by $-\alpha_{PG}\Delta V_{PG}$. Here α_{PG} is called lever arm of the PG and describes the strength of the capacitive coupling to the QD.

Applying a suitable voltage to the PG, one can arrive in a situation illustrated in Fig. 12.3b. Here, μ_S and μ_D are aligned with the dot electrochemical potential μ_N . The total energy is conserved when electrons tunnel elastically between source or drain and the QD. Therefore conductance through the QD increases resonantly in this case. An exemplary measurement of conductance versus voltage applied to the PG is shown in Fig. 12.2. Intervals of zero conductance correspond to the Coulomb blockade situation (Fig. 12.3a), while sharp conductance peaks correspond to elastic transport through the QD (Fig. 12.3b).

If a finite voltage $V_{\rm SD}$ is applied symmetrically between source and drain, we can arrive in the situation depicted in the upper left of Fig. 12.3. Here, the conductance is sketched schematically as a function of $V_{\rm PG}$ and $V_{\rm SD}$. The conductance approaches zero in white diamond-shaped regions, while a finite current is observed in the gray regions. At zero source-drain bias Coulomb blockade (a) or Coulomb resonances (b) are observed. As $V_{\rm SD}$ is increased, the voltage window in which Coulomb blockade is observed shrinks linearly. At the boundaries of the Coulomb blockaded regions, either $\mu_{\rm S}$ or $\mu_{\rm D}$ are aligned with the electrochemical potential in the QD

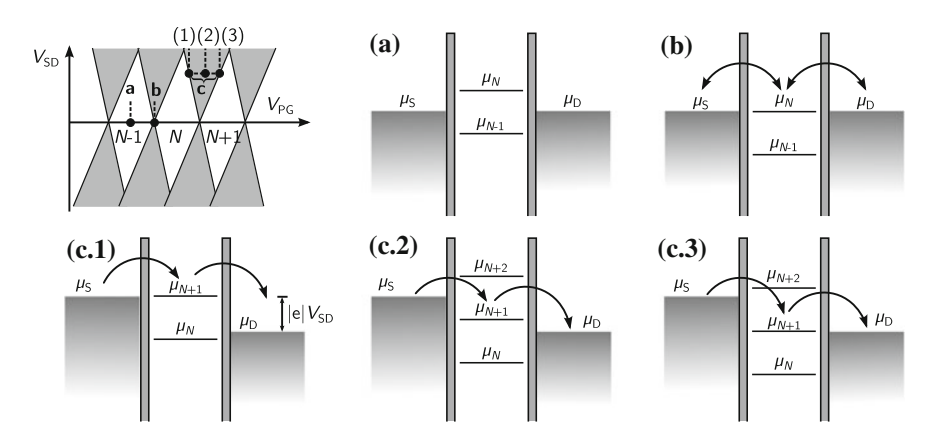


Fig. 12.3 Schematic of Coulomb blockade diamonds when V_{PG} and V_{SD} are varied simultaneously. *Gray* or *white* regions indicate finite or zero current. At zero source-drain voltage V_{SD} , Coulomb blockade (a) or Coulomb resonances (b) are found. At finite source-drain biases, current flows whenever the electrochemical potential of the QD lies in the bias window (c.2). The *diamond shaped* boundary of zero current is determined by alignment of the electrochemical potential of the QD with source (c.1) or drain (c.3) electrochemical potentials

(Fig. 12.3c.1, c.3). The slope of this boundary in the V_{SD} – V_{PG} plane is determined by the lever arm α_{PG} (the slope is negative for alignment with μ_{S} and positive for alignment with μ_{D}). Whenever the electrochemical potential of the QD lies within the bias window (Fig. 12.3c.2), transport from source to drain or vice-versa is possible and a finite conductance is observed.

12.2.3 Principle of Charge Detection

In the view of full counting statistics where all measurable physical quantities can be deduced from probability distributions [19], a time-resolved measurement of the QD occupation is a powerful tool that can give additional insight into correlations and internal structures. Transport processes in QDs where a resonant current can be measured (Fig. 12.2) are extremely fast and cannot be individually resolved in an experiment. Hence a different approach has to be chosen, in order to track the QD occupation as a function of time. This is accomplished by charge detection techniques. Here, the conductance of a QPC in close proximity to the QD is measured [20–23]. Due to the capacitive coupling of this charge detector (CD) to the QD, adding an electron to the QD will shift the CD conductance curve to more positive gate voltages. This situation is depicted schematically in Fig. 12.4. Here, the CD conductance is plotted versus the dot's PG voltage. Lowering V_{PG} decreases the QD population, resulting in an abrupt shift of the CD conductance curve to the left and hence an increase of G_{CD} . In addition to changing the QD population, lowering V_{PG}

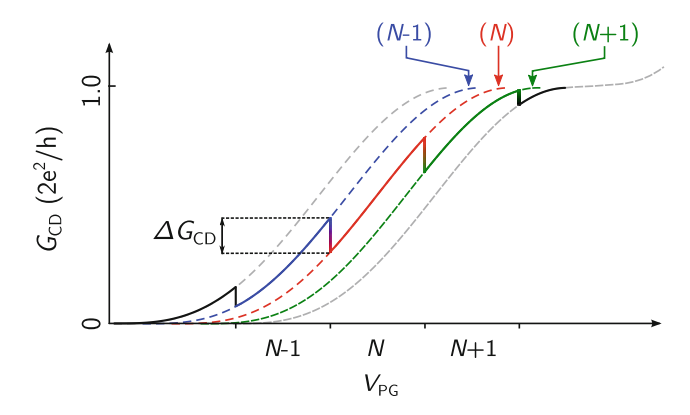


Fig. 12.4 Charge detector conductance as a function of the PG voltage and the occupation N-1, N, N+1,... of the QD. Whenever the QD occupation changes by one, the CD conductance curve is shifted to a more positive $V_{\rm PG}$ voltage, due to the capacitive coupling between CD and QD. This leads to a detectable change $\Delta G_{\rm CD}$ in the charge detector conductance

also closes the CD due to the capacitive cross-talk. Overall, a QPC conductance curve with sharp jumps (Fig. 12.4) is observed. Here, the tunneling coupling between QD and source and drain can be arbitrarily small, as the signal strength $\Delta G_{\rm CD}$ depends only on the CD sensitivity. Measuring $\Delta G_{\rm CD}$ as a function of time gives access to a time-resolved probe of the occupation of the QD.

12.3 Improving the Charge Detection Sensitivity

Charge detection experiments which rely on an extremely fast time-resolution, like the read-out of charge qubits [24, 25], require a high charge detector sensitivity. The charge detector response ΔG_{CD} to a variation $\Delta \mu_{QD}$ of the electrochemical potential of the QD is given in linear approximation as:

$$\Delta G_{\rm CD} \propto \frac{C_{\rm tot}}{C_{\rm OD-CD}} \frac{dG_{CD}}{d\mu_{\rm CD}} \Delta \mu_{\rm QD}$$
 (12.2)

Here, $dG_{CD}/d\mu_{CD}$ is the slope of the charge detector conductance and C_{tot}/C_{QD-CD} describes the strength of capacitive coupling between QD and CD, where C_{tot} is the total capacitance of the QD and C_{QD-CD} is the cross capacitance between CD and QD. Hence the CD slope and the strength of the capacitive coupling are the main two levers for improving the CD sensitivity. If a QPC is employed as CD, the slope $dG_{CD}/d\mu_{CD}$ depends on the QPC confinement potential and is difficult to vary (see Chap. 9). Several experiments hence have used single-electron transistors [26–28] or QDs [29] as charge detectors. Here the slope is only limited by thermal broadening.

The simplest way to enhance the capacitive coupling between CD and QD is by placing them in close proximity. However, in transport experiments employing large QDs in the quantum Hall regime this is not possible. The diameter of the QDs is typically greater than 1 μm , hence the lower limit of the average QD-CD distance is already greater than 500 nm. The high-mobility 2DEGs employed in this chapter ($\mu=10\times10^6~cm^2/Vs$, $n_S=1.3\times10^{11}~cm^{-2}$) are defined 320 nm below the surface. Thus gate depletion lengths are of comparable magnitude and further decrease the capacitive coupling strength. It has been shown that the capacitive coupling between CD and QD can be increased by reducing lateral screening due to metallic top-gates [1]. In practice this is accomplished by leaving a slit on the sidebarrier of the QD, which points in the direction of the CD. Furthermore, coupling can be enhanced by utilizing floating top-gates that connect CD and QD [1], however at the price of decreased stability of the investigated QD.

Here, we present charge detection measurements on a QD with a greatly enhanced CD sensitivity, achieved by forming a localized state in the CD in close proximity to the QD. An atomic force micrograph of the device is shown in Fig. 12.5a. The

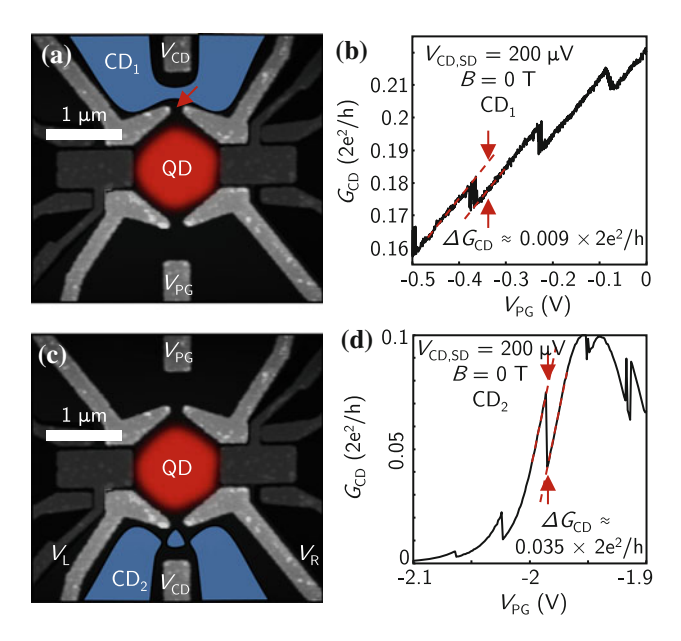


Fig. 12.5 a Atomic force micrograph of a quantum dot with two neighboring charge detectors. Bright gates are used to form CD and QD while *dark gray* gates are kept grounded. The QD (*red*) is defined by four gates. In the first configuration, CD₁ is defined as a QPC channel (*blue area*). **b** Conductance of CD₁ as a function of the plunger gate voltage. Steps related to Coulomb charging of the QD modulate the conductance curve. V_{CD} is tuned to the steepest point of the conductance curve. At the ideal operating point, $\Delta G \approx 0.009 \times 2e^2/h$ is obtained. When CD₂ is tuned such that a localized state forms (**c**, *blue area*), a sharp conductance resonance with shifts related to QD Coulomb charging is observed in the CD₂ conductance (**d**). Here, the sensitivity is significantly enhanced to approximately $0.035 \times 2e^2/h$

approximately 1 μ m \times 1 μ m large QD is defined by the four inner gates (bright gray). Dark gray gates are not used and are kept grounded. Bright gray gates at the top or bottom are either used to define a CD, or as PG of the QD. The top-gate layout is optimized such that the QD barrier is opened on the side pointing towards the CD (red arrow).

Figure 12.5a illustrates the situation in which a QPC is defined in the upper CD₁. The CD sensitivity has been optimized by applying a more negative voltage to the CD gate than to the QD gates, which pushes the CD channel (blue area) closer to the QD (red area). Due to the local minimum in the confinement potential which is defined by the three neighboring gates, the conductance of CD₁ versus CD gate voltage (Fig. 12.6) drops more sharply close to pinch-off than for an ordinary QPC with a smooth saddle-point potential.

In this situation, the measured CD conductance versus PG voltage is shown in Fig. 12.5b. The CD gate voltage has been chosen in order to set the CD at its optimal working point with the steepest slope in $G_{\rm CD}$. Due to the resonant conductance close to pinch-off, the steepest slope of the CD was found at around $0.2 \times 2e^2/h$ and not at $0.5 \times 2e^2/h$ as usually. For this well-tuned situation, $\Delta G_{\rm CD} \approx 0.009 \times 2e^2/h$ is obtained. This is comparable to sensitivities achieved in other experiments using QPCs as charge detector [29–32]. In a different configuration (Fig. 12.5c), where the confinement potential of CD₂ has been tuned such that a localized state forms in the CD in close proximity to the QD, a (tunneling-broadened) Coulomb resonance is found in the conductance of the CD (Fig. 12.5d) when the PG voltage is varied. Sharp kinks related to Coulomb charging of the QD modulate the CD conductance. Here, $\Delta G_{\rm CD} \approx 0.035 \times 2e^2/h$, nearly six times larger than for an optimized QPC charge detector, is found.

In order to tune the CD to such a resonance, V_L and V_R (see Fig. 12.5c) are varied, while $V_{\rm CD}$ is kept fixed. The CD transconductance obtained in this situation

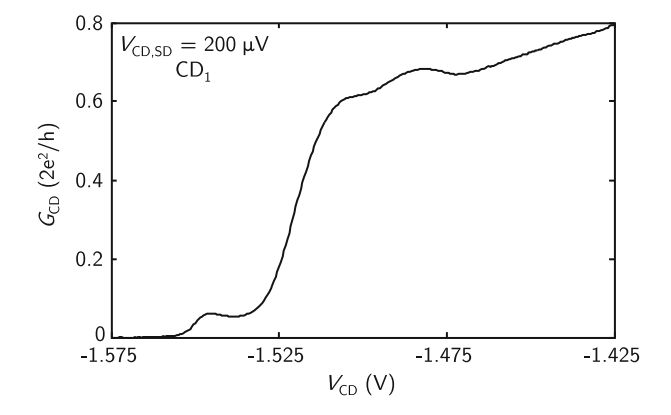


Fig. 12.6 Conductance of CD $_{\rm I}$ versus CD gate voltage. Here, the CD is not deliberately tuned in a situation with a strong localization. However, close to pinch-off, the CD conductance is steeper than an ordinary QPC due to the confinement potential which creates a local minimum

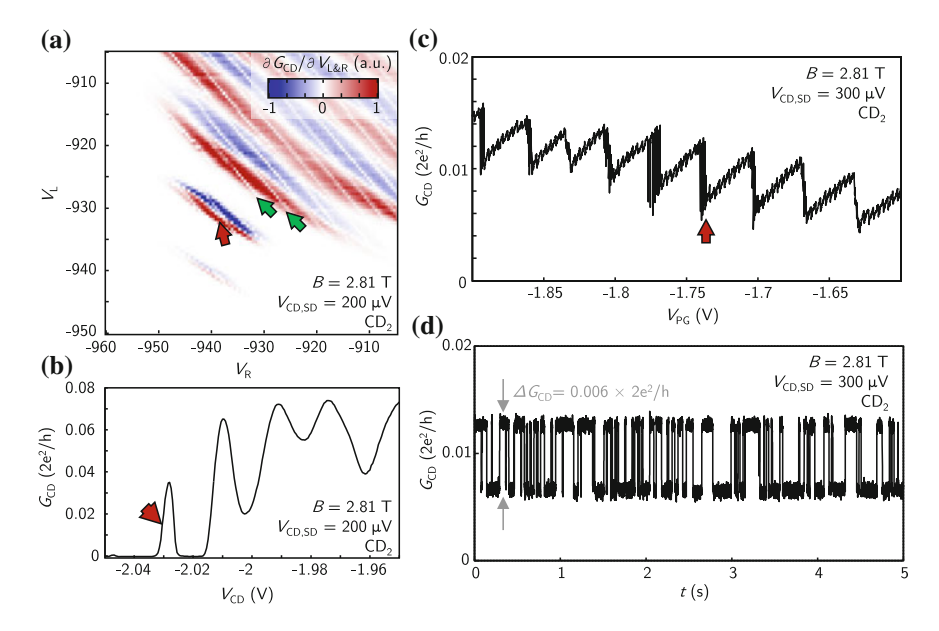


Fig. 12.7 a Transconductance of the charge detector versus left and right gate voltages $V_{\rm L}$ and $V_{\rm R}$. Charging events of the neighboring QD appear as *faint white lines* intersecting the sharp CD resonances (*green arrows*). b Charge detector conductance versus voltage applied to the CD gate. For single-electron counting, $V_{\rm CD}$ is set to the steepest point of the conductance curve (*red arrow*). c Charge detector conductance versus plunger gate voltage. Distinct steps at Coulomb charging events are visible. The charge detector is kept at the ideal operation point by adjustment of the CD voltage $V_{\rm CD}$, which explains the small kinks in the CD conductance, which arise due to the finite resolution of the voltage source. An exemplary time-resolved measurement of the CD conductance is shown in d. Single-electron charging events can clearly be resolved

is plotted in Fig. 12.7a. For the charge detection, $V_{\rm L}$ and $V_{\rm R}$ are set such that the transconductance is maximal (red arrow Fig. 12.7a). Apart from the Coulomb resonances in the CD, charging events in the QD are visible as faint white lines (green arrows). Coulomb resonances in CD and QD have non-identical slopes in the $V_{\rm L}-V_{\rm R}$ plane, which indicates different coupling strengths of these two gates to the QD and the CD localization.

Figure 12.7b shows the CD conductance as a function of the CD gate. To allow (time-resolved) charge detection across several Coulomb peaks, the CD voltage is set to the steepest point of the CD resonance (red arrow, Fig. 12.7b). Any change of the PG voltage is compensated by a smaller change of the CD voltage, in order to stay in the regime of the optimal sensitivity. A measurement of the CD conductance versus the PG voltage is shown in Fig. 12.7c. Here, large jumps in $G_{\rm CD}$ correspond to charging events from or to the QD, while small jumps arise due to the finite resolution of the voltage source when adjusting the CD voltage. The bulk filling factor $\nu_{\rm bulk}$ is tuned to two by application of an external magnetic field $B=2.81\,{\rm T}$. A time-resolved measurement of the CD conductance at a jump of $G_{\rm CD}$ (red arrow in Fig. 12.7c) is

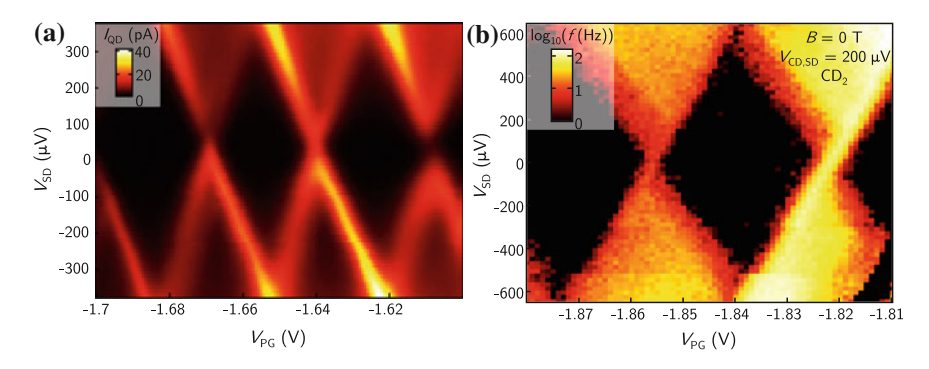


Fig. 12.8 a Current through the QD shown in Fig. 12.5a as a function of V_{PG} and V_{SD} . A charging energy of approximately 350 μ eV is found. b Single-electron tunneling rate as a function of plunger gate voltage and source-drain bias in a more pinched-off situation

shown in Fig. 12.7d. Two distinct levels, separated by $\Delta G_{\rm CD} \approx 0.006 \times 2e^2/h$ can be resolved, which allows to extract tunneling-in and -out rates. In this measurement, the CD bandwidth, which is mainly given by the I-V converter feedback resistance (here $R_{\rm F}=100~{\rm M}\Omega$), is of the order of 1 kHz.

Making use of the enhanced CD sensitivity, single-electron tunneling rates of several hundred Hertz can be clearly resolved, as demonstrated in the measurement of a Coulomb diamond in the counting signal shown in Fig. 12.8b. Here, the logarithmic single-electron tunneling rate is plotted versus PG voltage and source-drain voltage. For comparison, Coulomb diamonds in a less pinched-off regime are shown in Fig. 12.8a. Here, the direct current through the QD is plotted versus PG voltage and source-drain bias.

12.4 Conclusion

We have investigated methods for enhancing the charge detection sensitivity, for experiments that employ large quantum dots and high-mobility heterostructures in the quantum Hall regime. Introducing a gap in the barrier between QD and CD allowed us to enhance the capacitive coupling due to reduced screening and lead to a steeper QPC conductance slope of the CD.

The CD sensitivity could be even further enhanced by utilizing a localized state in the CD, which was defined in the gap of the QD barrier gates. Compared to when an ordinary QPC is used as CD, the sensitivity could be enhanced by nearly a factor of six. Finally, we demonstrated the applicability of this method by performing time-resolved charge detection on a large QD in the quantum Hall regime.

References 231

References

 C. Rössler, T. Krähenmann, S. Baer, T. Ihn, K. Ensslin, C. Reichl, W. Wegscheider, New J. Phys. 15, 033011 (2013). doi:10.1088/1367-2630/15/3/033011

- D. Goldhaber-Gordon, H. Shtrikman, D. Mahalu, D. Abusch-Magder, U. Meirav, M.A. Kastner, Nature 391, 156 (1998). doi:10.1038/34373
- S.M. Cronenwett, T.H. Oosterkamp, L.P. Kouwenhoven, Science 281, 540 (1998). doi:10.1126/ science.281.5376.540
- W.G.v.d. Wiel, S.D. Franceschi, T. Fujisawa, J.M. Elzerman, S. Tarucha, L.P. Kouwenhoven, Science 289, 2105 (2000). doi:10.1126/science.289.5487.2105
- J. Schmid, J. Weis, K. Eberl, K.v. Klitzing, Phys. Rev. Lett. 84, 5824 (2000). doi:10.1103/ PhysRevLett.84.5824
- A.C. Johnson, J.R. Petta, C.M. Marcus, M.P. Hanson, A.C. Gossard, Phys. Rev. B 72, 165308 (2005). doi:10.1103/PhysRevB.72.165308
- M. Ciorga, A.S. Sachrajda, P. Hawrylak, C. Gould, P. Zawadzki, S. Jullian, Y. Feng, Z. Wasilewski, Phys. Rev. B 61, R16315 (2000). doi:10.1103/PhysRevB.61.R16315
- 8. H.W. Liu, T. Fujisawa, Y. Ono, H. Inokawa, A. Fujiwara, K. Takashina, Y. Hirayama, Phys. Rev. B 77, 073310 (2008). doi:10.1103/PhysRevB.77.073310
- F.H.L. Koppens, C. Buizert, K.J. Tielrooij, I.T. Vink, K.C. Nowack, T. Meunier, L.P. Kouwenhoven, L.M.K. Vandersypen, Nature 442, 766 (2006). doi:10.1038/nature05065
- N. Shaji, C.B. Simmons, M. Thalakulam, L.J. Klein, H. Qin, H. Luo, D.E. Savage, M.G. Lagally, A.J. Rimberg, R. Joynt, M. Friesen, R.H. Blick, S.N. Coppersmith, M.A. Eriksson, Nat. Phys. 4, 540 (2008). doi:10.1038/nphys988
- E.A. Laird, J.M. Taylor, D.P. DiVincenzo, C.M. Marcus, M.P. Hanson, A.C. Gossard, Phys. Rev. B 82, 075403 (2010). doi:10.1103/PhysRevB.82.075403
- P. Maletinsky, A. Badolato, A. Imamoglu, Phys. Rev. Lett. 99, 056804 (2007). doi:10.1103/ PhysRevLett.99.056804
- 13. K. Ono, S. Tarucha, Phys. Rev. Lett. 92, 256803 (2004), doi:10.1103/PhysRevLett.92.256803
- F. Jelezko, T. Gaebel, I. Popa, M. Domhan, A. Gruber, J. Wrachtrup, Phys. Rev. Lett. 93, 130501 (2004). doi:10.1103/PhysRevLett.93.130501
- P. Roulleau, S. Baer, T. Choi, F. Molitor, J. Güttinger, T. Müller, S. Dröscher, K. Ensslin, T. Ihn, Nat. Commun. 2, 239 (2011). doi:10.1038/ncomms1241
- W.J.M. Naber, T. Fujisawa, H.W. Liu, W.G. van der Wiel, Phys. Rev. Lett. 96, 136807 (2006). doi:10.1103/PhysRevLett.96.136807
- T. Fujisawa, T.H. Oosterkamp, W.G.v.d. Wiel, B.W. Broer, R. Aguado, S. Tarucha, L.P. Kouwenhoven, Science 282, 932 (1998). doi:10.1126/science.282.5390.932
- T. Ihn, Semiconductor Nanostructures: Quantum States and Electronic Transport (OUP Oxford, 2010)
- 19. Y.V. Nazarov, Quantum Noise in Mesoscopic Physics (Springer, 2003)
- M. Field, C.G. Smith, M. Pepper, D.A. Ritchie, J.E.F. Frost, G.A.C. Jones, D.G. Hasko, Phys. Rev. Lett. 70, 1311 (1993). doi:10.1103/PhysRevLett.70.1311
- T. Ihn, S. Gustavsson, U. Gasser, B. Küng, T. Müller, R. Schleser, M. Sigrist, I. Shorubalko, R. Leturcq, K. Ensslin, Solid State Commun. 149, 1419 (2009). doi:10.1016/j.ssc.2009.04.040
- 22. J.M. Elzerman, R. Hanson, L.H. Willems van Beveren, B. Witkamp, L.M.K. Vandersypen, L.P. Kouwenhoven, Nature 430, 431 (2004). doi:10.1038/nature02693
- R. Schleser, E. Ruh, T. Ihn, K. Ensslin, D.C. Driscoll, A.C. Gossard, Appl. Phys. Lett. 85, 2005 (2004). doi:10.1063/1.1784875
- J.R. Petta, A.C. Johnson, J.M. Taylor, E.A. Laird, A. Yacoby, M.D. Lukin, C.M. Marcus, M.P. Hanson, A.C. Gossard, Science 309, 2180 (2005). doi:10.1126/science.1116955
- K.D. Petersson, J.R. Petta, H. Lu, A.C. Gossard, Phys. Rev. Lett. 105, 246804 (2010). doi:10. 1103/PhysRevLett.105.246804
- W. Lu, Z. Ji, L. Pfeiffer, K.W. West, A.J. Rimberg, Nature 423, 422 (2003). doi:10.1038/ nature01642

- S. Ilani, J. Martin, E. Teitelbaum, J.H. Smet, D. Mahalu, V. Umansky, A. Yacoby, Nature 427, 328 (2004). doi:10.1038/nature02230
- J. Martin, S. Ilani, B. Verdene, J. Smet, V. Umansky, D. Mahalu, D. Schuh, G. Abstreiter, A. Yacoby, Science 305, 980 (2004). doi:10.1126/science.1099950
- C. Barthel, M. Kjærgaard, J. Medford, M. Stopa, C.M. Marcus, M.P. Hanson, A.C. Gossard, Phys. Rev. B 81, 161308 (2010). doi:10.1103/PhysRevB.81.161308
- T. Müller, Radio-frequency quantum point contact charge detection, Ph.D. thesis, ETH Zürich (2011)
- 31. I.T. Vink, T. Nooitgedagt, R.N. Schouten, L.M.K. Vandersypen, W. Wegscheider, Appl. Phys. Lett. **91**, 123512 (2007). doi:10.1063/1.2783265
- 32. L.M.K. Vandersypen, J.M. Elzerman, R.N. Schouten, L.H.W.v. Beveren, R. Hanson, L.P. Kouwenhoven, Appl. Phys. Lett. 85, 4394 (2004). doi:10.1063/1.1815041

Chapter 13 Quantum Dots in the Quantum Hall Regime

Abstract We investigate magneto-transport through a $1.6~\mu m$ wide quantum dot (QD) with adjacent charge detector, for different integer filling factors in the QD and constrictions. When this system is operated at a high transmission, it acts as a Fabry-Pérot interferometer, where transport is governed by a Coulomb blockade mechanism. For lower transmissions where the barriers are in the tunneling regime, we can directly measure the charge stability diagram of two capacitively and tunnel coupled Landau levels. The tunneling regime has been investigated in direct transport, as well as in single electron counting. The edge states within the dot are non-cyclically depopulated, which can be explained by a simple capacitive model and allows to draw conclusions about the edge state geometry within the quantum dot.

13.1 Introduction

Two-dimensional electron systems at low temperatures and in strong magnetic fields show a rich spectrum of highly degenerate, incompressible ground states [2, 3]. Fractional quantum Hall states, occurring at a fractional filling factor ν with an odd denominator, are well described by the Laughlin wavefunction [4]. There exists a prominent exception from this hierarchy: the $\nu=\frac{5}{2}$ state [5], which is believed to obey non-Abelian statistics [6, 7]. This remarkable property could make it an interesting candidate for the realization of a topological qubit [8]. Theoretical ideas for probing the statistics of the $\nu=\frac{5}{2}$ state are based on quantum dots, operated as Fabry-Pérot interferometers as a basic building block [9–13].

Quantum dots exposed to a magnetic field also offer other interesting fields of study, as the investigation of the spin configuration [14] or few-electron addition spectra [15]. In the presence of a strong magnetic field, Coulomb blockade (CB) oscillations can no longer be described within a single-particle picture. Alternating compressible and incompressible regions are formed inside the dot, which can strongly modify the CB oscillations [16]. Previous experiments have allowed the extraction of mutual capacitances of these regions for different filling factors [17]. In

The following chapter is based on the article [1].

those experiments, alternating high and low CB peak currents have been observed, which was attributed to a double dot-like behavior of two edge states inside the dot. However, for the interpretation of recent experiments using quantum dots as Fabry-Pérot interferometers [19–21], it is important to understand the detailed structure of edge states inside the QD and the parameter range, where this description is valid.

Here we present investigations of a large quantum dot with a quantum point contact (QPC) serving as a charge detector. When the QD is operated as a Fabry-Pérot interferometer, we find resonances with a slope in voltage—magnetic field space and a periodicity characteristic for a Coulomb dominated effect, as already observed in previous experiments [19–21]. When the system is operated at a lower transmission where the barriers are in the tunneling regime, we observe a similar effect as in [17]. However, the amplitude modulation can be observed over a large parameter range for different filling factors, allowing the direct measurement of the charge stability diagram of capacitively and tunnel coupled edge states. As a consequence, we can estimate the width of the incompressible region separating the edge channels inside the QD. In contrast to previous experiments, this is accomplished by using capacitances, directly extracted from the measured charge stability diagram. Furthermore we are able to investigate the CB amplitude modulation by using (time-resolved) charge detection techniques, where it shows up as an increased/decreased tunneling rate. To our knowledge, single electron counting has never been performed with a QD of similar size. Direct transport measurements do not always reflect the full complexity of the edge state substructure inside a OD. In future experiments, single electron counting might provide additional important insight to charge localization and transport in micron-sized Fabry-Pérot interferometers. Most proposed Fabry-Pérot interferometry experiments for probing properties of fractional quantum Hall states assume edge states to be one-dimensional electron or composite Fermion channels with negligible interaction between compressible regions. We show, that when the edge states are confined to the QD, a complex behavior with compressible and incompressible regions is observed. The observed tunnel-coupling between the different compressible regions, i.e. the presence of tunnel-coupled alternative paths, might influence the outcomes of the proposed interferometry experiments.

13.2 Experimental Details

The quantum dot has been fabricated on a Hall-bar, defined by wet-etching of a single-side doped $GaAs/Al_xGa_{1-x}As$ heterostructure with a mobility of 8.1×10^6 cm²/Vs and an electron density of 1.15×10^{11} cm⁻². These structures employ a reduced proportion of Al in the spacer layer between the doping plane and the 2DEG (x = 0.24 compared to x = 0.30 or x = 0.33 which are most widely used), which was shown to favor the formation of the $\nu = \frac{5}{2}$ state [18]. The electron gas resides 340 nm below the surface. Optical lithography, combined with chemical etching and metal evaporation are used to define the mesa, Ohmic contacts and topgate leads. The quantum dot and charge detector gates are defined by electron-beam lithography

with subsequent metal evaporation. Applying a negative voltage of $V_{\rm G}\approx -0.5~{\rm V}$ to the topgates depletes the electron gas underneath. Compared to double-side doped quantum wells with δ -doped screening layers, this structure allows for a much better gateability [22]: the conductance of a single QPC is non-hysteretic and stable in time. Measurements have been conducted in a dry dilution refrigerator at a base temperature of $T_{\rm MC}\approx 10~{\rm mK}$ and in magnetic fields between $B=0~{\rm T}$ and $B=5~{\rm T}$, using standard four-terminal lock-in measurement techniques. A constant AC voltage modulation of an amplitude $<20~{\rm \mu V}$ has been applied via a current-to-voltage converter.

13.3 Results and Discussion

13.3.1 Zero Magnetic Field Transport

Figure 13.1a shows the topgate layout of the quantum dot that has been used for the measurements. The two 800 nm wide QPCs with a channel length of 600 nm serve as tunnel barriers of the 1.6 μ m wide quantum dot. The employed QPCs have shown to result in an almost harmonic confinement potential, apart from the regime very close to pinch-off [22]. The special geometry ensures a smooth QPC potential which is believed to favor the self-consistent formation of separated edge states.

In addition to the plunger gate (PG) that allows for the tuning of the electrochemical potential of the QD, a QPC that serves as a charge detector (CD) [23, 24] has been implemented. When QPC₁ and QPC₂ are in the tunneling regime, finite-bias measurements give rise to characteristic Coulomb diamonds (Fig. 13.1b), from which we extract charging energies of about 100 μ eV. The Coulomb diamond measurement also demonstrates the good stability and control of the QD. Sharp kinks in the CD current $I_{\rm CD}$ (Fig. 13.1d), aligned with peaks in the dot conductance $G_{\rm QD}$ indicate addition/depletion of a single electron from the quantum dot. By pinching off the tunnel barriers even more, time-resolved single electron counting [24–26] is possible for rates below approx. 50 Hz.

13.3.2 Non-cyclic Depopulation of Edge Channels

For a bulk filling factor of $\nu_{bulk}=2$, a filling factor in the quantum dot of $\nu_{QD}\approx 2$ and $\nu_{QPC}\approx 0$, i.e. when two spin-split edge states that are formed in the bulk, as well as in the dot are tunnel-coupled across the QPCs (see schematic inset Fig. 13.2a), CB oscillations are distinctly different from zero magnetic field measurements: the peak height of adjacent CB peaks alternates between two different values (Fig. 13.2a). After five peaks of high amplitude (marked by diamonds) and 6 peaks of low amplitude (squares), two peaks of similar height (filled circles) appear. The alternating peak

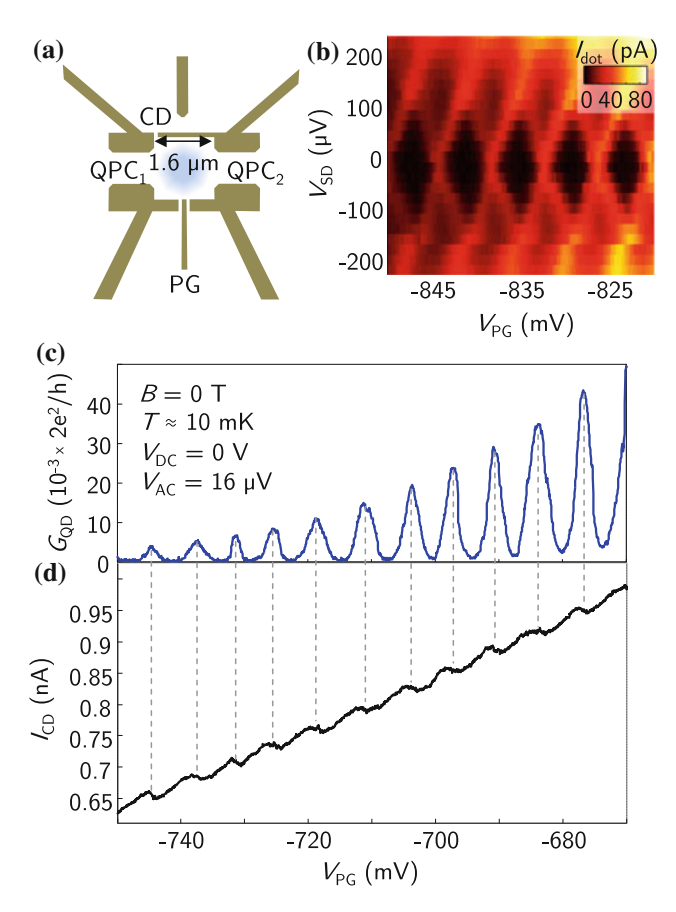


Fig. 13.1 a *Topgate* layout of the quantum dot. The two 800 nm wide QPCs (QPC $_1$ and QPC $_2$) were designed to provide a smooth saddle-point potential. A third, 600 nm wide QPC serves as a charge detector (CD). The sample stability is sufficient for measuring regular and stable Coulomb blockade *diamonds* (**b**). Despite of the dot's large size, single electron charging events can be resolved in the charge detector (**d**) small as well as in the direct current (**c**)

height can also be seen in the single electron counting regime (Fig. 13.2b). Here, the rate of tunnelling events between dot, source and drain (black line, extracted from a time-resolved measurement of the charge detector current) is plotted as a function of the plunger gate voltage V_{PG} . The contrast between peaks of high and low amplitude is lower than in the direct transport measurements. However, taking into account the amplitude dependence on the plunger gate voltage (decreased Coulomb peak height as V_{PG} is decreased), we still have a peak height difference of roughly 15%, bigger than our detection error. Tunneling-in (Γ_{in}) and tunneling-out (Γ_{out}) rates have been extracted from time-resolved measurements of the charge detector conductance. Apart from the different event rate at the Coulomb peak maxima, no further evidence of additional levels contributing to transport or more complex processes,

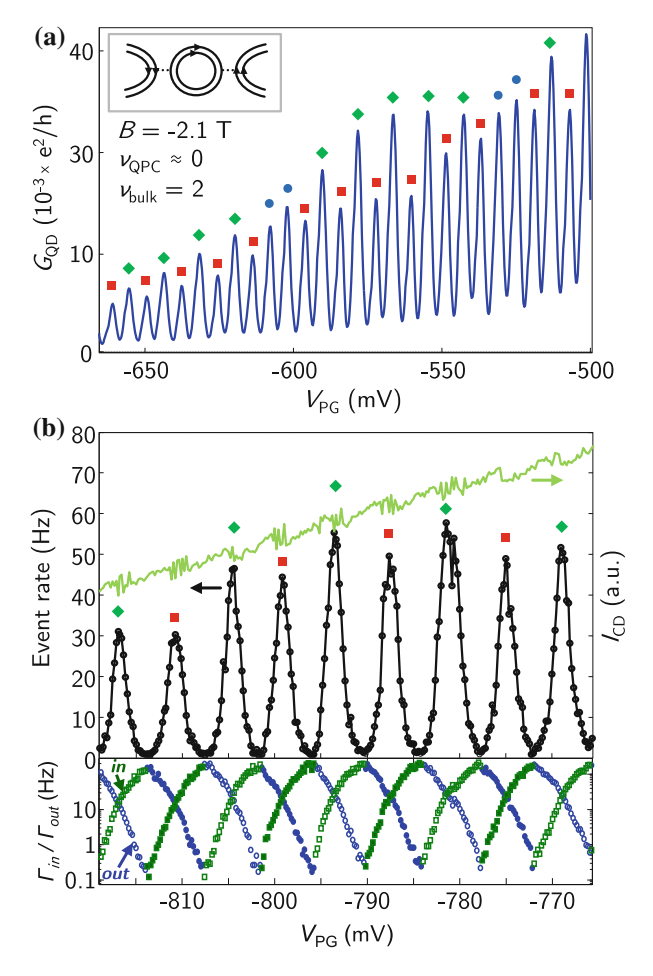


Fig. 13.2 a Coulomb blockade peaks for a bulk filling factor of two. When depleting the *dot* with the plunger gate (PG), Coulomb peaks with a *high/low* peak current (*diamonds/squares*) are observed, interrupted by two peaks of similar magnitude (*filled circles*). The alternating pattern also shows up in the number of single electron charging events in a more pinched-off regime (b). Here, the rate of events is shown in *black*, with the corresponding charge detector current I_{CD} (shifted and scaled) in *green*. Tunneling-in ($\Gamma_{\rm in}$) and tunneling-out ($\Gamma_{\rm out}$) rates for different Coulomb peaks are shown *below*

like electron bunching [27], could be found. As argued later, this means that tunneling processes within the dot are much faster than processes between the quantum dot and the leads. Measuring the CB oscillations as a function of PG voltage and magnetic field, a complex pattern of peak maxima is found (Fig. 13.3a). By extracting the peak amplitude minima (empty circles) and maxima (filled circles) numerically, it can be seen that they are distributed according to a tilted chessboard pattern, as indicated by the filled and empty circles in Fig. 13.3a. Along a Coulomb peak (black or blue line

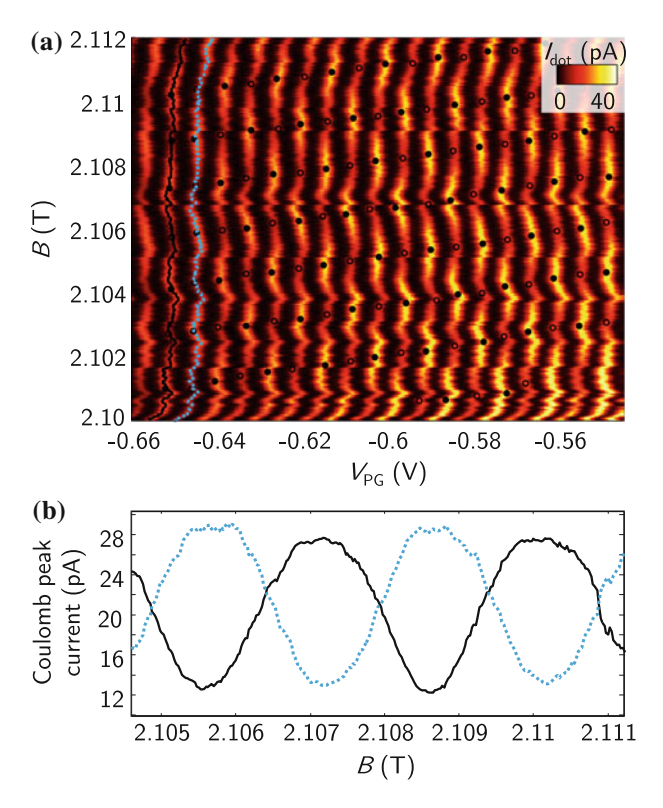


Fig. 13.3 a Coulomb blockade peaks, measured as a function of magnetic field and voltage applied to the plunger gate. Minima and maxima of the Coulomb peak current are extracted numerically and indicated by *filled/empty circles*. b Amplitude of two neighboring Coulomb peaks (position indicated in *black/blue* in (a) as a function of the magnetic field

in Fig. 13.3a, b), the peak current is modulated as a function of the magnetic field (Fig. 13.3b). Neighboring Coulomb peaks show opposite amplitude dependencies. Dominant shifts and drifts of the CB peaks in the measurement of Fig. 13.3a, make it impossible to investigate the absolute position of the peaks. However, modulations in the voltage spacing ΔV_{PG} of two adjacent peaks can clearly be observed (Fig. 13.4c). Here, we plot ΔV_{PG} of two successive CB peaks, offset in x-direction for better visibility. Similar measurements can be conducted for a bulk filling factor $\nu_{\text{bulk}} \approx 4$. In this case, bulk transport measurements suggest two spin-degenerate edge states separated by an incompressible region. Figure 13.4d shows the voltage distance between adjacent CB peaks for this case.

The described behavior can be explained by a capacitive model [17]: at a filling factor of $\nu_{QD}=2$ in the quantum dot, the edge states corresponding to the spin-split lowest Landau level (LL) form compressible regions inside the quantum dot. We denote the lower/upper spin branch of the lowest Landau level by LL1 and LL2. The width of these regions is dictated by self-consistency of the edge potential and

the electrostatic potential contribution of the electron density [28]. In-between the compressible rings (shown schematically in Fig. 13.4a as thick lines), an incompressible region with a magnetic field dependent width is formed (hatched region). In this situation, electrons in both LL1 and LL2 populate the whole disk-shaped area in the quantum dot. However, only the compressible regions contribute to electron transport. Both spin-split levels inside the OD are tunnel coupled to source and drain and capacitively coupled to the plunger gate, as well as to the leads. In addition there is mutual capacitive coupling between the two spin-split levels. Although they overlap spatially, the electronic states are only tunnel-coupled via the compressible regions of both discs. This configuration is an analogy to a double quantum dot system, which in this case is formed by energetically separated, but spatially overlapping electronic states. Here, two main effects determine the configuration of the quantum dot: first, increasing the magnetic field increases the degeneracy of the Landau levels. For a constant number of electrons in the dot, this corresponds to a redistribution of electrons between LL1 and LL2. In addition to that, an increased magnetic field also leads to an increased spin splitting, translating to a larger separation and therefore reduced tunnel coupling in between the compressible regions. However, for the magnetic field ranges studied here, this tunnel coupling variation can be neglected. Second, the total population of the OD can be tuned via the plunger gate, which couples to both LL1 and LL2. Due to the spatial overlap and common center of mass of LL1 and LL2, we expect that the capacitive coupling of both regions to the plunger gate is similarly strong. The conversion factors between energy and gate voltage, the lever arms α_1 and α_2 for discs 1 and 2 thus are expected to be very similar, with a slightly bigger α_1 , considering the larger contribution to the capacitive coupling at the edge closer to the plunger gate. In this configuration, each spin-split level, LL1 and LL2, can be seen as a separate QD with single-particle energies $\frac{1}{2}\hbar\omega_c \pm \frac{1}{2}g\mu_B B$ and charging energies of $\frac{e^2}{C_1}$ and $\frac{e^2}{C_2}$, where C_1 and C_2 are the self-capacitances of discs 1 and 2. With the mutual capacitance C_{1-2} , the total energy of the double quantum dot with N_1 electrons in LL 1 and N_2 electrons in LL 2 can be expressed as:

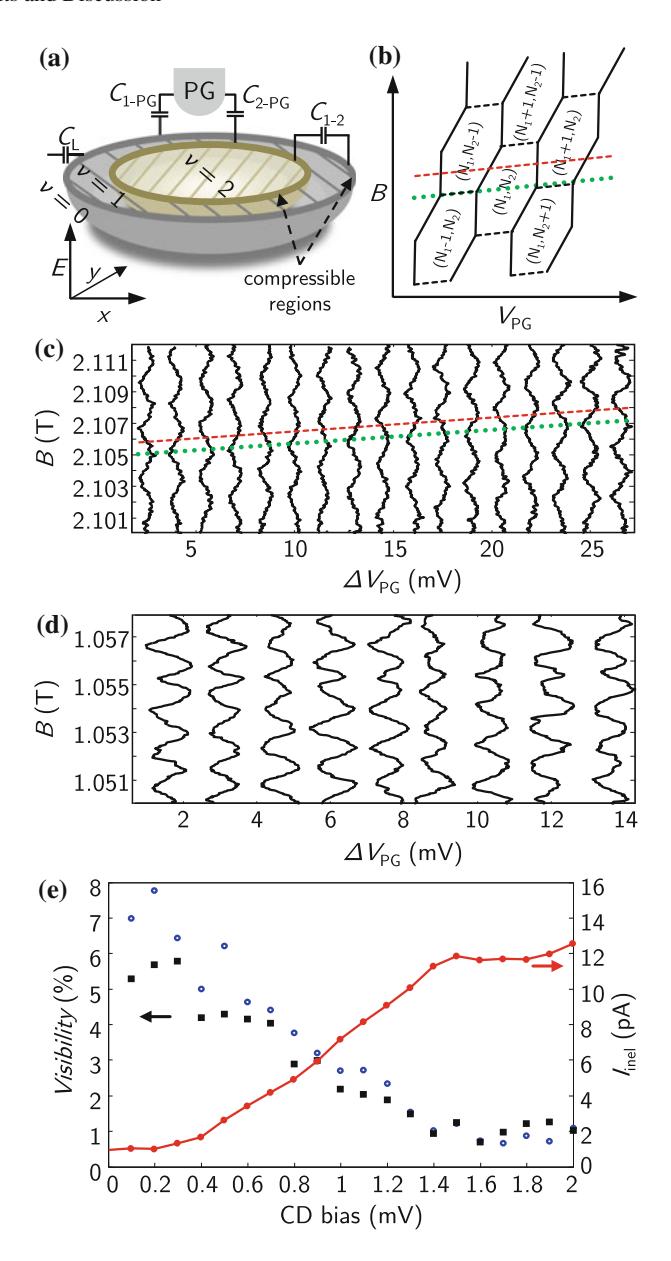
$$\begin{split} E(N_1,N_2) &= \frac{1}{2}\hbar\omega_c(N_1+N_2) - \frac{1}{2}g\mu_BBN_1 + \frac{1}{2}g\mu_BBN_2 \\ &- e\alpha_1V_{\rm PG}N_1 - e\alpha_2V_{\rm PG}N_2 \\ &+ \frac{e^2}{2C_1}N_1^2 + \frac{e^2}{2C_2}N_2^2 + \frac{e^2}{C_{1-2}}N_1N_2 \end{split}$$

where $\omega_c = \frac{eB}{m^*}$ is the cyclotron frequency. The charge configuration of such a double quantum dot system can be described by a charge stability diagram with hexagonal regions of constant charge configuration (N_1, N_2) [29, 30]. From the total energy, we may find conditions for the magnetic field and plunger gate voltage values along the boundary lines of this diagram (constant terms have been omitted):

Transition	$B - V_{\rm PG}$ dependence
$(N_1, N_2) \rightarrow (N_1 + 1, N_2 - 1)$	$B \propto \frac{e}{g\mu_B} (\alpha_2 - \alpha_1) V_{PG}$
	≈0
$(N_1, N_2) \to (N_1 + 1, N_2)$	$B \propto \frac{2e}{\frac{\hbar e}{m^*} - g\mu_B} \underbrace{\alpha_1}_{V_{PG}} V_{PG}$
	>0
$(N_1, N_2) \rightarrow (N_1, N_2 + 1)$	$B \propto \frac{2e}{\frac{\hbar e}{m^*} + g\mu_B} \underbrace{\alpha_2}_{V_{PG}} V_{PG}$
	>0

In Fig. 13.4b, such a charge stability diagram is shown schematically for given electron numbers in LL1 and LL2, (N_1, N_2) , as a function of the magnetic field B and the plunger gate voltage V_{PG} . Due to the comparable size of the capacitances C_1 , C_2 and C_{1-2} , the hexagons have a nearly rectangular shape (from the measured charge stability diagrams explained later, it can be extracted that $C_{1-2} \approx 0.87 \times C_1$). Coulomb peaks occur, whenever charge configurations of N_i and $N_i + 1$ electrons on LL1 (i=1) or LL2 (i=2) are energetically degenerate. A high CB peak current is observed if the electrochemical potential of LL1 is aligned with the Fermi energy in source and drain, a low peak current corresponds to the alignment of the electrochemical potential of LL2 with the Fermi energy. The reason for this peak height modulation is the different lateral tunneling distance. The dashed (red) line in Fig. 13.4b indicates a V_{PG} trace, in which the amplitude difference between adjacent peaks is maximal (alternating transport via LL1 or LL2). Along this line, the charge degeneracy lines are crossed at a maximum distance from the triple points. In contrast, the dotted (green) line corresponds to a case, where charge configurations that contribute to high and low amplitude are energetically close. From the slope of these lines, we can conclude $\alpha_1 < \alpha_2$, which might indicate a nonsymmetric charge distribution in the QD. Traversing the boundaries of the charge stability diagram near a triple point leads to thermal averaging of these two configurations, resulting in peaks of approximately equal height (as marked by the filled circles in Fig. 13.2a). Due to the slightly tilted hexagons, the high-low pattern is found again by further varying V_{PG}. In addition, slightly different charging energies of the two LLs lead to a distorted hexagon pattern.

A change of magnetic field has two effects: for a situation with a constant total number of charges, the addition of flux quanta to the interior of the QD increases the degeneracy of LL1 and LL2 and their energy splitting, thus redistributing electrons between LL1 and LL2. A change of the magnetic field also influences the total population of the dot, as it shifts QD energy levels relative to the Fermi energy in the leads. The red dashed line in Fig. 13.4c corresponds to the position of CB peaks with maximally modulated amplitudes. In agreement with the model illustrated in Fig. 13.4b, these lines correspond to approximately equal separation of adjacent peaks. For the second case, where the amplitude difference is thermally averaged (dotted green line in Fig. 13.4b), we expect and observe in Fig. 13.4c (along the green dotted line) alternating high and low ΔV_{PG} .



¬Fig. 13.4 a Capacitive model for two coupled edge channels. The discoidal energy levels LL1 and LL2 are separated in energy, but overlap spatially. Tunneling of charges is possible in between the compressible regions where the Landau levels cross the Fermi energy, b Exemplary charge stability diagram for a double quantum dot. Along the magnetic field axis, electrons mainly are redistributed in between LL1 and LL2 as well as slightly changing the total population by varying the total energy. A variation of the plunger gate voltage V_{PG} mainly influences the total electron population of the dot. The dashed red line indicates a situation in which the edge channels are cyclically depopulated, giving rise to a maximal height difference between neighboring peaks, as transport takes place alternatingly via LL1 or LL2. Along the dotted green line, neighboring Coulomb peaks lie close to the triple points and thus are thermally averaged and equally high. The plunger gate voltage difference between successive Coulomb peaks is shown in (c) for $\nu_{OD} \approx 2$ and (d) for $\nu_{OD} \approx 4$. The lines have been shifted closer together for better visibility. The dotted green line marks the position of Coulomb peaks of equal height, along the dashed red line, the peak height difference of neighboring peaks is maximal. e Visibility of two Coulomb peak pairs as a function of the charge detector bias $(G_{\rm CD} \approx 0.25 \frac{e^2}{h})$. Increasing the bias lowers the peak height difference visibility, while increasing the inelastic current through the quantum dot

To distinguish if the amplitude modulation is caused by only different lateral tunneling distances, or an activated tunneling process, we can look at Fig. 13.4e: here we measure the relative visibility $(G_{\rm LL1}-G_{\rm LL2})/(G_{\rm LL1}/2+G_{\rm LL2}/2)$ of two thermally broadened pairs of Coulomb peaks, as a function of the bias that has been applied to the charge detector QPC at its maximum sensitivity (in our case $G\approx 0.25\frac{e^2}{h}$ due to a localization in the QPC). The amplitude difference is observed to vanish when the bias is increased. The CD back-action is expected to increase the broadening of the Fermi-Dirac distribution of the leads. We are in the multilevel-transport regime $(h\Gamma\ll\Delta E\lesssim k_BT)$, however not $\Delta E\ll k_BT)$.

The tunneling rate to both regions increases, as additional levels lie within the broadening of the Fermi-Dirac distribution. The broadening also leads to an increased occupation of the excited states of LL1 compared to the ground state of LL2 and thus an increased activated tunneling rate to LL2, which could explain the why the amplitude difference vanishes. From the 40% maximum amplitude modulation between neighboring peaks, we can extract an energy-level separation of $\Delta E \approx 3~\mu\text{eV}$, using exp $(-\Delta E/k_BT)\approx 0.6$ and assuming a typical electron temperature of 60 mK. This is the order of magnitude expected for a dot of the given size.

One may ask, if there is any direct evidence that the second compressible region LL2 is involved in transport. In the situation where the electrochemical potential of LL2 is aligned with the potential of the leads (with a tunneling rate between LL1 and LL2 which is much slower than the tunneling rate between the leads and LL1), there are two sequential processes involved in an electron transfer from the leads to the QD: first, the fast activated tunneling of an electron to LL1 and back to the leads, second, slow tunneling from LL1 to LL2. Due to the very similar capacitive coupling of LL1 and LL2 to the charge detector, we are not able to resolve

¹In this regime, the Coulomb peak conductance is expected to have a small temperature dependence [31, 32], until either $k_B T \ll \Delta E$ or $k_B T \approx e^2/C$. (Note however, this does not hold whenever $h\Gamma \approx \Delta E$, where the amplitudes may have irregular and even nonmonotonic dependence on temperature [33].).

charge redistributions between those regions. From LL2, the electron can only escape with activated tunneling through LL1. While the electron has not left LL2, LL1 is blocked for further electron tunneling, due to the strong capacitive coupling C_{1-2} . The two tunneling processes would lead to electron bunching in the charge detector signal. However, such bunching is not observed in the experiment, suggesting that the interdot tunneling rate is very high (compared to the tunneling rate between QD and the leads) in our case.

Using the extracted interdot capacitance $C_{1-2} \approx 0.87 C_1$, we can make a rough statement about the spatial extent of the QD wave function. Modeling the interdotcapacitance as a simple plate-capacitor with a capacitance proportional to the plate area, we expect the area of LL2 to be roughly 87% of the area of LL1. The area of LL1 can be estimated from the lithographic size and the gate depletion lengths of the quantum dot, yielding $A \approx 0.64 \, (\mu \text{m})^2$. For rectangular QDs, this results in a difference of the side lengths of 54 nm. When the finite width of the edge states is neglected, this corresponds to a width of 27 nm of the incompressible region. Numerical calculations of bulk samples have predicted a width of approximately 20 nm for the incompressible region corresponding to a local filling factor of two [34]. The enhanced value for our case could be a result of the simplicity of the model used which just allows for an order of magnitude estimate, or a smoother confinement potential and increased electron-electron interaction due to confinement. Similarly, a width of approximately 50 nm can be extracted from $C_{1-2} \approx 0.77 C_1$ in the case of $\nu_{\rm OD} \approx$ 4. The increased width in this case is expected, as LL1 and LL2 are split by the larger cyclotron energy.

13.3.3 Transport in the Fabry-Pérot Regime

The Hall voltage drop across the QD ($V_{\rm diag}$, see inset Fig. 13.5a) gives access to the conductance through both constrictions [19]. When both QPCs are tuned to the same transmission ($G \approx 10 \frac{e^2}{h}$ at B=0) by applying a negative topgate voltage and the magnetic field is varied, we find conductances through the constrictions quantized in multiples of $\frac{e^2}{h}$ (Fig. 13.5a). In this configuration, edge states are formed in the bulk, in the QD and in the QPCs. In the QPCs, the filling factor is lower than in bulk and QD: $\nu_{\rm QPC} < \nu_{\rm QD}$, $\nu_{\rm bulk}$ (for our large dot $\nu_{\rm QD} \approx \nu_{\rm bulk}$). We note that $\nu_{\rm QPC}$ edge states pass the QD and contribute to the diagonal conductance, while ($\nu_{\rm QD} - \nu_{\rm QPC}$) edge states are confined inside the QD. On the riser of the conductance-plateaus (i.e. the low magnetic field side), periodic conductance oscillations are observed (Fig. 13.5b for $\nu_{\rm QPC} \approx 2$, Fig. 13.5c for $\nu_{\rm QPC} \approx 1$). The peaks of these oscillations are shifted to lower magnetic fields as the plunger gate voltage is decreased (Fig. 13.5b, c). The strength of this shift depends on the filling factor inside the QPCs ($\Delta B \approx 1.0$ mT for $\nu_{\rm QPC} \approx 2$, $\Delta B \approx 1.9$ mT for $\nu_{\rm QPC} \approx 1$, a smooth background has been subtracted in Fig. 13.5b, c). However, the plunger gate spacing $\Delta V_{\rm PG}$ is similar for both cases ($\Delta V_{\rm PG} \approx 7.2$ mV for $\nu_{\rm QPC} \approx 2$, $\Delta V_{\rm PG} \approx 7.9$ mV for

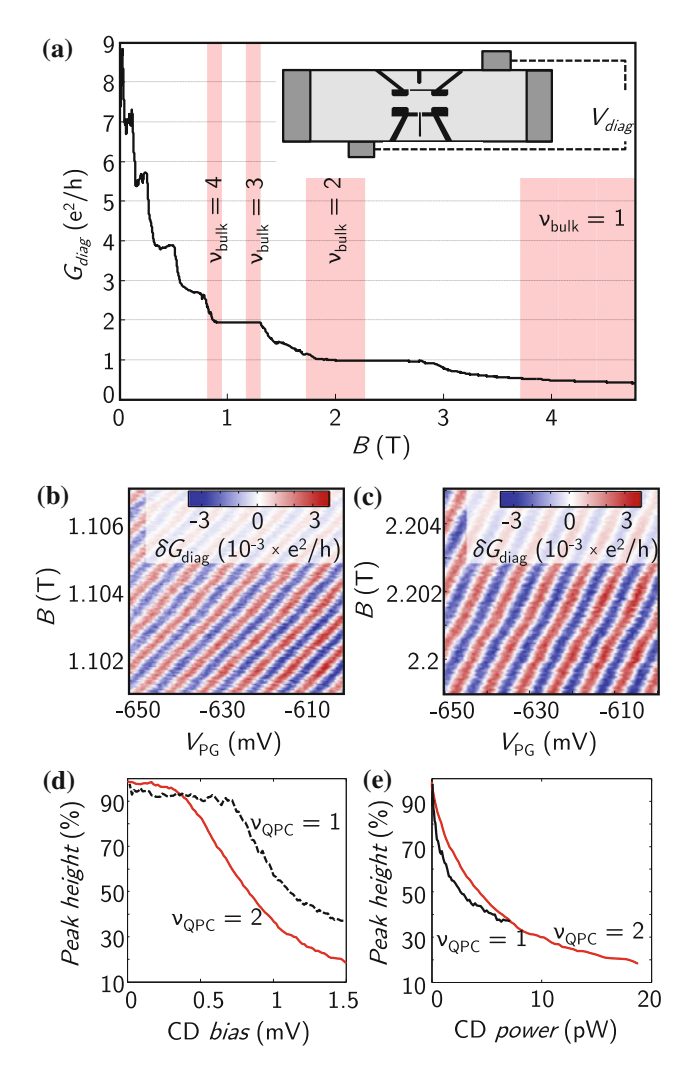


Fig. 13.5 a From the Hall voltage drop $V_{\rm diag}$ diagonally across the QD (*inset*), the effective conductance through the QD can be extracted. Here, we show $G_{\rm diag}$ for a fixed voltage applied to the topgates, as a function of magnetic field. $G_{\rm diag}$ is quantized in multiples of $\frac{e^2}{h}$. Shaded regions indicate the filling factor $\nu_{\rm bulk}$ of the bulk at the corresponding magnetic field values. On the riser of the conductance plateaus, magnetoresistance oscillations are observed. Their dependence on magnetic field and plunger gate voltages is shown in (b) for $\nu_{\rm QPC} \approx 2$, $\nu_{\rm bulk} \approx 4$ and in (c) for $\nu_{\rm QPC} \approx 1$, $\nu_{\rm bulk} \approx 2$. Increasing the bias and the power applied to the charge detector QPC respectively, greatly reduces the peak height of the observed magnetoresistance oscillations (d, e)

 $\nu_{\rm QPC} \approx 1$). This scaling with the QPC filling factor, as well as the direction of the shift are both contrary to what is expected for an Aharonov-Bohm interferometer [35]. Instead, the results are consistent with previous experiments and show that

transport is governed by a Coulomb blockade mechanism [19–21]. In this picture, the slope of the magnetoconductance oscillations is caused by the capacitive coupling of confined and transmitted edge states in the QD instead of a direct effect of the plunger gate on the interferometer area as in the Aharonov-Bohm case. Increasing the bias applied to the charge detector QPC ($G \approx 0.2 \frac{e^2}{h}$, Fig. 13.5d) decreases the amplitude of the oscillations, while the background of the conductance approaches its plateau value.

13.4 Conclusion

In summary, we have investigated transport through a large quantum dot, fabricated on a high-mobility wafer. Single-electron counting techniques, as well as direct current transport have been used to better understand the inner structure of the quantum dot for different filling factors. The periodic modulation of the conductance peak amplitude and spacing can be explained by a capacitive model, involving compressible and incompressible regions inside the dot. The high tunability of the device allowed the investigation of transport in the tunneling regime, as well as in a regime with edge states, perfectly transmitted through the dot (see Sect. 13.3.3). In this case, conductance oscillations, governed by a Coulomb blockade mechanism have been observed.

References

- S. Baer, C. Rössler, T. Ihn, K. Ensslin, C. Reichl, W. Wegscheider, New J. Phys. 15, 023035 (2013). doi:10.1088/1367-2630/15/2/023035
- H.L. Stormer, A. Chang, D.C. Tsui, J.C.M. Hwang, A.C. Gossard, W. Wiegmann, Phys. Rev. Lett. 50, 1953 (1983). doi:10.1103/PhysRevLett.50.1953
- D.C. Tsui, H.L. Stormer, A.C. Gossard, Phys. Rev. Lett. 48, 1559 (1982). doi:10.1103/ PhysRevLett.48.1559
- 4. R.B. Laughlin, Phys. Rev. Lett. 50, 1395 (1983). doi:10.1103/PhysRevLett.50.1395
- R. Willett, J.P. Eisenstein, H.L. Störmer, D.C. Tsui, A.C. Gossard, J.H. English, Phys. Rev. Lett. 59, 1776 (1987). doi:10.1103/PhysRevLett.59.1776
- 6. G. Moore, N. Read, Nucl. Phys. B 360, 362 (1991). doi:10.1016/0550-3213(91)90407-O
- 7. N. Read, E. Rezayi, Phys. Rev. B 59, 8084 (1999). doi:10.1103/PhysRevB.59.8084
- C. Nayak, S.H. Simon, A. Stern, M. Freedman, S.D. Sarma, Rev. Mod. Phys. 80, 1083 (2008). doi:10.1103/RevModPhys.80.1083
- A. Stern, B.I. Halperin, Phys. Rev. Lett. 96, 016802 (2006). doi:10.1103/PhysRevLett.96. 016802
- P. Bonderson, A. Kitaev, K. Shtengel, Phys. Rev. Lett. 96, 016803 (2006a). doi:10.1103/ PhysRevLett.96.016803
- S.D. Sarma, M. Freedman, C. Nayak, Phys. Rev. Lett. 94, 166802 (2005). doi:10.1103/ PhysRevLett.94.166802
- R. Ilan, E. Grosfeld, A. Stern, Phys. Rev. Lett. 100, 086803 (2008). doi:10.1103/PhysRevLett. 100.086803

- P. Bonderson, K. Shtengel, J.K. Slingerland, Phys. Rev. Lett. 97, 016401 (2006). doi:10.1103/ PhysRevLett.97.016401
- M.C. Rogge, C. Fühner, R.J. Haug, Phys. Rev. Lett. 97, 176801 (2006). doi:10.1103/ PhysRevLett.97.176801
- M. Ciorga, A.S. Sachrajda, P. Hawrylak, C. Gould, P. Zawadzki, S. Jullian, Y. Feng, Z. Wasilewski, Phys. Rev. B 61, R16315 (2000). doi:10.1103/PhysRevB.61.R16315
- A.A.M. Staring, B.W. Alphenaar, H. van Houten, L.W. Molenkamp, O.J.A. Buyk, M.A.A. Mabesoone, C.T. Foxon, Phys. Rev. B 46, 12869 (1992). doi:10.1103/PhysRevB.46.12869
- T. Heinzel, D.A. Wharam, J.P. Kotthaus, G. Böhm, W. Klein, G. Tränkle, G. Weimann, Phys. Rev. B 50, 15113 (1994). doi:10.1103/PhysRevB.50.15113
- 18. G. Gamez, K. Muraki, Phys. Rev. B 88, 075308 (2013). doi:10.1103/PhysRevB.88.075308
- Y. Zhang, D.T. McClure, E.M. Levenson-Falk, C.M. Marcus, L.N. Pfeiffer, K.W. West, Phys. Rev. B 79, 241304 (2009). doi:10.1103/PhysRevB.79.241304
- F.E. Camino, W. Zhou, V.J. Goldman, Phys. Rev. B 76, 155305 (2007). doi:10.1103/PhysRevB. 76.155305
- N. Ofek, A. Bid, M. Heiblum, A. Stern, V. Umansky, D. Mahalu, Proc. Natl. Acad. Sci. 107, 5276 (2010). doi:10.1073/pnas.0912624107
- C. Rössler, S. Baer, E. de Wiljes, P.-L. Ardelt, T. Ihn, K. Ensslin, C. Reichl, W. Wegscheider, New J. Phys. 13, 113006 (2011). doi:10.1088/1367-2630/13/11/113006
- M. Field, C.G. Smith, M. Pepper, D.A. Ritchie, J.E.F. Frost, G.A.C. Jones, D.G. Hasko, Phys. Rev. Lett. 70, 1311 (1993). doi:10.1103/PhysRevLett.70.1311
- T. Ihn, S. Gustavsson, U. Gasser, B. Küng, T. Müller, R. Schleser, M. Sigrist, I. Shorubalko, R. Leturcq, K. Ensslin, Solid State Commun. 149, 1419 (2009). doi:10.1016/j.ssc.2009.04.040
- J.M. Elzerman, R. Hanson, L.H. Willems van Beveren, B. Witkamp, L.M.K. Vandersypen, L.P. Kouwenhoven, Nature 430, 431 (2004). doi:10.1038/nature02693
- R. Schleser, E. Ruh, T. Ihn, K. Ensslin, D.C. Driscoll, A.C. Gossard, Appl. Phys. Lett. 85, 2005 (2004). doi:10.1063/1.1784875
- S. Gustavsson, R. Leturcq, B. Simovič, R. Schleser, P. Studerus, T. Ihn, K. Ensslin, D.C. Driscoll, A.C. Gossard, Phys. Rev. B 74, 195305 (2006). doi:10.1103/PhysRevB.74.195305
- D.B. Chklovskii, B.I. Shklovskii, L.I. Glazman, Phys. Rev. B 46, 4026 (1992). doi:10.1103/ PhysRevB.46.4026
- I.M. Ruzin, V. Chandrasekhar, E.I. Levin, L.I. Glazman, Phys. Rev. B 45, 13469 (1992). doi:10. 1103/PhysRevB.45.13469
- H. Pothier, P. Lafarge, C. Urbina, D. Esteve, M.H. Devoret, Europhys. Lett. 17, 249 (1992). doi:10.1209/0295-5075/17/3/011
- 31. C.W.J. Beenakker, Phys. Rev. B 44, 1646 (1991). doi:10.1103/PhysRevB.44.1646
- L.P. Kouwenhoven, C.M. Marcus, P. McEuen, S. Tarucha, R. Westervelt, N. Wingreen, in booktitle Mesoscopic electron transport, series and number proceedings of the NATO Advanced Study Institute on Mesoscopic Electron Transport, Curação, Netherland Antilles, 25 June–5 July 1996 (Kluwer Academic, 1997)
- 33. Y. Meir, N.S. Wingreen, P.A. Lee, Phys. Rev. Lett. **66**, 3048 (1991). doi:10.1103/PhysRevLett. 66 3048
- 34. K. Lier, R.R. Gerhardts, Phys. Rev. B 50, 7757 (1994). doi:10.1103/PhysRevB.50.7757
- B.I. Halperin, A. Stern, I. Neder, B. Rosenow, Phys. Rev. B 83, 155440 (2011). doi:10.1103/ PhysRevB.83.155440

Chapter 14 Preliminary Results of Interference Experiments in the Second Landau Level

Abstract Possible ways to implement a Fabry-Pérot interferometer for the investigation of the properties of the $\nu=5/2$ state are discussed. Defining structures on top of high mobility heterostructures is an experimental challenge and requires detailed study. The geometry of an interferometer has to be carefully chosen in order to be able to perform the envisioned experiments. In the present chapter, we give an overview of progress that we have made towards such an interference experiment at $\nu=5/2$. We present magnetotransport measurements of three different samples, based on heterostructures fabricated with different growth and doping techniques. Experimental challenges that arise and possible solutions are addressed. We demonstrate how a top-gate defined interferometer can be defined, transmitting a fully gapped $\nu=5/2$ FQH state with an energy gap exceeding 200 mK.

14.1 Introduction

"The noise is the signal."

Rolf Landauer-unfortunately not always true

Interference experiments employing Fabry-Pérot or Mach-Zehnder interferometers are expected to shed light on the nature of the FQH states in the second LL. We have discussed the physical foundations for these experiments in Sect. 5.3. In this chapter, we will approach the problem from a purely practical approach, i.e. how such a proposal could actually be implemented.

In order to implement a Fabry-Pérot interferometer with lowest order interference, the design of the interferometer and the 2DEG have to be optimized. The 2DEG should of course exhibit a pronounced $\nu = 5/2$ state, with a large energy gap. Ideally this should be achieved without illumination, as illumination typically degrades the gating properties. Furthermore, the 2DEG should allow to define top-gated structures

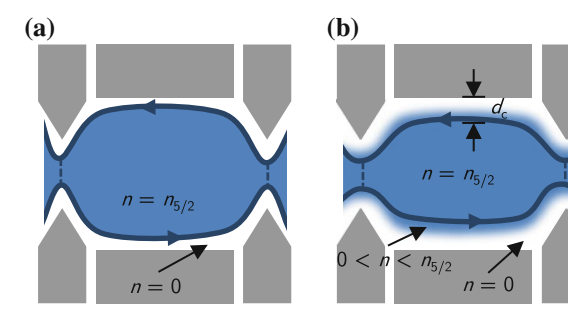
without leakage from the top-gates to the electron gas or charge fluctuations due to charge rearrangements in the doping or screening layers. Unfortunately, heterostructures that show a pronounced $\nu=5/2$ state are a precious and rare asset and are mostly not easily gateable. Thus experimental techniques that nevertheless allow working with the wafers available have to be developed. We have discussed in Sect. 10.3.5, how high-mobility heterostructures can be successfully gated by applying voltages at $T \geq 4\,\mathrm{K}$. Using this, we have implemented Fabry-Pérot interferometers on three different heterostructures, employing different growth and doping techniques. We will discuss the experimental challenges that arise when working with these structures. The most promising results were obtained using a conventionally DX-doped quantum well in combination with illumination. Here, a fully gapped $\nu=5/2$ state could be observed for transport through a top-gate defined interferometer, with an energy gap of more than 200 mK. Our results might open the way to future interference experiments at $\nu=5/2$.

14.2 Design Considerations

In order to guarantee a lowest-order interference process and the absence of Coulomb dominated physics, a puddle of filling factor $\nu=5/2$, strongly coupled to source and drain, has to be formed in the center of the interferometer. In an idealized interferometer (Fig. 14.1a), the density increases stepwise from n=0 to $n=n_{5/2}=5/2\times eB/h$ towards the center of the interferometer and disorder is absent. Here, the confinement potential is assumed to be infinitely steep. Edges are coupled weakly at the entrance and exit of the QPCs (dashed lines in Fig. 14.1a), leading to weak quasiparticle tunneling. In between the edge states (blue area), the density is homogeneous in the bulk, the center of the interferometer and the QPCs. This ensures that no compressible region, separated by an incompressible region from other compressible regions, can be formed in the interferometer. In this situation, we expect Coulomb dominated physics to be absent.

In a more realistic interferometer (Fig. 14.1b), the confinement potential is less steep and the density increases from n = 0 to $n = n_{5/2}$ over a finite length scale

Fig. 14.1 Ideal interferometer with infinitely steep confinement potential (a) versus realistic interferometer (b). Here, the density increases to the bulk value $n_{5/2}$ only over a length scale d_c away from the top-gates



 d_c . In this transition region, different compressible and incompressible regions may exist. If the density is not completely homogeneous throughout the QPCs and the interferometer, compressible puddles, which are insulated from other compressible regions by incompressible regions, may exist (see for example Chap. 13). In this case, the behavior of these puddles is described by Coulomb blockade physics, given their size is small enough [1, 2].

Thus we need to guarantee that the density in the QPCs and the interferometer is equal. We have discussed in Chaps. 10 and 11 how this is done for single QPCs and in weak quasiparticle tunneling experiments, by applying the top-gate voltages at T >4K. The diameter of the quantum dot is mainly determined by two critical length scales: first the length scale over which the bulk density is reduced towards the topgates, d_c , and second the coherence lengths of the candidate wavefunctions at $\nu = 5/2$. The first length scale is crucial, as we need to guarantee a filling factor $\nu = 5/2$ puddle in the center of the interferometer, around which quasiparticles can be braided. As we have seen in Chap. 11, weak backscattering in our high-mobility heterostructures is observed in QPCs of a width of approximately 1.1 µm. Hence, the central width of an interferometer should be much wider than this, as no backscattering of quasiparticles should occur here. In order to guarantee this crucial point, we have only implemented interferometer designs with a central width of at least approximately 2 \(\mu\)m. Ideally we would like to minimize the length d_c , that means we require an interferometer with a very steep confinement potential. We will discuss later, how this can be achieved by using an illumination technique. The second length scale, the coherence length of the candidate wavefunctions at $\nu = 5/2$, limits the size of the interferometer. The backscattered current due to lowest order interference of quasiparticles depends exponentially on a characteristic coherence length $L_{\phi}(T)$ or coherence temperature $T^*(L)$ [3]:

$$I_{12}^{(\mathrm{QP})} \propto e^{-T/T^*(L)} = e^{-L/L_{\phi}(T)}$$
 (14.1)

Hence, for a given electronic temperature, limited by our setup, the characteristic length L of the interferometer should be kept as short as possible. The coherence length $L_{\phi}(T)$ and coherence temperature $T^*(L)$ of the edge excitations depend on the scaling parameters of the charge and neutral scaling expontents, g_c and g_n (see [3]) and the velocities of charge and neutral modes v_c and v_n and can be written as [3]:

$$L_{\phi}(T) = \frac{1}{2\pi T} \left(\frac{g_c}{v_c} + \frac{g_n}{v_n} \right)^{-1}$$
 (14.2)

$$T^*(L) = \frac{1}{2\pi L} \left(\frac{g_c}{v_c} + \frac{g_n}{v_n} \right)^{-1}$$
 (14.3)

The coherence length L_{ϕ} scales linearly with the inverse temperature. Coherence lengths for the different e/4 edge excitations of the candidate wavefunctions have been calculated in [3], using the numerically calculated values for the velocities of charge and neutral modes v_c and v_n of [4].

e/4	MR Pf.	Pf, SU(2) ₂	K = 8	(3,3,1)	e/2
L_{ϕ} in μ m at T = 12.5 mK	2.8	1.0	38	1.4	9.6
T^* for $L = 1$ μ m	36	13	484	19	121

Table 14.1 Coherence lengths L_{ϕ} (at $T=12.5\,\mathrm{mK}$) and coherence temperatures T^* (for $L=1\,\mu\mathrm{m}$) for the e/4 quasiparticle excitations of the different candidate wavefunctions at $\nu=5/2$

The right column shows coherence length and coherence temperature of the Laughlin-type e/2 quasiparticles that are allowed for all candidate wavefunctions. Adapted from [3]

The L_{ϕ} (at a temperature $T=12.5\,\mathrm{mK}$) and coherence temperatures T^* (for $L=1\,\mu\mathrm{m}$) are shown in Table 14.1 for the different states. At our lowest electronic temperature L_{ϕ} is between 1 $\mu\mathrm{m}$ for the $\overline{\mathrm{Pf}}$ and SU(2)₂ states and 38 $\mu\mathrm{m}$ for the K=8 state. We remark that the results depend on the exact magnitude of the velocities of charge and neutral modes v_c and v_n and are thus also influenced by the steepness of the confinement potential and other effects. The rightmost column in Table 14.1 shows the coherence length and coherence temperature of the e/2 Laughlin type quasiparticles, which are common to all the candidate wavefunctions [3].

The interferometers used by us have a characteristic length L of approximately 2–2.5 μ m. Hence the interference signal is already expected to be damped because coherence lengths are of comparable magnitude. Since the lateral distances need to be larger than the QPC gap of typically 1.1 μ m, this cannot be circumvented, if we want to guarantee a gapped $\nu = 5/2$ state in the center of the interferometer. Hence it would be desirable to reduce the length scale d_c , by implementing a confinement potential of maximal steepness. We will discuss later, how this can be achieved by illumination and applying gate voltages at high temperatures. In this case, a fully gapped $\nu = 5/2$ state could be observed in QPCs as narrow as 950 nm.

14.3 Transport Measurements

In the following, we will present magnetotransport measurements through three different Fabry-Pérot interferometers, defined on heterostructures employing different growth techniques. Heterostructures employing quantum well doping, DX doping with screening quantum wells and ordinary DX doping have been studied. The wafers D120427C (sample A, $n_s \approx 2.2 \times 10^{11}$ cm⁻², $\mu \approx 1.9 \times 10^7$ cm²/Vs, quantum well doping) and D120702A (sample B, $n_s \approx 2.3 \times 10^{11}$ cm⁻², $\mu \approx 2.3 \times 10^7$ cm²/Vs, DX-doping with screening quantum wells) are optimized for the observation of the $\nu = 5/2$ state without prior LED illumination [5]. The wafer D110726B (sample C, $n_s \approx 3.1 \times 10^{11}$ cm⁻², $\mu \approx 1.8 \times 10^7$ cm²/Vs after illumination, conventional DX-doping) has to be illuminated at $T \approx 10$ K using a red LED, to allow for the observation of a fully quantized $\nu = 5/2$ state and pronounced RIQH states.

We discuss the two main problems that make the experimental realization of a Fabry-Pérot interferometer at $\nu=5/2$ difficult: first the insufficient stability of the heterostructures when voltages are applied to the top-gates or when those voltages are varied. The second difficulty is defining the interferometer area without reducing the density in the constrictions and hence inducing Coulomb dominated effects and strong backscattering.

14.3.1 Sample Stability Issues

The sample A uses a quantum well doping scheme, where X-band electrons provide additional screening. As we have seen in Sect. 10.3.5, screening electrons may lead to strong hysteretic processes when top-gate voltages are applied. This can be circumvented by applying gate voltages at $T \geq 4$ K, which has been done here. Figure 14.2a, b shows R_{xy} and R_{xx} measured in the bulk, and R_{diag} and R_{long} measured diagonally or longitudinally across the interferometer of sample A, versus the magnetic field B. Apart from IQH states, FQH states at $\nu = 5/2$, 7/3 and 8/3 and RIQH states are observed in the bulk. The interferometer is shown schematically in the inset of Fig. 14.2a. It is defined by applying negative top-gate voltages of -3.63 V (QPCL) or -3.8 V (QPCR) to the 1.2 μ m wide QPCs and applying -3.2 V to the plunger gates PG1 and PG2. The electron gas underneath the wide plunger gates is depleted at a top-gate voltage of approximately -2.5 V, while approximately -3.1 V have to be applied to deplete the electron gas underneath the narrow QPC gates.

In this configuration wide regions of vanishing R_{long} indicate the transmission of IQH states through the interferometer. The density in the constrictions is slightly reduced compared to the bulk density. This can be seen from the shift of the center of the IQH minima in R_{long} towards lower magnetic fields, compared to the center of the minima in R_{xx} .

In this situation, the top-gate voltages have been applied at $T \ge 4$ K and have not been changed at lower T. In this situation, conductance fluctuations for transport through the interferometer are only weak. However, for the observation of periodic conductance oscillations tuning the transmission of the QPCs is crucial. After the voltages of both QPCs have been changed at millikelvin temperatures in order to look for conductance oscillations, strong fluctuations in the longitudinal resistance appear. Figure 14.3 shows the longitudinal resistance, as a function of the magnetic field for different voltages applied to the left QPC, while the voltages applied to the other gates are not changed. Strong resistance fluctuations modulate the longitudinal resistance, making the observation of periodic conductance oscillations impossible.

The second Fabry-Pérot interferometer under study, sample B, uses a DX-doping scheme with additional quantum wells. The interferometer with 1.1 μ m wide QPCs has been defined by applying $-1.9\,\mathrm{V}$ to all top-gates at $T \geq 4\,\mathrm{K}$. The electron gas underneath the top-gates is depleted at voltages of approximately $-1.5\,\mathrm{V}$. Figure 14.4a, b shows R_{xy} in the bulk and R_{long} measured longitudinally across the interferometer. As before, IQH states are perfectly transmitted through the interferometer, whereas

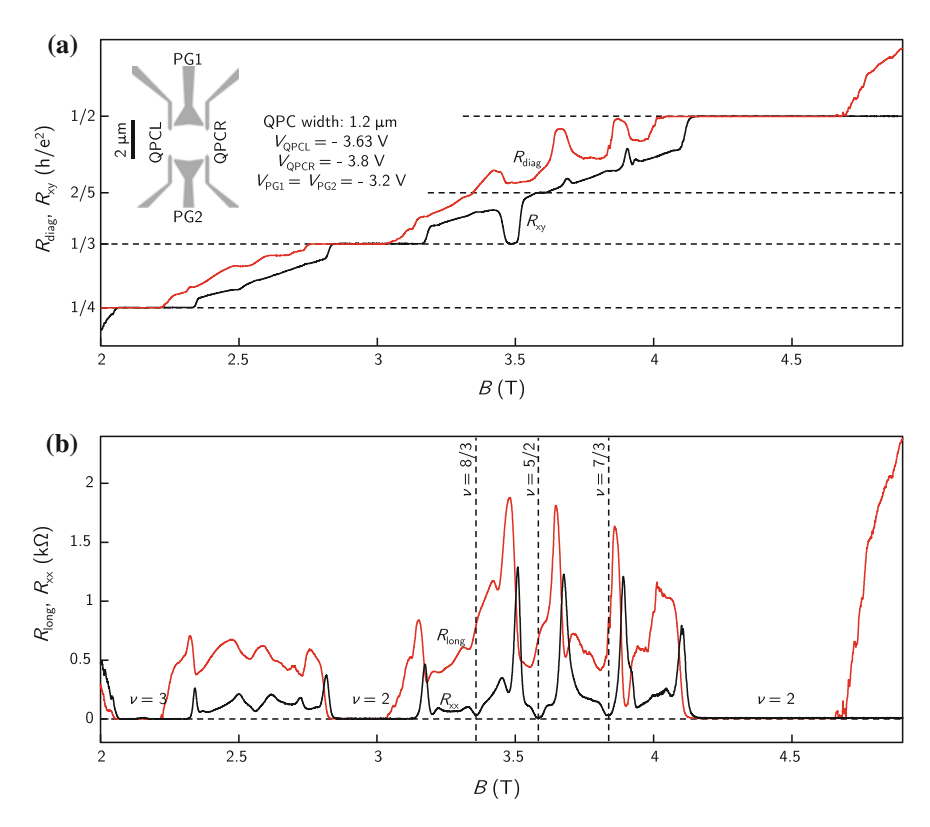


Fig. 14.2 a R_{xy} measured in the bulk and R_{diag} measured diagonally across the interferometer as a function of the magnetic field. The QPCs at the entrance and exit of the interferometer are 1.2 μ m wide and are biased to -3.63 and -3.8 V. **b** R_{xx} measured in the bulk and R_{long} measured longitudinally across the interferometer as a function of the magnetic field. (Sample D120427C-1C)

backscattering occurs in between IQH filling factors. At $\nu=5/2$, $R_{\rm long}\approx 260~\Omega$ is found. On the high magnetic field side of the IQH minima in $R_{\rm long}$, resistance fluctuations are observed (Fig. 14.4c–e). In contrast, on the low magnetic field side of the IQH minima no such behavior is observed. Similar observations have been made in [6]. At the magnetic fields where these resistance fluctuations occur, transport through the bulk is still quantized, whereas the filling factor of the QPCs is slightly reduced. This is exactly a configuration where we would expect lowest-order interference processes to occur. Here the transport through the interferometer is particularly sensitive to electrostatic fluctuations close to the QPCs, as counterpropagating edge states are only separated by a narrow incompressible region. The time-dependence of the fluctuations in the longitudinal resistance is shown in Fig. 14.5. Here, strong telegraph noise has been observed, even without changing the gate voltages at millikelvin temperatures. With this sample, no periodic conductance oscillations could be observed, even after intensive tuning of the QPCs. We have looked for periodic

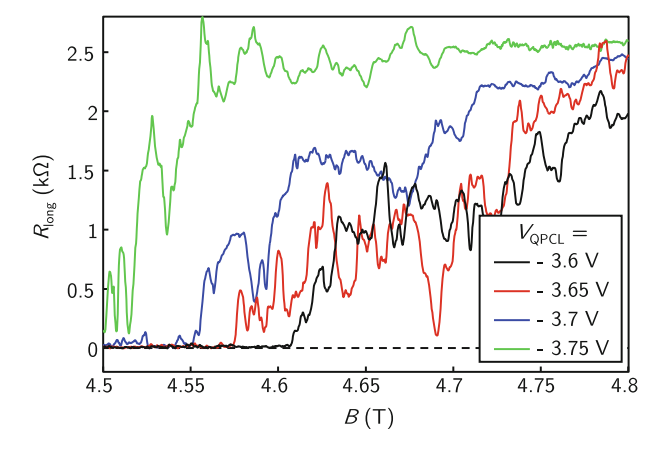


Fig. 14.3 Longitudinal resistance versus the magnetic field B, for different voltages applied to the *left* QPC. All other gate voltages are kept constant ($V_{PG1} = V_{PG2} = -3.2 \text{ V}$, $V_{QPCR} = -3.67 \text{ V}$). After the gate voltages have been varied at millikelvin temperatures, strong telegraph noise is observed. (Sample D120427C-1C)

conductance oscillations at the low- and high-magnetic field ends of IQH and FQH plateaus. In those configurations, the total transmission of the QPCs, as well as the asymmetry of the individual transmissions has been varied. In none of the configurations we were able to observe periodic conductance oscillations, neither by varying the *B*-field nor by varying the QPC voltage. Most likely the wafer stability is not sufficient for the observation of lowest-order interference. Tuning the system to a Coulomb dominated regime by strongly reducing the density in the QPCs was not possible either. The voltages that could be applied to the top-gates without damaging the sample were not sufficient for a substantial reduction of the density in the QPCs.

14.3.2 Optimizing the Transmission by Sample Illumination

The third sample that we investigated, sample C, utilizes a heterostructure with conventional DX-doping. The top-gate layout is shown in the inset of Fig. 14.6. Here, 950 nm wide QPCs and an interferometer with a maximum width of approximately 2.2 μ m have been defined by electron beam lithography and subsequent metal evaporation and lift-off. In the first measurements, the sample has not been illuminated before cooling it down to millikelvin temperatures. Negative voltages have been applied to the top-gates at $T \geq 4$ K, in order to allow a relaxation of the density in the QPCs ($V_{\rm QPCL} = -1.5$ V, $V_{\rm QPCL} = -1.6$ V, $V_{\rm PG1} = V_{\rm PG2} = -1.4$ V). The electron gas underneath the top-gates is depleted at approximately -1.1 V. The Hall resistance R_{xy} and longitudinal resistance R_{xx} are measured in the bulk, far away from the top-gates. In addition we measure the resistance longitudinally ($R_{\rm long}$) and diagonally

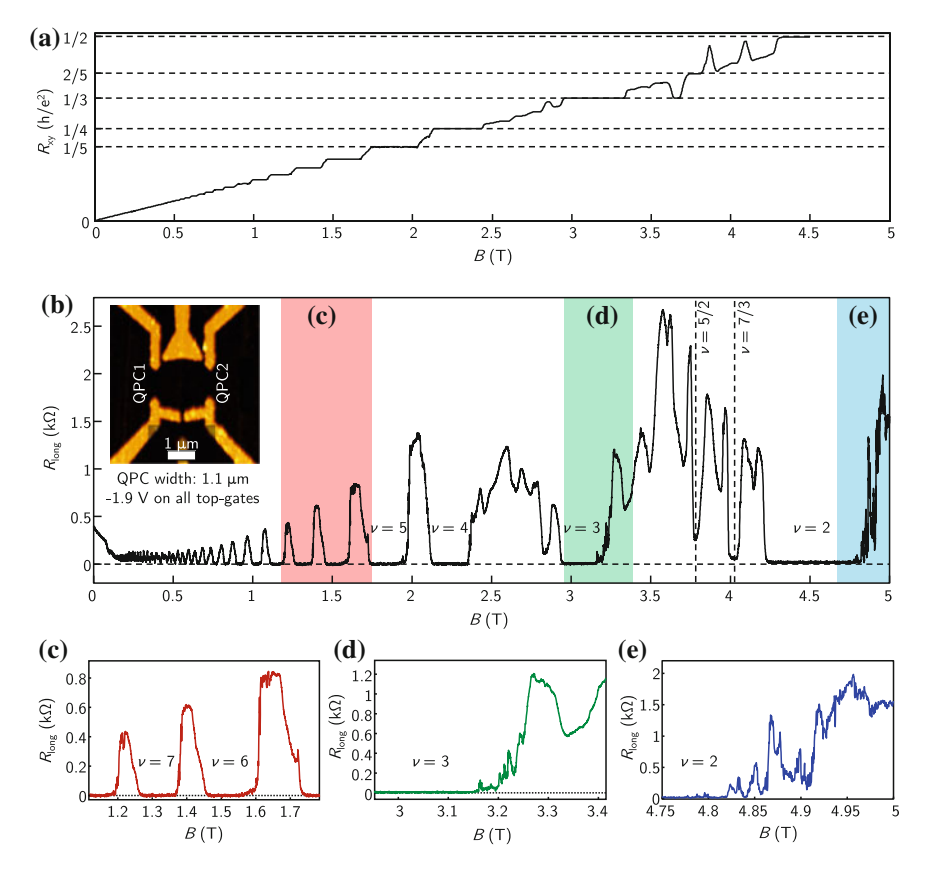


Fig. 14.4 a R_{xy} measured in the bulk versus the magnetic field B. b $R_{\rm long}$, measured longitudinally across the interferometer with 1.1 μ m wide QPCs (*inset*). While $R_{\rm long} \approx 0$ for IQH states, $R_{\rm long} \approx 260~\Omega$ is observed at $\nu = 5/2$. Close ups of the shaded regions in b are shown in (c-e). Non-periodic conductance fluctuations are observed at the high magnetic field end sides of the IQH minima in $R_{\rm long}$, while being absent on the low magnetic field end sides. (Sample D120702A-2C)

 $(R_{\rm diag})$ across the biased interferometer gates. Figure 14.6 shows R_{xx} (blue), R_{xy} (red), $R_{\rm diag}$ (turquoise) and $R_{\rm long}$ (green) as a function of the magnetic field. In the bulk, integer quantum Hall states with a quantized plateau in R_{xy} and vanishing R_{xx} are observed. Close to $\nu = 5/2$, R_{xx} drops, but does not reach zero (without illumination). The diagonal resistance $R_{\rm diag}$ exhibits plateaus, which are shifted to lower magnetic fields than the resistance plateaus in R_{xy} , indicating a reduced density within the constrictions. An effective filling factor of the QPCs, $\nu_{\rm QPC}$ can be extracted from $R_{\rm diag}$ via the relation $R_{\rm diag} = \frac{1}{\nu_{\rm QPC}}h/e^2$ [7]. A similar relation can be found for the longitudinal resistance: $R_{\rm long} = \left(\frac{1}{\nu_{\rm QPC}} - \frac{1}{\nu_{\rm bulk}}\right)h/e^2$. Hence, $R_{\rm long}$ exhibits a plateau in a situation where transport in bulk and QPC is quantized and the respective filling factors differ by one (Fig. 14.6). At the low-magnetic field ends of

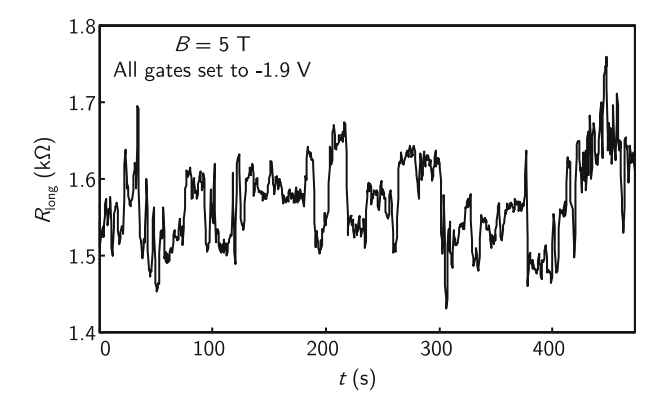


Fig. 14.5 Time dependence of the longitudinal resistance at B = 5 T. Strong telegraph noise modulates the resistance. (Sample D120702A-2C)

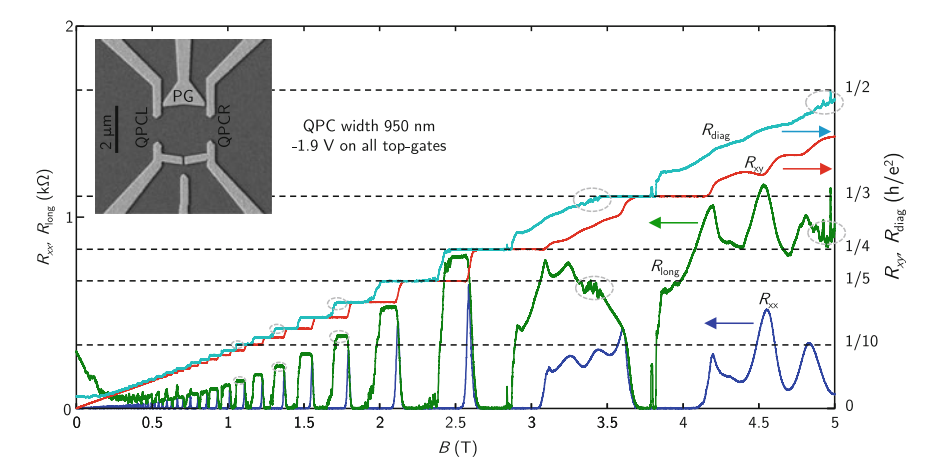


Fig. 14.6 Four-terminal resistances as a function of the magnetic field B. R_{xy} and R_{xx} indicate the filling factors of the bulk. R_{long} and R_{diag} are measured longitudinally and diagonally across the biased gates of the interferometer, which is shown in the inset. The filling factor of the QPCs is reduced compared to the filling factor of the bulk. At the low magnetic field sides of the resistance plateaus in R_{diag} , conductance oscillations are found (encircled areas). R_{long} reaches a quantized value whenever both R_{xy} and R_{diag} are quantized at a conductance plateau and bulk and QPC filling factors differ by one. (Sample D110726B-1A)

the resistance plateaus of $R_{\rm diag}$, conductance oscillations are observed in $R_{\rm diag}$ and $R_{\rm long}$ (encircled in gray in Fig. 14.6). Such conductance oscillations are observed for QPC filling factors $\nu_{\rm QPC}$ of 2, 3, 6, 8, 10, 12, 14, 16. The magnetic field period ΔB of the oscillations is extracted from a Fourier transformation of the data and is shown in Fig. 14.7a, as a function of $1/\nu_{\rm QPC}$. Clearly, a linear dependence of ΔB and $1/\nu_{\rm QPC}$ is observed, with a slope $\Delta B \times \nu_{\rm QPC} = 1.91$ mT.

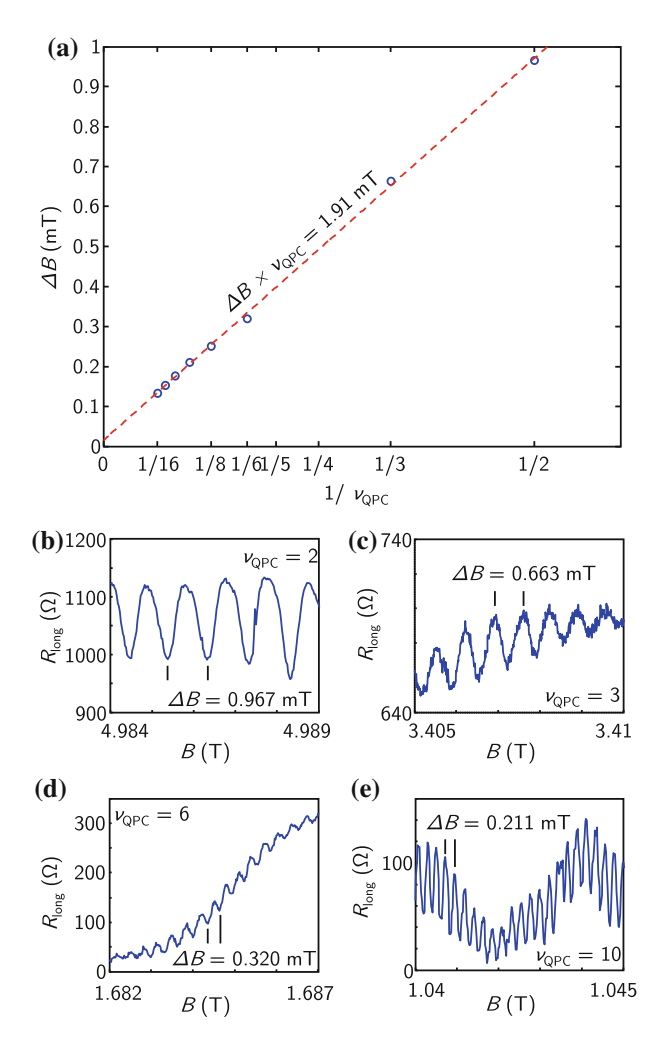


Fig. 14.7 a Magnetic field periodicity of the conductance oscillations in Fig. 14.6 as a function of the inverse QPC filling factor, $1/\nu_{\rm QPC}$. Oscillations for various filling factors are found. The periodicity scales linearly with $1/\nu_{\rm QPC}$. **b-e** Oscillations of the longitudinal resistance as a function of the magnetic field *B* for QPC filling factors 2, 3, 6 and 10. The width of the magnetic field interval of each individual plot is identical. (Sample D110726B-1A)

Assuming a circular QD, this corresponds to a dot diameter of 1.66 μ m, consistent with the top-gate layout and realistic gate depletion lengths. Conductance oscillations in R_{long} are shown for QPC filling factors $\nu_{QPC} = 2$, 3, 6 and 10 in Fig. 14.7b–e. Here, the width of the magnetic field axis of each individual plot is identical. With the heterostructure in use, it was not possible to observe conductance oscillations as a function of the voltage applied to the plunger gate at a fixed magnetic field. Here, changing the gate voltages created conductance fluctuations that made an

observation of the conductance oscillations impossible. Thus it was not possible to observe the characteristic signature of a Coulomb dominated process, which is the positive slope of the conductance oscillations when they are plotted as a function of plunger gate voltage and the magnetic field (see for example Fig. 13.5). However, from the reduced filling factor in the QPCs, the scaling of ΔB with $1/\nu_{QPC}$ and the size of the interferometer, a Coulomb dominated mechanism is strongly indicated. Although conductance oscillations could not be observed as a function of the plunger gate voltage, the fact that conductance oscillations with magnetic field periods as small as 130 μ T could be observed makes the sample promising for further study. Furthermore, magnetic field stability seems not to be an issue for our setup, down to small B-field periodicities.

In order to tune the interferometer to a situation where we expect lowest order interference and where the density is approximately constant through the QPCs, the system has been illuminated at T > 4 K using a red LED. By doing this, the density of the 2DEG has been increased from $n_s \approx 2.8 \times 10^{11} \text{ cm}^{-2}$ to $n_s \approx 3.1 \times 10^{11}$ cm⁻², while the mobility remained practically unchanged ($\mu \approx 1.8 \times 10^7$ cm²/Vs). Gate voltages of $-1.45 \,\mathrm{V}$ have been applied to all top-gates at $T > 4 \,\mathrm{K}$. After illumination, the electron gas underneath the gates is depleted at approximately -1.4 V. In this situation, we again measure R_{xy} in the bulk and R_{diag} and R_{long} across the interferometer (R_{xx} could not be measured due to a defective contact). The measured resistances are shown in Figs. 14.8a (R_{long}) and b (R_{xy} and R_{diag}). The quantization of FQH states has been drastically improved by the illumination—fully quantized FQH states with a clear plateau in R_{xy} are observed at $\nu = 8/3$, 5/2 and 7/3in the bulk. Furthermore, pronounced RIQH states are observed. Comparing R_{xy} and $R_{\rm diag}$, we see that resistance plateaus of the IQH states overlap, indicating perfect transmission and equal densities in bulk and QPCs. In between $\nu = 2$ and $\nu = 3$, we find $R_{\text{diag}} \geq R_{xy}$, which indicates an enhanced backscattering in the QPCs. At $\nu = 8/3$, 5/2 and 7/3, we observe $R_{\rm diag} = R_{xy}$ and $R_{\rm long} \approx 0$, indicating a perfect transmission of those FQH states through the interferometer. This is exactly the starting situation that is required for a lowest-order interference experiment. Due to the vanishing R_{long} for transport through the whole interferometer (with all top-gates biased to $-1.45 \,\mathrm{V}$), the $\nu = 5/2$ can be expected to remain fully gapped in the much wider central region of the interferometer, even if the QPCs are further closed.

Transport through the interferometer has also been investigated in a non-equilibrium situation. Here, a finite DC current $I_{\rm DC}$ has been added on top of the small AC current $I_{\rm AC}$ that was used for the lock-in measurement: $I_{\rm SD} = I_{\rm AC} + I_{\rm DC}$. The differential longitudinal resistance $dR_{\rm long}/dI_{\rm SD}$ is plotted in colorscale as a function of the magnetic field B and the DC current $I_{\rm DC}$ in Fig. 14.8c. Close to the RIQH states, bright diamond-shaped regions of large differential longitudinal resistance are found. This effect arises from the properties of the RIQH phases and is also observed in pure bulk measurements. This will be discussed in detail in Chap. 15.

The FQH states at $\nu = 5/2$, 7/3 and 8/3 show up as black diamond-shaped regions of small differential longitudinal resistance. The $\nu = 5/2$ and 7/3 states remain quantized until $I_{\rm DC} \approx 3.9$ nA or $I_{\rm DC} \approx 4.4$ nA, whereas the $\nu = 8/3$ state already disappears at $I_{\rm DC} \approx 1.5$ nA. These currents correspond to Hall voltage drops across the QPC

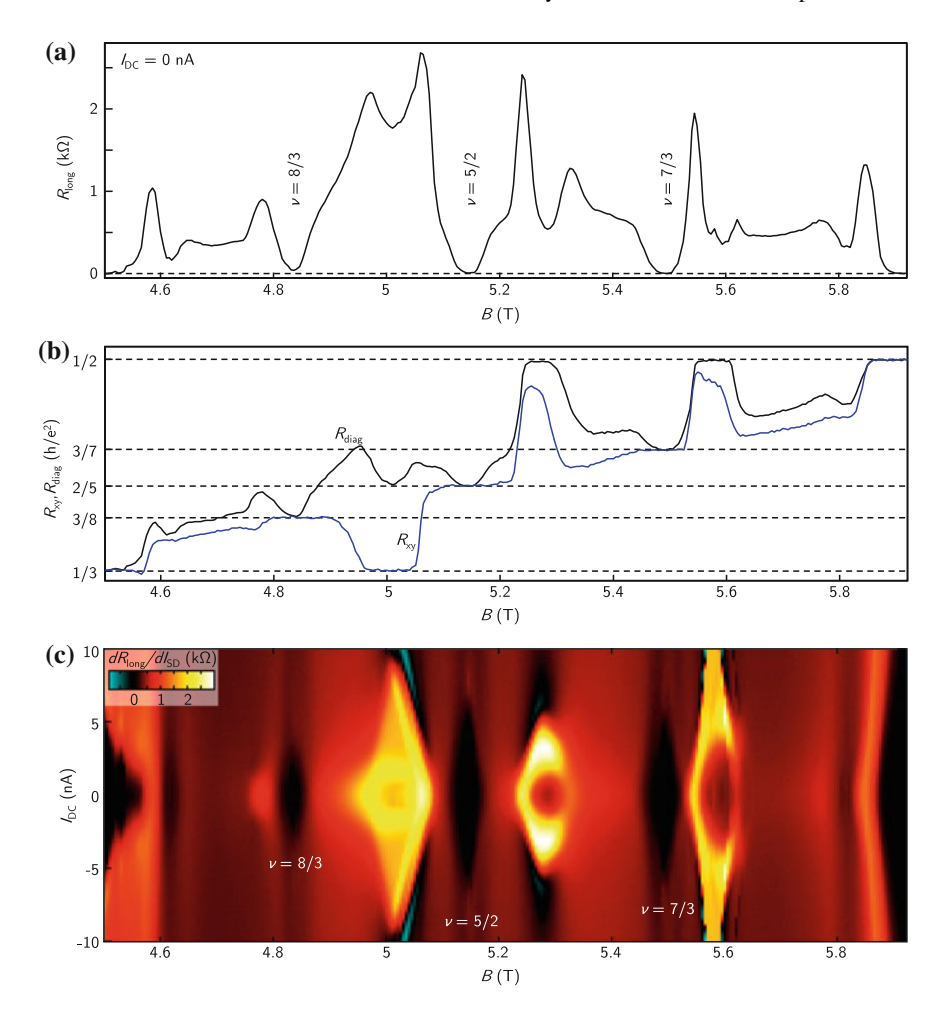


Fig. 14.8 a Longitudinal resistance, measured across the interferometer with -1.45 V applied to all top-gates, versus the magnetic field B. The transport through the interferometer is fully quantized at $\nu=8/3$, 5/2 and 7/3. b R_{xy} and $R_{\rm diag}$ versus the magnetic field B. While R_{xy} and $R_{\rm diag}$ overlap for $\nu=2$ and 3, $R_{\rm diag} \geq R_{xy}$ is found in between those two filling factors. At magnetic fields corresponding to the filling factors $\nu=8/3$, 5/2 and 7/3, R_{xy} and $R_{\rm diag}$ are identical, indicating perfect transmission. c Differential longitudinal resistance versus DC current and the magnetic field. The FQH states at $\nu=5/2$, 7/3 and 8/3 show up as black diamond shaped regions with vanishing differential longitudinal resistance. At $\nu=5/2$, 7/3 and 8/3 they remain fully quantized until $I_{\rm DC}\approx3.9$ nA, $I_{\rm DC}\approx4.4$ nA or $I_{\rm DC}\approx1.5$ nA, which corresponds to a Hall voltage drop of approximately 52 μ V, 44 μ V or 15 μ V. This energy scale is of the same magnitude as the energy gap of these states. (Sample D110726B-1A)

of approximately 15 μ V ($\nu=8/3$), 40 μ V ($\nu=5/2$) and 49 μ V ($\nu=7/3$). In similar measurements of dR_{xx}/dI_{SD} in the bulk (see for example Fig. 15.1a), FQH states remain fully quantized until much higher DC currents and FQH states show up as black stripes in the differential longitudinal resistance. Also, the bright diamond shaped regions in Fig. 14.8c which are related to the RIQH states are much more sensitive to temperature than the FQH states. We conclude that the FQH states are destroyed most likely by either local heating or a local breakdown effect in the QPC, but not due to heating the complete sample.

We have performed temperature-dependent measurements of the longitudinal resistance, in order to extract an energy gap of the FQH states in the QPC. Figure 14.9a shows $R_{\rm long}$ as a function of the magnetic field for temperatures from approximately 10 mK to approximately 120 mK. Close to the FQH minima in $R_{\rm long}$, an activated behavior $R_{\rm long} \propto e^{-E_{\rm gap}/2k_{\rm B}T}$ is observed (Fig. 14.9c, e, g). The energy gap $E_{\rm gap}/k_{\rm B}$ reaches maximum values of approximately 100 mK ($E_{\rm gap}=17.2~\mu eV$) for $\nu=8/3$, 200 mK ($E_{\rm gap}=34.5~\mu eV$) for $\nu=5/2$ and 270 mK ($E_{\rm gap}=46.5~\mu eV$) for $\nu=7/3$. The dependence of the extracted energy gap on the magnetic field is illustrated in Fig. 14.9b, d, f for the different filling factors. The size of the energy gaps is of the same magnitude as the Hall voltage drop at which the FQH states disappear. This might indicate that it is the voltage drop across the QPC and not a heating effect that destroys the FQH states.

In order to investigate if this is an activated process or a breakdown effect with a different voltage dependence, we investigate the dependence of the logarithm of the longitudinal resistance at $\nu=5/2$, 7/3 and 8/3 versus the inverse Hall voltage $1/V_{\rm H}$ (Fig. 14.10). For this the longitudinal resistance has been measured at a fixed magnetic field as a function of the DC current. The Hall voltage then is found from $V_{\rm H}=I_{\rm DC}\times R_{xy}$. For an activated behavior versus the Hall voltage drop, a behavior $R_{\rm long}\propto e^{-\frac{E_{\rm gap}}{eV_{\rm H}}}$ would be expected. Using the energy gaps extracted from the temperature measurements, we expect the logarithm of $R_{\rm long}$ to drop linearly with $1/V_{\rm H}$, with the slopes indicated by the black dashed lines in Fig. 14.10. While the agreement is still reasonable for $\nu=8/3$, the longitudinal resistance for $\nu=5/2$ and 7/3 falls off much faster and only agrees well with an activated behavior in a narrow Hall voltage range.

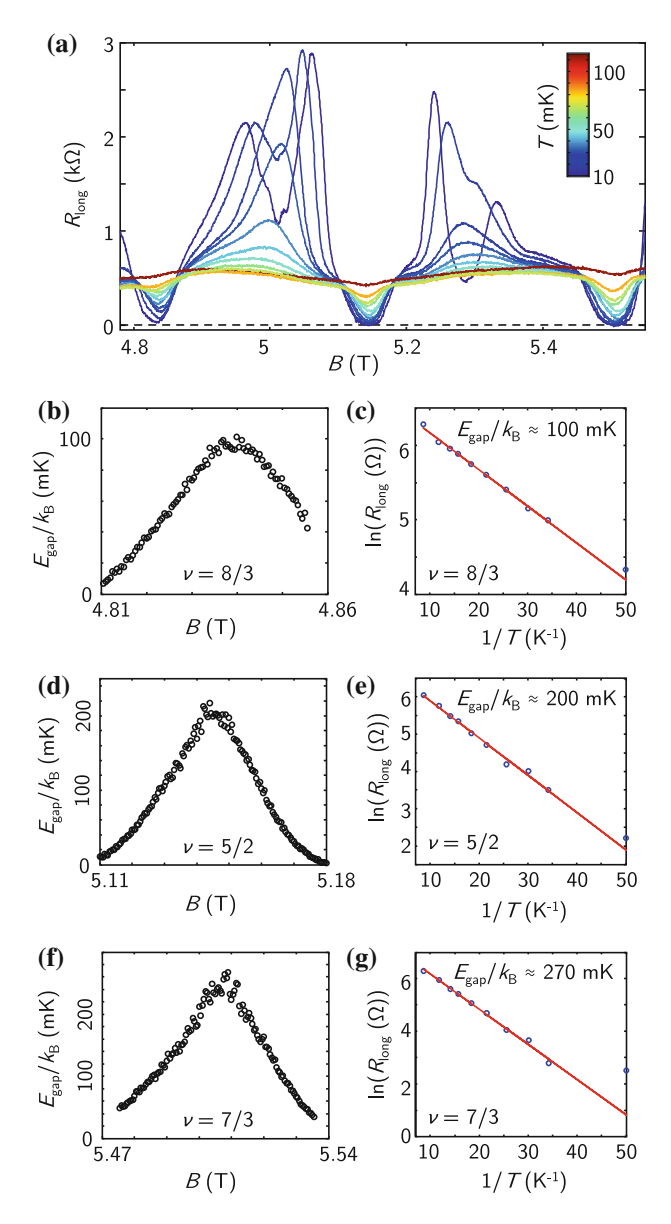
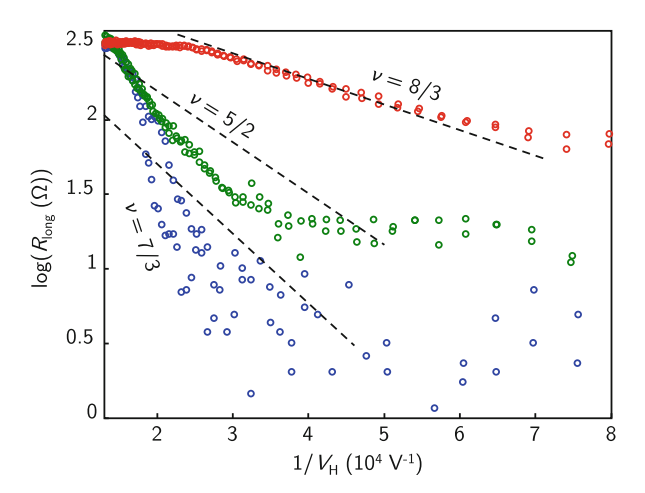


Fig. 14.9 a Temperature dependence of the resistance measured longitudinally across the interferometer with all *top-gates* set to $-1.45\,\mathrm{V}$, versus the magnetic field. The longitudinal resistance at filling factors $\nu=8/3$, 5/2 and 7/3 shows an activated behavior (\mathbf{c} , \mathbf{e} , \mathbf{g}) when varying the temperature. Maximum energy gaps of approximately $100\,\mathrm{mK}$ ($\nu=8/3$), $200\,\mathrm{mK}$ ($\nu=5/2$) and $270\,\mathrm{mK}$ ($\nu=7/3$) are found. The extracted energy gap values are maximal in a small region around the corresponding filling factor and are shown in \mathbf{b} , \mathbf{d} , \mathbf{f} as a function of the magnetic field B. (Sample D110726B-1A)

Fig. 14.10 Logarithm of the longitudinal resistance versus the inverse Hall voltage, $1/V_{\rm H}$, for filling factors $\nu = 5/2$, 7/3 and 8/3. Here the magnetic field is kept fixed and the Hall voltage is varied by changing the DC current: $V_{\rm H} = I_{\rm DC} \times R_{xy}$. Dashed lines indicate the slope that is expected for an activated behavior with the energy gaps extracted from the temperature measurements. (Sample D110726B-1A)



14.4 Conclusion and Outlook

To summarize, we have presented magnetotransport measurements of three Fabry-Pérot interferometers, employing three different heterostructures based on different growth and doping techniques. We have discussed experimental challenges that arise due to the difficult gating properties of high mobility electron gases. In one sample, we have observed a fully gapped $\nu=5/2$ state for transport through a top-gate defined interferometer, with an energy gap exceeding 200 mK. Here, the steepness of the confinement potential was enhanced by illumination, allowing a $\nu=5/2$ state through 950 nm wide QPCs without backscattering. Unfortunately the transmission through the QPCs was even too high for the implementation of a lowest-order interference experiment in this device: even at QPC gate voltages as low as approximately -4 V, IQH and FQH states were perfectly transmitted through the QPC. Pinching off further, transmission was reduced, but also telegraph-noise due to the very negative gate voltages started to set in. Hence in this device no periodic conductance oscillations were observed.

Further experiments with a similar sample layout, but more narrow QPCs seem promising. Our results show how small interferometers could be defined, using optimized illumination and gating techniques. We have demonstrated that the $\nu=5/2$ state may survive fully gapped in an approximately 2 μ m wide interferometer and even in 950 nm wide QPCs.

References

- B.I. Halperin, A. Stern, I. Neder, B. Rosenow, Phys. Rev. B 83, 155440 (2011). doi:10.1103/ PhysRevB.83.155440
- Y. Zhang, D.T. McClure, E.M. Levenson-Falk, C.M. Marcus, L.N. Pfeiffer, K.W. West, Phys. Rev. B 79, 241304 (2009). doi:10.1103/PhysRevB.79.241304

- W. Bishara, P. Bonderson, C. Nayak, K. Shtengel, J.K. Slingerland, Phys. Rev. B 80, 155303 (2009). doi:10.1103/PhysRevB.80.155303
- X. Wan, Z.-X. Hu, E.H. Rezayi, K. Yang, Phys. Rev. B 77, 165316 (2008). doi:10.1103/ PhysRevB.77.165316
- C. Reichl, J. Chen, S. Baer, C. Rössler, T. Ihn, K. Ensslin, W. Dietsche, W. Wegscheider, New J. Phys. 16, 023014 (2014). doi:10.1088/1367-2630/16/2/023014
- H. Choi, P. Jiang, M.D. Godfrey, W. Kang, S.H. Simon, L.N. Pfeiffer, K.W. West, K.W. Baldwin, New J. Phys. 13, 055007 (2011). doi:10.1088/1367-2630/13/5/055007
- 7. C.W.J. Beenakker, H. van Houten, cond-mat/0412664 (2004), Solid State Phys. 44, 1 (1991)

Part V Bulk Transport Experiments

Chapter 15 Non-equilibrium Transport in Density Modulated Phases of the Second Landau Level

Abstract We investigate non-equilibrium transport in the reentrant integer quantum Hall phases of the second Landau level. At high currents, we observe a transition from the reentrant integer quantum Hall phases to isotropic conduction. Surprisingly, this transition is markedly different for the hole- and electron sides of each spin-branch of the second Landau level. While the hole bubble phases exhibit a sharp transition to an isotropic compressible phase, the transition for the electron side occurs gradually via an intermediate phase. This behavior might be understood in terms of a current-driven two-dimensional melting transition, either taking place as a first order phase transition or as two continuous transitions involving an intermediate phase. The breaking of the particle-hole symmetry might have consequences for the physics at $\nu=5/2$ and other fractional quantum Hall states in the second Landau level.

15.1 Introduction

The properties of the lowest Landau level (N=0) are strongly influenced by fractional quantum Hall (FQH) physics, which gives rise to a large number of highly degenerate, incompressible ground states with a vanishing longitudinal resistance R_{xx} and a quantized Hall resistance $R_{xy} = h/\nu e^2$ at the corresponding filling factor ν . In contrast, the physics of higher Landau levels (LLs), $N \geq 2$, is dominated by density-modulated quantum Hall phases. Close to half-filling, highly anisotropic and nonlinear transport properties were found [2–4]. At $\nu \approx 4+1/4$ and $\nu \approx 4+3/4$, R_{xx} was found to vanish, while R_{xy} was restored to the value of the neighboring integer quantum Hall (IQH) plateau [2–4]. This effect was referred to as reentrant integer quantum Hall (RIQH) effect. Theoretical [5–10] and experimental [2–4, 11–14] evidence points to density modulated stripe or bubble phases which are responsible for the resistance anisotropy or the RIQH effect.

In the second Landau level, N = 1, a competition between FQH states and RIQH states is observed [15–22]. Here, theory suggests the existence of two electron and

Results shown in the following chapter have been partially published in the article [1]: Non-equilibrium transport in density modulated phases of the second Landau level.

Quantum Hall Systems, Springer Series in Solid-State Sciences 183,

[©] Springer International Publishing Switzerland 2015

S. Baer and K. Ensslin, *Transport Spectroscopy of Confined Fractional*

two hole bubble phases, which provide a lower ground-state energy than FQH states or an isotropic liquid [23, 24] at certain filling factors and are occupied with one or two electrons or holes per bubble.

The underlying physics of the FQH states in the second Landau level, like the $\nu = 5/2$ and $\nu = 12/5$ states is an open issue under intensive theoretical [25–42] and experimental [22, 43–48] investigation.

Experiments which investigate the RIQH phases of the second LL require very low temperatures and two-dimensional electron gases of very high mobility. Recently temperature-dependent measurements have revealed the importance of Coulomb interactions for the formation of RIQH states and indicated that a particle-hole asymmetry of the energy scales for the formation of electron and hole bubble phases occurs [18, 19]. Such a particle-hole symmetry breaking might have far-reaching consequences, for example for the ground-state wave function at $\nu = 5/2$. Hence a deeper understanding of the competing bubble phases in the second LL is desirable.

We report on magneto-transport measurements of high mobility two-dimensional electron gases. We investigate the RIQH states of the second LL in non-equilibrium transport by driving a finite DC current bias through the system. For large DC currents, RIQH states disappear and the Hall resistance approaches its high-temperature limit, where no density modulated phases are formed. We denote this phase as isotropic compressible phase. Surprisingly, the qualitative form of the transition from RIQH phases to isotropic compressible phases is different for electron and hole bubble states. While hole bubble states exhibit a sharp transition to the isotropic compressible phase, a gradual transition involving an intermediate phase is found for the electron bubble states. Qualitatively similar findings were obtained with three different samples, made from different high mobility heterostructures which employ different growth techniques. We furthermore extract and compare energy scales for the different RIQH states of the second LL. The local formation of RIQH states has been investigated by measuring transport through a quantum point contact (QPC). Here, signatures of the hole bubble states are completely absent, whereas signatures corresponding to the electron bubble states are most likely a pure bulk effect, while no RIQH phases are formed in the QPC channel. Finally, we investigate the direction dependence of the breakdown of the RIQH phases with respect to the current orientation. We observe that qualitative features of the transition to the isotropic compressible phase do not depend on the current orientation.

15.2 Experimental Details

Measurements have been performed on photolithographically defined Hall-bars contacted with Au/Ge/Ni Ohmic contacts in a standard four-terminal measurement scheme. A constant AC current (typically $I_{\rm AC}\approx 0.5$ nA) is passed from source to drain and $dV_{xx}/dI_{\rm SD}$ and $dV_{xy}/dI_{\rm SD}$ are measured using lock-in techniques. In non-equilibrium situations, an additional DC current is passed from source to drain,

on top of the AC current: $I_{SD} = I_{DC} + I_{AC}$. Currents are defined by applying a voltage across large resistors with typically $R = 100 \text{ M}\Omega - 1 \text{ G}\Omega$.

Three different high mobility structures have been used for the experiments. The wafers D120427C ($n_{\rm s}\approx 2.2\times 10^{11}~{\rm cm^{-2}},~\mu\approx 1.9\times 10^7~{\rm cm^2/Vs}$) and D120702A ($n_{\rm s}\approx 2.3\times 10^{11}~{\rm cm^{-2}},~\mu\approx 2.3\times 10^7~{\rm cm^2/Vs}$) are optimized for the observation of the $\nu=5/2$ state without prior LED illumination [49]. The wafer D110726B ($n_{\rm s}\approx 3.1\times 10^{11}~{\rm cm^{-2}},~\mu\approx 1.8\times 10^7~{\rm cm^2/Vs}$ after illumination) has been illuminated at $T\approx 10~{\rm K}$ using a red LED, to allow for the observation of a fully quantized $\nu=5/2$ state and pronounced RIQH states (see Appendix F).

Experiments have been conducted in a cryogen-free dilution refrigerator, with an electronic base temperature $T_{\rm el} \approx 12{\text -}13$ mK. This has been achieved by low-pass filtering and thermally anchoring the cabling at every temperature stage (see Chap. 7).

The filling factors of the RIQH states have been calculated from their magnetic field position relative to the center of the $\nu = 5/2$ plateau in R_{xy} . From this, we estimate an uncertainty in the filling factors of $\Delta \nu = \pm 0.007$.

15.3 Results and Discussion

In an equilibrium transport situation, only an AC current of typically 0.5 nA is passed along the long axis of a Hall-bar, from source to drain. In this situation, we measure the longitudinal voltage drop V_{xx} and the Hall voltage drop V_{xy} . Figure 15.1c, d (blue curves) show the differential longitudinal and Hall resistances, dV_{xx}/dI_{SD} and dV_{xy}/dI_{SD} , for filling factors between 2 and 3 in the bulk. The longitudinal resistance vanishes for the FQH states at $\nu=8/3,7/3$ and 5/2, while the Hall resistance shows a plateau at the same time.

Turning to a non-equilibrium transport situation, a DC current from source to drain is added on top of the AC current: $I_{SD} = I_{DC} + I_{AC}$. Figure 15.1a shows in colorscale the differential longitudinal resistance as a function of the magnetic field B and the DC current I_{DC} . The FQH states at $\nu = 8/3, 7/3$ and 5/2 show up as black stripes (small differential longitudinal resistance) at a constant magnetic field. When the differential Hall resistance is plotted as a function of the magnetic field B and the DC current I_{DC} (Fig. 15.1b), RIQH states with a quantized resistance of $h/(2e^2)$ (red) or $h/(3e^2)$ (blue) show up as diamond-shaped regions. We denote the RIQH states in the upper spin branch by R1A-R4A and in the lower spin branch by R1B-R4B. The RIQH state R1B is not observed in the measurement of Fig. 15.1. The width of the regions shrinks, as the DC current is enhanced, until an isotropic background is found at large currents ($I_{DC} \ge 12 \text{ nA}$). On the high magnetic field side of $\nu = 5/2$, the RIQH states are neighbored by strong side-peaks of smaller differential Hall resistance. Comparing Fig. 15.1b with Fig. 15.1a, we see that the boundaries of the RIQH phases in the longitudinal resistance are defined by two strong side peaks, with a region of small differential longitudinal resistance in-between. As I_{DC} is increased, the sidepeaks move together, resulting in a diamond shaped region. The outer boundary spanned by the side peaks at $B \approx 3.48$ T coincides with the extent of the RIQH

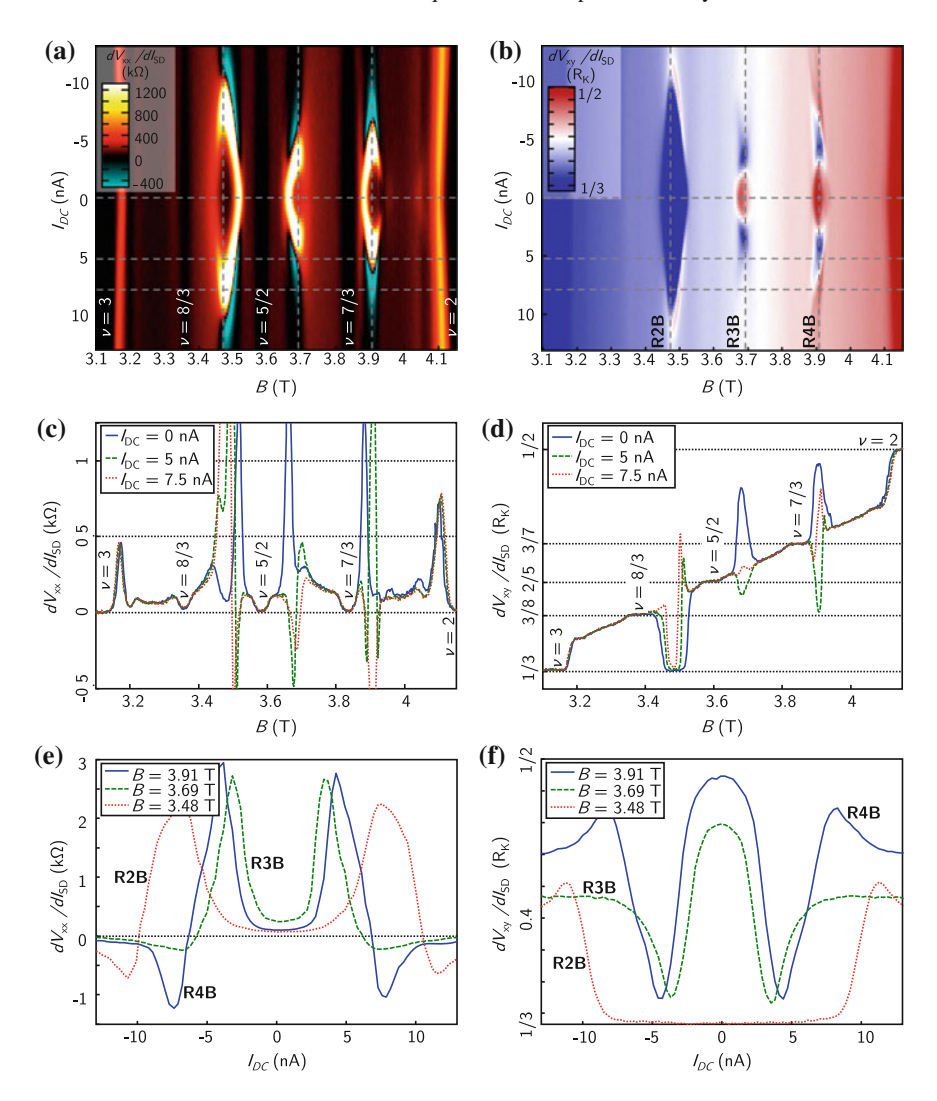


Fig. 15.1 a Differential longitudinal resistance versus magnetic field and DC current bias. Minima, associated with FQH states at $\nu=7/3$, 8/3 and 5/2 show up as black stripes. The RIQH states appear as a minimum in the longitudinal resistance with strong side-peaks and span diamond-shaped regions in the B-field - I_{DC} - plane. At larger I_{DC} biases, negative differential resistance is found (turquoise areas). Cuts in B-field and bias direction are shown in (\mathbf{c}, \mathbf{e}) . \mathbf{b} In the differential Hall resistance, RIQH states are visible as diamond-shaped regions, where the Hall resistance tends towards the quantized resistance value of a neighboring IQH plateau. As the current bias is increased, the RIQH states which we denote as R3B and R4B exhibit a strong decrease of the differential Hall resistance before they disappear in an isotropic background, corresponding to the isotropic compressible phase. In contrast, a sharp transition to the isotropic compressible phase is found for the RIQH state R2B. Traces of the differential longitudinal and Hall resistances in B-field and in current bias direction are shown in (\mathbf{d}, \mathbf{f}) . (Sample D120427C-1C)

phase at $\nu = h/(2e^2)$ in the differential Hall resistance. In contrast, the RIQH phase at $\nu = h/(3e^2)$ is defined by the inner boundary of the side peaks in dV_{xx}/dI_{SD} . At large currents where no RIQH phase is observed any more, regions of negative differential resistance are visible in dV_{xx}/dI_{SD} (turquoise areas in Fig. 15.1a). We remark that the ordinary resistance remains positive and that the negative differential resistance and the overall form of this measurement can be reproduced by numerically deriving a pure DC measurement (Fig. 15.11).

Figure 15.1c, d shows traces of the differential longitudinal and Hall resistance for three different DC currents. While the FQH states or the isotropic compressible phase show a weak dependence on current, differential resistance varies strongly close to the RIQH states. The DC current dependence of $dV_{xx}/dI_{\rm SD}$ and $dV_{xy}/dI_{\rm SD}$ in the center of the RIQH phases is shown in Fig. 15.1e, f. $dV_{xx}/dI_{\rm SD}$ is small at zero DC current, then grows rapidly as $I_{\rm DC}$ is increased. Finally, a region of negative differential resistance is found after which $dV_{xx}/dI_{\rm SD}$ returns to a constant background. $dV_{xy}/dI_{\rm SD}$ shows a different behavior for the RIQH phases on both sides of the $\nu=5/2$ state. For the RIQH state R2B (indicated in Fig. 15.1b), $dV_{xy}/dI_{\rm SD}$ increases sharply close to the classical background value, with only slight overshoots when the RIQH state is destroyed. In contrast, for the RIQH state R3B, $dV_{xy}/dI_{\rm SD}$ shows very pronounced undershoots, before it reaches the classical background value. The RIQH state R4B even shows a more complicated current dependence, where $dV_{xy}/dI_{\rm SD}$ first undershoots and then overshoots, before it reaches the classical background value.

Similar results have been obtained from measurements with other 2DEGs (Sample D120702A-2C, Fig. 15.2) and subsequent cooldowns (Sample D120427C-1C, Fig. 15.3). The differential longitudinal resistance $dV_{xx}/dI_{\rm SD}$ shows strong peaks at the boundaries of the RIQH phases (presumably due to a small density gradient in the sample [50, 51]). In the differential Hall resistance, a similar behavior as before is seen. The RIQH states at more than half filling of each spin branch of the second Landau level (R1A, R2A, R1B, R2B) show an abrupt transition to a classical Hall resistance (Fig. 15.2). On the other hand, RIQH states at less than half filling (R3A, R4A, R3B, R4B) have a less abrupt transition to a flat background, involving distinct undershoots of the differential Hall resistance.

15.3.1 Phase Diagram of Reentrant Integer Quantum Hall Phases

The DC current dependence of the Hall resistance allows us to extract a phase diagram for the different RIQH states. The critical current, $I_{\rm DC,crit}$, for which an RIQH state disappears is extracted from the measurements of Figs. 15.1, 15.2 and 15.3. The critical current is reached when the amplitude of the RIQH peak or dip in the differential Hall resistance has reached 30% of its maximum amplitude (i.e. 30% of the difference between the classical Hall background resistance and the quantized

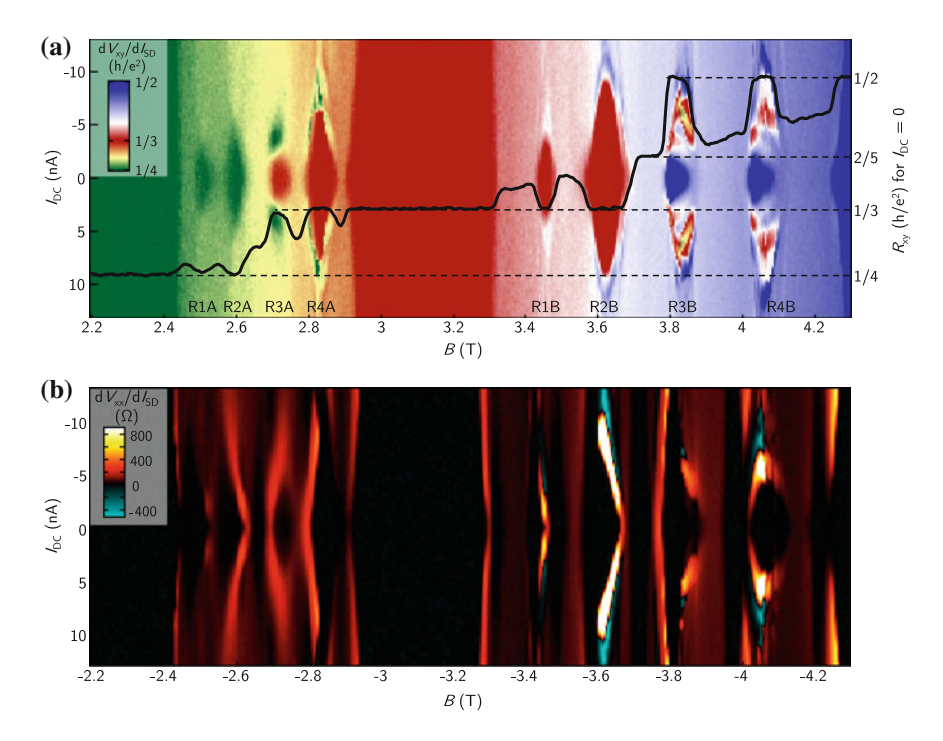


Fig. 15.2 Differential Hall (a) and longitudinal resistance (b), for a bulk filling factor $2 \le \nu \le 4$. The pair of RIQH states at the low-magnetic field sides of $\nu = 5/2$ and $\nu = 7/2$ show a sharp threshold to an isotropic compressible phase in the differential Hall resistance. RIQH states on the high-magnetic field side of $\nu = 5/2$ and $\nu = 7/2$ show a less abrupt transition which involves a region of smaller differential Hall resistance. (Sample D120702A-2C)

resistance of the neighboring IQH plateau). The same threshold, but with different sign is used for the intermediate current bias phase of the RIQH states R3A, R4A, R3B and R4B. As the relevant energy scale for the breakdown is the Hall voltage and not the current, we define a critical Hall voltage via $V_{\rm H,crit} = I_{\rm DC,crit} \times R_{xy,\rm quant.}$. Here, $R_{xy,\rm quant.} = h/(\nu e^2)$ is the quantized Hall resistance, corresponding to the RIQH state. The resulting critical Hall voltage is plotted as a function of the filling factor in Fig. 15.4.

The critical Hall voltage of the RIQH states R2A/B and R4A/B is larger than for R1A/B and R3A/B. In contrast to the critical current, the critical Hall voltage does increase monotonically with decreasing filling factor over $\nu = 7/2$ and $\nu = 5/2$. The critical current exhibits a non-monotonic behavior. A similar non-monotonic behavior has previously been observed for the critical temperatures T_c at which the RIQH states start to form [18, 52] and gives evidence for a particle-hole asymmetry in the corresponding energy scales.

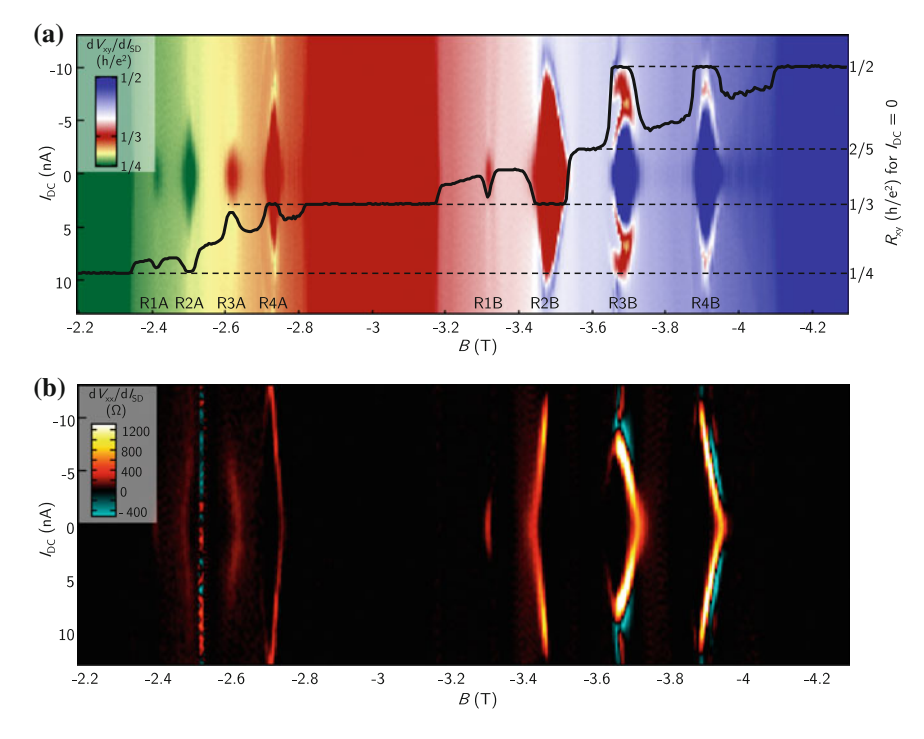


Fig. 15.3 Differential Hall (a) and longitudinal resistance (b), for a bulk filling factor $2 \le \nu \le 4$. The pair of RIQH states at the low-magnetic field sides of $\nu = 5/2$ and $\nu = 7/2$ show a sharp threshold to an isotropic compressible phase in the differential Hall resistance. RIQH states on the high-magnetic field side of $\nu = 5/2$ and $\nu = 7/2$ show a less abrupt transition which involves a region of smaller differential Hall resistance. (Sample D120427C-1C, second cooldown)

15.3.2 Transition from RIQH Phase to Isotropic Compressible Phase

We now turn to the question why the transition from a RIQH phase to an isotropic compressible phase occurs in a qualitatively different way for the RIQH states at both sides of $\nu = 5/2$ and $\nu = 7/2$. The behavior of the differential Hall resistance can be better understood from looking at the Hall voltage V_{xy} versus the DC current I_{DC} , $V_{xy}(I_{DC})$.

We schematically show the expected dependence of V_{xy} on I_{DC} in Fig. 15.5b.1 for a continuous transition between a RIQH phase and an isotropic compressible phase. For a constant filling factor, a linear slope $V_{xy} = h/(\nu e^2) \times I_{DC}$ is expected. Hence at a small DC current, where the RIQH state exists, the RIQH states R3B and R4B (with a plateau value of $h/2e^2$) exhibit a slope of $h/2e^2$ in the I_{DC} - V_{xy} diagram (green dashed line in Fig. 15.5b). Similarly, a slope of $h/3e^2$ is expected for the RIQH states R1B and R2B (red dashed line in Fig. 15.5b). In the limit of

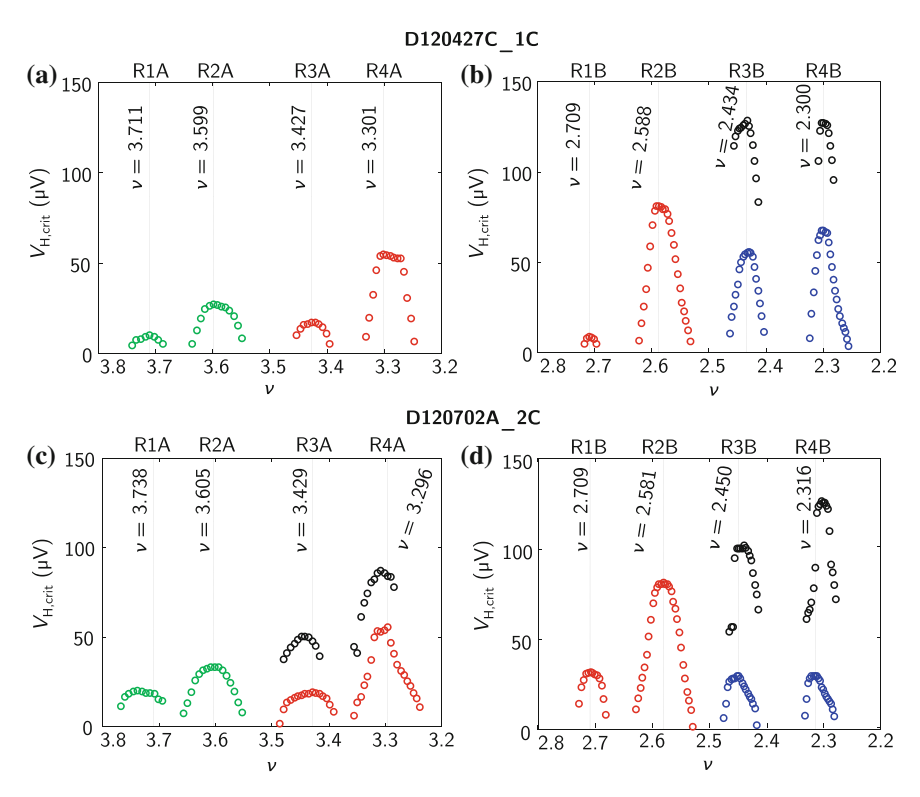


Fig. 15.4 a, c Critical Hall voltage for the breakdown of the RIQH states with $R_{xy} = 1/4 \times h/e^2$ (green) and $R_{xy} = 1/3 \times h/e^2$ (red) and for the transition to an isotropic background (black). **b**, **d** Critical Hall voltage for the breakdown of the RIQH states with $R_{xy} = 1/3 \times h/e^2$ (red) and $R_{xy} = 1/2 \times h/e^2$ (blue) and for the transition to an isotropic background (black)

large currents, the RIQH phase no longer exists, and a background Hall resistance, which is determined by the corresponding filling factor, is found (grey dashed lines in Fig. 15.5b). Thus, the curve $V_{xy}(I_{\rm DC})$ is expected to possess a slope of $h/\nu e^2$ for large DC currents, where $\nu \approx 2.43$ or 2.30 for the RIQH states R3B and R4B and $\nu \approx 2.71$ or 2.58 for R1B and R2B. In between the low- and high-current regime, a continuous transition occurs, while all linear slopes are expected to interpolate to the origin of the diagram. In order to satisfy these conditions, an intermediate regime with a smaller slope of $V_{xy}(I_{\rm DC})$ (hence smaller differential Hall resistance) is expected for the transition from $\nu = 2$ to the isotropic liquid. In contrast, for the transition from $\nu = 3$, we expect an intermediate regime with a greater slope in V_{xy} versus $I_{\rm DC}$. In the differential resistance, this would be visible as pronounced undershoots of the differential resistance for the RIQH states R3B and R4B, while strong overshoots should be visible for R1B and R2B. The expected $V_{xy}(I_{\rm DC})$ for such a continuous transition are shown schematically as black lines in Fig. 15.5b, where ν_1 and ν_2 denote the non-quantized "background" filling factors.

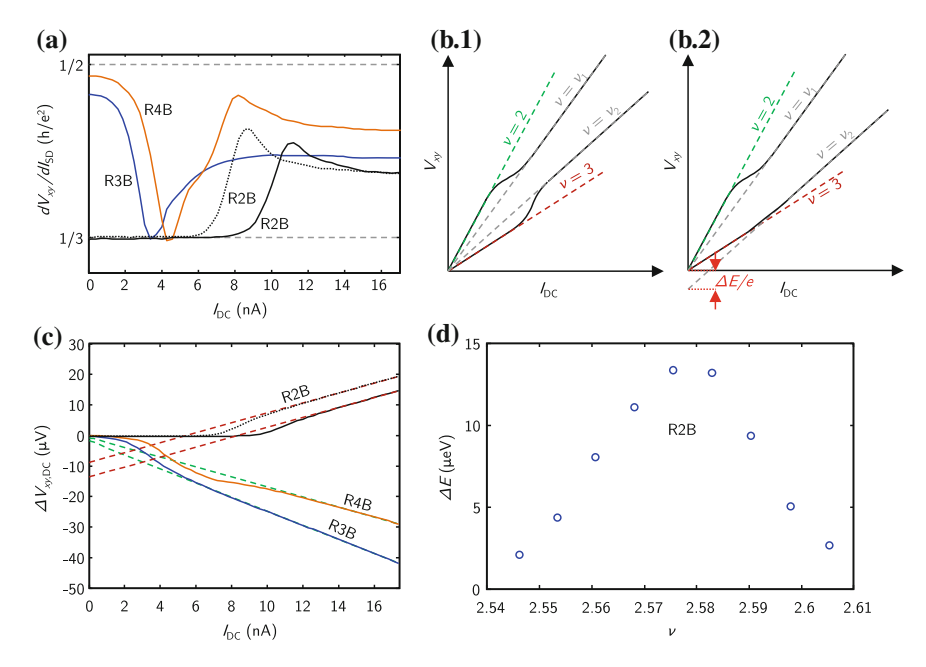


Fig. 15.5 a Differential Hall resistance for different filling factors. At large DC currents ≥10–15 nA, a constant differential resistance is found. **b.1** Schematic scenario for a continuous transition to the isotropic compressible phase with non-quantized filling factors ν_1 and ν_2 . **b.2** Schematic illustration of $V_{xy}(I_{DC})$ as obtained from the measurement. For the RIQH state R2B, the linear slope corresponding to the isotropic compressible phase is offset in V_{xx} by $\Delta E/e$. **c** Hall voltage versus the DC current. For better visibility, a linear slope corresponding to $V_{xy} = \frac{1}{3}h/e^2 \times I_{DC}$ or $V_{xy} = \frac{1}{2}h/e^2 \times I_{DC}$ has been subtracted from the DC Hall voltage. **d** Energy offset ΔE as a function of the filling factor. At the center of the RIQH phase, a maximum of ΔE of approximately 13 μeV is found. (Sample D120427C-1C)

In order to compare this scenario with our measurements, we calculate $V_{xy}(I_{DC})$ from the differential Hall resistance via integration:

$$V_{xy}(I_{\rm DC}) \approx \int_{0}^{I_{\rm DC}} \left(\frac{dV_{xy}}{dI_{\rm SD}}(\tilde{I}_{\rm DC})\right) d\tilde{I}_{\rm DC} + C$$
 (15.1)

where C is an unknown integration constant. The result obtained by this is schematically depicted in Fig. 15.5b.2. For the RIQH states R3B and R4B we indeed observe a similar behavior as expected for the scenario of a continuous transition, with a smooth transition between two different linear slopes, interpolating through the origin. In contrast, V_{xy} for the RIQH state R2B first moves with a slope corresponding to $\nu = 3$. As the DC current is increased, no gradual transition to the slope corresponding to the isotropic compressible phase is observed, but V_{xy} sharply changes slope at a certain DC current and moves with the slope of the isotropic compressible

phase. Surprisingly, the slope of this background resistance no longer interpolates to the origin of the V_{xy} – I_{DC} diagram when C is chosen such that V_{xy} ($I_{DC} = 0$) = 0.

The corresponding data, obtained by integrating the differential Hall resistance is shown in Fig. 15.5c. Here, a linear slope corresponding to $V_{xy} = \frac{1}{3}h/e^2 \times I_{DC}$ (R2B) or $V_{xy} = \frac{1}{2}h/e^2 \times I_{DC}$ (R3B, R4B) has been subtracted to guarantee better visibility of the important features. A distinct behavior of the RIQH states R3B and R4B (blue and orange solid lines), and R2B (black solid line) is observed. All slopes are close to zero at $I_{\rm DC} \approx 0$ due to the subtraction of the linear slope corresponding to $\nu = 2$ or $\nu = 3$. At large currents, $V_{xy}(I_{DC})$ reaches a slope, close to the expectation for the isotropic compressible phase at the given filling factor. When the slope of the isotropic compressible phase is linearly interpolated, it reaches zero voltage at zero DC current for the RIQH states R3B and R4B. This is clearly not the case for the RIQH state R2B, where the linear part of $V_{xy}(I_{DC})$ does not interpolate to the origin of the V_{xy} - I_{DC} diagram. This voltage shift is the largest for the filling factor corresponding to the center of the RIQH phase (black solid line in Fig. 15.5c) and decreases as the filling factor is increased or enhanced (for example black dashed line in Fig. 15.5c). The dependence of this energy shift on the filling factor is depicted in Fig. 15.5d. A maximum energy shift of approximately 13 μeV is found in the center of the RIQH phase.

We have investigated the transition from RIQH phases to the isotropic background in another sample using AC and DC measurements. The corresponding differential Hall resistance versus the magnetic field is shown in Fig. 15.6a. As the DC current is increased at the magnetic field values corresponding to the RIQH states R2B and R3B, a transition to an isotropic compressible background occurs at I_{DC} < 20 nA and the differential Hall resistance is constant at higher currents (Fig. 15.6b). The measured DC Hall and longitudinal voltages, $V_{xy,DC}$ and $V_{xx,DC}$ are shown in Fig. 15.6c–f. For better visibility, a linear slope corresponding to $V_{xy} = \frac{1}{3}h/e^2 \times I_{DC}$ or $V_{xy} = \frac{1}{2}h/e^2 \times I_{DC}$ has been subtracted from the DC Hall voltage. With this, the RIQH phases are seen as plateaus at $\Delta V_{xy,DC} = 0$. Dashed lines are fitted to the linear parts of the Hall voltage (for $-150 \text{ nA} < I_{DC} < 75 \text{ nA}$ and 75 nA $< I_{DC}$ < 150 nA). In contrast to before, slopes interpolate approximately through zero for all RIQH states (within the fit uncertainty). DC currents for the transition to the isotropic compressible phase are much larger for the RIQH state R2B than for R3B and R4B. In the longitudinal DC voltage, $V_{xx,DC}$, sharp jumps are observed for the RIQH states R2B (marked by red arrow in Fig. 15.6e), occurring at the DC current value where the RIQH phase is left. In contrast, $V_{xx,DC}$ varies smoothly as a function of DC current for the RIQH states R3B and R4B.

15.3.3 Discussion of the Bias Dependence

Let us turn to the question of a possible mechanism of the transition from the RIQH phases to the isotropic compressible phase. In the RIQH phase, the density of states

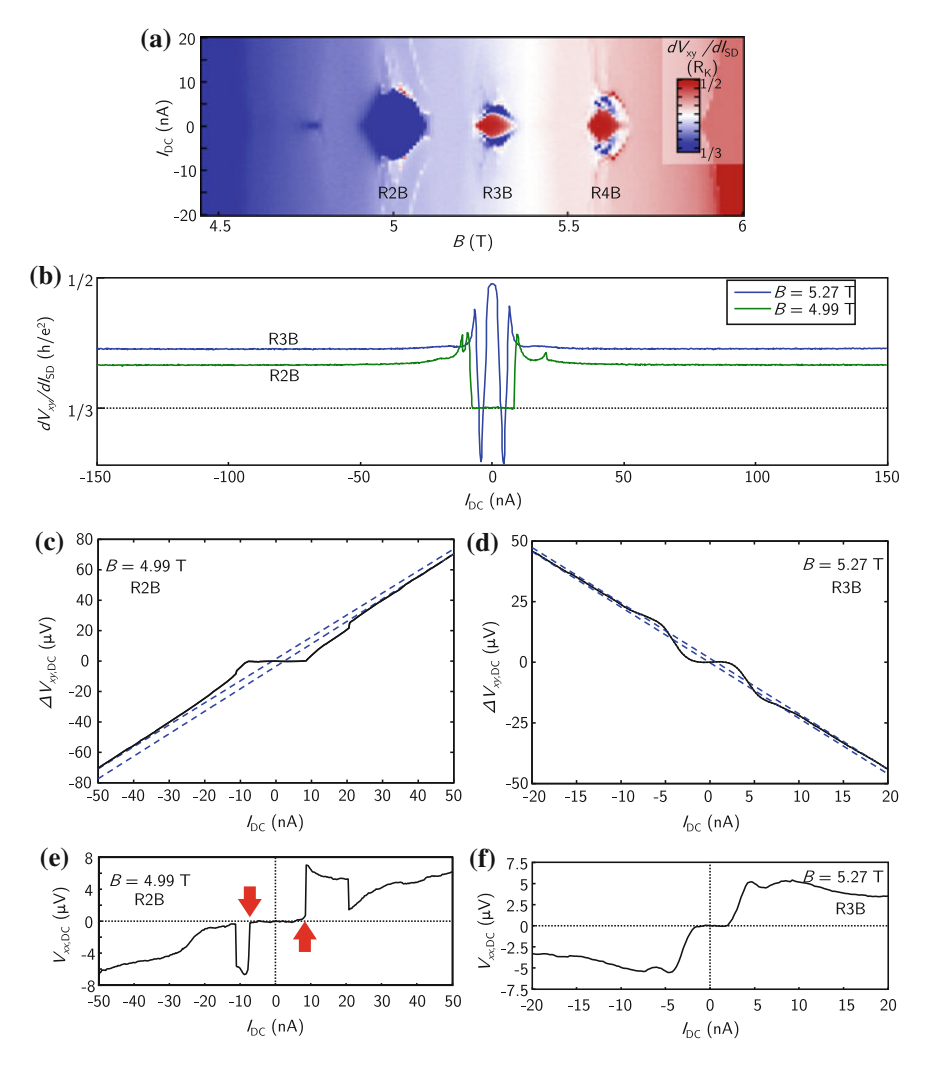


Fig. 15.6 a Differential Hall resistance versus DC current and the magnetic field. **b** Differential Hall resistance for the RIQH states R2B and R3B versus the DC current. At $I_{DC} > 20$ nA, the differential Hall resistance is approximately constant. **c**, **d** DC Hall voltage versus the DC current. Here, a linear slope corresponding to $V_{xy} = \frac{1}{3}h/e^2 \times I_{DC}$ (**c**) or $V_{xy} = \frac{1}{2}h/e^2 \times I_{DC}$ (**d**) has been subtracted. **e**, **f** DC longitudinal voltage $V_{xx,DC}$ versus the DC current. For the RIQH state R2B, jumps in the DC voltage ((**e**), marked by *red arrows*) are observed. (Sample D110726B-3D)

exhibits a small quasi-gap [9, 10]. In the bulk of the Hall-bar, the Fermi energy is pinned in the center of the quasi-gap by disorder, resulting in transport properties which are identical to those of an IQH state. These transport signatures are expected to survive as long as the Hall voltage drop across the bubble phase is smaller than the quasi-gap. Driving a DC current through the system in a RIQH state induces

a transition to an isotropic compressible phase, either by heating the system or by increasing the Hall voltage drop, until the Hall voltage drop becomes larger than the quasi-gap of the RIQH phase. These two possibilities cannot be easily distinguished.

The Kosterlitz, Thouless, Halperin, Nelson, Young (KTHNY) theory [53–56] predicts that an intermediate "hexatic" phase exists for a two-dimensional melting transition between a hexagonal solid and an isotropic liquid. In the electron liquid crystal picture, stripe crystal and Wigner crystal phases are expected to melt at finite temperatures, either via a first order phase transition, or by two sequential continuous transitions [57]. For the Wigner crystal, this intermediate phase is such a hexatic phase with short-range positional and quasi long-range orientational order [58]. The transition from the crystalline phase to the hexatic phase occurs via a dislocation unbinding transition [57]. Further increasing the temperature leads to a continuous disclination unbinding transition to the isotropic phase. For the bubble phases of the second LL, energy calculations indicate that such density modulated phases are formed via first order quantum phase transitions [24]. To our knowledge the possibility of a continuous transition from the bubble phase to an isotropic phase has not been studied in literature for such a system. However, KTHNY theory suggests that a hexatic phase might in principle exist for such a system.

The DC current dependence of the RIQH states R3B, R4B (and R3A, R4A) might be interpreted as a continuous transition, where the quasi-gap of the RIQH phase gradually disappears until finally an isotropic compressible phase is reached. The abrupt transition of the RIQH state R2B (and R1B, R1A, R2A) might in contrast be explained as a first-order phase transition with a discontinuous change of the electrochemical potential. This discontinuity might explain the energy offset ΔE , which in this interpretation can be seen as a measure for the quasi-gap of the RIQH phase. The jump that has been observed in $V_{xx,DC}$ might be caused by the jump of the electrochemical potential in such a transition.

15.3.4 Reentrant Integer Quantum Hall Phases in a QPC

The local formation of RIQH states can be investigated by utilizing a QPC. Figure 15.7a, b shows the differential Hall resistance, measured in the bulk of a high mobility Hall-bar (D120702A-2C). As before, R1B and R2B show a sharp threshold to an isotropic compressible phase, while a transition via an intermediate phase is observed for R3B and R4B. Now we turn to a situation, where a 1.1 μ m wide QPC, fabricated on top of the 2DEG is defined by applying negative voltages to the top-gates ($V_{\rm QPC} = -2.3$ V). We measure the voltage $V_{\rm diag}$ diagonally across the QPC, from which an effective filling factor of the QPC, $\nu_{\rm QPC}$, is obtained via $R_{\rm diag} = \frac{h}{e^2\nu_{\rm QPC}}$ [59]. The system is tuned to a weak backscattering situation, where bulk and QPC densities are identical, which can be seen from the overlap of the IQH plateaus in R_{xy} and $R_{\rm diag}$ (see Chap. 11). Figure 15.7c, d shows the differential diagonal resistance for this situation. While the IQH plateaus are still clearly

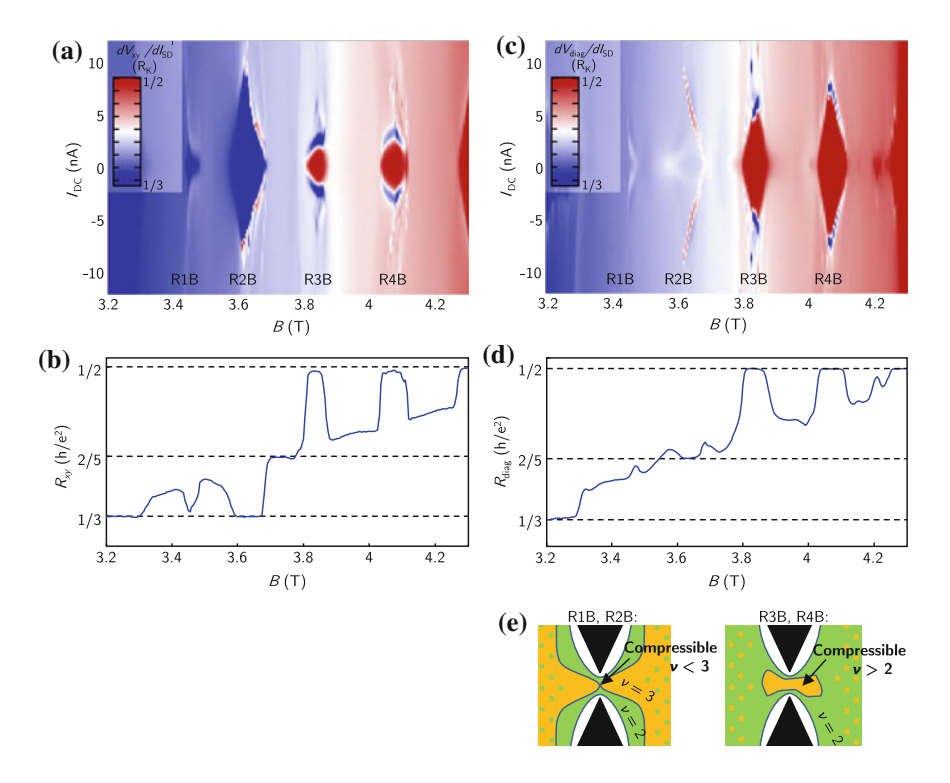


Fig. 15.7 a Differential bulk Hall resistance as a function of the DC current. b Differential Hall resistance at $I_{\rm DC}=0$. The RIQH states R1B–R4B are clearly visible. c Differential diagonal resistance across a 1.1 μ m wide QPC. Here, –2.3 V are applied to the top-gates. At zero DC current, the RIQH states R1B and R2B are no longer visible (d), whereas R3B and R4B are even more pronounced than in the bulk. e Schematic density distribution in the QPC and the bulk for the different RIQH states. (Sample D120702A-2C)

visible (Fig. 15.7d), FQH states can no longer be clearly identified. The reason for this is weak quasiparticle tunneling which destroys the FQH plateaus and gives rise to a power-law tunneling conductance between counterpropagating edge states (see Chap. 11). In this situation, the RIQH states R1B and R2B have vanished and are no longer seen in the diagonal resistance. In contrast, R3B and R4B are even more pronounced than in the bulk. The regions corresponding to a quantization at $h/(2e^2)$ have a larger extent in the $I_{\rm DC}$ direction than in the bulk.

The observation of the RIQH states R3B and R4B in the diagonal resistance however does not imply that they are formed in the QPC constriction. The relation $R_{\rm diag} = \frac{h}{e^2 \nu_{\rm QPC}}$ is only valid, if $\nu_{\rm QPC} \leq \nu_{\rm bulk}$, which is not necessarily the case for the density modulated bubble phases. In this case, the following relation holds: $R_{\rm diag} = \frac{h}{e^2 {\rm min}(\nu_{\rm QPC}, \nu_{\rm bulk})}$. A schematic of this situation is shown in Fig. 15.7e. For the RIQH states R1B and R2B, the innermost edge state (corresponding to $\nu = 3$) is

partially backscattered at the QPC and hence the quantization is lost, even if the RIQH states persist in the bulk. For the RIQH states R3B and R4B however, the innermost edge state of the bulk corresponds to $\nu=2$. If a compressible region is formed in the QPC, it has a larger filling factor than two, and hence the $\nu=2$ edge state is protected from backscattering. Hence, the quantized value of $dV_{\rm diag}/dI_{\rm DC}=h/(2e^2)$ can be interpreted as a bulk signature, where $\nu_{\rm bulk}=2$ describes the bulk transport properties and where a compressible phase is formed in the QPC, leading to $\nu_{\rm QPC}>2$.

We conclude that most likely no density modulated phases persist in the QPC channel. The different characteristics of the RIQH states R3B and R4B when measured in the bulk and across a QPC might result from a density gradient close to the QPC or from a variation in the current distribution and hence a partial local Hall voltage drop in the center of the QPC channel.

15.3.5 Orientation Dependence

In contrast to stripe phases in higher LLs, we expect the bubble phases of the second LL to be isotropic. However, it was shown that a large DC current can induce anisotropies in density modulated phases which are isotropic at small currents [60]. Figure 15.8 shows the differential Hall resistance for different orientations of the AC and DC current as a function of magnetic field and DC current. Insets show schematically the current configurations and the contact configuration used for each measurement. For parallel AC and DC currents, breakdown signatures of the RIOH states of the second LL are isotropic (Fig. 15.8a, b). When AC and DC current are passed either along the long axis of the Hall-bar (x-direction, Fig. 15.8a) or perpendicular to the long axis (y-direction, Fig. 15.8b), critical currents are of comparable magnitude. As before, R3B and R4B exhibit a transition to an isotropic phase with strong undershoots in the differential Hall resistance, while only weak overshoots are observed for R1B and R2B. Qualitatively, the breakdown for both current orientations looks similar, while details like the critical Hall voltage of the RIQH phases change slightly. In configurations where AC and DC currents are driven in perpendicular directions (Fig. 15.8c, d) the RIQH states R1B and R2B show an anisotropic behavior: here, the breakdown current depends strongly on the orientation of the DC current. In contrast, R3B and R4B only show a weak current direction dependence. This observation again highlights the different physical behavior of the electron and hole density modulated phases.

15.4 Conclusion 279

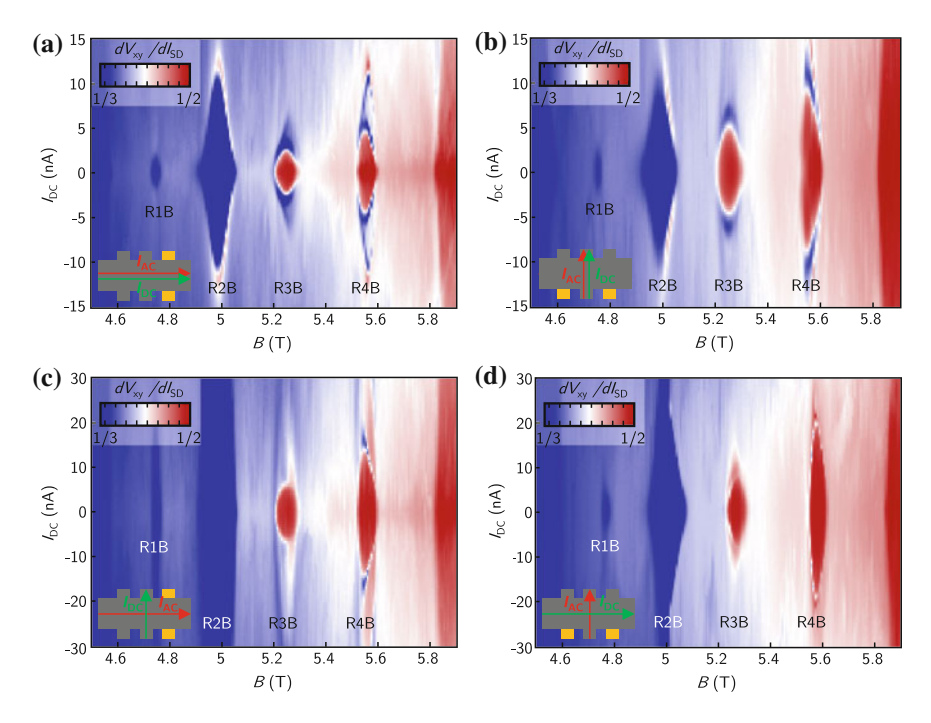


Fig. 15.8 Differential Hall resistance for different directions of DC and AC currents. The respective contact configurations and current directions are shown schematically as *insets*. Contacts used for measuring V_{xy} are emphasized in *orange*. Measurements where AC and DC currents flow in the x-direction (**a**) or the y-direction (**b**) show similar energy scales for the transition to an isotropic background. In configurations where AC and DC currents are applied perpendicular (**c**, **d**), critical currents for the RIQH states R1B and R2B are different. In a configuration with a small current density (**c**), R1B and R2B have larger critical currents than for a configuration with a higher current density (**d**). Critical currents for R3B and R4B are similar in both cases. (Sample 110726B-1D)

15.4 Conclusion

In conclusion, we have investigated magneto-transport in the RIQH phases of the second LL. Applying large DC currents induces a transition from density modulated bubble phases to an isotropic compressible phase. This transition is markedly different for hole and electron bubbles in both spin branches of the second Landau level. While hole bubbles exhibit a sharp transition to the isotropic compressible phase, a gradual transition involving an intermediate phase is found for the electron bubbles. This might be explained by different routes for a two-dimensional melting transition, either by a first-order phase transition or by two continuous transitions via an intermediate phase. We furthermore have investigated the breakdown of the RIQH phases in QPCs and their dependence on the current orientation. While the transport through the QPC is dominated by the bulk signatures of the RIQH phases, a distinct behavior of electron and hole bubble phases is observed for

different current directions. Further experiments are necessary in order to definitely clarify the physical origin of the different transitions of the RIQH phases. Our observations suggest that the particle-hole symmetry is broken for the density modulated phases in the second Landau level. This symmetry breaking has a strong influence on the properties of the density modulated phases and might also have an important impact on the physics of the FQH states in the second LL, like the $\nu=5/2$ FQH state.

Appendix

Dependence on Magnetic Field Direction

Changing the magnetic field direction does not change the qualitative behavior of the RIQH phases (see Fig. 15.9). However, details of the transition to the isotropic background may change.

Hysteresis of Current Sweeps

Figure 15.10 demonstrates that no strong hysteresis is observed for the transition from RIQH phases to the isotropic compressible phase. Here, three consecutive sweeps of the DC current (I_{DC} was changed from -57.5 nA $\rightarrow 57.5$ nA $\rightarrow -57.5$ nA $\rightarrow 57.5$ nA) are shown for the RIQH states R2B, R3B and R4B.

Negative Differential Resistance from DC Measurement

To exclude a measurement problem owing for example to unexpected frequency dependencies in an AC measurement, the longitudinal voltage drop V_{xx} has been measured in a pure DC measurement as a function of the magnetic field and the DC current. From this, the differential longitudinal resistance has been obtained by numerically deriving V_{xx} with respect to the current. The result is shown in Fig. 15.11. Apart from the increased noise level, this measurement perfectly agrees with the AC measurement of Fig. 15.1, excluding a problem with the AC measurement technique employed by us. Also here, pronounced regions of negative differential resistance are found (turquoise areas in Fig. 15.11). It should be noted that the ordinary resistance always remains positive.

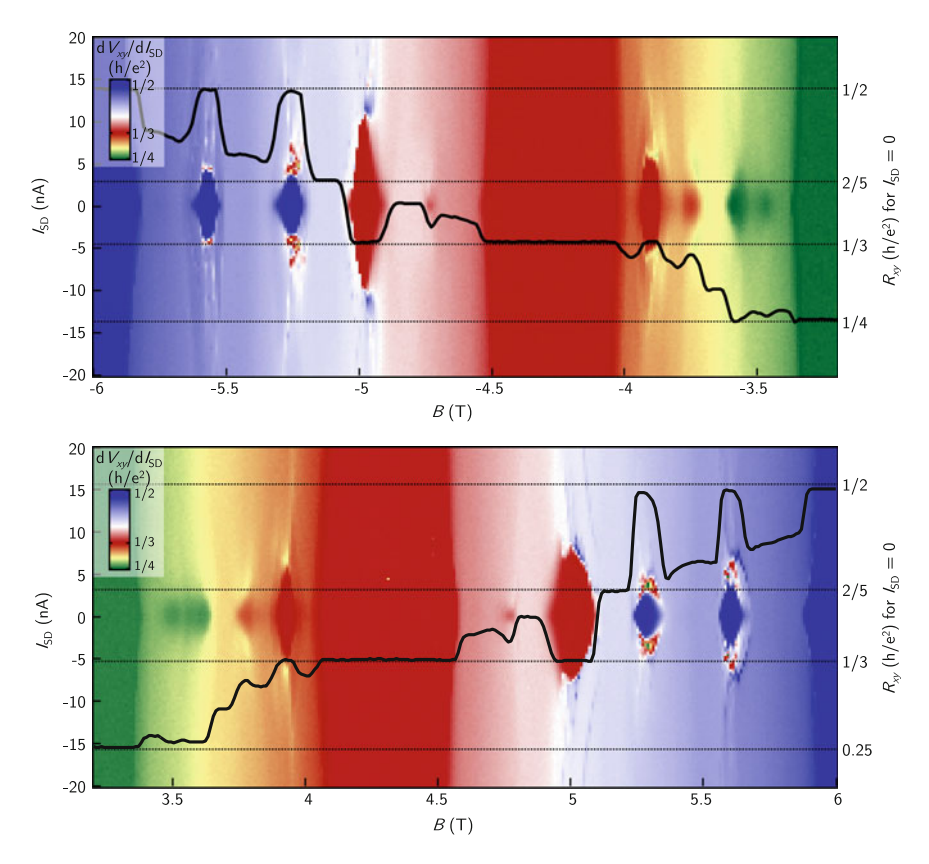


Fig. 15.9 Differential Hall resistance measured in two different magnetic field directions. (Sample D110726B-3D)

Bias Dependence of the Longitudinal Resistance

The bias dependence of the longitudinal resistance is shown in more detail in Fig. 15.12. At zero DC bias, R_{xx} shows a minimum at the B-field corresponding to the center of the RIQH phase, which is neighbored by two resistance maxima. When I_{DC} is increased, the minimum in R_{xx} is lifted and the magnetic field spacing between the side-peaks begins to shrink. At large biases, the side-peaks join to a single peak in R_{xx} , which then shrinks with subsequent increase of I_{DC} . This behavior is qualitatively similar to what is obtained when the temperature is increased [18, 52]. When the temperature is increased, the side-peaks move together until only a single peak is observed. The resistance peak shrinks as the temperature is further increased. This behavior is in sharp contrast to the activated behavior of FQH states.

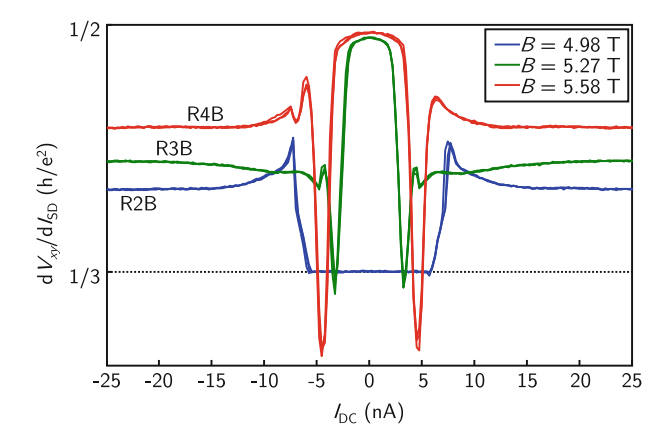


Fig. 15.10 Differential Hall resistance versus the DC current for RIQH states R2B, R3B and R4B. For each magnetic field, three consecutive sweeps of the current are shown (I_{DC} : –57.5 nA \rightarrow 57.5 nA \rightarrow -57.5 nA \rightarrow 57.5 nA). All curves lie nearly perfectly on top of each other. (Sample D110726B-3D)

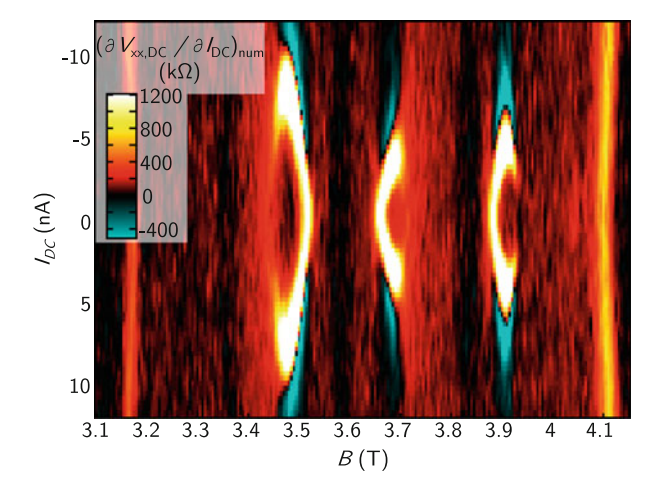


Fig. 15.11 Differential longitudinal resistance $\partial V_{xx,DC}/\partial I_{DC}$ versus the magnetic field and the DC current. $\partial V_{xx,DC}/\partial I_{DC}$ has been obtained by numerically deriving $V_{xx,DC}$ with respect to the applied DC current. The measurement agrees with Fig. 15.1, excluding a measurement problem as reason for the regions of negative differential resistance. (Sample D120427C-1C)

15.4 Conclusion 283

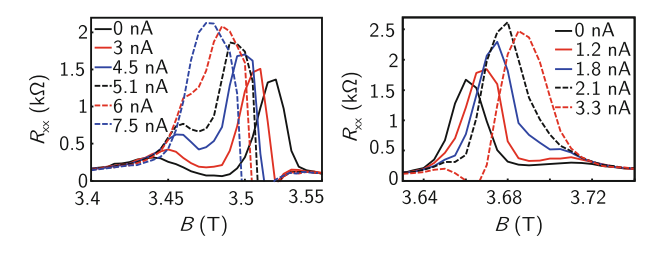


Fig. 15.12 DC current dependence of the RIQH minima in R_{xx} . At zero DC bias, R_{xx} shows a minimum at the *B*-field corresponding to the center of the RIQH phase, which is neighbored by two resistance maxima. When I_{DC} is increased, the minimum in R_{xx} is lifted and the magnetic field spacing between the side-peaks begins to shrink. At large biases, the side-peaks join to a single peak in R_{xx} , which then shrinks with subsequent increase of I_{DC} . (Sample D120427C-1C)

References

- S. Baer, C. Rössler, S. Hennel, H.C. Overweg, T. Ihn, K. Ensslin, C. Reichl, W. Wegscheider, Phys. Rev. B 91, 195414 (2015). doi:10.1103/PhysRevB.91.195414
- M.P. Lilly, K.B. Cooper, J.P. Eisenstein, L.N. Pfeiffer, K.W. West, Phys. Rev. Lett. 83, 824 (1999). doi:10.1103/PhysRevLett.83.824
- R.R. Du, D.C. Tsui, H.L. Stormer, L.N. Pfeiffer, K.W. Baldwin, K.W. West, Solid State Commun. 109, 389 (1999). doi:10.1016/S0038-1098(98)00578-X
- K.B. Cooper, M.P. Lilly, J.P. Eisenstein, L.N. Pfeiffer, K.W. West, Phys. Rev. B 60, R11285 (1999). doi:10.1103/PhysRevB.60.R11285
- M.M. Fogler, A.A. Koulakov, B.I. Shklovskii, Phys. Rev. B 54, 1853 (1996). doi:10.1103/ PhysRevB.54.1853
- 6. R. Moessner, J.T. Chalker, Phys. Rev. B 54, 5006 (1996). doi:10.1103/PhysRevB.54.5006
- 7. N. Shibata, D. Yoshioka, Phys. Rev. Lett. 86, 5755 (2001). doi:10.1103/PhysRevLett.86.5755
- A.A. Koulakov, M.M. Fogler, B.I. Shklovskii, Phys. Rev. Lett. 76, 499 (1996). doi:10.1103/ PhysRevLett.76.499
- M.M. Fogler, arXiv:cond-mat/0111001 (2001), pp. 98–138, in *High Magnetic Fields: Applications in Condensed Matter Physics and Spectroscopy*, eds. by C. Berthier, L.-P. Levy, G. Martinez (Springer, Berlin, 2002)
- R. Côté, C.B. Doiron, J. Bourassa, H.A. Fertig, Phys. Rev. B 68, 155327 (2003). doi:10.1103/ PhysRevB.68.155327
- R.M. Lewis, P.D. Ye, L.W. Engel, D.C. Tsui, L.N. Pfeiffer, K.W. West, Phys. Rev. Lett. 89, 136804 (2002). doi:10.1103/PhysRevLett.89.136804
- R.M. Lewis, Y. Chen, L.W. Engel, D.C. Tsui, P.D. Ye, L.N. Pfeiffer, K.W. West, Phys. Rev. Lett. 93, 176808 (2004). doi:10.1103/PhysRevLett.93.176808
- R.M. Lewis, Y.P. Chen, L.W. Engel, D.C. Tsui, L.N. Pfeiffer, K.W. West, Phys. Rev. B 71, 081301 (2005). doi:10.1103/PhysRevB.71.081301
- K.B. Cooper, J.P. Eisenstein, L.N. Pfeiffer, K.W. West, Phys. Rev. Lett. 90, 226803 (2003). doi:10.1103/PhysRevLett.90.226803
- J.P. Eisenstein, K.B. Cooper, L.N. Pfeiffer, K.W. West, Phys. Rev. Lett. 88, 076801 (2002). doi:10.1103/PhysRevLett.88.076801
- J.S. Xia, W. Pan, C.L. Vicente, E.D. Adams, N.S. Sullivan, H.L. Stormer, D.C. Tsui, L.N. Pfeiffer, K.W. Baldwin, K.W. West, Phys. Rev. Lett. 93, 176809 (2004). doi:10.1103/PhysRevLett. 93.176809

- A. Kumar, G.A. Csáthy, M.J. Manfra, L.N. Pfeiffer, K.W. West, Phys. Rev. Lett. 105, 246808 (2010). doi:10.1103/PhysRevLett.105.246808
- N. Deng, A. Kumar, M.J. Manfra, L.N. Pfeiffer, K.W. West, G.A. Csáthy, Phys. Rev. Lett. 108, 086803 (2012). doi:10.1103/PhysRevLett.100.086803
- N. Deng, G. Gardner, S. Mondal, E. Kleinbaum, M. Manfra, G. Csáthy, Phys. Rev. Lett. 112, 116804 (2014). doi:10.1103/PhysRevLett.112.116804
- G.A. Csáthy, J.S. Xia, C.L. Vicente, E.D. Adams, N.S. Sullivan, H.L. Stormer, D.C. Tsui, L.N. Pfeiffer, K.W. West, Phys. Rev. Lett. 94, 146801 (2005). doi:10.1103/PhysRevLett.94.146801
- W. Pan, J.S. Xia, H.L. Stormer, D.C. Tsui, C. Vicente, E.D. Adams, N.S. Sullivan, L.N. Pfeiffer, K.W. Baldwin, K.W. West, Phys. Rev. B 77, 075307 (2008). doi:10.1103/PhysRevB.77.075307
- J. Nuebler, V. Umansky, R. Morf, M. Heiblum, K. von Klitzing, J. Smet, Phys. Rev. B 81, 035316 (2010). doi:10.1103/PhysRevB.81.035316
- M.O. Goerbig, P. Lederer, C.M. Smith, Phys. Rev. B 68, 241302 (2003). doi:10.1103/ PhysRevB.68.241302
- M.O. Goerbig, P. Lederer, C.M. Smith, Phys. Rev. B 69, 115327 (2004). doi:10.1103/ PhysRevB.69.115327
- 25. G. Moore, N. Read, Nucl. Phys. B 360, 362 (1991). doi:10.1016/0550-3213(91)90407-O
- M. Levin, B.I. Halperin, B. Rosenow, Phys. Rev. Lett. 99, 236806 (2007). doi:10.1103/ PhysRevLett.99.236806
- S.-S. Lee, S. Ryu, C. Nayak, M.P.A. Fisher, Phys. Rev. Lett. 99, 236807 (2007). doi:10.1103/ PhysRevLett.99.236807
- 28. X.G. Wen, Phys. Rev. Lett. **66**, 802 (1991). doi:10.1103/PhysRevLett.66.802
- 29. B. Blok, X. Wen, Nucl. Phys. B 374, 615 (1992). doi:10.1016/0550-3213(92)90402-W
- 30. R.H. Morf, Phys. Rev. Lett. 80, 1505 (1998). doi:10.1103/PhysRevLett.80.1505
- E.H. Rezayi, F.D.M. Haldane, Phys. Rev. Lett. 84, 4685 (2000). doi:10.1103/PhysRevLett.84.
 4685
- 32. A.E. Feiguin, E. Rezayi, C. Nayak, S.D. Sarma, Phys. Rev. Lett. **100**, 166803 (2008). doi:10. 1103/PhysRevLett.100.166803
- 33. G. Möller, S.H. Simon, Phys. Rev. B 77, 075319 (2008). doi:10.1103/PhysRevB.77.075319
- 34. A.E. Feiguin, E. Rezayi, K. Yang, C. Nayak, S.D Sarma, Phys. Rev. B **79**, 115322 (2009). doi:10.1103/PhysRevB.79.115322
- 35. O.S. Zozulya, M. Haque, N. Regnault, Phys. Rev. B **79**, 045409 (2009). doi:10.1103/PhysRevB. 79.045409
- M. Storni, R.H. Morf, S.D. Sarma, Phys. Rev. Lett. 104, 076803 (2010). doi:10.1103/ PhysRevLett.104.076803
- G. Möller, A. Wójs, N.R. Cooper, Phys. Rev. Lett. 107, 036803 (2011). doi:10.1103/ PhysRevLett.107.036803
- 38. X. Wan, K. Yang, E.H. Rezayi, Phys. Rev. Lett. **97**, 256804 (2006). doi:10.1103/PhysRevLett. 97.256804
- X. Wan, Z.-X. Hu, E.H. Rezayi, K. Yang, Phys. Rev. B 77, 165316 (2008). doi:10.1103/ PhysRevB.77.165316
- I. Dimov, B.I. Halperin, C. Nayak, Phys. Rev. Lett. 100, 126804 (2008). doi:10.1103/ PhysRevLett.100.126804
- A. Wójs, C. Tőke, J.K. Jain, Phys. Rev. Lett. 105, 096802 (2010). doi:10.1103/PhysRevLett. 105.096802
- E.H. Rezayi, S.H. Simon, Phys. Rev. Lett. 106, 116801 (2011). doi:10.1103/PhysRevLett.106. 116801
- I.P. Radu, J.B. Miller, C.M. Marcus, M.A. Kastner, L.N. Pfeiffer, K.W. West, Science 320, 899 (2008). doi:10.1126/science.1157560
- L. Tiemann, G. Gamez, N. Kumada, K. Muraki, Science 335, 828 (2012). doi:10.1126/science. 1216697
- S. Baer, C. Rössler, T. Ihn, K. Ensslin, C. Reichl, W. Wegscheider, Phys. Rev. B 90, 075403 (2014). doi:10.1103/PhysRevB.90.075403

References 285

 U. Wurstbauer, K.W. West, L.N. Pfeiffer, A. Pinczuk, Phys. Rev. Lett. 110, 026801 (2013). doi:10.1103/PhysRevLett.110.026801

- M. Dolev, M. Heiblum, V. Umansky, A. Stern, D. Mahalu, Nature 452, 829 (2008). doi:10. 1038/nature06855
- 48. W. Pan, H.L. Stormer, D.C. Tsui, L.N. Pfeiffer, K.W. Baldwin, K.W. West, Solid State Commun. **119**, 641 (2001). doi:10.1016/S0038-1098(01)00311-8
- C. Reichl, J. Chen, S. Baer, C. Rössler, T. Ihn, K. Ensslin, W. Dietsche, W. Wegscheider, New J. Phys. 16, 023014 (2014). doi:10.1088/1367-2630/16/2/023014
- W. Pan, J.S. Xia, H.L. Stormer, D.C. Tsui, C.L. Vicente, E.D. Adams, N.S. Sullivan, L.N. Pfeiffer, K.W. Baldwin, K.W. West, Solid State Communications series Emergent phenomena in quantum Hall systems. Emergent Phenom. Quantum Hall Syst. 140, 88 (2006). doi:10.1016/j.ssc.2006.05.048
- W. Pan, J.S. Xia, H.L. Stormer, D.C. Tsui, C.L. Vicente, E.D. Adams, N.S. Sullivan, L.N. Pfeiffer, K.W. Baldwin, K.W. West, Phys. Rev. Lett. 95, 066808 (2005). doi:10.1103/PhysRevLett. 95.066808
- N. Deng, J.D. Watson, L.P. Rokhinson, M.J. Manfra, G.A. Csáthy, Phys. Rev. B 86, 201301 (2012). doi:10.1103/PhysRevB.86.201301
- J.M. Kosterlitz, D.J. Thouless, J. Phys. C: Solid State Phys. 6, 1181 (1973). doi:10.1088/0022-3719/6/7/010
- 54. J.M. Kosterlitz, J. Phys. C: Solid State Phys. 7, 1046 (1974). doi:10.1088/0022-3719/7/6/005
- 55. B.I. Halperin, D.R. Nelson, Phys. Rev. Lett. 41, 121 (1978). doi:10.1103/PhysRevLett.41.121
- 56. A.P. Young, Phys. Rev. B 19, 1855 (1979). doi:10.1103/PhysRevB.19.1855
- 57. E. Fradkin, S.A. Kivelson, Phys. Rev. B 59, 8065 (1999). doi:10.1103/PhysRevB.59.8065
- 58. C. Wexler, O. Ciftja, Int. J. Mod. Phys. B 20, 747 (2006). doi:10.1142/S0217979206033632
- C.W.J. Beenakker, H. van Houten, http://arxiv.org/abs/cond-mat/0412664cond-mat/0412664 (2004), Solid State Phys. 44, 1 (1991)
- J. Göres, G. Gamez, J.H. Smet, L. Pfeiffer, K. West, A. Yacoby, V. Umansky, K. von Klitzing, Phys. Rev. Lett. 99, 246402 (2007). doi:10.1103/PhysRevLett.99.246402

Part VI Conclusion

Chapter 16 Conclusion

In this book, we have presented experiments that investigated the properties of integer and fractional quantum Hall states by measurements in the bulk, using QPCs and QDs. By carefully optimizing our measurement setup and samples (Part II) we were able to investigate FQH states at extremely low electronic temperatures. This furthermore enabled us to study the RIQH states in the second LL in non-equilibrium transport (Part V). A detailed control and understanding of the transmission properties of single QPCs has allowed us to study the local formation of FQH states, their interaction with localization and their tunneling properties (Part III). Making use of this knowledge, we have investigated transport in QDs and interferometers in the quantum Hall regime (Part IV).

In the following we give a short conclusion of the individual experimental chapters of this book:

Chapter 7—Measurement Setup Optimization for Low Electron Temperatures and Chap. 8—Optimization of Samples and Sample Fabrication These two chapters described the considerable preliminary work which was necessary for the experiments presented in this book and might be of use for other experimentalists beginning in the field. We have removed heating sources, which arise in the cryostat due to vibrations and electronic noise. Furthermore, we have implemented a highly effective low-temperature filtering and thermal anchoring setup, which enabled us to reach electronic temperatures of approximately $12-13 \, \text{mK}$. We have studied the influence of the sample processing on the 2DEG quality and could identify a suitable process which does not degrade the mobility. We found that the Ohmic contact fabrication process and contact geometry were crucial in order to observe fragile FQH states, like the $\nu = 5/2 \, \text{state}$, in processed samples.

Chapter 9—Quantum Point Contacts In this chapter, we have investigated the transport properties of clean QPCs, which are the basic building block for the magnetotransport experiments discussed later in this book. Shifting the QPC channel position, we could demonstrate the absence of impurities and localizations. In finite

290 16 Conclusion

bias transport, conductance plateaus and half-plateaus were observed. The confinement potential was extracted and found to be well described by a harmonic potential, in agreement with numerical calculations. We have demonstrated how the confinement potential can be varied and have investigated the influence of this on the transmission of FQH states. Applying a finite magnetic field revealed interaction effects in the QPCs, like a strong *g*-factor enhancement or a large bias-dependence of the transmission in the FQH regime.

Chapter 10—Integer and Fractional Quantum Hall States in QPCs Here we have investigated the formation of integer and fractional quantum Hall states in QPCs. We found that the transmission properties of QPCs were strongly influenced by interference and localization effects, which we could explain in terms of single- and many-electron physics. In the FQH regime, we found indications for the localization of fractionally charged QPs in the QPC. Understanding these effects was important for the interpretation of tunneling and interference experiments in the quantum Hall regime. We furthermore demonstrated, how fragile quantum Hall states, like the $\nu = 5/2$ state, can be observed in QPCs using optimized growth and gating techniques.

Chapter 11—Quasiparticle Tunneling in the Second Landau Level In this chapter, we have investigated the most prominent FQH states at $\nu = 7/3$, 8/3 and 5/2, which are of great interest due to potential non-Abelian edge excitations. The bias and temperature dependence in a weak QP tunneling regime could be well described in terms of the chiral Luttinger liquid theory, which allowed us to extract characteristic properties of the edge excitations. For the $\nu = 5/2$ state, we found the best agreement with the Abelian (3,3,1) and (1,1,3)-states, for different backscattering strengths and in a finite range of magnetic fields. At $\nu = 8/3$, the tunneling behavior is best described by a particle-hole conjugate Laughlin state, while at $\nu = 7/3$ a rapid crossover to strong backscattering, where the theory is no longer applicable, occurs. Here, none of the candidate states was in preferential agreement with the experiment.

Chapter 12—Quantum Dots and Charge Detection Techniques Here we have described how charge detection techniques can be optimized to allow for a time-resolved detection of single electron charges in large quantum dots. With this, we were able to reach substantially higher charge detector sensitivities than reported in literature for dots of comparable size, making those techniques potentially interesting for the study of Coulomb-dominated interferometers in the quantum Hall regime.

Chapter 13—Quantum Dots in the Quantum Hall Regime This chapter describes transport experiments studying a large QD in a strong perpendicular magnetic field. For a high transmission of the QD barriers, the system was found to act as a Fabry-Pérot interferometer with a behavior governed by a Coulomb-dominated mechanism. When the barriers are in the tunneling regime, the transmission of the QD was found to be influenced by the presence of compressible and incompressible regions inside the QD. We could explain the behavior of the QD in analogy to the physics of a double QD, formed by two edge states. The corresponding charge droplets are cyclically

16 Conclusion 291

depopulated and are coupled to each other. We have extracted the charge stability diagram of this system and could draw conclusions about the edge state geometry within the QD.

Chapter 14—Preliminary Results of Interference Experiments in the Second Landau Level In this chapter, we have discussed experimental challenges that arise for the implementation of interference experiments with the FQH states of the second Landau level. We found that especially the gating of high mobility structures is experimentally challenging. We described how a fully gapped v = 5/2 state can be observed in an interferometer, with an energy gap of more than 200 mK. This is an important experimental step for the implementation of an interferometry experiment at v = 5/2, where the FQH state should be fully gapped in the center of the interferometer. This has to our knowledge not yet been demonstrated in literature.

Chapter 15—Non-equilibrium Transport in Density Modulated Phases of the Second Landau Level The last chapter discusses the transport properties of the RIQH phases in the second LL. We found that a transition to an isotropic compressible phase can be induced by applying large DC currents. This transition is markedly different for electron and hole bubble phases, which might indicate that the particle-hole symmetry in the second LL is broken or that the electron and hole bubble phases are more complex than currently anticipated by theory. A possible breaking of the particle-hole symmetry in the second LL might also have consequences for our understanding of the $\nu = 5/2$ FQH state.

A. Van der Pauw Measurement Method

The van der Pauw method allows the measurement of the sheet resistivity ρ_{\square} and hence mobility of a sample with an arbitrary geometry (see Fig. A.1a). By switching the current direction the following resistances are measured: $R_{12,34} = V_{34}/I_{12}$ (see Fig. A.1a) and $R_{23,41} = V_{41}/I_{23}$. Using conformal mapping methods, van der Pauw could show that the following relation holds independent of the sample geometry [1]:

$$\exp\left(-\frac{\pi}{\rho_{\square}}R_{12,34}\right) + \exp\left(-\frac{\pi}{\rho_{\square}}R_{23,41}\right) = 1 \tag{A.1}$$

Then the sheet resistivity can be calculated:

$$\rho_{\square} = \frac{\pi}{\ln 2} \frac{R_{12,34} + R_{23,41}}{2} f\left(R_{12,34}/R_{23,41}\right),\tag{A.2}$$

where f is a correction factor that is plotted in Fig. A.1b. A higher precision can be achieved by making use of reciprocity relations. The following conditions have to be met in order to apply the van der Pauw method [2]:

- Contacts are located at the edge of the sample
- The sample has to be singly connected (i.e. no holes)
- Contacts have to be small in size compared to the sample size
- Sheet resistivity is homogeneous

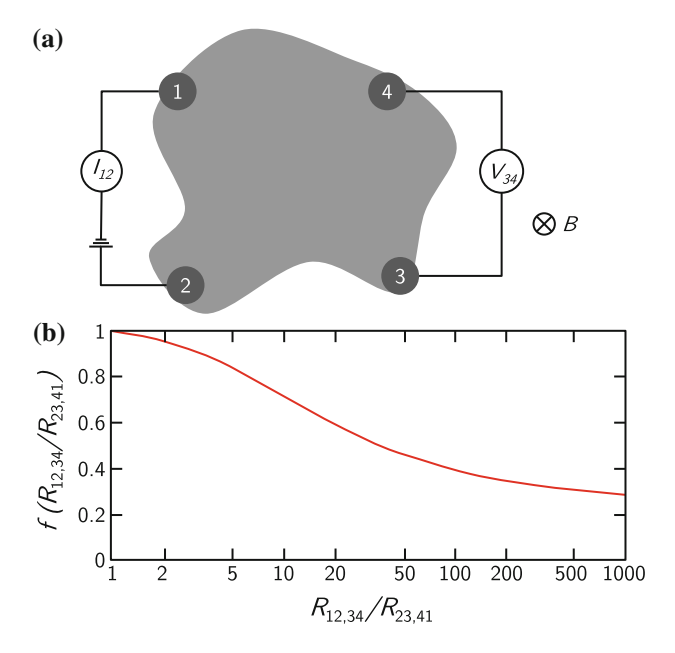


Fig. A.1 a Schematic setup for a van der Pauw measurement. **b** Correction factor f as a function of $R_{12,34}/R_{23,41}$. Adapted from [2]

B. Four-terminal Measurements in a Hall-bar

Four-terminal Measurement Across a QPC In order to relate the measured resistances in a Hall-bar measurement to the filling factors in bulk and QPC, we can treat the schematic Hall-bar depicted in Fig. A.2 with Landauer-Büttiker formalism. We assume that there are ν edge states in the bulk, each contributing e^2/h to the conductance. At the QPC, t edge states are transmitted while ($\nu - t$) edge states are reflected. Here, the current t is assumed to be flowing between contacts 1 and 4.

Applying the generalized multi-terminal Landauer-Büttiker formalism [3–5] to this case, we can write:

$$\begin{pmatrix}
I \\
0 \\
0 \\
-I \\
0 \\
0
\end{pmatrix} = \frac{e^2}{h} \begin{pmatrix}
\nu & 0 & 0 & 0 & 0 & -\nu \\
-\nu & \nu & 0 & 0 & 0 & 0 \\
0 & -t & \nu & 0 & -(\nu - t) & 0 \\
0 & 0 & -\nu & \nu & 0 & 0 \\
0 & 0 & 0 & -\nu & \nu & 0 \\
0 & 0 & 0 & -\nu & \nu & 0 \\
0 & -(\nu - t) & 0 & 0 & -t & \nu
\end{pmatrix} \begin{pmatrix}
V_1 \\
V_2 \\
V_3 \\
V_4 \\
V_5 \\
V_6
\end{pmatrix}$$
(A.3)

From (A.3) we find: $V_1 = V_2$ and $V_4 = V_5$. Using $V_{k,l} = V_k - V_l$ and choosing without loss of generality $V_4 = 0$, we obtain for the resistances $R_{m,n;k,l} = \frac{V_{k,l}}{I_{m,n}}$ in agreement with [6]:

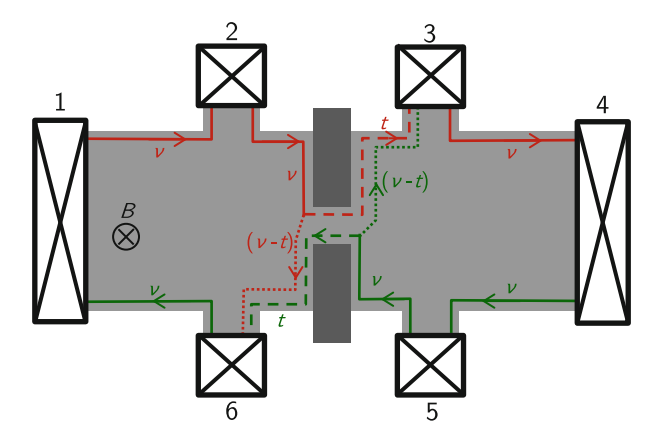


Fig. A.2 Hall-bar contact configuration. In the bulk, ν edge states contribute $\nu \times \frac{e^2}{h}$ to the conductance. t edge states are transmitted through the QPC, while the rest $(\nu - t)$ is reflected

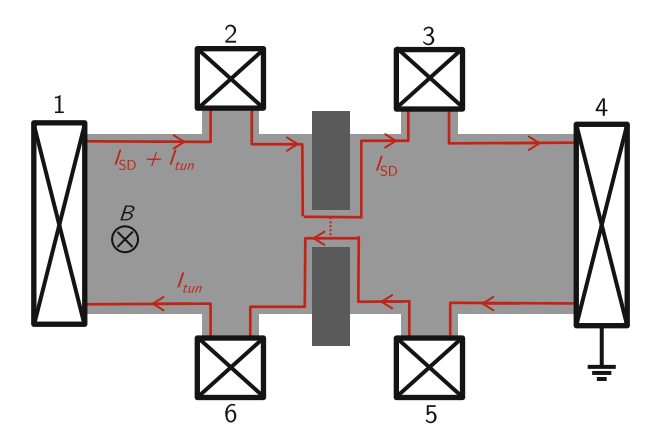


Fig. A.3 Currents in a weak tunneling setup. $I_{SD} + I_{tun}$ is inserted via contact 1. A current I_{tun} is backscattered at the QPC and only the current I_{SD} leaves the sample via contact 4, which is grounded

$$R_{xy} := R_{1,4;3,5} = R_{1,4;6,2} = \frac{h}{e^2} \left(\frac{1}{\nu}\right)$$
 (A.4)

$$R_{\text{long}} := R_{1,4;6,5} = R_{1,4;2,3} = \frac{h}{e^2} \left(\frac{1}{t} - \frac{1}{\nu} \right)$$
 (A.5)

$$R_{\text{diag}}^{+} := R_{1,4;2,5} = \frac{h}{e^2} \left(\frac{1}{t}\right)$$
 (A.6)

$$R_{\text{diag}}^- := R_{1,4;6,3} = \frac{h}{e^2} \left(\frac{2}{\nu} - \frac{1}{t} \right)$$
 (A.7)

When the transport in the system is quantized, the definition of an effective QPC filling factor $\nu_{\rm OPC}$ can be made via $\nu_{\rm OPC} = t$.

Tunneling conductance We now look at a QPC in a weak backscattering regime (Fig. A.3). Here, pin 4 is grounded, while a current $I_{SD} + I_{tun}$ is inserted at contact 1. At the QPC, the current I_{tun} (which is small compared to I_{SD}) is reflected.

The tunneling conductance can be derived analog to [7]: The voltage drop diagonally across the QPC is given by:

$$V_{2,5} = R_{xy} \left(I_{SD} + I_{tun}(V_{2,5}) \right) \tag{A.8}$$

where the tunneling current I_{tun} depends on the potential difference $V_{2,5}$. The differential diagonal resistance is measured and using (A.8) can be written as:

$$R_{\text{diag}}^{+} = \left(\frac{\partial V_{2,5}}{\partial I_{\text{SD}}}\right) = \left(\frac{\partial I_{\text{SD}}}{\partial V_{2,5}}\right)^{-1} = \left(\frac{\partial}{\partial V_{2,5}} \left(\frac{V_{2,5}}{R_{xy}} - I_{tun}(V_{2,5})\right)\right)^{-1}$$
(A.9)
$$= \frac{R_{xy}}{1 - R_{xy} \left(\frac{\partial I_{tun}}{\partial V}\right)|_{V_{2,5}}}$$
(A.10)

In the weak tunneling approximation, we have $V_{2,5} \approx R_{xy}I_{SD}$, where we have used $I_{SD} + I_{tun} \approx I_{SD}$. Using this and (A.9), we can now express the tunneling conductance g_{tun} as:

$$g_{tun} = \left(\frac{\partial I_{tun}}{\partial V}\right)\Big|_{V=R_{vv}I_{SD}} \approx \left(\frac{\partial I_{tun}}{\partial V}\right)\Big|_{V_{2.5}}$$
 (A.11)

$$= \frac{R_{\text{diag}}^{+} - R_{xy}}{R_{\text{diag}}^{+} R_{xy}} \approx \frac{R_{\text{diag}}^{+} - R_{xy}}{R_{xy}^{2}}$$
(A.12)

This result is used to extract the tunneling conductance in the weak tunneling experiments ([8, 9] and Chap. 11). We note that an exact measurement of the tunneling conductance is possible by grounding contacts 4 and 6 simultaneously [10, 11]. Due to the cold grounding scheme used for our experiments (see Chap. 7) we did not use this measurement scheme to prevent possible thermovoltage effects.

C. Calculation of the Probability Density Function of Residuals (for Chap. 11)

The residuals $\{\delta_{k,l}\}$ of measurement points $\{x_{k,l}\}$ (measured at T_k at $I_{DC,l}$) are given by:

$$\delta_{k,l} = \tilde{x}_{k,l} - g_{\infty} - Ag_{tun}(T_k, I_{DC,l}, e^*/e, g)$$
 (A.13)

where $\tilde{x}_{k,l} = x_{k,l} - \mu$ are offset measurement points, such that $\overline{\delta_{k,l}} = 0$.

Assuming a statistical error, the residuals follow a Gaussian distribution:

$$p\left(\{\delta_i\}|\sigma, g, e^*/e, A, g_\infty\right) \propto \exp\left(-\frac{1}{2\sigma^2} \sum_{k,l} \delta_{k,l}^2\right)$$
 (A.14)

After marginalization of the standard deviation σ , a Student-t distribution is obtained for the residuals [12]:

$$p(g, e^*/e, A, g_{\infty}|\{\delta_i\}) \propto \left(\sum_{k,l} \delta_{k,l}^2\right)^{-\frac{N-1}{2}}$$

$$= \frac{1}{\left(\sum_{k,l} (\tilde{x}_{k,l} - g_{\infty} - Ag_{tun}(T_k, I_{DC,l}, e^*/e, g))^2\right)^{\frac{N-1}{2}}}$$

$$= \frac{1}{\left(\alpha - 2g_{\infty}\beta - 2A\gamma + Ng_{\infty}^2 + 2g_{\infty}A\delta + A^2\epsilon\right)^{\frac{N-1}{2}}}$$

Here, we have used:

$$N = \sum_{k,l} 1$$

$$\alpha = \sum_{k,l} \tilde{x}_{k,l}^2$$

$$\beta = \sum_{k,l} \tilde{x}_{k,l}$$

$$\gamma = \sum_{k,l} \tilde{x}_{k,l} g_{tun}(T_k, I_{DC,l}, e^*/e, g)$$

$$\delta = \sum_{k,l} g_{tun}(T_k, I_{DC,l}, e^*/e, g)$$

$$\epsilon = \sum_{k,l} g_{tun}^2(T_k, I_{DC,l}, e^*/e, g)$$

With this:

$$\begin{split} p\left(g,e^*/e,A,g_{\infty}|\{\delta_i\}\right) &\propto \frac{1}{\left(Ng_{\infty}^2\right)^{\frac{N-1}{2}} \left(1+\frac{\frac{1}{2}\frac{N-1}{N}(\alpha-2g_{\infty}\beta-2A\gamma+2g_{\infty}A\delta+A^2\epsilon)}{\frac{N-1}{2}g_{\infty}^2}\right)^{\frac{N-1}{2}}} \\ &\approx \left(Ng_{\infty}^2\right)^{-\frac{N-1}{2}} \exp\left(-\frac{1}{2g_{\infty}^2}\frac{N-1}{N}(\alpha-2g_{\infty}\beta-2A\gamma+2g_{\infty}A\delta+A^2\epsilon)\right) \end{split}$$

Here, the Student-t distribution has been approximated by an exponential expression for the limit of large N. To the end, we are looking for the posterior probability density function:

$$p\left(g, e^*/e | \{\delta_i\}\right) = \int_{-\infty}^{\infty} \int_{-\infty}^{\infty} p\left(g, e^*/e, A, g_{\infty} | \{\delta_i\}\right) dA dg_{\infty}$$
 (A.15)

The first integration can be computed analytically, yielding:

$$\int_{-\infty}^{\infty} p\left(g, e^*/e, A, g_{\infty} | \{\delta_i\}\right) dA \propto \frac{\sqrt{2\pi}N^{\frac{3}{2} - \frac{N}{2}} |g_{\infty}| g_{\infty}^{1-N} \exp\left(\frac{(N-1)\left(-\alpha\epsilon + \gamma^2 + \delta^2 g_{\infty}^2 + 2\beta g_{\infty}\epsilon - 2\gamma\delta g_{\infty}\right)}{2g_{\infty}^2 N\epsilon}\right)}{\sqrt{(N-1)N\epsilon}} \tag{A.16}$$

A second, numerical integration over g_{∞} yields the desired result, $p(g, e^*/e|\{\delta_i\})$.

D. ν = 5/2 Sample Fabrication Recipe

The following process is a based on the standard photolithography recipe of the Ensslin group. Some modifications were made to minimize degradation of the 2DEG mobility for experiments at $\nu = 5/2$. Other processes which seem to yield good results can for example be found in [13, 14].

Cleave

- Typical sample size: $4.5 \, \text{mm} \times 4.5 \, \text{mm}$
- Leave at least 300 \(\mu \) m space from the structure to the edge

Initial cleaning

 Leave sample for approx. 3 min in acetone, 3 min in isopropanole, rinse for 30 s in water. No ultrasound, samples break easily! Blow dry with N₂

• Heat for 2 min, 120 °C, to remove water vapor and to prevent sticking problems of the resist. This might otherwise cause underetching.

Mesa lithography

- Spin with resist AZ5214E: 3s at 2000 rpm, 45s at 4500 rpm, use minimal ramp time
- Bake 2 min at 90 °C
- Align mesa structure with Karl Süss MJB3 mask aligner, soft contact mode. Illuminate for 12 s with CH2, $10.0 \,\mathrm{mW/cm^2}$ (at $\lambda = 405 \,\mathrm{nm}$).
- Develop in MF319, 30 s. Rinse in water, 20 s.
- Check result in microscope. There should be no resist residues outside the mesa.

Mesa etching

- Etch using highly dilute Piranha: $H_2O:H_2O_2:H_2SO_4 = 100:3:3$
- Calibrate etching rate with dummy chip. Typical rate: 2–3 nm/s (depends on age of the etching solution).
- Target etching depths: For single side-doped heterostructures: depth of doping plane, for double-side doped structures: 2DEG depth. 1
- After etching: rinse in water, at least 1 min
- Resist removal: leave sample for approx. 3 min in warm acetone (50°C), 3 min in warm isopropanole (50°C), rinse for 30 s in water. No ultrasound! Blow dry with N₂
- Measure etching depth with step profiler. Do not scratch over vital parts of the mesa! Ideally measure at alignment markers.

Contact lithography

- Clean again: leave sample for approx. 3 min in acetone, 3 min in isopropanole, rinse for 30 s in water. No ultrasound! Blow dry with N₂
- Spin with resist AZ5214E: 3 s at 2000 rpm, 45 s at 4500 rpm, use minimal ramp time
- Bake 2 min at 90 °C
- Align contact structure with Karl Süss MJB3 mask aligner, soft contact mode. Illuminate for 3 s with CH2, 10.0 mW/cm².
- Bake 2 min at 115 °C
- Illuminate whole sample surface for 30 s with CH2, 10.0 mW/cm².
- Develop in MF319, 30 s. Rinse in water, 20 s.
- Check result in microscope. There should be no resist residues inside the contact pads. (Residues burn during the contact annealing and degrade the 2DEG)

Au/Ge/Ni evaporation

• Dip etch to remove oxide layers before evaporation: 3 s in HCl (38%), rinse 60 s in water, blow dry with N₂.

 $^{^{1}}$ Comment: if the mesa structure is too high, it is difficult to evaporate connected gate leads over the edge.

 Lose no time and try to bring the samples in the evaporator vacuum as fast as possible!

- Evaporate eutectic mixture with Plassys II: (Ge/Au/Ge/Au/Ni/Au) (52.8/107.2/52.8/107.2/80/100 nm).
- Liftoff in warm acetone (50 °C). Rinse in water, 60 s.
- Clean again thoroughly: leave sample for approx. 3 min in warm acetone (50 °C), 3 min in warm isopropanole (50 °C), rinse for 30 s in water. No ultrasound! Blow dry with N₂
- Check under microscope if the surface is sufficiently clean. This is crucial before the annealing step.
- Leave for 30 min in Ultra Violet Ozone Cleaning system (UVOCS).

Au/Ge/Ni annealing

- Use J.I.P.Elec JetFirst 100 rapid thermal annealing oven.
- Important: use carrier spacer to avoid scratching the sample surface. The sample is covered by the upper part of the carrier.
- First step: Flush chamber, then leave 5 min at 120 °C to remove water vapor, 200 sccm H₂/N₂ (5%) flow
- Second step: 5 min at 500 °C, 200 sccm H_2/N_2 (5 %) flow
- Ramp speeds: 60 s-120 °C, 40 s from 120 °C to 450 °C, 20 s from 450 °C to 500 °C to avoid overshoot

Gate lead lithography

- Clean again: leave sample for approx. 3 min in acetone, 3 min in isopropanole, rinse for 30 s in water. No ultrasound! Blow dry with N₂
- Spin with resist AZ5214E: 3s at 2000 rpm, 45s at 4500 rpm, use minimal ramp time
- Bake 2 min at 90 °C
- Align gate lead structures with Karl Süss MJB3 mask aligner, soft contact mode. Illuminate for 3 s with CH2, 10.0 mW/cm².
- Bake 2 min at 115 °C
- Illuminate whole sample surface for 30 s with CH2, 10.0 mW/cm².
- Develop in MF319, 30 s. Rinse in water, 20 s.
- Check result in microscope

Gate lead evaporation

- Evaporate topgate leads with Plassys II: (Ti/Au) (10/80 nm)
- Liftoff in warm acetone (50°C). If the gold film does not flake by itself, use a pipette and blow carefully acetone to the surface (while the sample remains fully in the liquid). Rinse in water, 60 s.
- Before e-beam lithography, again thoroughly clean the surface: leave sample for approx. 3 min in warm acetone (50°C), 3 min in warm isopropanole (50°C), rinse for 30 s in water. No ultrasound! Blow dry with N₂

E-beam lithography

- Spin with PMMA 950 K in pure anisol, 45 s at 6000 rmp, minimal ramp time.
- Bake 5 min at 180 °C.
- E-beam exposure (RAITH150, 30 kV): aperture 10, doses: 2400 pC/cm (single pixel line) or 280 µC/cm² (polygons).
- Develop in MIBK:isopropanole 1:3, 60 s, rinse in isopropanole, 30 s.
- Check under microscope (µm-sized structures should be visible).

E-beam gate evaporation

- Evaporate e-beam leads with Plassys II: (Ti/Au) (2/28 nm)
- Liftoff in warm acetone (50 °C). If the gold film does not flake by itself, use a pipette and blow carefully acetone to the surface (while the sample remains fully in the liquid). In the worst case, quickly use ultrasound (<1 min, minimum power). Rinse in water, 60 s.
- Clean again: leave sample for approx. 3 min in acetone, 3 min in isopropanole, rinse for 30 s in water. No ultrasound! Blow dry with N₂

Bonding

- Cleave samples if necessary.
- Glue sample in chip carrier using conductive silver. Heat to 120 °C for approx. 2 min to dry.
- Bond with aluminum wire. Gold offers a better thermal conductance, but sticks much worse. The risk of breaking the sample is just too high!

E. Silver Annealing Process

The silver cold finger has been brazed from different parts using non-superconducting solder. Subsequently, it has been thermally annealed, in order to improve the thermal conductivity. The respective processes are shown in the following (Fig. A.4):

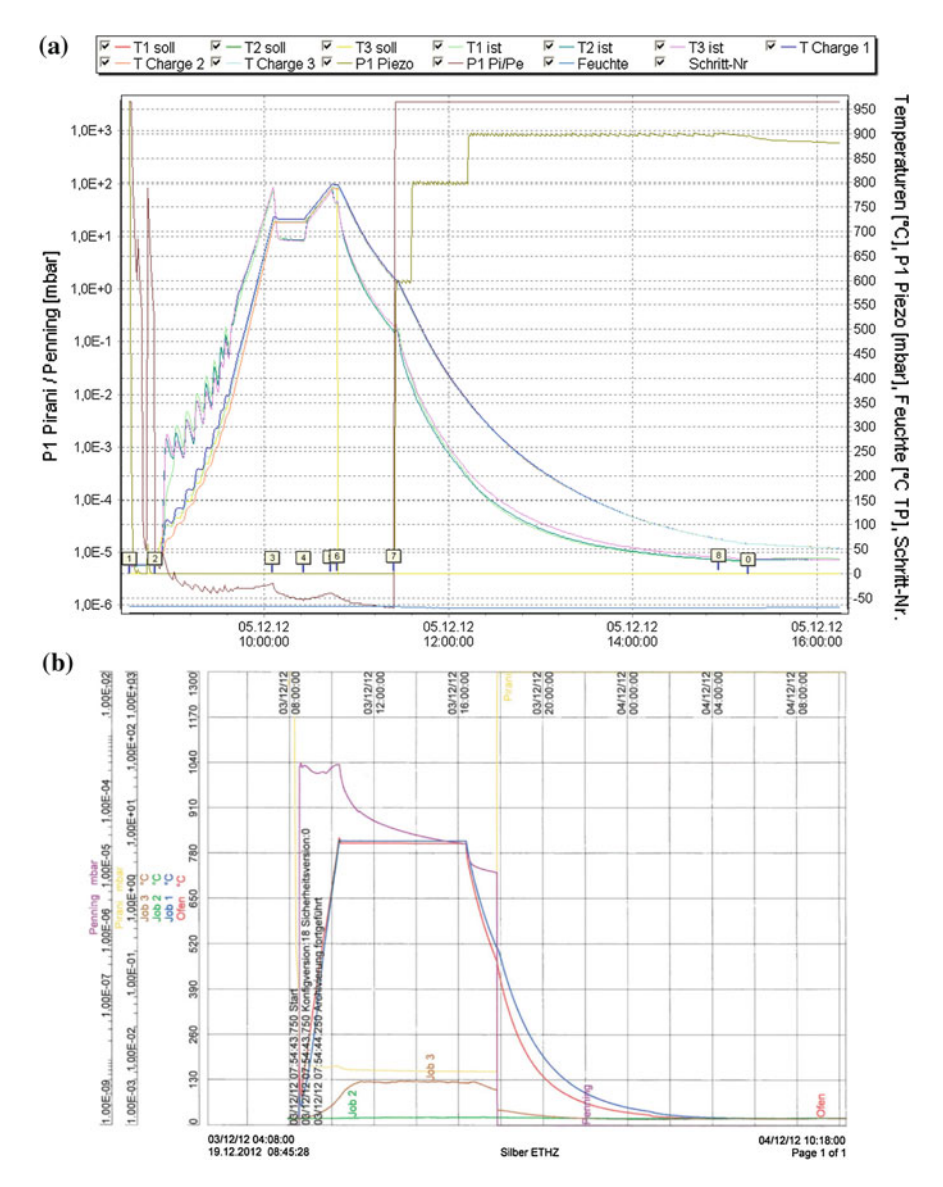


Fig. A.4 a Silver brazing process, b Silver annealing process, 6 h at 820 °C

F. LED Illumination Recipe

The following procedure was used to illuminate samples made from the wafer D110726B:

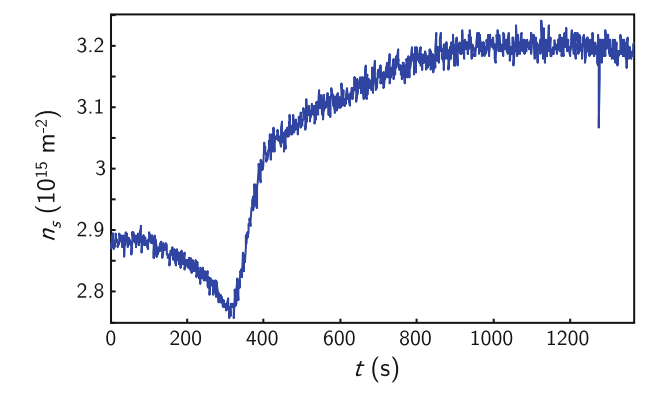


Fig. A.5 2DEG electron density as a function of time for an LED illumination process at $T=4\,\mathrm{K}$. (Sample D110726B-3B)

- Setup: use red LED, model number HLMP-3201. A constant current is applied with a Yokogawa current/voltage source. Distance from LED to sample: approximately 5–10 mm
- Cool sample to 4 K.
- Set B-field to 100 mT and measure the Hall resistance to monitor the density.
- t = 0: Open pin connection from LED to Yokogawa, $I_{LED} = 0$ nA.
- $t = 30 \text{ s: Set } I_{\text{LED}} = 100 \text{ nA}.$
- $t = 80 \text{ s: Set } I_{\text{LED}} = 300 \text{ nA}.$
- t = 230 s: Set $I_{\text{LED}} = 500 \text{ nA}$.
- $t = 290 \text{ s: Set } I_{\text{LED}} = 700 \text{ nA}.$
- The density increases now quickly (see Fig. A.5). Wait until the density has saturated.
- t = 1000 s: slowly set I_{LED} to zero.
- t = 1280 s: close LED pin.

References

- 1. L.J. van der Pauw, Philips Tech. Rev. 20, 220 (1958)
- 2. L.J. van der Pauw, Philips Res. Rep. 13, 1 (1958)
- 3. R. Landauer, IBM J. Res. Dev. 32, 306 (1988). doi:10.1147/rd.323.0306
- 4. A.D. Stone, A. Szafer, IBM J. Res. Dev. 32, 384 (1988). doi:10.1147/rd.323.0384
- 5. M. Buttiker, IBM J. Res. Dev. 32, 317 (1988). doi:10.1147/rd.323.0317
- 6. C.W.J. Beenakker, H. van Houten, cond-mat/0412664 (2004), Solid State Phys. 44, 1 (1991)
- I. Radu, Electron transport in confined structures in very high mobility GaAs in Perpendicular magnetic fields, Ph.D. thesis, Massachusetts Institute of Technology, Cambridge, Massachusetts (2009)
- I.P. Radu, J.B. Miller, C.M. Marcus, M.A. Kastner, L.N. Pfeiffer, K.W. West, Science 320, 899 (2008). doi:10.1126/science.1157560

 X. Lin, C. Dillard, M.A. Kastner, L.N. Pfeiffer, K.W. West, Phys. Rev. B 85, 165321 (2012). doi:10.1103/PhysRevB.85.165321

- S. Roddaro, V. Pellegrini, F. Beltram, G. Biasiol, L. Sorba, Phys. Rev. Lett. 93, 046801 (2004). doi:10.1103/PhysRevLett.93.046801
- S. Roddaro, V. Pellegrini, F. Beltram, Solid State Commun. 131, 565 (2004). doi:10.1016/j. ssc.2004.05.049
- 12. D.S. Sivia, J. Skilling, *Data Analysis: A Bayesian Tutorial* (Oxford University Press, Oxford, 2006)
- 13. J.B. Miller, Electron transport in GaAs heterostructures at various magnetic field strengths, Ph.D. thesis, Harvard University, Cambridge, Massachusetts (2007)
- 14. Douglas Templeton McClure III, Interferometer-based studies of quantum hall phenomena, Ph.D. thesis, Harvard University, Cambridge, Massachusetts (2012)

Symbols	quasiparticle tunneling, 82, 84
Λ -level, 32	shot noise measurements, 75
$\nu = 1/3, 30, 167, 181$	spin polarization, 76–82
energy gap in a QPC, 180, 181	tilted field measurements, 79
$\nu = 1/m, 31$	tunneling conductance, 191, 207
$\nu = 12/5, 41, 42$	$\nu = 7/3, 35, 39, 204$
candidate states, 41	candidate states, 39
$\nu = 2/3, 30, 167, 182$	edge paramters, 196, 199
energy gap, 182	energy gap, 259
$\nu = 4/11, 33$	quasiparticle charge, 76
$\nu = 5/13, 33$	$\nu = 8/3, 35, 39, 202$
$\nu = 5/2, 18, 35, 69, 73, 74, 76, 78, 80, 82,$	candidate states, 39
84–86, 88–90, 92, 203	edge paramters, 196
Aharonov-Bohm versus Coulomb-	energy gap, 259
dominated interferometer, 67	tunneling conductance, 194, 196, 207
candidate states, 35	113-state, 36, 38, 196, 203
coherence length, 250	2DEG, 9
coherence temperature, 250	gating, 251
Coulomb blockade, 69	hysteresis, 251
edge paramters, 196, 199	331-state, 36, 38, 69, 74, 193, 196, 203
edge properties, 82, 84, 85	
energy gap, 77, 259	\mathbf{A}
in a QPC, 179	Activation law, 26, 181
in an interferometer, 257	Activation measurement, 181, 182
interferometry, 66, 86–89, 247, 248, 251	Adiabatic demagnetization, 114
local compressibility measurements, 76	Anti-331-state, 36, 38, 193, 196
neutral modes, 84, 86	Anti- $K = 8$ state, 36, 37
NMR experiments, 81	Anti-Pfaffian state, 36, 37, 69, 74, 193, 196,
non-Abelian statistics, 64, 89	203
numerical studies, 74	Anti-SU(2) ₂ -state, 39, 193, 196
optical experiments, 80	Anyons, 41, 63, 64, 66, 67, 69
perfect transmission, 257	Arrhenius law, 26, 117, 119, 181, 182
quasiparticle charge, 75, 89	Arrhenius plot, see Arrhenius law119

В	compressible region, 48, 49, 165, 166
Bad contact, 125	current distribution, 48
Bonderson-Slingerland state, 39, 40, 42,	density distribution, 49, 50
196, 202	diamagnetic currents, 48
Breakdown of quantum Hall effect, 153	extended states, 28
Bubble phase, 35, 265	filling factor, 52
Bulk-edge correspondence, 58	incompressible region, 49, 165, 166
	Edge channels, see Edge states
	Edge effects, 27, 47
C	Edge states, 26, 28, 47, 49, 50
Charge mode, 36	composite Fermion picture, 52–54
Chern-Simons approach, 31	energetic picture, 55
Chiral Luttinger liquid, 55, 188	fractional quantum Hall effect, 50
Classical cyclotron radius, 13	hydrodynamic theory, 55–57
Cold finger, 113, 301	non-cyclic depopulation, 238
Composite Fermion, 31, 32, 52, 54	smooth confinement potential, 52
Composite Fermion theory, 31	steep confinement potential, 51
Contact annealing, 127, 128, 300	Effective mass, 12
Contact geometry, 125	Elastic mean free path, 12
Contact resistance, 127, 128	Electron density, 12, 15
Corbino contact, 125	Electron Liquid Crystal picture, 35
Coulomb blockade, 223, 235	Electron mobility, 12, 15, 18, 19
signature of non-Abelian statistics, 69	• • • • • • • • • • • • • • • • • • • •
Coulomb energy, 14	Electron temperature, 98
2.	estimation, 117, 118, 120
Coulomb interaction parameter, 35, 40, 60,	Electronic noise, 106
188, 190, 192, 195–198	Energy gap, 18
Cyclotron energy, 13	Energy spectrum in a magnetic field, 21
Cyclotron frequency, 22	Excess current, 50
Cyclotron radius, 13, 22	Exchange statistics, 63
D	F
Density modulated phases, 35, 265	Fabry-Pérot interferometer, 243, 247
Density of states, 12	Coulomb dominated, 255
Diagonal resistance, 294	Fermi energy, 13
Diffusive transport, 15	Fermi velocity, 13
Dilution refrigerator, 98	Fermi wavelength, 13
cabling, 108	Fermi wavevector, 13
cryostat frame, 105	Filling factor, 28, 32
dry fridge, 98	Filters, 108
forepump, 105	attenuation, 115, 116
pulse tube refrigerator, 98, 101, 102	Pi-Filters, 111
pulse tube rotary valve, 103	RC-Filters, 113
turbomolecular pump, 101, 105	Flux quantum, 32
	*
vibrations, 101 Disorder, 23, 24, 28, 169, 172	Four-terminal measurement in a Hall-bar, 294
Doping, 16	Fractional quantum Hall effect, 21, 29–32,
DX center, 16, 20	34–39, 41
DX doping, 16, 19	
E	H Haldana Halparin stata 42
Eddy currents, 114	Haldane-Halperin state, 42 Hall-bar, 126, 294
	Hall effect, 14, 21
Edge	11all Ellect, 14, 21

Hall resistance, 26, 28	Mobility, see Electron mobility
Halperin nnm-state, 38	Molecular beam epitaxy, 16
Heat sinks, 112	Moore-Read Pfaffian state, 36, 37, 41, 64,
Heterostructure, 10	69, 74, 193, 196, 203
Hopping transport, 119	
	N
I	Neutral mode, 37, 39
Ideal quantum wire, 135	Non-Abelian Anyons, 63, 64, 66, 67, 69
Integer quantum Hall effect, 25	Nuclear magnetic resonance, 81
Interference experiments, 86, 247	
Interferometer	0
$\nu = 5/2, 257$	0
$\nu = 7/3, 257$	Ohmic contacts, 127, 128, 299
$\nu = 8/3, 257$	
Aharonov-Bohm regime, 67	P
backscattered current, 67	Pfaffian state, <i>see</i> Moore-Read Pfaffian state
bias breakdown, 259	Trainian state, see Woore-Read Framan state
conductance oscillations, 255	
confinement potential, 248	Q
Coulomb dominated, 67, 255	QPC, see Quantum point contact
design considerations, 248	Quantum dot, 221–223
energy gap, 259	charge detection, 225, 228, 235
even-odd effect, 67	charge stability diagram for $\nu = 2,242$
filling factors, 251, 252, 254	charging energy, 223, 235
sample stability, 251	confinement energy, 223
telegraph noise, 251	Coulomb blockade, 223, 235
transmission, 252, 254	coulomb diamonds, 235
	electrochemical potential, 223
with non-Abelian anyons, 66, 67	energy scales, 222
	Fabry-Pérot regime, 243
K	filling factor, 243
K = 8 state, 36, 37, 196	interferometer, 247
Kapitza thermal resistance, 97	quantum Hall regime, 233
Kapitza thermai resistance, 77	single-electron counting, 228
	Quantum Hall effect, 21
L	localization, 76
Landau Fan, 23	Quantum point contact, 133
Landau levels, 22, 23, 32	$\nu = 5/2 \text{ state}, 179$
Landauer formula, 138	bias dependence in quantum Hall regime,
Landauer-Büttiker formalism, 26, 27	153
Laughlin state, 30, 39, 40, 196, 202	compressible and incompressible re-
Laughlin's wavefunction, see Laughlin state	gions, 165, 166, 169, 170
LED illumination, 19, 253, 302	conductance oscillations, 168, 173
Localized states, 24, 28, 169, 172	conductance quantization, 134
	confinement potential, 145
Longitudinal resistance, 294	density distribution, 141, 166, 167
	density hysteresis, 178, 179
M	effect of confinement potential on B-field
Magnetic length, 13	transmission, 149
Magnetoresistance, 14	filling factors, 162, 164
Majorana Fermions, 65	finite bias transmission, 143
Many-body wavefunction, 29	fractional quantum Hall states, 159, 177
Mesa geometry, 125	integer quantum Hall states, 159, 177
17100a Scottica y, 120	moser quantum man states, 137

lateral shifting of the channel, 142, 143,	S
174	Sample fabrication, 298–301
localization, 169, 170	Scanning SET, 76
magneto-electric depopulation, 139	Self-consistent edge, 48, 49
modes, 141	Shubnikov-de Haas effect, 24, 25
quantum Hall phase diagram, 162, 164	Silver annealing, 301
reentrant integer quantum Hall effect,	Silver cold finger, <i>see</i> Cold finger
276, 277	Statistical phase, 64
saddle-point potential, 138, 147	Stripe phase, 35, 265
screening, 169, 170	SU(2) ₂ -state, 36, 39, 69, 196
simulations, 139	30(2)2-state, 30, 39, 09, 190
spatial dependence of resonances, 174	
spin-resolved transport, 151	
subband energies, 142	T
transmission, 137, 138, 294	Thermal conductivity, 109
tuning the confinement potential, 147	of solid-solid joints, 110
tunneling, 58, 233	Thermal resistance, 97
tunneling conductance, 59, 60, 296	Thermocoax cables, 111
weak tunneling, 60	Two-dimensional electron gas, see 2DEG
Quantum well, 16	
gating, 251	
hysteresis, 251	\mathbf{v}
Quantum well doping, 16	Van der Pauw method, 293
Quartz heat sinks, see Heat sinks	Variable range hopping, 119
Quasiparticle, 31	variable range nopping, 119
charge, 35, 40, 188, 190, 192, 195–198	
tunneling, 233	
tunneling conductance, 190	\mathbf{W}
,	Weak tunneling, 58, 59, 190
	breakdown, 201
R	FWHM of tunneling peaks, 206
Read-Rezayi state, 39–42, 196	
Rectification via noise, 108	
Reentrant integer quantum Hall effect, 34,	X
265	X-band screening, 18
breakdown, 271, 273, 275	11 cana servening, 10
in a QPC, 276, 277	
non-equilibrium transport, 268–271	_
orientation dependence, 278, 279	<u>Z</u>
phase diagram, 272	Zeeman energy, 14
Resistivity tensor, 15	Zeeman splitting, 14, 22